

THESIS

UNIVERSITÉ DE PAU ET DES PAYS DE L'ADOUR
École doctorale des sciences exactes et de leurs applications

Defended on the 14th of December 2022
by Aurélie Labeur

To obtain the degree of doctor of the Université de Pau et des Pays de l'Adour
Speciality : Earth Sciences

**PALEOPIEZOMETRY OF SEDIMENTARY STYLOLITES IN FOLD-
AND-THRUST BELTS: CASE OF THE UMBRIA-MARCHE RIDGE,
APENNINES, ITALY**

MEMBERS OF THE JURY

REVIEWERS

- Juliette LAMARCHE
- Stefano TAVANI

MCF HDR / Université Aix Marseilles
Professor / University of Naples Federico II

EXAMINERS

- Daniel KOEHN
- Antonio BENEDICTO

Professor/ University of Erlangen-Nürnberg
MCF HDR/ Université Paris Sud

DIRECTORS

- Nicolas BEAUDOIN
- Jean-Paul CALLOT
- Olivier LACOMBE

MCF HDR / Université de Pau et des Pays de l'Adour
Professor / Université de Pau et des Pays de l'Adour
Professor / Sorbonne Université

À mon grand père, Henri Fievet, et mon grand-oncle, Michel Vannereau.

Abstract

Stylolite are rough structures developed by pressure solution, usually related either to burial stress or to tectonic contraction. The stylolite roughness, *i.e.*, the difference distribution in height between 2 points separated by a given distance along a track, yields quantitative information about stress magnitude applied normal to stylolite plane. Signal analysis onto a stylolite track, returning a characteristic length (cross-over length, L_c) at which two regimes of self-affine properties switch. In the case of a sedimentary, bedding-parallel stylolite (BPS), L_c scales to the magnitude of the vertical principal stress σ_1 , hence to the burial depth at the end of the stylolite life. Albeit being rather confidential, the application of the Stylolite Roughness Inversion Technique (SRIT) to BPS in foreland basins and fold-and-thrust belts (FTB) potentially sheds light on otherwise poorly constrained data, such as paleo-depths at which first increments of contraction started, and burial history as well, without requirement for paleo-temperatures, a data arguable in compressive settings.

The Umbria-Marche Apennine Ridge (UMAR, Central Apennines, Italy), a young folded belt where thick Mesozoic carbonates deformation developed stylolite intensively since burial and during contraction, provides a natural laboratory to further validate and expand SRIT applications on BPS, and to question its contribution to the understanding of burial-deformation history in foreland and FTB contexts during the pre to early folding compressional stage. Combining field and laboratory work, this project proposes methodological developments of SRIT that validates and will facilitate its broader use, and couples this innovative paleopiezometric method with other analyses (*e.g.* mesostructural and geochemical) to meet the objectives set out in the thesis, namely: (i) to unlock limitations of this paleopiezometer application, especially concerning the L_c estimate that could vary depending on signal analysis method applied. Using all data collected in the UMAR, we argue the discrepancy can be explained by limited roughness range from finite length signals. That can be improved tremendously by concatenating stylolites of the same morphology together. The outcome is that in most cases (> 90%), L_c values of on individual stylolite is valid, but can be improved by signal preparation, *e.g.* using a detrend function that put signal extremities to 0; (ii) to characterize compressive meso-structures in folds by classical methods of fracturing analysis and deduce a fracturing sequence then integrated in the global deformation sequence; (iii) to characterize the maximum burial undergone by strata before contraction, *i.e.* maximum vertical stress of BPS activity. The first case of study is the Cingoli Anticline, where vertical stress related to BPS roughness inversions varies from 17 ± 2 MPa and 43 ± 5 MPa, corresponding to burial depths comprised between 720 ± 85 m and 1840 ± 220 m. In the youngest formation, the maximum depth recorded by stylolites is 1200 ± 145 m (*i.e.* vertical stress of 28 ± 3.4 MPa). The latter data is used to estimate the onset of contraction, set at ~ 6 Ma. The application of this methodology in other folded structures located at the western and eastern ends of the UMAR, respectively the Subasio and Conero anticlines, allows to propose a model of the evolution of the onset of contraction at the scale of the ridge: from ~ 10 Ma (Tortonian) to ~ 4 Ma (Zanclean) from west to east, with shift of ~ 6 Ma over a distance of about 100 km without overlap in the ages. These data are consistent with the regional deformation sequence, well calibrated and constrained by more classical methods.

Overall, this work demonstrates the potential of this analytical method coupling SRIT and burial modeling, and its potential contribution to our understanding of the deformation history at the regional scale

Résumé

Les stylolites sont des structures rugueuses formées par pression-solution, généralement par enfouissement ou une contraction tectonique. Leur rugosité, définie comme la différence de hauteur entre 2 points séparés d'une distance donnée le long du stylolite, donne des informations quantitatives sur la grandeur de la contrainte appliquée perpendiculairement à son plan. L'analyse du signal appliquée à la trace d'un stylolite renvoie une longueur de coupure caractéristique L_c située à l'interface de 2 régimes aux propriétés auto-affines. Pour un stylolite sédimentaire parallèle à la stratification (BPS), la L_c est proportionnelle à la contrainte principale verticale σ_1 , et donc à la profondeur d'enfouissement enregistrée quand le développement du stylolite cesse. Bien que peu répandue, l'application de la technique d'inversion de la rugosité des stylolites (SRIT) aux BPS dans les bassins d'avant-pays et les chaînes plissées (FTB) apporte potentiellement des données autrement peu contraintes, comme les paléo-profondeurs associées aux premiers incréments de la contraction, et une partie de l'histoire de l'enfouissement sans besoin des paléo-températures, donnée discutable en contexte compressif.

L'Ombrie-Marche (UMAR, Apennins centraux, Italie), jeune chaîne plissée où l'enfouissement et la contraction ont engendré l'intense stylolitisation des carbonates méso-cénozoïques, est un cas d'étude de choix pour valider et étendre les applications de la SRIT aux BPS, et questionner son apport à la compréhension de l'histoire de l'enfouissement et de la déformation en contexte d'avant-pays et de FTB lors de la compression anté-plissement. Combinant terrain et laboratoire, ce projet propose des développements méthodologiques de cette méthode d'inversion pour valider et faciliter son plus large usage et couple cette technique innovante avec d'autres analyses (*e.g.* mésostructurales et géochimiques) pour répondre aux objectifs fixés dans la thèse : (i) débloquent les limites d'application de ce paléopiézomètre, notamment l'estimation variable de la L_c selon le traitement du signal utilisé. Son application aux BPS de l'UMAR relie potentiellement cette variabilité à une gamme de rugosité limitée pour de courts signaux, ce qui peut être considérablement amélioré en concaténant des stylolites de même morphologie. Les résultats démontrent que, dans plus de 90% des cas, les L_c sont valides pour des BPS individuels, mais peuvent être améliorées en préparant le signal en amont de l'inversion, (*e.g.* fonction detrend positionnant les extrémités du signal à 0) ; (ii) caractériser les méso-structures compressives dans les plis par l'analyse classique de la fracturation, et en déduire une séquence de fracturation ensuite intégrée dans la séquence de déformation globale; (iii) caractériser l'enfouissement maximal subi par les sédiments avant le début de la contraction, soit le σ_1 pour lequel l'activité des BPS est maximale. Le premier cas d'étude est l'Anticlinal de Cingoli, où σ_1 varie de 17 ± 2 MPa à 43 ± 5 MPa, correspondant à des profondeurs d'enfouissement comprises entre 720 ± 85 m et 1840 ± 220 m. Dans la formation la plus jeune, la profondeur maximale enregistrée par les BPS est de 1200 ± 145 m (*i.e.* $\sigma_1 = 28 \pm 3.4$ MPa). Cette donnée est utilisée pour estimer le début de la contraction, fixé à ~ 6 Ma. L'application de cette méthode à des plis situés aux extrémités ouest et est de l'UMAR, *i.e.* anticlinaux de Subasio et de Conero, permet de proposer un modèle d'évolution du début de la contraction à l'échelle de la chaîne, estimé de ~ 10 Ma (Tortonien) à ~ 4 Ma (Zancléen) d'ouest en est, avec un décalage de ~ 6 Ma sur environ 100 km sans chevauchement des âges. Ces données sont cohérentes avec la séquence de déformation régionale, bien calibrée et contrainte par des méthodes plus classiques.

Ce travail démontre le potentiel de cette méthode couplant SRIT et modélisation de l'enfouissement, ainsi que sa contribution potentielle à la compréhension de l'histoire de la déformation à l'échelle régionale.

Acknowledgements

Ce manuscrit met un point final à plusieurs années de dur labeur (ceci sans mauvais jeu de mots, bien entendu). Lors de cette escale à Pau qui a débuté en 2019, j'ai rencontré de nombreuses personnes qui ont contribué, chacune à leur manière, à la réalisation et à l'aboutissement de ce projet, et que je tiens à remercier aujourd'hui. Ces quelques lignes leur sont donc dédiées et, comme vous le constaterez assez rapidement, illustrent mon inaptitude à être concise en écriture.

A first paragraph to thank **Daniel Koehn**, **Juliette Lamarche**, **Stefano Tavani** and **Antonio Benedicto** for agreeing to be part of this jury and for doing me the honor of reporting and evaluating my work. I hope that this manuscript will be up to the task and that you will enjoy reading it.

Le chemin parcouru ces dernières années n'a pas toujours été évident à suivre. Je ne peux que remercier mes directeurs de thèse de m'avoir accompagnée et aidée à mener à bien ce joli projet.

Nicolas, merci de ta confiance et de ton implication durant ces 3 années. J'imagine qu'encadrer une thèse pour la première fois ne doit pas être une tâche facile, et pourtant, tu as toujours été attentif et disponible pour permettre que le projet avance. Tu m'as énormément appris, sur le monde merveilleux des stylolites d'une part, mais aussi sur l'art et la manière d'emballer les couches géologiques, ou la capacité d'un Q_8 à transporter 500 kg d'échantillons. La découverte de l'Italie et des Apennins, c'est aussi en grande partie à toi que je la dois, et je t'en suis infiniment reconnaissante. J'ai vraiment apprécié travailler avec toi, tant humainement que professionnellement. Ce fut une belle expérience, et maintenant arrivée en fin de course, je mesure la chance que j'ai eu d'avoir pu y prendre part. Merci de m'avoir donné ma chance, ainsi que de l'aide et du soutien dont tu as fait preuve du début à la fin. J'espère sincèrement que ce travail est à la hauteur de ce que tu espérais.

Jean-Paul, notre Chuck Norris palois, et As du volant des Apennins. L'âme du laboratoire ne serait pas la même sans toi. Je te remercie de la disponibilité et de l'implication dont tu as fait preuve, malgré une armée de nombreux thésards à encadrer, et ton engagement croissant dans l'administration. Ton écoute et ta bienveillance, ainsi que le temps passé sur mes « quelques » écrits, m'ont été d'une aide précieuse et ont permis d'en arriver ici aujourd'hui. Je garderai en mémoire ta capacité à passer du coq à l'âne en un dixième de seconde, ainsi que ta faculté à faire le tour du labo et à présenter l'équipe en moins de dix minutes (Speedy Gonzales n'a qu'à bien se tenir). Également merci pour tous ces bons moments partagés, des repas le midi sur les bancs de la fac, aux terrains et congrès en terres italiennes et autrichiennes. J'ai beaucoup appris et aussi énormément ri, je pense avoir gagné quelques années de vie grâce à tout ça ! Je profite aussi de ces quelques lignes pour remercier ton adorable famille, **Sarah et les garçons**, pour leur gentillesse et l'accueil chaleureux dont ils ont toujours fait preuve.

Et pour finir, **Olivier**, merci de ton investissement tout au long de ce projet. Outre l'initiation à l'inversion des macles de la calcite, je te dois de nombreuses corrections et relectures, ainsi que des conseils avisés qui ont largement contribué à ce que cette thèse aboutisse. Tu as pris le temps de nous accompagner sur le terrain, malgré ton emploi du temps chargé et tes nombreuses obligations, et je t'en

remercie également. Malgré les quelques changements de dernière minute concernant le sujet de la thèse, et mon anglais parfois un peu bancal, j'espère que tu es satisfait du résultat de ces 3 années de travail.

Cosa sarebbe una tesi in geologia senza un terreno di gioco? Un gran ringraziamento all'Italia, questa così bella terra d'accoglienza e agli scienziati che ci hanno accompagnato lungo le nostre peregrinazioni : **Lorenzo Petracchini** durante la missione sul campo a Cingoli, ma anche **Stefano Tavani, Fabrizio Agosta, Fabrizio Balsamo, Kei Ogata e Luca Smeraglia**, per la loro guida e durante il "fieldtrip" negli Appennini. Un infinito grazie per la scoperta di tutte queste belle curiosità geologiche appenniniche e per la vostra bella cultura !

Quelques remerciements s'imposent aussi pour toutes les personnes qui m'ont encouragées à entreprendre cette thèse, et qui m'ont donné envie poursuivre en géologie.

Un grand merci à l'ENSEGID, grâce à qui j'ai pu faire mes armes et vivre 3 années magnifiques en école d'ingénieur. **Philippe, Carine, Raph**, merci pour l'implication et l'écoute dont vous faites preuve tout au long de notre cursus. Le choix de poursuivre en géologie, tant à l'école avec l'option Géoresources qu'en doctorat, c'est en grande partie à vous que je le dois ! Également merci aux ensegidiens rencontrés lors de cette belle aventure, "les copains d'abord" comme disait Brassens : **Justine, Nadège, Marine P., Maximilien, Antoine, Pierre M. & Pierre G.**, loin des yeux pour certains, mais toujours près du cœur ! Merci d'être vous, et présents en toutes circonstances !

Mon expérience à Total aura mis sur ma route quelques personnes que j'aimerais également remercier. **Jean-Claude et Charlotte R.**, merci de l'aide que vous m'avez apportée, tant pour le stage que pour la thèse. Vos conseils et votre soutien m'ont été précieux, et sans ça, je ne suis pas certaine que j'en serai arrivée là aujourd'hui. **Inès, Marie, François, Valérie, Marc-Antoine, Thomas M. et Mathilde**, merci pour tous ces moments merveilleux que l'on partage encore aujourd'hui, et le soutien indéfectible dont vous avez fait toujours preuve à mon égard. Je ne vous serai jamais assez reconnaissante pour tout ça.

Je tiens également à remercier le laboratoire, au sein duquel j'ai évolué ces trois dernières années.

Merci à **Daniel** qui a su maintenir la cohésion de l'équipe en dépit des difficultés imposées par la COVID. Les réunions d'équipe (en présentiel ou en visio), les pots à la fac, et l'attention constante que tu portes aux jeunes doctorants que nous sommes (et dont j'ai largement bénéficié) ont su maintenir l'unité et la bonne ambiance au sein du groupe. Merci à toi !

Marie-Laure, à la fois merci et félicitations ! Outre ton aide précieuse pour la partie administrative, tu as toujours eu des petits gestes et attentions qui ont rendu cette aventure plus douce (je n'oublierai pas les prises de nouvelles régulières et discussions sur la terrasse, ni les pots de friandises qui auront

réchauffé bien des cœurs et rempli quelques estomacs). Merci pour ta bienveillance et ta bonne humeur. Et plein de bonheur pour la petite merveille qui ne devrait plus tarder à pointer le bout de son nez, vous méritez !

Anne et **Olivia**, découvertes de cette dernière année. De vraies doses d'oxygène et de bonne humeur quotidiennes. Merci pour ces moments partagés, aussi bien à la fac qu'à l'extérieur (mention spéciale pour l'initiation escalade. Sans vous j'aurais encore les pieds sur terre), et d'avoir été aussi attentives et à l'écoute lors de cette dernière ligne droite. Merci mille fois !

Venons-en maintenant aux copains de galère. Car un bateau ne se maintient pas à flots tout seul.

Aux anciens, et tout d'abord à mes colocataires de bureau **Naïm** et **Geoffrey**. On se connaissait un peu de l'école, et ces années communes dans ce bureau ont été une occasion fabuleuse de tisser des liens plus robustes. Merci pour la bonne ambiance, les longues discussions, et les moments de rire et de partage. Mais aussi et surtout, merci d'être toujours là aujourd'hui, et plus seulement comme de simples collègues mais aussi comme amis. J'espère que tout ceci perdurera encore longtemps ! Second hommage aux "vieux partis trop tôt" » : **Pierre-Alexandre**, reparti dans ta belle Normandie, et **Stephen**, chasseur de kangourous en devenir. **Stephen**, je ne pourrai jamais assez te remercier du soutien dont tu as fait preuve, et tout particulièrement lors des derniers moments de l'écriture. Sans ça, la cadence aurait été difficile à maintenir. Je ne peux vous souhaiter que de bonheur à tous les deux, en espérant qu'on ne tarde pas trop à se revoir (pour une session bretzels peut-être, qui sait !).

Thomas, **Gabriel**, **Francho**, un marathon de 3 ans, pour franchir la ligne d'arrivée quasiment en même temps ! 3 années de rires, de bons moments, de galères aussi, mais si c'était à refaire ça serait sans hésitation. Je ne pouvais espérer meilleurs acolytes pour vivre cette grande épopée ! Une team un peu cosmopolite (de l'Espagne à Agen, en passant par le bordelais et le 06), une belle salade niçoise un peu épicée et vineuse, et riche en tomates de mamie. Une fine équipe de collègues devenus potos en somme, qui j'espère perturbera à l'identique (*mea culpa*, Thomas j'ai esquivé les rimes en alexandrin ... mais je reste plus à l'aise avec les stylolites qu'avec la poésie ... Et comme dirait un grand poète, faut pas pousser Mémé avant les bœufs ... ou dans la charrue ?!). En résumé, merci les copains pour tous ces beaux moments !

Et parce qu'une équipe n'est rien sans relève, un grand merci aux nouveaux de la bande : **les Marine²**, **Salsa**, **Sepideh**, **Keanu**, **Anies** pour votre gentillesse et votre bonne humeur quotidienne. **Marine du Chnord**, même si je pense que je ne comprendrai jamais rien à tes carrés dans tes ronds (ou l'inverse ?), merci de prendre le temps de me réexpliquer à chaque fois. Comme l'a écrit Voltaire, "il faut cultiver notre jardin", et nos sessions plantage de graines partagées avec toi et **Salsa** resteront dans les annales. Merci d'être vous, et surtout restez ainsi ! **Marine du Sud-Ouest** (pour ne froisser ni les basques ni les béarnais), 6 ans que l'on se connaît, et qu'on se suit de près. Je suis heureuse que tu aies intégré la team paloise. Je te souhaite vraiment d'arriver à ce que tu désires (même si tu as l'air en bien partie), et qu'on puisse se suivre encore un peu par la suite !

Et sans oublier la fine équipe : **Ben** et **Alexis**. Dans les bons comme les mauvais moments, vous avez toujours répondu présents ! Un immense merci à tous les deux pour votre bienveillance, votre soutien, les discussions et bons moments partagés. **Ben**, je tiens à saluer ton imagination pour les blagues et jeux de mots (plus ou moins bons, à l'appréciation du correcteur). Et sache que non, je n'ai pas oublié l'épisode des bureaux intégralement emballés et intervertis ... ça n'est que partie remise ! **Alexis**, à la fois expert bulles et maître son, mais aussi poète et philosophe, tu m'auras appris que deux opposés ne sont pas nécessairement rébarbatifs (pour ne pas dire rédhibitoires) et qu'un "c'est pas faux" peut faire office de réponse à n'importe quelle question. Tout ça pour dire qu'on a vécu de sacrés bons moments depuis votre arrivée, et j'espère sincèrement que d'autres aussi incroyables et délirants que ceux déjà vécus nous attendent à l'avenir !

Un salut à la **team Escrime**, qui m'a également accompagnée durant ces 3 années. On mésestime souvent le poids du sport et de ceux qui le pratiquent dans une expérience comme celle-ci. **Jeff, Dario** et **Irina, Julien, Brice O., Laurent**, merci à tous d'avoir suivi et partagé cette expérience en temps réel. Merci également à **Ilana** et **Stephen, Fred** et **Karine, Paul** et **Morgane, Jérôme**, et sans oublier notre conseiller municipal **Jfp**, d'avoir intégré le train en marche et pris part à l'aventure ! Et parce que tout travail mérite sa bière, ou qu'après l'effort vient le réconfort, un immense merci à notre **Dimitri** national, ainsi qu'à **Brice, Laura** et **Charles-Aymeric**, pour nous avoir permis de nous ravitailler après l'entraînement, sur la terrasse de l'**Imparfait** ou sur les bancs de **La Cuisine**. Merci de nous avoir tant donné, et malgré ce chapitre qui se clôt aussi en cette fin d'année, j'espère d'autres moments partagés nous attendent (à Pau pour les uns, à Barèges pour les autres, qui sait). Une chose est sûre, vous nous manquerez !

Un petit mot pour mes proches sans qui je ne serai jamais devenue la personne que je suis aujourd'hui. Cette thèse est aussi la vôtre, pour tout l'amour, le temps et le soutien que vous m'apportez depuis tant d'années.

Maman, Papa, merci d'avoir toujours répondu présents. Grandir et se construire est un processus long et parfois compliqué, et malgré la difficulté de la tâche, vous m'avez aidée à maintenir le cap ces 28 dernières années. Vous avez essuyé mes doutes et consolé mes peines. Vous m'avez aidée à me sentir forte quand le courage m'abandonnait. Merci d'avoir toujours cru en moi, malgré les échecs et les faux pas. Merci de cet amour et de ce soutien indéfectible que vous me donnez depuis tant d'années. Cet accomplissement, c'est aussi le vôtre, et j'espère qu'il vous rendra heureux et fiers.

Mamie, Taton, les deux sœurs inséparables. Merci de m'aimer et de me choyer comme vous le faites depuis toujours. Je suis heureuse que vous soyez présentes pour me voir franchir cette étape de ma vie. Mon unique regret est de ne pas vous voir accompagnées de **Papi** et **Michel**, deux grands hommes que nous aimerions encore avoir à nos côtés aujourd'hui, et à qui je dédie ce travail avec bonheur et fierté.

Axel, mon "petit" frère. Petit bonhomme dans un corps de géant. Comme tu me l'as rappelé à juste titre très récemment, on ne se dit pas suffisamment les choses. Alors, je vais profiter de ces quelques

lignes pour te rappeler que je t'aime très fort, et que ça ne changera jamais (promis, la période où je te haïssais de voler mes poneys en plastique et de décapiter mes Barbies est révolue). Et comme d'autres l'ont fait pour moi, sache que je crois en toi. Je sais que l'avenir paraît parfois insurmontable, mais je suis intimement persuadée que tu finiras par trouver la voie et l'équilibre dont tu as besoin. Crois en toi et en tes rêves, et ça finira par fonctionner !

Je n'oublie par **Caro**, **Pampi** et **Louise**, ainsi que **Minou** et **Nini**, pour leurs petits mots d'encouragements et leurs attentions régulières. Je profite aussi de ce paragraphe pour remercier tous les membres de **L'Été à Pau** de m'avoir accueillie à bras ouverts il y a presque 4 ans maintenant, et d'avoir toujours été compréhensifs et bienveillants à mon égard. Promis, le temps où je troquais les sessions plages ou tyroliennes contre des heures de rédaction sur ordinateur, et où j'arrivais à 23h30 pour souffler les bougies, est désormais révolu. Un grand merci à tous !

Petite mention spéciale pour **Morgane C.**. Mon amie et ma confidente de toujours, tu m'as vue grandir et évoluer, et accompagnée en dépit des obstacles et des difficultés de la vie. Malgré la distance et ma capacité profonde à m'effacer de la surface de la Terre en période de stress (et il y en a eu...) tu as toujours été présente et maintenu le contact. Merci de m'avoir toujours écoutée, épaulée et soutenue. Je souhaite que cette amitié qui nous unit soit longue et heureuse, et être un jour à la hauteur de la formidable personne que tu es.

Maxime, mon amour, les mots ne suffiront jamais à exprimer mon infinie gratitude. Cette thèse, tu l'as vécue autant que moi, et je suis heureuse de tourner cette page avec toi à mes côtés. Je ne te remercierai jamais assez de ton soutien, de tes attentions quotidiennes, et de tout l'amour que tu me portes jour après jour. Merci d'être toi, tout simplement, et d'être mon pilier dans les bons comme dans les mauvais moments. Nous deux ça n'a pas toujours été simple, un peu long au démarrage, mais je pense pouvoir dire aujourd'hui que c'est une évidence. Et j'espère sincèrement que ce chemin que l'on parcourt ensemble nous mènera loin, afin de pouvoir te rendre tout ce que tu m'as apporté. *Ti amo*

Table of contents

▪ ABSTRACT	2
▪ RÉSUMÉ	4
▪ ACKNOWLEDGEMENTS	6
▪ TABLE OF CONTENTS	14
▪ TABLE OF ILLUSTRATIONS	20
▪ INTRODUCTION	34
I- SCIENTIFIC CONTEXT AND PROBLEMATIC	36
II- THESIS LAYOUT	39
▪ CHAPTER 1-BURIAL EVOLUTION AND STRESS DISTRIBUTION IN FORELAND BASINS AND FOLD-AND-THRUST BELTS: STATE OF THE ART	42
I- FORELAND BASINS AND FOLD-AND-THRUST BELT: NATURAL LABORATORIES FOR STUDY AND THE UNDERSTANDING OF GEOLOGICAL PROCESSES	44
1- DEFINITION	44
2- BASIN MODELING	47
II- MESOSCALE FRACTURE NETWORK IN FORELAND BASINS AND FOLD-AND-THRUST BELTS	48
1- CHARACTERIZATION OF FRACTURE NETWORK	49
1.1- Fracture definition and classification	49
1.2- Stylolites: general definition	51
2- DISTRIBUTION IN THE FORELAND BASINS AND FTB	51
2.1- Distribution within FTB	52
2.2- Distribution within fold	53
III- PALEOPIEZOMETRY IN THE STUDY OF FORELAND BASINS AND FOLD-AND-THRUST BELTS	54
1- INTRODUCTION TO PALEOPIEZOMETRY: CONCEPT AND CONTRIBUTIONS	54
2- FOCUS ON STYLOLITE PALEOPIEZOMETRY	56
2.1- Stylolites as paleopiezometers: definition, classifications, and growth mode	56
2.2- History and principles of the inversion method	61
2.3- Signal processing methods	63
2.4- Application to sedimentary stylolites: Sedimentary Stylolites Roughness Inversion Technique (SRIT)	65
IV- RECONSTRUCTION OF THE MESO-STRUCTURAL PATTERN AND BURIAL: METHODS	66
1- UNDERSTANDING OF THE FRACTURE NETWORK	66
1.1- Reconstruction of fracture sequence	66
1.2- U-Pb absolute radiochronology	68
1.3- Inversion of striated fault planes	68
2- SEDIMENT BURIAL MODELING	70
3- ROCK PROPERTIES ESTIMATION	72
3.1- Mechanical properties: Young modulus estimation for SRIT application	72

3.2-	Chemical compaction estimate for burial modelling	72
4-	STUDY OF VERTICAL STRESSES BY INVERSION OF THE ROUGHNESS OF SEDIMENTARY STYLOLITES (SRIT)	74
4.1-	Samples preparation	74
4.2-	Stress and burial depth computation	75
▪	CHAPTER 2-GEOLOGICAL SETTING: THE APENNINES AND THE UMBRIA APENNINE RIDGE	78
I-	GLOBAL GEODYNAMIC CONTEXT: EVOLUTION OF MEDITERRANEAN DOMAINS	80
II-	THE APENNINES, GLOBAL CONTEXT OF THE STUDY AREA	82
1-	GEOGNAMIC AND STRUCTURAL CONTEXT	82
2-	PALEOGEOGRAPHIC EVOLUTION	84
III-	THE UMBRIA MARCHE APENNINE RIDGE: CENTRAL PART OF THE APENNINES	88
1-	STRATIGRAPHIC SEQUENCE CHARACTERISTIC OF THE UMBRIA-MARCHE	88
1.1-	Facies of the UMAR stratigraphic sequence	88
1.1-	Paleogeographic evolution: link between tectonics and sedimentation	89
2-	STRUCTURAL CHARACTERISTICS AND PROPOSED MODELS	92
3-	KINEMATIC EVOLUTION	96
4-	MESOSTRUCTURAL CHARACTERISTICS	97
▪	CHAPTER 3-SEDIMENTARY STYLOLITE ROUGHNESS INVERSION TECHNIQUE: APPLICATION, LIMITATIONS, AND OPTIMIZATION	100
I-	INTRODUCTION	102
II-	OVERVIEW OF THE DATASET	104
1-	LOCATION AND PREPARATION OF SAMPLES	104
2-	TYOLOGY OF THE STUDIED STYLOLITE TRACKS	109
III-	VARIABILITY OVER THE STYLOLITE TRACK ACQUISITION AND TREATMENT	109
1-	COMPUTER-ASSISTED TRACK SEGMENTATION	109
2-	FINDING THE L_c	111
IV-	IDENTIFYING AND OVERCOMING THE METHODOLOGICAL LIMITATIONS OF SRIT	112
1-	IDENTIFIED LOCKS	112
1.1-	Validity of the L_c : is the signal analysis convincing ?	114
1.2-	Consistency of the L_c : are the results similar within the uncertainty between the two signal analysis techniques?	115
2-	OVERCOMING THE LIMITATIONS	116
2.1-	Optimization of the track for the signal analysis	116
2.2-	Stylolite morphology influence	118
2.3-	Concatenation of signals using the composite method: construction and inversion of composite sedimentary stylolites	119

2.4- Tests and validation of composite stylolites inversion	120
V- CONCLUSIONS	123
▪ CHAPTER 4-USING BEDDING PARALLEL STYLOLITE TO RECONSTRUCT THE BURIAL-DEFORMATION CALENDAR: EXAMPLES OF FOLDED CARBONATES IN THE CINGOLI ANTICLINE, UMBRIA-MARCHE, NORTHERN ITALY	124
I- GENERAL INTRODUCTION	126
II- BURIAL-DEFORMATION HISTORY OF FOLDED ROCKS UNRAVELED BY FRACTURE ANALYSIS, STYLOLITE PALEOPIEZOMETRY AND VEIN CEMENT GEOCHEMISTRY: A CASE STUDY IN THE CINGOLI ANTICLINE (UMBRIA-MARCHE, NORTHERN APENNINES)	128
III- GENERAL CONCLUSIONS	158
▪ CHAPTER 5-ASSESSING THE TIMING AND PROPAGATION OF LAYER-PARALLEL APENNINIC SHORTENING FROM THE UMBRIA-MARCHE APENNINE RIDGE TO THE CONERO ANTICLINE: INSIGHTS FROM PARALLEL TO BEDDING STYLOLITE ROUGHNESS PALEOPIEZOMETRY	160
I- INTRODUCTION	162
II- THE SUBASIO AND THE CONERO ANTICLINES: TWO OTHER FIELD EXAMPLES OF BURIAL-DEFORMATION RECONSTRUCTION	163
1- GEOLOGICAL SETTING	163
1.1- The Subasio Anticline	163
1.2- The Conero Anticline	165
2- MESOSTRUCTURAL CONTEXT	167
2.1- The Subasio Anticline	167
2.2- The Conero Anticline	173
2.3- Timing of regional deformation: evolution of flexure and folding	177
3- SEDIMENTARY STYLOLITES PALEOPIEZOMETRY	178
3.1- Young modulus estimation	178
3.2- Sedimentary stylolite roughness inversions	178
3.3- Vertical stress and burial depths computation	180
4- BURIAL DEPTHS EVOLUTION	182
III- INTERPRETATION OF THE COMPILED RESULTS: FROM THE FOLD SCALE TO THE FOLD-AND-THRUST BELT SCALE	184
1- SEDIMENTARY ROUGHNESS INVERSION: COMPILATION OF DATA	184
2- BURIAL CURVES	184
3- BURIAL DEPTHS EVOLUTION ALONG THE TRANSECT	187
4- DETERMINATION OF THE ONSET OF OROGENIC CONTRACTION	187
IV- CONCLUSIONS	188
▪ GENERAL DISCUSSION	190
I- INTRODUCTION	192

II- METHODOLOGICAL LIMITATIONS AND IMPROVEMENTS	192
1- HOW TO EXPLAIN INCONSISTENCY OF RESULTS?	192
2- IMPACT OF STYLOLITE MORPHOLOGY	194
3- VALIDITY AND INCONSISTENCY OF RESULTS, WHAT SOLUTION(S) ?	195
III- EVOLUTION OF FRACTURE SEQUENCE IN THE STUDIED FOLDS	196
1- FRACTURE SEQUENCE RELATED TO DEFORMATION HISTORY	196
2- CONTRIBUTIONS TO THE UNDERSTANDING OF LOCAL AND LARGE-SCALE EFFECTS	198
IV- TIMING AND PROPAGATION OF FOLDING	199
1- AT THE FOLD SCALE: CASE OF THE CINGOLI ANTICLINE	199
1.1- Impact of the chemical compaction on the timing of deformations?	199
1.2- Impact of the geothermal gradient on timing of deformations	204
1.3- Impact of the stylolite sampling	206
2- AT THE FOLD-AND-THRUST BELT SCALE	208
2.1- Shape of burial curves	208
2.2- Determination of the onset and of the duration of the LPS	208
2.3- Dating and quantifying the horizontal stresses build up	210
2.4- Debate on structural style	212
▪ GENERAL CONCLUSION	214
▪ REFERENCES	218
▪ APPENDICES	250

Table of illustrations

Figure 1.1-(A) Schematic map view of a “typical” foreland basin, limited longitudinally by two marginal ocean basins. The scale is not specified. The vertical line corresponds to the orientation of the cross-section represented in (B). **(B)** Schematic cross-section illustrating the geometry of the foreland basins. The boundary between the basin and the FTB is exaggerated vertically by a factor of 10. **(C)** Schematic cross-section illustrating a revised concept of foreland basin architecture, positioning the four depositional zones, the topographic front of the FTB (TF), a duplex zone (D), the front of a triangular zone (TZ), as well as progressive deformation represented by the short fan lines associated with the thrust tips. The interface between the front of the orogenic wedge and the foreland system is marked by the presence of extensive thrusting; after DeCelles & Giles (1996)..... 44

Figure 1.2-(A) Representation of the principal loading processes in peripheral foreland systems, with topographic and sediment load, and also subduction load related to vertical shear (V) and bending moment (M) on the end of the subducted slab potentially existing at depths of -50-200 km (Royden, 1993). **(B)** Representation of retroarc foreland basin systems. **(C)** Accumulation in wedge-top depozone, resulting from the competition between regional, load-driven subsidence (downward pointing arrows) and local uplift of the orogenic wedge related to shortening and thickening (upward pointing arrows); after DeCelles & Giles (1996). 45

Figure 1.3-(A) Fracture propagation modes, and **(B)** associated Mohr circles. Mode I: opening, mode II: shear; mode III: tearing; modified from Bons *et al.* (2012). 49

Figure 1.4-Classification of Bons *et al.*, (2012). Interpretation of vein opening patterns on field data; after Bons *et al.*, (2012). 51

Figure 1.5-Foreland flexuring, along-foredeep stretching and layer-parallel shortening (LPS) deformation stages, and associated macroscale structures. Foreland flexuring leads the development of extensional structures oriented parallel to the forebulge-foredeep belt system, and sometimes of transverse structures as secondary features. Along-foredeep stretching deformation stage provides the development of extensional fractures striking perpendicular to the forebulge-foredeep belt system, and of longitudinal fractures as secondary characteristics. LPS favors the development of mesoscale deformation patterns including either layer-parallel or layer-perpendicular elongation; modified from Tavani *et al.* (2015)..... 52

Figure 1.6-Deformation structures commonly observed in anticlines related to FTB. The spatial distribution and geometries associated with these mesostructures are shown at the scale of one strata (left scheme) in the limb and the hinge, and for several strata (right scheme) considering a section orthogonal to the fold axis. The section plane A-A' is oriented with respect to the fold on the left side of the figure; modified from Tavani *et al.* (2015). 54

Figure 1.7-Stylolites observed at outcrop in platform carbonates (Monte Nero, Apennines, Italy). Stylolites are represented by red lines; modified from Beaudoin *et al.* (2016) 57

Figure 1.8-Schematic representation of sedimentary and tectonic stylolites; modified from Ebner *et al.* (2010b). Principal stress σ_1 is represented in red. 57

Figure 1.9 -Classification of stylolites according to morphology and tooth amplitude, modified from Semeniuk & Logan (1976).	58
Figure 1.10 -Morphological classification of stylolites based on the work of Park & Schot (1968) and numerical simulations, modified from Koehn et al. (2016). 4 classes of stylolites are discriminated: 1) rectangular layer type, 2) seismogram pinning type, 3) suture and sharp peak type, 4) simple wave-like type.....	59
Figure 1.11 -Stylolite growth model and influence of roughness, modified from Koehn <i>et al.</i> (2016).....	59
Figure 1.12 -Summary of physical and morphological characteristics of stylolites. Notions of roughness, amplitude, compaction and spacing are defined on the middle and upper parts of the figure. Morphologies are also redrawn and detailed on the right-hand side.....	61
Figure 1.13 -Simulation results for a 14 mm linear fault, i.e., between -7 and +7 mm with the Spring Network Model; modified from Rolland (2013) and Aharonov & Katsman (2009). These curves represent cumulative dissolution for different time periods in three configurations (i) under stress and no clay; (ii) under no stress with clay; (iii) under stress and clay. For the same time interval, the cumulative dissolution is up to doubled in the presence of clay, whether a stress is applied or not.....	61
Figure 1.14 -Representation of the two scaling regimes on the Fourier Power Spectrum (FPS) and Average Wavelet Coefficients (AWC), associated with Hurst coefficients and separated by a characteristic cross-over length; modified from Ebner <i>et al.</i> (2008).....	62
Figure 1.15 -Example of stereodiagrams obtained after statistical processing of the field data (Stereonet), in current/rotated (R) and unrotated (U) positions. The dotted lines represent the stratification, and the color scale the density of poles. In the present case, the 50 measurements carried out and processed (whose planes have not been represented for reasons of readability) are used to discriminate two main orientations of fractures, whose average planes are represented by the solid black lines.....	67
Figure 1.16 -Illustration of fault measurements (blue) and tensor data calculated by Angelier's method s: orientation of the streak, σ_N : normal stress, σ : applied resultant stress, τ : shear stress, u : vector between the calculated shear stress and the streak, α : angle between these two vectors; after Beaudoin (2012), modified from Angelier (1990).....	69
Figure 1.17 -Schematic representation of the modeling steps of the burial curves. The mentioned parameters are detailed in the following paragraphs. The logo used is that of the Backstrip© software.....	70
Figure 1.18 -Detail of the application of Schmidt hammer method on the field, and example of results used for Young modulus calculation. Piston is pressed orthogonally against the rock surface (grey arrow). Values of sliding average R are plotted as a function of the number of measurements incorporated (orange curve), from which stabilized R value is deduced and used to compute Young modulus value with Equation 1.15.....	72

Figure 1.19 -Workflow the SRIT processing steps applied to BPS, including major assumptions and parameters.....	76
Figure 2.1 -Reconstruction of the geodynamic evolution of the Mediterranean area from the Jurassic to the present; after Jolivet et al. (2016).....	80
Figure 2.2 -(A) Generalized structural map of the Mediterranean, modified from Roure <i>et al.</i> (2012). (B) Location of the Northern, Central and Southern Apennines, with main thrusts structuring the area (C) Structural sketch map of the central-southern Italy, redrawn after Cosentino <i>et al.</i> (2010). (D) Geological scheme of the Umbria-Romagna-Marche Apennines and surrounding areas, modified from Guerrera <i>et al.</i> (2012).....	82
Figure 2.3 -Main steps of the late Triassic- middle Miocene evolution of the platform-basin system in central Italy; after Cosentino <i>et al.</i> (2010), modified from Accordi <i>et al.</i> (1986). Facies are numbered as follow : (1) evaporites; (2) dolomites and laminated dolomitic limestones; (3) clays and marls with intercalations of oolitic and organogenous wackstone-grainstone; (4) marls;(5) bioclastic wackstone-packstone; (6) mudstone with biotrititic and microclastic intercalations ; (7) marls, clays and pelagic micrites; (8) pelagic mudstonewackstone and hardground with nodular structures; (9) carbonate platform limestones; (10) organogenous grainstone-rudstone; (11) packstone-grainstone with intercalations of marly pelagic mudstone; (12) organogenous wackstone-grainstone; (13) carbonate basement; (14) supratidal deposits and alteration soils. CP: carbonate platform; PCP: pelagic carbonate platform. Paleogeographic maps of Tethys realm are related to these different stages: (A) late Triassic, (B) late Jurassic and (C) early Cretaceous maps; after Cosentino <i>et al.</i> (2010), modified from Yilmaz <i>et al.</i> (1996). The paleogeographic evolution of the UMAR is represented by the dotted black box	85
Figure 2.4 -(A) Location, geological map and SW-NE transect of the Apennines and the Umbria-Marche ridge. (B) Stratigraphic sequence characteristic of the UMAR. (C) Cross-section of the UMAR, along a SW-NE transect across the main anticlines of the FTB; modified from Beaudoin <i>et al.</i> (2020a).....	90
Figure 2.5 -Stratigraphy of the Marnoso-Arenacea Formation. Lateral evolution, diachronism of boundaries and deposits, absence of the Marnoso-Arenacea in more external areas and marker beds and correlation detailed in text are represented; modified after Guerrera <i>et al.</i> (2012), compilation of data from Delle Rose <i>et al.</i> (1990, 1991, 1994b; a), Dubbini <i>et al.</i> (1991), de Feyter, (1991), Montanari <i>et al.</i> (1991), Capuano & D'Antonio (1992), Carlini <i>et al.</i> (1995) and Capuano <i>et al.</i> (2009).	91
Figure 2.6 -Structural map of the UMAR from the Umbrian Valley to the Laga Basin; modified from Scisciani <i>et al.</i> (2014) and Bigi <i>et al.</i> (1992).; redrawn from Tavarnelli <i>et al.</i> (2004).	93
Figure 2.7 -Proposed structural models for the UMAR: i) thin-skinned model (a) modified from Bally <i>et al.</i> (1986); ii) thick-skinned model (b) modified from Calamita <i>et al.</i> (2000) and (d) modified from Mirabella <i>et al.</i> (2008); iii) inversion tectonics (c) modified from Tavarnelli <i>et al.</i> (2004).	94
Figure 2.8 -(A) Chronology of compressive events in the external zones of the UMAR, and associated among of shortening (Sh, in km) and rate of slip (Rs, in mm/yr). (B) Sequence of regional deformation	

underwent in the UMAR, where order and ages of folding/thrusting events are referenced by circled numbers 1 to 6 and numbers below these circles, respectively; after Lacombe *et al.* (2021)..... 97

Figure 2.9-Cartographic view of the main directions of stresses and meso-structures developed within the Monte Nero Anticline. Regional stress directions are represented by the black arrows, and local stresses by the gray arrows. Number and lengths of mesostructure are not representative; modified from Beaudoin *et al.* (2016). 98

Figure 3.1-Location of samples across the UMAR. The numbers locate the examples of outcrops, samples and results presented in Figures 3.2, 3.3 and 3.4 respectively: (1) the Subasio Anticline, Scaglia Bianca Formation; (2) the Subasio Anticline, Maiolica Formation, sample SUB72_BPS1; (3) the Cingoli Anticline, Scaglia Rossa Formation, sample C15_BPS2; (4) the Cingoli Anticline, Maiolica Formation; (5) the Cingoli Anticline, Scaglia Bianca Formation; (6) the Conero Anticline, Maiolica Formation, sample CON6_BPS1; (7) the Subasio Anticline, Scaglia Bianca Formation, sample SUB113_BPS1; (8) the San Vicino Anticline, Maiolica Formation, sample A104_BPS13; (9) the Conero Anticline, Scaglia Bianca Formation, sample CON20; modified from Beaudoin *et al.* (2020a)..... 104

Figure 3.2-Examples of outcrops studied across the UMAR, located by the numbers on the map in Figure 3.1..... 105

Figure 3.3-Examples of BPS studied across the UMAR, located by the numbers on the map in Figure 3.1..... 106

Figure 3.4-Results corresponding to BPS presented in Figure 3.3, and located in Figure 3.1 107

Figure 3.5-(**A**) Statistical distribution of signal widths corresponding to analyzed stylolites (Violin plot). The distribution is unimodal, with a width modulus of 2.98 cm. (**B**) Evolution of the cross-over lengths as a function of signal widths, for FPS and AWC treatments, considering 23% uncertainty on these L_c values (Rolland *et al.*, 2014); For these (**A**) and (**B**) graphical representations, the entire dataset is considered (*i.e.* 186 values of track and cross-over lengths). (**C**) Examples of stylolite track, with two different morphologies: columnar type (1-2) on the left and peak type (3) on the right, sampled in Subasio in the Maiolica and Scaglia Rossa formations respectively..... 108

Figure 3.6-Workflow and result of image processing, using Photoshop® and Matlab® computer interfaces, and comparison with the hand drawing method (2 users considered). The computer-assisted method (and associated steps, left-hand side) is mentioned in purple, the hand drawing (right-hand side) in dark. Regression curves obtained from FPS analysis are also presented, showing the calculated cross-over lengths. 111

Figure 3.7-Examples of results of piecewise linear regressions applied to stylolite data. Both roughness regimes are shown, with a characteristic break in slope at the interface. The minimum is reached for $b = 7$ for the FPS and $b = 5$ for the AWC. 112

Figure 3.8-Practical cases where (**A**) the AWC curves are not usable, because the break in slope is not well-marked. (**B**) the two regressions are unusable: for the FPS, the regression lines pass through too

few points; for the AWC, no break in slope is identified. The calculated cross-over length is therefore aberrant, being positioned outside the curve. 113

Figure 3.9-Value of the cross-over lengths per sample according to the signal analysis technique used (FPS as squares and AWC as circles). Color relates to the validity criterion as defined in Table 3.1. Red values correspond to invalid results (15 for AWC, 21 for FPS). For better readability, a logarithmic vertical scale is considered. 114

Figure 3.10-Degree of difference between L_c returned by AWC and FPS, quantified by calculating Δ (Equation 3.1). **(A)** Graphical representation of the value of Δ per sample. **(B)** Statistical distribution of Δ (Violin plot). The vertical scale is the same for both plots, on which the uncertainty associated with the non-linear regression methods is represented (23%). Above this value, the L_c is considered as not self-confident. The data set consists of the 158 stylolites for which inversions are valid..... 115

Figure 3.11-Comparative examples of signal corrections including or not slope and border effects. Data without correction, on those associated with the classical and new corrections are presented on the left (in purple), in the middle (in orange), and on the right (in green) of the figure, respectively..... 117

Figure 3.12-Statistical distribution and probabilistic model (Violin plot) of the cross-over lengths obtained by applying the classical method, for FPS and AWC regressions, for peak and columnar morphologies..... 118

Figure 3.13-Variation rate as a function of stylolite width (in cm). Only the results of the 158 valid inversions are considered. 119

Figure 3.14-Concatenation of stylolites of the same morphology and belonging to the same formation. The tracks are digitised, assembled and inverted. The right-hand side of the figure shows the results of the inversions for the individual and composite tracks. The L_c values are more consistent after concatenation ($\Delta = 17\%$) than for the individual stylolites ($\Delta = 55\%$ and 63%)..... 121

Figure 3.15-Representation of the L_c returned by inversion of concatenated stylolites, for both AWC (circles) and FPS (squares), considering the colorimetric scale defined in Table 3.1. Red values correspond to invalid results (3 for AWC, 1 for FPS). For better readability, a logarithmic vertical scale is used considered. 122

Figure 3.16-**(A)** Representation of L_c distribution considering the signal analysis method applied (*i.e.* FPS on the left and AWC on the right) and the type of stylolite studied (*i.e.* individual in yellow and composite in purple). **(B)** Comparison of the results after inversion of individual and composite stylolites, considering the Δ value (Equation 5.1). The dotted line represents the 23% uncertainty bar. Only the results of valid inversions are considered. 122

Figure 5.1-Illustration of the main formations studied in the Subasio Anticline. Each formation is associated with 2 field photographs. 164

Figure 5.2-Simplified geological map of the Subasio Anticline, redrawn from existing geological maps (Servizio Geologica d'Italia, 1969). Measurement sites are positioned thanks to the black dots, sampling

and measurement sites by red dots. Associated stratigraphic column (Servizio Geologica d'Italia, 1969) and cross-section (modified from Scisciani *et al.*, 2014)..... 165

Figure 5.3-Simplified geological map of the Conero Anticline, redrawn from existing geological maps (Fancelli & Radrizzani, 1964b). Measurement sites are positioned thanks to the black dots, sampling and measurement sites by red dots. Associated stratigraphic column (Fancelli & Radrizzani, 1964b) and cross-section(modified from Mussi *et al.*, 2017)..... 166

Figure 5.4-Illustration of the main formations studied in the Conero Anticline. The case of the Maiolica is illustrated with 2 field photographs..... 167

Figure 5.5-Chronological relationships (*i.e.* crosscutting), observed at mesoscopic scale, between: **(A)** a vein N060 belonging to set I (blue) and a BPS, **(B, C)** sets I and II (pink), **(D)** sets II and III (orange). **(D)** Interpretative scheme of the formation of the E-W set..... 168

Figure 5.6-Location of fracture planes measured on the geological map of the Subasio Anticline. Each measurement point is associated with two stereodiagrams (lower hemisphere), representing main fracture orientations in current (R) and unfolded attitude (U); on each stereodiagram, the bedding is reported as dashed lines, and fracture planes by solid-colored lines, each color relating to one of the three major fracture sets defined (blue: N040 ±20°, pink: N130±20°, orange: ~N-S). 169

Figure 5.7-Location and plot of measured tectonic stylolites on the geological map of the Subasio Anticline. Each measurement point is associated with two stereodiagrams (lower hemisphere), representing main orientations of tectonic stylolites peaks measured (current and unfolded attitude). On each stereodiagram, the bedding is reported as dashed lines, and peaks orientation (*i.e.* σ_1 orientation) is given by high pole density zones. Stereodiagrams with fault-slip data and principal stress axes are also reported; 170

Figure 5.8-Interpretative model of the history of deformation in the Subasio Anticline. The structural evolution of the area is represented in in map view. For each stage of deformation, the main principal stress σ_1 is represented as red arrows, as well as the associated mesostructures (blue: sets I and III, pink: set II, orange: set IV). Thrusts and faults are represented by red lines in map view, in transparency when it is inactive. 172

Figure 5.9-Location of fracture planes measured on the geological map of the Conero Anticline. Each measurement point is associated with two stereodiagrams (lower hemisphere), representing main fracture orientations in current (R) and unfolded attitude (U); on each stereodiagram, the bedding is reported as dashed lines, and fracture planes by solid-colored lines, each color relating to one of the four major fracture sets defined (green: set I, blue: set II, pink: set III, orange: set IV). Major sets are represented in bold on the stereodiagrams as on the map. 174

Figure 5.10-Location and plot of measured tectonic stylolites on the geological map of the Conero Anticline. Each measurement site is associated with two stereodiagrams (lower hemisphere), representing main orientations of tectonic stylolites peaks measured (current and unfolded attitude). On each stereodiagram, the bedding is reported as dashed lines, and peaks orientation (*i.e.* σ_1

orientation) is given by high pole density zones. Stereodiagrams with fault-slip data and principal stress axes are also reported. 175

Figure 5.11-Interpretative model of the history of deformation in the Conero Anticline. The structural evolution of the area is represented in map view. For each stage of deformation, the main principal stress σ_1 is represented as red arrows, as well as the associated mesostructures (green: set I, blue: set II, pink: set III, orange: set IV). Orogenic thrusts and faults are represented by red lines in map view, in transparency when it is inactive..... 176

Figure 5.12-Summary chart of the evolution of flexure and folding/thrust ages at the scale of the UMAR, through the 4 folds studied: Subasio, San-Vicino and Cingoli, and Monte Conero. The associated ages are given in italics, each color corresponding to the bibliographic source: in dark blue Guerrera *et al.* (2012), in orange Curzi *et al.* (2020), in light blue Calamita *et al.* (1994) and in purple Lacombe *et al.* (2021)..... 177

Figure 5.13-Summary of inversion results considering the longitude and the formation of sampling. Each box shows the distribution of values, with the median represented by a vertical line, and the extrema by the straight lines. **(A)** Distribution of cross-over lengths L_c given in millimeters. **(B)** Distribution of depths deduced from the vertical stresses obtained after inversions..... 181

Figure 5.14-Burial models constructed for the **(A)** Subasio and **(B)** Conero anticlines considering thickness from stratigraphic and well data corrected for chemical and physical compaction. In Subasio, model is taken from works of Caricchi *et al.* (2015). The range of depths reconstructed from BPS roughness inversion (with uncertainty shaded in light grey) are reported for each formation as grey levels. The corresponding timing and depth of active dissolution are reported on the x axis and left y axis, respectively. Onsets of LPS, *i.e.* the moment when σ_1 switches from vertical to horizontal, is deduced from the results of the roughness inversion process applied on sedimentary stylolites. 183

Figure 5.15-Summary of inversion results considering the anticline and the formation. For greater readability, all values are not represented. Each box shows the distribution of values with the median represented by a vertical line, and the extrema by the error bars. **(A)** Distribution of L_c obtained from the signal processing of single tracks by AWC/FPS, given in millimeters. **(B)** Distribution of depths deduced from the vertical stresses obtained after inversions. **(C)** Normalization of burial depths relative, here the top of the Maiolica top, by fold..... 185

Figure 5.16-Burial models constructed for the Subasio **(1)**, San Vicino **(2)**, Cingoli **(3)** and Conero **(4)** anticlines considering thickness from stratigraphic and well data corrected for chemical and physical compaction. In Subasio, San Vicino and Cingoli, models are taken from works of Caricchi *et al.* (2015), Lacombe *et al.*, (2021) and Labour *et al.*, (2021), respectively. The range of depths reconstructed from BPS roughness inversion (with uncertainty shaded in light grey) are reported for each formation as grey levels. The corresponding timing and depth of active dissolution are reported on the x axis and left y axis, respectively. Onsets of LPS, *i.e.*, the moment when σ_1 switches from vertical to horizontal, is deduced from the results of the roughness inversion process applied on sedimentary stylolites. 186

Figure 6.1-Concatenation of one single track 5 times. Non-linear regression curves are represented. Inversions are invalid before and after concatenation, demonstrating that signal length has no impact on the quality of the results..... 193

Figure 6.2-Comparison between (i) L_c returned by the classical FPS (green) and (ii) AWC (orange), their mean value (in grey) and (iv) the mean L_c obtained after concatenation (purple). 12 cases are considered, for which the inversions by the classical method return valid but inconsistent results... 195

Figure 6.3-Synthesis of fracturing data at the UMAR scale. Fractures are represented by thick green, blue, pink or orange lines depending on the stage of deformation represented. The orientation of the inherited faults controlling the folding is given by the thick red lines. Red arrows indicate the direction of the maximum horizontal principal stress..... 197

Figure 6.4-Model of stylolite growth and end over time. Two cases are illustrated: (i) linked to a large-scale effect, with simultaneous development and end of stylolites throughout the stratigraphic column; (ii) subject to local effects (*e.g.* reservoir, overpressure), causing diachronic development and end of stylolites in the different strata. Developing stylolites are represented in grey, those that are fully grown in black..... 198

Figure 6.5-Determination of chemical compaction: processing and calculation steps..... 200

Figure 6.6-Distribution of chemical compaction data on the Cingoli Anticline, in map view. Per GPS point is indicated: the number of strata (*stra*) and the number of stylolites (*styl*) measured to calculate the compaction, and the average number of stylolites per meter of strata and the associated average deviation when the data allowed it (*NC*: not computed). The latter is calculated from field measurements: counting the number of BPS for a given rock height on each outcrop, then calculating the number of BPS per metre. Some of the outcrops studied are illustrated by field photos associated with the measurement site..... 201

Figure 6.7-Impact of the chemical compaction on burial curves construction..... 203

Figure 6.8-Impact of the chemical compaction on timing of deformation interpreted..... 204

Figure 6.9-Burial models for geothermal gradients of 20°C/km, 23°C/km, and 30°C/km, considering a surface temperature of 10°C. The stratigraphic data and methodology are identical to those used in the work of Labeur *et al* (2021)...... 207

Figure 6.10-Comparison of results for the different cases considered: synthesis in terms of timing and deformation sequence; 208

Figure 6.11-Synthesis of flexure, LPS and folding stages across the UMAR. The colours green, blue and red are associated with the onset and duration for each of these stages of deformation: green for the flexural stage and given by bibliographic data (Calamita *et al.*, 1994); Guerrero *et al.*, 2012), blue for the

LPS and given by these studies, red for the folding stage and given by the work of Lacombe *et al.* (2021)..... 209

Figure 6.12-Spatial and temporal evolution of σ_v and σ_H magnitudes, in map view, cross-section and graphically. Maps and cross-sections are represented in sketch form. Vertical shortening is not calculated, and vertical scale is exaggerated on cross-sections. Magnitudes are deduced from depths returned by SRIT application on BPS and these given by burial models. The evolution of the LPS is also represented on these sections, indicated by the blue areas in transparency. 211

Figure 6.13-(A) Relation between durations of deformation stages of folding event, fold style (*i.e.* final fold geometry) and sequence of regional deformation. Circles 1 to 6 indicate the order of structural style development, *i.e.* sequence of folding/thrusting, with corresponding ages in Ma (in parentheses). The colour code is: blue for the LPS, red for the fold growth, green for the LSFT and yellow for the post-folding extension/compression; from Lacombe *et al.* (2021). **(B)** Structural style proposed for Umbria-Marche based on data from this study and previous works (Beaudoin *et al.*, 2020b; Lacombe *et al.*, 2021). The suggested model proposes a propagation of the deformation through the level of decollement, *i.e.* the diachronous formation from west to east of fault-bend folds along a flat-ramp decollement. 213

Table 1.1 - Porosity values and associated coefficient, deduced from curves and equations of Allen & Allen (1990b) and Watts (2001).....	71
Table 1.2 - Corrections associated with the type of basin considered, based on the equations of Allen & Allen (1990) and Watts (2001).....	71
Table 2.1 - Synthesis of the tectono-stratigraphic evolution of the Umbria-Marche basin and adjacent.....	87
Table 3.1 - Criteria used to assess the validity degree of L_c , defined after the inversion of the signals.....	114
Table 5.1 - Fault inversion results using the Angelier (1984, 1989, 1990). Azimut and dip are given for each principal stress σ_1 , σ_2 and σ_3 , the associated ϕ ratio, as well as the number of faults and the method used for inversions.	171
Table 5.2 - Fault inversion results using the inversion of striated fault plane of Angelier (1984, 1989, 1990). Azimut and dip are given for each principal stress σ_1 , σ_2 and σ_3 , the associated ϕ ratio, as well as the number of faults and the method used for inversions.	176
Table 5.3 - Stabilized R values averaged for the Maiolica, Scaglia Bianca, and Scaglia Rossa formations in Subasio and Conero anticlines, and associated Young moduli E. The number of measurement sites is indicated for each formation in brackets (n), as well as the number of points used for the calculation of the stabilized R value (m). The uncertainty on the R and E values is given by the standard deviation. Values Young moduli are deduced from the Equation 1.15 (Chapter 1).....	178
Table 5.4 - Results of Bedding Parallel Stylolite roughness inversions. Values are grouped considering the location and the formation of sampling. *Crossover length given within 23% uncertainty. **Vertical stress σ_v given within 12% uncertainty calculated according to Equation 1.12.2 (Chapter 1), with following parameters: a Young modulus depending on formation and location, a Poisson ratio $\nu = 0.25$, and interfacial energy $\gamma = 0.32 \text{ J.m}^{-2}$. Dry density of rock considered for calculation $d = 2400 \text{ g.m}^{-3}$, acceleration of gravity $g = 9.81 \text{ m.s}^{-2}$	180

« Sans la curiosité de l'esprit, que serions-nous ? Telle est bien la beauté et la noblesse de la science : désir sans fin de repousser les frontières du savoir, de traquer les secrets de la matière et de la vie sans idée préconçue des conséquences éventuelles ».

Marie Curie

Introduction

I- SCIENTIFIC CONTEXT AND PROBLEMATIC

The quantitative estimates of past stress magnitudes over time is a challenging, but essential task for the understanding of the mechanical and palaeohydrological behavior of the sedimentary basins (Beaudoin *et al.*, 2019, 2020a). Several implications are driven by their understanding: (i) the direction and magnitude of stresses directly impact the physical properties of rocks, *e.g.* fracture permeability and are thus important for the reservoir aspect (*e.g.* Li *et al.*, 2021); (ii) the understanding of distribution of stresses can help to understand major geodynamic changes, *e.g.* slab-lower crust coupling in the Sevier-Laramide (*e.g.* Cross, 1986) (iii) the evolution of stress magnitudes can help to determine the activation of faults, (*e.g.* stress field perturbation at the edge of a fault, Kattenhorn *et al.*, 2000), or the rheology of the crust (*e.g.* debate on the possible impact of structural style on stress magnitudes in forelands, Beaudoin *et al.*, 2020b).

Reconstruction of paleostresses deal with stresses related to tectonic deformation rocks at depth (Lacombe, 2007). Paleopiezometers are commonly observed structures in rocks, developed under the application of stress. They are calibrated in a specific pressure-temperature range and provide quantitative information on the directions and magnitudes of stresses applied to the sediments. In addition, they record a single, time-averaged stress field. Some palaeopiezometers have the advantage of (i) being applicable to fold-and-thrust belts (FTB) as well as sedimentary basins, (ii) being calibrated in the diagenetic domain (P,T), and (iii) giving the absolute or differential magnitude of the principal stresses (Beaudoin & Lacombe, 2018). The inversion of calcite twins (Etchecopar, 1984), as well as a recent method of inversion of stylolite roughness properties (Schmittbuhl *et al.*, 2004), meet these criteria and allow to assess the magnitudes of principal stresses. Calcite twins and stylolites are both formed during early deformation, *i.e.* under low stress differentials, and are, therefore, good outcrop markers. But, whereas calcite twins average the orientations and magnitudes of the stresses in space and time, stylolites alone record these parameters at a defined moment, corresponding to the end of their growth.

Stress magnitudes are dependent on the depth of deformation. Knowing the depth at which they are recorded is thus important. One of the methodological challenges in reconstructing past stresses is to determine at what depth the deformation occurred, the reconstruction of these paleodepths and of their evolution being essential to understand and to constrain the sedimentary, thermal and tectonic history of sedimentary basins (Guidish *et al.*, 1985; Yalçın *et al.*, 1997; Beaudoin & Lacombe, 2018). The importance of a correct estimate of burial was demonstrated by numerical fluid flow models (Gonzalez-Mercado, 2007), showing the impact of overestimating paleoburial and erosion on the prediction of potential source rock maturity and hydrocarbon migration, and on the erosion/sedimentation mass balance between the belt and the adjacent basin. Thus, a wrong estimate of burial can bias the understanding of the petrophysical evolution of potential source rocks and reservoirs, past vertical movements and hydrocarbon prospects. As an example, paleoburial was underestimated in the Veracruz

petroleum province of eastern Mexico (Ferket *et al.*, 2000, 2003, 2006). This misunderstanding of burial and therefore of erosion rates potentially leads to misinterpretation in terms of timing of deformation, reservoir properties, and fluid evolution of the system. Study of burial and deformation thus raises the questions of processes responsible for the temporal evolution of sedimentary basins, and of the underlying issues of mechanical behavior of the upper crustal strata. Other less fundamental aspects are also raised, related to society, such as storage potential and hydrocarbon resources, as well as green resources, CO₂, geothermal energy, climate, earthquakes.

Sedimentary basins (both ancient and modern) provide some of the best natural laboratories for studying and constraining the aforementioned geological processes. They can be assimilated to containers, whose contents must be studied to understand their dynamics and control factors. Thus, the record of sedimentation, burial, erosion, and uplift provides access to most of the stages of evolution of the basin. Several types of sedimentary basins can be defined: (i) basin formed in extensional context, *i.e.* rift to passive margins (*e.g.* Fundy rift basin, Canada, Withjack *et al.*, 1995), (ii) basin formed in compressional context (accretionary wedges, foreland basins, *e.g.* Cordilleran basin, Utah, Horton *et al.*, 2004) and (iii) basin in intraplate context, like diffuse flexure, dynamic topography, pull apart basin, etc... (*e.g.* Dead Sea Basin, Ten Brink & Ben-Avraham, 1989). Among those, foreland basins record most of the phases of the related orogenic evolution, where constraining the evolution of burial and deformation over long time scales remains a challenge because foreland basin-FTB systems are particularly prone to vertical movements (subsidence and tectonic uplift), including flexural subsidence and sedimentation in the foreland basin, and thrusting and associated erosion in the FTB.

Three main tools can be used to attempt the quantification of the depths associated with past deformations: (i) paleothermometers, with limitations specific to each method (*e.g.* clay transformations such as illite-smectite, fluid inclusions, oxygen isotopy, CO₂ clumped isotopy ...), and that require an estimate of the geothermal gradient to convert the past temperature to depth; (ii) Thermochronometers that includes apatite fission-tracks (*e.g.* Donelick *et al.*, 2005; Tagami, 2005), zircon fission-tracks, and apatite and zircon (U-Th)/He dating (Farley, 2002; Ehlers & Farley, 2003), or ⁴⁰Ar/³⁹Ar dating in white mica and potassium feldspars with higher closure temperature. They provide access to absolute ages at which the rock cooled down below a temperature depending on the thermometer. That age, in turn, is usually translated into rate of exhumation; (iii) barometers, giving access to a pressure from which depth can be deduced, and fairly poorly represented: thermodynamic mineralogical equilibria typical of metamorphism (*e.g.* apatite inclusions in garnets), HC+H₂O fluid inclusions, and sedimentary stylolites. Sedimentary stylolites, although widely represented in sedimentary basins, have seen little use to estimate deformation depths.

Stylolites are defined as rough pressure-solution interfaces, frequently observed in carbonate rocks (Stockdale, 1922, 1926, 1936; Paris B. Stockdale, 1943; H. V. Dunnington, 1954; Bushinskiy, 1961; Park & Schot, 1968; Bathurst, 1972; Buxton & Sibley, 1981; Railsback, 1993), and of which peaks developed perpendicular to the maximum stress σ_1 applied during their growth (Rolland, 2013). Two main types

of stylolites are discriminated according to the nature of the applied stress: (i) burial-related stylolites, formed under the effect of the weight of the overburden (under a vertical principal stress), during burial prior to contraction and during exhumation; (ii) tectonic stylolites, related to horizontal contraction, likely observed during the evolution of the foreland basin and in other contexts such as stable carbonate forelands. Empiric studies of open stylolite surfaces characterized stylolite roughness as a signal displaying self-affine properties (Renard *et al.*, 2004). The log-log graphical representation of the signal analysis returns two slopes characterized by specific roughness coefficients (*i.e.* Hurst coefficients) related to the regimes of growth, dominated by the surface energy at small-scale (*i.e.* below 1mm) and by the elastic energy at large-scale (*i.e.* above 1mm) (Schmittbuhl *et al.*, 2004; Ebner *et al.*, 2009a; b; Rolland *et al.*, 2012, 2014). The spatial scale related to the switch from elastic energy to surface energy dominated corresponds to a cross-over length (L_c), spatial scale on which of Stylolite Roughness Inversion Technique (SRIT) is based. This L_c depends on chemical (*i.e.* surface energy at the solid-fluid interface) and mechanical (*i.e.* Poisson ratio and Young modulus) properties of the host, and on the applied differential and mean stresses (Schmittbuhl *et al.*, 2004). The use of SRIT applied to bedding-parallel sedimentary stylolites (BPS) enables the quantification of the principal vertical stress during the burial, provided the hypothesis of uniaxial strain is checked in the stylolite plane (*e.g.* Ebner *et al.*, 2009a). Then, the computed σ_v values can be converted into paleodepth independently from the past geothermal gradient, providing the maximum depth at which BPS developed, that can be, in FTB context, related to the maximum depth at which $\sigma_v > \sigma_H$. This relation was exploited by Beaudoin *et al.* (2020) in the Bighorn Basin (Wyoming, USA), who projected SRIT results on burial models to access the timing at which $\sigma_v > \sigma_H$. This absolute age was successfully confronted to the absolute datation by the mean of U-Pb of the first tectonic cement related to the contraction. When it comes to apply SRIT in this way, that has a lot of implications on the ages of the deformation, it is important to consider that SRIT faces some methodological limitations: (i) in the choice of the signal processing used, as several methods exists, *e.g.* Average Wavelet Coefficient (AWC, Simonsen *et al.*, 1998; Renard *et al.*, 2004; Candela *et al.*, 2009), Fourier Power Transform (FPS, Renard *et al.*, 2004; Candela *et al.*, 2009), correlation function (COR, Santucci *et al.*, 2007; Candela *et al.*, 2009), and as results sometimes differ (*e.g.* Schmittbuhl *et al.*, 1995; Simonsen *et al.*, 1998; Beaudoin *et al.*, 2019); (ii) identified variation in reconstructed stress according to the texture of the host rock and/or the morphology of the stylolite (Beaudoin *et al.*, 2019; Bah *et al.*, 2022). These issues partly relate to the fact BPS has not widely been used as palaeopiezometers in geological studies, limiting the dataset to discuss the reliability and robustness of this method.

This project, entitled “**Paleopiezometry of sedimentary stylolites in fold and thrust belts: case of the Umbria-Marche Ridge, Apennines, Italy**”, aims to: (i) understand and overcome the methodological limitations encountered when using the SRIT; (ii) test the reliability and robustness of the methodology presented in the Bighorn Basin study (Beaudoin *et al.*, 2019) by applying it to different study cases, and by confronting these results with thermometers or chronometers associated with

identified structures; (iii) extend the study to FTB and see if the timing obtained is consistent with a well-constrained deformation history, and estimate how far the method can be used to quantify compressive stresses. The Umbria-Marche Ridge (Central Apennines, Italy), where burial and contraction led to extensive pressure-solution processes in thick Meso-Cenozoic carbonates (Lavecchia *et al.*, 1988), constitutes the case study. This young FTB built during the Neogene (Lavecchia *et al.*, 1988; Scisciani *et al.*, 2014) in a sequence of fold development constrained by growth strata, provides a natural laboratory to apply and validate the SRIT to BPS, and also to highlight its potential contributions to the understanding of burial and timing of deformations in forelands and FTB.

This work proposes several approaches to this inversion method to force its understanding, to detail its strengths and limitations, and to demonstrate its contributions to the study of geological systems such as foreland-FTB, with the case of the UMAR:

- (i) the first stage is to understand and to unlock methodological limitations encountered related to SRIT application. This new methodology is then applied to a large set of data sampled in the whole UMAR, to test the method and perform a statistical analysis of the SRIT results (*i.e.* L_c values). The aim is to identify the impact factors, the methodological limits, as well as to test the reliability and robustness of the method based on the criteria of validity and coherence of the results, in order to validate its use and to propose adapted optimization paths.
- (ii) once the methodology has been validated and optimized, this work proposes to apply it to three real geological cases considered individually. The methodology combines fracture analysis, application of SRIT to BPS and construction of burial curves based on field data. The idea is to estimate the burial-deformation calendar for each of these structures, and to test its consistency with data from previous studies in the area and more conventional analysis methods (*e.g.* thermometers and chronometers known in the area).
- (iii) the study is finally extended to the scale of the UMAR, by coupling the results obtained for each structure studied independently. The reconstructed timing is compared with existing data to verify its consistency, and to push the limits of the method as far as possible in order to highlight its contribution to the estimation of compressive stresses.

II- THESIS LAYOUT

Chapter 1 provides a synthesis of the requested literature data related to foreland basins and FTBs, associated mesostructures. The classical methodologies used in these contexts are developed, as well as those applied in this work. The study of fracturing and palaeopiezometry of sedimentary stylolites is more extensively documented, as at the focus of this work.

Chapter 2 presents the literature review focused on the study area: **I-** the global geodynamic context, relating to the evolution of the Mediterranean domains; **II-** the Apennines, detailing the geodynamic and structural context, and the palaeogeographic evolution related to them; **III-** the Umbria-Marche Apennine Ridge (UMAR), with the description of the typical stratigraphic sequence, the

structural characteristics and the various models proposed, the kinematic scenario and the mesostructural characteristics described at the scale of the belt.

Chapter 3 consists of a statistical study of the SRIT results applied to the BPS. The geological aspect is not considered in this first chapter of results, the idea being to test the method on a large dataset (*i.e.* all the data available for the UMAR), in order to evaluate quantitatively and statistically the reliability of the method. The chapter is divided into a non-exhaustive description of the analyzed samples (location, facies, morphology and length of stylolites), followed by the presentation of two methodological contributions proposed in the present work, *e.g.* a first image processing workflow by a computer-assisted track segmentation and the inversion of concatenated stylolites. These methodological contributions aim at reinforcing the reliability and robustness of the inversion results and facilitating the use of the method.

Chapter 4 presents a first geological case of the study: the Cingoli Anticline. This case study presents a coupled methodology, involving palaeopiezometric inversions applied to BPS, classical fracture studies and vein cement geochemistry, in order to study the burial and deformation history of the anticline. These results were published on 13 January 2021 in the peer-reviewed journal *Geosciences*.

Chapter 5 presents two other case studies: the Conero and Subasio anticlines, for which fracture and BPS inversion data are detailed. This chapter also forms a synthesis of the fracture and burial data obtained at the FTB scale. This up-scaling to the regional scale, coupled with data of Chapter 4, demonstrates the robustness of the SRIT applied to natural and large-scale geological cases, as well as the contribution to follow the evolution of the onset and of the duration of the LPS at the scale of the FTB.

Chapter 6 discusses the various contributions and limitations of the method, both from a methodological and application point of view. Firstly, it aims to highlight the limitations of the method, and the elements that can be used to understand and overcome them. Then, a large-scale analysis of the fracture sequence is proposed. A last part dedicated to the understanding of the timing and propagation of the folding demonstrates the methodological contributions to the understanding of pre-compressive damage in foreland basin-FTB systems. This section (i) discusses the assumptions used for the study of the geological cases considered, (ii) shows how the use of this methodology allows the monitoring of vertical and horizontal stresses at the scale of the FTB and (iii) proposes elements of interpretation as to the structural style considered for the study sector.

*Chapter 1- Burial evolution and stress distribution in foreland
basins and fold-and-thrust belts: state of the art*

I- FORELAND BASINS AND FOLD-AND-THRUST BELT: NATURAL LABORATORIES FOR STUDY AND THE UNDERSTANDING OF GEOLOGICAL PROCESSES

1- Definition

Fold-and-thrust belt (FTB)-stable foreland systems were widely documented on Earth (Cooper, 2007; Nemcok *et al.*, 2009), and characteristic of orogenic belts formed in compressive context. They are extensively encountered in convergence zones, at tectonic plate collision boundaries (*e.g.* Himalayas, Coward *et al.*, 1986; Sandvol *et al.*, 1997, and Apennines, Cosentino *et al.*, 2010), in subduction zones and oceanic accretionary prisms (*e.g.* Andes, Oncken *et al.*, 2006), as well as in intraplate areas influenced by the convergence of neighbouring plates (*e.g.*, Yinshan and western Ordos belts, China, Davis *et al.*, 1998; Ritts *et al.*, 2009). Foreland basins are defined as sedimentary basins developed between the front of the active FTB and the adjacent craton (Figure 1.1), forming elongated areas of plate flexuration in response to tectonic loading in continental convergence domain.

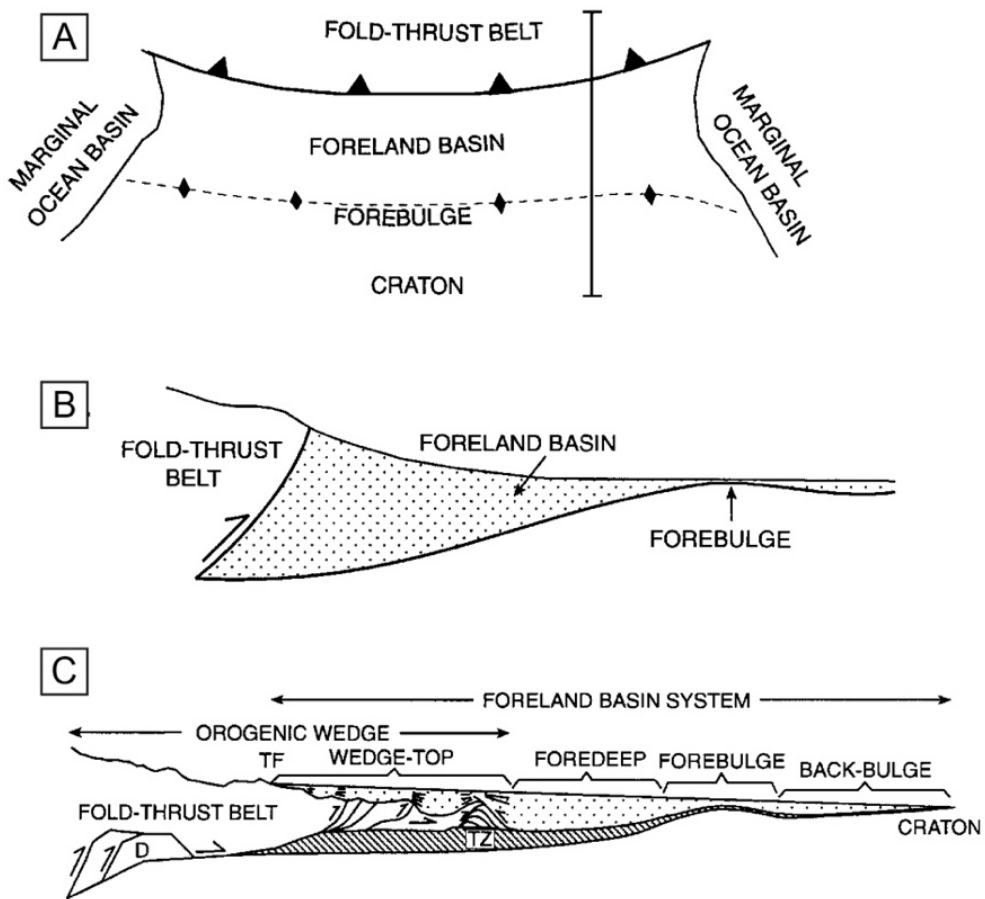


Figure 1.1- (A) Schematic map view of a “typical” foreland basin, limited longitudinally by two marginal ocean basins. The scale is not specified. The vertical line corresponds to the orientation of the cross-section represented in (B). (B) Schematic cross-section illustrating the geometry of the foreland basins. The boundary between the basin and the FTB is exaggerated vertically by a factor of 10. (C) Schematic cross-section illustrating a revised concept of foreland basin architecture, positioning the four depositional zones, the topographic front of the FTB (TF), a duplex zone (D), the front of a triangular zone (TZ), as well as progressive deformation represented by the short fan lines associated with the thrust tips. The interface between the front of the orogenic wedge and the foreland system is marked by the presence of extensive thrusting; after DeCelles & Giles (1996).

In the front of FTB-stable foreland systems, three main processes, not exclusive, are responsible for lithospheric flexure (Figure 1.2) (*e.g.* Royden, 1993): (i) topographic loads, related to the weight of orogenic nappes, at the origine of a flexure over distances of several hundred kilometers in the stable craton (*e.g.* Price, 1973; Beaumont, 1981); (ii) subduction loads which generate subsidence greater and/or more widespread than expected from the topographic load in foredeep depozones because of the location of the foreland on the subducting plate (Karner & Watts, 1983; Royden & Karner, 1984); and (iii) subducted slabs, in the case of retroarc forelands located on continental plates above subducting slabs (*e.g.* Cross, 1986).

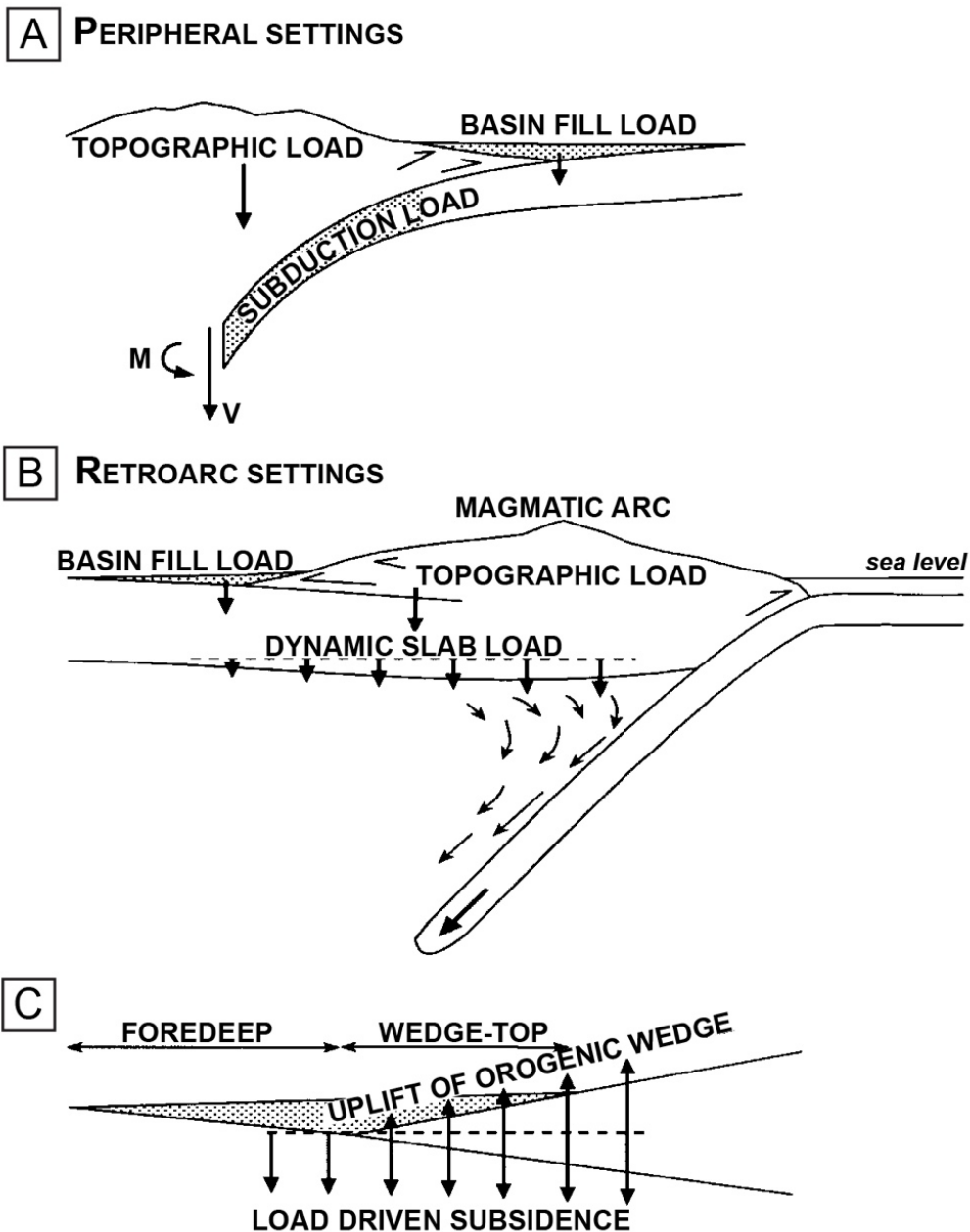


Figure 1.2- (A) Representation of the principal loading processes in peripheral foreland systems, with topographic and sediment load, and also subduction load related to vertical shear (V) and bending moment (M) on the end of the subducted slab potentially existing at depths of -50-200 km (Royden, 1993). (B) Representation of retroarc foreland basin systems. (C) Accumulation in wedge-top depozone, resulting from the competition between regional, load-driven subsidence (downward pointing arrows) and local uplift of the orogenic wedge related to shortening and thickening (upward pointing arrows); after DeCelles & Giles (1996).

Foreland basins are divided into four distinct zones (Figure 1.1, DeCelles & Giles, 1996), namely wedge-top, foredeep, forebulge and back-bulge, which boundaries sometimes shift laterally over time. Sedimentary deposits within these zones depend on the position of the front over time: the front advanced towards the inside of the craton and progressively incorporated the deposits.

The wedge-top depozone (Figure 1.1C) corresponds to the accumulation of sediments on top of the frontal part of the orogenic wedge. The limit of deformation associated with the frontal tip of underlying orogenic wedge defines the extent of this depozone toward the foreland (DeCelles & Giles, 1996). Length of this depositional zone was estimated of several tens of kilometers, and tapers onto orogenic wedge (*e.g.* the Sevier thrust belt, length of 75 km, Utah and Wyoming, Coogan *et al.*, 1992, 50 km of the active northern Apennines thrust belt, Ricci Lucchi, 1986). The deposits differ according to the nature of the system: rather coarse, alluvial and fluvial near high topographic relief in subaerial contexts, the subaqueous areas present mass-flows and fine grained shelf sediments (*e.g.* Ori *et al.*, 1986). Main processes favour sediment accumulation, such as regional, load-driven subsidence, and regional and local uplift of the orogenic wedge related to crustal thickening or isostatic rebound. Uplift in the FTB frontal foothills, responsible for local wedge-top sediment accumulation (Lawton & Trexler Jr, 1991; Talling *et al.*, 1995), as well as eustatic sea-level, have also an important role in development and destruction of sediment deposits.

The foredeep depozone (Figure 1.1C) constitute the mass of sediments accumulated between the frontal tip of the orogenic wedge and forebulge. Subaerial deposits are fluvial and alluvial, while subaqueous deposits are shallow lacustrine and marine, from deltaic to shallow shelf and turbidite fans. Several major processes drive sediment accommodation such as : (i) the loading by the adjacent orogenic wedge and the erosion of wedge sediments, as well as loading subsurface, and (ii) the regional isostatic uplift during erosion of the orogenic load, (iii) the uplift linked with the progress of the orogenic thrust wedge or the retrograde migration of the forebulge, or even (iv) variations in relative sea level (Price, 1973; Beaumont, 1981; Jordan, 1981; Quinlan & Beaumont, 1984; Heller *et al.*, 1988; Mitrovica *et al.*, 1989; Flemings & Jordan, 1990; Allen *et al.*, 1991; Royden, 1993).

The forebulge (Figure 1.1C) is the area of potential uplift along the cratonic side of the foredeep (DeCelles & Giles, 1996). Dependent on flexural rigidity of the lithosphere (DeCelles & Giles, 1996), its width was estimated to between 60 and 470 km, and its high range between tens to hundreds meters high. The forebulge is normally a subaerial and erosional zone (Crampton & Allen, 1995), *i.e.* elevated area considered as a non-deposition or erosion zone, where the resulting unconformity gives access to its position over time (*e.g.* Jacobi, 1981; Stockmal *et al.*, 1986; Mussman & Read, 1986; Patton & O'connor, 1988; Bosellini, 1989; Sinclair *et al.*, 1991; 1992; Currie, 1994). However, in some forelands, the forebulge contains buried syn-orogenic sediments, possibly related to regional, long-wavelength subsidence linked to a dynamic slab in retroarc system, as well as aggradation up to base level or an equilibrium drainage profile across the forebulge crest.

The back-bulge depozone (Figure 1.1C) is the area of sediments accumulation between the forebulge and the craton (DeCelles & Giles, 1996). Sediment bulk is mainly related to orogenic belt, with possible significant contributions from craton and carbonate platform development in submarine system. It is characterized by a regional closure around a central thick zone, suggesting the possible involvement of some components of flexural subsidence in the accommodation of sediments towards the front of the craton. Because of the low subsidence rate, it is overfilled over time (like the foredeep). Hence, stratigraphic units deposited in this area are much thinner than those of the foredeep, and time planes are sub-parallel over lateral distances of several hundred kilometres and perpendicular to the orogenic belt (Flemings & Jordan, 1989; DeCelles & Burden, 1992). Deposits are essentially shallow and non-marine, with a predominantly fine grain size because of a large distance to the source in orogenic belt, except on the flank of the uplifted forebulge area where coarse sediments sometimes accumulate.

2- Basin modeling

Basin modeling involves the reconstruction of the deposition, compaction and erosion of strata over time and space, and the simultaneous evolution of the thermal history of the basin (Peters *et al.*, 2012). Often used in the petroleum industry (Basin and Petroleum System Modeling, BPSM), the method consists of modeling the hydrocarbon-generation process to estimate volumes, predict location and characterize the properties of hydrocarbon accumulations available for entrapment and fluid flows (Al-Hajeri *et al.*, 2009). Several dynamic processes, *e.g.* sediment deposition, faulting, burial, as well as kerogen maturation kinetics and multiphase fluid flow in case of petroleum simulations, are considered during modeling. They may be examined from 1D to 4D modeling, with a complexity typically increases with spatial dimensionality. For instance, while the 1D modeling only simulates burial history at a single point, the others are used to reconstruct petroleum systems at the scale of a cross section (*i.e.* 2D modeling), as well as at the reservoir and basin scale (*i.e.* 3D or 4D modeling whether time dimension is considered). Several preliminary steps are necessary to build these models, *e.g.* the construction of a structural model and the identification of the chronology of deposition and physical properties of each strata, on the basis of geophysical, geologic and geochemical data. The model can be adjusted by the comparison of model outputs, *i.e.* porosity, temperature, pressure, vitrinite reflectance, accumulation volume or fluid composition, with independent calibration information (Al-Hajeri *et al.*, 2009). In the context of this modelling, there are several approaches to temperature more or less time dependent.

The use of thermochronometers is common in the study of thermal history of sedimentary basins (*e.g.* Arne *et al.*, 2002). Two main thermochronometers can be distinguished considering the closing temperatures associated with these systems: low and high temperature thermochronometers. Low temperature thermochronometers are associated with closure temperature ranges, between 70°C and > 200°C. They include apatite fission-track (AFT) and apatite (U-Th)/He dating methods (Armstrong, 2005). AFT and apatite (U-Th)/He dating are used to study the tectonic processes behind the cooling of rocks. They are highly accurate for rapid cooling, and strongly influenced by thermal variations in the shallow crust (Ehlers & Farley, 2003). In contrast, high temperature thermochronometers, *i.e.* zircon

fission-track (ZFT) and $^{40}\text{Ar}/^{39}\text{Ar}$ methods in mica and potassium feldspars, as well as zircon (U-Th)/He dating, are associated with high and disjointed temperature ranges. While closure temperatures for ZFT range from 185°C to 240°C (e.g. Brandon *et al.*, 1998; Tagami, 2005), temperatures associated with argon systems vary depending on the mineral considered: 350°C-420°C for white mica (McDougall & Harrison, 1999; Hodges *et al.*, 2005) and 150-200°C for K-feldspar. Zircon (U-Th)/He dates are associated with temperatures between 180°C and 200°C (Reiners *et al.*, 2002; Reiners, 2005). These thermochronometers have a lower sensitivity to the temperature ranges of most sedimentary basins. They are rather used for assessing source region parameters from the study of detrital grain composition, ages and characteristics (Armstrong, 2005).

The coupling of these thermochronometers, and particularly of AFT analysis, with maximum paleotemperature indicators such as vitrinite reflectance (e.g. Bray *et al.*, 1992; Green *et al.*, 1995; Ventura *et al.*, 2001), or $^{40}\text{Ar}/^{39}\text{Ar}$ (e.g. Kohn *et al.*, 1997) provides some of the best indicators of both magnitude and timing of basin inversion in sedimentary basins. A potential barrier to the application of these maximum paleotemperature techniques are the major assumptions they require and their strong impact on the resulting age and depth estimates. For example, vitrinite reflectance consists in the measure of the incident light percentage reflected from a statistically meaningful sample of vitrinite particles. Moreover, the analysis of illite crystallinity consists of an indirect measurement of the mean consecutive illite layers contained in coherent scattering domains of mixed-layer illite-smectite. This measurement value is strongly dependent on the size of studied fraction (Kubler, 1984) and on many experimental parameters (Kubler, 1967; Warr & Rice, 1994; Kübler & Jaboyedoff, 2000), such as: shape and material of sample holder, age of the X-Ray tube, geometry of the diffractometer, type of counter, rotation speed of the diffractometer and of the chart of recorder, size of the divergent and receiving slits, whether or not a monochromator was used and the counting sensitivity. For these reason, numerous calibrations are required.

II- MESOSCALE FRACTURE NETWORK IN FORELAND BASINS AND FOLD-AND-THRUST BELTS

Faults, fractures, stylolites are accommodative structures for deformation generated by small-scale processes (e.g. Evans *et al.*, 2003; Marfil *et al.*, 2005; Evans & Elmore, 2006;). They are spatially and temporally distributed and develop in foreland-FTBs from the early stages of convergence, even before folding. They have been extensively studied by universities and industries for several decades, because much information can be deduced from the analysis of these deformation structures: (i) they provide information on the deformation patterns within foreland and FTBs (e.g. Tavani *et al.*, 2008; Quintà & Tavani, 2012; Beaudoin *et al.*, 2020b); (ii) they impact the properties of source rocks, and thus control the migration and circulation of fluids within the reservoirs (e.g. Fisher & Knipe, 2001; Tavani *et al.*, 2008; Beaudoin *et al.*, 2020a). This section aims to characterize deformation structures frequently developed in carbonate rocks, as well as their distribution in the foreland and FTB.

1- Characterization of fracture network

1.1- Fracture definition and classification

Sensu stricto, a fracture is defined as a small planar or subplanar discontinuity formed under the application of an external (e.g., tectonic) or internal (thermal, chemical or residual) stress, disrupting the mechanical and mineralogical properties of the rocks (e.g., loss of cohesion, ...).

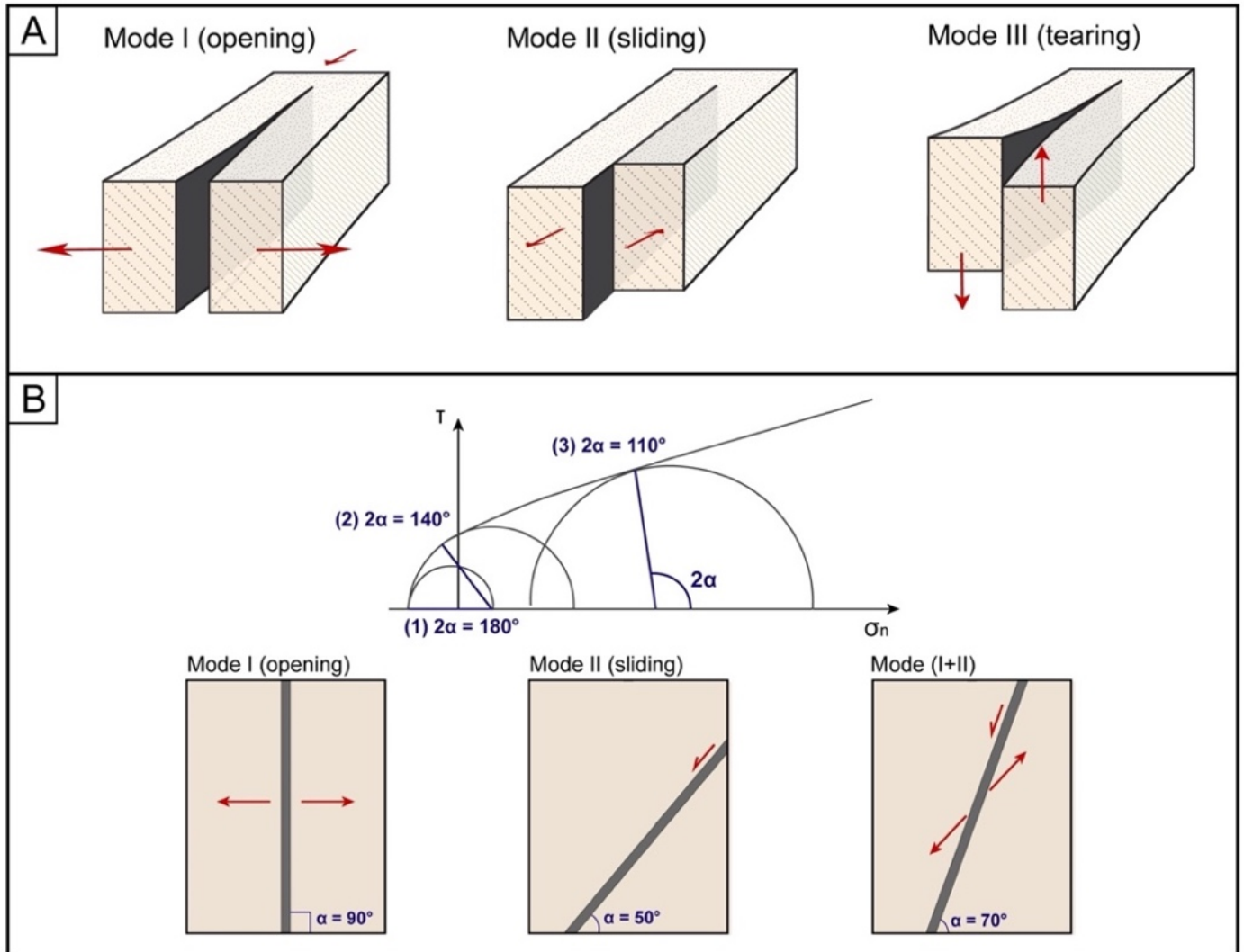


Figure 1.3- (A) Fracture propagation modes, and (B) associated Mohr circles. Mode I: opening, mode II: shear; mode III: tearing; modified from Bons *et al.* (2012).

Three mechanisms of fracture opening and propagation have been characterized (Figure 1.3, Bons *et al.*, 2012): (i) mode I, associated with extensional dynamics. The displacement is perpendicular to the fracture plane, giving access to the direction of minimum stress σ_3 (itself perpendicular to this plane); mode II, in a shear context. The displacement is parallel to the fracture plane; mode III, or tearing, involving sliding parallel to the fracture plane. A last mode is also considered since it occurs in natural conditions. This mode, called mixed mode, is a coupling between modes I and II defined above. Mode I and mixed mode I+II fracture networks initiate and develop only if the applied stresses (extensive or effective) are sufficient. Several parameters condition their formation. First, some factors control the orientation of the fractures during their growth: the orientations of the applied stress (*i.e.* the main

controlling factor), as well as lithology, mechanical contrasts, and burial depth because of the anisotropy generated by this applied stress (André *et al.*, 2006). Second, the spacing of fractures varies according to lithology, thickness of the beds, tectonic context (*e.g.* compressive, extensive). These mechanisms of fracture propagation are the subject of several studies, *e.g.* Bieniawski, (1967a; b), Engelder, (1987, 1999), Stoeckhert *et al.* (2015), and some work showed that these mechanisms are closely correlated to the propagation environment of the fracture network, and more specifically to its heterogeneities. For example, the study of Renard *et al.* (2009), based on the monitoring of fracture propagation by X-ray microtomography, confirms that this propagation is essentially conditioned by the presence of heterogeneities: while the fractures bypass and/or stop against the grains, which constitute zones of resistance, they easily cross the pores which constitute zones of weakness favorable to the propagation of the fracturing.

Two main types of fractures are discriminated, related to specific stress states: (i) joints and veins, opened in mode I. When the open mode I fracture is mineralized, it is a vein, otherwise it is a joint; (ii) faults, opened in mode I+II or mode II. In mode I+II, when the offset is much smaller than the size of the plane along which the displacement occurs, fracture is defined as a shear vein, otherwise it's a fault.

Several categories of veins (*i.e.* mineralized mode I fractures) are recognized according to the morphology of the minerals (Hilgers & Urai, 2002), namely (Figure 1.4): (i) antitaxial veins, corresponding to a growth of fibrous minerals from the center to the edge of the vein; (ii) syntaxial veins, associated with a mineral growth from the edge to the center; (iii) ataxial veins, for which the direction of mineral growth is impossible to define. Bons *et al.* (2012) refined this textural classification by discriminating five types of textures, giving more or less precise information concerning the opening kinematics (Figure 1.4): (i) blocky texture, corresponding to a mineral precipitation without privileged direction and a growth initiated from the edge of the veins (*i.e.* ataxial veins); (ii) elongate blocky texture, related to a mineral precipitation with privileged direction, the growth being initiated from the edge towards the center of the veins (*i.e.* syntaxial veins); (iii) crack-seal texture, suggested as all associated with the so-called ataxial veins and including (iv) a stretched texture (fibrous close). These two textures correspond to multiple phases of opening and filling, crack-seal process consisting of the development of fibrous veins by repeated increments of the microcrack opening, followed by sealing of the microcrack by deposition of material from solution. It occurs where accumulation of elastic strain is followed by brittle failure, release elastic strain, solution transfer of material to the microfracture site, and deposition therein. Once sealing of the microfracture is accomplished, stresses can once again be transmitted across the region of the initial microcrack, and elastic strains again build up until there is renewed microfracture (Ramsay, 1980; Cox & Etheridge, 1983); (v) fibrous texture of the antitaxial veins, the fibrous minerals growing from the center to the edge of the vein.

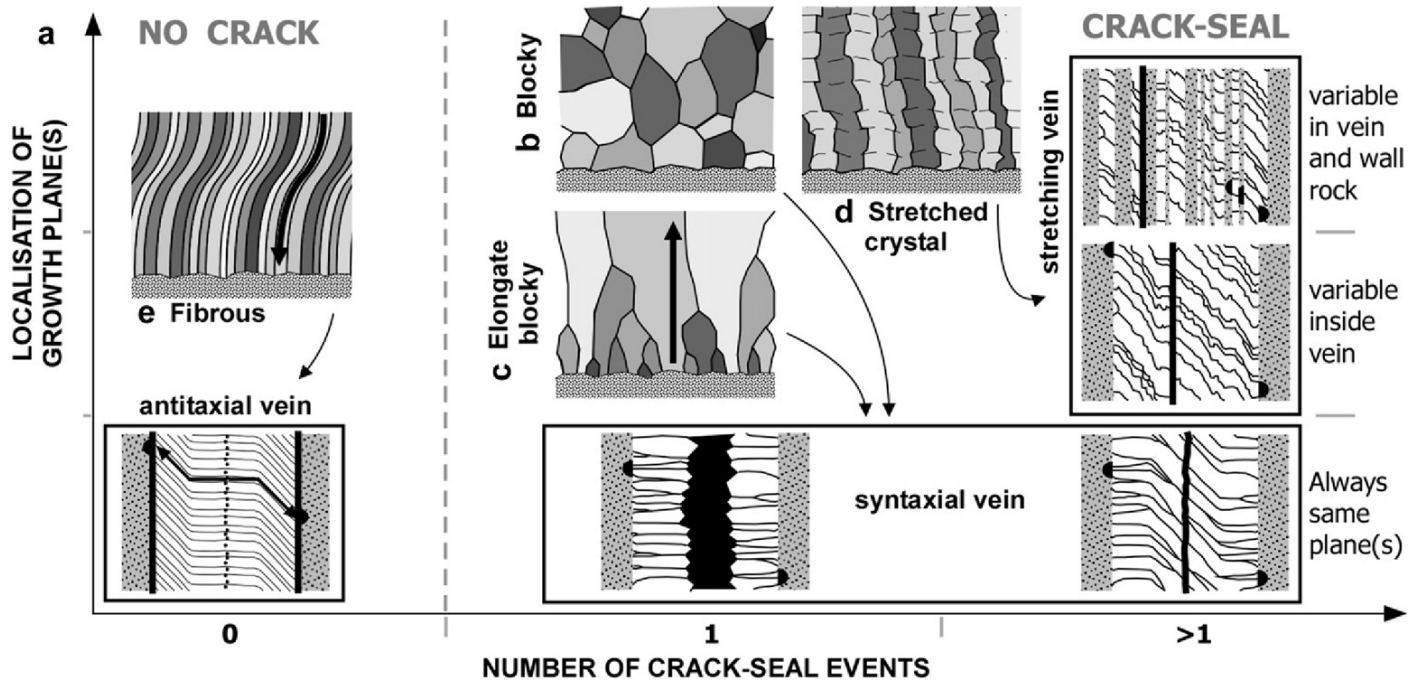


Figure 1.4- Classification of Bons *et al.*, (2012). Interpretation of vein opening patterns on field data; after Bons *et al.*, (2012).

1.2- Stylolites: general definition

Stylolites are defined as pressure-dissolution interfaces frequently observed in carbonate rocks (*e.g.* Paris B. Stockdale, 1943; H. V. Dunnington, 1954; Park & Schot, 1968; Bathurst, 1972; Railsback, 1993), and developed perpendicular to the maximum stress applied during their growth. Two main types of stylolites were discriminated according to the nature of the applied stress: (i) sedimentary stylolites, formed during burial prior to contraction and during exhumation in foreland basins, under the effect of the weight of the sediments (*i.e.* vertical stress); (ii) tectonic stylolites, related to horizontal contraction. They form serrated and rough surfaces, called “sutures”, at the interface of two rock masses which grain size rarely exceeds the amplitude of the teeth which intersect them. They are distinguished from dissolution veins, or flasers, which adjoin the edge of the grains rather than splitting them (Bathurst, 1987). Stylolites are further detailed in a later section of this chapter, as they constitute the major theme of this thesis.

2- Distribution in the foreland basins and FTB

For orogenic systems, the tectonic model considered is the Andersonian model (Anderson, 1951). In addition, the deformation models for foreland basins and FTBs are associated with the following six major tectonic processes (Tavani *et al.*, 2015): (i) foreland flexure in the peripheral bulge and the ultraperipheral region of the foredeep; (ii) longitudinal extension along the foredeep; (iii) layer-parallel shortening (LPS), both in the inner zone of the foredeep and at the ends of thrusts; (iv) syn-folding deformation, during the formation of anticlines (*i.e.* folding *sensu-stricto*); (v) contraction of the system, related to a late folding stage of tightening (LSFT). A recent study grouped this stages (iii), (iv) and (v) into a single stage called the folding event (Lacombe *et al.*, 2021); (vi) extensive deformation generated by gravity. Each of these events are associated with one or more types of meso-structures.

2.1- Distribution within FTB

Forelands recorded macroscale deformation in the early stages of the shortening, related to foreland flexure and pre-folding compression. The foreland flexure extensional stage is associated with outer arc extension in the peripheral bulge, accommodated by deformation structures well referenced in forelands (Figure 1.5) (e.g. Calamita & Deiana, 1980; Scisciani *et al.*, 2001; Mazzoli *et al.*, 2005; Tavani *et al.*, 2012b): (i) longitudinal extensional faults, with a rather constant, high cut-off angles; (ii) a network of longitudinal mesostructures, including joints, veins, and dilatation bands perpendicular to bedding. Their position within the system depends on factors such as the thickness of syn-orogenic sediments, curvature and elastic thickness of the lithosphere (Tavani *et al.*, 2015). In doing so, joints are expected to form preferentially in the zone of maximum curvature and at the shallower structural levels; (iii) a second network of extensional transverse faults, perpendicular to the longitudinal structures. This network also includes faults that accommodate hanging wall fault-parallel stretching induced by the lateral decrease of fault displacement (Destro, 1995; Medwedeff & Krantz, 2002).

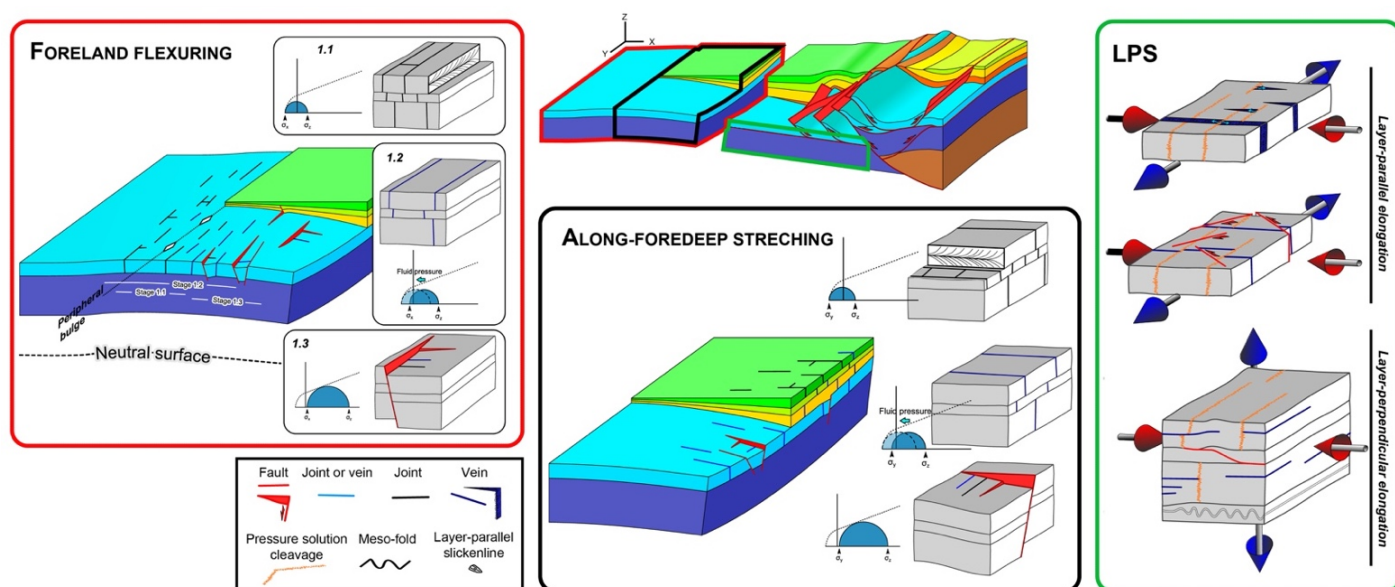


Figure 1.5- Foreland flexuring, along-foredeep stretching and layer-parallel shortening (LPS) deformation stages, and associated macroscale structures. Foreland flexuring leads the development of extensional structures oriented parallel to the forebulge-foredeep belt system, and sometimes of transverse structures as secondary features. Along-foredeep stretching deformation stage provides the development of extensional fractures striking perpendicular to the forebulge-foredeep belt system, and of longitudinal fractures as secondary characteristics. LPS favors the development of mesoscale deformation patterns including either layer-parallel or layer-perpendicular elongation; modified from Tavani *et al.* (2015).

The along-strike stretching stage is defined as the rock migration from the foreland flexured zone into the monoclinical dipping area of the foredeep caused by progressive underthrusting of the lower plate lithosphere. Lateral variability and terminations of orogenic systems impose along-strike curved profiles to foredeeps attained by along-strike stretching (Tavani *et al.*, 2015). This foredeep-parallel lengthening can lead the development of two kind of fractures: (i) as primary features, transverse extensional structures striking perpendicular to the forebulge-foredeep-belt system; (ii) longitudinal fractures can develop as a secondary characteristic (Figure 1.5).

During the LPS, mesostructures develop in the innermost area of the foredeep and at the top of thrust wedges (Tavani *et al.*, 2015). The most common structures are stylolites (Figure 1.5), coupled with synchronous calcite removal processes and re-precipitation into neighbouring pores (*e.g.* Renard *et al.*, 1997; Amrouch *et al.*, 2010b). This stylolites-vein pairs system oriented at a high angle to bedding was widely documented in carbonate rocks, in the foreland and in adjacent FTBs (*e.g.* Engelder & Geiser, 1980; Tavarnelli, 1997; Amrouch *et al.*, 2010a; Beaudoin *et al.*, 2020a; b). For non-carbonate rocks (*i.e.* less affected by pressure-solution processes), this stylolite-vein coupling was replaced by conjugate fault systems at a high angle to bedding (Figure 1.5, Tavani *et al.*, 2015).

2.2- Distribution within fold

Considering their geometry, three categories of meso-structures characterize the foreland and the FTB (Tavani *et al.*, 2015): (i) longitudinal structures parallel to the fold axis, related to contraction and extension; (ii) extensive structures perpendicular to the fold axis; (iii) steeply dipping structures with respect to the fold axis, related to the play of conjugate strike-slip faults (Figure 1.7).

During folding, six intermediate deformation processes are superposed (Figure 1.7): (i) tangential deformation; (ii) flexural slip; (iii) synchronous folding of LPS; (iv) fracturing related to fault propagation; (v) deformation of the base of the fold; (vi) extensive deformation due to gravity. They cause certain types of meso-structures, such as fractures, faults, pressure-solution cleavages, ... (Tavani *et al.*, 2015).

In particular, many pressure-dissolution seams may characterize this stage of deformation (*e.g.* northern Apennines, Tavani *et al.*, 2012b) and show specific characteristics of the folding process: (i) decrease in their frequency from the limbs to the crest of the anticlines; (ii) marked inclination with respect to the bedding, but still less than 90°. When they were replaced to the horizontal, shear figures are observed at the fold hinge; (iii) slight obliquity of these structures with respect to the direction of the anticlines. They are also directed perpendicular to the direction of advance of the tectonic structures. For this Apennine example, all of these features indicate stress channeling during folding in the northern Apennines: the maximum stress is parallel to the regional shortening, and rotated in the vertical plane to maintain an angle of about 30° to the bedding (Tavani *et al.*, 2012b).

The fold development is initiated and continue as long as the rotation of the limbs and the curvature of the strata accommodates the shortening. At this so-called “locking” stage, or Late Stage Fold Tightening (LSFT), the rocks still undergo shortening, but the contraction that causesthe folding is strongly inclined to the bedding. Specific deformation structures are associated with this late contraction phase, crossing the strata and accommodating the shortening: (i) fore-thrusts and back-thrusts observed respectively in the front and back limbs of the folds (Gutiérrez-Alonso & Gross, 1999; Tavani *et al.*, 2008); (ii) pressure-dissolution seams parallel to the bedding, offsetting pre- and syn-fold deformation structures (Tavarnelli, 1997); (iii) conjugate strike-slip faults recording the maximum stress σ_1 (Tavani *et al.*, 2015).

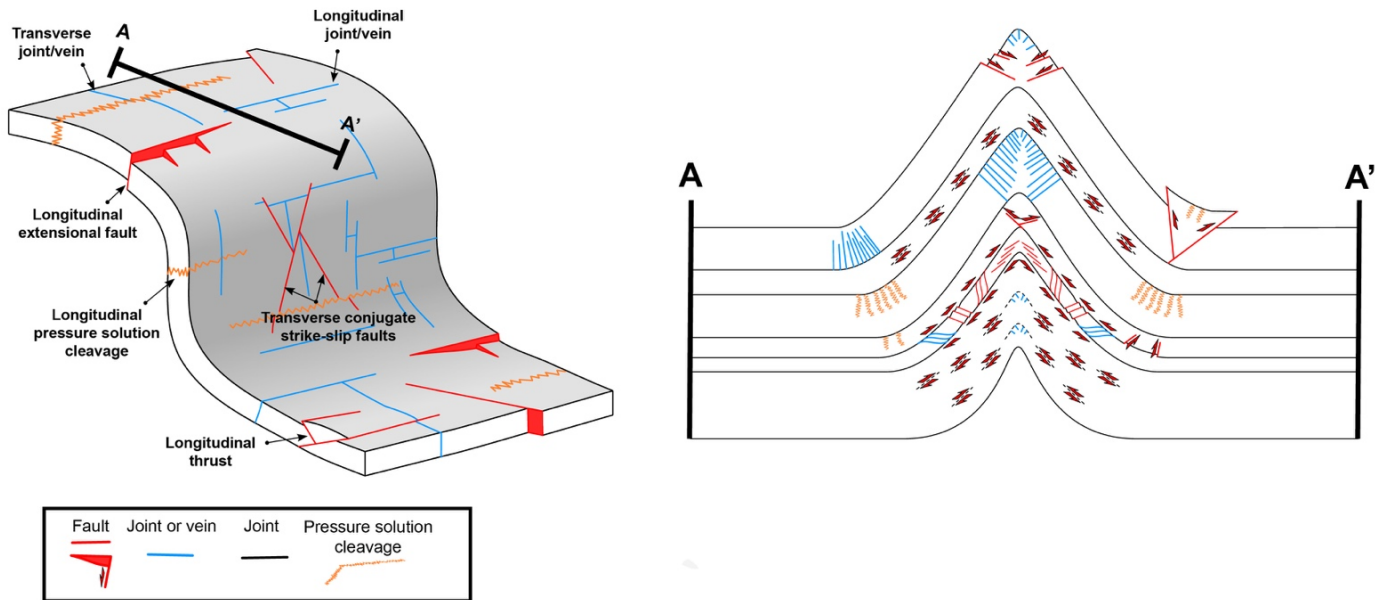


Figure 1.6- Deformation structures commonly observed in anticlines related to FTB. The spatial distribution and geometries associated with these mesostructures are shown at the scale of one strata (left scheme) in the limb and the hinge, and for several strata (right scheme) considering a section orthogonal to the fold axis. The section plane A-A' is oriented with respect to the fold on the left side of the figure; modified from Tavani *et al.* (2015).

During folding and thrusting affecting the foredeep and foreland, the dip of the monoclinical strata and associated subsidence determine whether the total uplift of the fold will be positive or negative (Doglioni & Prosser, 1997; Doglioni *et al.*, 1999). In the case of positive uplift, gravity induces the development of extensional faults: (i) longitudinal in the shallow parts of the fold limbs (Morley, 2007; Laird & Morley, 2011); (ii) transverse in steeply dipping periclinal zones (Guillaume *et al.*, 2008). Other examples of gravity-generated extensional faults exist in the continental domain, within anticlinal structures (Tavani *et al.*, 2014).

III- PALEOPIEZOMETRY IN THE STUDY OF FORELAND BASINS AND FOLD-AND-THRUST BELTS

1- Introduction to paleopiezometry: concept and contributions

Paleopiezometers are commonly observed structures in rocks, developed under the application of stress. Calibrated in a specific pressure-temperature domain, they provide quantitative information on the directions and magnitudes of stresses applied to the sediment. In addition, they have the advantage of recording a single, time-averaged stress field. Paleopiezometric inversion methods were therefore developed in the 20th century. They are applied to networks of meso- and micro-structures (*i.e.* faults, fractures, stylolites, calcite twins) which record deformations linked to contraction in foreland basins or to extensive processes. Ultimately, they allow to estimate and characterize the magnitude and orientation of the stresses generated in these different contexts, and to reconstruct their distribution over long-time scales. Magnitudes and orientations returned by these studies are averaged in space and time (*e.g.*, Lacombe, 2007).

Many palaeopiezometers are used to reconstruct the succession of past stresses in various tectonic settings: their initiation is related to a stress tensor with three orthogonal principal components (σ_1 , σ_2 , σ_3) characterized by their magnitude and orientation ($\sigma_1 > \sigma_2 > \sigma_3$). The reconstruction of the real palaeostress tensor therefore requires the quantification of six parameters: (i) the orientation of the principal stresses (σ_1 , σ_2 , σ_3); (ii) the value of the associated differentials ($\sigma_1 - \sigma_3$) and ($\sigma_2 - \sigma_3$); (iii) the normal stress, related to the effect of isotropic pressure and fluid pressure. Paleopiezometric inversion methods, and more particularly the inversion of calcite twins (Lacombe *et al.*, 2007), do not consider the effect of this normal stress. They only allow the characterization of a so-called 'deviatoric' stress tensor, without giving access to its isotropic component. As this isotropic component help to estimate the global magnitude of stress, the complete tensor recorded during deformation cannot be deduced from calcite twinning inversions (Lacombe *et al.*, 2007; Parlangeau, 2017; Parlangeau *et al.*, 2018, 2019). The analysis of sedimentary thicknesses and the study of the associated mechanics is classically used to estimate the global magnitude of the stresses. Access to the complete stress tensor, and thus to its isotropic component, implies the use of complementary methods based on fault striation analysis and rock mechanics laws to determine the missing parameter (*i.e.* the value of one of the main stresses, or a complementary relation linking the magnitudes of these three stresses).

Some palaeopiezometers are applicable in FTB and sedimentary basins. They are calibrated in the diagenetic domain (P,T), and give the absolute or differential magnitude of the principal stresses (Beaudoin & Lacombe, 2018). The inversion of calcite twins (Etchecopar, 1984), as well as a second recent method of inversion of stylolite roughness property (Schmittbuhl *et al.*, 2004), satisfy these criteria and allow estimation of principal stress magnitudes. Calcite twins and stylolites have in common to be formed during early deformation, *i.e.* under low stress differentials. They are therefore good outcrop markers of these early deformation. But, whereas calcite twins, micro-structures characterized by their thickness, average the orientations and magnitudes of the stresses in space and time, the stylolite alone records these parameters at a defined moment, corresponding to the cessation of its growth. This raises the question of the accuracy of the stress magnitudes recorded when using these two methodologies.

Paleopiezometric methods have several contributions in the study and reconstruction of past stresses within geological systems:

- (i) quantification of physical parameters of rock, such as the Young modulus. Otherwise known as the modulus of elasticity, this physical parameter is defined as the constant relating the tensile/compressive stress and the onset of strain of an isotropic elastic material, by Hooke's law: $\sigma = E \times \varepsilon$ (1.1), with σ the stress (in Pa), E the Young modulus (in Pa), and ε the relative elongation (dimensionless). An example of Young modulus estimation by paleopiezometric inversion methods was given by the work of Ebner *et al.* (2009), applying a series of inversions on bedding-parallel sedimentary stylolites (BPS) collected in the Cirque de Navacelle. This paleopiezometric inversion method, developed in the following sections,

links Young modulus E and principal stress in an inversely proportional relationship. The other physical parameters involved (*e.g.* solid-fluid interfacial energy, Poisson's ratio) being known, and the inversions allowing to estimate the vertical principal stresses, the inversions allow the estimation of a Young modulus of 15 GPa for these Jurassic limestones.

- (ii) in case of sedimentary stylolites, the use of paleopiezometric inversion provide the quantification of vertical stress experienced by strata during burial, prior contraction and/or during exhumation (*e.g.* Beaudoin *et al.*, 2019, 2020b). Burial depths reached by the strata can be deduced from vertical stresses to which these inversions give access.
- (iii) paleopiezometry of calcite twins and of tectonic stylolites are two complementary methods to assess the orientations and magnitudes of horizontal stresses (*e.g.* Beaudoin *et al.*, 2016, 2020b). They provide the reconstruction of the three principal main stresses orientation, as well as differential stress magnitudes experienced by sediments.

Paleopiezometry of stylolite roughness is at the core of this thesis. The remainder of this chapter aims to introduce this paleopiezometric method by presenting the basics and fundamentals, and then to detail the applicative aspect.

2- Focus on stylolite paleopiezometry

2.1- Stylolites as paleopiezometers: definition, classifications, and growth mode

Stylolites are pressure-solution figures frequently observed in sedimentary rocks (Figure 1.7). This compaction mechanism includes a set of dissolution-recrystallization processes carried out under stress in the upper part of the crust. Observed at various scales (grains, veins, bed interfaces), the elementary process of these pressure-solution mechanisms was mainly performed at the grain scale (Zhang, 2010). In carbonate rocks, compaction related to pressure-solution prevails over mechanical compaction (Croizé *et al.*, 2010), the latter often inhibited by rapid cementation events. Other processes dominate diagenesis, not related to pressure-solution processes, *e.g.* grain crushing and plasticity, pore collapse (Wong & Baud, 1999; Croizé *et al.*, 2010). Nevertheless, the preponderance of these processes also depends on the pressure-temperature conditions of carbonate reservoirs. These conditions (P,T) being often too low to promote these compaction processes, pressure-solution generally dominates the diagenesis of carbonate rocks (Zhang, 2010).

Stylolites are generally filled with insoluble materials such as clay particles, oxides, and organic matter (Heald, 1955; Tada & Siever, 2003; Harris, 2006). Some authors agree in defining them as local barriers to fluid flow (Koehn *et al.*, 2016), able to (i) concentrate impermeable materials and thus form a barrier, (ii) intensify sealing properties of the strata, and (iii) accentuate the effect of existing barriers. Their differential permeability permits the circulation of fluids along the flanks of stylolite teeth without crossing the interface, and thus causes (i) the formation of dissolution holes, probably as the consequence of the lixiviation fluids localized along the teeth, (ii) the existence of veins, always localized on the flanks of the stylolite teeth.

Sometimes, these rough interfaces interact with other meso- and microstructures such as cracks and veins (Rispoli, 1981; Andre *et al.*, 2010), or compaction figures such as deformation and compaction bands (Tondi *et al.*, 2006). This strong interaction between pressure-solution and compaction figures is notably observed in the Majella carbonates (Italy), where compaction bands and pressure-solution veins developed parallel to bedding (Rustichelli *et al.*, 2012).

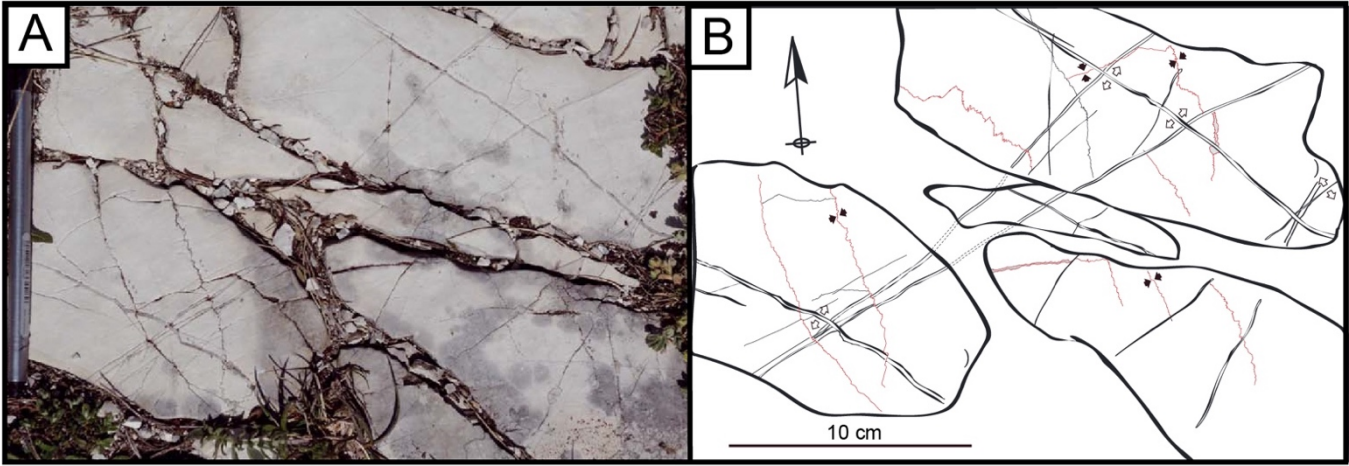


Figure 1.7- Stylolites observed at outcrop in platform carbonates (Monte Nero, Apennines, Italy). Stylolites are represented by red lines; modified from Beaudoin *et al.* (2016)

Numerous classifications and terminologies result from observation and studies of stylolites based on the tectonic context related to their formation, their morphology, and their growth mode and process.

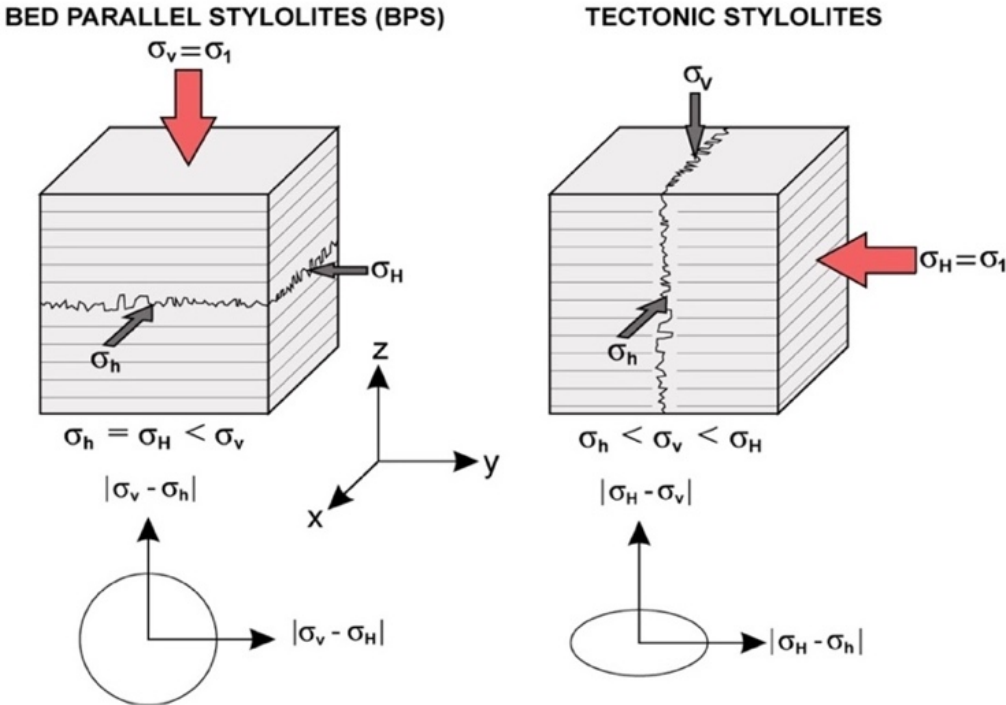


Figure 1.8- Schematic representation of sedimentary and tectonic stylolites; modified from Ebner *et al.* (2010b). Principal stress σ_1 is represented in red.

In most cases, stylolites grow perpendicular to the maximum stress applied during their growth (σ_1) (Koehn *et al.*, 2007) (Figure 1.8). Two major types of stylolites are discriminated depending on the nature of the stress: (i) sedimentary stylolites, formed under the weight of the sedimentary column

during burial preceding the first deformation generated by contraction in foreland basins. Sedimentary stylolites are sometimes oblique to the layers, when burial is post tilting; (ii) tectonic stylolites, related to horizontal contraction. Some bed-parallel stylolites may be tectonic in origin, when they are formed in the vicinity of a normal fault and related to displacement of the latter, as well as formed during the LSFT and thus necessarily developed parallel to the strata. Nevertheless, if the stylolite developed along a preferential plane such as a bedding or a crack, the orthogonality between the principal stress and the mean plane of the stylolite is no longer observed (Stockdale, 1922). In this case, the term used is slickolites and then defined a stylolite which mean plane is not perpendicular to σ_1 but subparallel to the tooth edge (Ebner *et al.*, 2010b).

A second typology, presented in Figure 1.9, classified stylolites into six categories according to their morphology and the amplitude of their teeth (Semeniuk & Logan, 1976).

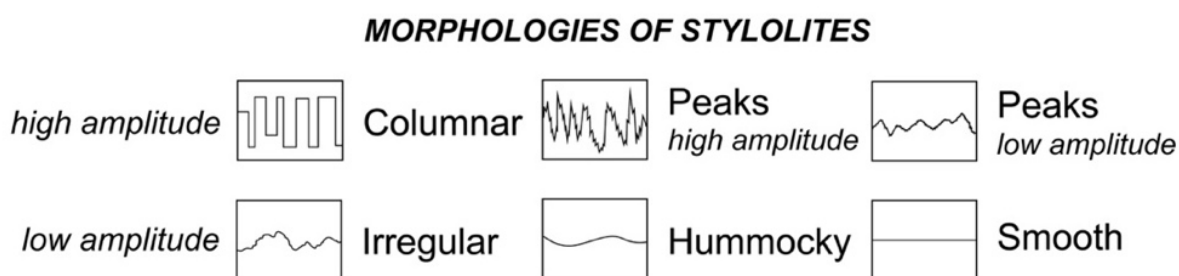
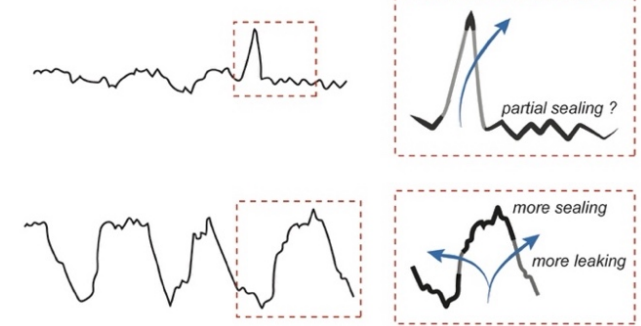
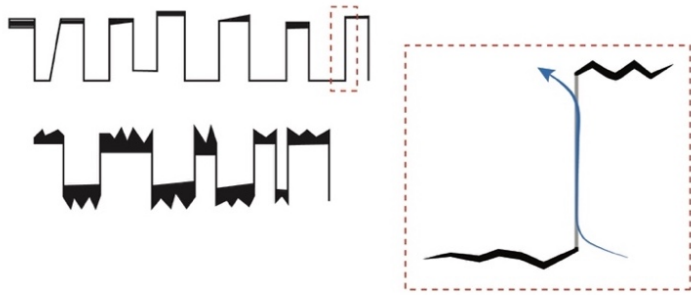


Figure 1.9- Classification of stylolites according to morphology and tooth amplitude, modified from Semeniuk & Logan (1976).

A new classification was established based on numerical simulations and studies of natural stylolites identified within the Permian Zechstein Basin gas reservoir in northern Germany (Koehn *et al.*, 2016). Four classes are discriminated based on the classification of Park & Schot (1968), without considering interconnections between stylolites (Figure 1.10). The first class, called rectangular layer type, groups together the columnar stylolites, formed by large, juxtaposed columns, rough on the plateaus (Figure 1.10). Their growth is linear. The extremities of the teeth are impermeable and thus form a barrier to fluid flow, promoting its circulation along the flanks (Figure 1.10). This type of stylolite is thus characterized by strong permeability anisotropy (Koehn *et al.*, 2016). The second category includes another type of columnar stylolite, with linear growth but variable roughness: seismogram pinning (Figure 1.10). Two cases can be distinguished in terms of permeability: (i) if layer residues are preserved at the teeth, the permeability behaviour will be the same as for the rectangular layer type, *i.e.*, a strongly anisotropic permeability; (ii) otherwise, the permeability varies with the nature and quantity of the material. So, if the material is tight and the surface not very rough, the stylolite is a mostly impermeable barrier, only porous at the large teeth (Koehn *et al.*, 2016). A non-columnar type of stylolite is also defined: the suture and sharp peak (Figure 1.10). Their growth is non-linear. The last class, the simple wave-like type, consists of sparsely roughened stylolites with an undulated morphology compared to a wave (Figure 1.10). They form an tight barrier when impermeable materials are collected (Koehn *et al.*, 2016).

RECTANGULAR LAYER-TYPE WITH RESIDUE LAYER

SUTURE AND SHARP PEAK TYPE



SEISMOGRAM PINNING TYPE WITH A VERY VARIABLE ROUGHNESS

SIMPLE WAVE-LIKE TYPE

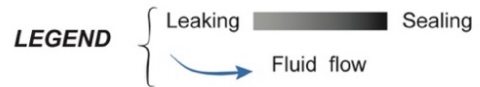
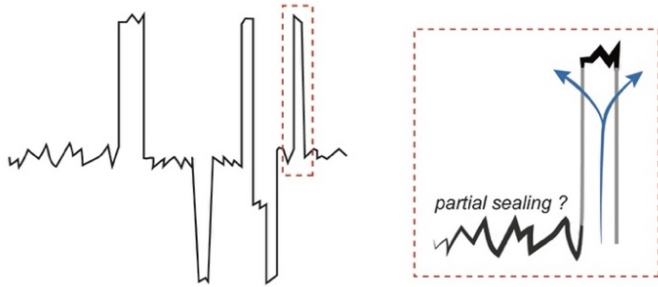


Figure 1.10- Morphological classification of stylolites based on the work of Park & Schot (1968) and numerical simulations, modified from Koehn *et al.* (2016). 4 classes of stylolites are discriminated: 1) rectangular layer type, 2) seismogram pinning type, 3) suture and sharp peak type, 4) simple wave-like type.

Other factors impact and constrain the morphology of stylolites: the lithology of the rocks, and more particularly that of carbonates, as well as the clay content. Notably, referring to Dunham's classification (Dunham, 1962), serrated morphologies are observed more in packstones, grainstones and boundstones than in finer limestones (mudstones to wackestones) (Ebner *et al.*, 2009b).

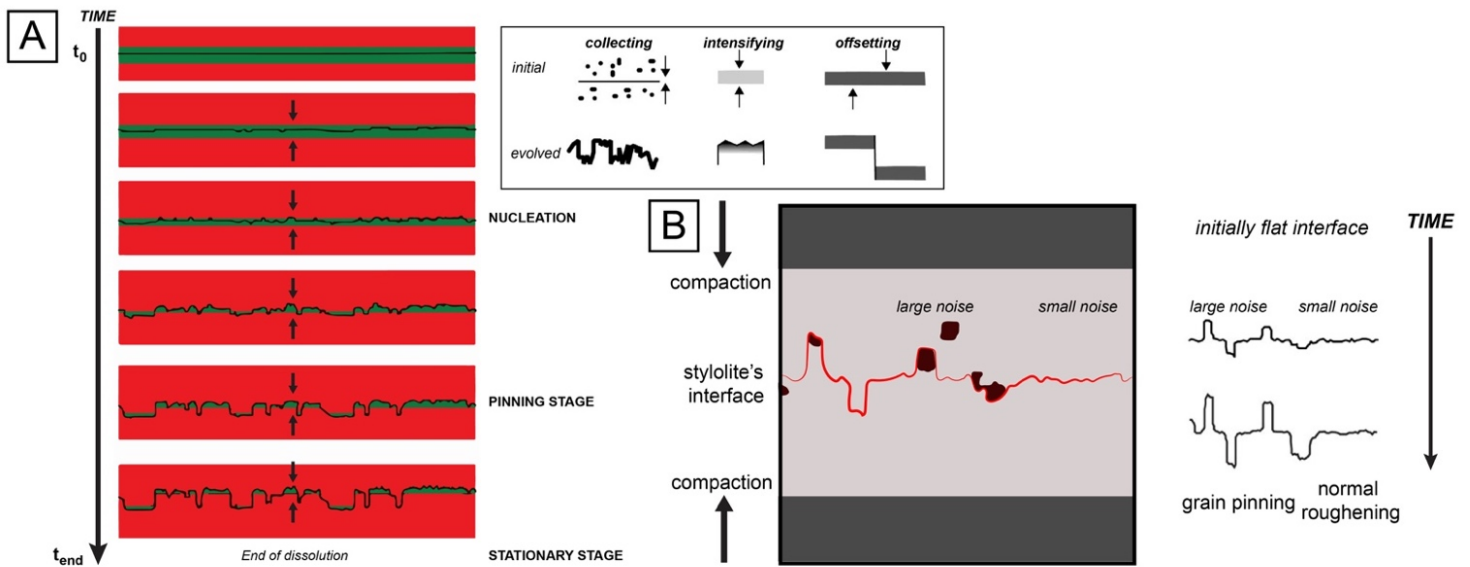


Figure 1.11- Stylolite growth model and influence of roughness, modified from Koehn *et al.* (2016).

Stylolite growth (differentiated from lateral propagation) is divided into three successive phases (Koehn *et al.*, 2016) (Figure 1.11). First, roughness is initiated in a slow and nonlinear growth pattern: this is the nucleation stage (Figure 1.11). The teeth of stylolites develop during the second phase of growth, called pinning stage. It is generally associated with a phenomenon of punching (or pinning),

explained according to the models by the existence of instabilities or by a resistance of some particles to dissolution at the stylolite interface, becoming rough (Figure 1.11). At this stage, growth is rapid and linear. Growth ends when the dissolution process was completed. The stylolite no longer grows and reaches a stationary stage (Figure 1.11). Two models explain the processes that initiate the roughness development. The first one, called instability concept, links the existence of instabilities and the initiation of roughness. In contrast, the heterogeneity concept is based on the idea that the roughness of stylolites is the consequence of heterogeneities in the sediment (Figure 1.11). In this second model, stresses stabilize the system and do not generate any instability. It was often used for numerical simulations, aiming to generate synthetic surfaces of orders of magnitude similar to those of natural stylolites (Renard *et al.*, 2004; Schmittbuhl *et al.*, 2004; Brouste *et al.*, 2007; Koehn *et al.*, 2007; Ebner *et al.*, 2009b). Koehn *et al.* (2007) gave the example of pinning particles as potential heterogeneities within layers, where the pinning process is associated with slow dissolution of particle(s) located on one side of the stylolite interface, such that only the other side dissolves (Koehn *et al.*, 2016). According to this definition, tooth growth is downward if these pinning particles arrive from the top of the interface, and upward if they arrive from the bottom. In carbonates, the most frequent pinning particles are quartz grains and clay particles (Ebner *et al.*, 2010b). Their main characteristic is that they differ from the surrounding sediment in strength and/or dissolution kinetics, and thus promote the initiation of stylolite roughness during pressure-solution processes. The indentation of quartz grains in clay layers has a notable impact on the morphology of the stylolite in formation and favours the initiation of large columns and thus the columnar type. This model of stylolitization, validated by Ebner *et al.* (2010b) at various scales in carbonates, nevertheless implies that the heterogeneities identified in the matrix are identical to those present along the stylolitic interface. Other types of heterogeneities thus exist in non-carbonate lithologies. In addition, the magnitude of roughness varies with scale (Koehn *et al.*, 2016). At small scales, heterogeneity is related to the effect of a single pinning particle. Pinning impacts both sides of the stylolite interface, and elastic and surface energies are sufficient to dissolve the particles. The effect of heterogeneities is reduced, and the roughness of a lower amplitude (Figure 1.11B). On the other hand, the large-grain pinning observed on a large scale increases the amplitude of the roughness (Figure 1.11); the size of the teeth only depends on the time taken by the grain to reach the stylolite and its dissolution kinetics.

As a synthesis, Figure 1.12 summarizes main characteristics stated and described in the previous sections. Physical characteristics, *i.e.* roughness, amplitude, compaction and spacing, are illustrated in order to highlight their characteristics and differences. The three main types of morphologies are also represented, *i.e.* columnar, peaks and simple wave-like type.

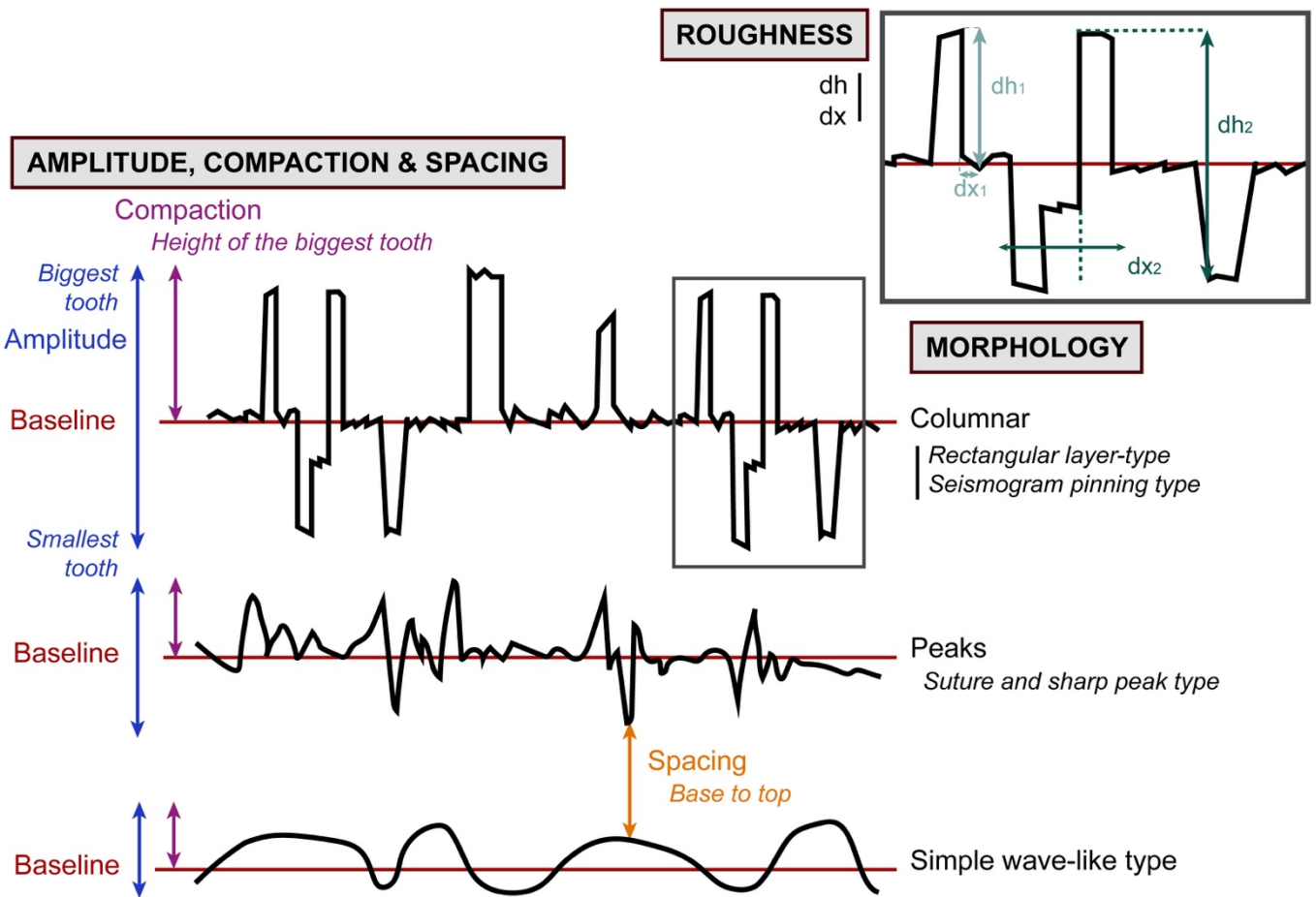


Figure 1.12- Summary of physical and morphological characteristics of stylolites. Notions of roughness, amplitude, compaction and spacing are defined on the middle and upper parts of the figure. Morphologies are also redrawn and detailed on the right-hand side.

2.2- History and principles of the inversion method

Stylolites are the subject of numerous studies that lead to the numerical and analytical models that are known and accepted today.

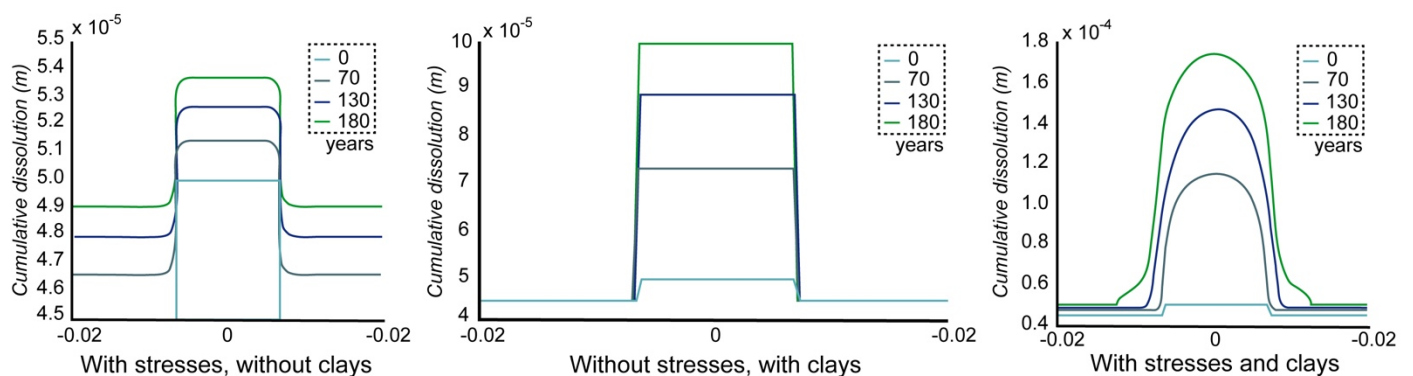


Figure 1.13- Simulation results for a 14 mm linear fault, i.e., between -7 and +7 mm with the Spring Network Model; modified from Rolland (2013) and Aharonov & Katsman (2009). These curves represent cumulative dissolution for different time periods in three configurations (i) under stress and no clay; (ii) under no stress with clay; (iii) under stress and clay. For the same time interval, the cumulative dissolution is up to doubled in the presence of clay, whether a stress is applied or not.

The study of the effect of clay particles on pressure-solution processes by numerical simulations (Aharonov & Katsman, 2009) demonstrated the influence of the presence of clay on pressure-dissolution mechanisms: dissolution phenomena are amplified and stylolites propagate if stresses are applied. In

this model, stylolite growth was studied with the Spring Network Model, starting from a linear defect, in an elastic medium where clay is uniformly distributed and represents 1.5% of the volume fraction (Figure 1.13).

The development of stylolite roughness from an initial preferential surface (called anti-crack), in the absence of clay, was also numerically simulated (Koehn *et al.*, 2007). The prerequisites for this study are the basics of molecular dynamics, and especially the one that considers the dissolution rate as dependent on the local free energy (itself varying according to the applied stress and the surface energy). Chemical compaction is then expressed using the following proportionality law (Koehn *et al.*, 2007; Ebner *et al.*, 2009a):

$$D = kV(1 - e^{-\frac{(\Delta\Psi + \Delta\sigma_n)V}{RT}}) \quad (1.2)$$

where D is the dissolution rate (m.s⁻¹); k the dissolution constant rate (mol.m⁻².s⁻¹); V the molecular volume of the solid (m³.mol⁻¹); R the molar gaz constant (8.314 J.mol⁻¹. °K⁻¹); T the temperature (°K); ΔΨ variations of Helmholtz free energy upon dissolution of a solid element (J.m⁻³), with Helmholtz free energy accounting for elastic and surface energy variations; Δσ_n the normal stress gradients along the interface.

Two scaling regimes are identified: (i) a small-scale regime, in which the surface energy is dominant and the roughness strongly fluctuating; (ii) a large-scale regime, in which the elastic energy predominates. Subsequent numerical simulations, modelling stylolites, demonstrate that the imposed stress would largely impact the cross-over length located at the interface of these two regimes (Figure 1.14). Small-scale analyses, coupled with a detailed study of microstructures, complete this work (Ebner *et al.*, 2009b, 2010b). They allow to characterize the disorder observed at small scale (in terms of nature and structure), its impact on the dissolution of the grains, and to understand its modes of interaction with the grains present around the stylolite.

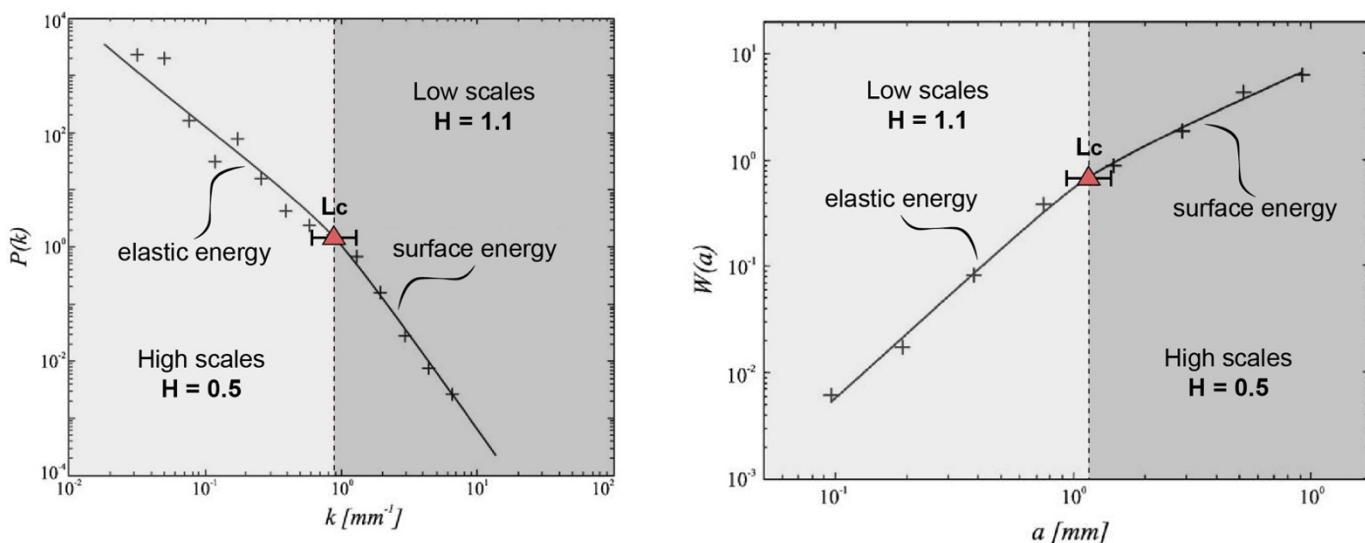


Figure 1.14- Representation of the two scaling regimes on the Fourier Power Spectrum (FPS) and Average Wavelet Coefficients (AWC), associated with Hurst coefficients and separated by a characteristic cross-over length; modified from Ebner *et al.* (2008).

In addition, these localized pressure-solution interfaces in the rock are sometimes compared to other geological objects such as compaction bands (*e.g.*; Baud *et al.*, 2004; Katsman *et al.*, 2006;) which are compacted subperpendicular to the direction of maximum compression and often observed in sandstones of intermediate porosity (13 to 28%) (Baud *et al.*, 2004). Based on this comparison, stylolites and compaction bands were modelled as anti-cracks (Fletcher & Pollard, 1981; Rispoli, 1981; Mollema & Antonellini, 1996). As a result of these studies, Fletcher & Pollard (1981) observed differential dissolution within the same stylolite, *i.e.* less marked at the ends than in the central part. Then, they made an analogy between the propagation of stylolites and that of mode I (extensional) fractures of this elliptical dissolution pattern: stresses would be perpendicular to the plane of stylolite and concentrated at the ends of the teeth. Nevertheless, this analogy is challenged by some studies conducted in the 2000s, including laboratory work simulating the volume losses observed within these pressure-solution figures (Katsman *et al.*, 2006; Katsman, 2010).

2.3- Signal processing methods

Several signal analysis methods exist for the treatment of stylolite profiles. Two main methods are then used to evaluate the self-affine character of the resulting signal and to characterize the associated Hurst coefficient (Ebner *et al.*, 2009a).

The first function considered is the Fourier Power Spectrum (FPS, Renard *et al.*, 2004; Candela *et al.*, 2009), consisting of the analysis of the signal spatial frequencies to reconstruct it as a sum of cosines and sines. The modulus square of the Fourier transform (FT) of the profile or surface under consideration is calculated as a function of the wave number k_i defined as follows: $k_i = \frac{2\pi}{L_i}$ (1.3.1), where i and L represent the dimension and size of the object respectively. The resulting 1D profile or 2D surface are defined as follows:

$$FPS_{1D}(k) = \sum_{j=1}^N h(j)e^{-ik(j-1)(k-1)} \quad (1.3.2)$$

$$FPS_{2D}(k_x, k_y) = \sum_{m=1}^M \sum_{n=1}^N h(m, n)e^{-ik_x m} e^{-ik_y n} \quad (1.3.3)$$

where FPS_{1D} is the 1D profil of length N , and FPS_{2D} is the 2D surface of size $M \times N$.

To avoid the phenomenon of aliasing (*i.e.* spatial overlap) linked to the periodicity of the signal, the limit frequency relative to the spectrum, known as the Nyquist frequency, is then calculated using the relation $f_{NY} = \frac{1}{2L}$ (1.3.4), where L is the size of the object under study. In the case of objects with self-affine geometry such as stylolites, the frequency spectrum becomes :

$$FPS(k) \sim k^{-(1+2H)} \quad (1.3.5)$$

In this configuration, the power spectrum $FPS(k)$ is a function of k , and the use of a logarithmic scale results in a linear, self-affine function, whose slope p depends on the Hurst coefficient (Renard *et al.*, 2004; Schmittbuhl *et al.*, 2004), with $p = -(1+2H)$ (1.3.6).

The second signal processing method used is the Average Wavelet Coefficient (AWC, Simonsen *et al.*, 1998; Renard *et al.*, 2004; Candela *et al.*, 2009), consisting of a decomposition of the 1D signal into wavelets whose amplitudes depend on the position and scale of study. The mathematical basis for this method is derived from Simonsen *et al.* (1998). The signal is reconstructed as a wavelet sum from a reference wavelet ψ translated, expanded and compared to the signal by sliding window. The wavelet transform $W_{a,b}$ considering a 1D profile h is defined as follows:

$$W_{a,b} = \frac{1}{\sqrt{a}} \int_{-\infty}^{+\infty} \psi\left(\frac{x-b}{a}\right) |h(x)| dx \quad (1.4.1)$$

where ψ is the basic wavelet (Daubechies wavelet of order 12), parameterized by $a > 0$ (dilatation parameter) and $-\infty < b < +\infty$ (translation parameter), and h is the original single-valued function. For each length scale a , the resulting wavelet coefficients are averaged over the parameter b , according to the relation $W_a = \langle W_{a,b} \rangle_b$ (1.4.2), simplified as follows for objects with self-affine geometry: $W[h(ax)]_{a,b} = a^H W_{a,b}$ (1.4.3). Thus, for a self-affine input signal, relation 1.4.3 becomes:

$$W(a) \sim a^{H+\frac{1}{2}} \quad (1.4.4)$$

where $W(a)$ is the average wavelet coefficient. The linear regression is performed by representing $W(a)$ as a function of a on a logarithmic scale, the slope thus depending on the Hurst coefficient (Ebner *et al.*, 2009a), with $p = H + \frac{1}{2}$ (1.4.5)

Several other statistical methods exist for the characterization of roughness at various spatial wavelengths:

- The Root-Mean-Square Correlation (RMS): along the stylolitic profile, calculating the square root of the average of the squared heights $h(x)$ over sliding windows δx , whose size varies from the resolution to the maximum length of the system. The self-affinity property of the profile is expressed as follows: $\langle \text{RMS}(\delta x) \rangle \sim \delta x^H$ (1.5)
- The Maximum-Minimum Height Difference (MM): computation of the height difference $h(\delta x)$ between the minimum and maximum heights of the stylolitic profile over sliding windows of widths δx , and averaged over each window width. The self-affinity of the signal gives the relation: $\langle h(\delta x) \rangle \sim \delta x^H$ (1.6)
- The suture functions (Santucci *et al.*, 2007; Candela *et al.*, 2009): calculation of the k^{th} root of the k^{th} moment of the height increment $|\Delta(h)| = |h(x+\delta x) - h(x)|$ (1.7.1). Once averaged over x , and for a self-affine function, the k -order suture functions are expressed as a power law proportional to the roughness exponent H (Equation 1.7.2): $\langle C_k(\delta x) \rangle_x \sim \delta x^H$ (1.7.2)
- The height correlation function (COR, Candela *et al.*, 2009): second-order suture function, calculated by increments of the heights and obeying the power law defined in Equation 1.8 for self-affine functions:

$$C(\delta x) = [|\Delta h(x)|^2]^{\frac{1}{2}} \quad (1.8)$$

Tests of these all methods conducted by Candela *et al.* (2009) on anisotropic synthetic self-affine surfaces demonstrate a better determination of Hurst coefficients by applying the FPS and AWC whatever the direction studied. Their use is therefore favored in the framework.

2.4- Application to sedimentary stylolites: Sedimentary Stylolites Roughness Inversion Technique (SRIT)

The analytical model used for sedimentary stylolites is detailed below.

The dissolution rate at the fluid-solid interface considers several parameters, and particularly the local perturbations related to surface irregularities.

$$\partial_t z = \underbrace{\partial_{xx} z}_{\text{Surface tension} \leftrightarrow \text{effects induced by the curvature of the surface}} - \frac{1}{L_c} \underbrace{\int_{-\infty}^{+\infty} \frac{\partial_y z}{x-y} dy}_{\text{Elastic interactions} \leftrightarrow \text{surface deformation}} + \underbrace{\eta(x, z(x))}_{\text{Frozen noise} \leftrightarrow \text{disorder present in the host rock; independent of time}} \quad (1.9)$$

The dissolution is thus a function of three major components: (i) surface tension, considering effects induced by the surface curvature; (ii) elastic interactions, witnesses of the surface deformation; (iii) frozen noise, independent of time, which transcribes the disorder present in the host rock. It also depends on a quantity called the cross-over length (L_c), which separates two large scale regimes, and is calculated using relation 1.10 :

$$L_c = \frac{\gamma E}{\beta \sigma_m \sigma_d} \quad (1.10)$$

β being a dimensionless constant (Equation 1.11), E the Young's modulus, γ the surface tension, σ_m the average stress and σ_d the differential stress.

$$\beta = \frac{\nu(1-2\nu)}{\Pi} \quad (1.11)$$

These relationships, and in particular Equation 1.10, thus illustrate the two major physical processes that predominate in the stylolite growth. The first of these physical processes is surface tension, which is dominant at small scales. In this model, which ultimately corresponds to the Edwards-Wilkinson model (Edwards & Wilkinson, 1982) associated with a notion of disorder, elastic interactions are negligible. The surface roughness, associated with a coefficient called the Hurst coefficient, is estimated to be $H \approx 1$ for small scales (Schmittbuhl *et al.*, 2004). In contrast, the surface tension is negligible in front of the elastic interactions at large scales (*i.e.*, $l \gg L_c$). This model is equivalent to the propagation of an elastic line, or a fracture front generated in mode I, in an unordered medium. Finally, the combination of these two scaling laws (and associated models) yields a resulting model that predicts the growth of a self-affine surface, which roughness varies depending on whether the scale is less than or greater than the cross-over length.

Studies conducted on natural stylolites sampled in open quarries give similar results to those obtained from numerical simulations and predictive models (Renard *et al.*, 2004; Schmittbuhl *et al.*, 2004). The roughness values retained from this work are $H = 1.1$ for small scales and $H = 0.5$ for large scales, as well as a cross-over length of the order of a millimeter. These values are accepted as quasi-

universal for sedimentary stylolites, as they are defined as independent of rock lithology and location (Renard *et al.*, 2004; Schmittbuhl *et al.*, 2004; Brouste *et al.*, 2007; Ebner *et al.*, 2009a)

The application of this model to sedimentary stylolites, parallel to the bedding (BPS) in horizontal strata (Figure 1.8), is based on three main assumptions: (i) the maximum principal stress is vertical; (ii) horizontal stresses are isotropic and in the plane of the stylolite ($\sigma_h = \sigma_H$); (iii) deformation is uniaxial. No horizontal displacement is thus realized, and the stylolites would initiate during the first phase of basin formation. The vertical stresses are then expressed by the relations:

$$\sigma_h = \sigma_H = \frac{\nu}{1-\nu} \sigma_v \quad (1.12.1) \quad \sigma_v^2 = \frac{\gamma E}{\alpha \beta L_c} \quad (1.12.2)$$

ν being the Poisson's ratio, α a dimensionless parameter depending on ν . These simplified formulas give access to the vertical stress, *i.e.* the lithostatic stress applied to the rock during stylolite development.

Definitions, theories, and concepts associated with palaeopiezometric methods, and more specifically with palaeopiezometry applied to BPS, have been detailed in this section. The contributions of this methodology to the understanding of geological systems, and more particularly of foreland basins and FTBs, motivate its use in this thesis. Beyond the theoretical aspect, the following section aims to present the applicative aspect of the different methods used to answer the expectations and questions raised during this study.

IV- RECONSTRUCTION OF THE MESO-STRUCTURAL PATTERN AND BURIAL: METHODS

1- *Understanding of the fracture network*

1.1- *Reconstruction of fracture sequence*

Fractures are very present in carbonate rocks and are essential indicators of deformation on a meso-structural scale. In order to relate these meso-scale structures to regional tectonic events, fractures that share similar orientations, mode of deformation and relative chronology with respect to other sets of fracture can be grouped. Considering a study area, the first step consists in measuring fracture orientations. Main orientations of are then inferred by statistical tests performed on the field data, using tools for processing and statistical representation of fracturing data, *e.g.* Stereonet (Allmendinger *et al.*, 2013; Cardozo & Allmendinger, 2013) and Openstereo (Grohmann & Campanha, 2010) softwares. Orientation data are first projected on Schmidt stereodiagrams (lower hemisphere), in the current attitude of the strata (raw) and after unfolding (unfolded), *i.e.*, corrected for stratification dip by rotating the dip angle of the strata back to horizontal around a horizontal axis (normally corresponding to the direction of the fold, locally to the direction of the strata). The Fisher statistical test is then performed on these folded and unfolded datasets, applied to the projections of the poles of the fracture planes. Then, stereodiagrams giving the planes and the density of the poles are generated as output for these folded

and unfolded datasets. Main orientations are then discriminated by considering the areas of highest pole density (Figure 1.15).

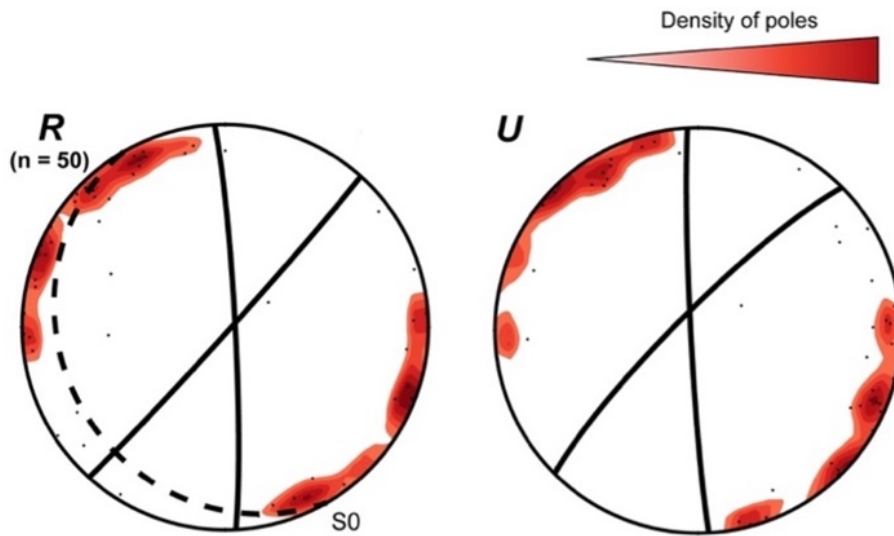


Figure 1.15- Example of stereodiagrams obtained after statistical processing of the field data (Stereonet), in current/rotated (R) and unrotated (U) positions. The dotted lines represent the stratification, and the color scale the density of poles. In the present case, the 50 measurements carried out and processed (whose planes have not been represented for reasons of readability) are used to discriminate two main orientations of fractures, whose average planes are represented by the solid black lines.

The second step is the characterization of the deformation mode, *e.g.* opening, shearing, contraction, defined through thin sections observed using an optical microscope. In case of veins, several observations help to characterize the opening kinematics. The first is to look for evidence of offset of one or more ante-fracture features (*e.g.* veins, pressure-solution figures, fossils, *etc.*), with this offset giving clues to the opening kinematics (Bons *et al.*, 2012) (Figure 1.5). A second method is the observation and characterization of the shape and/or possible offsets of the fracture edges, also indicative of the vein opening direction. Analysis of vein textures gives partial or total information on the kinematics of opening, certain textures allowing to define the direction of mineral growth, and/or the characteristic of opening mechanism of the vein studied (Figure 1.3).

Then chronological relationships between the main fractures identified according to their orientation and their deformation mode are defined, to group them in sets. Once defined, the idea is to position these sets in a fracture sequence, and then related to deformation. Several methods help to define the relative chronology of fractures. To define if a fracture pre- or post-dates another one, their relative chronology can be defined by studying their structural relationship at meso- and micro-scale. These chronological relationships are thus deduced from criteria of overlap, abutment, and offset/opening, described below. Another method is to determine if fractures pre- or post-date folding, such as the fold test inspired by paleomagnetic methods (Graham, 1949): if the fractures are better adjusted in untitled position than in the current state, then the pre-tilt origin of these fractures is preferred. Although this fold test is sufficient, Andersonian theory can also be used to determine these chronologies in cases where Anderson's conditions are met.

Finally, fracture sets are then defined considering (1) their common orientations (2) their deformation mode and (3) their relative chronologies. The characterization of fracture sets provides the definition of fracture sequence characteristic of the area, then related to a deformation sequence related to the area studied. Once the sets have been defined, geochemical analyses can be performed to access to the mineralogical composition, temperatures, and/or ages associated with the fractures studied.

1.2- U-Pb absolute radiochronology

In this work, U-Pb dates are used as a support for some of the fracture studies carried out. The broad outlines are given, without going into the details of the method.

U-Pb dating of carbonates by laser ablation inductively coupled plasma mass spectrometry (LA-ICPMS) is an absolute dating method for dating carbonate deposits (Drost *et al.*, 2018), speleothems (Woodhead & Hergt, 2001), as well as reservoir porosity-filling cements (*e.g.*, Li *et al.*, 2014; Godeau *et al.*, 2018). In addition, its many advantages also explains its democratization in research community: (i) a high spatial resolution, allowing the detection and exploitation of uranium heterogeneities at the submillimeter scale, and the quantification of the initial lead concentration; (ii) the ability of ablation cells to host and analyze several samples simultaneously, and therefore to multiply the dating performed (*i.e.*, several samples per day); (iii) the correction of U/Pb ratio shifts related to matrix, thanks to the recent characterization of carbonate standards (Roberts *et al.*, 2020). This method is based on isotopic maps constructed for elements of interest for dating (*i.e.*, U, Pb, Th) from ablation along lines, as well as calculation of ages from pixel values (Drost *et al.*, 2018; Hoareau *et al.*, 2021a; Motte *et al.*, 2021). Two main types of mapping are performed in these analyses. The first type is related to the heterogeneity of the carbonate lithologies, and implies a preliminary step of petrographic and geochemical characterization of the samples in order to optimize the dating process (Roberts *et al.*, 2020). One of the methods used is the initial screening of samples by LAICP-MS. It provides the mapping of samples in terms of concentrations of diagnostic trace elements (U, Pb, Th), and thus the location of unaltered zones rich in uranium (*i.e.*, preferential zones for obtaining precise and significant ages, Roberts *et al.*, 2020). The second type of mapping is based on point ablations with sizes between 80 and 235 μm (*e.g.*, Ring & Gerdes, 2016; Roberts & Walker, 2016; Parrish *et al.*, 2018). It enables the construction of isochrones by combining several tens of ablation craters made on the same crystal, or on adjacent crystals when they are too small (*e.g.*, micrite), to finally deduce ages with high accuracy (< 3% in the most favorable cases) (Roberts *et al.*, 2020).

1.3- Inversion of striated fault planes

Striated fault planes are also important in the characterization of associated stresses and strains. Indeed, from field analyses consisting in the measurement of several striated planes and the determination of their relative movements, the inverse method developed by Angelier (1984, 1989, 1990) allows to characterize the 4-parameter reduced stress tensor, *i.e.*, the orientation of the principal stresses σ_1 , σ_2 et σ_3 , and the ϕ ratio that describes the shape of the stress ellipsoid (Equation 1.13).

$$0 \leq \Phi = \frac{\sigma_2 \cdot \sigma_3}{\sigma_1 \cdot \sigma_3} \leq 1 \quad (1.13)$$

This method consists of a series of steps leading to the calculation of this reduced tensor, including the ϕ ratio and principal stresses (Equation 1.13), and explaining a maximum of mechanically compatible faults: (i) encoding the data in computer; (ii) applying the method of right dihedra (Angelier, 1984) to group the mechanically compatible faults. For each fault, the difference between the measured fault striation and the applied shear stress (*i.e.*, angle α and/or vector u , Figure 1.17) is reduced; (iii) application of the least squares method to each fault, for calculation of the reduced stress tensor (for details of matrix calculations, refer to Angelier, 1984).

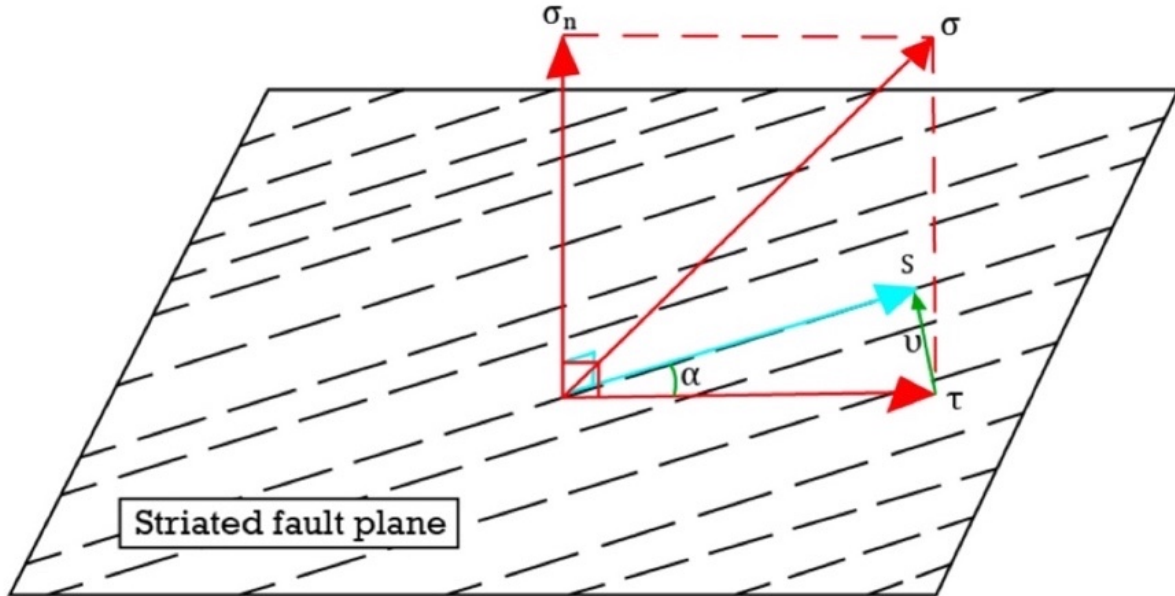


Figure 1.16- Illustration of fault measurements (blue) and tensor data calculated by Angelier's method s: orientation of the streak, σ_n : normal stress, σ : applied resultant stress, τ : shear stress, u : vector between the calculated shear stress and the streak, α : angle between these two vectors; after Beaudoin (2012), modified from Angelier (1990).

The quality of the computed tensor depends on two parameters: (i) the value of the angle α , the lower the value of α the better the quality of the tensor and (ii) the mechanical consistency of the faults. The degree of constraint applied to the computed tensor is also user-dependent: the user can choose to constrain it strongly, by separating a fault population into several subcategories. On the contrary, he can choose to increase the number of faults explained by the tensor by creating classes incorporating faults with a lower degree of compatibility, based on qualitative criteria such as chronology, and thus increase the degree of constraints applied to this tensor. In addition, the creation of fault classes and the calculation of the reduced stress tensor are automatically weighted by the program, considering the quantity of measurements and the level of confidence. Two last specificities of the program condition the final calculation of the stress tensor and the resulting interpretations: (i) for faults of the same geometry, the ϕ ratio (Equation 1.13) is not calculable; (ii) the Anderson conditions (Anderson, 1951) are not respected by the calculated tensors. The calculation is therefore performed in the current position of the strata, and the interpretation given by the user, who chooses to interpret the calculated tensor as pre- or syn-tilt, or in position observed today in outcrop.

2- Sediment burial modeling

Burial model is built from the stratigraphic and well data collected in the study area considered. Thicknesses are corrected from compaction to obtain the maximum burial depths recorded by layers. Two types of corrections are then applied, considering the effects of physical and chemical compaction.

The computer interface used to produce these burial curves is the Backstrip© software (Cardozo, 2011) and implies the input of some parameters for the modeling. The first set of parameters to be defined provides the estimation of physical compaction undergone by the strata, generated by the weight of the sedimentary column and possibly the water column, depending on the type of basin considered (Figure 1.17).

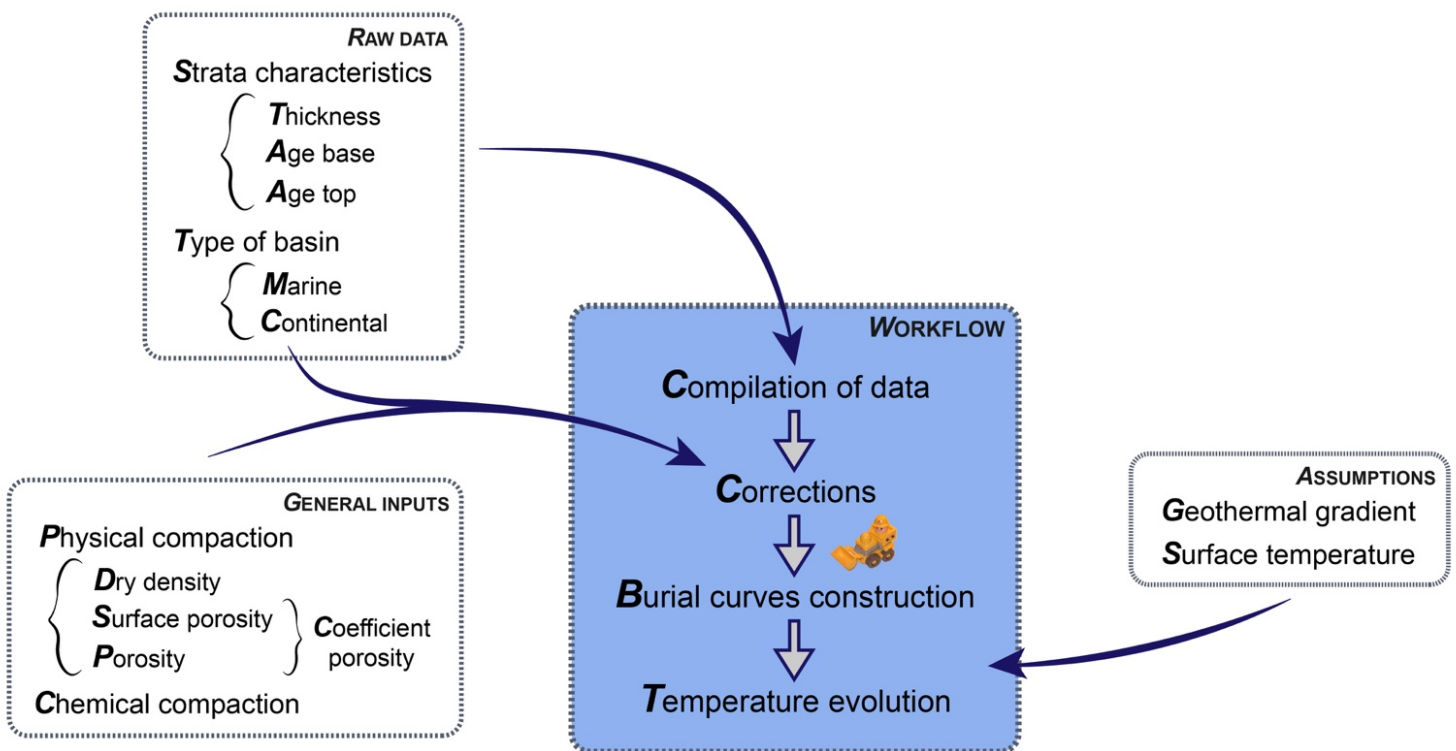


Figure 1.17- Schematic representation of the modeling steps of the burial curves. The mentioned parameters are detailed in the following paragraphs. The logo used is that of the Backstrip© software.

These parameters are defined based on bibliographic data, and in particular on the work of Allen & Allen (1990b) and Watts (2001). Thus, the dry density ρ_c is evaluated at 2.4 kg/m^3 for carbonates and 1.8 kg/m^3 for other lithologies (Manger, 1963). The porosity coefficient c is also calculated on the basis of the equations and curves of Allen & Allen (1990), Watts (2001) and Lee *et al.* (2020): the curves porosity = $f(\text{depth})$ are used to estimate the porosity and the surface porosity for each lithology considered, and to deduce then the porosity coefficient thanks to the relations :

$$\phi = \phi_0 e^{-cy} \quad (1.14.1) \quad \text{and} \quad c = -\frac{1}{y} \ln\left(\frac{\phi}{\phi_0}\right) \quad (1.14.2)$$

where ϕ is the porosity at a considered depth y , ϕ_0 the surface porosity and c the porosity coefficient. The values used are summarized in Table 1.1.

Lithology	Surface porosity ϕ_0	Porosity ϕ (y = 2 km)	Porosity coefficient (c)
Carbonates	70%	25%	0.51
Clays	62%	20%	0.57
Sandstones	45%	23%	0.34

Table 1.1 - Porosity values and associated coefficient, deduced from curves and equations of Allen & Allen (1990b) and Watts (2001)

Since the corrections for sediment and water weight differ significantly (Table 1.2), the basin type is also defined in the software (0 for a marine basin, 1 for a continental basin), so as not to bias the resulting burial curves.

	Sediment loading correction	Water loading correction
Marine	$Y = S \frac{\rho_m \cdot \rho_s}{\rho_m \cdot \rho_w}$	$Y_t = Y \cdot \Delta_{SL} \frac{\rho_w}{\rho_m \cdot \rho_w}$
Continental	$Y = S \frac{\rho_m \cdot \rho_s}{\rho_w}$	$Y_t = Y \cdot \Delta_{SL}$

Table 1.2 - Corrections associated with the type of basin considered, based on the equations of Allen & Allen (1990) and Watts (2001).

Thicknesses given by stratigraphic studies or well data (*i.e.*, the actual thicknesses of the formations) are corrected for this chemical compaction effect according to one of the above methods.

The constructed burial models are 1D models in effects related to flexural bulging of the foreland are not considered. Indeed, laws used in classical basin modelling link porosity and vertical stresses, deformation being considered as essentially driven by overburden sediments (*e.g.* Athy, 1930; Smith, 1971; Schneider *et al.*, 1996). Nevertheless, the effective horizontal stress can equal or even exceed the effective vertical stress in tectonically active basins (Zoback *et al.*, 1989). Moreover, in orogenic forelands, LPS is associated with significant damage of strata (Robion *et al.*, 2007; Tavani *et al.*, 2015), as well as with a decrease in porosity (Couzens-Schultz & Azbel, 2014) and a partial control of fluid migration (Roure *et al.*, 2005, 2010). Considering the geological context of this study, the following question arises: can the horizontal stress be neglected in this kind of models without impacting the results? This issue may be answered to some extent by the two following points:

- (i) classical 1D methods used in research and industry systematically overlook horizontal stresses (*e.g.* Petroleum System Modelling, PSM);
- (ii) modelling of the horizontal tectonic effects involves 3D modelling processes sometimes complex and using relatively specific tools. In particular, classical 1D models are coupled with geomechanical models to overcome this difficulty and to include this missing parameter in the models (*e.g.* Bruch *et al.*, 2021). They also provide a quantification of shortening rates, which are potentially overestimated due to 3D modelling complexities (Berthelon *et al.*, 2021).

These complex methodologies, which are constantly being improved, do not currently allow the impact of horizontal contraction to be estimated and modelled, and constrain the use of classic models in which only the sediment weight is considered. Therefore, the choice of neglecting the horizontal tectonic component for burial model construction seems acceptable in the context of these 1D basin models.

3- Rock properties estimation

3.1- Mechanical properties: Young modulus estimation for SRIT application

Studies of fractures and burial also involve the determination of the physical parameters of the rocks. In particular, paleopiezometric inversions imply the quantification of the Young modulus value. The method used in this work is the Schmidt rebound hammer technique, which is a non-destructive method used for the estimation of the uniaxial compressive strength and Young modulus of natural rocks (e.g. Aydin & Basu, 2005). It implies the use of a spring-loaded piston (the Schmidt hammer), pressed orthogonally against a surface of rock. The energy created by the resistance of the surface to the impact enables the piston to rebound. The distance traveled by the piston after the rebound is called the rebound value R, which is considered to be a proxy of the surface hardness (Aydin & Basu, 2005), itself used to quantify uniaxial compressive strength and Young modulus of the rock (Katz *et al.*, 2000). The sliding average of representative R values is computed. The resulting stabilized value of rebound (Figure 1.19) is used for calculation of the Young modulus, deduced from the following empiric relationship determined for sedimentary rocks (Katz *et al.*, 2000): $E = 0.00013 \times R^{3.09074}$ (1.15)

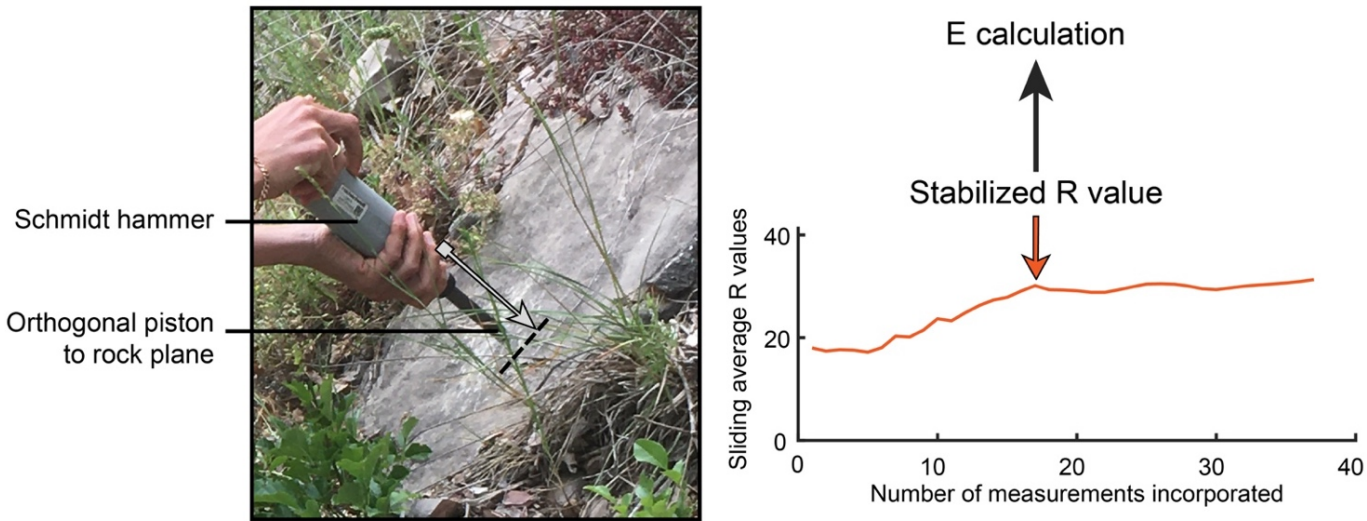


Figure 1.18- Detail of the application of Schmidt hammer method on the field, and example of results used for Young modulus calculation. Piston is pressed orthogonally against the rock surface (grey arrow). Values of sliding average R are plotted as a function of the number of measurements incorporated (orange curve), from which stabilized R value is deduced and used to compute Young modulus value with Equation 1.15

3.2- Chemical compaction estimate for burial modelling

Compaction of sediments is related to two types of phenomena: (i) pure mechanical compaction, related to the grains rearrangement during burial and (ii) mechano-chemical compaction associated

with dissolution-precipitation mechanisms and generally induced by pressure-solution. While mechanical compaction is dominant at the surface, chemical compaction predominates at depth (Schmidt & McDonald, 1979; Schneider *et al.*, 1996). Chemical compaction is therefore an important parameter when studying the burial of strata (*e.g.* Bah *et al.*, 2022). However, its exact estimation remains a delicate and questionable process for several reasons. A first element is the plurality of processes responsible for porosity loss in carbonates, namely pressure-solution creep and fluid-rock interactions (Croize *et al.*, 2013). Mesosstructures resulting from pressure-solution processes depend mainly on lithology and structural resistance, and are of various natures, such as sutured grain contacts and truncations, indentations, clay seams, and stylolites (Wanless, 1979; Buxton & Sibley, 1981). Several authors agreed that stylolites play an important role in this chemical compaction process : while Finkel & Wilkinson (1990) described local dissolution along stylolites as participating in the occlusion of porosity due to the diffusion of material into the surrounding media that it generates, Bjørlykke (2006) and Ehrenberg *et al.* (2006) closely correlated the loss of porosity by cementation with the presence of stylolites. There are therefore different methods to attempt to quantify the compaction associated with stylolites.

Classical estimation of the amount of dissolution is achieved using geochemical methods consisting of the quantification of insoluble species accumulated in dissolved zones. In particular, these methods can be used to determine the amount of dissolution associated with stylolites (Toussaint *et al.*, 2018), by comparing the quantity of insoluble species passively concentrated in stylolite seams to the initial amount of the same species in undeformed rock. In this methodology, the underlying assumption is that a dissolution process is occurring, and errors are related to spatial heterogeneities related to these insoluble species. The first possible calculation is the relative mass balance (Equation 1.16), considering the concentration of insoluble elements in the undeformed rock I_p and that related to dissolution I_e , the representative elemental volume before deformation M_0 , and assuming an initial homogeneous distribution of species: The calculation of volume variations of these insoluble elements is also a method of quantifying the amount of dissolution, but only applicable in the case where the density difference between the two parts of the rock is known (Gresens, 1967; Grant, 2005).

$$\frac{\Delta M}{\Delta M_0} = \frac{I_p}{I_e} - 1 \quad (1.16)$$

Analysis of stylolite geometry provides determination of the amount of dissolution related to stylolite development. In particular, a vein intersected by a dissolving stylolite records a displacement. The measurement of this the apparent displacement related to this dissolution effect allows the estimation of the dissolved thickness e , which is then a function of this displacement noted d_s and the angle α between the vein and the solution seam:

$$e = d_s \times \tan(\alpha) \quad (1.17)$$

Another method of quantification consists in the measurement of stylolite tooth height. The underlying assumption is that all the roughness is generated during stylolite formation, implying an

underestimation of the amount of dissolution (*i.e.* calculation of a minimal value, Toussaint *et al.*, 2018). However, several studies detailed the tests and applications of this quantification method on numerical and natural cases:

- in microdynamic simulations of stylolite roughness (Koehn *et al.*, 2007), based on the design of a 2D numerical model considering: (i) an initial flat interface representing the stylolite during the early phases of formation (*i.e.* initial “anticrack”, Fletcher & Pollard, 1981; Katsman *et al.*, 2006), where dissolution can take place and the solid can only dissolve and not precipitate (*i.e.* contact of a solid with an undersaturated fluid); (ii) all the dissolved elements along the interface instantaneously transported into the fluid outside the system; (iii) fluid of constant solute concentration. This numerical study demonstrates that roughness can be reliably and robustly modelled numerically, according to the two known roughness regimes, and strongly similar to the observed natural cases. Furthermore, it concludes that the geometry of the stylolite teeth enables to estimate the direction of the finite compaction or the main compressional stress, but that the quantification of dissolution is necessarily underestimated.
- the study of six reservoir cores in two units of the Zechstein carbonate (Koehn *et al.*, 2012) allowed the application and comparison of two methods of calculating chemical compaction, based on measurements of stylolite tooth amplitudes: (i) a first method consisting of the classical estimation of compaction, *i.e.* calculated as the sum of stylolite tooth amplitudes, yields values between 3% and 5.6%; (ii) a second, less conventional method, consisting of estimating the number of stylolites per meter and then integrating their amplitude into the compaction calculation, returns dissolution percentages between 25 and 39% (close to the initial porosity of carbonates studied of 42%, Bruns *et al.*, 2013).
- a more recent study based on numerical and natural data (Koehn *et al.*, 2022) proposed a calculation of the compaction at the stylolite through time expanding the scaling law of Ben-Itzhak *et al.* (2012).

Thus, these various methods can be used to estimate the dissolution related to stylolitization, although potentially underestimated depending on the methodology used. Nevertheless, its estimation remains necessary for the study of sediment burial in foreland contexts, and particularly for lithologies such as carbonates where pressure-solution processes frequently occur.

4- Study of vertical stresses by inversion of the roughness of sedimentary stylolites (SRIT)

4.1- Samples preparation

The first step of the data acquisition and treatment is to cut and polish samples to visualize the track of the stylolite to be analyzed. For sedimentary stylolites, a cut is made perpendicular to the stylolite plane. Then, the flat surface of the rock is scanned with a resolution of 12800 × 12800 dpi. The resulting file is an image in JPEG or TIFF format, with sufficient quality to be analyzed with image processing

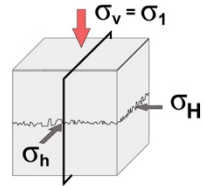
software (Gimp® or Photoshop®). Initially, the stylolite track is redrawn on a touch-sensitive graphics tablet, using the pencil tool (line size: 5), at $\times 200$ and $\times 400$ zooms for greater accuracy. The image is then converted to greyscale and exported as a JPEG file (still with a resolution of 12800 dpi), to be then numerically processed.

4.2- Stress and burial depth computation

Signal treatments previously defined, *i.e.* FPS and AWC, are applied under computer (*i.e.* Matlab®) on redrawn BPS tracks, using already existing scripts derived from the work of Ebner (2009) and Rolland (2013), and optimized during this work. They provide quantification of vertical stress recorded by sedimentary stylolites during burial under the assumption of uniaxial strain previously detailed (Figure 1.19).. This hypothesis is nevertheless verified by making two orthogonal cuts for the same stylolite. If the stylolite is anisotropic, the values returned by the inversions will be significantly different. The input parameters of the program are the L_c value previously defined, and the physico-chemical characteristics of the rocks studied. Although the methodology is applicable in other lithologies, the length scales required imply its application to carbonate-dominated lithologies in the context of this thesis work. The associated input parameters are therefore defined as follows: (i) Young modulus, or modulus of elasticity, estimated by mechanical tests carried out by the Schmidt Hammer method; (ii) Poisson's ratio (μ), between 0.2 and 0.3 and fixed for this treatment at 0.25 (Rolland *et al.*, 2014; Beaudoin *et al.*, 2016); (iii) the interfacial energy of solubility, equal to 0.32 for calcite and 0.247 for dolomites (Wright *et al.*, 2001) .

Finally, burial depth associated with vertical stress obtained is calculated using the relation $\sigma_v = \rho g z$ **(1.20)** (Figure 1.20). The following assumption is then made on the density, estimated at 2.4, and corresponding to the average density calculated for dry sandstones and carbonates. The use of this averaged value is justified by (i) the consistency of the results obtained in the previous studies which also re-inject this value for depth calculation (*e.g.* Beaudoin *et al.*, 2020b; a) and (ii) neglecting the impact of the fluid overpressure in the weight of the column in this methodology. Figure 1.20 summarizes the successive stages of this inversion methodology applied to BPS, as well as the dominant hypotheses and input parameters allowing the initiation of the computer processing stages.

SEDIMENTARY STYLOLITES



$$z = \frac{\sigma_v}{\rho g}$$

VERTICAL STRESS [Pa]

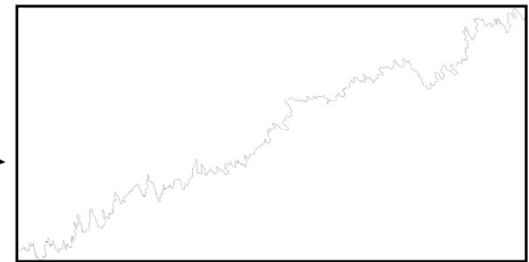
BURIAL DEPTH [m]

$$\sigma_v^2 = \frac{\gamma E}{\alpha \beta L_c} \quad \text{Uniaxial strain hypothesis}$$

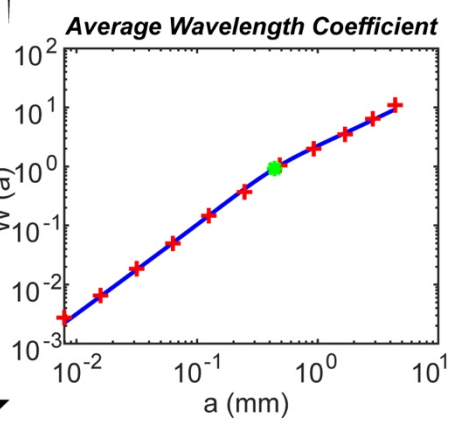
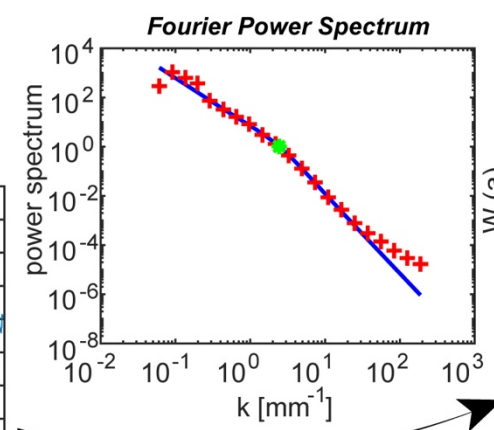
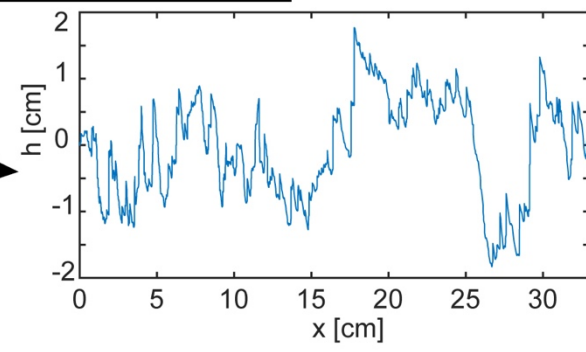
Fixed parameters depending on materials

CROSSOVER LENGTH SCALE [mm]

drawing



digitalization



signal processing
2 non-linear regressions

+ original data * Lc value [mm]
— modelled fit

Figure 1.19- Workflow the SRIT processing steps applied to BPS, including major assumptions and parameters.

To conclude, this chapter aims to define the foreland basins and FTBs associated, as well as mesostructures related to this system. In addition, methodologies for the study of foreland basins and FTBs are described both from a theoretical and an application perspective. A special interest is given to the study of fractures and palaeopiezometry of BPS roughness, as applied in the framework of this work. The question now arises of which case study should be considered to apply all these methodologies and attempt to answer to the expectations and problems raised. The choice focused on the Apennines, and more specifically on the Umbria-Marche Apennine Ridge (Italy), where many characteristics are combined to approach the issues of the thesis and apply these methodologies. The purpose of the next chapter is therefore to present the characteristics of this case study, from the large scale to that of mesostructures.

*Chapter 2- Geological setting: the Apennines and the Umbria
Apennine Ridge*

I- GLOBAL GEODYNAMIC CONTEXT: EVOLUTION OF MEDITERRANEAN DOMAINS

The history of the Apennines is closely linked to the geodynamic evolution of the Mediterranean, where various major tectonic features such as the European, African and Apulian plates evolved (Figure 2.1). Since the Mesozoic, Africa has been in an extensional phase, sometimes coupled with compressive episodes (Jolivet *et al.*, 2016); these compressions are generally associated with ophiolite obduction processes, mainly on the northern margin. Notably, the closure of the Neo-Tethys Ocean in the Late Cretaceous was responsible for a major obduction from the Mediterranean to the Himalayas (on the Arabian margin particularly, from Cyprus to Oman), resulting in a Cretaceous compressive event recorded in the African-European convergence zone.

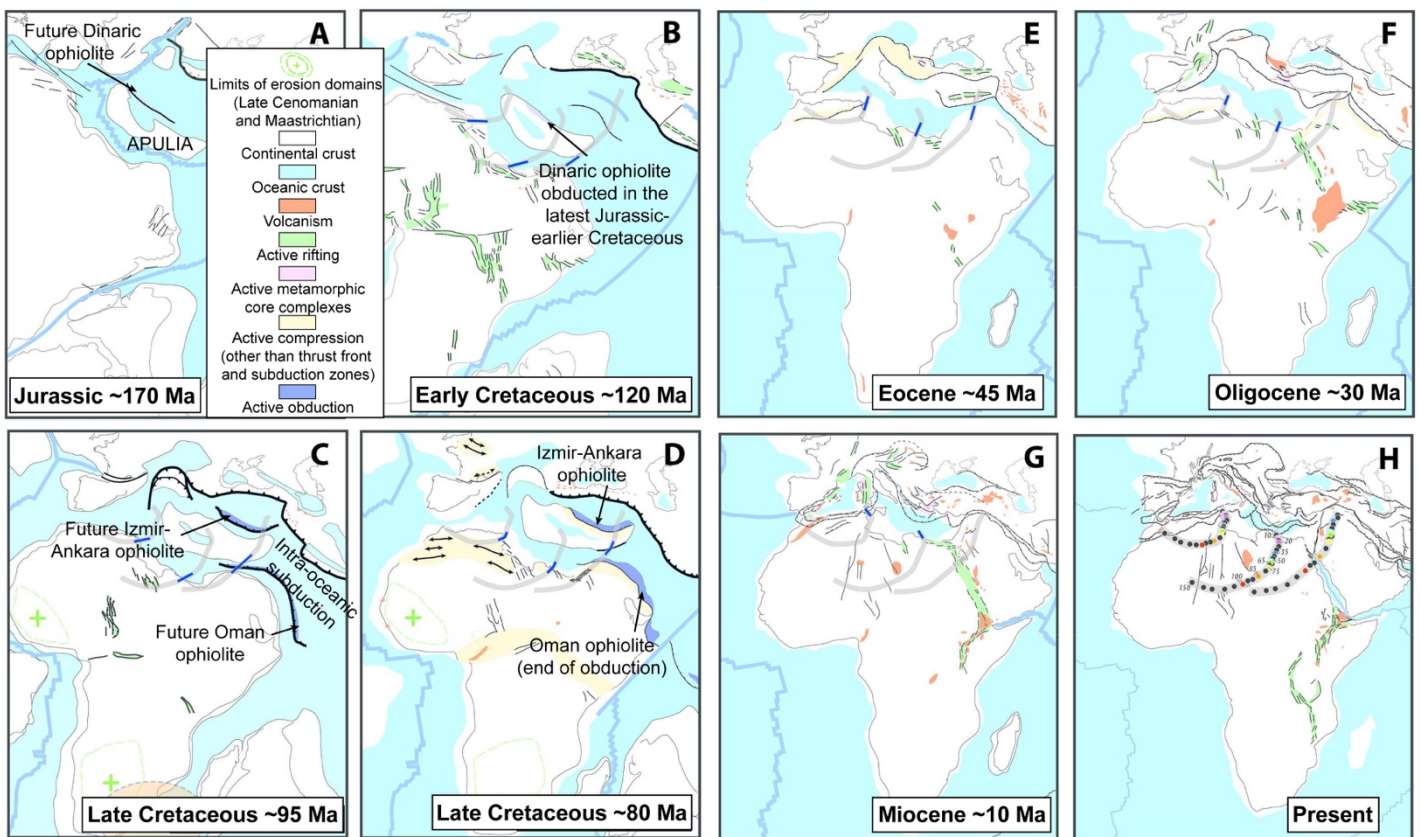


Figure 2.1- Reconstruction of the geodynamic evolution of the Mediterranean area from the Jurassic to the present; after Jolivet *et al.* (2016).

The tectonic evolution of Africa and of the Neo-Tethys ocean consists of a succession of geological events occurring since the Jurassic. The story began in the Middle Jurassic (-170 Ma) (Figure 2.1A), with the subduction of the Neo-Tethys below the southern Eurasian margin, already well opened in the eastern part (Agard *et al.*, 2011). While the Adriatic continent migrated towards north Africa, the rifting built the eastern Mediterranean basin and a second order African basin called Ionian basin (Frizon de Lamotte *et al.*, 2011). At the same time, the rifting between India and Africa caused the opening of the west Indian Ocean (Frizon de Lamotte *et al.*, 2015). Several obductions are also related to this rifting episode. For example, the Dinaric ophiolites were obducted at the onset of intra-oceanic subduction

during the late Jurassic (-175 and -160 Ma) in the northern margin of the Apulian block (Jolivet *et al.*, 2016).

During the early Cretaceous (-120 Ma) a major rifting phase between Africa and Arabia occurred (Nikishin *et al.*, 1998, 2015; Guiraud *et al.*, 2005), as well as the opening of the south Atlantic (Figure 2.1B). Intra-oceanic subduction that began in the Jurassic continued, causing the obduction of ophiolites in the Armenian part of the Apulian margin (Hässig *et al.*, 2013, 2016). The African-Eurasian convergence intensified around -118 Ma as plate movements resumed (Agard *et al.*, 2007). The last tectonic event, called the "Austrian phase", was recorded around -125 Ma, *i.e.* during the late Barremian (Smith *et al.*, 2006); it consisted in the reactivation of north-south structures independent of the African-Eurasian convergence and mostly observed in the western part of Africa (Jolivet *et al.*, 2016). A major compressive phase was then recorded in the late Cretaceous (-100 to -75 Ma), initiated after the intra-oceanic subduction at the origin of the obduction of the major ophiolitic nappes observed today at outcrop: the Izmir-Ankara and Oman ophiolites (Figure 2.1C) (Jolivet *et al.*, 2016). Its propagation over most of Africa generated undulations in the basement, as well as the reactivation of inherited rifts: this was the "Santonian event" (-85 Ma) (Benkhelil *et al.*, 1988; Benkhelil, 1989; Genik, 1993; Bosworth *et al.*, 1999; Guiraud *et al.*, 2005; Bevan & Moustafa, 2012; Arsenikos *et al.*, 2013), during which only northern Africa and Arabia and the sub-Saharan rift were reactivated (Figure 2.1D) (Jolivet *et al.*, 2016). This compression was also recorded across western Europe: (i) in the Pyrenees, where it began in the Santonian (Jolivet *et al.*, 1999; Jammes *et al.*, 2010), and southeastern France; (ii) in the Paris Basin and North Sea (Guillocheau *et al.*, 2000); (iii) and ended in the western Mediterranean with the slow initiation of a subduction, the future Apennine subduction zone (Jolivet *et al.*, 2016).

A period of relative stability was recorded between -65 and -45 Ma (Rosenbaum *et al.*, 2002), followed by a compressive phase beginning in the middle to late Miocene in the Atlas and Syrian belts, as well as in the northern part of the west Mediterranean subduction (Iberian ridge and Pyrenees) (Figure 2.1E). After this compressive stage, the Oligocene uplift affected most of Africa (Burke *et al.*, 2003, 2008): the northern part underwent an elevation of 200 to 300 m, while the north African volcanic area started to build (Wilson & Guiraud, 1992; Wilson, 1993; Liégeois *et al.*, 2005). At the same time, extensive deformation was recorded in the upper part of the African plate, near the convergence zone (Jolivet *et al.*, 2016).

Finally, between -30 and -35 Ma, several tectonic events occurred (Figure 2.1F). Back-arc basins developed in the Mediterranean area (Jolivet & Faccenna, 2000). Rifts were also initiated in the future Gulf of Aden and the Red Sea, while the ancient sub-Saharan rifts were reactivated. From the late Eocene onward, the separation of Arabia from Africa was generated by similar tectonic and geodynamic processes to those previously described (Figures 2.1G and 2.1H). However the resulting collision was contemporary with these processes, since the oceanic lithosphere was strongly reduced at this stage (Jolivet & Faccenna, 2000).

II- THE APENNINES, GLOBAL CONTEXT OF THE STUDY AREA

1- Geodynamic and structural context

The Apennines are in the Central and southern part of Italy (Figures 2.2A and 2.2B), in a pericratonic region where deformation events directly linked with the interaction between European and Africa plates during the Neogene are recorded. The Apennines extend from the Po Plain to the Calabrian arc for 1500 km, and form the backbone of the Italian peninsula (Scisciani *et al.*, 2014). The central area is considered as an overlap zone between two oceanic domains (Figure 2.2B): (i) the Tethys Ocean, whose opening is linked to the Triassic rifting and to the extension between the Adriatic and European margins; (ii) the Neo-Tethys Ionian domain, or East Mediterranean Ocean, related to the propagation of the Neo-Tethys Ocean opened during the Permo-Triassic (Finetti *et al.*, 2005).

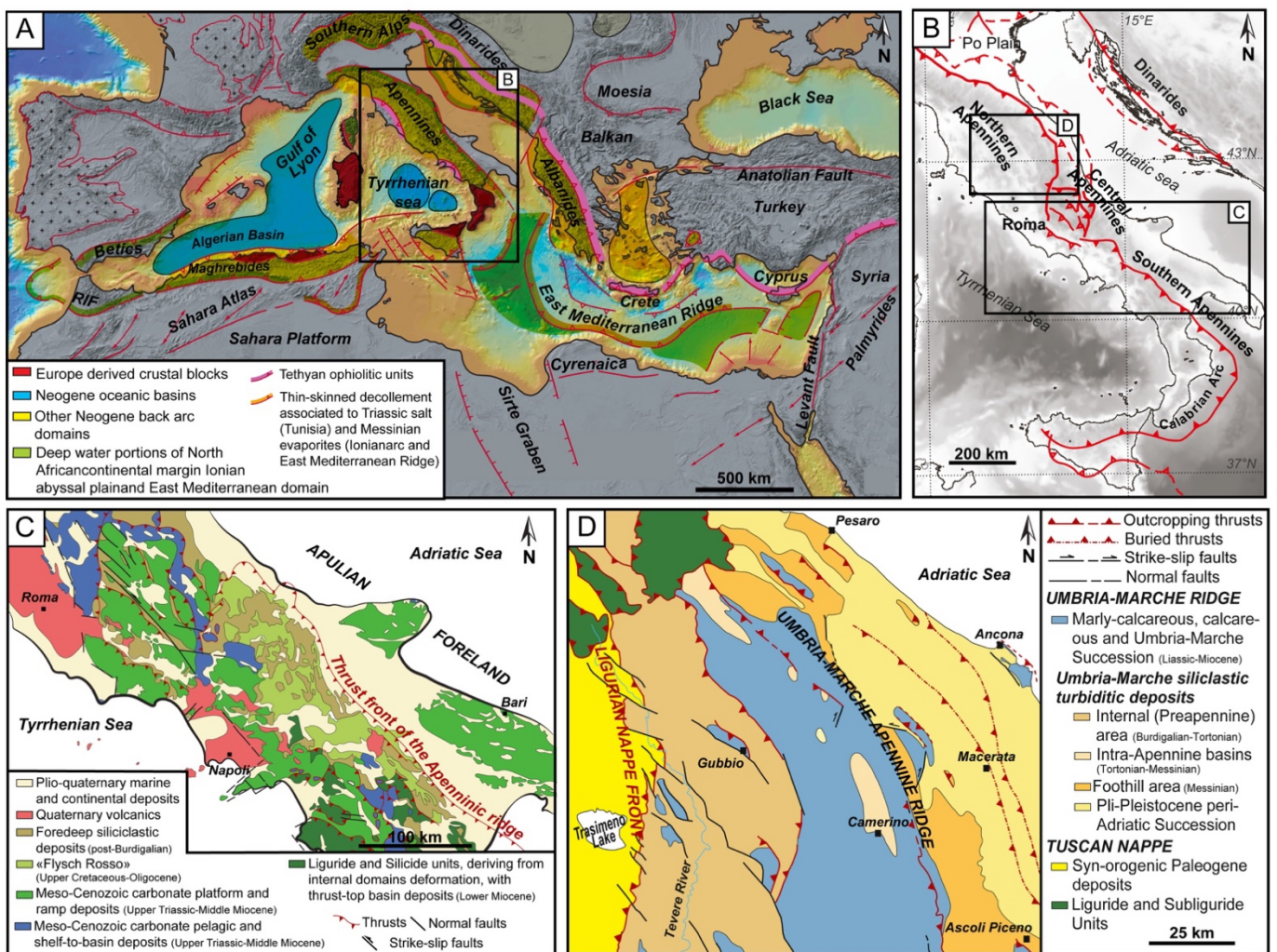


Figure 2.2- (A) Generalized structural map of the Mediterranean, modified from Roure *et al.* (2012). (B) Location of the Northern, Central and Southern Apennines, with main thrusts structuring the area (C) Structural sketch map of the central-southern Italy, redrawn after Cosentino *et al.* (2010). (D) Geological scheme of the Umbria-Romagna-Marche Apennines and surrounding areas, modified from Guerrera *et al.* (2012).

Three distinct tectonic events succeeded on another and contributed to the building of the Apennines (Scisciani *et al.*, 2014). A major extension was recorded from the end of the Permo-Triassic to the middle Jurassic, associated with the opening of the Ligurian Ocean (Bernoulli & Jenkyns, 1974; Aldinucci *et*

al., 2008). This rifting phase generated extensional structures affecting the Hercynian basement, *i.e.* normal fault systems and horsts and grabens building the passive margin in formation (future Adriatic margin). The depositional environments progressively evolved from continental to pelagic environments (Figure 2.2C) and favored the development of a carbonate platform. Sedimentary deposits reached a maximum thickness during the early Cretaceous (Guerrera *et al.*, 2012), because of a general subsidence related to the middle Liassic tectonic phase. This tectonic phase is directly linked with the Neothethys Jurassic rifting that affected the whole Neothethyan domain. Thus, this extensional tectonics was responsible for the break-up of the shallow-water platform domain widespread in almost all of central Italy and created platform-basin systems including: (i) downthrown sectors with dominant pelagic deposits (*i.e.* deeper-water sedimentation) and local clastic carbonates from shallower areas; (ii) upthrown sectors with shallow water carbonates (Figure 2.2C). During the late Cretaceous, the extensional tectonics recorded in the carbonate platform domains (*e.g.* Shiner *et al.*, 2004) was probably responsible for pulses of accelerated subsidence recorded by Cretaceous basin carbonate sediments (Marchegiani *et al.*, 1999). The compression that began in the late Miocene-early Pliocene marked the beginning of the Apennine orogeny. Folds and thrusts were oriented NNW-SSE (Figure 2.2C), and sedimentary processes were therefore directly controlled by the evolution of the Apennines, involving a shift from carbonate to clastic sedimentation. The late Pliocene-Quaternary extension, associated with the activity of NW-SE oriented normal faults, is at the origin of the formation of intermountain basins contemporary with the present seismic activity (Calamita *et al.*, 2000; Pizzi & Scisciani, 2000).

The Apennines form a FTB with an eastern convexity, becoming younger and younger from west to east (Figure 2.2C): while the internal arc built at the end of the Oligocene, the external zones are dated to the Pliocene-Pleistocene (Lavecchia *et al.*, 1988). The Apennines are divided into two main arcs: the Northern Apennines and the Southern Apennines arcs (Figure 2.2B), each associated with its own geological and structural characteristics such as structural evolution, rotation patterns, shortening rates and outcrop formations (Boccaletti *et al.*, 2005; Satolli *et al.*, 2014). The Northern Apennines were developed during the Cenozoic, at the time of the closure of the Ligurian Ocean (eastern branch of the Tethys Ocean) and the collision of the European and African continental margins (Corsica-Sardinia and Adria blocks, respectively) (Malinverno & Ryan, 1986; Carmignani & Kligfield, 1990). They were formed by the stacking of large overlapping tectonic units, mainly oriented towards the east: the Tuscan and Umbrian nappes, overlain by the Ligurian nappe and the sedimentary cover (Scisciani *et al.*, 2014). The Southern Arc is characterized by the stacking of two tectonic units: (i) the Massa-Apuane units, made of Permian to Oligocene metamorphic sediments, stacked tectonically then deformed into a duplex during the Oligo-Miocene (Carmignani & Kligfield, 1990); (ii) the Tuscan nappe, overlapping these metamorphic units. From a structural point of view, the Apennines are characterized by a succession of asymmetrical anticlines with an eastern vergence, separated by narrower and often asymmetrical synclines. Numerous faults also affected the Mesozoic-Tertiary sedimentary succession and the Hercynian basement (basement faults) (Figures 2.2C and 2.2D) (Guerrera *et al.*, 2012). They result from

the succession of tectonic units related to the deformation Meso-Cenozoic carbonates (*i.e.* shallow water limestones in carbonate platform domains and deeper-water carbonates in slope and pelagic domains), and consist of basement and cover thrust-sheets developed in an ensialic context (Cosentino *et al.*, 2010). This structural setting is the result of the superimposition of two tectonic episodes that occurred at different times: (i) the piggyback sequence of main thrusts followed by a general northeastward migration of the orogenic system, that provided the out-of-sequence reactivation of some sectors previously involved in the thrust belt; (ii) post-orogenic extensional and strike-slip tectonics. Under this general context, main thrusts activated during different piggy-back migration phases of the orogenic system, as well as main out-of-sequence thrust fronts, bound the main tectonic units (Cosentino *et al.*, 2010): (i) one thrust on the border of the Liguride and Silicidic units, (ii) others that distinguish sequences belonging to the Apennines thrust belt and related foredeep deposits and (iii) the thrust front Apennines, bordering the allochthonous Apennine units (Figures 2.2C and 2.2D).

2- Paleogeographic evolution

As for any complex tectonic frameworks, paleogeographical models for the peri-Mediterranean domain are difficult to build, because of a high tectonic activity related to recent orogenic processes, new oceanic basin formation, lithospheric bloc rotations, ... Thus, the reconstruction of the pre-deformational paleogeography implies to unravel kinematic evolution and to quantify shortening or/and extension during deformations (Cosentino *et al.*, 2010). Despite these uncertainties, models were proposed for the western Tethyan realm considering all these parameters (Dercourt *et al.*, 1993; Ciarapica & Passeri, 1998, 2002).

During the late Triassic, a wide shallow-water platform developed, dividing two continental emerged areas: the Iberic-Provencal sector to the north and the North-African sector to the South (Figure 2.3A). Then, the rifting that occurred caused the break-up of a huge carbonate sedimentation domain and, with the synchronous opening of N-S lateral branches affecting pelagic sedimentation, favored the creation of Triassic basins. Pelagic facies (*i.e.*, bituminous dolostones) observed in central Italy are probably related to the tectono-sedimentary evolution of intra-platforms that divided shallow water carbonate facies from dolomitic domains. The middle Liassic then recorded an important extensional phase, directly associated with the western propagation of the continental rifting that affected the more eastern regions during the late Triassic. This caused the break-up of the huge shallow-water platform and development of wide platform-basin systems preserved until the Mesozoic. In the peri-Tethyan area, this shallow-water platform developed under peri-oceanic conditions, providing the rise of confining pelagic basins and the isolation of Apulian platform, separated from the Apennine platform by intermediate basins (Figure 2.3B). This stage marked the maximum development of the Ligure-Piemontese oceanic basin, with sectors with oceanic lithosphere (Cosentino *et al.*, 2010). The subsidence resulting from these first rifting stages, coupled with extensional processes and followed by the building of the Adriatic margin, continued and prevailed until the pre-orogenic stage (early Miocene) (Guerrera *et al.*, 2012).

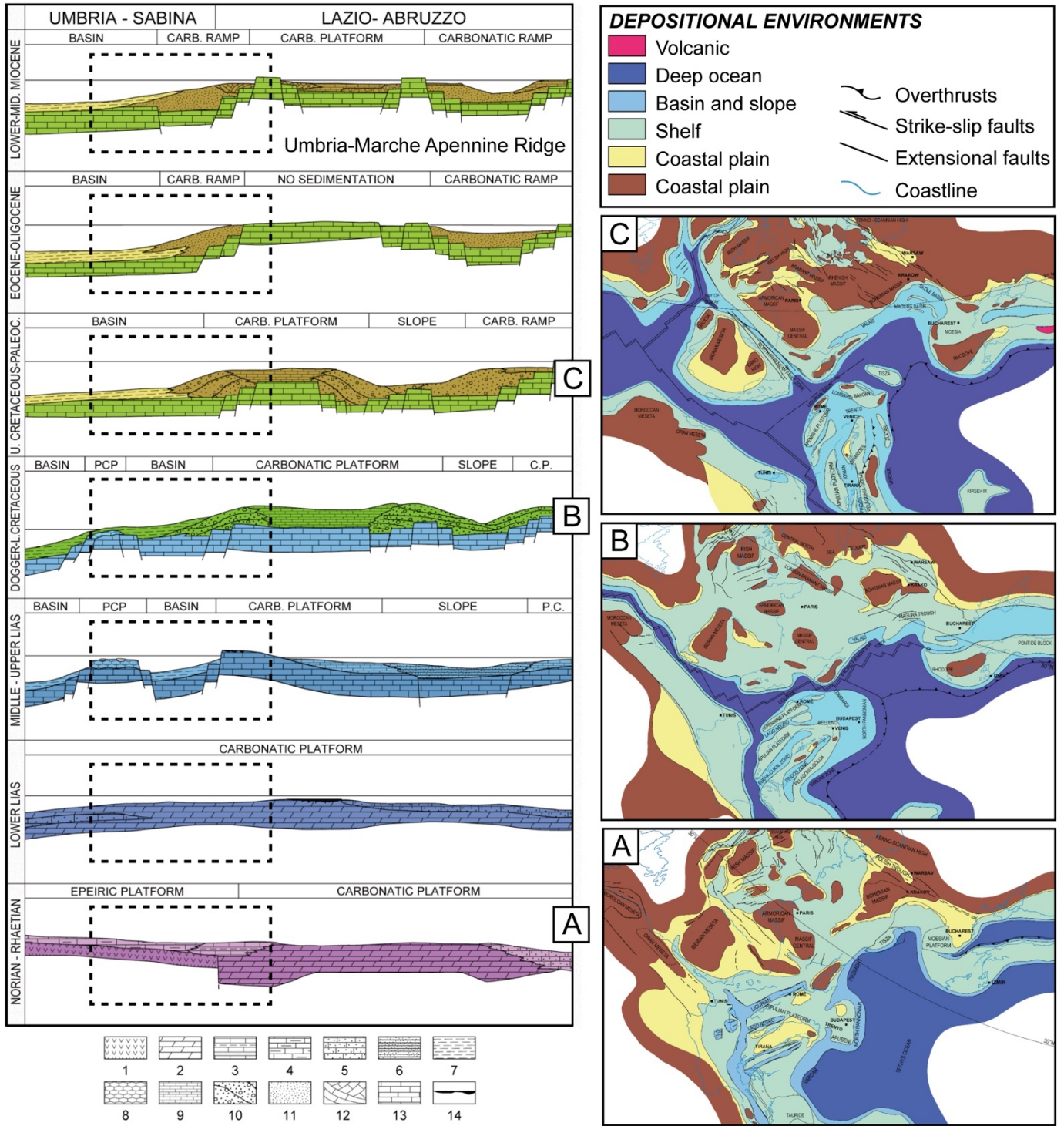


Figure 2.3- Main steps of the late Triassic- middle Miocene evolution of the platform-basin system in central Italy; after Cosentino *et al.* (2010), modified from Accordi *et al.* (1986). Facies are numbered as follow : (1) evaporites; (2) dolomites and laminated dolomitic limestones; (3) clays and marls with intercalations of oolitic and organogenous wackstone-grainstone; (4) marls; (5) bioclastic wackstone-packstone; (6) mudstone with biotrititic and microclastic intercalations ; (7) marls, clays and pelagic micrites; (8) pelagic mudstonewackstone and hardground with nodular structures; (9) carbonate platform limestones; (10) organogenous grainstone-rudstone; (11) packstone-grainstone with intercalations of marly pelagic mudstone; (12) organogenous wackstone-grainstone; (13) carbonate basement; (14) supratidal deposits and alteration soils. CP: carbonate platform; PCP: pelagic carbonate platform. Paleogeographic maps of Tethys realm are related to these different stages: **(A)** late Triassic, **(B)** late Jurassic and **(C)** early Cretaceous maps; after Cosentino *et al.* (2010), modified from Yilmaz *et al.* (1996). The paleogeographic evolution of the UMAR is represented by the dotted black box

Geodynamic processes drastically changed during the late Cretaceous (Cosentino *et al.*, 2010). A first stage of compression occurred during the early Cretaceous, only active in the more eastern sector. It was related to a general regressive trend in the northern area, which is synchronous of a period of relative tectonic rest in the central sector. That's why the middle Liassic platform-basin systems continued to develop. Moreover, the transgression that occurred in the southern margin was responsible for the large spread of shallow-water platforms (Figure 2.3B). During the late Cretaceous (Figure 2.3C), extensional processes recorded in the whole area only persisted in the more eastern sector, while compressional tectonics was recorded in the more northern area (Cosentino *et al.*, 2010).

In the late Miocene, the basin entered a foredeep stage, and progressively migrated eastward (in relation to the retreat of the subduction zone). Due to an increasing clastic influx, the sedimentation progressively evolved towards a silici-clastic system, with sandstone (flysch) and marl deposits (Guerrera *et al.*, 2012). These deposits were diachronous from the inner to the outer areas, and coevally with the eastward migration of the deformation, the contraction beginning in the early Serravalian in the inner areas and ending in the Tortonian-Messinian in the outer parts. In the Adriatic sector (*i.e.* the foreland ramp), the non-deposition of these sand-rich flyschs indicates a late onset of the foredeep stage, dated to the late Messinian. Although the hypothesis of tectonically controlled sedimentation is debated (*e.g.* Ricci-Lucchi, 1975; de Jager, 1979;; Martelli *et al.*, 1994; Mutti *et al.*, 2002), the Miocene Marnoso-Aranacea Basin is considered as a complex foredeep basin built during a diachronous syn-sedimentary tectonics, divided into seven sub-basins formed during the propagation of the main thrust (Van Wamel & Zwart, 1990; Martelli *et al.*, 1994; Lucente, 2004) or into large and distinct depositional zones (Guerrera *et al.*, 2012). In addition, the diversity of sedimentary deposits can also depend on the complex paleotopography inherited from tectonic deformation migrating progressively eastward and controlling depositional processes and sediment distribution.

The transition to the forebulge stage, followed by a new compressional phase, initiated deformations. Sediments deposited were mainly silico-clastic, but also evaporitic and post-evaporitic in the Adriatic sector (in connection with the Messinian salinity crisis) (Table 2.1). The history of the basin continued and ended in the Pliocene, in a context of foredeep coupled with compressive and thrust processes. Deposits were then mainly formed by pelites and arenites, and most of the basin was deformed and emersive, except for the Adriatic sector (Guerrera *et al.*, 2012) (Table 2.1).

MAIN ROCK SUITE	EXTERNAL TOSCANA BASIN	UMBRIA-ROMAGNA BASIN					MARCHE BASIN				MAIN REGIONAL EVENTS
		INTERNAL Elements		EXTERNAL Elements			INTERNAL Elements		EXTERNAL		
		Falterona Unit	Monte Nero	Poggio Castellaccio	Pietralunga	Borgo Pace	Monte Vicino	Sant'Angelo in Vado	Urbania	Urbino Element	
pelites and subordinate arenites	deformed and emerged					emerged				Cella Marls - Argille Azzurre Fms (Plio-Quaternary <i>p.p.</i>)	Pliocene foredeep and Thrust-top Stages (compression)
black shales, evaporites, siliciclastic and marly deposits						deformed and probably emerged					
mainly marly deposits	Vicchio Marls Fm (Burdigalian - Serraval. <i>p.p.</i>)	?	Verghereto Marls Mbr (MAR) (Serrav. <i>p.p.</i> - Torton. <i>p.p.</i>)	?			Campo Marls Mbr (MAM) (Early Tortonian)	Belvedere Marls Mbr (MAM) (Late Torton. - Early Mess.)	Pre-orogenic Schlier Fm (Late Burdigal. - Early Messinian)		Miocene foredeep stage (progressive eastward migration)
siliciclastic deposits (flysch)	Mt. Falterona Sandstones Fm	Marnoso-Arenacea Romagnola Fm (MAR)					Marnoso-Arenacea Marchigiana Fm (MAM)				
	Late Aquitanian	Latest Burdig.-Langhian <i>p.p.</i>	Langhian - Serravallian <i>p.p.</i>	Langhian <i>p.p.</i> - Serravallian	Latest Langhian - Earliest Tortonian	Late Serraval. - Early Tortonian	Latest Serravallian - Tortonian <i>p.p.</i>				
clays, marly-clays, marls and calcareous deposits	Marne Varicolori, Villore Fm (Chattian - Aquitan. <i>p.p.</i>)	Schlier Fm (Late Burdigalian)		Schlier Fm		Top Schlier Fm	Top Schlier Fm			Pre-orogenic stage (prevailing subsidence)	
				?	Burdigal. <i>p.p.</i> - Langhian <i>p.p.</i>	Earliest Serrav.	Middle Serravallian	Late Serravallian - Earliest Tortonian			
marls, marly-clays, black shales, chert, limestones, volcanogenic materials	Mesozoic-Tertiary Succession					Marne a Fuocidi to Bisciario succession (Early Cretaceous <i>p.p.</i> - Early Miocene <i>p.p.</i>)				Rifting/driftng (extensional process, subsidence)	
neritic and pelagic limestones						From Calcare Massiccio Fm to Maiolica Fm (Early Jurassic - Early Cretaceous <i>p.p.</i>)					

Table 2.1 - Synthesis of the tectono-stratigraphic evolution of the Umbria-Marche basin and adjacent

III- THE UMBRIA MARCHE APENNINE RIDGE: CENTRAL PART OF THE APENNINES

The Umbria-Marche Apennine Ridge (UMAR) is the central part of the Apennines and belongs to the foreland area. It extends for about 450 km and culminates to over 2000 m above sea level (Scisciani *et al.*, 2014) and is described as a succession of east-verging arcuate folds and thrusts (piggy-back type basin) oriented NNW-SSE (Figure 2.4A) (Bally *et al.*, 1986; Calamita & Deiana, 1988; Barchi *et al.*, 2012). This region is tectonically active and is currently in a post-orogenic extension phase.

1- *Stratigraphic sequence characteristic of the Umbria-Marche*

1.1- *Facies of the UMAR stratigraphic sequence*

The characteristic stratigraphic sequence of the Northern Apennines is divided into several large stratigraphic units (Figure 2.4B). At the base of the succession, the late Triassic formations underlain the Hercynian basement rarely to never exposed (Lavecchia *et al.*, 1988). Two types of lithologies are described within these Triassic formations: (i) in the lower part, shallow water dolomites and anhydrites, otherwise named Anidriti di burano; (ii) interbedded euxinic marls in the upper part, characterized by the presence of bivalves belonging to the species *Rhaetacivula Contorta* (Scisciani *et al.*, 2014). Their thickness, evaluated at 1000 m before the Mio-Pliocene deformations, is estimated to be 2000 m. These Triassic sediments are overlain by early Jurassic carbonates (Figure 2.4B), the Calcarea Massiccio, at the base of Jurassic sequence. They are formed by massive peridital limestones, poorly bedded and about 700 m thick (Lavecchia *et al.*, 1988). These carbonates pass upwards to the Umbria-Marche pelagic succession, composed by Jurassic-Cretaceous limestones sporadically interbedded with shales and cherts (Scisciani *et al.*, 2014). Two associations of facies characterized this Jurassic carbonate succession (Figure 2.4B). The first consists of four successive carbonate formations, such as: (i) biomicritic limestones with chert bed intercalations of the Corniola, enriched in radiolarians; (ii) the Rosso Ammonitico, composed by nodular marly limestones; (iii) marls and cherty limestones of the Calcari e Marne a Posidonia; (iv) the Calcari Diasprigni, radiolarian-rich cherty limestones and cherts evolving from towards micritic limestones and marls bearing abundant *Saccocoma* sp. fragments at the top. The second, named the Bugarone group, formed by the combination of finely bedded nodular limestones with argillites (Lavecchia *et al.*, 1988). From the early Cretaceous to the late Miocene, sedimentation was characterized by predominantly carbonate (fine limestones) and marly deposits (Figure 2.4B). During the early Cretaceous, micritic limestones associated with chert beds shales of the Maiolica, and marls of the Marne a Fucoidi, were successively deposited and overlain by limestones with cherts intercalations. This limestone unit, the Scaglia Group, is subdivided into three successive members: (i) the Scaglia Bianca; (ii) the Scaglia Rossa; (iii) the Scaglia Cinerea and Variegata. Then, the first Miocene unit deposited is the Bisciario Formation, marly limestones and marls essentially composed of volcanogenic materials. The Miocene series continues with the deposition of the Schlier

Formation, differing from the Biscario by its low volcanoclastic component. The overlying Mio-Pliocene silicoclastic flyschs form the last unit of this stratigraphic sequence (Figure 2.4B), with clastic turbiditic and arenitic facies of the Marnoso-Arenacea, Arenarie di Camerino and Laga formations, and overlain by Plio-Quaternary sediments.

1.1- Paleogeographic evolution: link between tectonics and sedimentation

The classical stratigraphic sequence of the UMAR is therefore composed by Triassic to Miocene pre-orogenic carbonates, overlain by syn-orogenic marine Mio-Pliocene deposits, and overlying Plio-Quaternary continental sediments. The geodynamic and tectonic context thus impacted the sedimentation across the UMAR over time (Figure 2.3 and Table 2.1).

During the early Jurassic, the platform limestones of the Calcare Massiccio was deposited in shallow marine environments. The second succession, called the Bugarone Group, is formed by platform carbonates deposited in a pelagic environment during the late Jurassic. The syn-rift extension impacted the sedimentation of this carbonate succession because of the activity of normal faults that generated a system of horsts and grabens, where the space available for sedimentation varied strongly. Consequently, these carbonates are discontinuous and form a condensed level in the horst areas, where the space dedicated to sedimentation was strongly reduced. In contrast, in the grabens, the stratigraphic equivalent of this condensed series was deposited. This so-called “complete” carbonate succession is constituted from the base to the top by the Corniola, Rosso Ammonitico, Calcari a Posidonia and Calcari Diasprigni formations. The Maiolica, a post-rift marly-limestone formation dated to the late Jurassic, stratigraphically overlaps these complete and condensed series (Mazzoli *et al.*, 2002). Lateral variations in facies and thickness are therefore observed within these pelagic basins, related to extensive dynamics and passive margin building; in particular, sediment thickness is reduced on structural highs, while the complete Jurassic sequence is deposited and preserved in deep troughs (Bernoulli & Jenkyns, 1974; Lavecchia *et al.*, 1988; Ciarapica & Passeri, 2002; Scisciani *et al.*, 2014).

Then, the marls of the Marne a Fucoidi deposited during the early Cretaceous constitute a first marly interval, continuous on the scale of the FTB, and thus a stratigraphic marker providing calibration of seismic data with the surface geology (Figure 2.5) (Scisciani *et al.*, 2014). They are overlain by the hemipelagic limestones of the Scaglia group deposited from the late Aptian to the Aquitanian. The Miocene compressive tectonics then initiated the transition from carbonate to silico-clastic sedimentation (Lavecchia *et al.*, 1988), and provided the deposit of the hemipelagic units of Bisciaro and Schlier. While volcanogenic materials of Bisciaro are essentially associated with the volcanic activity recorded during the early Miocene, the Schlier is characterized by a strong variability of facies and a diachronism of the deposits (Figure 2.5). Thus, it is dated to the Langhian in the inner areas and to the late Tortonian-early Messinian in the outer areas (where hemipelagic lithofacies predominate). This diachronism reflects the progressive migration of the FTB from west to east and is observed in the foredeep deposits of the Marnoso-Arenacea, Arenarie di Camerino and Laga formations, whose sedimentation is diachronous from the inner to the outer areas

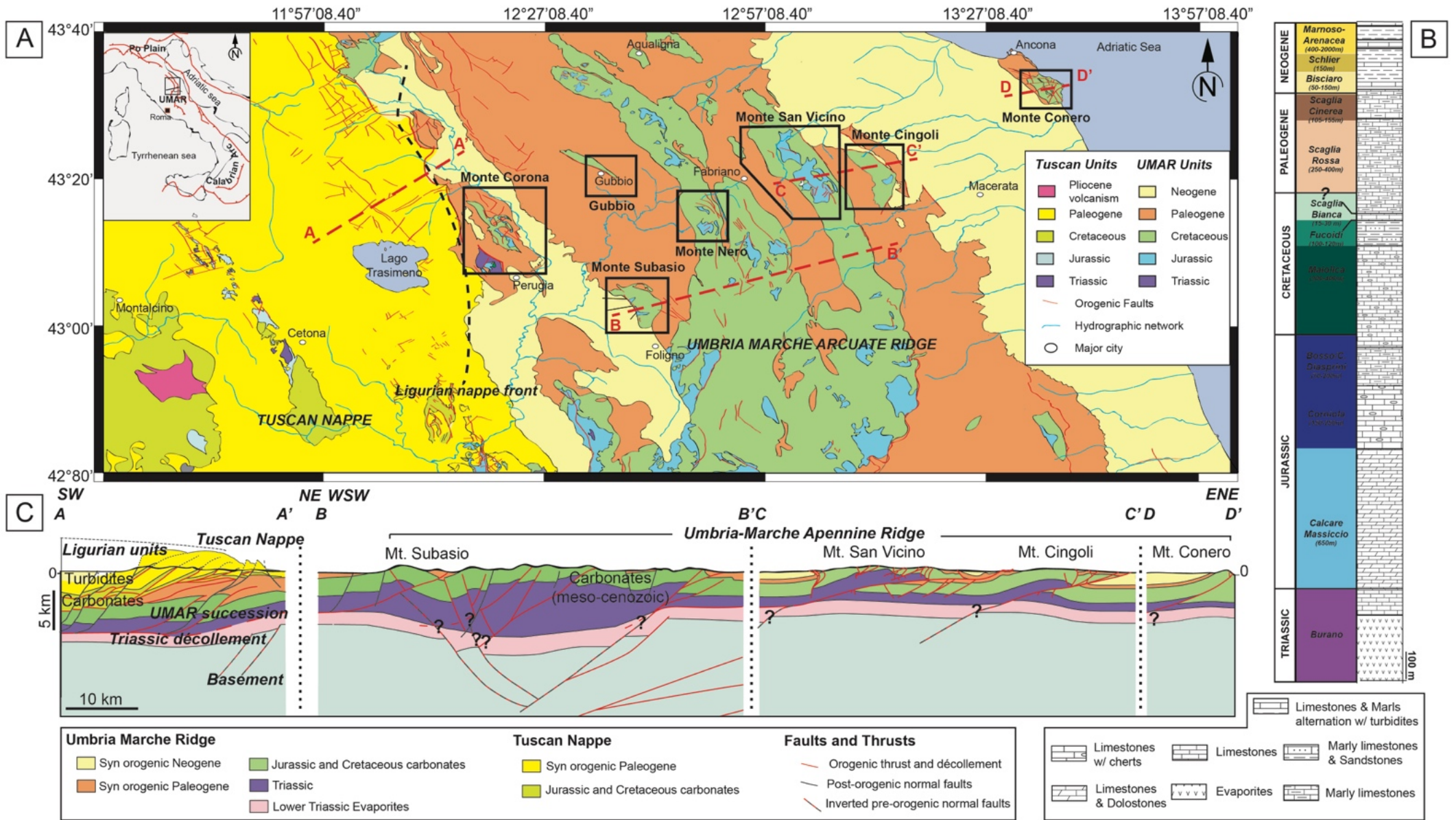


Figure 2.4- (A) Location, geological map and SW-NE transect of the Apennines and the Umbria-Marche ridge. (B) Stratigraphic sequence characteristic of the UMAR. (C) Cross-section of the UMAR, along a SW-NE transect across the main anticlines of the FTB; modified from Beaudoin *et al.* (2020a).

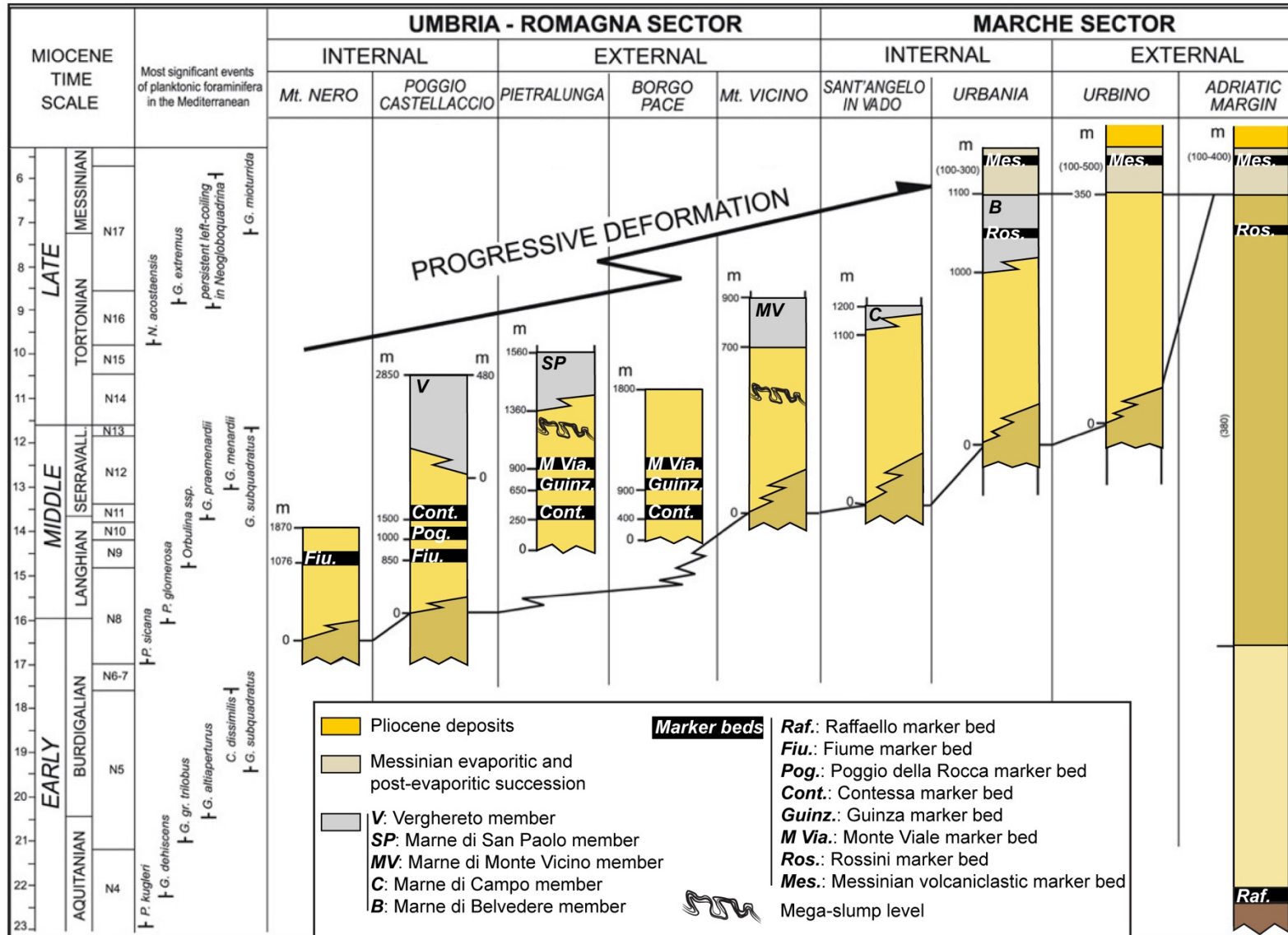


Figure 2.5- Stratigraphy of the Marnoso-Arenacea Formation. Lateral evolution, diachronism of boundaries and deposits, absence of the Marnoso-Arenacea in more external areas and marker beds and correlation detailed in text are represented; modified after Guerrera *et al.* (2012), compilation of data from Delle Rose *et al.* (1990, 1991, 1994b; a), Dubbini *et al.* (1991), de Feyter, (1991), Montanari *et al.* (1991), Capuano & D'Antonio (1992), Carlini *et al.* (1995) and Capuano *et al.* (2009).

Thus, while clastic turbidites and marls were deposited in the hinterland between the Serravallian and Tortonian (Marnoso-Arenacea), the Tortonian to Messinian series of the Arenarie di Camerino was deposited in the central area. The deposits are younger in the hinterland, dated to the Messinian (Laga Formation). Furthermore, from late Miocene, the foreland basins subsidence is also associated with the activity of normal faults related to flexure pre-dating the growth of compressional structures (Scisciani *et al.*, 2014). Considering the diachronism of the extension linked to the eastward migration of the basin, studies carried out in the UMAR enabled to date the flexure and normal faults as syn-development of the deposition of these flyschs, and therefore as predating the Miocene thrusts. The extensional process is therefore related to bending or buckling of the foreland (Scisciani *et al.*, 2001; Mazzoli *et al.*, 2002; Mirabella *et al.*, 2004). Finally, Plio-Quaternary continental sediments were unconformably deposited on top of the Jurassic and Cretaceous marine units, with a maximum thickness in the inter-mountain basins such as the Colfiorito basin and the Umbrian valley.

Several marker beds are identified within these Cretaceous to Miocene deposits, closely related to the tectonic-sedimentary evolution of the region (Figure 2.5). These are major widespread stratigraphic markers enabling large-scale correlations to be made. The first marker bed identified is the Selli; at the base of the Marne a Fucoidi, this bituminous horizon enriched in radiolarites constitutes one of the main episodes of organic matter deposition in the early Aptian (Coccioni *et al.*, 1987). It is associated with a global palaeoceanographic event: the Anoxic Ocean Event 1a (AEO1a) (Baudin *et al.*, 1998). The Bonarelli is a regional stratigraphic marker bed located at the top of the Scaglia Bianca, at the Cenomanian/Turonian interface. It consists of organic-rich sediments, related to a second anoxic event, the so-called "Oceanic Anoxic Event 2" (OAE2) (Turgeon & Brumsack, 2006; Guerrera *et al.*, 2012). The Cretaceous/Tertiary boundary, located in the mid-upper part of the Scaglia Rossa, corresponds to a clay bed characterized by an anomalous concentration of iridium (Alvarez, 2009). The Raffaello is the lithostratigraphic limit between the Scaglia Cinerea and Bisciaro formations; it is the first volcanoclastic interval observed in the Miocene succession (Montanari *et al.*, 1994).

2- Structural characteristics and proposed models

The UMAR belongs to the central part of the Apennines (Figure 2.6). The structure of the Apennines and of the UMAR is still debated in the scientific community. In particular, seismic data from the CROP project (Barchi *et al.*, 1998; Noguera & Rea, 2000; Finetti *et al.*, 2001), aeromagnetic data, as well as field and subsurface data helped to image this structure, leading to a revision of the structural model classically considered.

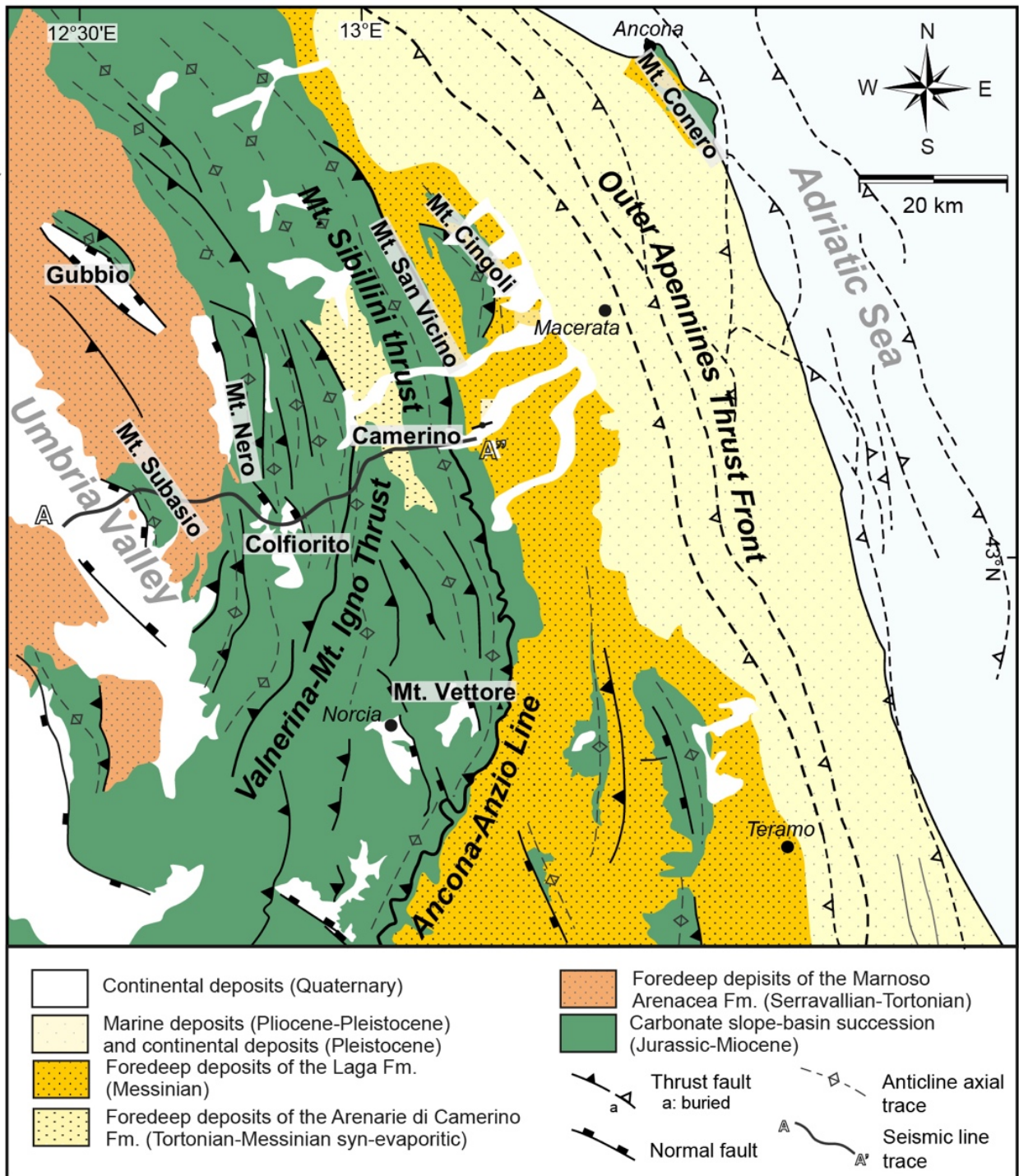


Figure 2.6- Structural map of the UMAR from the Umbrian Valley to the Laga Basin; modified from Sciscianni *et al.* (2014) and Bigi *et al.* (1992).; redrawn from Tavarnelli *et al.* (2004).

The classic interpretation of the UMAR considers the Triassic evaporites as the major decoupling level between the basement and the cover, enabling the detachment and disharmonic deformation of the cover during the first phase of shortening (Guerrera *et al.*, 2012). In this thin-skinned tectonics model (Figure 2.7A), thin tectonic slices related to thrusts are decoupled along the Triassic evaporites and late Paleozoic clastic rocks. The crystalline basement, which does not crop out, is not involved in shortening (Bally *et al.*, 1986; Ghisetti & Vezzani, 1988; Hill & Hayward, 1988). The amount of orogenic contraction is important and the shortening rates are abnormally high (15-50 mm/yr) compared to

similar FTB. Nevertheless, the interpretation of the seismic and aeromagnetic imagery challenges this classical model, locating the thrusts on inherited pre-orogenic normal faults formed either during the evolution of the Mesozoic passive margin or during flexure of the foreland (e.g. Mazzoli *et al.*, 2000; Scisciani *et al.*, 2001; Calamita *et al.*, 2003; Pace & Calamita, 2014). In addition, some geophysical data such as deep seismic reflection profiles, gravity modeling, P- and S-wave conversion of teleseismic events, and refraction seismic highlight the Moho overthrust beneath the Apennines (e.g. Ponziani *et al.*, 1995; Barchi *et al.*, 1998; Scarascia *et al.*, 1998; Mele *et al.*, 2006). This tectonic contact is thought to be the result of subduction of the Adriatic plate beneath the Apennines (Royden *et al.*, 1987; Carminati & Doglioni, 2012), or crustal shortening generated by lithospheric thrusting (Calamita *et al.*, 2004; Boccaletti *et al.*, 2005; Finetti *et al.*, 2005).

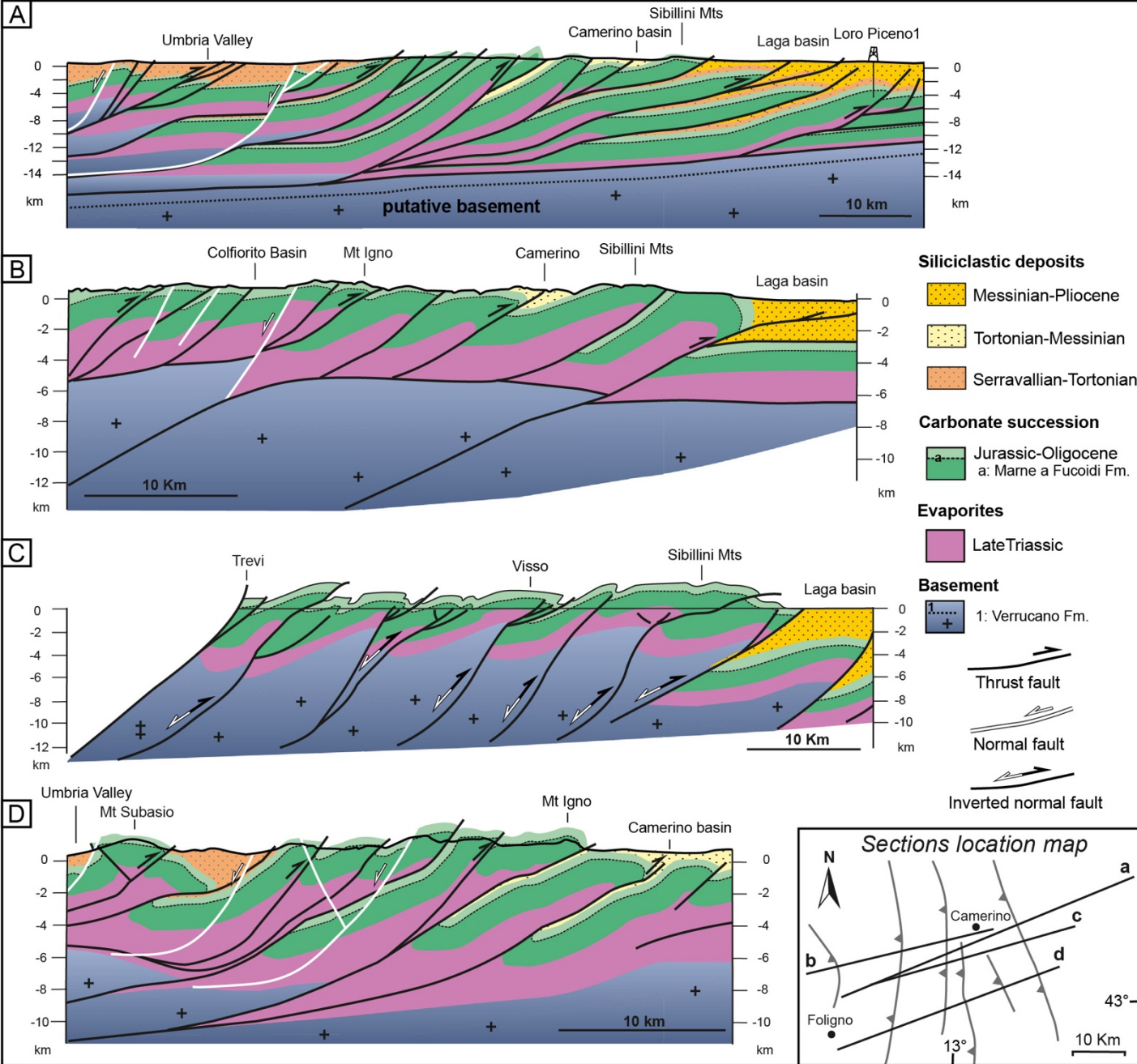


Figure 2.7- Proposed structural models for the UMAR: i) thin-skinned model (a) modified from Bally *et al.* (1986); ii) thick-skinned model (b) modified from Calamita *et al.* (2000) and (d) modified from Mirabella *et al.* (2008); iii) inversion tectonics (c) modified from Tavarnelli *et al.* (2004).

Thick-skinned (Figures 2.7B and 2.7D) and inversion tectonics (Figure 2.7C) models also emerged from these observations, with the dominant ideas being: (i) imbricated thrusts involving both the basement and the cover and high angle thrusts resulting from the inversion of steeply dipping normal faults (thick-skinned tectonics); (ii) inversion of Permo-Triassic basins coupled with reactivation of basement faults (inversion tectonics) (Coward *et al.*, 1999; Mirabella *et al.*, 2008). In the inversion model, Miocene thrusts reactivated pre-orogenic normal faults. Tavarnelli *et al.* (2004) applied this model to the Apennines: a network of transverse Mesozoic faults would compartmentalize the folded and thrust structures of the Apennines by their repeated reactivation during the Cenozoic. The Ancona-Anzio Line appears to be the most continuous of this set of transverse faults (Castellarin *et al.*, 1982), separating Umbria-Marche from Abruzzo, and merging with the Sibillini Mountains thrust front (*i.e.*, lateral ramp) (Figure 2.6). This syn-sedimentary normal fault initiated in the Jurassic would have undergone two successive phases of reactivation, in connection with the Miocene compressional tectonics: it was reactivated as a dextral strike-slip fault in the Miocene, then as a thrust fault during the Pliocene. Other examples of reactivated faults would also have affected the Apennines and Umbria-Marche, such as the Valeria Line (Decandia, 1982) in the southern part of the UMAR which was reactivated as a sinistral strike-slip fault in the Oligo-Miocene, then as a dextral transpression in the Mio-Pliocene, and associated with a succession of N-S folds and thrusts.

This central area of the Apennines is composed of a series of NE-verging folds (Figure 2.6). In the western part, the Subasio Anticline is a double plunging fold whose backlimb (*i.e.* western limb) was affected by a W-dipping normal fault called the Mt. Subasio Fault, as well as by a backthrust fault (Deiana, 1965). Pliocene–Quaternary continental deposits widely crop out along the Umbria Valley and in the hanging-wall of this W-dipping normal fault (Scisciani *et al.*, 2014). The eastern part is more complex and is constituted by four major anticlines. The Mount Igno-Valnerina is the most continuous fold in this eastern part, overturned in its lower part. It was affected by normal faults related to the Jurassic pre-thrusting extension, synchronous with Mesozoic deposits and reactivated during the Miocene. The amount of shortening recorded in the Mount Igno-Valnerina was about 1.7 km (Scisciani *et al.*, 2014).

Northeast of Mount Igno, two major anticlines with axes NNW-oriented disappear under the Camerino basin. This basin was filled with Miocene turbidites and was affected by Miocene normal faults (Scisciani *et al.*, 2000). The eastern edge of the basin bounds the eastern part of the UMAR and forms a faulted area (west dipping thrust fault) where the Sibillini Mountains culminate. The Monte Vettore belongs to this massif and is the apex of the arc. It recorded a maximum shortening of about 10 km, as well as a maximum structural elevation with an exhumation of Jurassic rocks to more than 2000 m asl (Scisciani *et al.*, 2014). Another major structural unit compartmentalizes this eastern part of the Central Apennines: the Fiastrone Valley (eastern end of the area), where the main thrusts are located. In this sector, the pelagic limestones of the early Jurassic overlaps the Tortonian and Messinian formations, and the strata are highly dipping, even overturned. The recorded shortening was about 4

km (Di Domenico *et al.*, 2012); however, it is lower by 2 km in the Mount Vettore area (northern area), where the orogenic contraction is reduced towards the northwest (Mazzoli *et al.*, 2005). In addition, the Sibillini Mountains thrusts are responsible for minor folded structures affecting the overlying Paleogene-Miocene marl units and Messinian silico-clastic deposits (Koopman & Anton, 1983; Scisciani & Montefalcone, 2005). The total shortening is estimated about 7.7 km, each of thrust-related fold structures recording an amount of shortening from 1 to 3 km. The front of the thrust belt confines the Pliocene foredeep to the east. This frontal zone is composed by tectonic duplications of Mesozoic carbonate cover and underlying basement related to an imbricate leading edge thrust system (Scisciani *et al.*, 2006; Fantoni & Franciosi, 2010). In addition, these anticline structures were sometimes affected by NW-SE trending Quaternary normal faults (Scisciani *et al.*, 2014). These faults are related to recent seismic activity, *i.e.* the 1997 Umbria-Marche seismic sequence, and juxtapose Quaternary continental deposits with Jurassic and Miocene carbonates (Calamita *et al.*, 2000). Actually, the NE-SW extension recorded during the Quaternary was at the origin of the almost synchronous activation of the normal faults in the whole axial zone of the central Apennines (estimated around 1.1 Ma) (Calamita *et al.*, 2000). Two tectonic phases were then distinguished: (i) a first active phase until the early Pleistocene, characterized by the migration of the fold-and-thrust belt (FTB) and the foreland. The front of the Apennines, located under the Adriatic, tended to deepen towards the west, until it involved the Moho under the Tiber valley (Calamita *et al.*, 2000). This tectonic event was also marked by the development of the Altotiberina Fault, a weakly eastward dipping normal fault located in the inner zone (Barchi *et al.*, 1998; Calamita *et al.*, 2000); (ii) a second phase, starting in the early Pleistocene, associated with the development of inversion ramp systems and steeply dipping normal faults (Calamita *et al.*, 2000). Furthermore, the increase in seismic activity at 6-7 Ma recorded towards the SE (Westaway, 1992; Ekström *et al.*, 1998), would have as a potential origin the counterclockwise rotation of the Apulean block around a pole located in northern Italy, as suggested by Anderson & Jackson (1987).

3- Kinematic evolution

Although its structural style is still a matter of debate, the UMAR is described as a succession of several thrust sheets successively formed over time according to a west-east diachronism. These thrust sheets are thus related to Late Messinian-Early Pliocene deformation in the western part (Sibillini thrusts, San Vicino) and Plio-Pleistocene in the eastern part (Ancona, Conero), and with an average slip rate of 8 mm/yr (Calamita *et al.*, 1994). The chronology of the compressional events in the external zones of the UMAR are detailed in the work of Calamita *et al.* (1994), in which the timing of the deformations and the associated rates were quantified using restored sections across the different external zone (Figure 2.8A). Guerrera *et al.* (2012) also studied the space/time evolution of the UMAR and of the northern Apennine Miocene foredeep, using information provided by the study of turbidite silicoclastic sedimentation. Furthermore, the multi-disciplinary approach of Curzi *et al.* (2020) aimed to estimate shortening and post compressional tectonic inversion coupling fieldwork data (*i.e.* detailed geological mapping and multi-scale structural analyses) with (i) illite-smectite paleogeotherm, (ii)

Considering these various studies, and based on the example presented by Beaudoin *et al.* (2016) at the scale of the fold (Figure 2.9), the following first-order fracture sequence can be proposed for the UMAR: four sets of joints and veins, and three sets of tectonic stylolites can be discriminated and associated with a deformation stage. The ante-fold contraction stage (N045 compression) is related to joints/veins of sets I and II striking N020 to N050 and to stylolites of set II-S with N020 to N050 striking teeth. The 20/30° variation in compression direction can be assumed to be related to strata rotation around a vertical axis on a fold or regional scale. The early folding stage is associated with: (i) E-W (N080–110) striking joints/veins of set III, (ii) ~E-W σ_1 -trending compressional and strike-slip compatible stress tensors and (iii) ~E-W trending tectonic stylolite teeth of set III-S. Sets III and III-S teeth are roughly perpendicular to the axis of the fold and can be related to the LPS. The ~E-W compression is interpreted as developed due to perturbation of the regional Apenninic compression because of the reactivation of the N180 striking fault inherited from the Jurassic. The curvature-related synfolding extension is related to N135 striking joints/veins of the set IV compatible with an extensional stress tensor with a horizontal σ_3 trending NE-SW. The LSFT is associated with E-W trending tectonic stylolite teeth of set IV-S, developed under an E-W striking σ_1 , and still consistent with the stress field under which the anticline grew. The second post-tilting event is associated with the occurrence of tail-cracks on the N090 striking fractures of set III related to the NE-SW post folding Apenninic contraction.

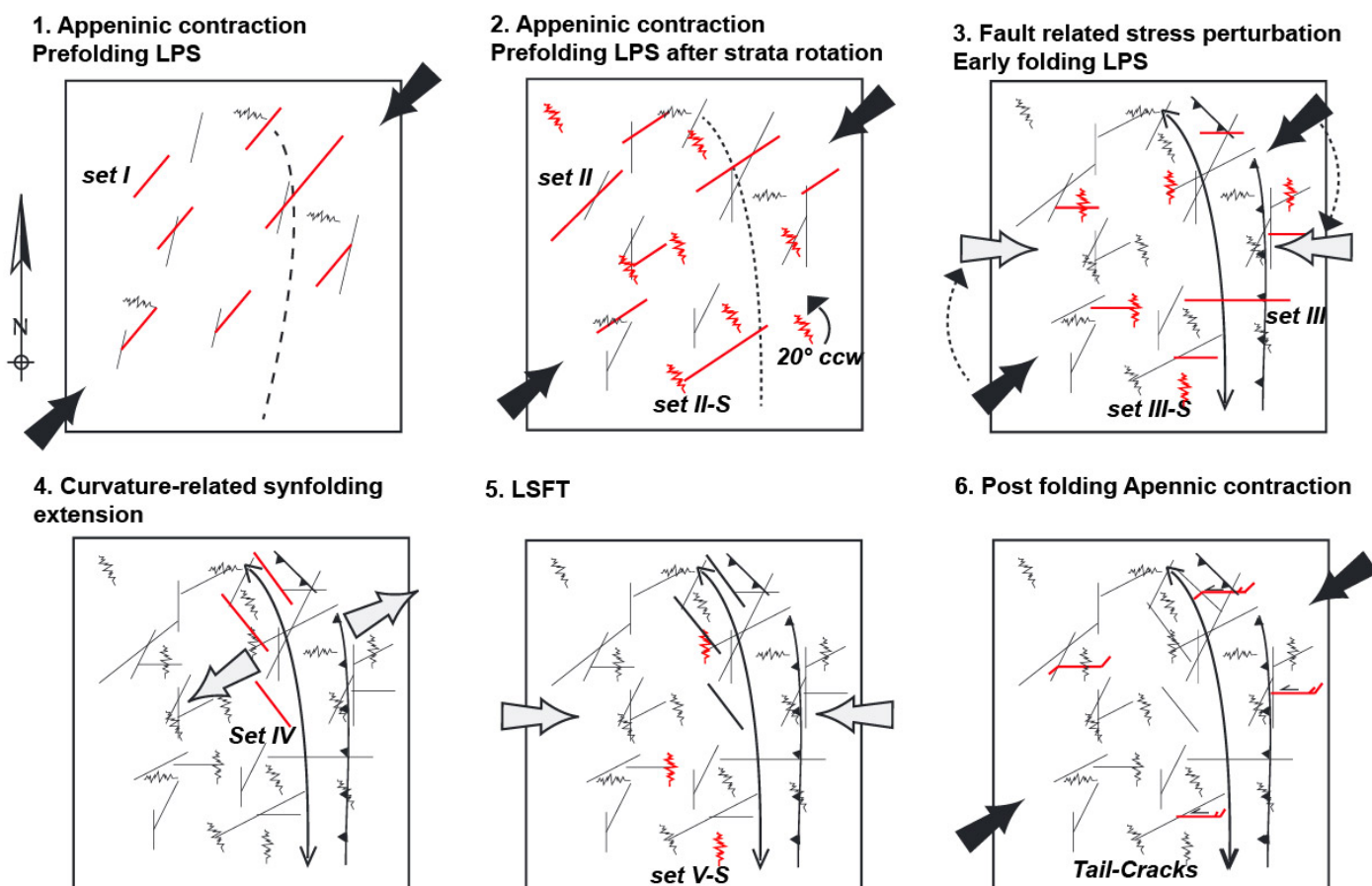


Figure 2.9- Cartographic view of the main directions of stresses and meso-structures developed within the Monte Nero Anticline. Regional stress directions are represented by the black arrows, and local stresses by the gray arrows. Number and lengths of mesostructures are not representative; modified from Beaudoin *et al.* (2016).

Chapter 3- Sedimentary Stylolite Roughness Inversion
Technique: application, limitations, and optimization

I- INTRODUCTION

Paleopiezometry applied to the roughness of sedimentary stylolites is a recent method of analysis of the magnitudes of the principal stresses (Schmittbuhl *et al.*, 2004). Today, this approach is used in a few tectonic studies (*e.g.* Beaudoin *et al.*, 2016, 2019, 2020c; a; Beaudoin & Lacombe, 2018; Lacombe *et al.*, 2021; Bah *et al.*, 2022; Zeboudj *et al.*, 2022) while being further explored through numerical simulations (Ebner *et al.*, 2009a; Koehn *et al.*, 2012, 2022; Rolland *et al.*, 2012). In these studies, stylolites are used as strain and stress gauges to estimate the orientation of paleo-stresses, but also their absolute values of formation stresses and amounts of compaction (Koehn *et al.*, 2022). Specifically, the SRIT of BPS allows to assess the vertical stress experienced at the time dissolution stopped along the pressure-resolution planes and thus assists in the reconstruction of the burial and contractional history (*e.g.* Beaudoin *et al.*, 2020c). As the SRIT relies on signal analysis of a stylolite track, various signal processing methods were tested for this methodology (Chapter 1), *i.e.* FPS (Simonsen *et al.*, 1998; Renard *et al.*, 2004), AWC (Renard *et al.*, 2004), RMS (Candela *et al.*, 2009), MM (Candela *et al.*, 2009), and the suture functions including COR (Candela *et al.*, 2009). Candela *et al.* (2009) generated synthetic self-affine surfaces with azimuthal variation of the scaling exponent (between 0.5 and 1) to quantitatively test the reliability and accuracy of all these methods. Then, they demonstrated that: (i) AWC and FPS are the methods that best determine the Hurst coefficients over the entire variability tested, regardless of the direction studied; (ii) RMS and COR tend to underestimate and overestimate the Hurst coefficient, respectively. To date, no consensus appears to exist about the choice of the more appropriate signal processing method. Numerical simulations carried out by Ebner *et al.* (2009a) demonstrated similarities of L_c returned by either FPS or AWC. These similarities were also observed in the study of BPS of the Cirque de Navacelles limestones (Ebner *et al.*, 2009b), highlighting L_c value with an equivalent order of magnitude for both signal analyses. On the contrary, the error analysis of Schmittbuhl *et al.* (1995), using synthetic signals with known properties, highlighted a systematic offset between FPS and AWC. This offset was also observed when applying the method to field cases of study, *e.g.* works of Beaudoin *et al.* (2019) in the Paris Basin. Simonsen *et al.* (1998) also demonstrated that AWC significantly outperforms FPS in case of a small number of samples. Other results reinforced the controversy, such as the work of Karcz & Scholz (2003) which studied stylolites from the Calcare Massiccio (Apennines) and determined their fractal properties using the method of Eke *et al.* (2002), implying two successive methods of signal processing and digital analysis, *i.e.* FPS and Scaled Windowed Method (SWL, Cannon *et al.*, 1997). They demonstrated that some of them are related to fractal signal, *i.e.* recording of a single self-affine scaling regime with no characteristic cross-over length. In the literature, the FPS analysis was somehow favored (*e.g.* Beaudoin *et al.*, 2016, 2020b; Bah *et al.*, 2022; Zeboudj *et al.*, 2022). In particular Rolland *et al.* (2012) and Rolland (2013), on the basis of the work of Candela *et al.* (2009), quantified the error on the surface anisotropy estimation and showed that FPS is associated with the lowest errors. In contrast, other works used preferentially AWC compared to FPS. For example, in the

study of vertical stress in the Bighorn Basin (Wyoming, Beaudoin et al., 2020c), AWC was chosen to conduct the signal analysis, because it was proven to be less sensitive to the quantity and quality of the samples. Likewise, in the Paris Basin study (Beaudoin *et al.*, 2019) for which past maximum burial depths were derived using SRIT on a large dataset and compared to independent thermal burial modelling, results showed a better consistency of the results using AWC than the COR function. In addition, studies reported some impact of natural factors on the crossover length resulting from signal analysis, correlating the reliability of the SRIT with (1) the morphology of the stylolites and (2) the sedimentary texture of the carbonate host rock (*e.g.* Beaudoin *et al.*, 2019; Bah *et al.*, 2022). Point (1) can be summarized as follows: depending on the morphology of the stylolite considered (Figure 1.12), *i.e.* columnar dominated (1-2) *versus* peak dominated (3), the resulting depth derived from the inversion does not have the same significance. While stylolites belonging to classes 1 and 2 systematically underestimate the maximum depth of burial experienced by the strata under a vertical maximum principal stress, stylolites belonging to the type 3 are more likely to record a L_c consistent with the maximum principal stress experienced by the strata, particularly in mud-supported lithologies (Bah *et al.*, 2022). Thus, the depths associated with the columnar types tend to be interpreted as intermediate depths, while the peak-type stylolites are reliable indicators of the maximum depth of burial. Stylolites from class 4 do not show any systematic behavior as a function of depth, and therefore do not allow a reliable estimate of burial depth (Beaudoin *et al.*, 2019). Point (2) is based on the few studies where the crossover length (L_c) seemingly depends on the depositional texture (*e.g.* Beaudoin *et al.*, 2019; Bah *et al.*, 2022). In the Paris Basin, the L_c are different according to the texture, wackstone, floatstone and packstone lithologies being to be the most likely to record the maximum burial depth (Beaudoin *et al.*, 2019). In the TOCA formation in offshore Congo, the study of a large population of stylolites unravels that the L_c values are significantly lower in mud-supported textures (mudstone/wackestone) than in grain supported textures (packstones) (Bah *et al.*, 2022). It is worth noting that the relationship between stylolite morphology and L_c tends to be replicated in various cases. Nevertheless, the effect of depositional texture on L_c is highly debatable because of the overall low number of data, as recent studies using a large data set to understand stylolite distribution and morphology neglected L_c values (Peacock *et al.*, 2017; Humphrey *et al.*, 2020).

All these considerations, and especially the timing estimation, highlight the limitations of the application of the SRIT to natural cases, and thus raise the question of its reliability and conditions of use. Moreover, this questioning is even more meaningful considering the increasing geological implications of this methodology in basin studies as for instance derivation of the timing of deformation (*e.g.* Beaudoin *et al.*, 2019; Bah *et al.*, 2022; Zeboudj *et al.*, 2022). Building on the large set of stylolites (186) sampled throughout the UMAR, this first chapter aims at (1) identifying the reasons that explain discrepancy between the results of AWC and FPS applied to natural stylolites, and (2) proposing practical solutions to improve the reliability and consistency of the results of this palaeopiezometric technique. The idea is not to critically discuss the signal analysis process behind the SRIT, but instead

to refine the conditions and limitations of its application, to provide the community with a new reliable and easy-to-use paleopiezometric tool for basin analysis.

II- OVERVIEW OF THE DATASET

1- Location and preparation of samples

The studied bedding-parallel stylolites were collected across the central portion of the UMAR, a young carbonate-dominated FTB of which sedimentological and structural characteristics are presented in Chapter 2. The dataset consists of 186 stylolites sampled across the UMAR, along a large SW-NE transect including 7 folded structures (Figure 3.1): the Corona, Gubbio, Subasio, San Vicino, Cingoli and Conero anticlines. Samples were collected from the Meso-Cenozoic carbonates outcropping in this area, in the Maiolica and Scaglia Bianca, Rossa and Variegata formations (Figures 2.4 and 3.2). The dominant lithologies are mud-supported platform carbonates, in which stylolites of various morphologies are referenced, *i.e.* columnar (1-2) or peak (3) types. A more detailed geological description of the structures studied is given in Chapters 4 and 5.

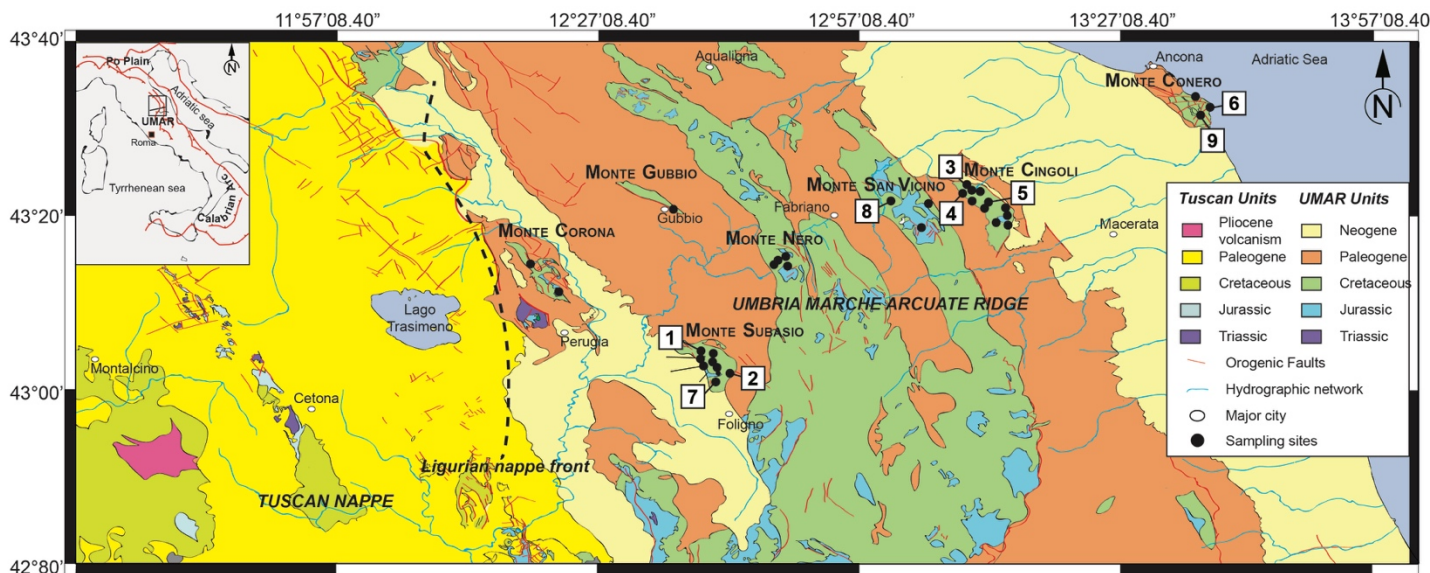


Figure 3.1- Location of samples across the UMAR. The numbers locate the examples of outcrops, samples and results presented in Figures 3.2, 3.3 and 3.4 respectively: (1) the Subasio Anticline, Scaglia Bianca Formation; (2) the Subasio Anticline, Maiolica Formation, sample SUB72_BPS1; (3) the Cingoli Anticline, Scaglia Rossa Formation, sample C15_BPS2; (4) the Cingoli Anticline, Maiolica Formation; (5) the Cingoli Anticline, Scaglia Bianca Formation; (6) the Conero Anticline, Maiolica Formation, sample CON6_BPS1; (7) the Subasio Anticline, Scaglia Bianca Formation, sample SUB113_BPS1; (8) the San Vicino Anticline, Maiolica Formation, sample A104_BPS13; (9) the Conero Anticline, Scaglia Bianca Formation, sample CON20; modified from Beaudoin *et al.* (2020a).

Samples are prepared in laboratory for subsequent analysis and cut in perpendicular planes to the stylolite plane. The resulting faces are then polished and scanned at high resolution, so that the stylolite track can be extracted and used for inversions following the protocol described in Chapter 1. As examples, Figures 3.3 and 3.4 present the tracks of 6 stylolites studied across the UMAR (located by numbers in Figure 3.1), as well as the associated inversion results.

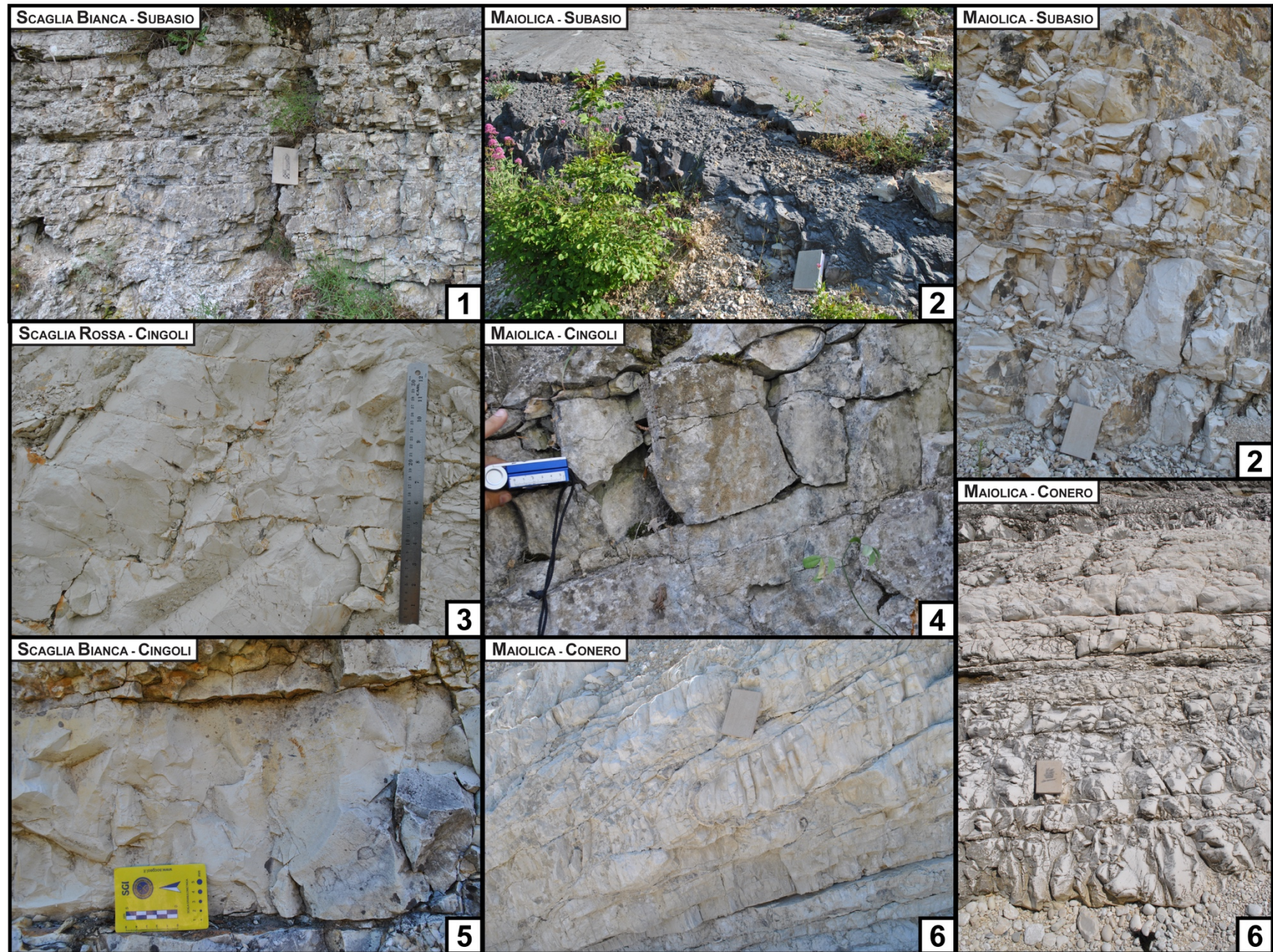


Figure 3.2- Examples of outcrops studied across the UMAR, located by the numbers on the map in Figure 3.1.

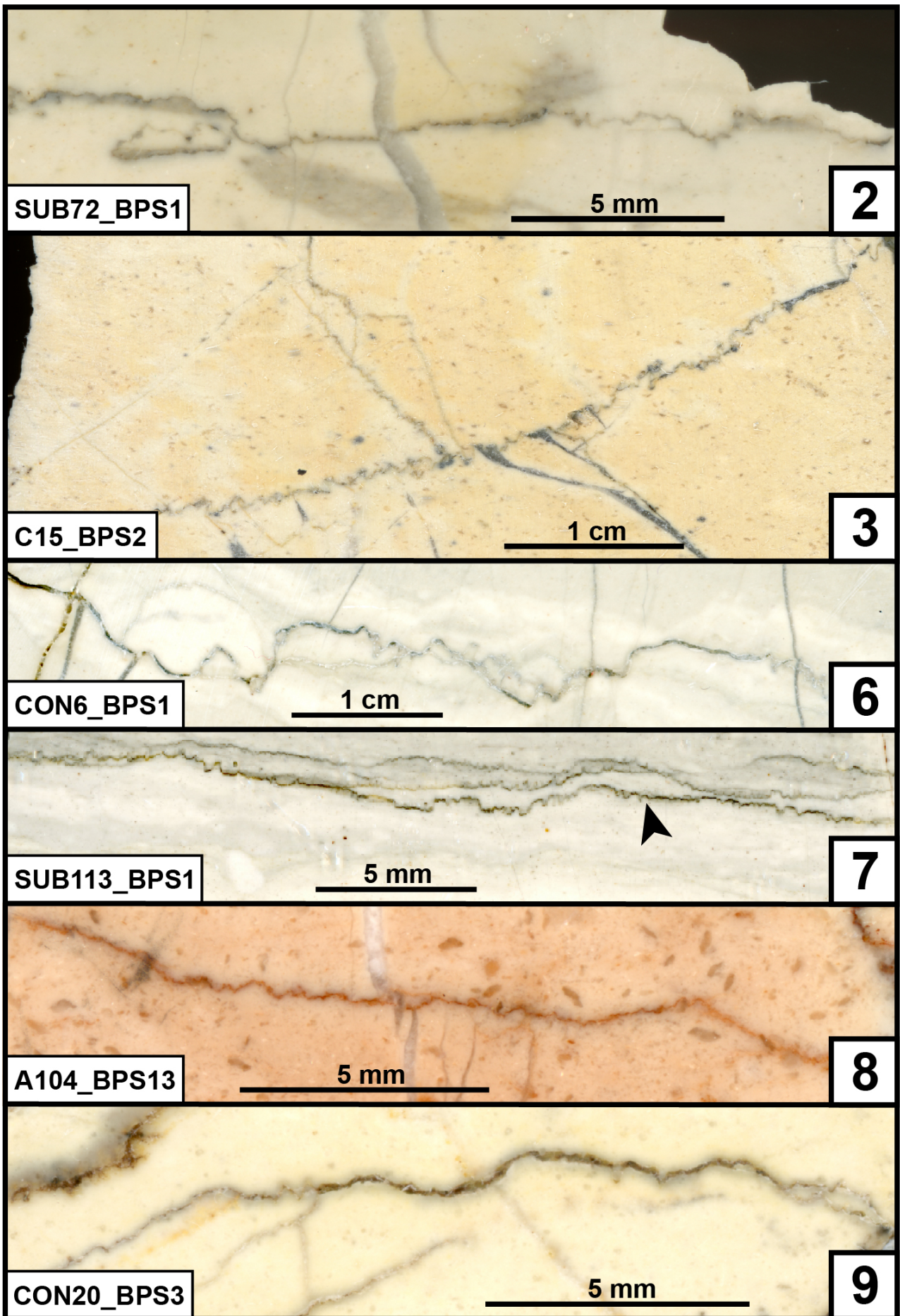


Figure 3.3- Examples of BPS studied across the UMAR, located by the numbers on the map in Figure 3.1.

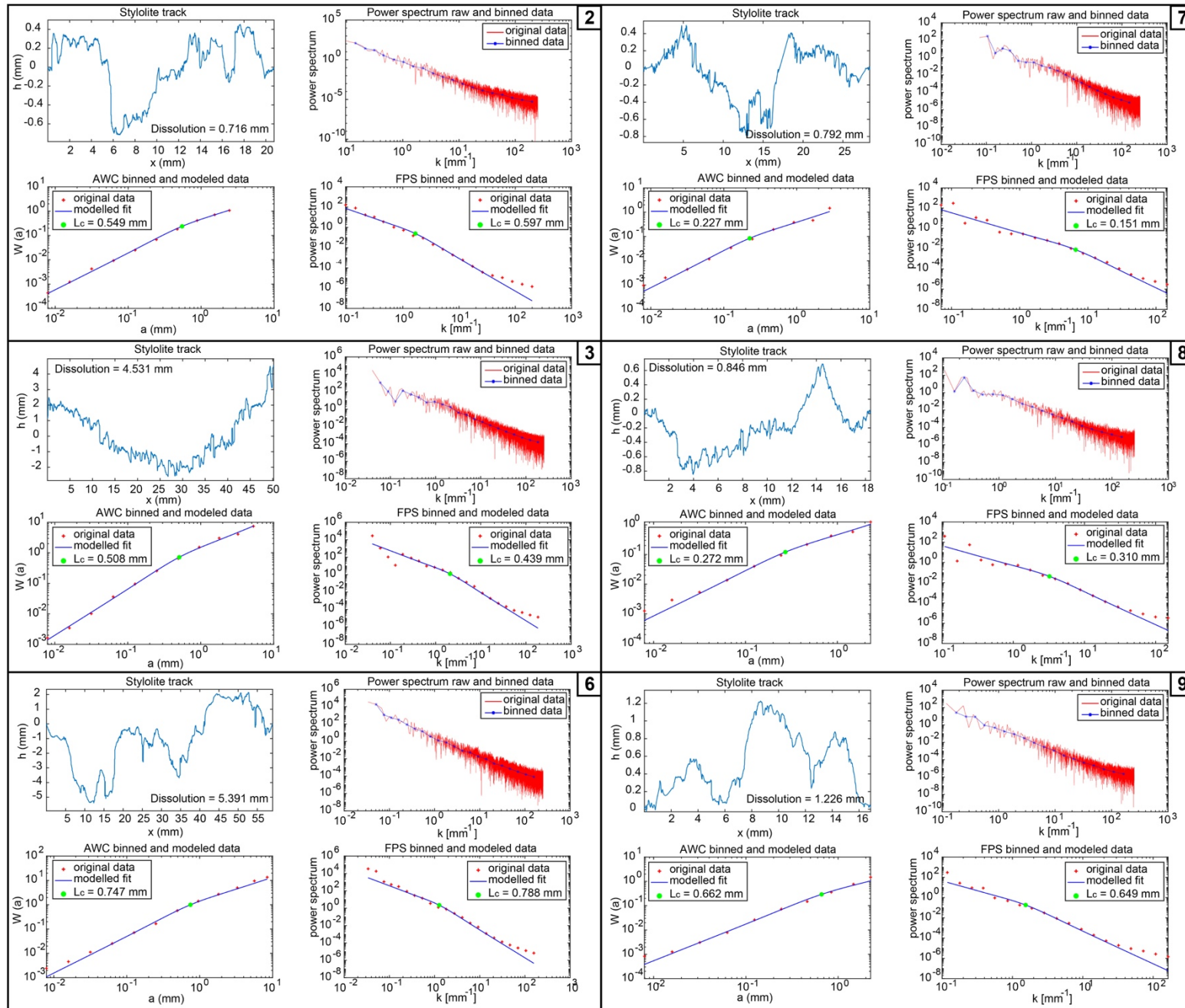


Figure 3.4- Results corresponding to BPS presented in Figure 3.3, and located in Figure 3.1

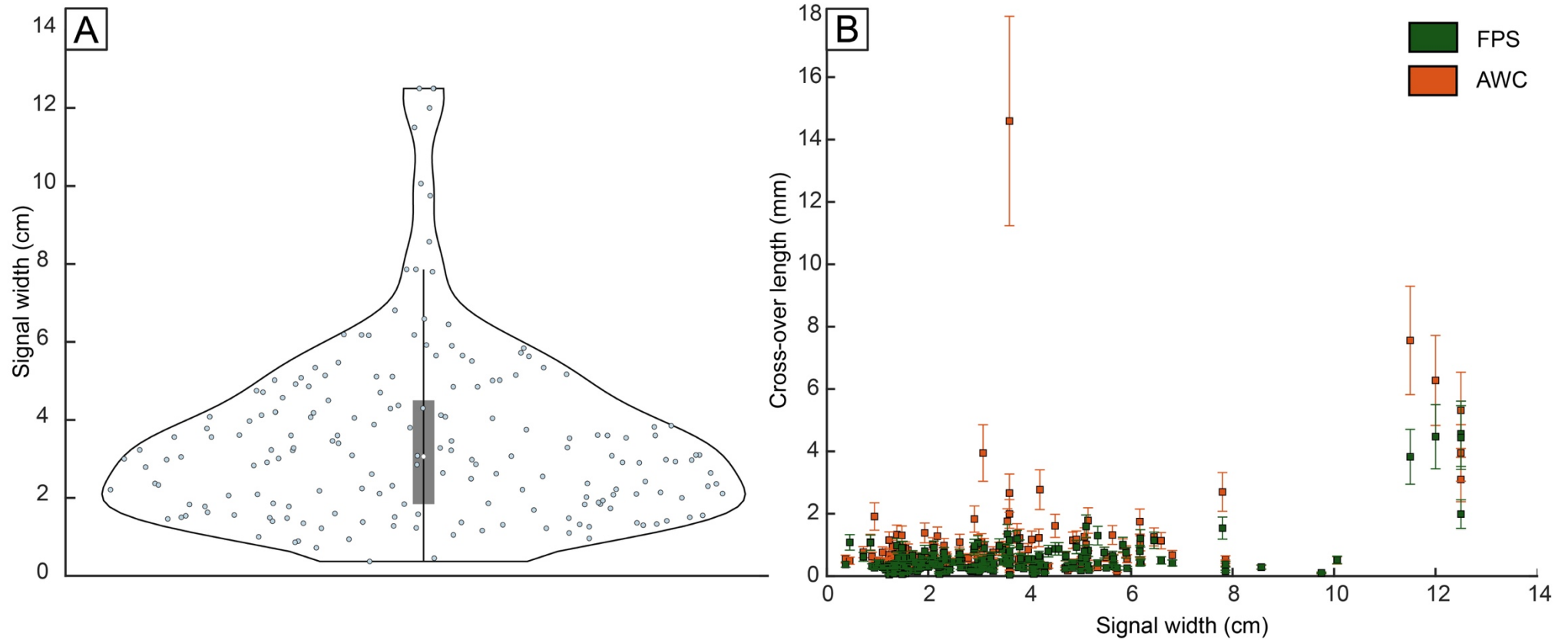


Figure 3.5- (A) Statistical distribution of signal widths corresponding to analyzed stylolites (Violin plot). The distribution is unimodal, with a width modulus of 2.98 cm. (B) Evolution of the cross-over lengths as a function of signal widths, for FPS and AWC treatments, considering 23% uncertainty on these L_c values (Rolland *et al.*, 2014); For these (A) and (B) graphical representations, the entire dataset is considered (*i.e.* 186 values of track and cross-over lengths). (C) Examples of stylolite track, with two different morphologies: columnar type (1-2) on the left and peak type (3) on the right, sampled in Subasio in the Maiolica and Scaglia Rossa formations respectively.

2- Typology of the studied stylolite tracks

Stylolite tracks are characterized by their roughness, their morphology, and their width. Note that the width corresponds to the width of the treated signal, and not that of the stylolite in the rock. Distribution of widths in the whole population is represented as a Violin plot (Figure 3.5A), a plot that represents both the distribution of a population (median value, quartiles and some deciles), along with the individual values in an envelope of which the width corresponds to the probability of the distribution modeled from the data (Hintze & Nelson, 1998). In other words, a random individual stylolite in a population will have more chance to correspond to the width(s) at which the wider envelope is predicted. The cross-over lengths (L_c) obtained after inversion of the 186 stylolites are also plotted as a function of stylolite track lengths, for both signal analysis methods (*i.e.* AWC and FPS, Figure 3.5B).

The population studied is characterized by the stylolites displaying a peak morphology (75%, versus 25% columnar, *e.g.* in Figure 3.5C), and the studied signal widths rarely exceed 8 cm, following an unimodal distribution with a modulus of 2.98 cm (Figure 3.5A). Provided that all results are considered valid, two ranges of L_c values seem to appear considering the size of the stylolite track. For track widths less than or equal to 10 cm (*i.e.* the size range containing the majority of stylolites studied), the cross-over lengths oscillate mostly between 0 and 3 mm, for both AWC and FPS. For longer tracks ($n=5$), L_c values vary between 2 and 8 mm.

These results highlight that a long track is required for finding high L_c , explaining a trend between the width of the stylolite and the cross-over length value. Note however that relatively low L_c values (3 mm) can be found in the long track samples, discarding a correlation *sensu stricto*. The second part of the study deals with the validity and consistency of the inversion process.

III- VARIABILITY OVER THE STYLOLITE TRACK ACQUISITION AND TREATMENT

1- Computer-assisted track segmentation

The SRIT uses 2D tracks of stylolite, that are in most studies drawn by hand from high resolution scan (*e.g.* Beaudoin *et al.*, 2016, 2020b). That leaves room for discrepancy on the track from one user to another, which can lead to differences in L_c values (Figure. 3.6). An image-analysis was developed, based on segmentation similar in concept to the one proposed by Rolland (2013). The stylolite is separated from the surrounding host rock using color thresholding process of the high-resolution picture (12800 dpi) using an image processing software (Photoshop®). The resulting image processing is then carried out in Matlab®, which main steps are detailed in Figure 3.6:

- (i) loading the image and conversion to greyscale;
- (ii) binarization of the image with a global threshold calculated using the Otsu method (Otsu, 1979), which chooses the threshold to minimize the intra-class variance of the thresholded black and white pixels;

- (iii) compute the complement of the binary image: black becomes white and white becomes black;
- (iv) fill operation on the background pixels of the binary input image. The points to be filled are specified here as the holes in the input binary image, a hole being defined as a set of background pixels that cannot be reached by filling the background from the edge of the image;
- (v) removal of all connected components (objects) that have less than a certain number of pixels of the original binary image, here initially set to 5000, producing a second binary image. The generated binary image is displayed on the screen so that the user can validate, or not, the segmentation performed. If the user validates the segmentation, the complement of the binary image obtained is generated and then converted to 8 bits. Otherwise, the user can repeat this processing step by changing the threshold number of pixels initially set until an optimal segmentation is obtained, *i.e.* a binary image without residue and for which the stylolite track is continuous.
- (vi) a final step is to transform the resulting image into a matrix, and to automatically extract the height and length information associated with the drawn stylolite.

These two drawing methods, *i.e.*, hand-drawing and computer-assisted, were tested to verify their agreement and reliability. A stylolite track was hand-drawn by two users and segmented using image analysis. For these three cases, tracks appear visually equivalent (Figure 3.6). However, L_c values resulting of the inversion process on the tracks highlight the impact of the drawing method on the cross-over length. Indeed, L_c obtained from the 2 hand-drawn tracks (*i.e.* redrawn manually by 2 different users) are different, *i.e.* 0.363 ± 0.08 mm for user 1 and 0.560 ± 0.13 mm for user 2, but overlap considering the uncertainty of 23% (Rolland *et al.*, 2014). The value obtained by the computer-assisted method (0.464 ± 0.11 mm) is intermediate.

Considering the uncertainty of 23% related to the estimate method of L_c (Rolland *et al.*, 2014), these ranges of values overlap, and these two drawing methods can be considered as valid and equivalent. Obtaining a track using image analysis is then a good method that allow a larger number of stylolites to be processed in a short time span, enabling the user to build a statistically viable population. It is worth noting that in specific cases, as for instance when the color contrasts between the stylolite and the matrix are not sufficient, the color thresholding is not an efficient method.

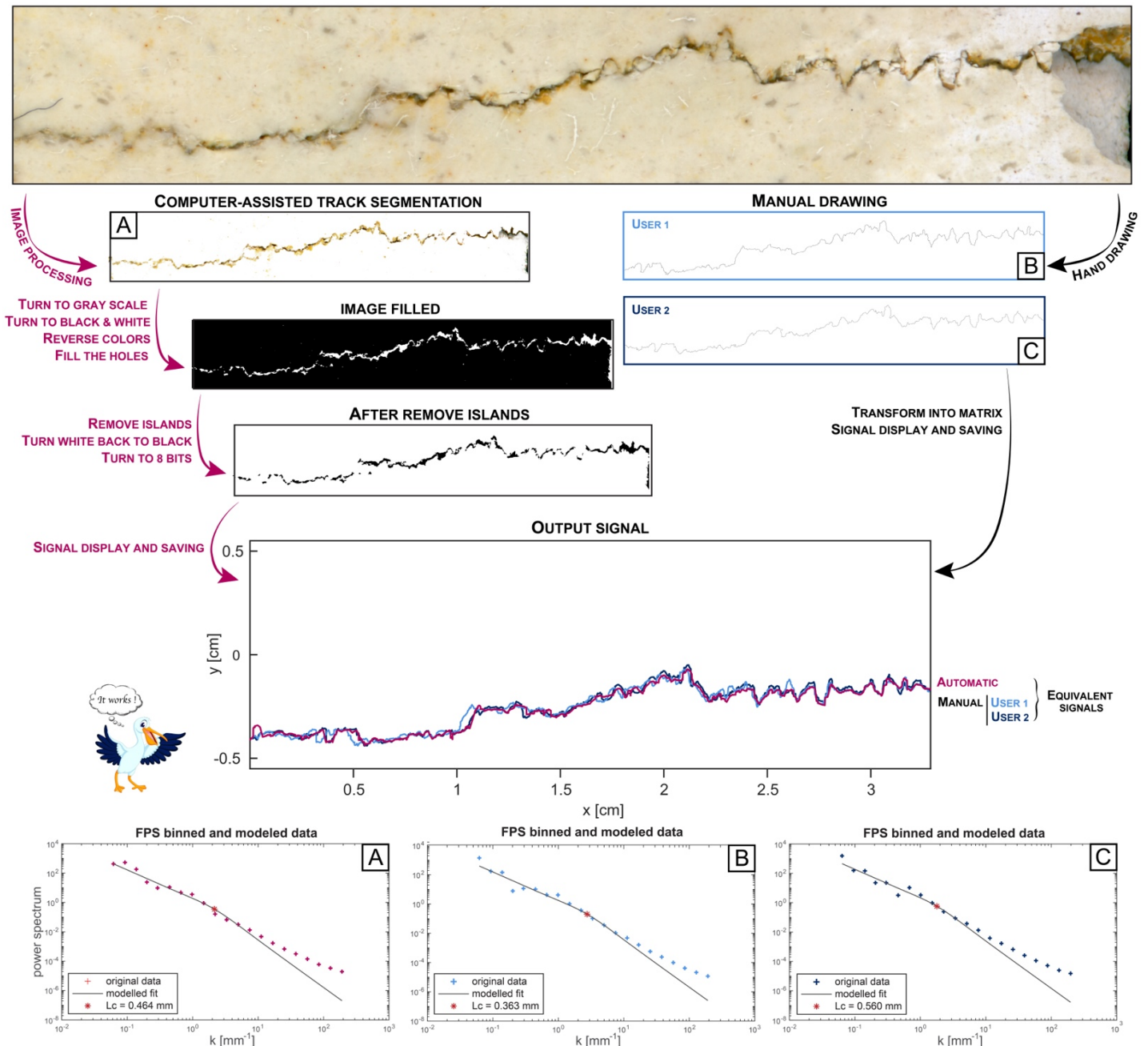


Figure 3.6- Workflow and result of image processing, using Photoshop® and Matlab® computer interfaces, and comparison with the hand drawing method (2 users considered). The computer-assisted method (and associated steps, left-hand side) is mentioned in purple, the hand drawing (right-hand side) in dark. Regression curves obtained from FPS analysis are also presented, showing the calculated cross-over lengths.

2- Finding the L_c

The accepted method to find the L_c is to use non-linear regression on a binned result of a signal analysis of a track, with the Hurst exponents (the slope in a log-log space) fixed to 0.5 and 1.1 (Schmittbuhl et al., 2004). This comes with an uncertainty calculated by Rolland *et al.* (2014) of about 23% on the value of L_c . That uncertainty can be accepted as acknowledgment of the fact the L_c is actually a space of transition between to roughness regime, unlikely being a single value. However, the question of minimizing this uncertainty in the determination of the cross-over length was the subject of a Master 1 internship (5 weeks) I co-supervised with Pr. D. Brito during the year 2022. The idea was to apply

alternative regression methods to a given stylolite track. Piecewise linear regression methods were therefore explored, looking for the minimum deviation between the model and the real data, and thus reducing the uncertainty on the determination of the slope break (Figure 3.7). The workflow is as follows: (i) reading and editing (if necessary) of the data, application of the FPS, AWC and logarithmic binning; (ii) construction of a linear regression matrix, then calculation of the sum of the squares of the deviations in values between the model and the data. This step is iterative and calculates this matrix, noted SRR, for each possible separator value (*i.e.* break in slope, noted b), the value b varying between the first and the last data point at regular intervals of 0.01; (iii) finding the minimum deviation corresponding to the linear regression of the data. The tests were carried out on real stylolite data, and clearly demonstrate the existence of two scaling regimes for stylolite roughness, as well as a characteristic break in slope located at the interface of these two regimes (Figure 3.7). However, the regression slopes, as well as the value of the slope break, remain dependent on the points chosen by the user for calculating the regression. Thus, although this work reinforces the validity of the models underlying the use of the SRIT, it has not minimized this 23% uncertainty in the determination of the cross-over length.

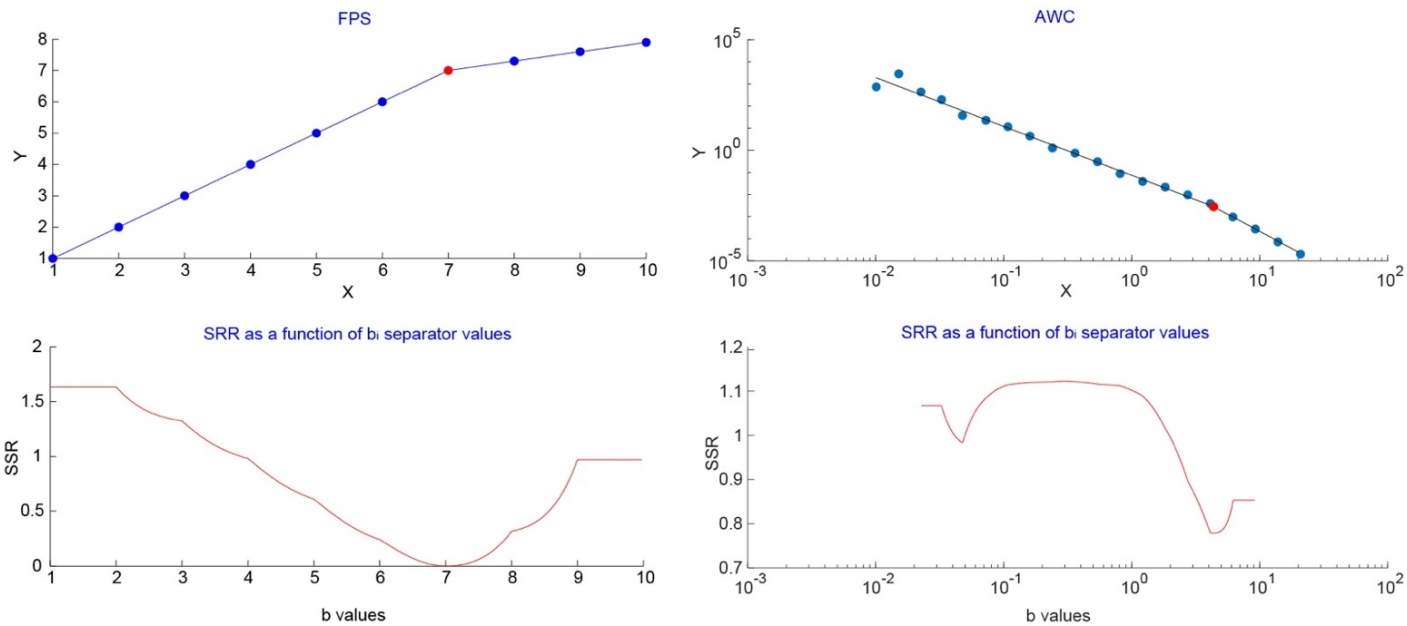


Figure 3.7- Examples of results of piecewise linear regressions applied to stylolite data. Both roughness regimes are shown, with a characteristic break in slope at the interface. The minimum is reached for $b = 7$ for the FPS and $b = 5$ for the AWC.

IV- IDENTIFYING AND OVERCOMING THE METHODOLOGICAL LIMITATIONS OF SRIT

1- Identified locks

Several cases of SRIT application highlighted some locks that constitute potential constraints for its use. In particular, some studies showed that inversions do not necessarily work, some stylolites displaying one scaling law, *i.e.* being described by a single Hurst exponent (*e.g.* Karcz & Scholz, 2003 Rolland *et al.*, 2014). The percentage of "waste", *i.e.* inversions that do not yield a cross-over length value

(Figure 3.8), was estimated to be between 20% and 40%, *e.g.* works of Rolland *et al.* (2014) and Beaudoin *et al.* (2019). In addition, differences between the two signal processing methods were also observed in some works. The Paris Basin study (Beaudoin *et al.*, 2019) showed that, depending on the signal processing used, the percentage of inversion that do not work varies, *i.e.* 27% for AWC, against 46% for FPS. Furthermore, the error analysis of Schmittbuhl *et al.* (1995) highlighted a systematic offset between FPS and AWC, and Simonsen *et al.* (1998) showed that AWC outperforms FPS in case of small number of samples.

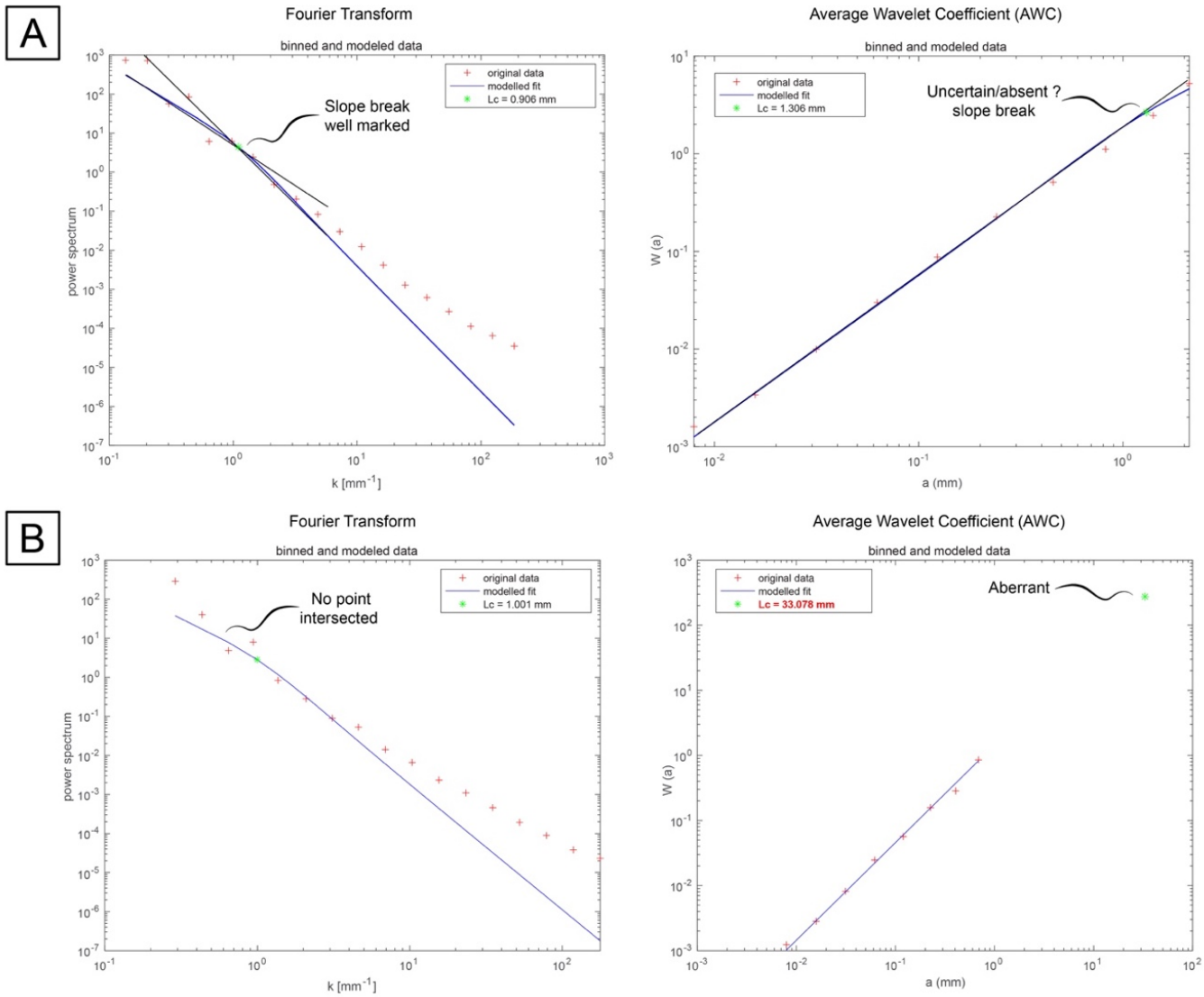


Figure 3.8- Practical cases where (A) the AWC curves are not usable, because the break in slope is not well-marked. (B) the two regressions are unusable: for the FPS, the regression lines pass through too few points; for the AWC, no break in slope is identified. The calculated cross-over length is therefore aberrant, being positioned outside the curve.

The question of the SRIT robustness is then raised: to what extent are the results exploitable and usable? Two criteria are therefore explored in order to provide elements of an answer: (i) a first criterion of validity, to judge whether the inversion is convincing, *i.e.* two slopes with a well-marked break in slope at the interface; (ii) a second criterion of consistency, *i.e.* similar results for the two signal processing methods. SRIT is applied on the dataset previously presented, using the classical method described in Chapter 1.

1.1- Validity of the L_c : is the signal analysis convincing ?

Resulting cross-over lengths are first classified using a qualitative color scale presented in Table 3.1. All the results, classified according to this colorimetric scale, are listed in Appendix 3.1, are plotted in the Figure 3.9, per sample and for the two signal processing inversion methods.

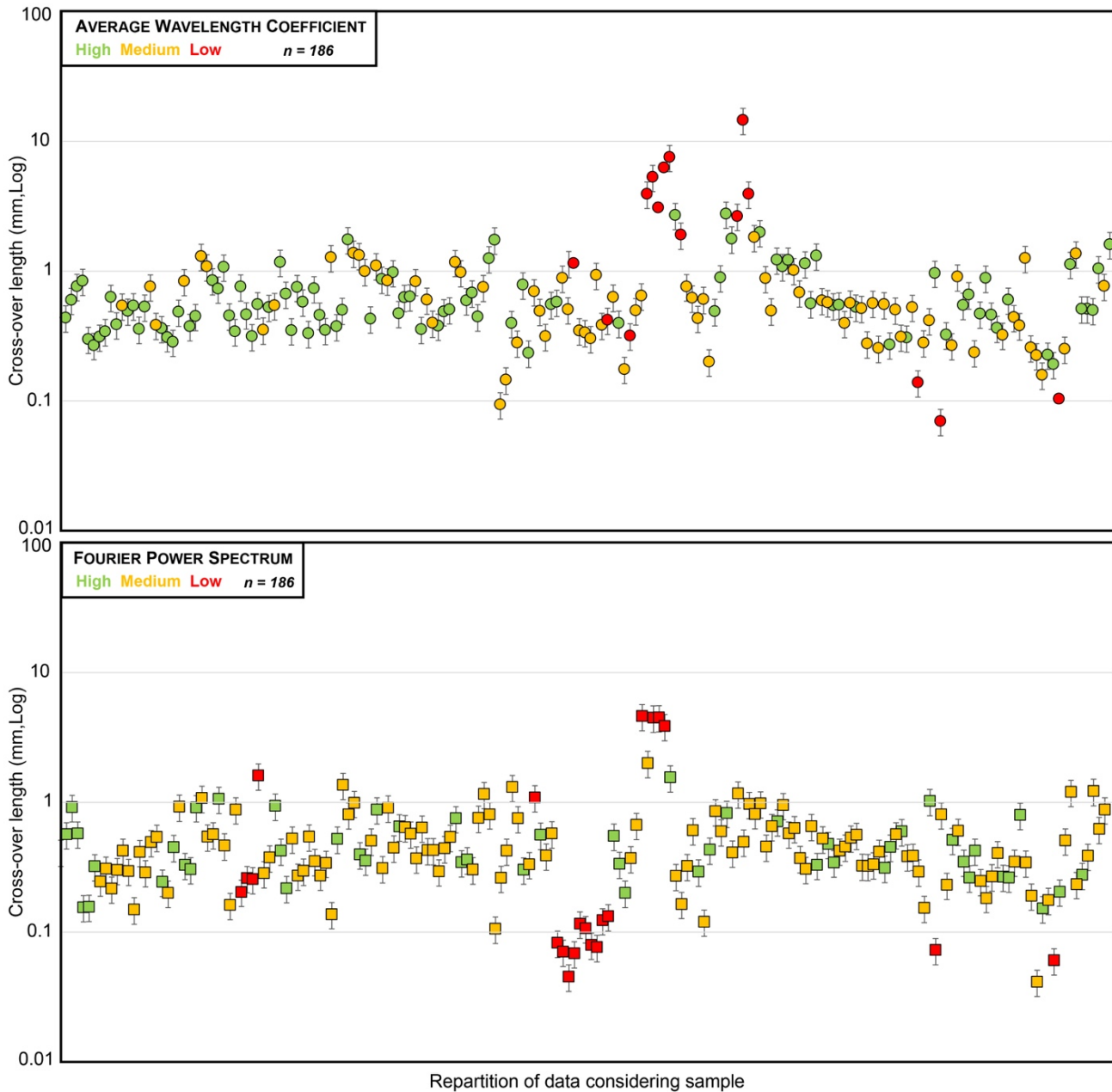


Figure 3.9- Value of the cross-over lengths per sample according to the signal analysis technique used (FPS as squares and AWC as circles). Color relates to the validity criterion as defined in Table 3.1. Red values correspond to invalid results (15 for AWC, 21 for FPS). For better readability, a logarithmic vertical scale is considered.

High	2 slopes with a well-marked break in slope
Medium	Both slopes exist, but pass through less than 3 points. Slope break is visible, but sometimes difficult to identify. L_c is on binned point.
Low	Only one line is observed, with no real break in slope. L_c value is an outlier (order of magnitude much larger than 1 mm). The inversion result is not used

Table 3.1 - Criteria used to assess the validity degree of L_c , defined after the inversion of the signals.

Considering the curves obtained and the above criteria, 28 inversions out of the 186 are inconclusive (*i.e.* abnormal L_c values and/or curves without a break in slope, Figure 3.9), distributed as follows: 15 for the AWC (*i.e.*, 8% of the 186 initial data, top graph on Figure 3.9), 21 for the FPS (*i.e.*, 11.2% of the 186 initial data bottom graph on Figure 3.9), and 7 cases for which neither of the two methods works (*i.e.*, 4%). This first analysis therefore provides a qualitative sorting of this dataset by distinguishing exploitable inversions from those that are not. 85% of the inversions are therefore conclusive, which is a first support to the validity of the method.

1.2- Consistency of the L_c : are the results similar within the uncertainty between the two signal analysis techniques?

As mentioned above, the L_c values returned after inversion sometimes can diverge significantly from one method to another. The variation rate (Δ), defined as the difference between AWC and FPS L_c values normalized to the AWC (Equation 3.1, percentage value), is calculated to quantitatively estimate if two L_c obtained by FPS or AWC are consistent with each other's:

$$\Delta = \frac{|L_c(\text{AWC}) - L_c(\text{FT})|}{L_c(\text{AWC})} \times 100 \quad (3.1)$$

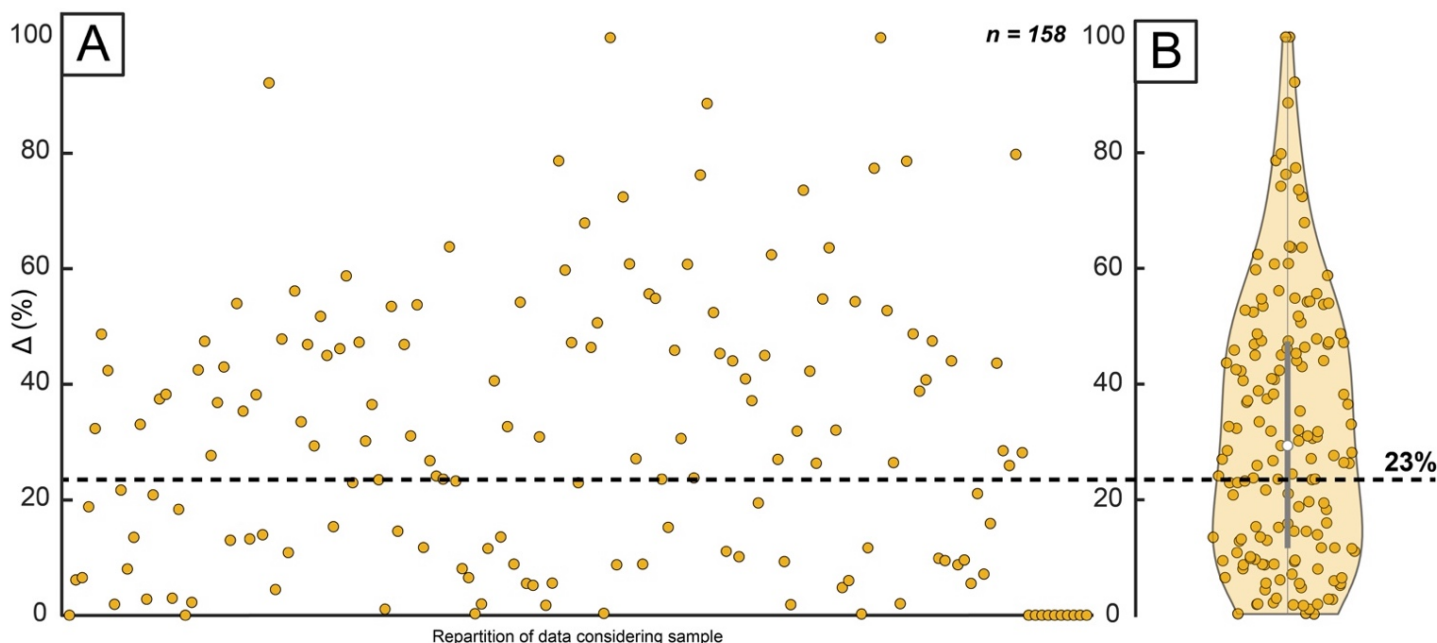


Figure 3.10- Degree of difference between L_c returned by AWC and FPS, quantified by calculating Δ (Equation 3.1). **(A)** Graphical representation of the value of Δ per sample. **(B)** Statistical distribution of Δ (Violin plot). The vertical scale is the same for both plots, on which the uncertainty associated with the non-linear regression methods is represented (23%). Above this value, the L_c is considered as not self-confident. The data set consists of the 158 stylolites for which inversions are valid.

Considering the uncertainty associated the estimation of the L_c (23%), L_c can be considered as self-consistent (*i.e.* similar with both techniques) if the $\Delta < 23\%$. Applied on a population of 158 stylolites for which inversions are valid, only 34% of the stylolite track inversions showed a self-consistency in the L_c results (Figure 3.10). In other words, if a vast majority of stylolite tracks can be analyzed successfully with either AWC or FPS (*i.e.* returning the 2 regimes of control separated by a L_c value), the comparison of the L_c value between AWC and FPS, that should be similar, fail in most cases. That makes the use of

the SRIT complicated as one might have to choose between two valid yet significantly different L_c , and as exemplified by the literature, the signal analysis method varies from one publication to another. This questions the robustness of the SRIT, and the following part is dedicated to find explanation and solution to this problem.

2- Overcoming the limitations

2.1- Optimization of the track for the signal analysis

The first step of the inversion process consists in preparing the stylolite track to facilitate its analysis. For instance, the average trend of the track needs to be horizontal in order to properly consider the roughness, *i.e.* the variation of height along the track. To do so, previous studies (*e.g.* Ebner *et al.*, 2009a; b, 2010; Rolland *et al.*, 2012; Rolland, 2013) applied the detrend function that restores the average trend of the stylolite track to the horizontal. This correction of the average slope of the track is made by locally applying the difference between the height of the track point and the correction of this average slope. The remaining data is returned as a residual vector, which is then processed by the AWC and FPS. Within the framework of this methodology, additional corrections are considered in order to improve the quality of the signal to be processed, and consequently the signal analyses (*i.e.* FPS and AWC) which are applied to it afterwards. These corrections consist of:

- (i) applying the detrend function on the raw signal (vector h grouping the successive values of the peak heights of the stylolite studied; the associated indexes are grouped in a vector x). The resulting vector h corresponds to the initial vector deduced from the values of the best straight-fit line applied on the raw data;
- (ii) correcting these residual data for slope effects. This correction step is based on an iterative process which calculates, over the whole signal, the absolute difference between 2 average heights, the first calculated over the first 20 points, the second over the rest of the signal. As long as this difference in height remains above a certain threshold value (fixed here at 10^{-10} mm), a second vector h_1 is generated, equal to the height values of the h vector corrected for the slope (*i.e.* at the point considered, subtraction of the h value and a quantity depending on the slope and the position). When this height difference becomes less than or equal to this threshold value, iterations end. The last average height difference returned corresponds to the dissolution value (in mm) associated with the stylolite studied, and the resulting h_1 vector becomes the signal to be inverted;
- (iii) set the extremities of the signal h_1 to 0 (when it is not already the case), by difference of the entire values of h_1 with the initial value of the vector.

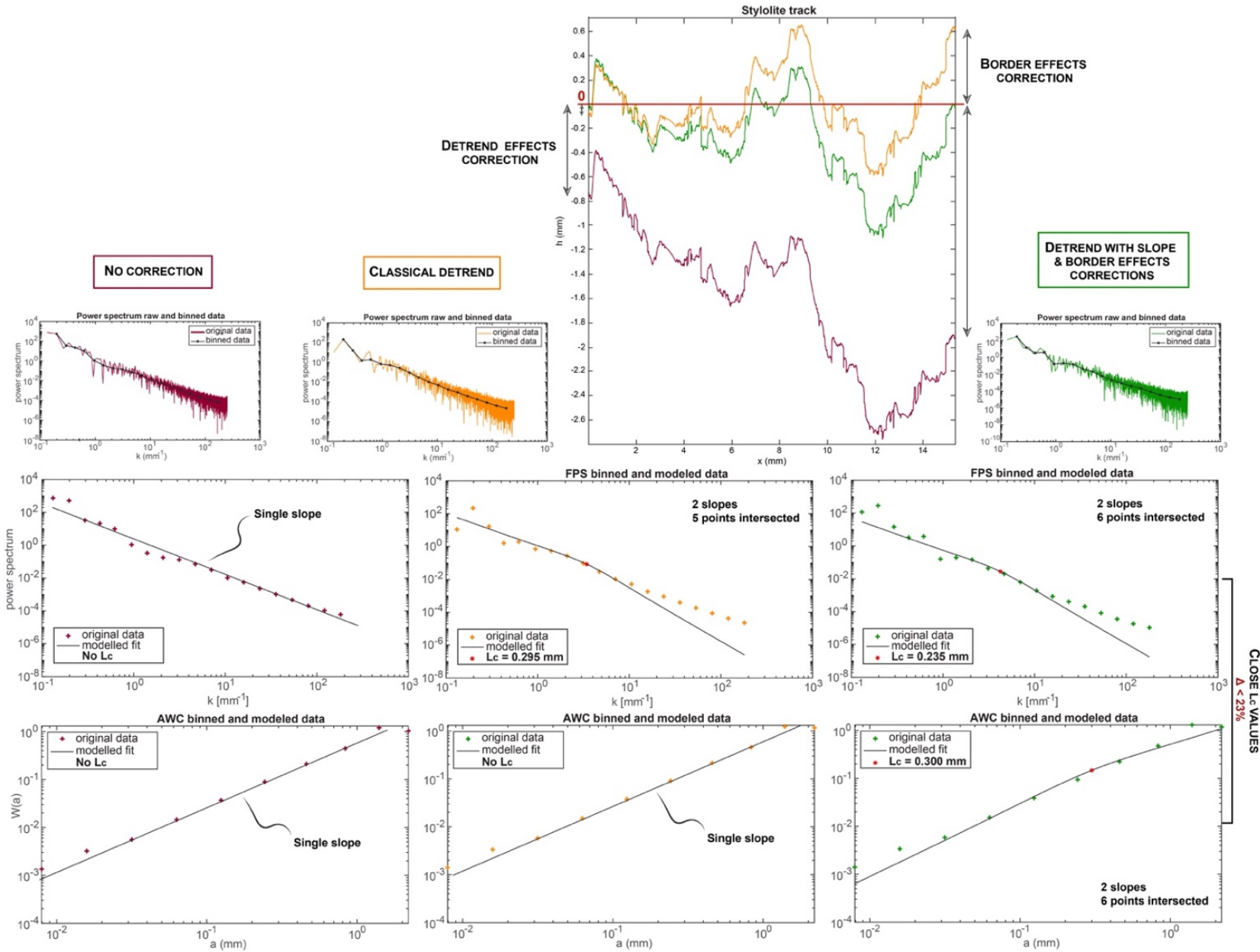


Figure 3.11- Comparative examples of signal corrections including or not slope and border effects. Data without correction, on those associated with the classical and new corrections are presented on the left (in purple), in the middle (in orange), and on the right (in green) of the figure, respectively.

Figure 3.11 presents the results of three cases of inversion applied on the same stylolite, differing in the type of correction applied to the stylolite track before the signal analysis step: (1) no correction is applied before the signal processing (Figure 3.11, left side, in purple). The resulting signal is neither reset to 0 nor corrected for border effects. The inversions are not valid, as the AWC and FPS return only one slope; (2) the track is corrected by the classical detrend (Figure 3.11, central part, in orange). The inversion by the FPS is valid, as both slopes are marked and pass through a finite number of points (5 intersected points in total). In contrast, the AWC inversion is not valid, as only one slope is returned; (3) the new methodology is applied, combining classical detrend and border effect correction (Figure 3.11, right side, in green). The signal analysis is convincing, returning 2 control regimes separated by a L_c for both AWC and FPS. The inversions are also consistent, L_c values being close, and the associated variation rate less than 23%.

These results demonstrate that these corrections favor a convincing signal analysis and consistent L_c values. Other tests and studies are then carried out to test the robustness of the method and to propose solutions to overcome methodological locks.

2.2- Stylolite morphology influence

The impact of morphology on L_c values is also studied. The morphologies considered are column (1-2) and peak (3) types, sampled in mudstone lithologies. Local effects related to the location of the samples are neglected, both types of morphologies being observed on all the sampling sites.

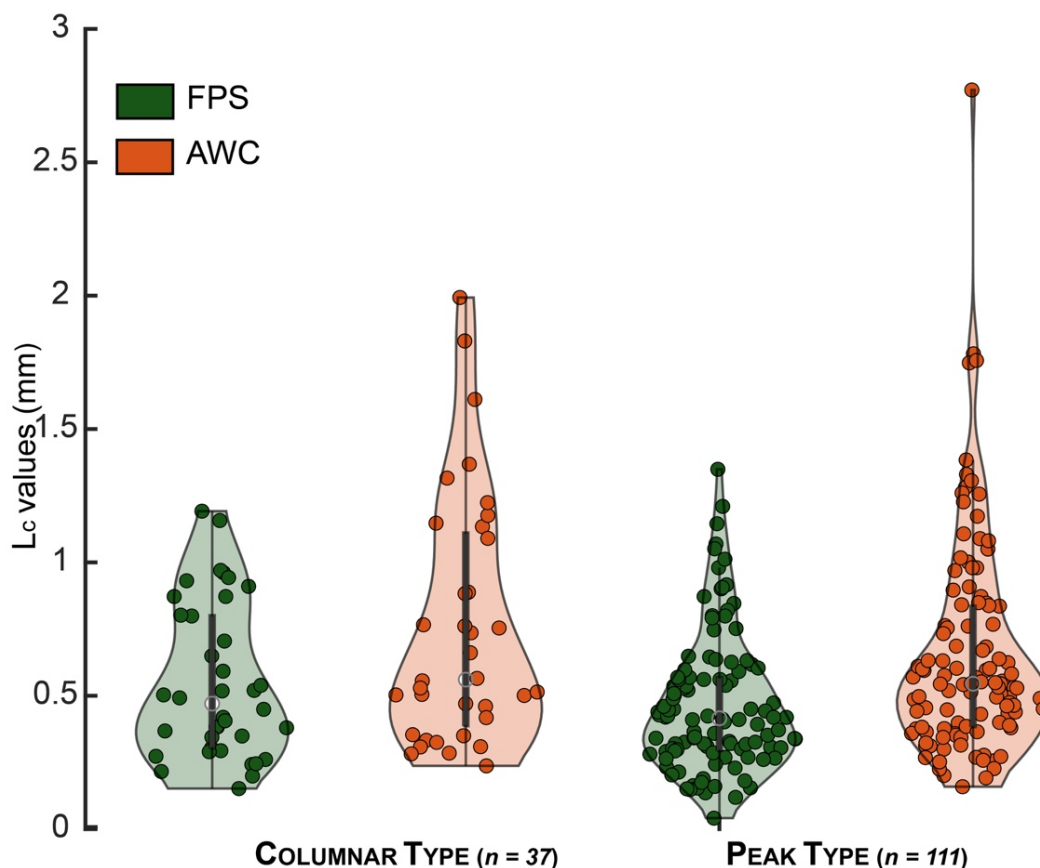


Figure 3.12- Statistical distribution and probabilistic model (Violin plot) of the cross-over lengths obtained by applying the classical method, for FPS and AWC regressions, for peak and columnar morphologies.

Figure 3.12 represents L_c values as a function of morphology and signal processing (*i.e.* FPS and AWC), and shows differences according to morphology: for columnar morphologies, the distribution is bimodal and L_c values are higher (considering median and quartile values). However, for peak morphologies, the distribution is unimodal, and the L_c values are lower (still considering medians and quartiles).

2.3- Concatenation of signals using the composite method: construction and inversion of composite sedimentary stylolites

The significant differences in the L_c values between FPS and AWC raise the question of the consistency of these two methods of signal analysis. Regarding the previous results (Figure 3.10), 66% of the inversions present significant variations in the L_c values achieved AWC and FPS. A plausible explanation would be the sensitivity of the latter to the number of points constituting the signal to be inverted. This width sensitivity was already intuited by Figure 3.5C, which shows variations in L_c with signal width (*i.e.* increase in L_c with stylolite track size). To confirm or deny this possible impact of stylolite size on L_c consistency, the variation rate Δ is plotted as a function of this parameter, by considering only the 158 valid inversions (Figure 3.13).

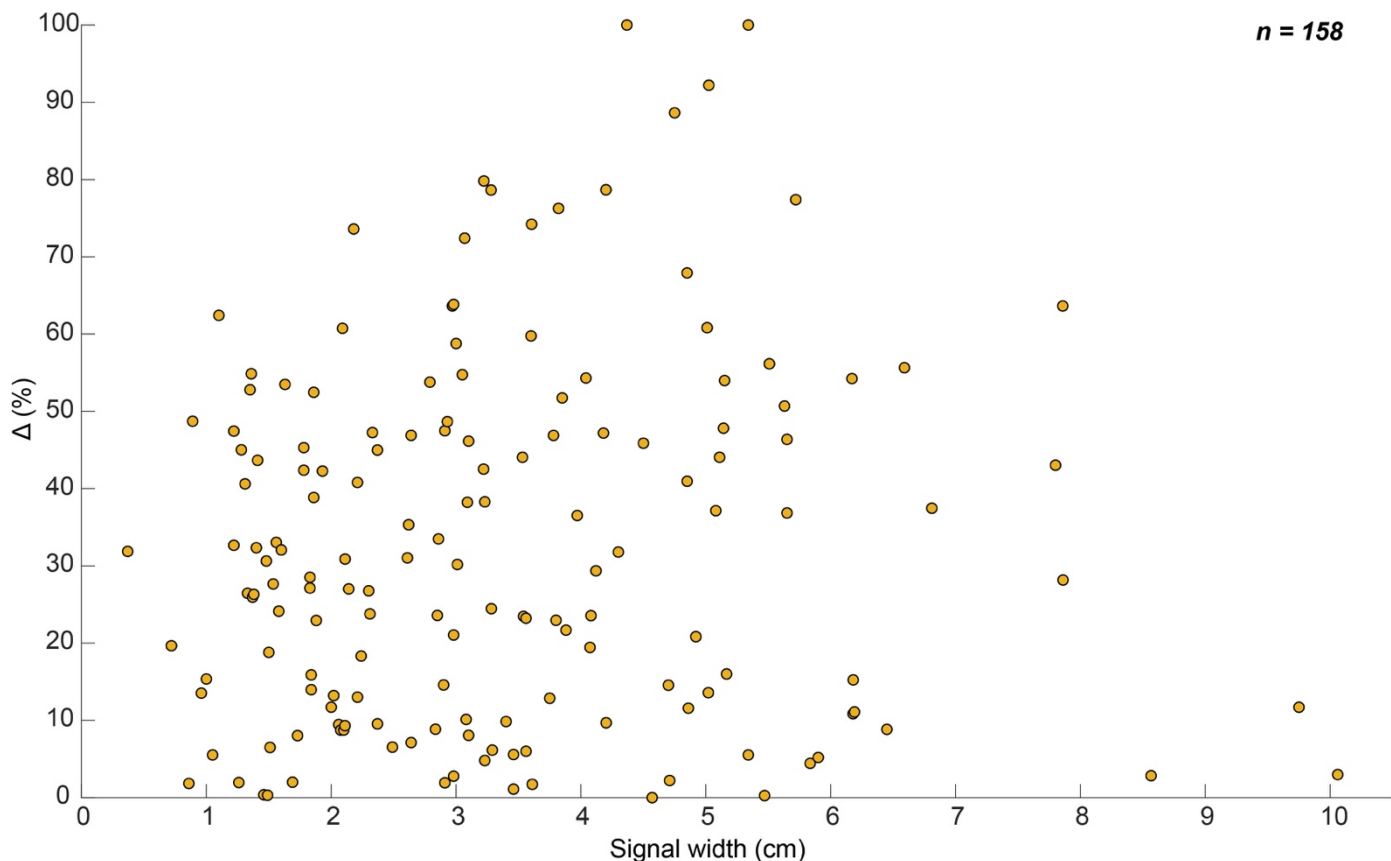


Figure 3.13- Variation rate as a function of stylolite width (in cm). Only the results of the 158 valid inversions are considered.

The distribution of Δ values is relatively scattered, and no trend can be defined between Δ and with the width of treated signals. This first test tends to refute the hypothesis previously put forward, as the width of the track does not seem to impact the consistency of the inversions. However, a finite stylolite implies

fixed roughness ranges. In addition, AWC and FPS are not sensitive to the same parameters: while FPS has a high sensitivity to vertical features, AWC has proven to be less impacted by sample quality and number (Simonsen *et al.*, 1998; Ebner *et al.*, 2009b). These two factors could explain the differences observed in the inversion results. The idea is now to test stylolites with larger roughness ranges. Composite stylolites are thus created by concatenation of stylolites belonging to the same formation and having common morphological characteristics. The method is detailed in Figure 3.14, and consists in: (i) scanning, digitalization and correction (*i.e.* detrend and border effects) of tracks, (ii) their concatenation and (iii) concatenated signal analysis (*i.e.* AWC and FPS application).

2.4- Tests and validation of composite stylolites inversion

56 concatenated stylolites were therefore generated and then analyzed with AWC and FPS methods. At least two stylolites are required, and up to 16 tracks were assembled. The resulting L_c values are given in Appendix 3.2 and represented in Figure 3.15, classified qualitatively according to the color scale given in Table 3.1. Only 4 inversions are considered unsuccessful (1 for the FPS, representing less than 2% of the data, and 3 for the AWC, *i.e.* 5% of the data), and 52 inversions (*i.e.* 93%) are conclusive (Figure 3.15). This first result demonstrates the validity of the inversions of composite stylolites.

Values of L_c and associated variation rates are plotted using Violin plot in Figure 3.16. Statistical distributions of both L_c values (Figure 3.16A) and Δ percentages (Figure 3.16B) overlap before and after concatenation, even though the extremes are higher for non-concatenated stylolite inversion. Ranges of values are more overlapping in the case of the AWC, where the statistical distributions of cross-over lengths are almost equivalent (Figure 3.16A). In addition, 54% of the data have a percentage Δ of less than 23%, compared to 34% for the classical method (Figure 3.16B). Thus, the inversion of composite stylolites seems to enhance consistency of L_c returned by the AWC and the FPS, the latter giving more consistent results after concatenation.

Thus, concatenation has two notable impacts: (i) the reduction of the number of failed inversions with the FPS and (ii) the increase the consistency of results between AWC and FPS. In addition, the values of L_c obtained with and without concatenation remain in similar ranges of values. The concatenation thus supports the robustness of the classical method, which remains valid despite the lack of consistency.

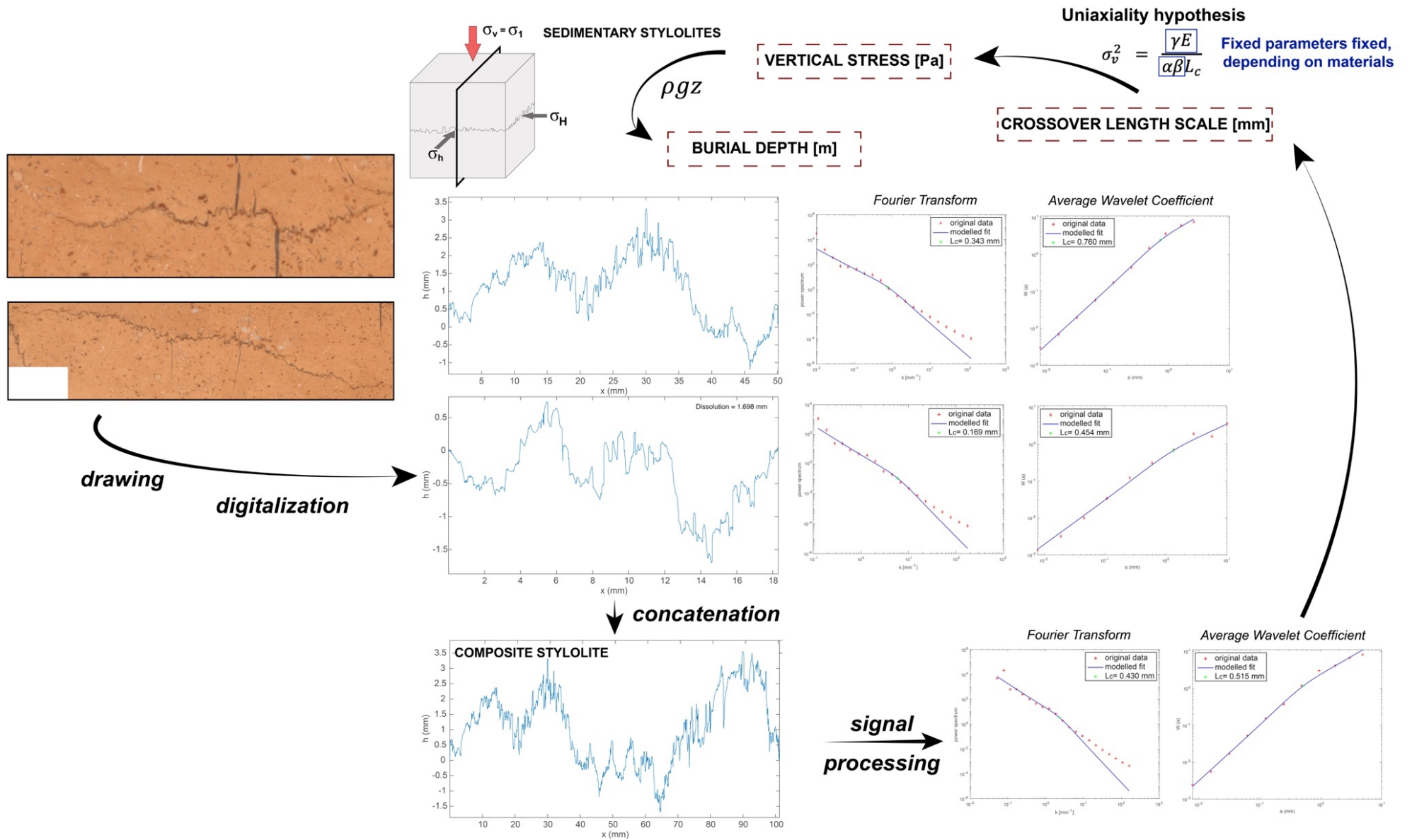


Figure 3.14- Concatenation of stylolites of the same morphology and belonging to the same formation. The tracks are digitised, assembled and inverted. The right-hand side of the figure shows the results of the inversions for the individual and composite tracks. The L_c values are more consistent after concatenation ($\Delta = 17\%$) than for the individual stylolites ($\Delta = 55\%$ and 63%)

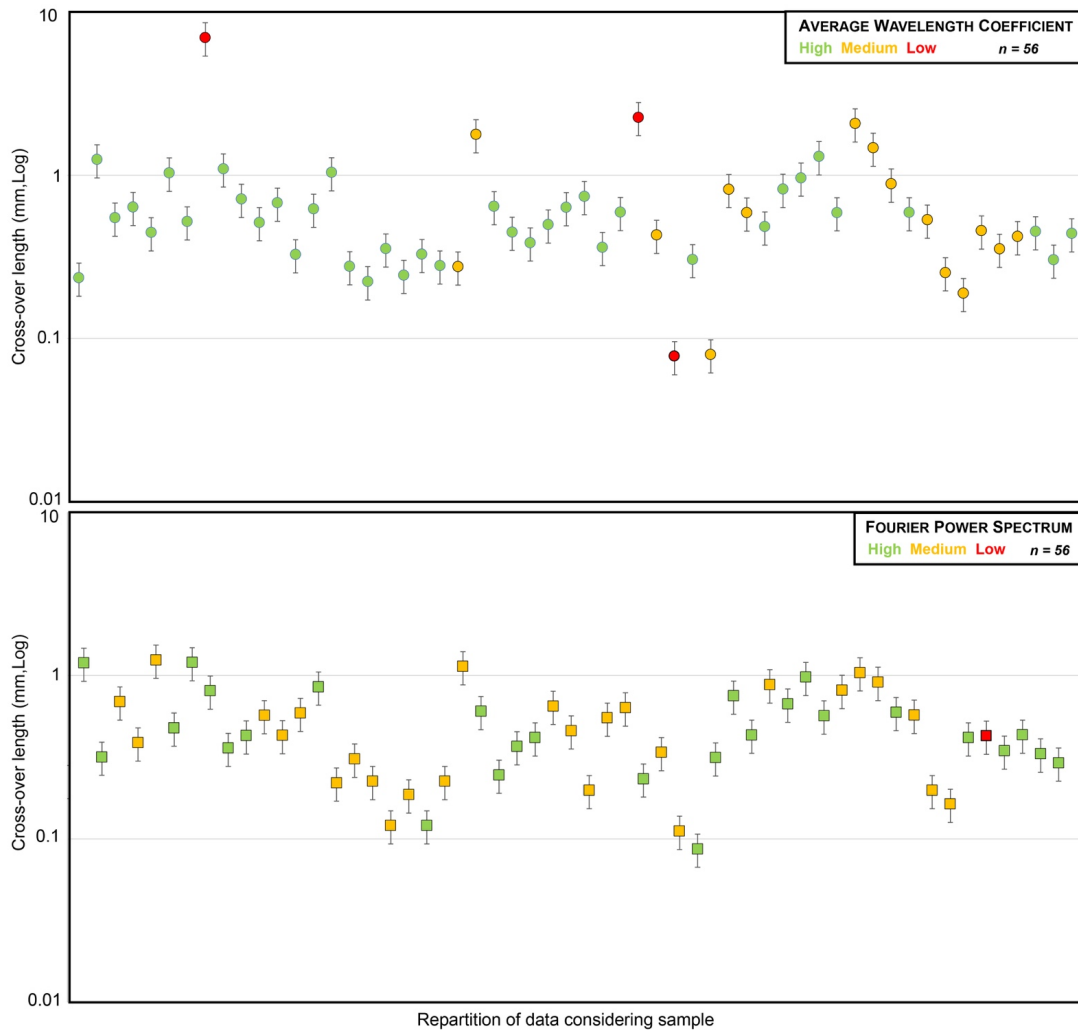


Figure 3.15- Representation of the L_c returned by inversion of concatenated stylolites, for both AWC (circles) and FPS (squares), considering the colorimetric scale defined in Table 3.1. Red values correspond to invalid results (3 for AWC, 1 for FPS). For better readability, a logarithmic vertical scale is used considered.

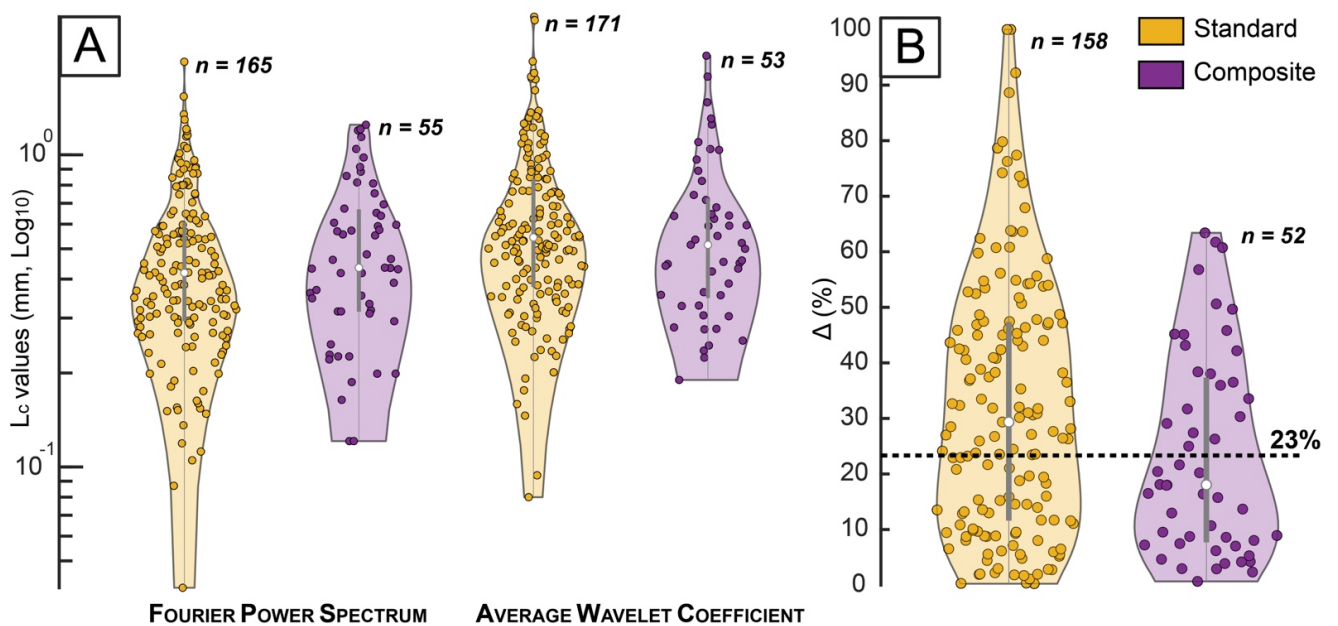


Figure 3.16- (A) Representation of L_c distribution considering the signal analysis method applied (*i.e.* FPS on the left and AWC on the right) and the type of stylolite studied (*i.e.* individual in yellow and composite in purple). (B) Comparison of the results after inversion of individual and composite stylolites, considering the Δ value (Equation 5.1). The dotted line represents the 23% uncertainty bar. Only the results of valid inversions are considered.

V- CONCLUSIONS

Several conclusions can be drawn from the different analyses conducted. Firstly, the improvement of the drawing and digitization phases by the computer-assisted segmentation process leads to a time gain, with an accuracy often equivalent to manual drawing, which is important especially for large datasets. Then, compared to previous work (*e.g.* Ebner *et al.*, 2009a; b, 2010; Rolland *et al.*, 2012; Rolland, 2013), the corrections applied to the signal during the first part of the processing, *i.e.* correction of border and slope effects, improve the validity and consistency of inversions for both signal processing, and more particularly for the AWC which seems to show a higher sensitivity to slope and edge effects. The study of composite stylolites brings answers to overcome the locks and limits of the inversion method. By increasing the number of valid and consistent results, concatenation confirms the reliability of the inversion method. The criterion of validity then prevails over that of consistency, a result being usable if the inversion is valid. However, the inversion of composite stylolites also raises questions as to why the analysis of a stylolite track by two signal processing methods does not necessarily return consistent results: what could explain that concatenation improves the quality and consistency of inversions? When AWC and FPS return valid but inconsistent results, what is the result of concatenation? In this configuration, what value of L_c should be chosen? Additional tests are therefore carried out to try to provide some answers, that are presented and discussed in a later chapter (Chapter 6).

*Chapter 4- Using bedding parallel stylolite to reconstruct the
burial-deformation calendar: examples of folded carbonates in
the Cingoli Anticline, Umbria-Marche, Northern Italy*

I- GENERAL INTRODUCTION

Understanding the tectonic-sedimentary evolution in foreland basins and FTB, as well as thermal phenomena and associated fluid systems, requires reconstructing history of burial during deformation, and thus quantifying burial depths and associated stress magnitudes. Mesostructures observed in these geological settings, *i.e.*, faults, veins, and stylolites, are local markers of deformation, and thus provide characterization of the deformation pattern (Tavani *et al.*, 2012b) and estimation of the evolution of associated paleostresses (*e.g.* Engelder, 1987; Bellahsen *et al.*, 2006a; b; Lacombe *et al.*, 2011; Tavani *et al.*, 2012, 2015; Beaudoin *et al.*, 2012). In contrast, depths and timing of deformation remain difficult to estimate. Indeed, the methods used are often thermo-dependent, very specific, and return only partial information regarding burial and deformation timing. Furthermore, they involve assumptions about the geothermal gradient, which is difficult to estimate in these tectonic settings that are strongly impacted by uplift and erosion phenomena. In particular, estimation of rock burial during deformation is often complicated by these assumptions about the geothermal gradient (Beaudoin & Lacombe, 2018).

The purpose of this chapter is therefore to propose another way to reconstruct part of the burial-deformation calendar providing to overcome a part of the limitations of the previously mentioned methods. The timing of deformation in FTBs and foreland basins is better constrained thanks to several recent improvement of the geochemical structural geology (see Beaudoin *et al.*, 2022 for a review regarding carbonates). The development of U-Pb dating on calcite cement, as well as syn-kinematic clay minerals, and K-Ar and Ar-Ar geochronologic data of illite-mica in folds and shear zones, enable absolute dating on the tectonic vein filling related to tectonic activity (*e.g.* Garduño-Martínez *et al.*, 2015; Beaudoin *et al.*, 2018; Roberts & Holdsworth, 2022). Clumped isotopes can be reliably used to reconstruct the exact temperature of precipitation under 90–100°C (Hoareau *et al.*, 2021b), and its combination to fluid inclusion microthermometry can be used to reconstruct the temperature-pressure-time path in sedimentary sequence (Mangenot *et al.*, 2017). Moreover, the understanding of how stylolites can be used as stress gauges (Renard *et al.*, 2004; Schmittbuhl *et al.*, 2004) enables quantification of the burial depths recorded by sedimentary rocks (*e.g.* Koehn *et al.*, 2016b; Bertotti *et al.*, 2017; Beaudoin *et al.*, 2020). Together, these methods rely on the ubiquitous features of carbonate rocks. This contribution proposes to combine paleopiezometry and isotope-based thermometry as a new methodology widely applicable to carbonates to constrain the timing of burial and this of the onset of contraction. This approach consisting of the coupling of data from burial models and BPS roughness inversion was already tested in the Bighorn Basin and compared to U-Pb dating (Beaudoin *et al.*, 2019). Nevertheless, U-Pb dating being not always successful (Appendix 4.1), it is important to test other approaches and methodologies.

In this perspective, this approach is detailed using the example of the Cingoli Anticline for which the most complete set of data and methods are applied. The results and interpretations are presented in the article **“Burial-deformation history of folded rocks unraveled by fracture analysis,**

stylolite paleopiezometry and vein cement geochemistry: a case study in the Cingoli Anticline (Umbria-Marche, Northern Apennines)". I first authored this paper, which was published on the 13 January 2021 in the peer-reviewed journal *Geosciences* (Labeur *et al.* in 2021). This paper reports a combination of BPS inversion results with burial model that I fully led, throwing the bases of the new methodology to assess contraction timing that I expanded during my PhD. To validate the outcome of this method, an unprecedented confrontation to paleofluid flow reconstruction, that uses CO₂ clumped isotope temperatures, is done as a collaborative work.

Article

Burial-deformation History of Folded Rocks Unraveled by Fracture Analysis, Stylolite Paleopiezometry and Vein Cement Geochemistry: A Case Study in the Cingoli Anticline (Umbria-Marche, Northern Apennines)

Aurélie Labeur ¹, Nicolas E. Beaudoin ¹, Olivier Lacombe ^{2,*}, Laurent Emmanuel ², Lorenzo Petracchini ³, Mathieu Daëron ⁴, Sebastian Klimowicz ² and Jean-Paul Callot ¹

¹ Laboratoire des Fluides Complexes et Leurs Réservoirs, Université de Pau et des Pays de l'Adour, E2S UPPA, CNRS, TOTAL, LFCR 64000 Pau, France; alabeur@univ-pau.fr (A.L.); nicolas.beaudoin@univ-pau.fr (N.E.B.); jean-paul.callot@univ-pau.fr (J.-P.C.)

² Institut des Sciences de la Terre de Paris–ISTeP, CNRS-INSU, Sorbonne Université, 75252 Paris, France; laurent.emmanuel@sorbonne-universite.fr (L.E.); sebastian.klimowicz.sk@gmail.com (S.K.)

³ Consiglio Nazionale delle Ricerche, IGAG, 00015 Roma, Italy; lorenzo.petracchini@igag.cnr.it

⁴ Laboratoire des Sciences du Climat et de l'Environnement, UMR82212, LCE/IPSL, CEA-CNRS-UVSQ, Université Paris-Saclay, Gif-sur-Yvette, 91190 Saclay, France; daeron@lsce.ipsl.fr

* Correspondence: olivier.lacombe@sorbonne-universite.fr



Citation: Labeur, A.; Beaudoin, N.E.; Lacombe, O.; Emmanuel, L.;

Petracchini, L.; Daëron, M.;

Klimowicz, S.; Callot, J.-P.

Burial-deformation History of Folded Rocks Unraveled by Fracture Analysis, Stylolite Paleopiezometry and Vein Cement Geochemistry: A Case Study in the Cingoli Anticline (Umbria-Marche, Northern Apennines). *Geosciences* **2021**, *11*, 135. <https://doi.org/10.3390/geosciences11030135>

Academic Editors: Domenico Liotta, Giancarlo Molli, Angelo Cipriani and Jesus Martinez-Frias

Received: 30 January 2021

Accepted: 1 March 2021

Published: 13 March 2021

Publisher's Note: MDPI stays neutral with regard to jurisdictional claims in published maps and institutional affiliations.



Copyright: © 2021 by the authors. Licensee MDPI, Basel, Switzerland. This article is an open access article distributed under the terms and conditions of the Creative Commons Attribution (CC BY) license (<https://creativecommons.org/licenses/by/4.0/>).

Abstract: Unravelling the burial-deformation history of sedimentary rocks is prerequisite information to understand the regional tectonic, sedimentary, thermal, and fluid-flow evolution of foreland basins. We use a combination of microstructural analysis, stylolites paleopiezometry, and paleofluid geochemistry to reconstruct the burial-deformation history of the Meso-Cenozoic carbonate sequence of the Cingoli Anticline (Northern Apennines, central Italy). Four major sets of mesostructures were linked to the regional deformation sequence: (i) pre-folding foreland flexure/forebulge; (ii) fold-scale layer-parallel shortening under a N045 σ_1 ; (iii) syn-folding curvature of which the variable trend between the north and the south of the anticline is consistent with the arcuate shape of the anticline; (iv) the late stage of fold tightening. The maximum depth experienced by the strata prior to contraction, up to 1850 m, was quantified by sedimentary stylolite paleopiezometry and projected on the reconstructed burial curve to assess the timing of the contraction. As isotope geochemistry points towards fluid precipitation at thermal equilibrium, the carbonate clumped isotope thermometry (Δ_{47}) considered for each fracture set yields the absolute timing of the development and exhumation of the Cingoli Anticline: layer-parallel shortening occurred from ~6.3 to 5.8 Ma, followed by fold growth that lasted from ~5.8 to 3.9 Ma.

Keywords: Apennines; fold-and-thrust belt; burial and tectonic history; fractures; stylolites; fluid flow; clumped isotope thermometry; paleopiezometry

1. Introduction

The reconstruction of the burial-deformation history of sedimentary rocks is a complex issue but an essential exercise to understand the tectonic and sedimentary history in fold-and-thrust belts and foreland basins, with numerous implications spanning from the evolution of the fluid-flow system and associated resources to the understanding of the long-term behavior of the upper crust [1–7]. Mesostructures observed in fold-and-thrust belts and related forelands, such as faults, veins, and stylolites provide essential information for understanding the deformation pattern [8]. Numerous studies have indeed linked the development of fractures to the large-scale long-term folding history and geometry, either through a descriptive field-based approach [9–11], paleostain and paleostress reconstructions [12–17], mechanical simulation (e.g., [18,19]), or through geochemical approaches (e.g., [20]). Besides, studies of distributed subseismic fractures demonstrated

that mesostructures are markers of the local deformation sequences and provide access to the evolution of the associated paleostresses [8–10,15,21–36]. When it comes to the burial history, however, the depth-time paths are reconstructed from temperature-dependent proxies, such as organic matter thermal maturity, temperature-dependent clay minerals (e.g., [37–39]), fluid inclusion microthermometry, or low temperature thermochronology (apatite fission tracks, U-Th/He on apatite crystals [40–46]). All these methods rely on the occurrence of specific features (organic matter, fluid inclusions, specific minerals like zircons, or Ar-rich clays) and return only partial information (e.g., maximum temperature, timing of reaching closure temperature . . .) while requiring assumptions about the past geothermal gradient. The latter is often argued over in fold-and-thrust belts and foreland basins where uplift and erosion are common events, thus it remains strongly challenging to reconstruct the burial at which the deformation occurred [7].

We propose to build on recent methodological advances to better constrain the timing of deformation in fold-and-thrust belts and foreland basins. The development of U-Pb dating on calcite cement enables absolute dating on the tectonic vein filling and synkinematic clay minerals (e.g., [47–49]), clumped isotopes can be reliably used to reconstruct the exact temperature of precipitation under 90–100 °C [50], and its combination to fluid inclusion microthermometry allows to reconstruct the temperature-pressure-time path in sedimentary sequence [51]. Moreover, the understanding of how stylolites can be used as stress gauges [52,53] enables reconstruction of the burial experienced by sedimentary rocks (e.g., [7,54–60]). These methods rely on the ubiquitous features of carbonate rocks, and we propose in this contribution to combine paleopiezometry and isotope-based thermometry as a new methodology widely applicable to carbonates in order to assess the timing and depth of burial/contraction during deformation history. We present an original application by reconstructing the burial-deformation history of the carbonate sedimentary sequence of the Cingoli Anticline, an arcuate fold in the Umbria-Marche Apennines Ridge (UMAR, Northern Apennines, central Italy; Figure 1). The Cingoli Anticline is an excellent case study for testing such new methodologies: (i) it is a rather simple symmetrical fold, mainly formed by carbonate rocks exhibiting pervasive fractures and stylolites [61]; (ii) there is an abundant literature that discusses the timing of folding, based on sedimentologic and tectonic studies [62–64]; (iii) the geothermal gradient is known [65]; and (iv) it belongs to a young mountain belt where the past mesostructures received relatively poor attention [60,61,66–70] compared to their active counterparts.

In this study, we aim at identifying, characterizing and dating the mesostructures related to the main stages of deformation, i.e., faults, fractures, and stylolites linked to layer-parallel shortening (LPS), folding, and late-stage fold tightening (LSFT). For this purpose, we first carry out a classical field-based mesostructural study. We further reconstruct the burial history of strata by building burial curves using present strata thickness corrected for physical and chemical compaction and by applying the roughness inversion technique to sedimentary stylolites in order to quantify the maximal vertical stress, and hence the maximum burial depth experienced by the sedimentary sequence prior to contraction and during exhumation.

The timing of the deformation is further constrained by the temperatures derived from isotopic data (^{18}O , ^{13}C and clumped isotopes), showing a thermal equilibrium with the host rocks considering previously published geothermal gradients, and compared to previous studies carried out in nearby folds [60,71]. This original and transferable approach reveals the burial evolution, the timing of deformation, and the fluid system in the Cingoli Anticline during the Apennine contraction in eastern UMAR.

2. Geological Setting

2.1. The Umbria Marche Apennine Ridge (UMAR)

The Apennines fold-and-thrust belt extends from the Po Plain to the Calabrian Arc over a distance of 1500 km, and it is the result of the Eurasian and African Plates convergence [72,73]. The Apennine belt accommodated significant orogenic contraction, estimated

up to 50% through cross section balancing [74], and recorded shortening rates ranging from 6 mm/year up to 15–50 mm/year [74,75]. From a structural point of view, the Apennine belt is characterized by a succession of asymmetrical anticlines with eastward vergence, separated by narrower and often asymmetrical synclines. The Apennines are commonly divided into two main arcs, the Northern and the Southern Apennines arcs, each associated with its own geological and structural characteristics [76–78]. Moreover, this curved belt, with eastward convexity, is increasingly younger from west to east (from Oligocene to Pleistocene; [72,79]). This is the result of a roughly eastward migration of the deformation front (and its associated successive foredeep basin), which is related to the eastward retreating subduction of the Adriatic Plate under the European Plate, superimposed by post-orogenic extension at the rear of the propagating orogenic belt [29,72,80,81].

The UMAR represents the central-southern part of the Northern Apennines arc developed during late Miocene–Pliocene when the area was involved in the Apennines build-up. It is about 450 km long and rises to over 2000 m above sea level [75]. The sedimentary succession observed in the UMAR can be divided into three main units as follows: (i) Upper Triassic evaporites, the thickness of which is estimated at 1000 m before deformations and considered as a décollement level. They unconformably overlie crystalline rocks of the basement, which is barely or not even observable at the outcrop [72]; (ii) the Umbria-Marche carbonate-dominated succession (~2500 m thick), divided in several formations deposited from the earliest Jurassic to Oligocene [72,82–84]; (iii) Miocene hemipelagites and turbidites, deposited above these carbonate rocks, which record the progressive eastward involvement of the Meso-Cenozoic succession into the fold-and-thrust belt [62,85]. Indeed, during the foredeep stage, more than 3000 m of turbidites were deposited ahead of the advancing fold-and-thrust belt.

Both thick- and thin-skinned structural styles of deformation have been proposed for the Apennines. The thin-skinned interpretation considers a disharmonic deformation of the crust with the sedimentary units detached along the Triassic evaporites [86–88]. The thin-skinned model is opposed to the thick-skinned which considers the involvement of the basement during compressional deformation (e.g., [89]). Furthermore, several studies suggest that many thrusts are rooted on inherited pre-orogenic structures, mostly pre-existing normal faults formed either during the evolution of the Mesozoic passive margin or during the foreland flexure [90–96].

The UMAR undergoes the following main stages of regional deformation: (i) the forebulge stage consisting of the foreland flexuring [8], dated from late Oligocene–early Miocene in the western part of the ridge (i.e., eastern Tuscany–Monte Nero) and from middle Miocene in the eastern part of the ridge (i.e., Gubbio, San Vicino, and Cingoli areas) [79]; (ii) the LPS event, a pre/early-folding compressional stage NE–SW-oriented related to the Apenninic contraction [66,97–99], occurred by early Miocene to the west, and by middle Pliocene to the east [79]; (iii) the folding stage, started by early Miocene in the western part of the UMAR, and by middle Miocene in the eastern part. This stage is characterized by a maximum stress trending parallel to regional shortening, i.e., NE–SW-oriented [29], and local extension perpendicular to fold axis and associated with strata curvature at fold hinge [60]; (iv) the LSFT, associated with a NE–SW contractional trend. This stage corresponds to the moment when shortening is no longer accommodated, by e.g., limb rotation [60]; (v) a post-orogenic extension, starting by Miocene times in the western UMAR [99] and by early Pliocene times in the eastern part of the ridge [62,63], and continuing today. This extensional stage is associated with NNW–SSE trending related normal faults causing the downfaulting of the fold succession [86,99,100].

2.2. The Cingoli Anticline

2.2.1. Structural Pattern

The Cingoli Anticline is located in the eastern part of the UMAR along the footwall of the Sibillini Mountains (Figure 1A). This anticline is characterized by an arcuate geometry; its main NW–SE axis evolves toward a N–S orientation in its southern part; it is characterized

by gently dipping limbs and its hinge is relatively flat. The fold has a spatial extension of about 15 km from north to south, and about 5 km from west to east and it culminates ~400 m above the local land (770 m above sea level). An WNW-ESE oriented left-lateral fault and a NNE-SSW oriented right-lateral fault bound the Cingoli Anticline to the north and south, respectively (Figure 1A). In addition, [101] and [63] suggest that inherited pre-contractural structures striking ~N-S (i.e., the Jurassic rifting and the late Miocene foreland flexure) strongly controlled the subsequent contractural tectonic evolution of the area (Figure 1A,C).

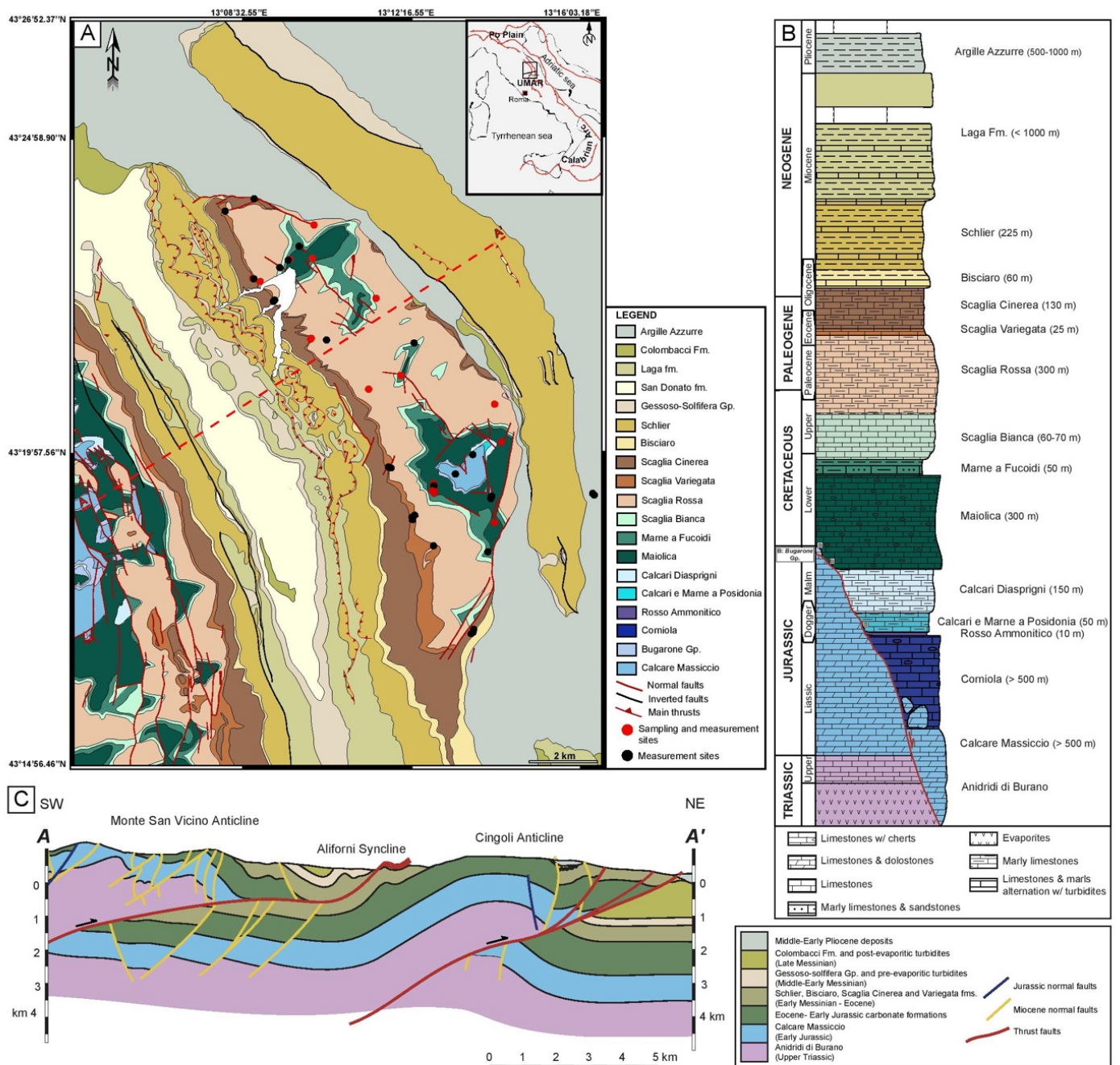


Figure 1. (A) Location and simplified geological map of the Cingoli Anticline. Red points represent the sampling sites for sedimentary stylolites analysis, and black points represent the measurement sites. (B) Stratigraphic column, not to scale, of the Umbria-Marche area, with thicknesses valid for the Cingoli Anticline area (modified from [61]). (C) SW-NE geological cross section through the northern part of the Cingoli Anticline [63].

2.2.2. Sedimentary Succession

Where not specified, the lithostratigraphic units described below are traditional and validated units [102], and correspond with formation-rank units.

The deformed units comprise Mesozoic and Cenozoic marine deposits, consisting of evaporites and platform carbonates at the base overlain by pelagic carbonates [63,64,101,103] (Figure 1B). The succession comprises:

- (1) Upper Triassic anhydrites and dolostones, grouped in the Anidridi di Burano, unconformably deposited above the continental deposits of the Verrucano and the Hercynian basement; at the top of the Anidridi di Burano, euxinic interstratified marls are present.
- (2) The Calcare Massiccio, formed by massive peridital limestones dated from Hettangian to Sinemurian (ca. 201–191 Ma).
- (3) Four main Jurassic formations: (i) the Corniola, limestones with cherts beds (early Sinemurian–early Toarcian, ca. 199–183 Ma); (ii) the Rosso Ammonitico, nodular marly limestones dated Toarcian (ca. 183–174 Ma); (iii) the marls and cherty limestones of the Calcari e Marne a Posidonia (late Toarcian–early Bajocian, ca. 174–170 Ma); (iv) the Calcari Diasprigni, dominated by radiolarian-rich cherty limestones and cherts and, on top, by micritic limestones and marls bearing abundant *Saccocoma* sp. fragments (late Bajocian–early Tithonian, ca. 170–152 Ma). Because of the horst and graben structures related to the Jurassic extensional tectonics, these deposits accumulated in the hanging wall basins forming thick (hundreds of meters) “basinal” successions, while thin (up to few tens of meters), fossil-rich and condensed successions (Bugarone Group) accumulated on top of footwall blocks of Jurassic faults during the same time span (i.e., from early Pliensbachian to early Tithonian; ca. 191–152 Ma) [82,83,104–106].
- (4) The Maiolica, micritic limestones associated with chert beds (Tithonian–earliest Aptian, ca. 152–124 Ma).
- (5) Shales and marls of the Marne a Fucoidi (Aptian–Albian, ca. 124–100 Ma).
- (6) The “Scaglia” group is composed of micritic limestones with cherts intercalations (late Aptian–Aquitainian, ca. 113–21 Ma), and divided into four formations: (i) the Scaglia Bianca (Cenomanian–earliest Turonian, ca. 100–94 Ma); (ii) the Scaglia Rossa (earliest Turonian–Lutetian, ca. 94–41 Ma), subdivided into three members; (iii) the Scaglia Variegata (Lutetian–Priabonian, ca. 48–34 Ma) and (iv) the Scaglia Cinerea (Rupelian–earliest Aquitainian, ca. 34–22 Ma).
- (7) Bisciaro (Aquitainian–Burdigalian, ca. 22–16 Ma) and Schlier (Langhian–Tortonian, ca. 16–7 Ma) formations, hemipelagic limestones, marly limestones and marls.
- (8) Siliciclastic foredeep deposits, grouped in two major sequences: (i) Messinian arenitic and pelitic turbidites (ca. 7–5 Ma), composed by the Laga formation and the Gessoso-Solfifera Group with the San Donato and Colombacci formations; (ii) arenites, pelites and fossiliferous marine clays and marls of the Argille Azzurre, early to middle Pliocene in age (ca. 5–3 Ma). In this area, the Messinian and Pliocene deposits are continuous and widespread, and provide an almost complete record of the deformation history of the ridge’s outer domains. In particular, growth strata observed in the San Donato and Colombacci formations within the Aliforni Syncline postdate flexural turbidites of the Laga formation, consequently broadly constraining fold growth to late Messinian–Zanclean (ca. 6–4 Ma) [62,63].

3. Materials and Methods

3.1. Fracture-Stylolite Network Characterization and Striated Fault Planes Analysis

The structural data collection and sampling sites are distributed along the whole anticline (Figure 1). The characterization of the fracture-stylolite network is based on field observations and measurements and analyses of joints, veins, striated faults, and tectonic stylolites. The dataset comprises more than 2300 orientations of mesostructures from the Cingoli Anticline. Furthermore, abutment and crosscutting relationships were carefully

observed and analysed to establish the relative chronology of fracture sets. Fracture orientation data were projected on Schmidt stereodiagrams (lower hemisphere), in the current attitude of the strata (raw) and after unfolding (unfolded). In addition, the major sets of joints and/or veins (i.e., the most documented and representative at fold scale) were grouped and averaged by a Fisher statistical analysis, based on the following assumptions: (i) similar orientation considering natural variability (i.e., within 20°); (ii) deformation mode (e.g., opening, shearing, contraction), defined through thin sections observed with optical microscope; and (iii) chronological relationships.

Considering that stylolite peaks grow parallel to the main shortening direction [107], with respect to the distribution of dissolution gradients (i.e., non-soluble particles) [108], the orientation of the horizontal maximum principal stress (σ_1) was inferred from the maximum density of the peak orientation of tectonic stylolites. The early, syn-, and late folding sets of mesostructures were discriminated with the OpenStereo software [109]. Data were corrected for bedding attitude, by rotation about a horizontal axis to remove the dip angle of the strata, in order to investigate the relationships between fracturing and folding. Thus, fractures were grouped according to their geographical and structural position (respectively north/south and forelimb/backlimb), and according to the main stages of deformation.

Approximately 40 mesoscale striated faults were also measured to complement this mesostructural analysis, in 3 sites of measurements located in the northern and southern ends of the anticline. We used Angelier's inversion technique [110] which, under specific assumptions [111], allowed us to calculate paleostress orientations (i.e., local trend and plunge of principal stress axes) and stress ratios for each site of measurement.

3.2. Rock Mechanical Properties

To calculate the mechanical properties of the studied rocks, we used the Schmidt rebound hammer technique, which is a non-destructive method used for the estimation of the uniaxial compressive strength and Young modulus of concrete and natural rocks (e.g., [112]). It implies the use of a spring-loaded piston (the Schmidt hammer), pressed orthogonally against a surface of rock. The energy created by the resistance of the surface to the impact enables the piston to rebound. The distance traveled by the piston after the rebound is called the rebound value R, which is considered to be a proxy of the surface hardness [112], itself used to quantify uniaxial compressive strength and Young modulus of the rock [113]. A Silver Schmidt OS8200 (manufactured by PROCEQ) was used on 12 sites in various localities and sedimentary units of the fold. Each site consists of 50 to 90 rebounds performed perpendicularly to the surface, in most case lying flat (i.e., the hammer being vertical), from which rebound values were averaged as a single rebound value valid for the site. In order to ensure that this value is free from any outlier due to local heterogeneity, we calculated a moving average incremental mean until the mean rebound value stabilizes (supplementary material, Figure S1, Table S1).

3.3. Sedimentary Stylolite Roughness Inversion

Sedimentary stylolites are pressure-solution surfaces usually developed parallel to bedding in sub-horizontal strata during burial, i.e., when σ_1 was vertical. They are frequently observed in sedimentary rocks, and especially in carbonates. The 1D roughness of a track along these dissolution surfaces, i.e., the difference in height between two points along the track (sensu [53]), results from a competition between two forces [53]: (i) roughening forces, i.e., pinning on non-soluble particles in the rocks, and (ii) smoothing forces, associated with the surface energy at scale <1 mm and the elastic energy at scale >1 mm. Two main scaling regimes are discriminated by the stylolite growth model [56,107,108,114] depending on the predominant energy and the associated Hurst exponent (i.e., roughness exponent): the surface energy-controlled scale, characterized by a steep-slope and a roughness exponent of 1.1 ± 0.1 , and the elastic energy-controlled scale, associated with a gentle slope and a Hurst exponent between 0.5 and 0.6. At the transition of these scale regimes,

the change in roughness exponent is associated with a crossover length, estimated in mm by the signal processing approach. The authors in [53] directly link this crossover length L_c to the magnitude of prevalent mean stress σ_m and differential stress σ_d in the strata at the time the stylolite stopped to be an active dissolution surface, with Equation (1):

$$L_c = \frac{\gamma E}{\beta \sigma_m \sigma_d} \quad (1)$$

where L_c is the crossover length converted to m, E the Young modulus of the rock (in Pa), γ is the solid-fluid interfacial energy (in $\text{J}\cdot\text{m}^{-2}$), and β a dimensionless constant depending on the Poisson ratio (ν) and calculated with the relation:

$$\beta = \frac{\nu(1-2\nu)}{\pi} \quad (2)$$

The mean stress and the differential stress, are defined in Pa according to the Equations (3) and (4):

$$\sigma_m = \frac{\sigma_1 + \sigma_2 + \sigma_3}{3} \quad (3)$$

$$\sigma_d = \sigma_1 - \sigma_3 \quad (4)$$

Several studies successfully applied this approach, establishing the spectral analysis of the roughness of sedimentary stylolites as a robust paleopiezometry tool [54,57,59,60,108,115–118], especially because the final roughness is acquired quickly at the end of the stylolite's growth, thus depends only on stress and no longer on strain rate [108].

More than 100 sedimentary stylolites, with peaks perpendicular to the dissolution plane, were sampled in several localities of the Cingoli Anticline (Figure 1A) in the Maiolica, Scaglia Rossa, and Scaglia Variegata. The samples were cut and polished to better analyze the stylolite track. Each cut was made perpendicular to the plane of the stylolite and scanned with a resolution of 12,800 pixels per inches; the resulting file is an image on which the 1D track was hand drawn at magnifications 200% and 400% for greater precision. Then, each track was analyzed as a periodic signal. Usual analyses involve the Fourier Power Spectrum (FPS) and Average Wavelet Coefficient (AWC) methods [115]. We chose the method of Average Wavelet spectrum with Daubechies D4 wavelets [115,119], which is proven to be more stable and less sensitive to resolution effects. We used a non-linear regression with fixed Hurst coefficients of 0.5 and 1.1, corresponding to elastic and surface regimes, respectively (please refer to supplementary material, Figure S2, for the plots). The uncertainty for this regression approach to estimate L_c has been previously estimated to 23% [57]. To calculate the vertical stress magnitude, the horizontal stress was then considered as isotropic (i.e., uniaxial strain hypothesis, $\sigma_v > \sigma_h = \sigma_H$) in the case of sedimentary stylolites. Thus, the Equation (1) established by [53] is simplified as:

$$\sigma_v^2 = \frac{\gamma E}{\alpha L_c} \quad (5)$$

α being a constant defined as follows:

$$\alpha = \frac{(1-2\nu)(1+\nu)^2}{30\pi(1-\nu)^2} \quad (6)$$

To verify this assumption, sections perpendicular to the stylolite plane were cut for several samples and treated following the same inversion method, the isotropy of the horizontal stress implying a constant value of the crossover length regardless of the track direction [53,115].

While the solid-fluid interfacial energy γ is well-known and stable, fixed to $0.24 \text{ J}\cdot\text{m}^{-2}$ for dolomite and of $0.32 \text{ J}\cdot\text{m}^{-2}$ for calcite [120], and while the Poisson ratio ν is rather stable in carbonates and can be approximated to 0.25 ± 0.05 , a major source of uncertainty lies in

the values of the Young modulus E [57,121]. With known E , ν , and γ , the uncertainty on the calculated stress is 12% [57]. As in previous works [57,60,117,118] the calculated vertical stress $\sigma_v = \sigma_1$ was translated directly into the burial depth (z) of rocks using the relation

$$\sigma_v = \rho g z \quad (7)$$

with ρ the average dry density of overlying rocks and g the gravity acceleration. Indeed, the stylolite roughness can be considered as unaffected by local fluid overpressure because the dissolution is located along a fluidic film [56,108,116], an assumption that remains valid until the system is fluidized [122]. For this reasons, ρ was considered as the average dry rock density for clastic and carbonate sediments (evaluated mean value at $2400 \text{ kg}\cdot\text{m}^{-3}$), without any additional assumption on the past thermal gradient or fluid pressure [7], and g the gravity acceleration, fixed at $9.8 \text{ m}\cdot\text{s}^{-2}$.

3.4. O-C Stable Isotopes

The analysis of stable oxygen and carbon isotopes, associated with the study of the diagenetic state of the rocks, allows for the identification and characterization of fluid generations at the origin of mineralization and vein filling within sedimentary rocks [20,123–129]. We focus hereinafter on the calcite cements filling the tectonic veins related either to LPS or to strata curvature at fold hinges. The mineralogy of some host-rock was checked with X-ray diffraction (supplementary material, Figure S3) using a Bruker D2 Phaser diffractometer from the IStEP laboratory (Sorbonne Université) with X-Ray wavelength of 1.54056 \AA . The resulting X-ray patterns showing mostly pure calcite with minor amounts of quartz. The diagenetic state of calcite veins was checked under cathodoluminescence microscopy and were performed on a cold cathode Cathodyne platform (CITL CCL 8200 Mk4) at stable vacuum of 60 mThor, a voltage of 12 kV, and a current of 200 μA , corresponding to the ideal voltage-current conditions to activate the luminescence of the carbonates.

We selected vein cements where the vein texture [130] and the diagenetic state support a single phase of filling, occurring at the same time or soon after fracture development (e.g., elongated blocky, Figure 2).

The isotope ratios of oxygen ($^{18}\text{O}/^{16}\text{O}$) and carbon ($^{13}\text{C}/^{12}\text{C}$) of samples collected in several localities of the Cingoli Anticline were obtained by Isotope-Ratio Mass Spectrometry (IRMS). The spectrometric equipment couples an automatic sample preparation line (KIEL IV) and an analysis section (DELTA V advantage) from Thermo Fisher Scientific at the IStEP laboratory (Paris). We first selected veins of which (i) the cement witnessed a single growth step, unaltered by later diagenetic events, checked with cathodoluminescence microscopy; and (ii) the cement was likely related to vein opening, considering antitaxial or elongated blocky textures [130]. Thirty (30) to 50 μg of powder were sampled from the vein and the surrounding host-rocks as well, using a computer assisted micromill drill. The powder was reacted with anhydrous orthophosphoric acid at $70 \text{ }^\circ\text{C}$ to extract CO_2 gas, itself ionized in the spectrometer. The measured isotopic ratio reported in permil relative to the Vienna Pee Dee Belemnite (‰ VPDB) are with an accuracy of 0.05 ‰ and 0.1 ‰ for carbon and oxygen, respectively.

3.5. Carbonate Clumped-Isotope Paleothermometry (Δ_{47})

All analyses were performed at the Laboratoire des Sciences du Climat et de l'Environnement (LSCE, Gif sur Yvette). Eight samples of homogenized carbonate powder were converted to CO_2 by anhydrous phosphoric acid reaction at $90 \text{ }^\circ\text{C}$ in a common, stirred acid bath for 15 minutes. Initial phosphoric acid concentration was 103% ($1.91 \text{ g}/\text{cm}^3$) and each batch of acid was used for 7 days. After the cryogenic removal of the water, the evolved CO_2 was helium-flushed at $25 \text{ mL}/\text{mn}$ through a purification column packed with Porapak Q (50/80 mesh, 1 m length, 2.1 mm ID) and held at $-20 \text{ }^\circ\text{C}$, and then quantitatively recollected by cryogenic trapping and transferred into an Isoprime 100 dual-inlet mass spectrometer equipped with six Faraday collectors (m/z 44–49). Each analysis took about 2.5 hours, during which the analyte gas and working reference gas were allowed to flow

from matching, 10 mL reservoirs into the Nier-type ion source through deactivated fused silica capillaries (65 cm length, 110 μm ID). Every 20 minutes, gas pressures were adjusted to achieve $m/z = 44$ current of 80 nA, with differences between analyte gas and working gas generally below 0.1 nA. Pressure-dependent background current corrections were measured 12 times for each analysis. All background measurements from a given analytical session are then used to determine a mass-specific relationship linking background intensity (Z_m), total $m/z = 44$ intensity (I_{44}), and time (t):

$$Z_m = a + bI_{44} + ct + dt^2 \quad (8)$$

Background-corrected ion current ratios (δ^{45} to δ^{49}) were converted to $\delta^{13}\text{C}$, $\delta^{18}\text{O}$, and “raw” Δ_{47} values as described by [131], using the IUPAC oxygen-17 correction parameters. The isotopic composition ($\delta^{13}\text{C}$, $\delta^{18}\text{O}$) of our working reference gas was computed based on the nominal isotopic composition of carbonate standard ETH-3 [132] and an oxygen-18 acid fractionation factor of 1.00813 [133]. Raw Δ_{47} values were then converted to the “absolute” Δ_{47} reference frame defined by the “ETH” carbonate standards [132] using regression methods detailed by [134]. Full analytical errors are derived from the external reproducibility of unknowns and standards ($N_f = 78$) and conservatively account for the uncertainties in raw Δ_{47} measurements as well as those associated with the conversion to the “absolute” Δ_{47} reference frame. The precipitation temperature was calculated using the calibration proposed by [135] and updated by [132].

3.6. Burial Model

The burial model associated with the Cingoli Anticline area was constructed from the open access well data collection of the ViDEPI project selected around the Cingoli Anticline (i.e., Misa1, Rosora1, Burano1, Treia1 wells). Thicknesses were sequentially uncompacted to obtain burial depths of the strata of interest through time. Two kinds of corrections were therefore applied, considering the effects of both physical and chemical compaction. The computer interface used to produce these burial curves is the Backstrip software, which performs 1D backstripping of sedimentary strata [136] and involves several parameters for modeling.

First, the layer thicknesses were corrected for chemical compaction, in order to be referenced in the software. Thickness information was provided by stratigraphic studies or well data (i.e., current formation thicknesses). In this case, thicknesses were corrected for chemical compaction, considering spacing and amplitudes of bedding-parallel stylolites (BPS) for each formation studied. The average number of sedimentary stylolites per meter was estimated from outcrop data. The height of the highest tooth (i.e., the height from tooth to base line) associated with each analyzed stylolite was also computed from the samples. Chemical compaction was then deduced from these two parameters, calculated as their product, and expressed as a percentage of bed thickness.

The second step consisted of defining parameters needed to evaluate physical compaction undergone by the different layers, related to the weight of the sedimentary column and possibly of the water column (according to the type of basin considered). These parameters, such as the dry density ρ and the porosity coefficient c , were defined on the basis of the work by [137,138], as follows: (i) the dry density ρ was chosen at 2700 kg/m^3 for carbonate rocks and 1800 kg/m^3 for other lithologies; (ii) the porosity coefficient c was calculated with the following equations and the porosity-depth curves established by [137,138]. Φ is the porosity at depth y , while Φ_0 the surface porosity, both given by the curves.

$$\Phi = \Phi_0 e^{-cy} \text{ with } c = \frac{1}{y} \ln\left(\frac{\Phi}{\Phi_0}\right) \quad (9)$$

Thus, c is equal to 0.58 for carbonate rocks and to 0.3 for other lithologies. Corrections related to the weight of sediments and water being significantly different [137,138], the type of basin was also defined (0 for a marine basin, 1 for a continental basin), in order not to introduce bias into the resulting burial curves.

4. Results

4.1. Fracture-Stylolite Network Characterization and Striated Fault Planes Analysis

The fracture deformation mode was defined through thin sections observed with optical microscope, either by considering the texture (i.e., elongate blocky or crack-seal), or the object shift in the matrix (Figure 2).

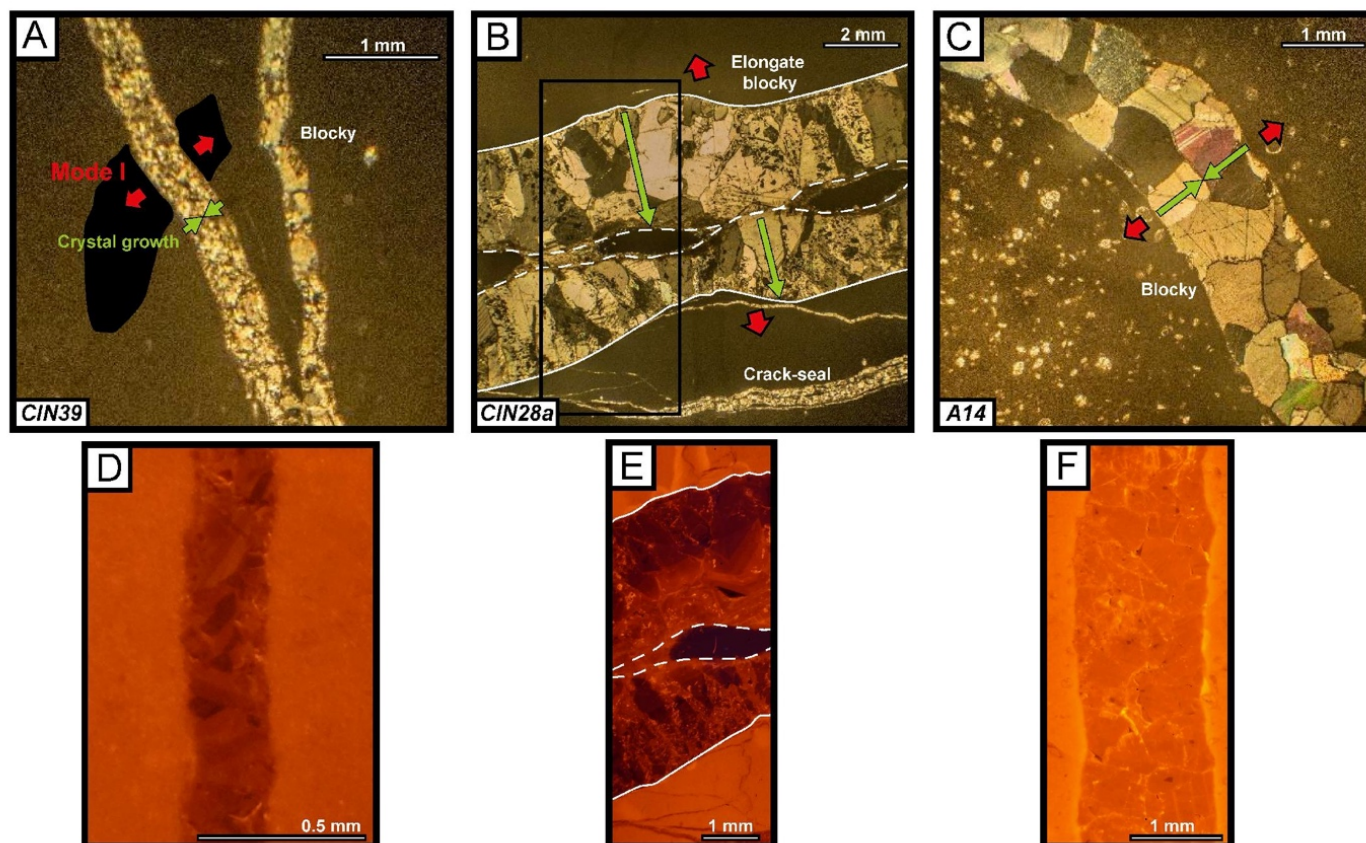


Figure 2. Observation of the different types of fractures in optical microscopy. (A) N-S fractures, (B) N045 fractures and (C) N135-160 fractures. Textures and shifts in the matrix were characterized, in order to verify the deformation mode, based on the classification of [130]. Red arrows represent the direction of the opening (mode I), and green arrows the direction of calcite crystal growth. (D–F) observation of these different sets in cathodoluminescence, indicating a single crystallization phase, synchronous with the mode I opening.

Three major sets of fractures were discriminated on the basis of their average orientation (Figures 3 and 4A,B) whereas their chronological sequence was established through abutment and crosscutting relationships at different scales (from outcrop to thin section):

- set I gathers bedding-perpendicular joints oriented N180 to N020 (after unfolding). This set is observed over the entire anticline, predates sets II and III, because it is intersected and abutted by a set of stylolites with peaks oriented N045, which are themselves intersected and abutted by the joints/veins of set II (Figure 4C).
- set II gathers joints and veins with $N045 \pm 10^\circ$ orientation, present throughout the study area. They are perpendicular to bedding strike. This set postdates set I and predates set III.
- set III comprises bedding-perpendicular N130 to N160-oriented joints parallel to bedding strike (i.e., N135-140 in the North and N160 in the South). They are mainly parallel to the axis of the anticline and crosscut or abut all other joint/vein sets (Figure 4C).
- another set of E-W fractures, poorly represented at the scale of the anticline (i.e., only in the northern part, in three sites of measurements), includes N070 to N110-oriented joints (after unfolding) and perpendicular to the bedding, developed after set II.

Because of the low number of measurements (i.e., 25 of 3000 fractures analyzed) and because they systematically developed near faults (Figure 3), this family of fractures is considered as minor and of local meaning only, and therefore not affiliated to a major set. Consequently, it will not be interpreted thereafter.

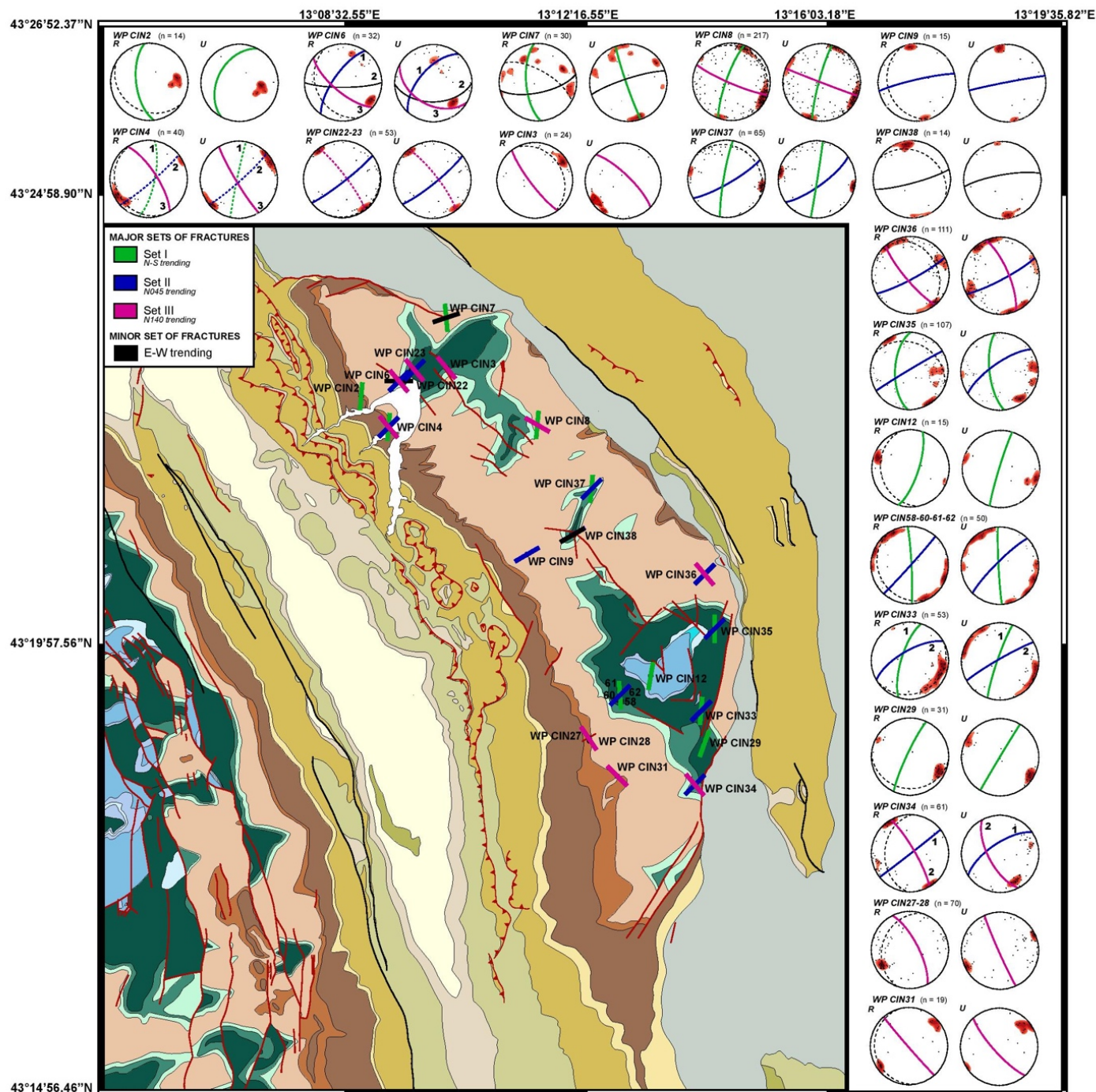


Figure 3. Location of fracture planes measured on the geological map (GPS locations are provided in the supplementary material, Table S2). Each measurement point is associated with two stereodiagrams (lower hemisphere), representing main fracture orientations in current (R) and unfolded attitude (U); on each stereodiagram, the bedding is reported as dashed lines, and fracture planes by solid-colored lines, each color relating to one of the three major fracture sets defined (green: set I, blue: set II, pink: set III).

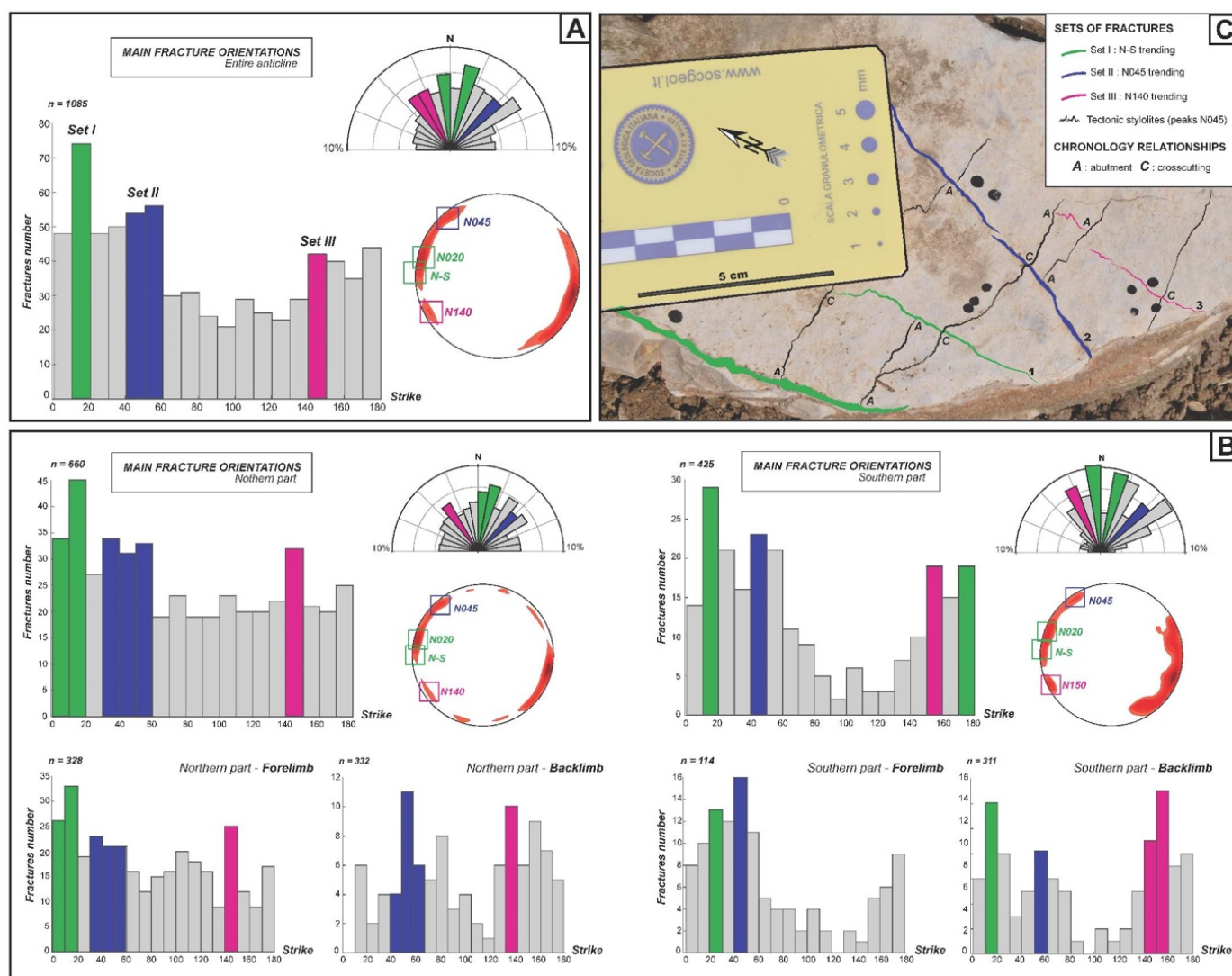


Figure 4. Main fractures orientations (after unfolding) plotted on histograms, stereograms and rose diagrams for (A) the whole anticline and (B) northern and southern parts of the anticline, discriminating forelimb and backlimb measurements. Three major sets of fractures discriminated according these orientations are represented with their specific color (green: set I, blue: set II, pink: set III). (C) Chronological relationships between fractures and stylolites (i.e., abutment and crosscutting), observed at mesoscopic scale.

Tectonic stylolite peaks are mostly oriented N045 (Figure 5). The continuous change in dip of the stylolite plane from vertical to oblique suggests that part of the tectonic stylolites developed before folding and other after folding. Few prefolding stylolites peaks are oriented N140 (WP CIN 37 and WP CIN 27–28) in the Maiolica and Scaglia in the southern backlimb, and N090 in Calcare Massiccio in the southern part of the anticline (WP CIN 12).

The inversion of striated faults for stress was carried out in few sites in the anticline (Figure 5):

- in the northern backlimb, conjugate NW-SE trending reverse faults reveal a compressional stress regime with a σ_1 axis roughly oriented N045;
- in the northern forelimb, N170–180-oriented normal faults indicate either an extensional regime with σ_3 oriented N045, or, more likely correspond to tilted oblique-slip reverse faults consistent with a pre-tilting N020 compression;
- in the southern backlimb, the few fault-slip data preclude any reliable stress tensor calculation. The dataset is however consistent with a post-tilting σ_1 oriented N045 and σ_3 oriented N135.

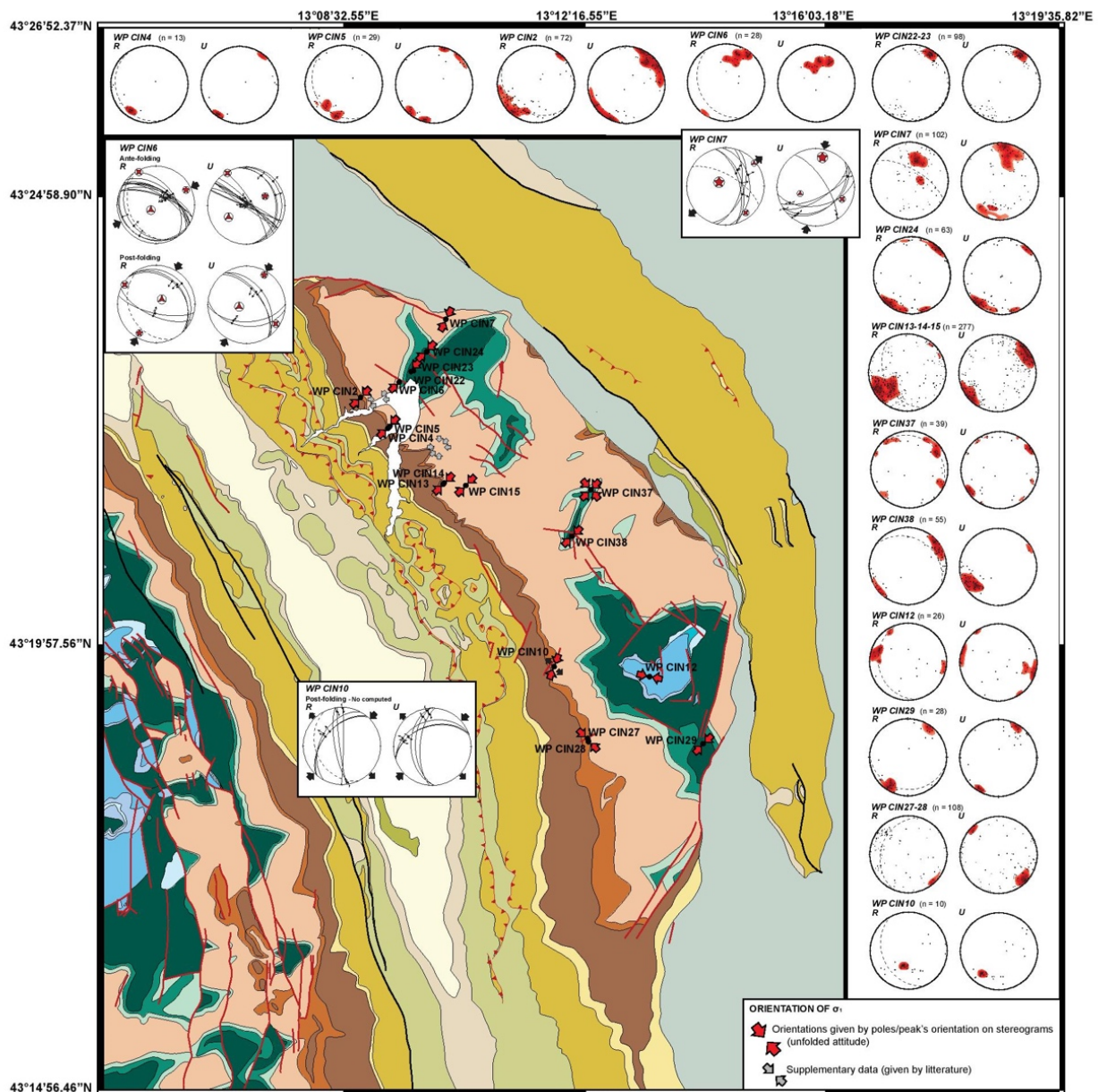


Figure 5. Location and plot of measured tectonic stylolites on the geological map. Each measurement point is associated with two stereodiagrams (lower hemisphere), representing main orientations of tectonic stylolites peaks measured (current and unfolded attitude). On each stereodiagram, the bedding is reported as dashed lines, and peaks orientation (i.e., σ_1 orientation) is given by high pole density zones. Stereodiagrams with fault-slip data and principal stress axes are also reported.

4.2. Young Modulus Estimate

Rock elastic properties were measured on flat homogeneous surfaces, for Maiolica, Scaglia Rossa and Scaglia Variegata, corresponding to 12 sites of measurement ($n = 1063$). For each site, the mean for rebound value R was represented as a function of the number of rebound incorporated in the mean calculation (supplementary material, Figure S1, Table S1); the stabilized R value (represented as a plateau on the graph) is then believed to be corrected from heterogenous effect and outliers, and so represent the rebound value R for the rock studied. Strikingly, the average of these representative R values is similar in the Maiolica, Scaglia Rossa and Scaglia Variegata formations, with values of 45 ± 8.4 , 48 ± 5.8 and 46 ± 8.5 , respectively. R values were further interpreted as Young moduli following the empiric relationship determined in [113] for sedimentary rocks and return a

E value similar for the 3 formations at about 20 GPa, very similar to the one reconstructed from stylolite inversion by [121] of 23 GPa.

4.3. Sedimentary Stylolite Roughness Inversion

The stylolite roughness inversion method was applied on 112 BPS sampled in the northern, central and southern parts of the Cingoli Anticline (Figure 1A), within the Cretaceous to Eocene carbonate formations. The inversion was successful (i.e., returning a value of crossover length L_c) on 77 BPS covering the anticline and distributed as follows: Maiolica (early Cretaceous, $n = 56$), Scaglia Rossa (late Cretaceous-early Eocene, $n = 18$) and Scaglia Variegata (middle to late Eocene, $n = 3$). For several stylolites, this paleopiezometric inversion was applied on two orthogonal tracks, in order to ensure that the stress on the horizontal plane was isotropic. L_c values are summarized in Table 1, and reported as an interval for each formation studied, considering an uncertainty of 23%:

- Maiolica: $[0.27 \pm 0.06; 1.76 \pm 0.40]$ mm
- Scaglia Rossa: $[0.36 \pm 0.08; 1.17 \pm 0.27]$ mm
- Scaglia Variegata: $[0.75 \pm 0.17; 1.75 \pm 0.40]$ mm

Table 1. Results of stylolite roughness inversion, applied on bedding-parallel stylolites.

Sample	GPS	Formation	L_c (mm)	σ_v (MPa) *	Depth (m)
CIN13	58	Maiolica	0.44 ± 0.10	34	1440
			0.60 ± 0.14	29	1250
			0.77 ± 0.18	26	1100
			0.84 ± 0.19	24	1040
			0.30 ± 0.07	41	1740
			0.27 ± 0.06	43	1840
CIN14	59	Maiolica	0.31 ± 0.07	40	1700
			0.34 ± 0.08	38	1630
CIN3	60	Maiolica	0.63 ± 0.14	28	1200
			0.39 ± 0.09	36	1540
CIN6	60	Maiolica	0.54 ± 0.12	30	1300
			0.49 ± 0.11	32	1360
			0.36 ± 0.08	37	1550
CIN8	60	Maiolica	0.53 ± 0.12	30	1300
			0.76 ± 0.17	26	1100
CIN9	60	Maiolica	0.39 ± 0.09	36	1540
CIN10	60	Maiolica	0.36 ± 0.08	37	1600
			0.31 ± 0.07	40	1700
			0.29 ± 0.07	42	1800
CIN15	61	Maiolica	0.49 ± 0.11	32	1360
			0.84 ± 0.19	25	1040
			0.38 ± 0.09	37	1550
CIN17	61	Maiolica	0.85 ± 0.20	25	1040
CIN18	61	Maiolica	0.45 ± 0.10	33	1400
			0.91 ± 0.21	23	1000
			1.09 ± 0.25	22	900
CIN33	64	Maiolica	0.73 ± 0.17	26	1100
			1.08 ± 0.25	22	900
			0.46 ± 0.11	33	1400
			0.34 ± 0.08	38	1630
CIN38	64	Maiolica	0.53 ± 0.12	30	1300
			0.55 ± 0.13	30	1300
CIN40	64	Maiolica	0.76 ± 0.17	26	1100
			0.46 ± 0.11	33	1400
			0.32 ± 0.07	40	1700
			0.56 ± 0.13	30	1300
			0.35 ± 0.08	38	1600

Table 1. Cont.

Sample	GPS	Formation	L_c (mm)	σ_v (MPa) *	Depth (m)
C3	WP_CIN3	Maiolica	1.76 ± 0.40	17	720
			1.38 ± 0.32	19	810
C51	WP_CIN23	Maiolica	1.18 ± 0.27	21	880
			0.67 ± 0.15	27	1150
C56	WP_CIN23	Maiolica	0.35 ± 0.08	38	1600
C67'	WP_CIN29	Maiolica	0.75 ± 0.17	26	1100
			0.58 ± 0.13	29	1250
C68	WP_CIN29	Maiolica	0.33 ± 0.08	39	1650
C69	WP_CIN29	Maiolica	0.74 ± 0.17	26	1100
			0.46 ± 0.11	33	1400
C70	WP_CIN29	Maiolica	0.35 ± 0.08	38	1600
			0.34 ± 0.08	38	1600
C71	WP_CIN29	Maiolica	0.38 ± 0.09	36	1540
C72	WP_CIN29	Maiolica	0.50 ± 0.12	32	1350
C86	WP_CIN38	Maiolica	1.33 ± 0.31	20	850
			0.39 ± 0.09	36	1540
			0.43 ± 0.10	34	1450
			1.11 ± 0.26	22	900
C79	WP_CIN36	Scaglia Rossa	0.38 ± 0.09	37	1550
C15	WP_CIN7	Scaglia Rossa	0.49 ± 0.11	32	1300
			0.51 ± 0.12	32	1300
C87	WP_CIN8	Scaglia Rossa	1.17 ± 0.27	21	880
			0.75 ± 0.17	26	1100
C21	WP_CIN9	Scaglia Rossa	0.59 ± 0.14	29	1250
			0.68 ± 0.16	27	1150
			0.45 ± 0.10	34	1420
C26	WP_CIN13	Scaglia Rossa	0.87 ± 0.20	24	1020
			0.85 ± 0.20	24	1020
			0.98 ± 0.23	23	960
C28	WP_CIN13	Scaglia Rossa	0.45 ± 0.10	33	1400
C29	WP_CIN13	Scaglia Rossa	0.63 ± 0.14	28	1200
			0.64 ± 0.15	28	1200
			0.84 ± 0.19	25	1040
C30	WP_CIN14	Scaglia Rossa	0.36 ± 0.08	38	1600
			0.60 ± 0.14	29	1230
			0.40 ± 0.09	35	1500
C2	WP_CIN2	Scaglia Variegata	0.75 ± 0.17	26	1100
			1.26 ± 0.29	20	850
			1.75 ± 0.40	17	720

* Crossover length given within 23% uncertainty. Vertical stress σ_v given within 12% uncertainty calculated according to Equation (5), considering a Young modulus $E = 23$ GPa ([139], this study), a Poisson ratio $\nu = 0.25$, and interfacial energy $\gamma = 0.32$ J·m⁻². Depth calculated using dry density of rock $d = 2400$ g·m⁻³, acceleration of gravity $g = 9.81$ m·s⁻².

4.4. Burial Model

The burial curves resulting from the backstripping process are presented in Figure 6.

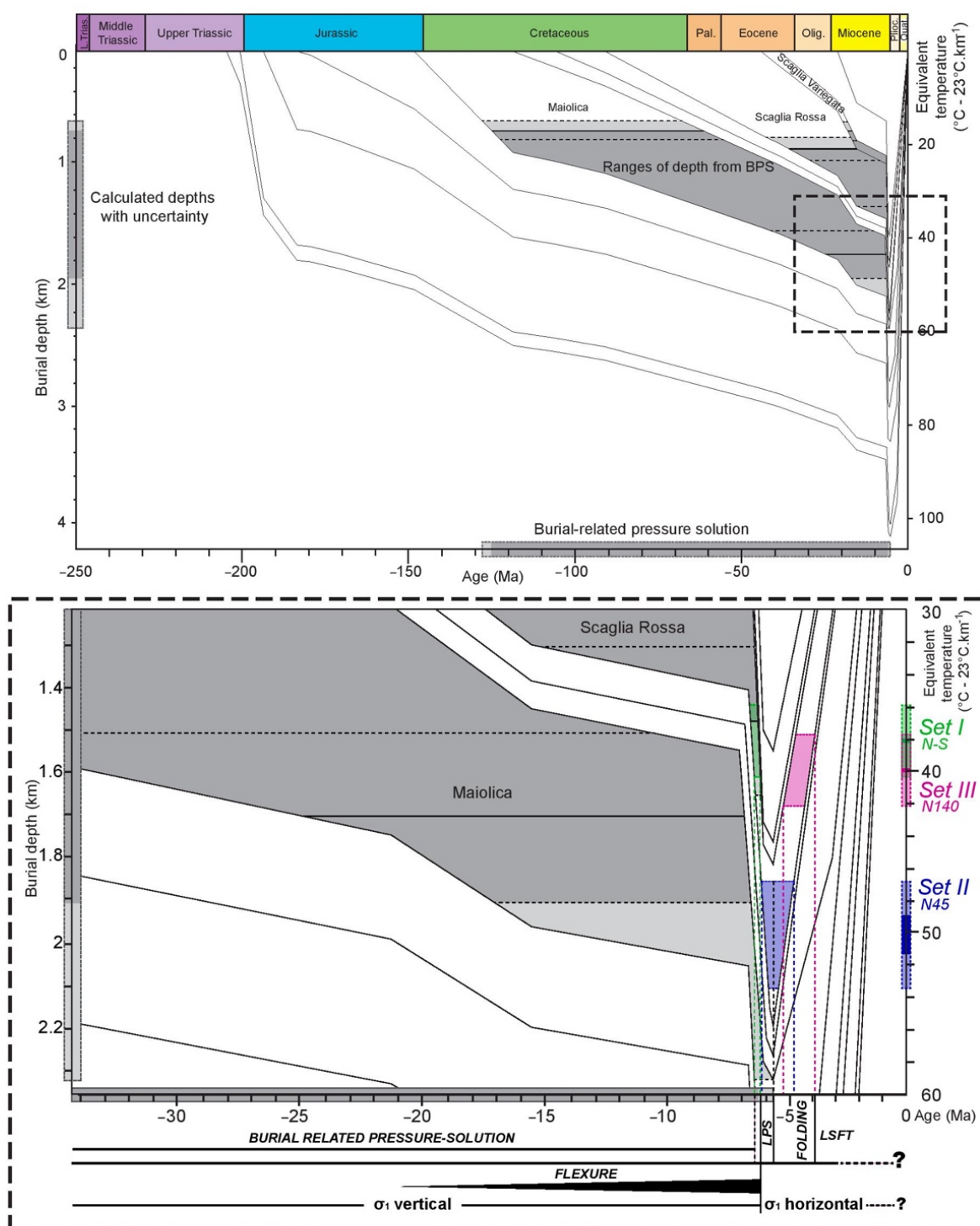


Figure 6. Burial model constructed considering thickness from stratigraphic and well data corrected for chemical and physical compaction. The range of depths reconstructed from BPS roughness inversion (with uncertainty shaded in light grey) are reported for each formation as grey levels. The corresponding timing and depth of active dissolution are reported on the x axis and left y axis, respectively. The results of clumped isotope analysis (i.e., temperatures of precipitation of vein cements at thermal equilibrium with the host rock) are reported on the right y axis. The timing of the deformation is reported on the right-hand side in the insert. Onsets of LPS, folding stage and LSFT are deduced from the results of the roughness inversion process applied on sedimentary stylolites, as well as from clumped isotope data.

They were reconstructed for the Triassic to Pliocene formations in the Cingoli area, considering: (i) the chemical compaction calculated at 8% for Maiolica, and 3% for Scaglia Rossa and Scaglia Variegata considering spacing and amplitude of BPS (following [108]); (ii) physical compaction by using the open-source software BackStrip [136]. The temperatures linked to these depths were calculated by considering a geothermal gradient of 23 °C·km⁻¹ reconstructed in the outermost western part of the UMAR from organic matter thermal maturity [65] and clay minerals [140] (Figure 6). These curves illustrate a first phase of increasing burial, corresponding to the deepening of the Umbria-Marche basin and a second phase of exhumation since early Pliocene. The maximum burial depths computed for the formations of interest, and equivalent temperatures, can be deduced from the left and right *y*-axis of Figure 6, respectively. These curves are consistent with models established for the inner part of the belt in the area of the Monte Tancia thrust [71].

4.5. Oxygen and Carbon Stable Isotopes

Twenty-eight (28) vein calcite cements and surrounding calcite host-rocks from the Scaglia Rossa were analyzed for $\delta^{18}\text{O}$ and $\delta^{13}\text{C}$ (Table 2, Figure 7).

Table 2. Results of Stable Isotopic Analyses of Oxygen and Carbon Isotopes.

Sample	Set	Vein		Host-Rock	
		$\delta^{13}\text{C}$ (‰VPDB)	$\delta^{18}\text{O}$ (‰VPDB) Calcite	$\delta^{13}\text{C}$ (‰VPDB)	$\delta^{18}\text{O}$ (‰VPDB) Calcite
CIN23-V1	I	2.04	2.19	2.15	−2.95
CIN23-V2	I	1.90	−0.44	2.15	−2.95
CIN23-V3	I	1.91	−1.56	2.15	−2.95
CIN23-V4	I	1.98	−0.68	2.15	−2.95
CIN25-V1	I	2.06	1.79	2.10	−2.27
CIN25-V2	I	2.06	−0.97	2.10	−2.27
CIN25-V3	I	2.08	2.07	2.10	−2.27
CIN39-V1	I	0.05	−0.74	1.08	−1.59
CIN39-V2	I	0.10	−0.30	1.08	−1.59
CIN39-V3	I	0.31	−0.66	1.08	−1.59
CIN7-V1	II	2.48	1.37	2.47	−1.68
CIN7-V2	II	2.97	2.09	2.47	−1.68
CIN28a-V1	II	2.07	1.21	2.01	−1.82
CIN28a-V2	II	1.81	0.58	2.01	−1.82
CIN28a-V3	II	1.95	2.22	2.01	−1.82
CIN26-V1	II	2.00	2.59	2.02	−1.74
CIN26-V2	II	1.95	2.34	2.02	−1.74
CIN26-V3	II	2.14	1.47	2.02	−1.74
CIN26-V4	II	2.05	1.38	2.02	−1.74
CIN28b-V1	II	2.08	2.20	2.03	−1.64
CIN28b-V2	II	1.98	1.68	2.03	−1.64
A13-V1	III	3.23	0.79	3.08	−1.45
A14-V1	III	3.21	0.21	2.89	−1.53
A14-V2	III	3.19	0.61	2.89	−1.53
CIN37-V1	III	1.39	−0.59	1.09	−1.55
CIN37-V2	III	1.25	0.46	1.09	−1.55
CIN37-V3	III	1.10	−1.12	1.09	−1.55
CIN37-V3	III	1.10	−1.12	1.09	−1.55

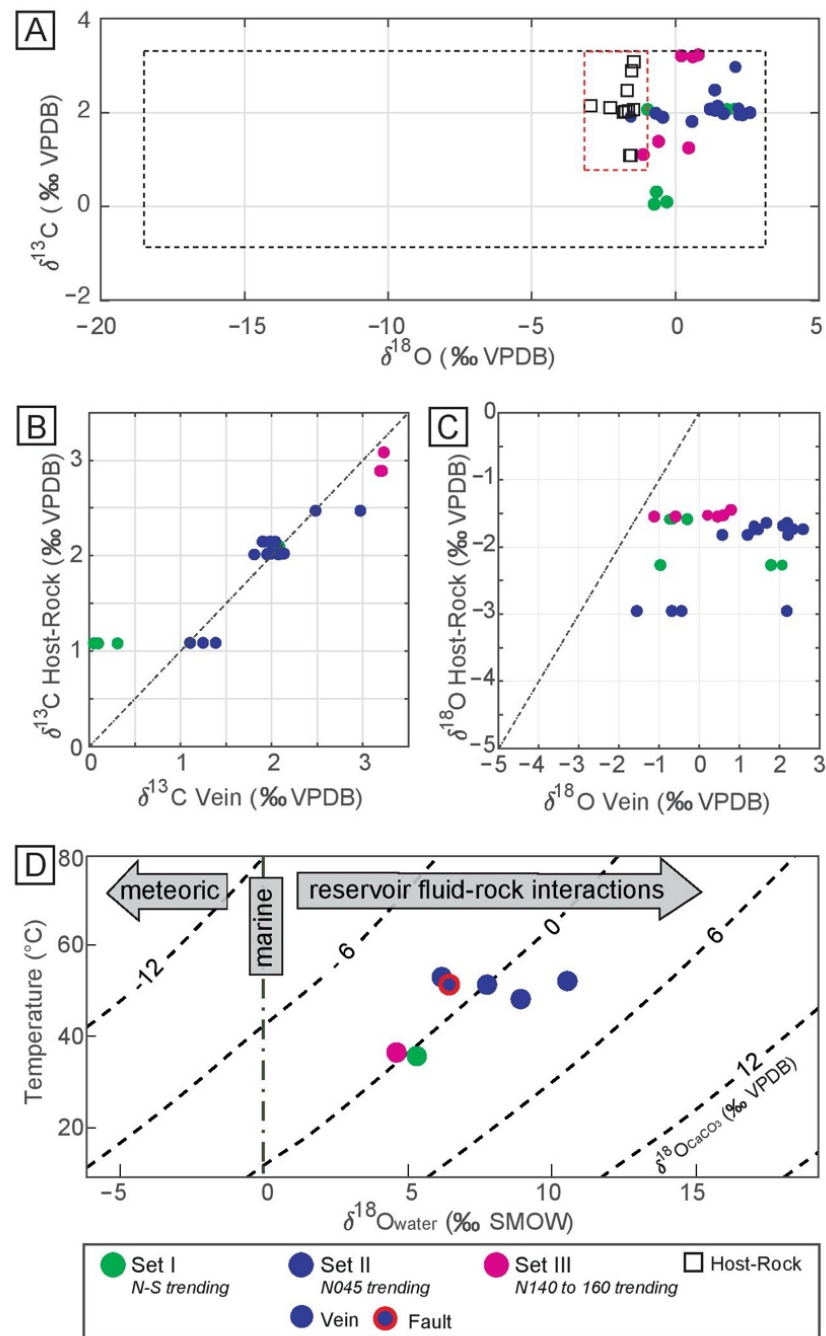


Figure 7. Isotopic data from tectonic veins, faults and host-rocks sampled in the Scaglia Rossa. (A) Oxygen versus Carbon stable isotopic ratio (‰ VPDB) of host rocks (black squares), and vein cements according to the vein sets. Red dotted frame represents the range of isotopic values documented in the UMAR from the Hettangian to Aquitanian carbonates, black dotted frame represents the range of isotopic values documented in tectonic related fracture fillings at the scale of the range [60]. (B) $\delta^{13}\text{C}$ values of vein cements versus $\delta^{13}\text{C}$ values of the surrounding host rocks (‰ VPDB), according to the vein sets. (C) $\delta^{18}\text{O}$ values of vein cements versus $\delta^{18}\text{O}$ values of the surrounding host rocks (‰ VPDB), according to the vein sets. (D) $\Delta_{47}\text{CO}_2$ measured temperature of precipitation (°C) versus $\delta^{18}\text{O}$ values of calcite cements (‰ VPDB, oblique dotted lines) and corresponding $\delta^{18}\text{O}$ values of the related fluids (‰ SMOW) calculated from temperature-dependent fractionation equation $\text{CaCO}_3\text{-H}_2\text{O}$ of [141]. For A-D, tectonic veins are reported as full circles of which color relates to the set they belong to (green: N-S, blue: N045, purple: N140). Note that the circle with red contour on D correspond to an LPS-related fault.

In the host-rock ($n = 11$), the $\delta^{18}\text{O}$ isotopic values range from -2.95 to -1.45‰ VPDB while the $\delta^{13}\text{C}$ isotopic values range from 1.08 to 3.08‰ VPDB. In the calcite veins ($n = 28$), the $\delta^{18}\text{O}$ isotopic values range from -1.56 to 2.59‰ VPDB while the $\delta^{13}\text{C}$ isotopic values range from 0.05 to 3.23‰ VPDB. The vein cements show variable isotopic values: for the set I (N-S, $n = 10$), $\delta^{18}\text{O}$ ratio ranges from -1.56 to 2.19‰ VPDB while $\delta^{13}\text{C}$ ratio ranges from 0.05 to 2.08‰ VPDB; for the set II (N045, $n = 11$), $\delta^{18}\text{O}$ ratio ranges from 0.58 to 2.59‰ VPDB while $\delta^{13}\text{C}$ ratio ranges from 1.81 to 2.97‰ VPDB; for the set III N140 ($n = 7$), $\delta^{18}\text{O}$ ratio ranges from -1.12 to 0.79‰ VPDB while $\delta^{13}\text{C}$ ratio ranges from 1.1 to 3.23‰ VPDB; $\delta^{18}\text{O}$ ratio ranges from -1.57 to 1.93‰ VPDB while $\delta^{13}\text{C}$ ratio ranges from 2.02 to 2.21‰ VPDB (Table 2, Figure 7A). In order to account for possible rock buffering effect, the isotopic values of the veins were plotted against isotopic values of the surrounding host-rock, for both carbon (Figure 7B) and oxygen (Figure 7C). Results show that most veins have a $\delta^{13}\text{C}$ value similar to their host rock, with a difference ranging from -0.50 to 0.25‰ VPDB in all sets except in the set I where this difference reaches -1.05‰ VPDB. Considering the difference in $\delta^{18}\text{O}$ values, the results are more scattered, ranging from -0.12 to 5.14‰ VPDB. Notably, the difference in the set II is higher than the one in the set III.

4.6. Carbonate Clumped-Isotope Paleothermometry ($\Delta 47$)

Eight of the 9 samples presented in the Supplementary Material were selected as being unambiguously related to a major fracture set. Consequently, 7 samples of vein cements and 1 sample of striated coating of fault plane were selected for $\Delta 47$ clumped isotope measurements (Table 3), with $\Delta 47$ values ranging from $0.593 \pm 0.006\text{‰}$ to $0.630 \pm 0.006\text{‰}$, (1SE) corresponding to precipitation temperature (T_{47}) ranging from $38.30 \pm 1.9\text{ °C}$ to $51.4 \pm 2.2\text{ °C}$ (1SE). Veins belonging to different tectonic sets appear to yield distinct temperatures of precipitation, with T_{47} ranging from $48.7 \pm 2.1\text{ °C}$ to $51.4 \pm 2.2\text{ °C}$ for the set II ($n = 5$) and related fault cements, while vein cements from sets I and III have T_{47} ranging from $38.8 \pm 2.0\text{ °C}$ to $45.1 \pm 2.1\text{ °C}$.

Table 3. Results of clumped isotope measurements, with $\Delta 47$ ratio and associated temperature of precipitation T_{47} .

Sample	N	Set	$\delta^{13}\text{C}$ (‰ VPDB)	$\delta^{18}\text{O}$ (‰ VPDB, Calcite)	$\Delta 47$ (‰, 1 σ)	T_{47} (°C \pm 1 σ)
NB_CIN23_V1	3	I	1.77	-0.40	0.6299 ± 0.0058	38.3 ± 1.9
NB_CIN25_V1prime	3	I	1.93	1.68	0.6006 ± 0.0058	48.7 ± 2.1
NB_CIN26_V1	3	II	1.92	2.13	0.5933 ± 0.0058	51.4 ± 2.2
NB_CIN28a_V1	3	II	1.73	-0.03	0.5968 ± 0.0057	50.0 ± 2.2
NB_CIN28b_V1	3	II	2.01	1.95	0.5944 ± 0.0058	51.0 ± 2.2
NB_CIN7_V1	3	II	2.44	0.86	0.6103 ± 0.0058	45.1 ± 2.1
NB_A14_V1	3	III	3.08	0.45	0.6283 ± 0.0058	38.8 ± 2.0
NB_CIN25_FAILLE	3	/	2.01	1.77	0.5985 ± 0.0058	49.4 ± 2.2

5. Interpretation of Results

5.1. Sequence of Mesostructures in Relation to Folding

The main stages of regional deformation, already described in the literature [29,60–63,68,121,142], were associated with sets of fracture-stylolite network identified in this domain of the UMAR.

Set I (N-S to N020-oriented fractures) is the oldest set encountered in the Cingoli Anticline. Because of its orientation and opening mode, we propose to interpret it as an along-strike joint set related to the flexure stage associated with forebulge development (sensu [8]).

Vertical, bedding, and fold-axis perpendicular set II joints/veins, associated with early folding stylolites with N045-oriented peaks likely reflects a stage of LPS with σ_1 striking perpendicular to the northern part of the UMAR structure axes. This is confirmed by reverse faulting associated with a N045 σ_1 after unfolding (Figure 5). Local complexities are interpreted as resulting from LPS related stress perturbation, resulting in a slight local

stress rotation in the vicinity of local heterogeneities such as inherited faults (Figure 3, e.g., [23,143,144]). For instance, we interpret the N020 contraction in the northern part of the fold as a local rotation around the WNW-ESE fault. We also consider that stylolites with peaks-oriented E-W documented in the Calcare Massiccio relate to LPS perturbed by the reactivation of N-S striking inherited normal fault.

The joints/veins of set III postdate those of set II (Figure 4C) and are bedding-perpendicular and strike parallel to the local fold axis and bedding strike. We propose to relate this set to the folding stage, reflecting outer-arc extension associated to strata curvature at fold hinge. The $\sim 20^\circ$ variation of the orientation of this set between the north and south of the fold (N140 in the northern part and N160 in the southern part, Figure 3 and Figure 4) is consistent with the arcuate shape of the fold and then strengthen this interpretation.

Late folding, tectonic stylolites with horizontal peaks striking N045, along with post-tilting strike-slip faults (Figure 5) are interpreted to be related to horizontal NE-SW contraction affecting the strata after the fold was locked, corresponding to LSFT [8,15].

Our results therefore demonstrate that the N045 compression prevailed during the entire contractional history, i.e., from LPS to LSFT.

5.2. Evolution of the Burial Depth

The calculation of vertical stress involves the use of the following mechanical parameters: (i) crossover lengths L_c values, calculated by considering an uncertainty of 23% and reported in Table 1; (ii) mechanical and chemical parameters, defined in the literature and given above (i.e., Young modulus E , Poisson ratio ν and the solid-fluid interfacial energy γ). Then, the burial depths were calculated from each value of the vertical stress using Equation (2) and rounded to the closest 10 m (Table 1). The corresponding depth ranges for each formation are:

- Maiolica: from 720 ± 85 m to 1840 ± 220 m;
- Scaglia Rossa: from 880 ± 100 m to 1590 ± 190 m;
- Scaglia Variegata: from 720 ± 85 m to 1100 ± 130 m.

These ranges of burial depth correspond to the ranges of depth in which pressure solution along sedimentary stylolites was active, i.e., at the time vertical shortening (σ_1 vertical) was prevailing over horizontal shortening [60,145]. Figure 6 shows these ranges of depth reported on the burial model for comparison. The inversion and modeling data appear to be consistent as the maximum burial recorded by sedimentary stylolites never exceeds the maximum depth of the formation they belong to (Figure 6). In addition, the largest range of depths is associated with the Maiolica (i.e., the oldest formation); for the Scaglia Rossa and Variegata, intervals are overall narrower, and the more recent the formation, the narrower the depth range and the shallower the depth returned. In the case of the Scaglia Variegata (i.e., the youngest), the maximum burial recorded by the stylolites does not exceed 1200 m. Thus, BPS would not develop between 1200 and 1750 m, i.e., at the maximum burial values associated with the Scaglia Variegata (Figure 6). However, these data indicate that the burial was continuous from the Cretaceous to the late Miocene until the maximum burial depths of the sedimentary layers studied were reached. The reconstruction of the complete burial/exhumation history in relation to the deformation stages requires the combination of these data with isotope analyses.

5.3. Fluid System

The fluid system in the Cingoli Anticline can be partially characterized using stable O, C and clumped isotope dataset. The positive difference of isotopic values between vein cements and related host-rock, being low to null for $\delta^{13}\text{C}$ values (Figure 7B) yet significant for $\delta^{18}\text{O}$ values (Figure 7C), argues against rock buffered fluid precipitation as well as diagenesis related to burial. Instead, it strongly suggests that cements precipitated from local fluids originated from the studied sedimentary sequence (hence with identical $\delta^{13}\text{C}$ signature), with various but limited degrees of fluid-rock interaction likely related

to migration, leading to an increase of the $\delta^{18}\text{O}$ ratios. The Δ_{47} results complement and support this interpretation as the combination of the temperature of precipitation T_{47} with the $\delta^{18}\text{O}$ value of the cement yields the $\delta^{18}\text{O}$ values of the precipitating fluid (Figure 7D) using the temperature dependent equation of fractionation of [141]. The reconstructed $\delta^{18}\text{O}$ values of the precipitating fluids range from 4.80 to 10.50‰ SMOW, irrespective of the tectonic vein sets where fluids precipitated. Positive $\delta^{18}\text{O}$ values points towards a more or less evolved brine origin for the fluid, which is consistent with a scenario involving a migration of Turonian-Lutetian marine fluids inside the host Scaglia Rossa and precipitating at thermal equilibrium within the host. It is noteworthy that these characteristics of the fluid system in the Cingoli Anticline are consistent with the fluid systems reconstructed in most of the other folds and thrusts of the UMAR, except for the Subasio Anticline [60] and Monte Tancia thrust [71]. Interestingly, our dataset does not document a rock buffering of external fluids as interpreted in the Monte Tancia thrust (southern part of the UMAR) by [71], and it does not reflect the late meteoric derived fluid infiltration documented there and related to the currently active extensional tectonics. When considering the tectonic vein sets, temperature of precipitation T_{47} differs significantly between set I, set II, and set III, supporting the interpretation of a thermal equilibrium between local fluids and the host rocks throughout the burial history. Moreover, the difference in $\delta^{18}\text{O}_{\text{fluids}}$ values between set II, related to LPS, and set III, related to local curvature of the strata at fold hinge, suggest that the degree of lateral fluid-rock interaction was higher during LPS than during folding, as is the case elsewhere [139].

6. Discussion

The results of mesostructural and isotopic analyses, together with inversion of the roughness of the sedimentary stylolites for maximum burial depth, have been combined in order to unravel the history of deformation in the Cingoli area. Moreover, because the fluid system appears to be at thermal equilibrium during deformation and that each fracture set has a specific T_{47} signature, it is possible to infer the timing of fracture development by comparing the range of precipitation temperatures T_{47} measured in the vein cements from each set with burial curves and maximum depths of active pressure-solution reconstructed from inversion of stylolite roughness. The stages of deformation (Figure 8), together with their absolute timing and sequence were therefore characterized, and compared with existing data for this study area [60,71], as well as in other localities of the belt, i.e., the anticlines of Monte Nero [121], Monte Catria [66] and Monte Conero [68]; the ages determined using the isotopic data are given with an uncertainty of 0.2 Ma, due to uncertainties on temperature (± 2 °C) (Figure 6):

- (i) pre-contractual stage, marked by burial, vertical compaction and dissolution along BPS recognized at the scale of the fold-and-thrust belt [60,61,66,68,121], under a vertical σ_1 . It lasted until the early Messinian (ca. 6.4 Ma);
- (ii) this pre-contractual stage is partly coeval with an E-W extension related to the flexure of the Adriatic foreland [63,101], the onset of which is set to early Burdigalian (ca. 21 Ma, as defined by the inflection point of the burial curves), and which ended by middle Messinian (ca. 6.3 Ma, Figure 8). This E-W extension would be at the origin of the development of a network of N-S fractures (set I). Pre-folding N-S striking joints have already been described in this anticline [61], and in other anticlines, Monte Nero [121] and Monte Catria [66], without being related to regional extension. In the Conero anticline, however, [68] related a set of N-S, high angle to bedding, joints and veins associated with normal faults to a flexural event. Further considerations provide the existence of polyphase syndepositional normal faulting: the Barremian [146–148] and late Cretaceous phases of stretching (e.g., [95,149,150], well known in the Umbria-Marche-Sabina area, could have developed set I joints in the Maiolica and Scaglia Rossa, as well as the development of stylolites in the Mesozoic rocks.
- (iii) LPS stage, a pre/early-folding compressional stage with σ_1 NE-SW-oriented related to the Apenninic contraction [66,97–99]. The onset of this stage corresponds to the

switch from formerly vertical to horizontal σ_1 , associated with a N045 compression marked by the fractures and stylolites of set II. This stage of deformation is consistent regionally as it has been documented in the Monte Nero [121], Conero [68], and Monte Catria [66] anticlines, and identified in numerous folds of the UMAR [52,54]. Based on T_{47} precipitation temperature and burial history, the LPS stage started since the middle Messinian (ca. 6.3 Ma). It has been reported in other case studies that the fold growth and associated underlying ramp activation is likely to be responsible for the uplift we reconstructed ca. 5.8 Ma [60]. Thus, we consider the LPS stage to have lasted from 6.3 Ma to 5.8 Ma;

- (iv) fold growth stage, characterized by a compression parallel to regional shortening, i.e., NE-SW-oriented [29] and local extension perpendicular to fold axis and related with strata curvature at fold hinge [60]. Based on the dating of the LPS, fold growth started at 5.8 Ma yet the T_{47} points towards a related N135 striking joints/veins development during the latest Neogene-early Pliocene (ca. 5.2 to 3.9 Ma, Figure 8). That difference in timing suggests a 0.6 My long fault activity and strata tilting before curvature became high enough to developed outer-arc extension fractures;
- (v) LSFT, post-dating the fold growth stage and still associated with a NE-SW contractional trend. At this stage shortening is no longer accommodated by e.g., limb rotation [60] and is associated with tectonic stylolites with N045-oriented peaks. The E-W fractures locally measured cannot be associated with this deformation stage, because no consistent chronological relationships with the syn-folding fracture sets were identified. Isotopic analyses (Figure 8) suggest the onset of the LSFT by the Pliocene (ca. 3.9 Ma). Despite the record of recent seismic activity in this northern part of the Apennines, linked to a post-orogenic NE-SW extension [151], the end of this deformation stage can precisely be determined neither from previous studies carried out in Cingoli [61] nor from data collected during this study.

This deformation scenario is in line to the one proposed by [61], that discriminates seven sets of stylolites, of which complexity can be related to more local effect of the fold evolution.

The fold growth duration in Cingoli as constrained by the above results (ca. 1.9 My, from 5.8 to 3.9 Ma) is consistent with that established by [62] using the age of foredeep deposits. The age of the end of the foreland flexure, evaluated at ca. 6.3 Ma in our study, is also consistent within uncertainties with the early Messinian age (ca. 7.2–6.5 Ma) derived from the sedimentary dating of the flexure-related normal faults [63,64]. The abrupt increase in the slope of the burial curves (Figure 6) likely reflects the initiation of this flexure at about 21 Ma, which is older than the late Burdigalian (ca. 16 Ma) age previously proposed on the basis of the distribution and variations in thickness of the Schlier (Aquitainian-Serravallian) marking the deepening of the basin [63], and older than Serravallian (ca. 13.8 Ma) proposed at the west of the Cingoli Anticline, in the western part of the belt [79]. The horizontal isotropy of the compaction-related sedimentary stylolites, along which dissolution was active until 7 Ma, however, suggests a very limited imprint of the flexure on the magnitude of the horizontal stresses in the Cretaceous-Paleogene rocks until the early Messinian, when the flexure became important enough to cause fractures and large-scale normal faults [63].

The folding duration, estimated in our work at ~ 2 My (from 5.8 to 3.9 Ma) is consistent with the results of previous studies carried out in the more internal areas of the belt, using absolute dating methods to reconstruct the duration and timing of the deformations [60,71]: the difference in timing is in line with [62], and the duration of the folding is consistent with [60,71], which respectively dated the folding from 8 to 5 Ma [60], and from 9 to 7 Ma [71] (i.e., a duration of 2 to 3 My).

This case study illustrates the potential of the combination of mesostructural, paleo-piezometric, and isotopic analyses, which reveals a regionally consistent sequence and timing of deformation stages, despite multiple sources of uncertainties. Namely, the refining of the timing of the flexure expression on the sedimentary reservoir is an example of how the study of mesostructures can provide insights on the large-scale structures.

Another example of such upscaling lies in the interpretation of the arcuate shape of the Cingoli Anticline, that the distribution and timing of LPS related veins (set II) bounds to be a primary feature of the fold development, likely linked to the reactivation of an inherited N-S normal fault during folding (Figure 8).

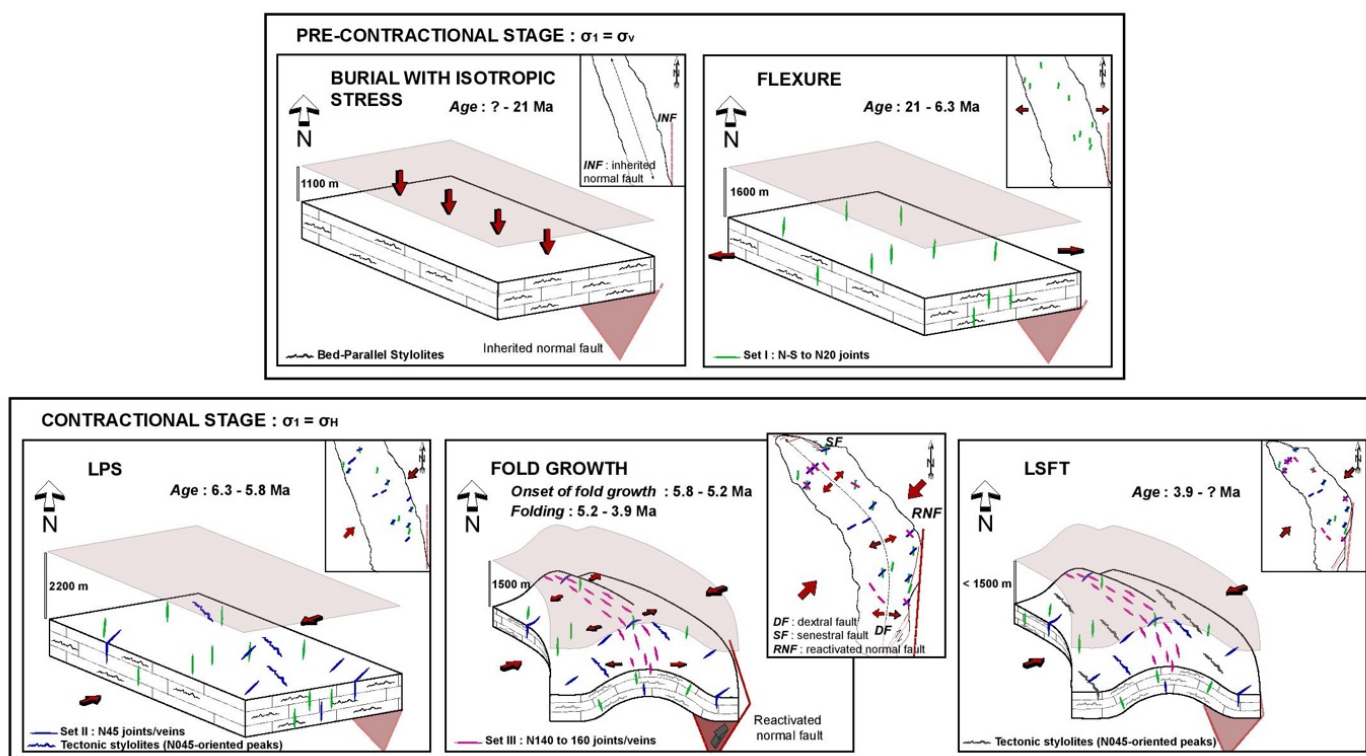


Figure 8. Interpretative model of the history of deformation in the Cingoli Anticline. The structural evolution of the area is represented in 3D and in map view. For each stage of deformation, the main principal stress σ_1 is represented as red arrows, as well as the associated mesostructures (green: set I, blue: set II, pink: set III) and burial depths recorded by the Scaglia Rossa (deduced from burial curves). Faults are represented by red lines in map view, dotted lines when inactive, and solid lines when active. The inherited normal fault is also represented on the 3D block, by a red plane in transparency when it is inactive.

7. Conclusions

This work, focused on the Cingoli Anticline in eastern UMAR, shows how the burial-deformation history of folded rocks can be unraveled using an original combination of ubiquitous features of carbonate rocks: fracture analysis, BPS paleopiezometry and vein cement geochemistry. The main conclusions are:

- different stages of deformation were recognized: (i) E-W extension related to foreland flexure (σ_1 vertical); (ii) N045 oriented LPS; (iii) fold growth; (iv) LSFT, under a horizontal N045 contraction. Mesostructural analyses also support that the arcuate geometry of the Cingoli Anticline is a primary feature, probably linked to the oblique reactivation of a N-S inherited normal fault.
- the burial history of strata was reconstructed with high resolution using roughness inversion applied to sedimentary stylolites. Our results highlight that this paleopiezometric technique yields consistent maximum depth estimates down to 2500 m, in agreement with previous studies in the western part of the UMAR.
- the timing of deformation, and particularly the duration of the Apenninic contractional stages, was reconstructed from combined paleopiezometric, isotopic and mesostructural data. Following foreland flexure (ca. 21.2 to 6.3 Ma), LPS was dated from middle Messinian to early Pliocene (ca. 6.3 to 5.8 Ma) and fold growth occurred between early

and middle Pliocene (ca. 5.8 to 3.9 Ma). The precise duration of LSFT remains out of reach. The duration of the fold growth phase is in line with previous estimates based on other proxies such as K-Ar and U-Pb absolute dating [71].

- the O and C stable isotope signatures and clumped isotopes of Δ_{47} of vein cements imply that the paleofluid system that prevailed during LPS and folding in this structure involve marine local fluids with limited interaction with the host rock, in agreement with earlier findings in the eastern UMAR.

Beyond regional implications, this study demonstrates the high potential of our new approach combining paleopiezometric, isotopic, and mesostructural data to reconstruct the sequence and to constrain the timing not only of local mesoscale deformation, but also of regional tectonic events in an orogenic system. Our results further confirm that the paleopiezometric inversion of the roughness of sedimentary stylolites for the vertical stresses is a reliable and powerful tool to unravel the amount and timing of burial without any assumption about the past geothermal gradient.

Supplementary Materials: The following are available online at <https://www.mdpi.com/2076-3263/11/3/135/s1>, Figure S1: graphical representation of the incremental mobile average value of the elastic rebound as a function of the number of measurements incorporated in the calculation, for each measurement site, Table S1: stabilized average rebound value R for the Maiolica, Scaglia Rossa and Scaglia Variegata. Standard deviation and number of measures are detailed for each site of measurement, Figure S2: Average Wavelet analysis of the stylolite roughness for all studied samples, Table S2: GPS coordinates of measurement and sampling sites, Figure S3: interpreted X-ray diffractometry spectrum of the Scaglia Rossa, Figure S4: Δ_{47} analysis report, detailing analysis and results.

Author Contributions: Conceptualization, A.L., N.E.B., O.L., and J.-P.C.; methodology, A.L., N.E.B. and S.K.; formal analysis, A.L., N.E.B., M.D., S.K. and L.E.; fieldwork, O.L., N.E.B., J.-P.C. and L.P.; writing—original draft preparation, A.L.; writing—review and editing, A.L., N.E.B., O.L., L.E., L.P., M.D. and J.-P.C.; project administration, N.E.B.; funding acquisition, N.E.B., O.L., J.-P.C. All authors have read and agreed to the published version of the manuscript.

Funding: This research was funded by the Sorbonne Université, grant number C14313, the Région Nouvelle-Aquitaine, and the Agence Nationale de la Recherche (Projet Investissement d’Avenir (programme E2S)).

Acknowledgments: A.L and N.E.B are funded through the ISITE programme E2S, supported by ANR PIA and Région Nouvelle-Aquitaine. Authors also thank two anonymous reviewers for insightful comments that improved the manuscript and Giancarlo Molli, Angelo Cipriani and Domenico Liotta, for their editorial work.

Conflicts of Interest: The authors declare no conflict of interest. The funders had no role in the design of the study; in the collection, analyses, or interpretation of data; in the writing of the manuscript, or in the decision to publish the results.

References

1. Barton, C.A.; Zoback, M.D. Stress perturbations associated with active faults penetrated by boreholes: Possible evidence for near-complete stress drop and a new technique for stress magnitude measurement. *J. Geophys. Res.* **1994**, *99*, 9373–9390. [[CrossRef](#)]
2. Zoback, M.L.; Zoback, M.D. Chapter 24: Tectonic stress field of the continental United States. *Mem. Geol. Soc. Am.* **1989**, *172*, 523–539. [[CrossRef](#)]
3. Sibson, R.H. Crustal stress, faulting and fluid flow. *Geol. Soc. Spec. Publ.* **1994**, *78*, 69–84. [[CrossRef](#)]
4. Sanderson, D.J.; Zhang, X. Stress-controlled localization of deformation and fluid flow in fractured rocks. *Geol. Soc. Spec. Publ.* **2004**, *231*, 299–314. [[CrossRef](#)]
5. Sanderson, D.J.; Zhang, X. Critical stress localization of flow associated with deformation of well-fractured rock masses, with implications for mineral deposits. *Geol. Soc. Spec. Publ.* **1999**, *155*, 69–81. [[CrossRef](#)]
6. Mourgues, R.; Gressier, J.B.; Bodet, L.; Bureau, D.; Gay, A. “Basin scale” versus “localized” pore pressure/stress coupling—Implications for trap integrity evaluation. *Mar. Pet. Geol.* **2011**, *28*, 1111–1121. [[CrossRef](#)]
7. Beaudoin, N.; Lacombe, O. Recent and future trends in paleopiezometry in the diagenetic domain: Insights into the tectonic paleostress and burial depth history of fold-and-thrust belts and sedimentary basins. *J. Struct. Geol.* **2018**, *114*, 357–365. [[CrossRef](#)]

8. Tavani, S.; Storti, F.; Lacombe, O.; Corradetti, A.; Muñoz, J.A.; Mazzoli, S. A review of deformation pattern templates in foreland basin systems and fold-and-thrust belts: Implications for the state of stress in the frontal regions of thrust wedges. *Earth-Sci. Rev.* **2015**, *141*, 82–104. [[CrossRef](#)]
9. Bergbauer, S.; Pollard, D.D. A new conceptual fold-fracture model including prefolding joints, based on the Emigrant Gap anticline, Wyoming. *Bull. Geol. Soc. Am.* **2004**, *116*, 294–307. [[CrossRef](#)]
10. Bellahsen, N.; Fiore, P.; Pollard, D.D. The role of fractures in the structural interpretation of Sheep Mountain Anticline, Wyoming. *J. Struct. Geol.* **2006**, *28*, 850–867. [[CrossRef](#)]
11. La Bruna, V.; Lamarche, J.; Agosta, F.; Rustichelli, A.; Giuffrida, A.; Saldon, R.; Marie, L. Structural Diagenesis, Early Embrittlement and Fracture Setting in Shallow-Water Platform Carbonates (Monte Alpi Southern Apennines, Italy). In *Proceedings of the Fifth International Conference on Fault and Top Seals*; European Association of Geoscientists & Engineers: Houten, The Netherlands, 2019; Volume 2019, pp. 1–5.
12. Rocher, M.; Lacombe, O.; Angelier, J.; Chen, H.W. Mechanical twin sets in calcite as markers of recent collisional events in a fold-and-thrust belt: Evidence from the reefal limestones of southwestern Taiwan. *Tectonics* **1996**, *15*, 984–996. [[CrossRef](#)]
13. Lacombe, O.; Angelier, J.; Rocher, M.; Bergues, J.; Deffontaines, B.; Chu, H.T.; Hu, J.C.; Lee, J.C. Stress patterns associated with folding at the front of a collision belt: Example from the Pliocene reef limestones of Yutengping (Taiwan). *Bull. Soc. Geol. Fr.* **1996**, *167*, 361–374.
14. Rocher, M.; Lacombe, O.; Angelier, J.; Deffontaines, B.; Verdier, F. Cenozoic folding and faulting in the south Aquitaine Basin (France): Insights from combined structural and paleostress analyses. *J. Struct. Geol.* **2000**, *22*, 627–645. [[CrossRef](#)]
15. Amrouch, K.; Lacombe, O.; Bellahsen, N.; Daniel, J.M.; Callot, J.P. Stress and strain patterns, kinematics and deformation mechanisms in a basement-cored anticline: Sheep Mountain Anticline, Wyoming. *Tectonics* **2010**, *29*. [[CrossRef](#)]
16. Amrouch, K.; Beaudoin, N.; Lacombe, O.; Bellahsen, N.; Daniel, J.M. Paleostress magnitudes in folded sedimentary rocks. *Geophys. Res. Lett.* **2011**, *38*. [[CrossRef](#)]
17. Callot, J.P.; Breesch, L.; Guilhaumou, N.; Roue, F.; Swennen, R.; Vilasi, N. Paleo-fluids characterisation and fluid flow modelling along a regional transect in Northern United Arab Emirates (UAE). *Arab. J. Geosci.* **2010**, *3*, 413–437. [[CrossRef](#)]
18. Sassi, W.; Guiton, M.L.E.; Leroy, Y.M.; Daniel, J.M.; Callot, J.P. Constraints on bed scale fracture chronology with a FEM mechanical model of folding: The case of Split Mountain (Utah, USA). *Tectonophysics* **2012**, *576–577*, 197–215. [[CrossRef](#)]
19. Smart, K.J.; Ferrill, D.A.; Morris, A.P.; McGinnis, R.N. Geomechanical modeling of stress and strain evolution during contractional fault-related folding. *Tectonophysics* **2012**, *576–577*, 171–196. [[CrossRef](#)]
20. Beaudoin, N.; Bellahsen, N.; Lacombe, O.; Emmanuel, L. Fracture-controlled paleohydrogeology in a basement-cored, fault-related fold: Sheep Mountain Anticline, Wyoming, United States. *Geochem. Geophys. Geosyst.* **2011**, *12*. [[CrossRef](#)]
21. Saintot, A.; Stephenson, R.; Brem, A.; Stovba, S.; Privalov, V. Paleostress field reconstruction and revised tectonic history of the Donbas fold and thrust belt (Ukraine and Russia). *Tectonics* **2003**, *22*. [[CrossRef](#)]
22. Laubach, S.E.; Olson, J.E.; Gale, J.F.W. Are open fractures necessarily aligned with maximum horizontal stress? *Earth Planet. Sci. Lett.* **2004**, *222*, 191–195. [[CrossRef](#)]
23. Bellahsen, N.; Fiore, P.E.; Pollard, D.D. From spatial variation of fracture patterns to fold kinematics: A geomechanical approach. *Geophys. Res. Lett.* **2006**, *33*. [[CrossRef](#)]
24. Cooper, S.P.; Goodwin, L.B.; Lorenz, J.C. Fracture and fault patterns associated with basement-cored anticlines: The example of Teapot Dome, Wyoming. *Am. Assoc. Pet. Geol. Bull.* **2006**, *90*, 1903–1920. [[CrossRef](#)]
25. Ahmadhadi, F.; Lacombe, O.; Daniel, J.-M. Early Reactivation of Basement Faults in Central Zagros (SW Iran): Evidence from Pre-folding Fracture Populations in Asmari Formation and Lower Tertiary Paleogeography. In *Thrusts Belts and Foreland Basins. Frontiers in Earth Sciences*; Lacombe, O., Roue, F., Vergés, J., Eds.; Springer: Berlin/Heidelberg, Germany, 2007; pp. 205–228.
26. Ahmadhadi, F.; Daniel, J.M.; Azzizadeh, M.; Lacombe, O. Evidence for pre-folding vein development in the Oligo-Miocene Asmari Formation in the Central Zagros Fold Belt, Iran. *Tectonics* **2008**, *27*. [[CrossRef](#)]
27. Lacombe, O.; Bellahsen, N.; Mouthereau, F. Fracture patterns in the Zagros Simply Folded Belt (Fars, Iran): Constraints on early collisional tectonic history and role of basement faults. *Geol. Mag.* **2011**, *148*, 940–963. [[CrossRef](#)]
28. Casini, G.; Gillespie, P.A.; Vergés, J.; Romaire, I.; Fernández, N.; Casciello, E.; Saura, E.; Mehl, C.; Homke, S.; Embry, J.C.; et al. Sub-seismic fractures in foreland fold and thrust belts: Insight from the Lurestan Province, Zagros Mountains, Iran. *Pet. Geosci.* **2011**, *17*, 263–282. [[CrossRef](#)]
29. Tavani, S.; Storti, F.; Baus, J.; Muñoz, J.A. Late thrusting extensional collapse at the mountain front of the northern Apennines (Italy). *Tectonics* **2012**, *31*. [[CrossRef](#)]
30. Beaudoin, N.; Leprière, R.; Bellahsen, N.; Lacombe, O.; Amrouch, K.; Callot, J.P.; Emmanuel, L.; Daniel, J.M. Structural and microstructural evolution of the Rattlesnake Mountain Anticline (Wyoming, USA): New insights into the Sevier and Laramide orogenic stress build-up in the Bighorn Basin. *Tectonophysics* **2012**, *576–577*, 20–45. [[CrossRef](#)]
31. Stearns, D.W.; Friedman, M. Reservoirs in Fractured Rock. In *Stratigraphic Oil and Gas Fields—Classification, Exploration Methods, and Case Histories*. In *Stratigraphic Oil and Gas Fields—Classification, Exploration Methods, and Case Histories*; AAPG Special Volumes; Goud, H.R., Ed.; The American Association of petroleum Geologist: Tulsa, OK, USA, 1972; Volume 10, pp. 82–106.
32. Engelder, T. *Joints and Shear Fractures in Rock*; Department of Geoscience, Pennsylvania State University: State College, PA, USA, 1987; pp. 27–69. ISBN 0-12-066265-5.

33. Laubach, S.E. Subsurface fractures and their relationship to stress history in East Texas basin sandstone. *Tectonophysics* **1988**, *156*, 37–49. [[CrossRef](#)]
34. Laubach, S.E. Paleostress directions from the preferred orientation of closed microfractures (fluid-inclusion planes) in sandstone, East Texas basin, U.S.A. *J. Struct. Geol.* **1989**, *11*, 603–611. [[CrossRef](#)]
35. Fischer, M.P.; Woodward, N.B.; Mitchell, M.M. The kinematics of break-thrust folds. *J. Struct. Geol.* **1992**, *14*, 451–460. [[CrossRef](#)]
36. Cooke, M.L. Fracture localization along faults with spatially varying friction. *J. Geophys. Res. Solid Earth* **1997**, *102*, 22425–22434. [[CrossRef](#)]
37. Aldega, L.; Carminati, E.; Scharf, A.; Mattern, F.; Al-Wardi, M. Estimating original thickness and extent of the Semail Ophiolite in the eastern Oman Mountains by paleothermal indicators. *Mar. Pet. Geol.* **2017**, *84*, 18–33. [[CrossRef](#)]
38. Aldega, L.; Bigi, S.; Carminati, E.; Trippetta, F.; Corrado, S.; Kavooosi, M.A. The Zagros fold-and-thrust belt in the Fars province (Iran): II. Thermal evolution. *Mar. Pet. Geol.* **2018**, *93*, 376–390. [[CrossRef](#)]
39. Balestra, M.; Corrado, S.; Aldega, L.; Morticelli, M.G.; Sulli, A.; Rudkiewicz, J.-L.; Sassi, W. Thermal and structural modeling of the Scillato wedge-top basin source-to-sink system: Insights into the Sicilian fold-and-thrust belt evolution (Italy). *Bulletin* **2019**, *131*, 1763–1782. [[CrossRef](#)]
40. Anders, M.H.; Laubach, S.E.; Scholz, C.H. Microfractures: A review. *J. Struct. Geol.* **2014**, *69*, 377–394. [[CrossRef](#)]
41. Becker, S.P.; Eichhubl, P.; Laubach, S.E.; Reed, R.M.; Lander, R.H.; Bodnar, R.J. A 48 m.y. history of fracture opening, temperature, and fluid pressure: Cretaceous Travis Peak Formation, East Texas basin. *Bull. Geol. Soc. Am.* **2010**, *122*, 1081–1093. [[CrossRef](#)]
42. Laubach, S.E.; Fall, A.; Copley, L.K.; Marrett, R.; Wilkins, S.J. Fracture porosity creation and persistence in a basement-involved Laramide fold, Upper Cretaceous Frontier Formation, Green River Basin, USA. *Geol. Mag.* **2016**, *153*, 887–910. [[CrossRef](#)]
43. Fall, A.; Eichhubl, P.; Cumella, S.P.; Bodnar, R.J.; Laubach, S.E.; Becker, S.P. Testing the basin-centered gas accumulation model using fluid inclusion observations: Southern Piceance Basin, Colorado. *Am. Assoc. Pet. Geol. Bull.* **2012**, *96*, 2297–2318. [[CrossRef](#)]
44. Lespinasse, M. Are fluid inclusion planes useful in structural geology? *J. Struct. Geol.* **1999**, *21*, 1237–1243. [[CrossRef](#)]
45. Corrado, S.; Invernizzi, C.; Aldega, L.; D'errico, M.; Di Leo, P.; Mazzoli, S.; Zattin, M. Testing the validity of organic and inorganic thermal indicators in different tectonic settings from continental subduction to collision: The case history of the Calabria–Lucania border (southern Apennines, Italy). *J. Geol. Soc. London.* **2010**, *167*, 985–999. [[CrossRef](#)]
46. Schito, A.; Andreucci, B.; Aldega, L.; Corrado, S.; Di Paolo, L.; Zattin, M.; Szaniawski, R.; Jankowski, L.; Mazzoli, S. Burial and exhumation of the western border of the Ukrainian Shield (Podolia): A multi-disciplinary approach. *Basin Res.* **2018**, *30*, 532–549. [[CrossRef](#)]
47. Beaudoin, N.; Lacombe, O.; Roberts, N.M.W.; Koehn, D. U-Pb dating of calcite veins reveals complex stress evolution and thrust sequence in the Bighorn Basin, Wyoming, USA. *Geology* **2018**, *46*, 1015–1018. [[CrossRef](#)]
48. Hoareau, G.; Claverie, F.; Pécheyran, C.; Paroissin, C.; Grignard, P.-A.; Motte, G.; Chailan, O.; Girard, J.-P. Direct U-Pb dating of carbonates from micron-scale femtosecond laser ablation inductively coupled plasma mass spectrometry images using robust regression. *Geochronology* **2021**, *3*, 67–87. [[CrossRef](#)]
49. Aldega, L.; Viola, G.; Casas-Sainz, A.; Marcén, M.; Román-Berdiel, T.; Lelij, R. Unraveling Multiple Thermotectonic Events Accommodated by Crustal-Scale Faults in Northern Iberia, Spain: Insights From K-Ar Dating of Clay Gouges. *Tectonics* **2019**, *38*, 3629–3651. [[CrossRef](#)]
50. Hoareau, G.; Crognier, N.; Lacroix, B.; Aubourg, C.; Roberts, N.M.W.; Niemi, N.; Branellec, M.; Beaudoin, N.; Ruiz, I.S. Combination of $\Delta 47$ and U-Pb dating in tectonic calcite veins unravel the last pulses related to the Pyrenean Shortening (Spain). *Earth Planet. Sci. Lett.* **2021**, *553*, 116636. [[CrossRef](#)]
51. Mangenot, X.; Bonifacie, M.; Gasparini, M.; Götz, A.; Chaduteau, C.; Ader, M.; Rouchon, V. Coupling $\Delta 47$ and fluid inclusion thermometry on carbonate cements to precisely reconstruct the temperature, salinity and $\delta 18\text{O}$ of paleo-groundwater in sedimentary basins. *Chem. Geol.* **2017**, *472*, 44–57. [[CrossRef](#)]
52. Renard, F.; Schmittbuhl, J.; Gratier, J.P.; Meakin, P.; Merino, E. Three-dimensional roughness of stylolites in limestones. *J. Geophys. Res.* **2004**, *109*. [[CrossRef](#)]
53. Schmittbuhl, J.; Renard, F.; Gratier, J.P.; Toussaint, R. Roughness of stylolites: Implications of 3D high resolution topography measurements. *Phys. Rev. Lett.* **2004**, *93*, 238501. [[CrossRef](#)]
54. Ebner, M.; Piazzolo, S.; Renard, F.; Koehn, D. Stylolite interfaces and surrounding matrix material: Nature and role of heterogeneities in roughness and microstructural development. *J. Struct. Geol.* **2010**, *32*, 1070–1084. [[CrossRef](#)]
55. Ebner, M.; Toussaint, R.; Schmittbuhl, J.; Koehn, D.; Bons, P. Anisotropic scaling of tectonic stylolites: A fossilized signature of the stress field? *J. Geophys. Res.* **2010**, *115*, B06403. [[CrossRef](#)]
56. Rolland, A.; Toussaint, R.; Baud, P.; Schmittbuhl, J.; Conil, N.; Koehn, D.; Renard, F.; Gratier, J. Modeling the growth of stylolites in sedimentary rocks. *J. Geophys. Res. Solid Earth* **2012**, *117*, B6. [[CrossRef](#)]
57. Rolland, A.; Toussaint, R.; Baud, P.; Conil, N.; Landrein, P. Morphological analysis of stylolites for paleostress estimation in limestones. *Int. J. Rock Mech. Min. Sci.* **2014**, *67*, 212–225. [[CrossRef](#)]
58. Koehn, D.; Rood, M.P.; Beaudoin, N.; Chung, P.; Bons, P.D.; Gomez-Rivas, E. A new stylolite classification scheme to estimate compaction and local permeability variations. *Sediment. Geol.* **2016**, *346*, 60–71. [[CrossRef](#)]
59. Bertotti, G.; de Graaf, S.; Bisdorn, K.; Oskam, B.; Vonhof, H.B.; Bezerra, F.H.R.; Reijmer, J.J.G.; Cazarin, L.C. Fracturing and fluid-flow during post-rift subsidence in carbonates of the Jandaíra Formation, Potiguar Basin, NE Brazil. *Basin Res.* **2017**, *29*, 836–853. [[CrossRef](#)]

60. Beaudoin, N.; Labeur, A.; Lacombe, O.; Koehn, D.; Billi, A.; Hoareau, G.; Boyce, A.; John, C.M.; Marchegiano, M.; Roberts, N.M.; et al. Regional-scale paleofluid system across the Tuscan Nappe–Umbria Marche Arcuate Ridge (northern Apennines) as revealed by mesostructural and isotopic analyses of stylolite-vein networks. *Solid Earth* **2020**, *11*, 1617–1641. [[CrossRef](#)]
61. Petracchini, L.; Antonellini, M.; Billi, A.; Scrocca, D. Fault development through fractured pelagic carbonates of the Cingoli anticline, Italy: Possible analog for subsurface fluid-conductive fractures. *J. Struct. Geol.* **2012**, *45*, 21–37. [[CrossRef](#)]
62. Calamita, F.; Cello, G.; Deiana, G.; Paltrinieri, W. Structural styles, chronology rates of deformation, and time-space relationships in the Umbria-Marche thrust system (central Apennines, Italy). *Tectonics* **1994**, *13*, 873–881. [[CrossRef](#)]
63. Mazzoli, S.; Deiana, G.; Galdenzi, S.; Cello, G. Miocene fault-controlled sedimentation and thrust propagation in the previously faulted external zones of the Umbria-Marche Apennines, Italy. *EGU Stephan Mueller Spec. Publ. Ser.* **2002**, *1*, 195–209. [[CrossRef](#)]
64. Calamita, F.; Cello, G.; Invernizzi, C.; Paltrinieri, W. Stile strutturale e cronologia della deformazione lungo la traversa M. S. Vicino. *Stud. Geol. Camerti* **1990**, 69–86. [[CrossRef](#)]
65. Caricchi, C.; Aldega, L.; Corrado, S. Reconstruction of maximum burial along the Northern Apennines thrust wedge (Italy) by indicators of thermal exposure and modeling. *Bull. Geol. Soc. Am.* **2015**, *127*, 428–442. [[CrossRef](#)]
66. Tavani, S.; Storti, F.; Salvini, F.; Toscano, C. Stratigraphic versus structural control on the deformation pattern associated with the evolution of the Mt. Catria anticline, Italy. *J. Struct. Geol.* **2008**, *30*, 664–681. [[CrossRef](#)]
67. Petracchini, L.; Antonellini, M.; Billi, A.; Scrocca, D. Syn-thrusting polygonal normal faults exposed in the hinge of the Cingoli anticline, northern Apennines, Italy. *Front. Earth Sci.* **2015**, *3*, 67. [[CrossRef](#)]
68. Díaz General, E.N.; Mollema, P.N.; Antonellini, M. Fracture patterns and fault development in the pelagic limestones of the Monte Conero anticline (Italy). *Ital. J. Geosci.* **2015**, *134*, 495–512. [[CrossRef](#)]
69. Calamita, F.; Coppola, L.; Deiana, G.; Ivernizzi, C.; Mastrovincenzo, S. Le associazioni strutturali di Genge e M. Rotondo; un motivo ricorrente nella thrust belt umbro-marchigiana settentrionale. *Boll. Della Soc. Geol. Ital.* **1987**, *106*, 141–151.
70. Invernizzi, C. Low temperature deformation in naturally deformed marly limestones from the Umbria-Marche Apennines. *Ann. Tectonicae* **1994**, *8*, 119–133.
71. Curzi, M.; Aldega, L.; Bernasconi, S.M.; Berra, F.; Billi, A.; Boschi, C.; Franchini, S.; Van der Lelij, R.; Viola, G.; Carminati, E. Architecture and evolution of an extensionally-inverted thrust (Mt. Tancia Thrust, Central Apennines): Geological, structural, geochemical, and K–Ar geochronological constraints. *J. Struct. Geol.* **2020**, *136*, 104059. [[CrossRef](#)]
72. Lavecchia, G.; Minelli, G.; Piali, G. The Umbria-Marche arcuate fold belt (Italy). *Tectonophysics* **1988**, *146*, 125–137. [[CrossRef](#)]
73. Elter, F.M.; Elter, P.; Eva, C.; Eva, E.; Kraus, R.K.; Padovano, M.; Solarino, S. An alternative model for the recent evolution of the Northern-Central Apennines (Italy). *J. Geodyn.* **2012**, *54*, 55–63. [[CrossRef](#)]
74. Tozer, R.S.J.; Butler, R.W.H.; Corrado, S. Comparing thin- and thick-skinned thrust tectonic models of the Central Apennines, Italy. *Stephan Mueller Spec. Publ. Ser.* **2002**, *1*, 181–194. [[CrossRef](#)]
75. Scisciani, V.; Agostini, S.; Calamita, F.; Pace, P.; Cilli, A.; Giori, I.; Paltrinieri, W. Positive inversion tectonics in foreland fold-and-thrust belts: A reappraisal of the Umbria-Marche Northern Apennines (Central Italy) by integrating geological and geophysical data. *Tectonophysics* **2014**, *637*, 218–237. [[CrossRef](#)]
76. Mazzoli, S.; Aldega, L.; Corrado, S.; Invernizzi, C.; Zattin, M. Pliocene-Quaternary thrusting, syn-orogenic extension and tectonic exhumation in the Southern Apennines (Italy): Insights from the Monte Alpi area. *Spec. Pap. Soc. Am.* **2006**, *414*, 55.
77. Boccaletti, M.; Calamita, F.; Viandante, M.G. The lithospheric Apennine Neo-Chain developing since the Lower Pliocene as a result of the Africa-Europe convergence. *Boll. della Soc. Geol. Ital.* **2005**, *124*, 87–105.
78. Satolli, S.; Pace, P.; Viandante, M.; Calamita, F. Lateral variations in tectonic style across cross-strike discontinuities: An example from the Central Apennines belt (Italy). *Int. J. Earth Sci.* **2014**, *103*, 2301–2313. [[CrossRef](#)]
79. Brozzetti, F.; Cirillo, D.; Luchetti, L. Timing of Contractual Tectonics in the Miocene Foreland Basin System of the Umbria Pre-Apennines (Italy): An Updated Overview. *Geosciences* **2021**, *11*, 97. [[CrossRef](#)]
80. Cello, G.; Mazzoli, S.; Tondi, E.; Turco, E. Active tectonics in the central Apennines and possible implications for seismic hazard analysis in peninsular Italy. *Tectonophysics* **1997**, *272*, 43–68. [[CrossRef](#)]
81. Ghisetti, F.; Vezzani, L. Normal faulting, extension and uplift in the outer thrust belt of the central Apennines (Italy): Role of the Caramanico fault. *Basin Res.* **2002**, *14*, 225–236. [[CrossRef](#)]
82. Santantonio, M. Pelagic carbonate platforms in the geologic record: Their classification and sedimentary and paleotectonic evolution. *Am. Assoc. Pet. Geol. Bull.* **1994**, *78*, 122–141. [[CrossRef](#)]
83. Santantonio, M. Facies associations and evolution of pelagic carbonate platform/basin systems: Examples from the Italian Jurassic. *Sedimentology* **1993**, *40*, 1039–1067. [[CrossRef](#)]
84. Carminati, E.; Lustrino, M.; Cuffaro, M.; Doglioni, C. Tectonics, magmatism and geodynamics of Italy: What we know and what we imagine. *J. Virtual Explor.* **2010**, *36*, 10–3809. [[CrossRef](#)]
85. Bigi, S.; Milli, S.; Corrado, S.; Casero, P.; Aldega, L.; Botti, F.; Moscatelli, M.; Stanzione, O.; Falcini, F.; Marini, M.; et al. Stratigraphy, structural setting and burial history of the Messinian Laga basin in the context of Apennine foreland basin system. *J. Mediterr. Earth Sci.* **2009**, *1*, 61–84. [[CrossRef](#)]
86. Bally, A.W.; Burbi, W.; Cooper, J.C.; Ghelardoni, L. Balanced sections and seismic reflection profiles across the Central Apennines. *Mem. Soc. Geol. Ital.* **1986**, *107*, 109–130.
87. Ghisetti, F.; Vezzani, L. Geometric and kinematic complexities in the Marche-Abruzzi external zones (Central Apennines, Italy). *Geol. Rundschau* **1988**, *77*, 63–78. [[CrossRef](#)]

88. Hill, K.; Hayward, A. Structural constraints on the Tertiary plate tectonic evolution of Italy. *Mar. Pet. Geol.* **1988**, *5*, 2–16. [[CrossRef](#)]
89. Lacombe, O.; Bellahsen, N. Thick-skinned tectonics and basement-involved fold–thrust belts: Insights from selected Cenozoic orogens. *Geol. Mag.* **2016**, *153*, 763–810. [[CrossRef](#)]
90. Hippolyte, J.-C.; Angelier, J.; Barrier, E. Compressional and extensional tectonics in an arc system: Example of the Southern Apennines. *J. Struct. Geol.* **1995**, *17*, 1725–1740. [[CrossRef](#)]
91. Mazzoli, S.; Cello, G.; Deiana, G.; Galdenzi, S.; Gambini, R.; Mancinelli, A.; Mattioni, L.; Shiner, P.; Tondi, E. Modes of foreland deformation ahead of the Apennine thrust front. *J. Czech Geol. Soc.* **2000**, *45*, 246.
92. Scisciani, V.; Calamita, F.; Tavarnelli, E.; Rusciadelli, G.; Ori, G.-G.; Paltrinieri, W. Foreland-dipping normal faults in the inner edges of syn-orogenic basins: A case from the Central Apennines, Italy. *Tectonophysics* **2001**, *330*, 211–224. [[CrossRef](#)]
93. Calamita, F.; Paltrinieri, W.; Pelorosso, M.; Scisciani, V.; Tavarnelli, E. Inherited Mesozoic architecture of the Adria continental palaeomargin in the neogene central apennines orogenic system, Italy. *Boll. Della Soc. Geol. Ital.* **2003**, *122*, 307–318.
94. Rusciadelli, G.; Viandante, M.G.; Calamita, F.; Cook, A.C. Burial-exhumation history of the central Apennines (Italy), from the foreland to the chain building: Thermochronological and geological data. *Terra Nov.* **2005**, *17*, 560–572. [[CrossRef](#)]
95. Tavarnelli, E. Ancient synsedimentary structural control on thrust ramp development: An example from the Northern Apennines, Italy. *Terra Nov.* **2007**, *8*, 65–74. [[CrossRef](#)]
96. Pace, P.; Calamita, F. Push-up inversion structures v. fault-bend reactivation anticlines along oblique thrust ramps: Examples from the Apennines fold-and-thrust belt (Italy). *J. Geol. Soc. Lond.* **2014**, *171*, 227–238. [[CrossRef](#)]
97. Marshak, S.; Geiser, P.A.; Alvarez, W.; Engelder, T. Mesoscopic fault array of the northern Umbrian Apennine fold belt, Italy: Geometry of conjugate shear by pressure-solution slip. *Geol. Soc. Am. Bull.* **1982**, *93*, 1013–1022. [[CrossRef](#)]
98. Storti, F.; Rossetti, F.; Salvini, F. Structural architecture and displacement accommodation mechanisms at the termination of the Priestley Fault, northern Victoria Land, Antarctica. *Tectonophysics* **2001**, *341*, 141–161. [[CrossRef](#)]
99. Barchi, M.; Alvarez, W.; Shimabukuro, D.H. The Umbria-Marche Apennines as a double orogen: Observations and hypotheses. *Ital. J. Geosci.* **2012**, *131*, 258–271. [[CrossRef](#)]
100. Calamita, F.; Deiana, G. The arcuate shape of the Umbria-Marche-Sabina Apennines (Central Italy). *Tectonophysics* **1988**, *146*, 139–147. [[CrossRef](#)]
101. Deiana, G.; Cello, G.; Chiocchini, M.; Galdenzi, S.; Mazzoli, S.; Pistolesi, E.; Potetti, M.; Romano, A.; Turco, E.; Principi, M. Tectonic evolution of the external zones of the Umbria-Marche Apennines in the Monte San Vicino-Cingoli area. *Boll. Della Soc. Geol. Ital.* **2002**, *1*, 229–238.
102. Cita, M.B.; Abbate, E.; Ballini, M.; Conti, A.; Falorni, P.; Germani, D.; Petti, F.M. Carta Geologica d'Italia–1: 50.000, Catalogo delle Formazioni, Unità tradizionali. *Quad. Serv. Geol. D'It. Ser. III* **2007**, *7*, 382.
103. Menichetti, M. La sezione geologica Cingoli–M. Maggio-Tevere nell'Appennino umbro-marchigiano: Analisi cinematica e strutturale. *Stud. Geol. Camerti* **1991**, *special vo*, 315–328.
104. Centamore, E.; Chiocchini, M.; Deiana, G.; Micarelli, A.; Pieruccini, U. Contributo alla conoscenza del Giurassico dell'Appennino Umbro-Marchigiano. *Stud. Geol. Camerti* **1971**, *1*, 7–89. [[CrossRef](#)]
105. Farinacci, A. *Jurassic Sediments in the Umbro-Marchean Apennines: An Alternative Model*; Istituto di Geologia e Paleontologia: Roma, Italy, 1981.
106. Santantonio, M.; Carminati, E. Jurassic rifting evolution of the Apennines and Southern Alps (Italy): Parallels and differences. *Bulletin* **2011**, *123*, 468–484. [[CrossRef](#)]
107. Koehn, D.; Renard, F.; Toussaint, R.; Passchier, C.W. Growth of stylolite teeth patterns depending on normal stress and finite compaction. *Earth Planet. Sci. Lett.* **2007**, *257*, 582–595. [[CrossRef](#)]
108. Toussaint, R.; Aharonov, E.; Koehn, D.; Gratier, J.P.; Ebner, M.; Baud, P.; Rolland, A.; Renard, F. Stylolites: A review. *J. Struct. Geol.* **2018**, *114*, 163–195. [[CrossRef](#)]
109. Grohmann, C.H.; Campanha, G.A. OpenStereo: Open source, cross-platform software for structural geology analysis. *AGU Fall Meet. Abstr.* **2010**, *2010*, IN31C-06.
110. Angelier, J. Tectonic analysis of fault slip data sets. *J. Geophys. Res.* **1984**, *89*, 5835–5848. [[CrossRef](#)]
111. Lacombe, O. Do fault slip data inversions actually yield “paleostresses” that can be compared with contemporary stresses? A critical discussion. *Comptes Rendus-Geosci.* **2012**, *344*, 159–173. [[CrossRef](#)]
112. Aydin, A.; Basu, A. The Schmidt hammer in rock material characterization. *Eng. Geol.* **2005**, *81*, 1–14. [[CrossRef](#)]
113. Katz, O.; Reches, Z.; Roegiers, J.-C. Evaluation of mechanical rock properties using a Schmidt Hammer. *Int. J. Rock Mech. Min. Sci.* **2000**, *37*, 723–728. [[CrossRef](#)]
114. Ebner, M.; Koehn, D.; Toussaint, R.; Renard, F. The influence of rock heterogeneity on the scaling properties of simulated and natural stylolites. *J. Struct. Geol.* **2009**, *31*, 72–82. [[CrossRef](#)]
115. Ebner, M.; Koehn, D.; Toussaint, R.; Renard, F.; Schmittbuhl, J. Stress sensitivity of stylolite morphology. *Earth Planet. Sci. Lett.* **2009**, *277*, 394–398. [[CrossRef](#)]
116. Koehn, D.; Ebner, M.; Renard, F.; Toussaint, R.; Passchier, C.W. Modelling of stylolite geometries and stress scaling. *Earth Planet. Sci. Lett.* **2012**, *341–344*, 104–113. [[CrossRef](#)]

117. Beaudoin, N.; Gasparrini, M.; David, M.E.; Lacombe, O.; Koehn, D. Bedding-parallel stylolites as a tool to unravel maximum burial depth in sedimentary basins: Application to Middle Jurassic carbonate reservoirs in the Paris basin, France. *Bull. Geol. Soc. Am.* **2019**, *131*, 1239–1254. [CrossRef]
118. Beaudoin, N.; Lacombe, O.; David, M.E.; Koehn, D. Does stress transmission in forelands depend on structural style? Distinctive stress magnitudes during Sevier thin-skinned and Laramide thick-skinned layer-parallel shortening in the Bighorn Basin (USA) revealed by stylolite and calcite twinning paleopiez. *Terra Nov.* **2020**, *32*, 225–233. [CrossRef]
119. Simonsen, I.; Hansen, A.; Nes, O.M. Determination of the Hurst exponent by use of wavelet transforms. *Phys. Rev.* **1998**, *58*, 2779–2787. [CrossRef]
120. Wright, K.; Cygan, R.T.; Slater, B. Structure of the (1014) surfaces of calcite, dolomite and magnesite under wet and dry conditions. *Phys. Chem. Chem. Phys.* **2001**, *3*, 839–844. [CrossRef]
121. Beaudoin, N.; Koehn, D.; Lacombe, O.; Lecouty, A.; Billi, A.; Aharonov, E.; Parlangeau, C. Fingerprinting stress: Stylolite and calcite twinning paleopiezometry revealing the complexity of progressive stress patterns during folding—The case of the Monte Nero anticline in the Apennines, Italy. *Tectonics* **2016**, *34*, 1687–1712. [CrossRef]
122. Vass, A.; Koehn, D.; Toussaint, R.; Ghani, I.; Piazzolo, S. The importance of fracture-healing on the deformation of fluid-filled layered systems. *J. Struct. Geol.* **2014**, *67*, 94–106. [CrossRef]
123. Dietrich, D.; McKenzie, J.A.; Song, H. Origin of calcite in syntectonic veins as determined from carbon- isotope ratios. *Geology* **1983**, *11*, 547–551. [CrossRef]
124. Shemesh, A.; Ron, H.; Erel, Y.; Kolodny, Y.; Nur, A. Isotopic composition of vein calcite and its fluid inclusions: Implication to paleohydrological systems, tectonic events and vein formation processes. *Chem. Geol.* **1992**, *94*, 307–314. [CrossRef]
125. Templeton, A.S. Fluids and the Heart Mountain Fault revisited. *Geology* **1995**, *23*, 929–932. [CrossRef]
126. Douglas, T.A.; Chamberlain, C.P.; Poage, M.A.; Abruzzese, M.; Shultz, S.; Henneberry, J.; Layer, P. Fluid flow and the heart mountain fault: A stable isotopic, fluid inclusion, and geochronologic study. *Geofluids* **2003**, *3*, 13–32. [CrossRef]
127. Vilasi, N.; Malandain, J.; Barrier, L.; Callot, J.P.; Amrouch, K.; Guilhaumou, N.; Lacombe, O.; Muska, K.; Roure, F.; Swennen, R. From outcrop and petrographic studies to basin-scale fluid flow modelling: The use of the Albanian natural laboratory for carbonate reservoir characterisation. *Tectonophysics* **2009**, *474*, 367–392. [CrossRef]
128. Barbier, M.; Hamon, Y.; Callot, J.P.; Floquet, M.; Daniel, J.M. Sedimentary and diagenetic controls on the multiscale fracturing pattern of a carbonate reservoir: The Madison Formation (Sheep Mountain, Wyoming, USA). *Mar. Pet. Geol.* **2012**, *29*, 50–67. [CrossRef]
129. Gasparrini, M.; Lacombe, O.; Rohais, S.; Belkacemi, M.; Euzen, T. Natural mineralized fractures from the Montney-Doig unconventional reservoirs (Western Canada Sedimentary Basin): Timing and controlling factors. *Mar. Pet. Geol.* **2021**, *124*, 104826. [CrossRef]
130. Bons, P.D.; Elburg, M.A.; Gomez-Rivas, E. A review of the formation of tectonic veins and their microstructures. *J. Struct. Geol.* **2012**, *43*, 33–62. [CrossRef]
131. Daëron, M.; Blamart, D.; Peral, M.; Affek, H.P. Absolute isotopic abundance ratios and the accuracy of $\Delta 47$ measurements. *Chem. Geol.* **2016**, *442*, 83–96. [CrossRef]
132. Bernasconi, S.M.; Müller, I.A.; Bergmann, K.D.; Breitenbach, S.F.M.; Fernandez, A.; Hodell, D.A.; Jaggi, M.; Meckler, A.N.; Millan, I.; Ziegler, M. Reducing uncertainties in carbonate clumped isotope analysis through consistent carbonate-based standardization. *Geochem. Geophys. Geosyst.* **2018**, *19*, 2895–2914. [CrossRef] [PubMed]
133. Kim, S.T.; Mucci, A.; Taylor, B.E. Phosphoric acid fractionation factors for calcite and aragonite between 25 and 75 °C: Revisited. *Chem. Geol.* **2007**, *246*, 135–146. [CrossRef]
134. Daëron, M. Full propagation of analytical uncertainties in $\Delta 47$ measurements. *Geochem. Geophys. Geosyst.* **2020**, 1–26. [CrossRef]
135. Kele, S.; Breitenbach, S.F.M.; Capezzuoli, E.; Meckler, A.N.; Ziegler, M.; Millan, I.M.; Kluge, T.; Deák, J.; Hanselmann, K.; John, C.M.; et al. Temperature dependence of oxygen- and clumped isotope fractionation in carbonates: A study of travertines and tufas in the 6–95°C temperature range. *Geochim. Cosmochim. Acta* **2015**, *168*, 172–192. [CrossRef]
136. Cardozo, N. Backtrip: Performs 1D “Airy type” Backstripping of Sedimentary Strata. 2011. Available online: <https://downloadsfafer.com/software/osxbackstrip/> (accessed on 30 January 2021).
137. Allen, P.A.; Allen, J.R. *Basin Analysis: Principles and Applications*, Blackwell Scientific Publication, 1st ed.; Blackwell Scientific Publications: Oxford, UK; London, UK, 1990; ISBN 0632024224.
138. Watts, A.B. *Isostasy and Flexure of the Lithosphere*; Paperback; Cambridge University Press: Cambridge, UK, 2001; ISBN 9780521006002.
139. Beaudoin, N.; Bellahsen, N.; Lacombe, O.; Emmanuel, L.; Pironon, J. Crustal-scale fluid flow during the tectonic evolution of the Bighorn Basin (Wyoming, USA). *Basin Res.* **2014**, *26*, 403–435. [CrossRef]
140. Aldega, L.; Botti, F.; Corrado, S. Clay mineral assemblages and vitrinite reflectance in the Laga Basin (Central Apennines, Italy): What do they record? *Clays Clay Miner.* **2007**, *55*, 504–518. [CrossRef]
141. Kim, S.T.; O’Neil, J.R. Equilibrium and nonequilibrium oxygen isotope effects in synthetic carbonates. *Geochim. Cosmochim. Acta* **1997**, *61*, 3461–3475. [CrossRef]
142. Di Naccio, D.; Boncio, P.; Cirilli, S.; Casaglia, F.; Morettini, E.; Lavecchia, G.; Brozzetti, F. Role of mechanical stratigraphy on fracture development in carbonate reservoirs: Insights from outcropping shallow water carbonates in the Umbria-Marche Apennines, Italy. *J. Volcanol. Geotherm. Res.* **2005**, *148*, 98–115. [CrossRef]
143. Petit, J.; Barquins, M. Can natural faults propagate under mode II conditions? *Tectonics* **1988**, *7*, 1243–1256. [CrossRef]

144. Homberg, C.; Hu, J.C.; Angelier, J.; Bergerat, F.; Lacombe, O. Characterization of stress perturbations near major fault zones: Insights from 2-D distinct-element numerical modelling and field studies (Jura mountains). *J. Struct. Geol.* **1997**, *19*, 703–718. [[CrossRef](#)]
145. Beaudoin, N.; Lacombe, O.; Koehn, D.; David, M.E.; Farrell, N.; Healy, D. Vertical stress history and paleoburial in foreland basins unravelled by stylolite roughness paleopiezometry: Insights from bedding-parallel stylolites in the Bighorn Basin, Wyoming, USA. *J. Struct. Geol.* **2020**, *136*, 104061. [[CrossRef](#)]
146. Fabbi, S.; Citton, P.; Romano, M.; Cipriani, A. Detrital events within pelagic deposits of the Umbria-Marche Basin (Northern Apennines, Italy): Further evidence of Early Cretaceous tectonics. *J. Mediterr. Earth Sci.* **2016**, *8*, 39–52.
147. Cipriani, A.; Bottini, C. Early Cretaceous tectonic rejuvenation of an Early Jurassic margin in the Central Apennines: The “Mt. Cosce Breccia” . *Sediment. Geol.* **2019**, *387*, 57–74. [[CrossRef](#)]
148. Cipriani, A.; Bottini, C. Unconformities, neptunian dykes and mass-transport deposits as an evidence for Early Cretaceous syn-sedimentary tectonics: New insights from the Central Apennines. *Ital. J. Geosci.* **2019**, *138*, 333–354. [[CrossRef](#)]
149. Decandia, F.A. Geologia dei Monti di Spoleto (Provincia di Perugia). *Boll. Della Soc. Geol. Ital.* **1982**, *101*, 291–315.
150. Marchegiani, L.; Bertotti, G.; Cello, G.; Deiana, G.; Mazzoli, S.; Tondi, E. Pre-orogenic tectonics in the Umbria-Marche sector of the Afro-Adriatic continental margin. *Tectonophysics* **1999**, *315*, 123–143. [[CrossRef](#)]
151. Mazzoli, S.; Santini, S.; Macchiavelli, C.; Ascione, A. Active tectonics of the outer northern Apennines: Adriatic vs. Po Plain seismicity and stress fields. *J. Geodyn.* **2015**, *84*, 62–76. [[CrossRef](#)]

III- GENERAL CONCLUSIONS

This work, focused on the Cingoli Anticline, shows how the burial-deformation history of folded rocks can be unraveled using an original combination of ubiquitous features of carbonate rocks: fracture analysis, BPS paleopiezometry and vein cement geochemistry.

Regarding the case study, different stages of deformation were recognized: (i) E-W extension related to foreland flexure (σ_1 vertical); (ii) N045 oriented LPS; (iii) fold growth; (iv) LSFT, under a horizontal N045 contraction. Mesostructural analyses also support that the arcuate geometry of the Cingoli Anticline is a primary feature, probably linked to the oblique reactivation of a N-S inherited normal fault. The timing of deformation, and particularly the duration of the Apenninic contractional stages, was also reconstructed from combined paleopiezometric, isotopic and mesostructural data. Following foreland flexure (ca. 21.2 to 6.6 Ma), LPS was dated from middle Messinian to early Pliocene (ca. 6.3 to 5.8 Ma) and fold growth occurred between early and middle Pliocene (ca. 5.8 to 3.1 Ma). The precise duration of LSFT remains out of reach. The duration of the fold growth phase is in line with previous estimates based on other proxies such as K-Ar and U-Pb absolute dating of fault rocks in the Monte Tancia Thrust (Curzi *et al.*, 2020). The O and C stable isotope signatures and clumped isotopes of Δ_{47} of vein cements imply that the paleofluid system that prevailed during LPS and folding in this structure involve marine local fluids with limited interaction with the host rock, in agreement with earlier findings in the eastern UMAR. From a methodological point of view, the burial history of strata was reconstructed with high resolution using roughness inversion applied to sedimentary stylolites. These results highlight that this paleopiezometric technique yields consistent estimates of maximum depths experienced by strata down to 2500 m, in agreement with previous studies in the western part of the UMAR.

The final advantage is that this method is easier to use than classic methods in the application, as it is less expensive in terms of laboratory analysis. It also does not involve crushing, Rock Eval or vitrinite analysis, the treatment consisting only in the computer analysis of a stylolite scan performed on a cut and polished sample. The difficulty lies in the sampling part, which implies recovering and analyzing several hundred kilos of samples for a reasonable statistical representativeness. So, in the same way that sonic or rock eval field methods have been developed, it would be possible to consider the development of a field methodology specific to the study of sedimentary stylolites, involving, for example, the use of a polishing machine and a high-resolution camera allowing for the analysis and processing of stylolites directly in the field. Beyond regional implications, this study demonstrates the high potential of this new approach combining paleopiezometric, isotopic, and mesostructural data to reconstruct the sequence and to constrain the timing not only of local mesoscale deformation, but also of regional tectonic events in an orogenic system. These results further confirm that the paleopiezometric inversion of the roughness of sedimentary stylolites for the vertical stresses is a reliable and powerful tool to unravel the amount and timing of burial without any assumption about the past geothermal gradient.

Chapter 5- Assessing the timing and propagation of layer-parallel apenninic shortening from the Umbria-Marche Apennine Ridge to the Conero anticline: insights from parallel to bedding stylolite roughness paleopiezometry

I- INTRODUCTION

In previous chapters, the contribution of paleopiezometry on sedimentary stylolites roughness applied to the reconstruction of the burial-deformation calendar is demonstrated. Notably, the study of the Cingoli Anticline is a field example where this methodology is applied and provides the estimation of the onset of Apenninic contraction at the fold scale. Affordable, easily applicable, but less precise, this methodology is intended to complement the classical temperature-dependent methods used to reconstruct the burial history of strata. Albeit not widely spread, the application of SRIT to BPS populations in a single folded structure, but also at the scale of foreland basins and FTB, could potentially sheds light on otherwise poorly constrained data, such as the paleo-depths at which the first increments of the contraction started, and the burial history as well (Beaudoin *et al.*, 2020c; Labeur *et al.*, 2021).

In this context, the application of this innovative methodology coupling SRIT and burial curves is extended to the regional case of the UMAR, from the hinterland to the Adriatic coast. The first issue is then to test the reliability of this method, and in particular the SRIT accuracy on a larger study, by comparison with data already known in the area. The second one is to discuss contribution of this method to the understanding of pre-folding deformations in the context of foreland basins and FTB, notably the LPS evolution, concept which is still debated. In this analysis, the evolution of burial depths and of the timing of the LPS onset is tracked along a SW-NE transect across the UMAR. These results are then compared to various studies discussing the burial and timing of folding (Calamita *et al.*, 1990, 1994; Mazzoli *et al.*, 2002; Caricchi *et al.*, 2015). This study is therefore a relevant example of the reconstruction of burial evolution and of dating of the onset of contraction at the FTB scale. This work involves the study of several folded structures along a SW-NE transect across the UMAR. The present study couples mesostructural and burial data from the Cingoli Anticline with those from two other folds studied during this PhD, and with those from a published case study in which I participated as co-author for the acquisition and processing of data, as well as for the formatting of some figures. The studied folded structures are located along the transect on the Figure 3.1 (Chapter 3), using the black boxes, and described as follows: (i) the Cingoli Anticline, previously presented (Labeur *et al.*, 2021; Chapter 4); (ii) the Subasio and Conero anticlines, 2 folds distributed along the transect and studied during a field campaign in June 2021; (iii) additional data from published case studies of the San Vicino Anticline (Lacombe *et al.*, 2021), near Cingoli. The first part of this work is to set the geological framework of the study by summarizing the sedimentary and structural characteristics of these area of interest. Then, results of these individual studies are presented and linked to highlight the impact and contribution of this innovative methodology in this well constrained regional case study.

II- THE SUBASIO AND THE CONERO ANTICLINES: TWO OTHER FIELD EXAMPLES OF BURIAL-DEFORMATION RECONSTRUCTION

The case of Cingoli strengthens the robustness of this methodology. The latter is then applied to the Subasio and Conero anticlines to further test the replicability and consistency of the results at the fold scale and to assess how valid is the reconstructed calendar of deformation at the scale of the FTB. This section presents the folds of interest, then highlights (i) the mesostructural context through the analysis of fracture-stylolite networks, (ii) the burial of strata through the application of paleopiezometric methods of sedimentary stylolites, and (iii) the maximum burial undergone by the different formations through time using the reconstruction of burial curves.

1- Geological setting

1.1- The Subasio Anticline

The Subasio Anticline is an asymmetric folded structure belonging to eastern part of the UMAR located about 10 km southeast of Perugia (Figure 3.1, Chapter 3).

Characterized by a SW vergence, it extends for 12 km in N-S axis, *versus* a few tens of kilometers along its longitudinal direction (Damiani *et al.*, 1995). This compressional structure forms a doubly plunging fold (Scisciani *et al.*, 2014), characterized by : (i) a backlimb (western flank) affected by a W-dipping normal fault and a back-thrust fault (Deiana, 1965); (ii) a gently-dipping forelimb corresponding to the eastern flank (Figure 5.2).

The stratigraphic succession is similar to that classically described in Umbria-Marche. In particular, the Jurassic marine formations display typical facies of this stratigraphic sequence (Figures 5.1 and 5.2). There are, however, some lithological and thickness differences for the Mesozoic formations compared to the lithotypes of similar formations outcropping in other areas of the Apennines. The limestones of the Corniola Formation, for example, are sometimes finely crystalline in the Subasio area and present a regular alternation of gray to greenish calcareous-marl layers and clayey marls in thin layers at the top of the formation, thus progressively interdigitating with the overlying limestones.

Thickness and facies variations are also observed, more specifically in the core of this macro-anticline that hosts a reduced Jurassic succession related to the existence of a horst. Furthermore, the Miocene silicoclastic deposits (Burdigalian-Serravalian) are mostly characterized by facies typical of the Umbria-Marche sequence. Finally, the sedimentary complexes outcropping in the Assisi nappe are very close to those of the adjacent regions (Servizio Geologica d'Italia, 1969).

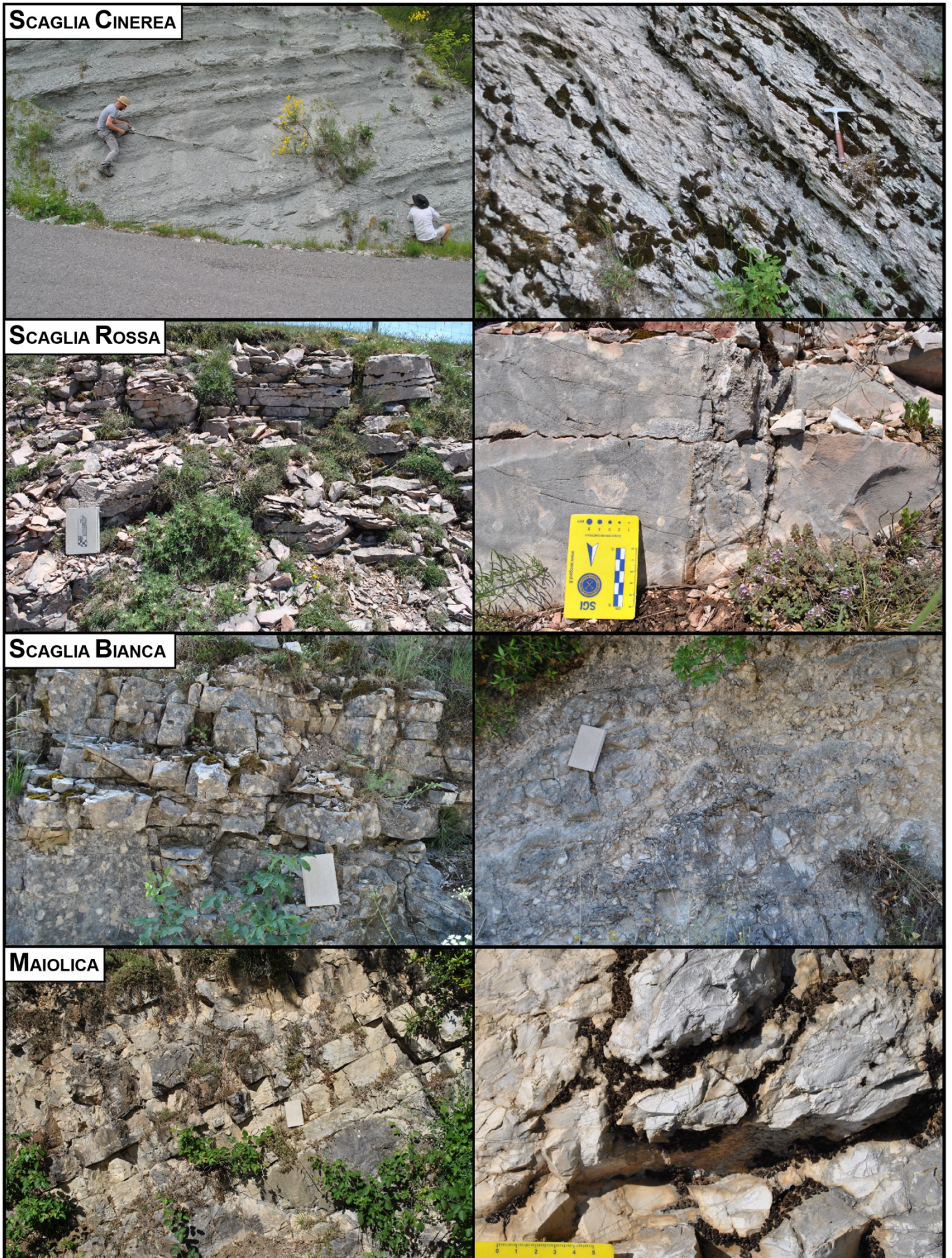


Figure 5.1- Illustration of the main formations studied in the Subasio Anticline. Each formation is associated with 2 field photographs.

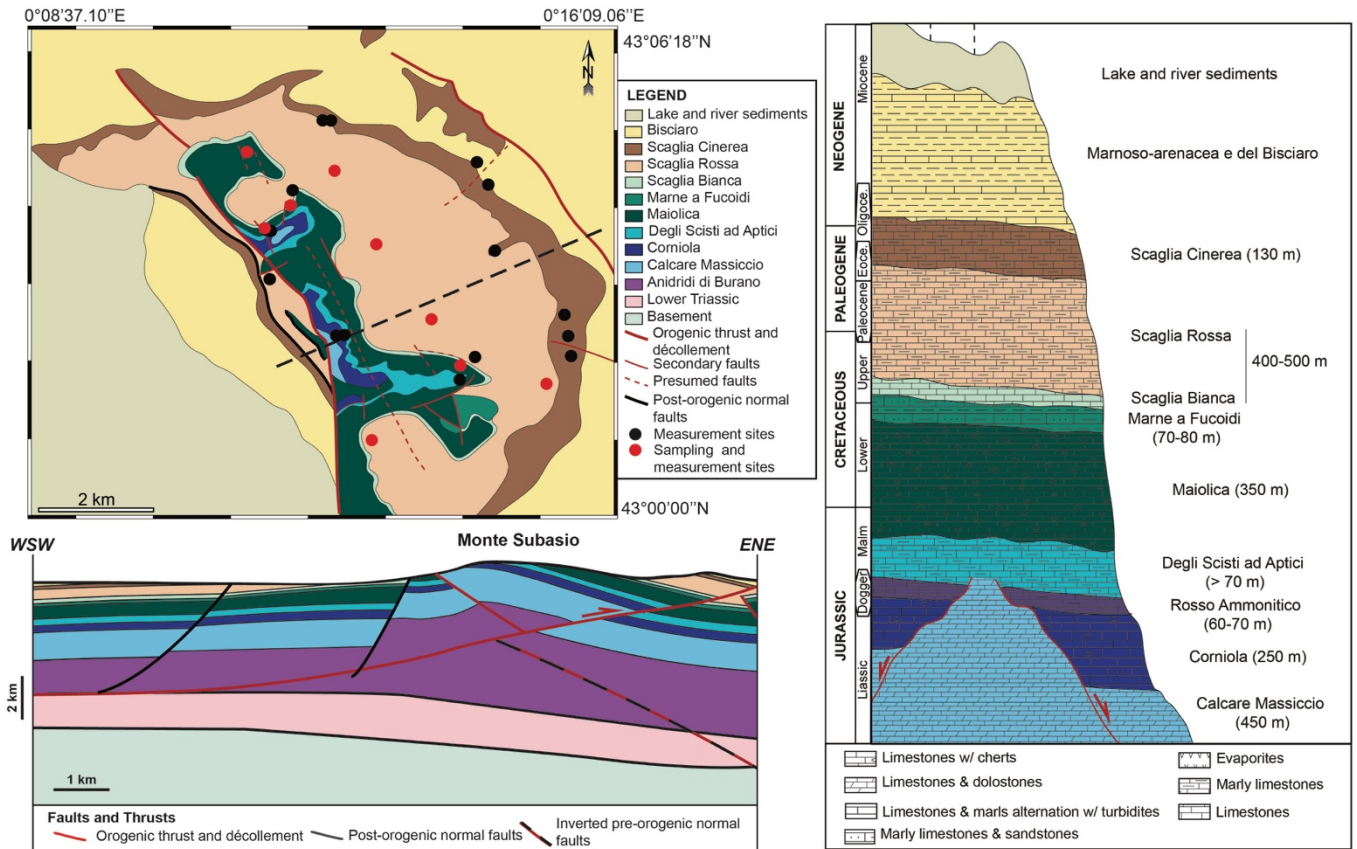


Figure 5.2- Simplified geological map of the Subasio Anticline, redrawn from existing geological maps (Servizio Geologica d'Italia, 1969). Measurement sites are positioned thanks to the black dots, sampling and measurement sites by red dots. Associated stratigraphic column (Servizio Geologica d'Italia, 1969) and cross-section (modified from Scisciani *et al.*, 2014)

1.2- The Conero Anticline

The Conero Anticline is located in the outermost part of the Apennine Ridge, south of Ancona, in the easternmost Marche region and bordering the Adriatic Sea (Figure 3.1, Chapter 3). This short, double vergence fold extends over 2.5 km along a NE-SW axis, with a wavelength of 3.5 km in a NW-SE direction, and culminates at 572 m above the sea level (Diaz General, 2013). It is bounded structurally by two major faults and cut laterally by perpendicular late normal and strike-slip faults.

This asymmetric anticline formed during the Pliocene compressional event associated with a SW-NE oriented σ_1 . It is characterized by a globally N140 oriented axis, with an eastern limb striking NE and steeper than the western flank (80° versus 20°) (Cello & Coppola, 1984; Diaz General, 2013) (Figure 5.3). Furthermore, a system of strike-slip left-lateral faults crossed this anticline. These faults are oriented at high angle to the fold axis (Cello & Cappola, 1984; Coccioni *et al.*, 1997) and are associated with a lateral offset of 100 to 200 meters (Fancelli & Radrizzani, 1964a) without impact on the orientation of the fold axis (Cello & Coppola, 1984). Some right-lateral faults oriented N030-040 are also reported, as well as some normal faults characterized by a spacing of a few tens to a few hundreds of meters and a length of several hundred meters along the fold axis (Diaz General, 2013).

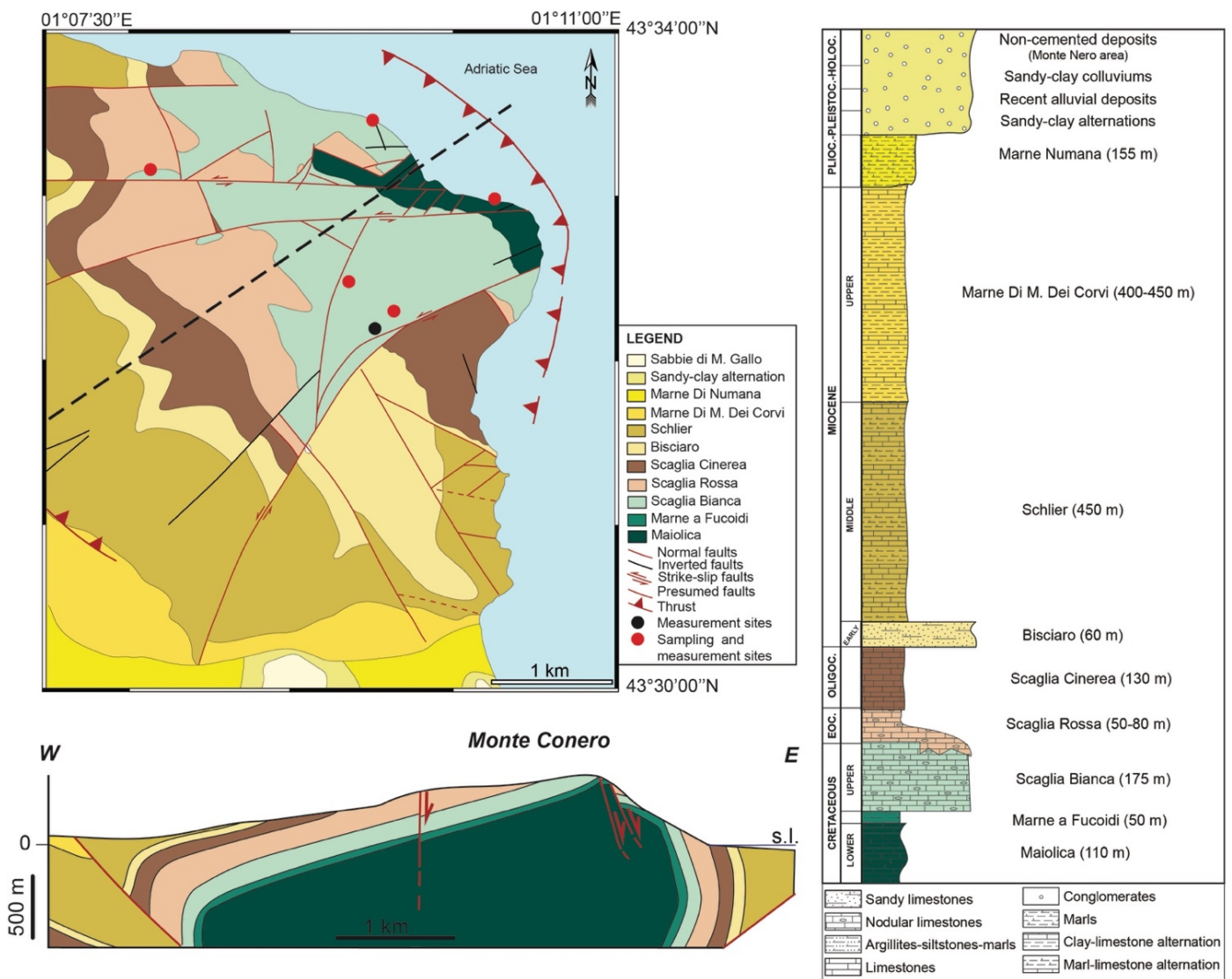


Figure 5.3- Simplified geological map of the Conero Anticline, redrawn from existing geological maps (Fancelli & Radrizzani, 1964b). Measurement sites are positioned thanks to the black dots, sampling and measurement sites by red dots. Associated stratigraphic column (Fancelli & Radrizzani, 1964b) and cross-section(modified from Mussi *et al.*, 2017).

Marine sedimentation is predominant in this area (Montanari & Sandroni, 1995). The outcropping stratigraphic sequence corresponds to the second part of the typical Umbria-Marche sequence, *i.e.* the carbonate sequence of the Meso-Cenozoic, then covered by turbiditic silicoclastic deposits and flysch of the Mio-Pleistocene (Figures 5.3 and 5.4). However, one can notice some differences with the classical sequence of the Umbria-Marche, namely: (i) variations in thickness in the silty, marly and calcareous formations, especially for the Marne a Fucoidi for which the thickness is largely reduced (10 m *versus* 60 m) (Diaz General, 2013); (ii) a stratigraphic gap between the Scaglia Bianca and the Scaglia Rossa, probably as the consequence of an earthquake that generated a big submarine landslide, the latter at the origin of the remobilization of these sediments and their migration into the deepest areas of the ancient marine basin (Montanari and Sandroni 1995).

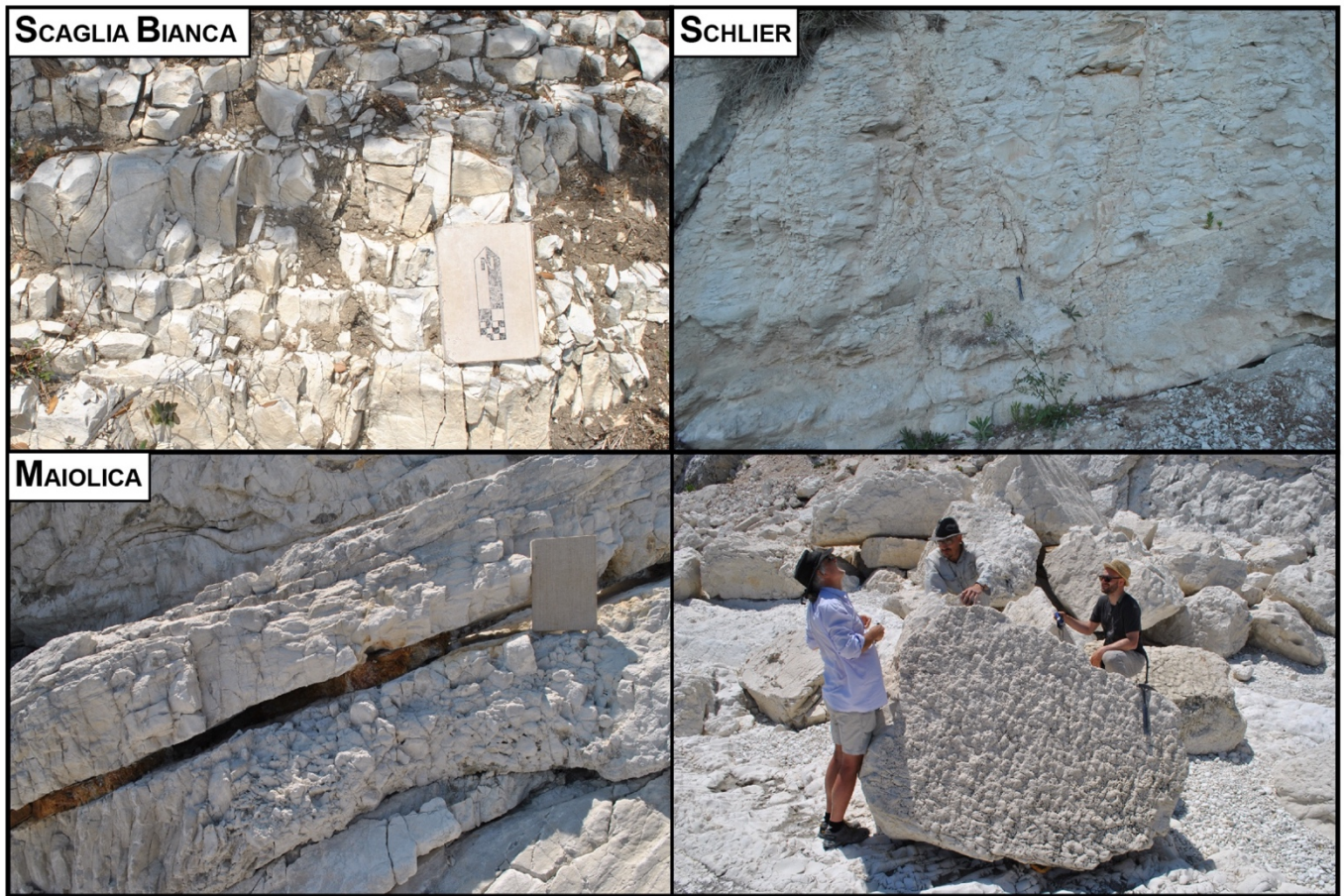


Figure 5.4- Illustration of the main formations studied in the Conero Anticline. The case of the Maiolica is illustrated with 2 field photographs.

2- *Mesostructural context*

The mesostructural context is defined for each anticlinal more succinctly than in Cingoli. Thus, applying the fracture analysis methods described above (Chapter 2), fractures observed and measured in the field are grouped by sets based only on their orientations and their structural position at first. Then, by considering the geometrical and chronological relationships between the different sets, and by relating them to the regional deformation stages, the fracture sequence is reconstructed for these two case studies.

2.1- *The Subasio Anticline*

The study fracture and tectonic stylolites orientations and chronology relationships provides the discrimination of 5 sets at first order, including joints, veins and/or tectonic stylolites: (i) veins and joints J_1 striking $N040 \pm 20^\circ$, *i.e.* $N050$ to $N060$ in the backlimb and hinge, and $N020$ to $N060$ in the forelimb. They are perpendicular to the bedding strike and observed on the entire fold (Figure 5.6). They intersect and then postdate BPS (Figure 5.5A). They are associated with tectonic stylolites S_1 whose peaks strike $N040 \pm 20^\circ$ and horizontal in untilted position (Figure 5.7); (ii) vertical veins and joints J_2 , whose planes strike $N110$ to $N150$ in the backlimb and $N110$ to $N130$ in the forelimb. They are vertical and sub-parallel to parallel to fold axis (Figures 5.6). This set post-dates set I, since associated fractures intersect fractures belonging to set I (Figures 5.5B and 5.5C); (iii) vertical fractures J_3 , striking N-S in the

backlimb and N030 in the forelimb and hinge. They intersect and thus post-dates fractures of set II (Figure 5.5C); (iv) tectonic stylolites S_2 , whose peaks strike $N040\pm 20^\circ$ and horizontal in current position. At second order, a set of fractures composed of vertical veins striking $N070$ to $N100$ is also identified, poorly represented at the scale of the anticline (4 measurement sites), and with no clear chronological relationship with the other sets.

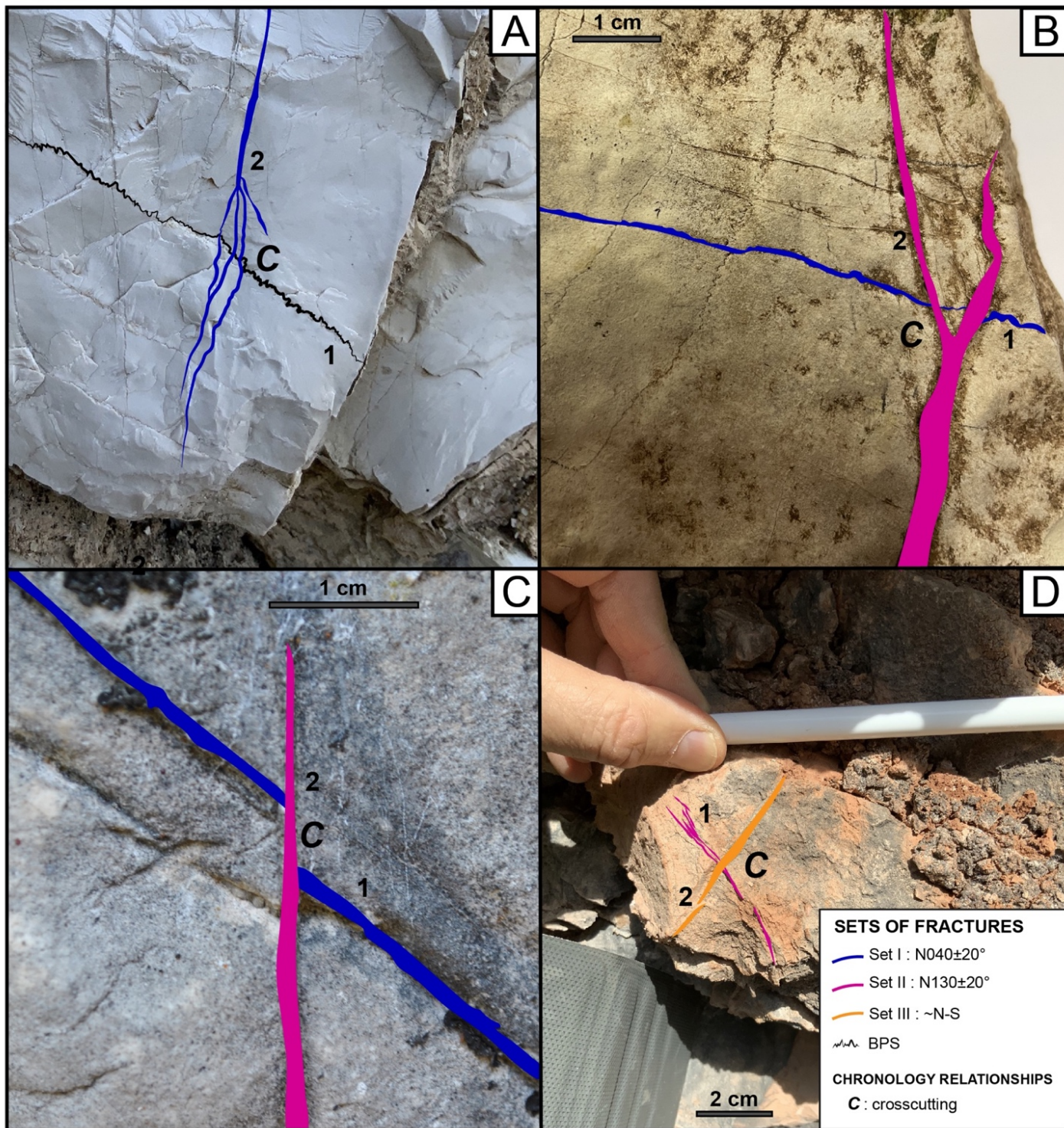


Figure 5.5- Chronological relationships (*i.e.* crosscutting), observed at mesoscopic scale, between: (A) a vein $N060$ belonging to set I (blue) and a BPS, (B, C) sets I and II (pink), (D) sets II and III (orange). (D) Interpretative scheme of the formation of the E-W set.

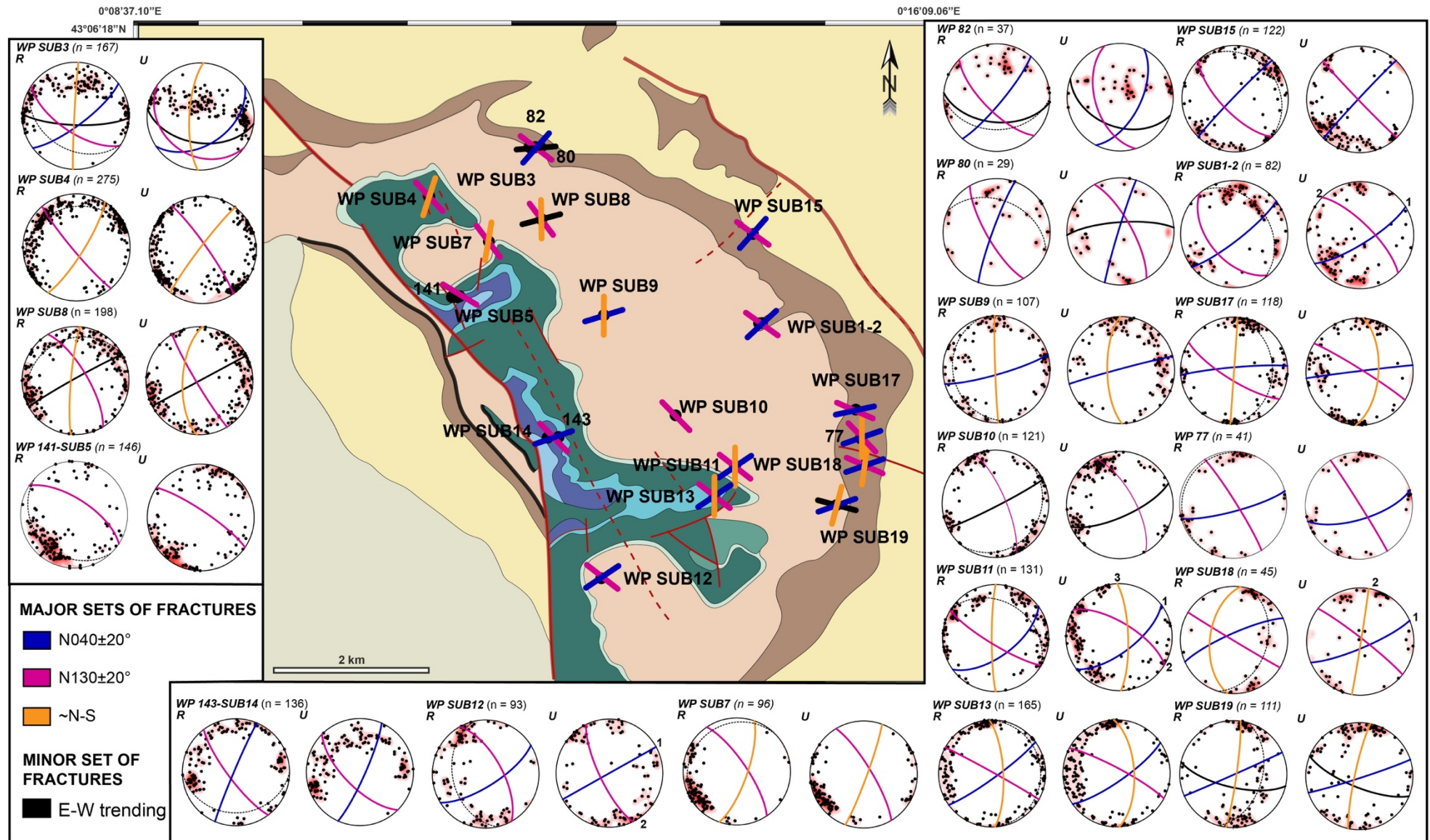


Figure 5.6- Location of fracture planes measured on the geological map of the Subasio Anticline. Each measurement point is associated with two stereonet diagrams (lower hemisphere), representing main fracture orientations in current (R) and unfolded attitude (U); on each stereonet diagram, the bedding is reported as dashed lines, and fracture planes by solid-colored lines, each color relating to one of the three major fracture sets defined (blue: $N040 \pm 20^\circ$, pink: $N130 \pm 20^\circ$, orange: $\sim N-S$).

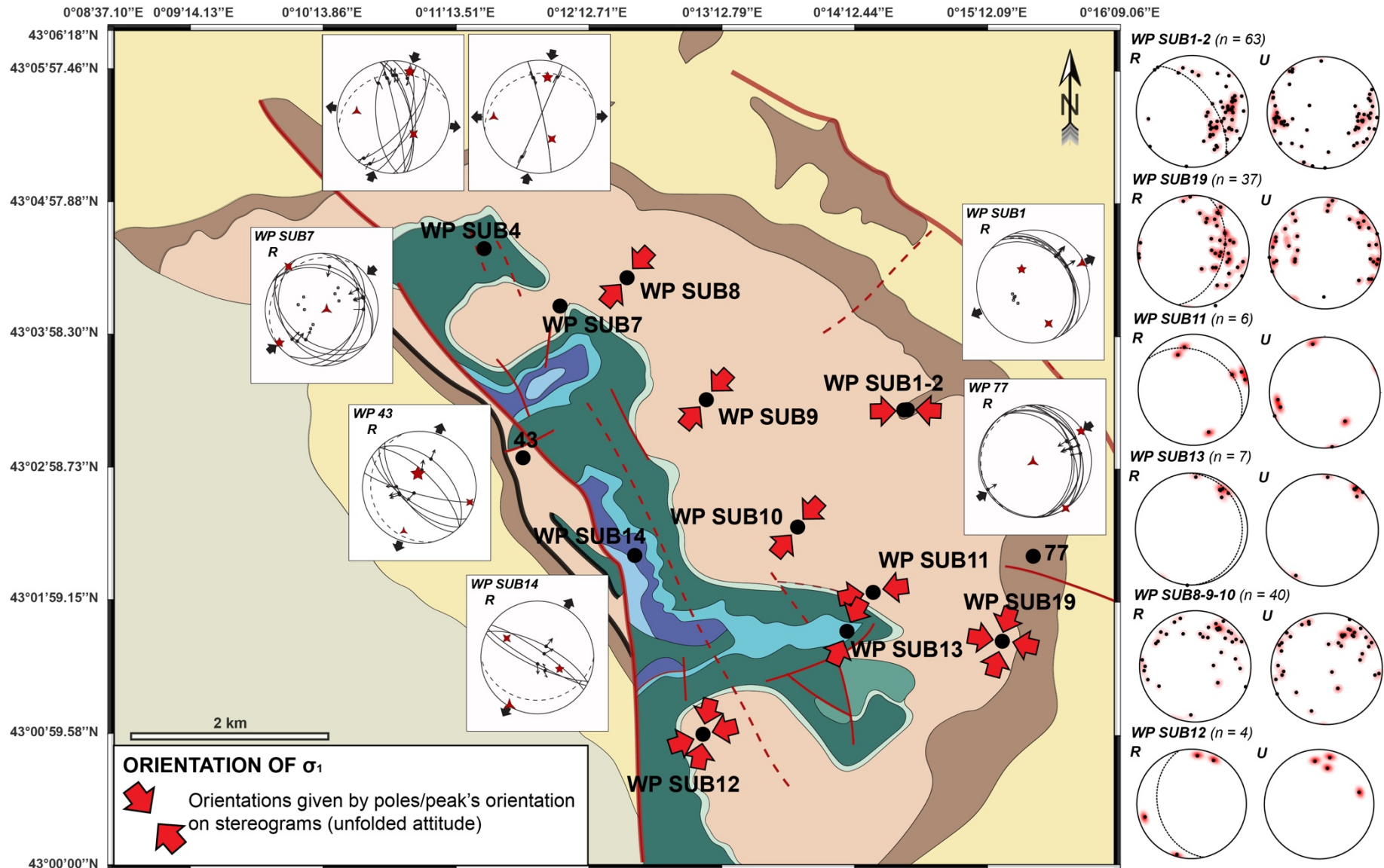


Figure 5.7- Location and plot of measured tectonic stylolites on the geological map of the Subasio Anticline. Each measurement point is associated with two stereodiagrams (lower hemisphere), representing main orientations of tectonic stylolites peaks measured (current and unfolded attitude). On each stereodiagram, the bedding is reported as dashed lines, and peaks orientation (*i.e.* σ_1 orientation) is given by high pole density zones. Stereodiagrams with fault-slip data and principal stress axes are also reported;

The inversion of the fault data using Angelier's method (Chapter 2) highlights several families of faults (Figure 5.7 and Table 5.1):

- 2 compressive tensors (WP SUB7 and 77), characterized by a σ_1 oriented N060 and horizontal in current position of strata, σ_2 oriented N050 and horizontal in current position of strata, and σ_3 vertical. Φ is constant (0.5);
- 2 extensive tensors (WP SUB14 and 43), with σ_3 axis striking N020, σ_2 axis striking N110 and σ_1 vertical. Faults are high angle (almost perpendicular) to bedding. Φ varies between 0.2 and 0.7;
- 1 extensive tensor (WP SUB1) with σ_3 axis striking N060, σ_2 axis striking N150 and σ_1 vertical. Faults are low angle to bedding (*i.e.* fault plane parallel to bedding). Φ is equal to 0.7
- 1 strike-slip fault (WP SUB4), with a σ_1 axis striking N010 and contained in the bedding (and thus horizontal after correction of strata bedding), a σ_3 axis striking E-W to N100 and perpendicular to the bedding, and σ_2 axis vertical. Φ is relatively constant, between 0.2 and 0.4.

GPS	Fault number	Method	σ_1		σ_2		σ_3		ϕ
			Az.	Dip	Az.	Dip	Az.	Dip	
WP SUB1	5	INVD	326	60	157	30	65	05	0.7
WP SUB4	9	INVD	020	16	130	51	279	35	0.4
WP SUB4	4	INVD	012	30	151	53	270	20	0.2
WP SUB7	8	INVD	232	06	322	04	089	83	0.5
WP SUB14	4	INVD	117	54	302	36	210	02	0.7
43	6	INVD	327	70	123	19	215	08	0.2
77	9	INVD	057	03	147	01	259	87	0.5

Table 5.1 - Fault inversion results using the Angelier (1984, 1989, 1990). Azimut and dip are given for each principal stress σ_1 , σ_2 and σ_3 , the associated ϕ ratio, as well as the number of faults and the method used for inversions.

Interpretation of these striated fault plane inversions help to distinguish 4 main stress regimes related to different stages of deformation recorded for the area. If possible, they are also linked with the 5 sets of fractures previously defined and represented in Figure 5.6:

- a post-tilting compressive regime, with σ_1 oriented N050 and horizontal in current position of strata, and kinematically consistent with tectonic stylolites S_2 , whose peaks are horizontal in current position and strike $N040\pm 20^\circ$.
- an extensive regime, with σ_3 oriented N020 and oblique to the fold axis. The extreme values of Φ show that tensors are close to the permutation. This stress regime cannot be linked to the syn-fold but could instead be associated with a late extension (post-LSFT). It might be kinematically consistent with vertical joints and veins J_3 striking ~N-S;
- an extensional regime, with σ_3 oriented N060 and horizontal in untilted position. This regime is kinematically consistent with flexural slip probably syn-folding, and with J_3 vertical joints and veins striking $N130\pm 20^\circ$.

- a strike-slip regime with a σ_1 axis striking N010 and horizontal after unfolding, *i.e.* ante-tilting.

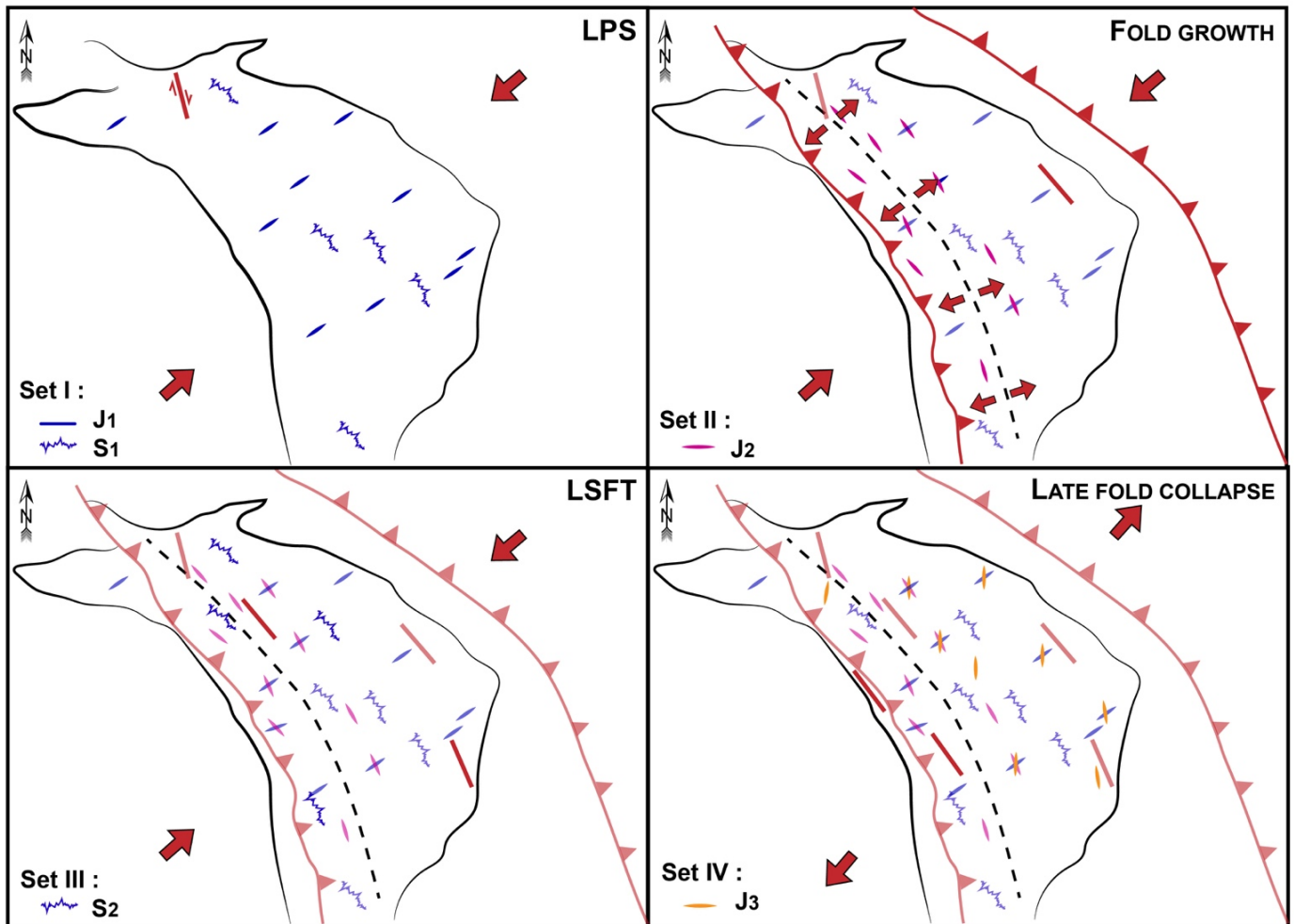


Figure 5.8- Interpretative model of the history of deformation in the Subasio Anticline. The structural evolution of the area is represented in in map view. For each stage of deformation, the main principal stress σ_1 is represented as red arrows, as well as the associated mesostructures (blue: sets I and III, pink: set II, orange: set IV). Thrusts and faults are represented by red lines in map view, in transparency when it is inactive.

Finally, the following fracturing and deformation sequence can be defined for the Subasio Anticline, illustrated by the interpretative model proposed in Figure 5.8:

- (i) set I, including tectonic stylolites S_1 , with peaks striking $N040\pm 20^\circ$ and horizontal in untilted position, and veins and joints J_1 , striking $N040\pm 20^\circ$ and perpendicular to bedding. This is the oldest set encountered in the Subasio Anticline, interpreted as related to LPS stage. The ante-tilting strike-slip fault, with a N010-oriented σ_1 , might be interpreted to be related to this NE-SW contraction;
- (ii) set II, composed by vertical veins and joints J_2 , striking $N130\pm 20^\circ$ and parallel to fold hinge, and flexural slip related to a $N060$ σ_3 after unfolding. These fractures can be interpreted as related to folding stage, reflecting extensions that occur at the hinge;
- (iii) set III of late folding, tectonic stylolites with horizontal peaks striking $N040\pm 20^\circ$, and kinematically consistent with N040 and post-tilting compression. This set can be related the

horizontal NE-SW contraction experienced by strata when the fold is locked, *i.e.* during the LSFT;

- (iv) set IV, composed by J_3 joints and veins ~N-S -oriented, assumed to be kinematically consistent with the N020 extension. Thus, they might be interpreted as generated during a late collapse of the fold, post-LSFT.

2.2- The Conero Anticline

As in Cingoli and Subasio, fracture network is analyzed in the Conero Anticline by the study of average orientations and relative chronology of fractures and tectonic stylolites (Figure 5.9). Three sets of fractures are discriminated according to these criteria:

- a first set of joints and veins J_1 , vertical and N-S to N170-oriented, and mainly oblique to bedding strike. They are located in the central and southern part of the anticline, synchronous or intersecting BPS;
- joints and veins J_2 with a strike $N060\pm 20^\circ$ and vertical. They are mainly perpendicular to the bedding strike and are represented on the whole fold. They are associated with tectonic stylolites S_1 horizontal after bedding correction, with peaks striking N040 to N060°, and mainly identified in the northern part (Figure 5.10). They abut and then post-dates the set J_1 ;
- veins and joints J_3 striking N160 and vertical in current position, only observed at the hinge. They are parallel to bedding strike and fold axis strike. They abut and then post-date J_1 and J_2 .

Another set of sub-vertical to vertical fractures E-W-oriented is also identified. As in Subasio and Cingoli, this fracture set is considered to be of second order, as it is poorly represented at the scale of the fold (low number of sites and measurements) and has no clear chronological relationship with the other fracture sets identified.

Using Angelier's inversion method on 2 sites of measurements (Chapter 2), two families of faults are characterized (Figure 5.9 and Table 5.2):

- 1 strike-slip tensor (WP CON3), with σ_1 axis striking N230 and σ_3 axis striking N140. σ_1 and σ_3 axes are both contained in bedding, and thus horizontal after correction of strata bedding. Faults related to this tensor are high angle to bedding (sub-vertical to vertical). Φ is equal to 0.1.
- a second strike-slip tensor (WP CON4), with σ_1 axis striking N040, and a dip of 80°, and σ_3 axis striking N150 contained in the bedding (*i.e.* horizontal after correction of strata bedding). It is associated with high angle to bedding faults, and a Φ 0.9.

The extreme values of Φ demonstrate that these tensors are close to the permutation. They can be interpreted as related to the main strike-slip stress regime, pre-tilting, and characterized by a σ_1 striking ~N045 and horizontal after unfolding, and a σ_3 striking NW-SE and horizontal after unfolding. This regime may be interpreted as kinematically consistent with the vertical veins/joints J_2 N060±20°-oriented.

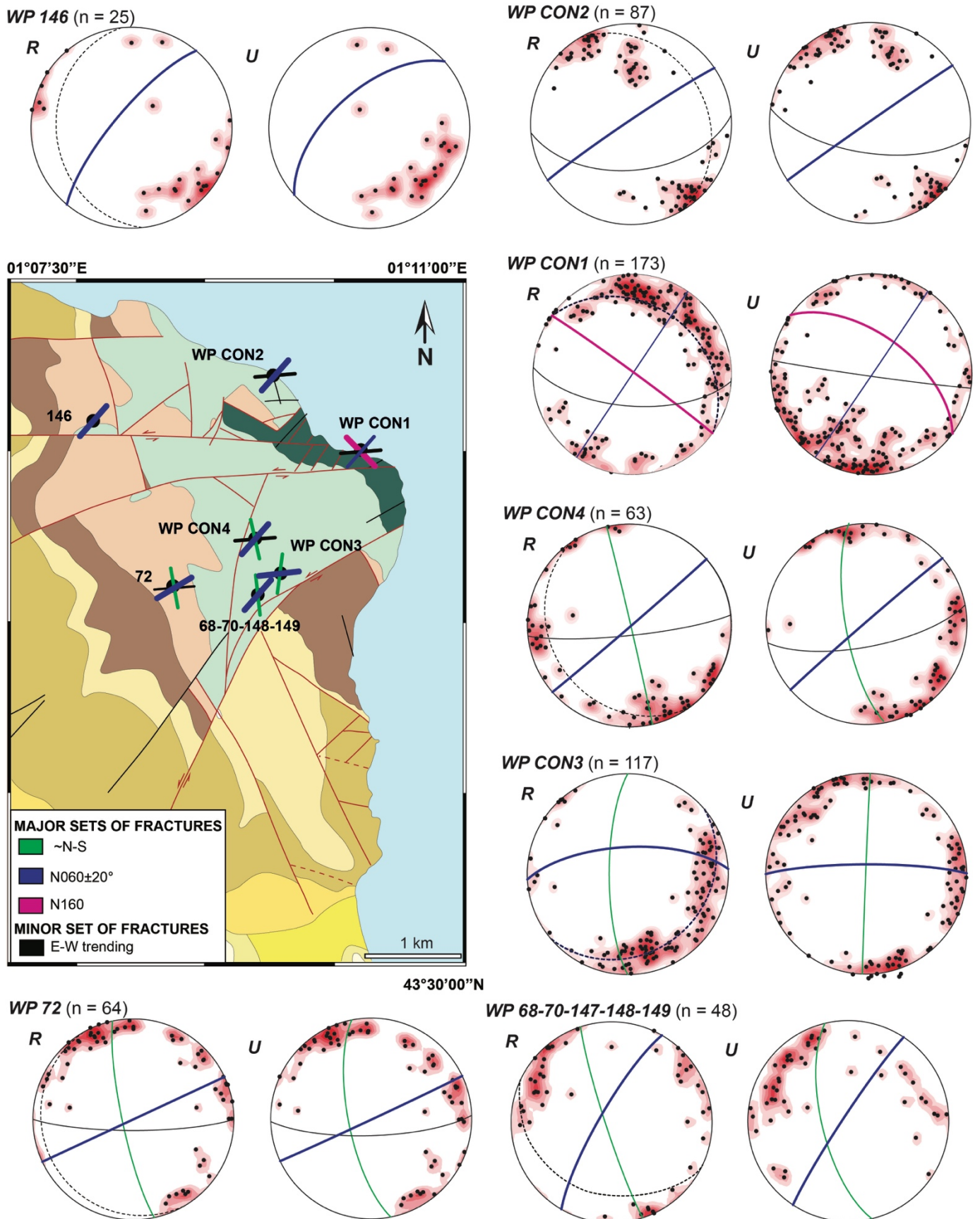


Figure 5.9- Location of fracture planes measured on the geological map of the Conero Anticline. Each measurement point is associated with two stereodiagrams (lower hemisphere), representing main fracture orientations in current (R) and unfolded attitude (U); on each stereodiagram, the bedding is reported as dashed lines, and fracture planes by solid-colored lines, each color relating to one of the four major fracture sets defined (green: set I, blue: set II, pink: set III, orange: set IV). Major sets are represented in bold on the stereodiagrams as on the map.

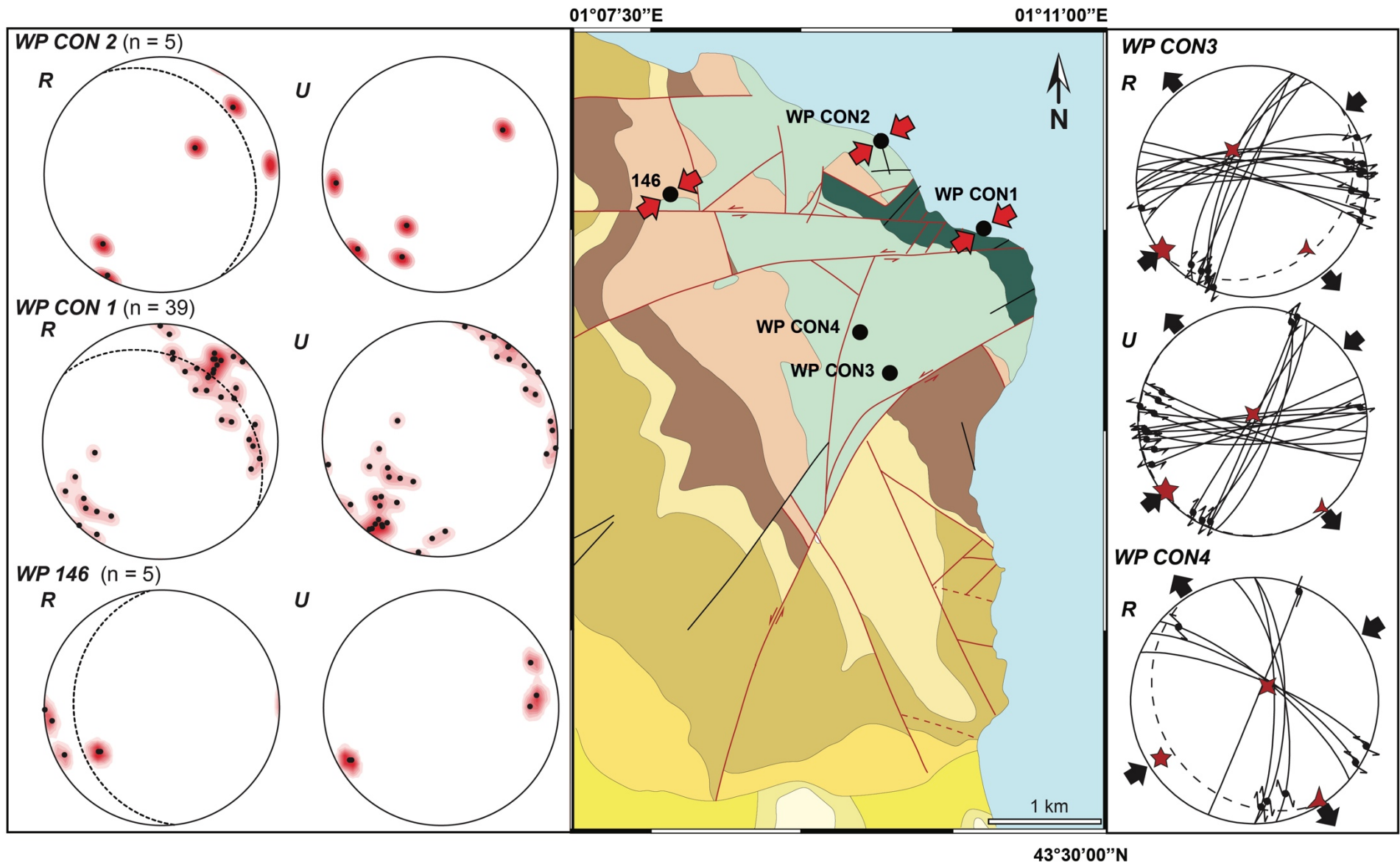


Figure 5.10- Location and plot of measured tectonic stylolites on the geological map of the Conero Anticline. Each measurement site is associated with two stereodiagrams (lower hemisphere), representing main orientations of tectonic stylolites peaks measured (current and unfolded attitude). On each stereodiagram, the bedding is reported as dashed lines, and peaks orientation (*i.e.* σ_1 orientation) is given by high pole density zones. Stereodiagrams with fault-slip data and principal stress axes are also reported.

GPS	Fault number	Method	σ_1		σ_2		σ_3		ϕ
			Az.	Dip	Az.	Dip	Az.	Dip	
WP CON3	16	INVD	233	03	328	64	141	26	0.1
WP CON4	7	INVD	042	77	238	12	147	03	0.9

Table 5.2 - Fault inversion results using the inversion of striated fault plane of Angelier (1984, 1989, 1990). Azimut and dip are given for each principal stress σ_1 , σ_2 and σ_3 , the associated ϕ ratio, as well as the number of faults and the method used for inversions.

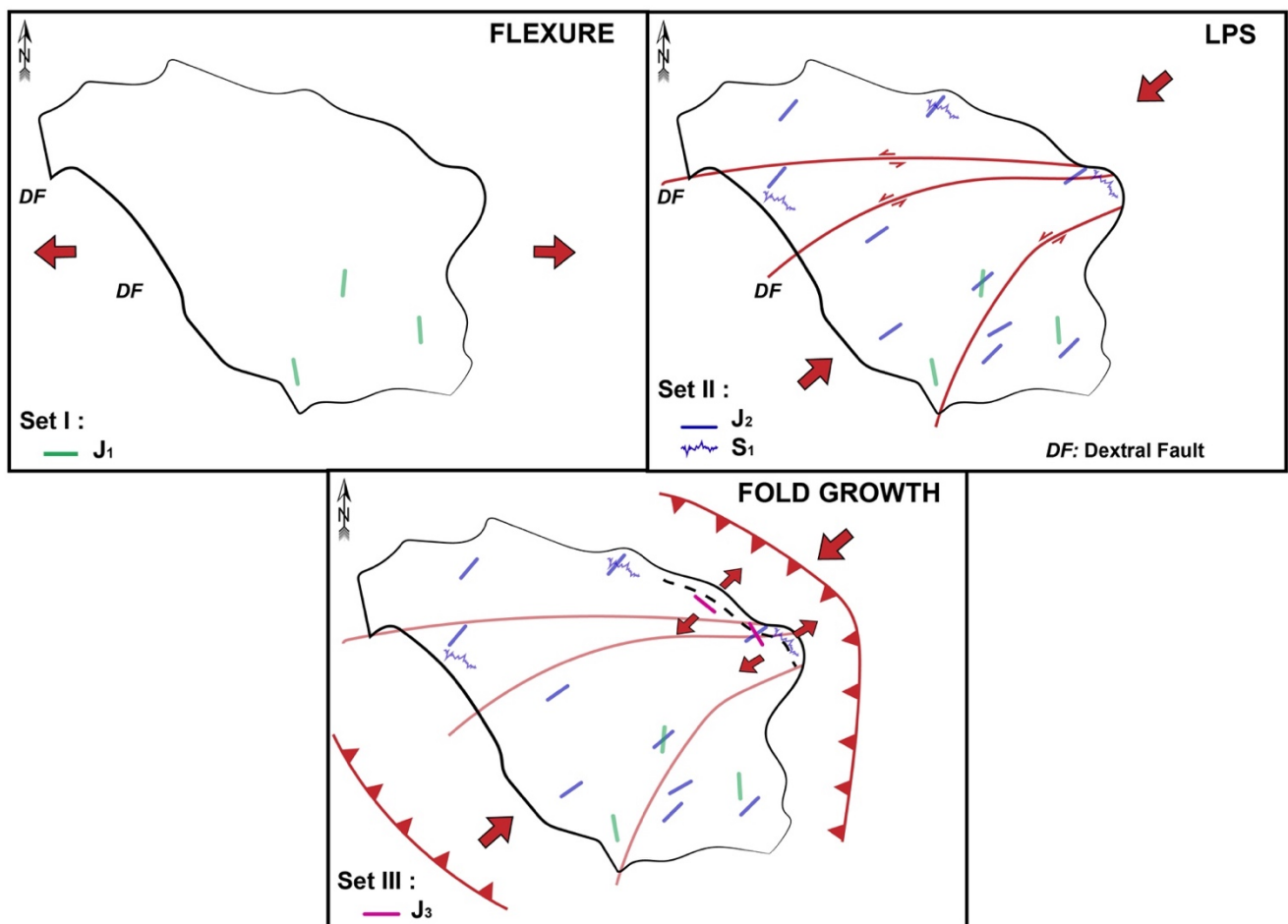


Figure 5.11- Interpretative model of the history of deformation in the Conero Anticline. The structural evolution of the area is represented in map view. For each stage of deformation, the main principal stress σ_1 is represented as red arrows, as well as the associated mesostructures (green: set I, blue: set II, pink: set III, orange: set IV). Orogenic thrusts and faults are represented by red lines in map view, in transparency when it is inactive.

The interpretative model of the history of deformation in the Conero Anticline is given in Figure 5.11 and links the main stages of regional deformation with the development of fractures-stylolites network. The proposed fracturing-deformation sequence is as follows:

- (i) the flexural stage, related to set I of fractures, including veins and joints J_1 N160-oriented, post-dating BPS and pre-dating other sets of fractures;
- (ii) set II of fractures-stylolites is related to LPS, stage associated with a NE-SW contraction that occurs before fold growth. This set includes vertical veins and joints J_2 , N060±20°-oriented whose strike is perpendicular to the bedding strike. They are related to tectonic stylolites S_1

whose peaks follow the same orientation. This set could also be associated with to the activity of strike-slip faults, under a stress regime characterized by a horizontal extensive component NE-SW-oriented;

- (iii) set III includes vertical joints/veins J_3 which post-date the other sets of fractures and strike parallel to the local fold axis (*i.e.* N160). They are assumed as related to outer-arc extension related to folding at the hinge.

2.3- Timing of regional deformation: evolution of flexure and folding

The diachronous propagation of flexural and folding stages at the scale of the UMAR, correlated with the eastward migration of the deformation front, is summarized in Figure 5.12, considering the data from literature available on the whole area.

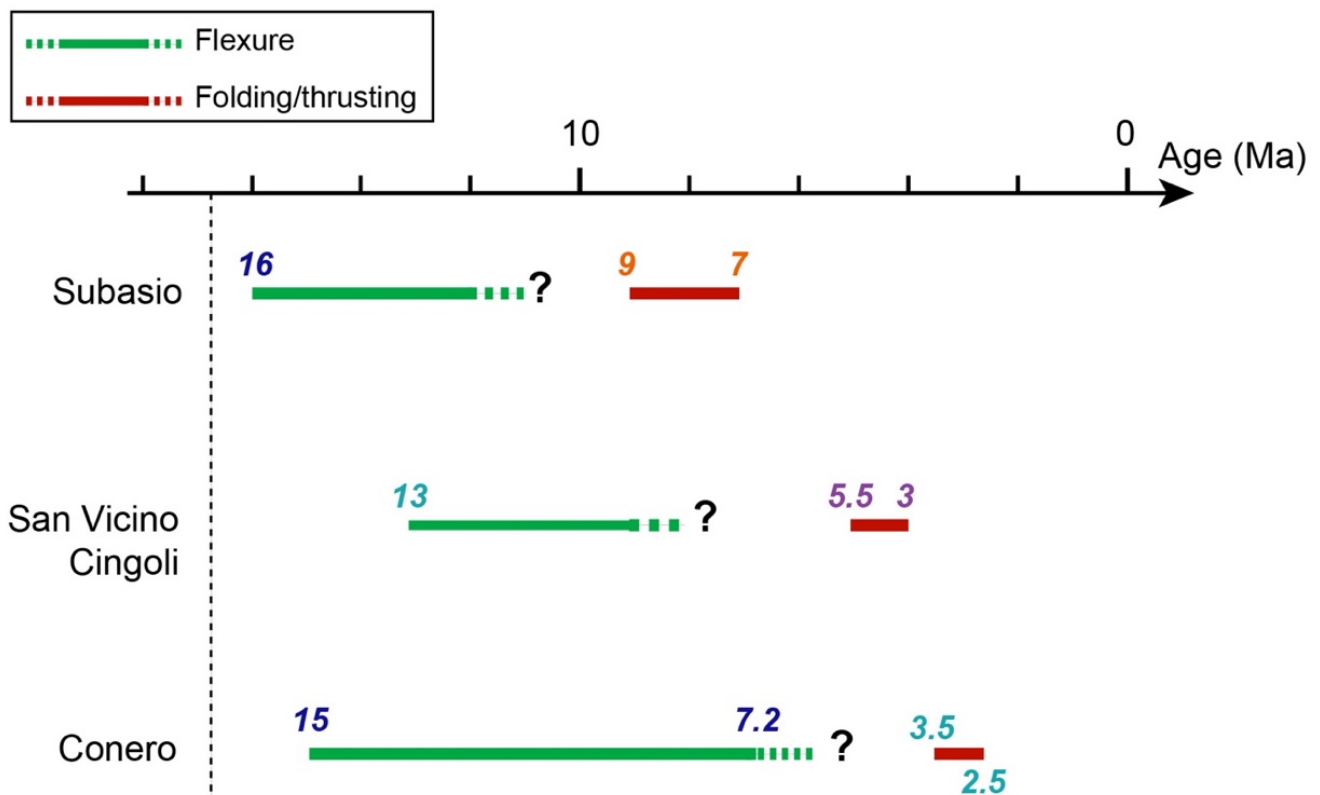


Figure 5.12- Summary chart of the evolution of flexure and folding/thrust ages at the scale of the UMAR, through the 4 folds studied: Subasio, San-Vicino and Cingoli, and Monte Conero. The associated ages are given in italics, each color corresponding to the bibliographic source: in dark blue Guerrera *et al.* (2012), in orange Curzi *et al.* (2020), in light blue Calamita *et al.* (1994) and in purple Lacombe *et al.* (2021).

In the work of Calamita *et al.* (1994), the timing and rate of deformation in the external zones of the UMAR was reconstructed (Figure 5.12, light blue) on the basis of a correlation between spacing and thickness of the thrust sheets, and on a time/space relationship between the end of the activity of each thrust and the distance from a reference point within the system. Guerrera *et al.* (2012) reconstructed the space/time evolution of the UMAR and the Apennine Miocene foredeep through the stratigraphic, biostratigraphic and chronostratigraphic study of the Miocene silicoclastic deposits (Figure 5.12, dark blue). Multi-analytical approach applied by Curzi *et al.* (2020) in the western part also complemented these data, combining field data (*i.e.* detailed mapping of the area and multiscale structural analyses)

with laboratory analyses (*i.e.* illite-smectite paleothermal indicators, clumped and oxygen-carbon isotopes applied to calcite mineralization and fault rock dating using K-Ar and/or syn-kinematic illite methods) (Figure 5.12, orange). The study of Lacombe *et al.*, 2021 gave the last missing ages by coupling meso-structural data and U-Pb dating of calcite veins (Figure 5.12, purple), and allowed finalization of the reconstruction of this evolutionary scheme of flexure and contraction ages (for more details on the kinematic part, please refer to Chapter 2).

3- *Sedimentary stylolites paleopiezometry*

3.1- *Young modulus estimation*

In 15 sites in Subasio and Conero anticlines, 542 R rebound values are measured on flat homogeneous surfaces to estimate rock elastic properties for the Maiolica, Scaglia Bianca, Scaglia Rossa formations as previously described (Chapter 2). All measurements are detailed in Appendices 5.1 and 5.2. The average of these representative R values and resulting Young moduli are reported in Table 5.3.

Location	Formation (n)	Stabilized R value (m)	Young modulus E (GPa)
Subasio	Maiolica (3)	56 ± 2.6 (141)	33 ± 4.8
Subasio	Scaglia Bianca (2)	61 ± 3 (80)	43 ± 6.5
Subasio	Scaglia Rossa (6)	56 ± 5.6 (241)	35 ± 10.8
Conero	Maiolica (2)	58 ± 6.1 (80)	36 ± 11.7

Table 5.3 - Stabilized R values averaged for the Maiolica, Scaglia Bianca, and Scaglia Rossa formations in Subasio and Conero anticlines, and associated Young moduli E. The number of measurement sites is indicated for each formation in brackets (n), as well as the number of points used for the calculation of the stabilized R value (m). The uncertainty on the R and E values is given by the standard deviation. Values Young moduli are deduced from the Equation 1.15 (Chapter 1).

For the same formations, studies previously carried out in Umbria-Marche gave values close to 20 GPa (Beaudoin *et al.*, 2016; Labeur *et al.*, 2021). Considering the uncertainty on the values of R and E obtained, E values used for inversions are those computed from these measurements and detailed in Table 5.3.

3.2- *Sedimentary stylolite roughness inversions*

Stylolites roughness inversions are successful for 60 BPS with peaks perpendicular to the dissolution plane, sampled within the Jurassic to Eocene carbonate formations in these two anticlines, and distributed as follows (Figures 5.6 and 5.9):

- Subasio: Maiolica, n=19; Scaglia Bianca, n=10; Scaglia Rossa, n=8;
- Conero : Maiolica, n=20; Scaglia Bianca, n=3.

To ensure the stress isotropy on the horizontal plane, paleopiezometric inversions are applied on two orthogonal tracks for several stylolites (Beaudoin *et al.*, 2016). All L_c values are reported in Table 5.4, given within an uncertainty of 23% (Rolland *et al.*, 2014), and their distribution summarized in Figure 5.13A.

Location	Sample	Formation	L_c (mm)*	E (GPa)	σ_v (MPa)**	Depth (m)	
Subasio	SUB25	Maiolica	0.45± 0.10	33	40	1690	
			0.56± 0.13		36	1510	
		SUB27		0.31±0.07		48	2040
		SUB28		0.53±0.12		37	1560
		SUB41		0.38±0.09		43	1830
		SUB45		0.29±0.07		49	2100
			0.15±0.03		68	2900	
				0.97±0.22		27	1150
		SUB65		0.33±0.08		47	1980
			0.27±0.06		51	2190	
		SUB70		0.51±0.12		37	1590
		SUB72		0.55±0.07		36	1530
			0.66±0.15		33	1390	
				0.26±0.06		52	2210
				0.47±0.11		39	1650
				0.89±0.20		28	1200
		SUB107		0.34±0.08		46	1940
			0.19±0.04		61	2600	
				0.16±0.04		67	2840
		SUB113	Scaglia Bianca	0.23±0.05	43	64	2720
				0.19±0.04		70	2960
		A165		1.13±0.26		29	1220
			1.37±0.39		26	1110	
				0.51±0.12		43	1810
				0.51±0.12		43	1810
				0.50±0.12		43	1830
				1.05±0.24		30	1270
			0.77±0.18		35	1480	
			1.61±0.37		24	1020	
	SUB80	Scaglia Rossa	0.46±0.11	35	33	1400	
			0.37±0.09		37	1580	
			0.40±0.09		35	1500	
	SUB85		0.26±0.06		53	2260	
		0.26±0.06		54	2280		
	SUB97		0.35±0.08		47	1980	
	SUB98		0.79±0.18		31	1310	
	SUB145		0.20±0.05		68	2880	

Location	Sample	Formation	L_c (mm)*	E (GPa)	σ_v (MPa)**	Depth (m)
Conero	CON3	Maiolica	0.26± 0.06	36	55	2340
			0.40 ± 0.09		45	1890
	0.28 ± 0.06		53		2250	
	CON6		0.79 ± 0.18		32	1340
			0.3 ± 0.07		51	2180
			0.70 ± 0.16		34	1430
	CON8		0.49 ± 0.11		40	1700
			0.56 ± 0.13		38	1600
			0.56 ± 0.13		38	1600
	CON10		0.58± 0.13		37	1570
			0.40 ± 0.09		44	1890
			0.33 ± 0.10		49	1890
	CON17		0.89 ± 0.20		30	1270
			0.51 ± 0.12		39	1680
			0.35 ± 0.08		48	2020
			0.34± 0.08		48	2050
			0.30 ± 0.07		51	2160
			0.94 ± 0.22		29	1230
			0.39 ± 0.09		45	1920
			0.63 ± 0.15		35	1500
CON20	Scaglia Bianca	0.32 ± 0.07	54	2300		
		0.50 ± 0.11	43	1840		
		0.65 ± 0.15	38	1610		

Table 5.4 - Results of Bedding Parallel Stylolite roughness inversions. Values are grouped considering the location and the formation of sampling. *Crossover length given within 23% uncertainty. **Vertical stress σ_v given within 12% uncertainty calculated according to Equation 1.12.2 (Chapter 1), with following parameters: a Young modulus depending on formation and location, a Poisson ratio $\nu = 0.25$, and interfacial energy $\gamma = 0.32 \text{ J.m}^{-2}$. Dry density of rock considered for calculation $d = 2400 \text{ g.m}^{-3}$, acceleration of gravity $g = 9.81 \text{ m.s}^{-2}$

3.3- Vertical stress and burial depths computation

Once the following parameters are defined, associated vertical stress are computed (Table 5.4): (i) crossover lengths L_c values reported considering an uncertainty of 23% (Rolland *et al.*, 2014) and (ii) mechanical and chemical parameters characteristic of the rocks studied, namely Young modulus E, Poisson ratio ν and the solid-fluid interfacial energy γ , defined in previous works and detailed above. Then, burial depths are calculated from each value of the vertical stress. They are rounded to the closest 10 m and summarized in Table 5.4. The corresponding depth ranges for each formation and each locality are graphically represented in Figure 5.13B.

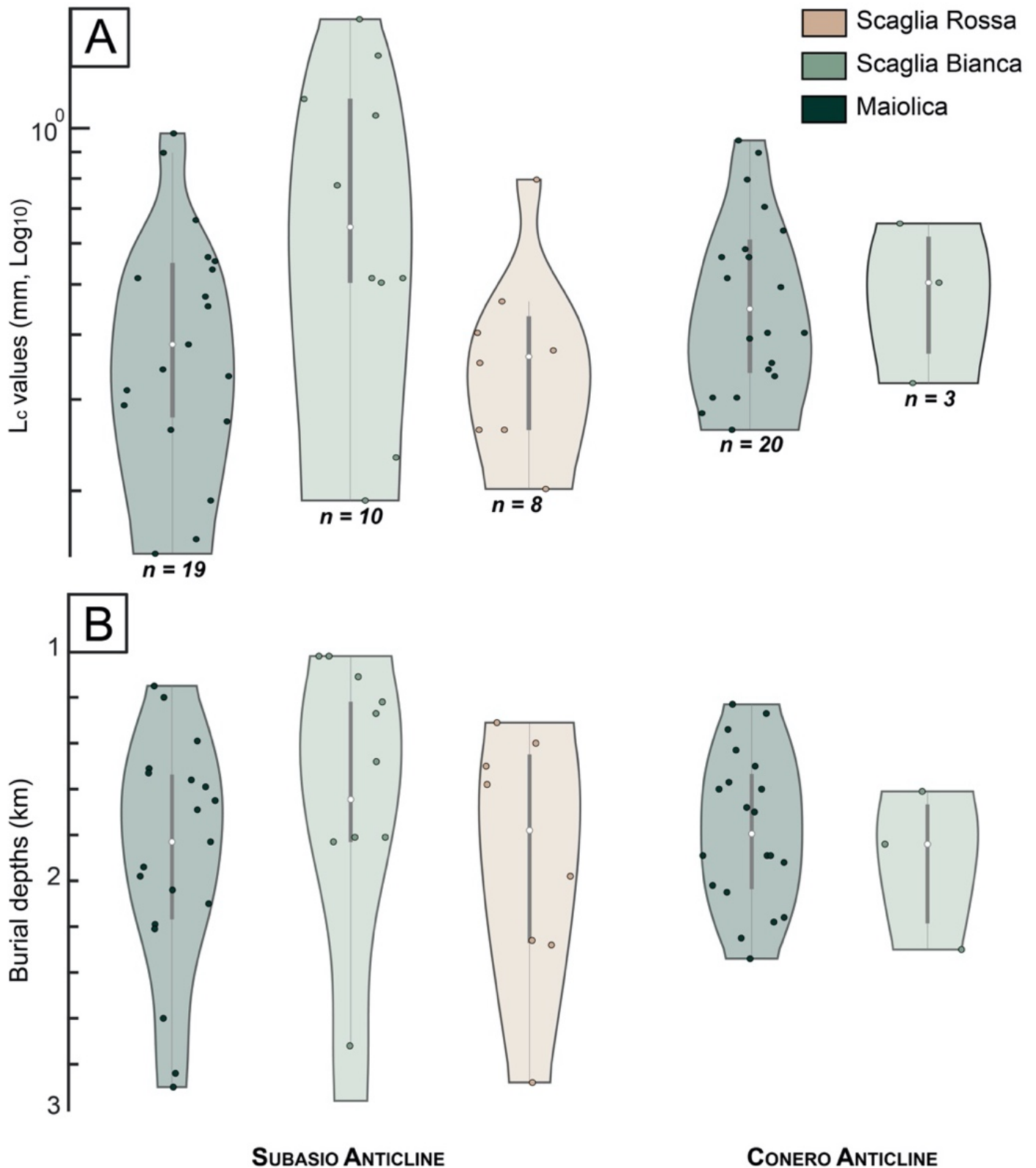


Figure 5.13- Summary of inversion results considering the longitude and the formation of sampling. Each box shows the distribution of values, with the median represented by a vertical line, and the extrema by the straight lines. **(A)** Distribution of cross-over lengths L_c given in millimeters. **(B)** Distribution of depths deduced from the vertical stresses obtained after inversions.

4- Burial depths evolution

Figure 5.14 presents burial curves reconstructed for the Subasio (Figure 5.14A) and the Conero (Figure 5.14B) anticlines, following the method applied in Cingoli. For the Subasio Anticline, burial model is derived from the work of Caricchi *et al.* (2015). In Conero, burial curves are reconstructed for the Jurassic to Pliocene formations, considering the chemical compaction and physical compaction, as previously detailed. Thus, considering field data and previous work carried out in Cingoli (Labeur *et al.*, 2021), chemical compaction is estimated at 8% for the Maiolica, and 3% for the Scaglia formations (*i.e.* Bianca, Rossa and Variegata). The value of the geothermal gradient considered remains $23^{\circ}\text{C.km}^{-1}$, as estimated by organic matter thermal maturity (Caricchi *et al.*, 2015) and clay minerals (Aldega *et al.*, 2007). As observed for the Cingoli Anticline, two main stages are illustrated by these curves for both anticlines (Figure 5.14): (i) a first phase of increasing burial, related to the deepening of the Umbria-Marche basin in a foreland setting, and (ii) an exhumation stage, the age of which is younger from west to east (*i.e.* from late Miocene in Subasio to middle Pliocene in Conero).

The internal consistency of burial depths values is demonstrated because the maximum burial recorded by sedimentary stylolites never exceeds the maximum depth of the formation they belong, from the data used in the construction of burial curves (Figures 5.14A and 5.14B). In addition, maximum depths recorded by BPS and maximum burial associated with the oldest formation studied in both anticlines provides information on burial duration (Figure 5.14): (i) in Subasio, considering the Scaglia Rossa, BPS would not develop between 2120 and 2850 m; (ii) in Conero, for the Scaglia Bianca, no BPS between 1830 and 3800 m. Thus, the burial was continuous from the Cretaceous to the late Miocene-early Pliocene, until the sedimentary layers studied reached the maximum burial depths.

Beyond the access to the maximum burial reached before the contraction begun, combination of results of SRIT inversion applied on BPS and burial curves provides access to the time at which the principal stress σ_1 changes from vertical to horizontal. The underlying assumption is to consider the end of stylolite growth as associated with the switch from formerly vertical to horizontal σ_1 , *i.e.* with the onset of the LPS stage. Indeed, this pre/early folding compressional stage is regionally recorded (*e.g.*, Tavani *et al.*, 2008; Díaz General *et al.*, 2015; Beaudoin *et al.*, 2016; Labeur *et al.*, 2021; Lacombe *et al.*, 2021), with a σ_1 NE-SW-oriented related to the Apenninic contraction. Furthermore, stylolites studied are bedding-parallel and horizontal in untilted position. Stylolitization is considered as directly linked to the burial of the strata under the weight of overburden before contraction. Thus, by plotting the estimated paleodepths on the reconstructed burial models, the onset of LPS (*i.e.* of horizontal contraction) is constrained for the both anticlines, 9.9 Ma in Subasio (Figure 5.14A) and 4.3 Ma in Conero respectively (Figure 5.14B).

This study therefore provides a first-order estimation of the LPS onset at the fold scale, for 3 cases of study. The accuracy of ages values remains questionable, as their estimation involves the use of some parameters for which the uncertainty is difficult to estimate (*e.g.* Young modulus, burial modelling, ...). Hence, the LPS onset ages are rounded for the rest of the study assuming an uncertainty of around one

million years, *i.e.* 10 Ma in Subasio, 6 Ma for Cingoli and 4 Ma for Conero. The comparison of these case studies, located on a transect crossing the UMAR, would give a potential idea of the evolution of this burial-deformation calendar on a larger scale.

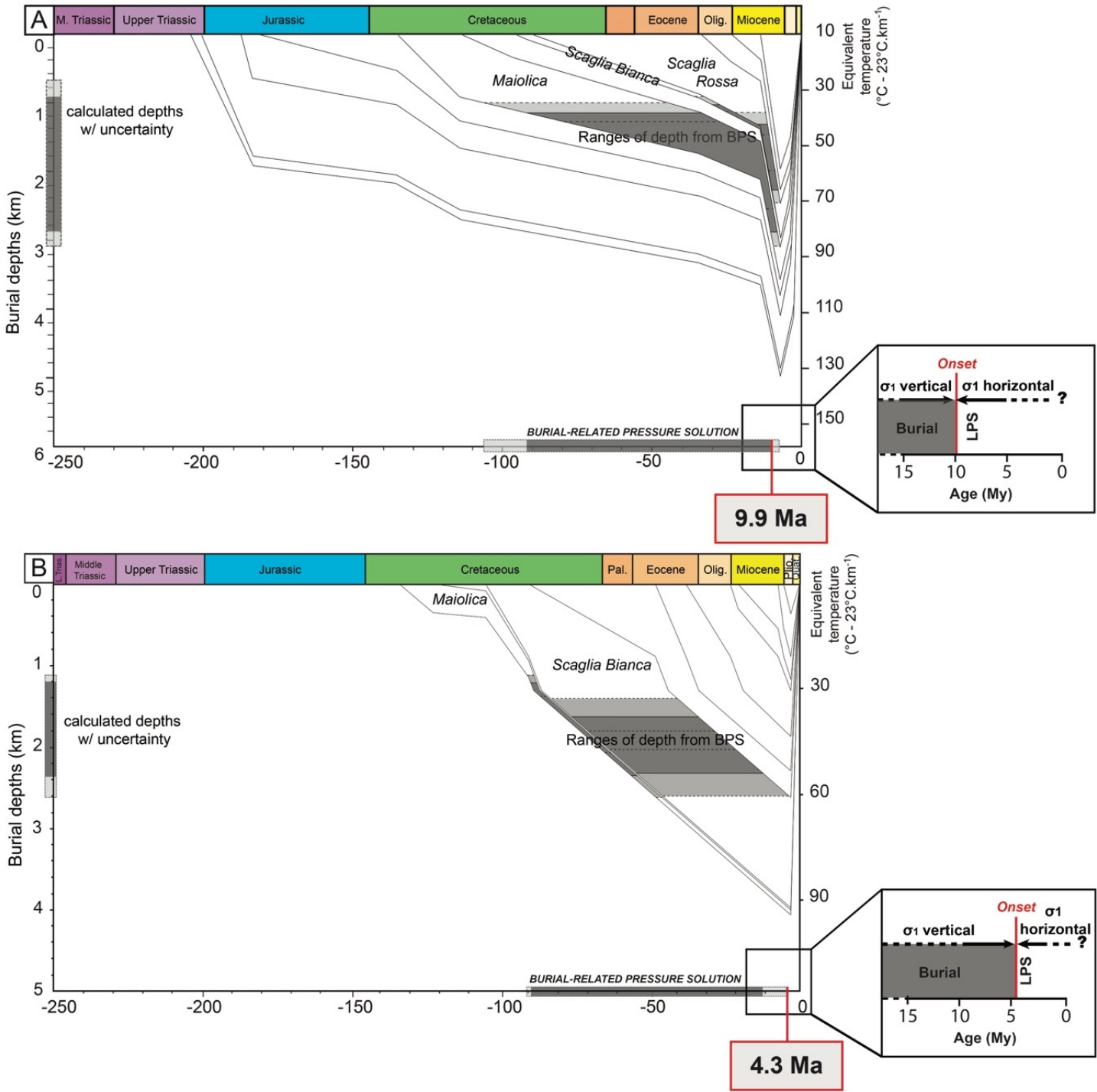


Figure 5.14- Burial models constructed for the **(A)** Subasio and **(B)** Conero anticlines considering thickness from stratigraphic and well data corrected for chemical and physical compaction. In Subasio, model is taken from works of Caricchi *et al.* (2015). The range of depths reconstructed from BPS roughness inversion (with uncertainty shaded in light grey) are reported for each formation as grey levels. The corresponding timing and depth of active dissolution are reported on the x axis and left y axis, respectively. Onsets of LPS, *i.e.* the moment when σ_1 switches from vertical to horizontal, is deduced from the results of the roughness inversion process applied on sedimentary stylolites.

III- INTERPRETATION OF THE COMPILED RESULTS: FROM THE FOLD SCALE TO THE FOLD-AND-THRUST BELT SCALE

1- *Sedimentary roughness inversion: compilation of data*

The results of the studies previously presented are compiled with those published for the San Vicino anticline (Lacombe *et al.*, 2021). 173 BPS sedimentary stylolites are therefore studied within the Jurassic to Eocene carbonate formations in these 4 anticlines located from west to east of the FTB, *i.e.* the Subasio, San Vicino, Cingoli and Conero anticlines (Figure 3.1, Chapter 3). Among this dataset, and considering the validation criteria discussed in Chapter 3, SRIT is successful for 165 BPS and thus returned a value of crossover length L_c , distributed as follows: Subasio: (Maiolica, n=19; Scaglia Bianca, n=11; Scaglia Rossa, n=7), San Vicino (Maiolica, n=28), Cingoli (Maiolica, n=56; Scaglia Rossa, n=18; Scaglia Variegata, n=3) and Conero (Maiolica, n=20; Scaglia Bianca, n=3). Figure 5.5A summarizes L_c distribution according to the anticline and sampled formations.

2- *Burial curves*

Figure 5.15 presents burial curves reconstructed for the Subasio, San Vicino, Cingoli and Conero anticlines, and already detailed in previous section. Major stages of deformation recorded in this area are represented on these are illustrated on these burial curves:

- (i) from Jurassic to Cretaceous, the slopes of burial curves are more or less important. The steepest curves illustrated successive stages of rapid tectonic subsidence related to the Jurassic rifting which occurred at the beginning of the Jurassic (during middle Liassic) and to the extensional stage recorded during the late Cretaceous (Cenomanian). When they are less steep, these curves are linked to subsidence phases that were probably thermally controlled during this same time span (*i.e.* syn- and post-rift);
- (ii) the significant deepening of the curves from Mio-Pliocene times, observed on all models except Conero, is related to the flexure of Adriatic foreland. The onset of this flexure is associated with the inflexion point of the curves;
- (i) the rapid diminution of burial depths is related to the exhumation stage, which started later from west to east (*i.e.*, from late Miocene to middle Pliocene).

The maximum burial depths reached by formations of interest, and equivalent temperatures, are deduced from the left and right y-axis of these models, respectively (Figure 5.15). All these models are consistent with each other, as well as with the model constructed for the inner part of the belt in the area of the Monte Tancia thrust (Curzi *et al.*, 2020). The only difference observed is for the Conero model, where the acceleration of burial due to flexure is not represented.

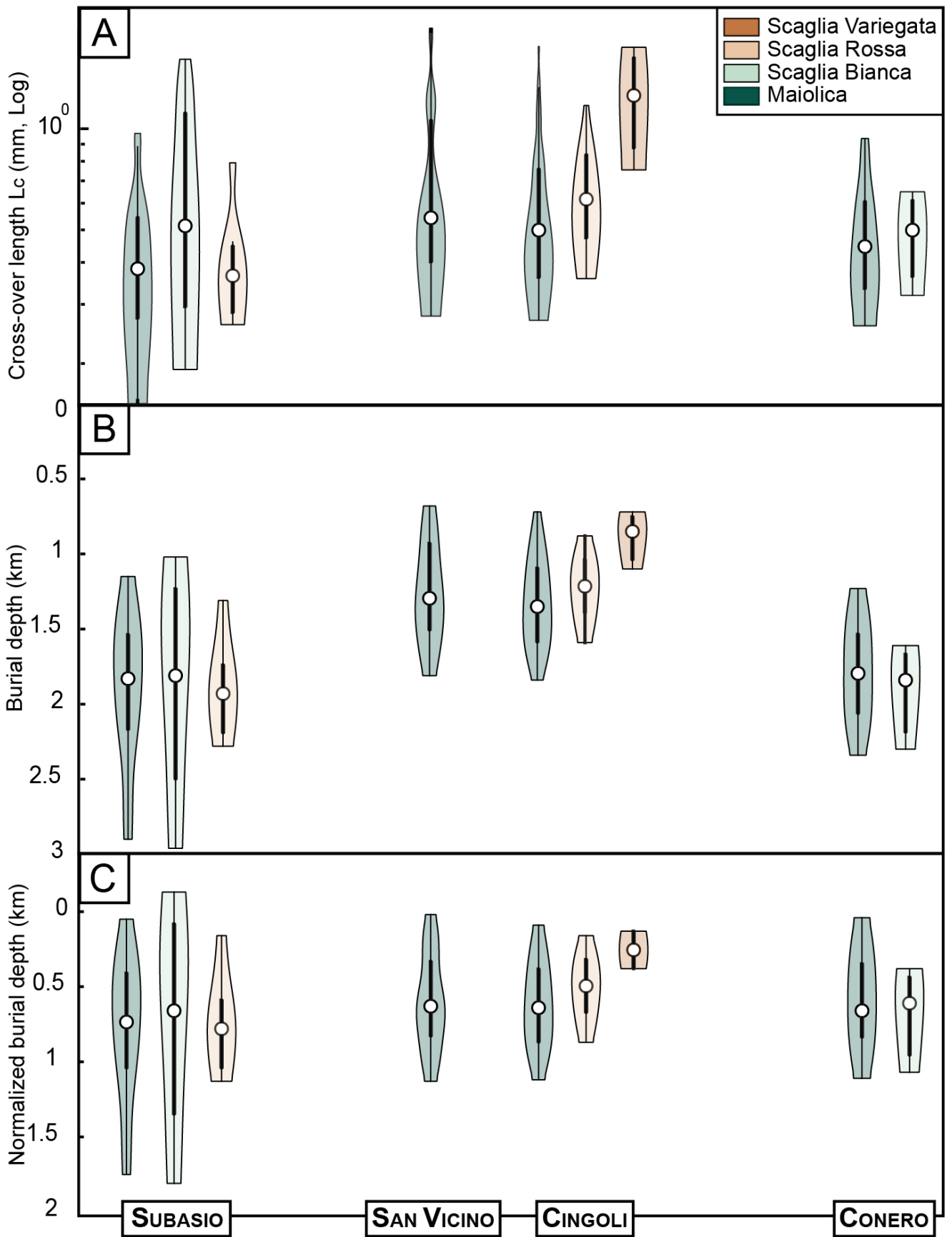


Figure 5.15- Summary of inversion results considering the anticline and the formation. For greater readability, all values are not represented. Each box shows the distribution of values with the median represented by a vertical line, and the extrema by the error bars. **(A)** Distribution of L_c obtained from the signal processing of single tracks by AWC/FPS, given in millimeters. **(B)** Distribution of depths deduced from the vertical stresses obtained after inversions. **(C)** Normalization of burial depths relative, here the top of the Maiolica top, by fold.

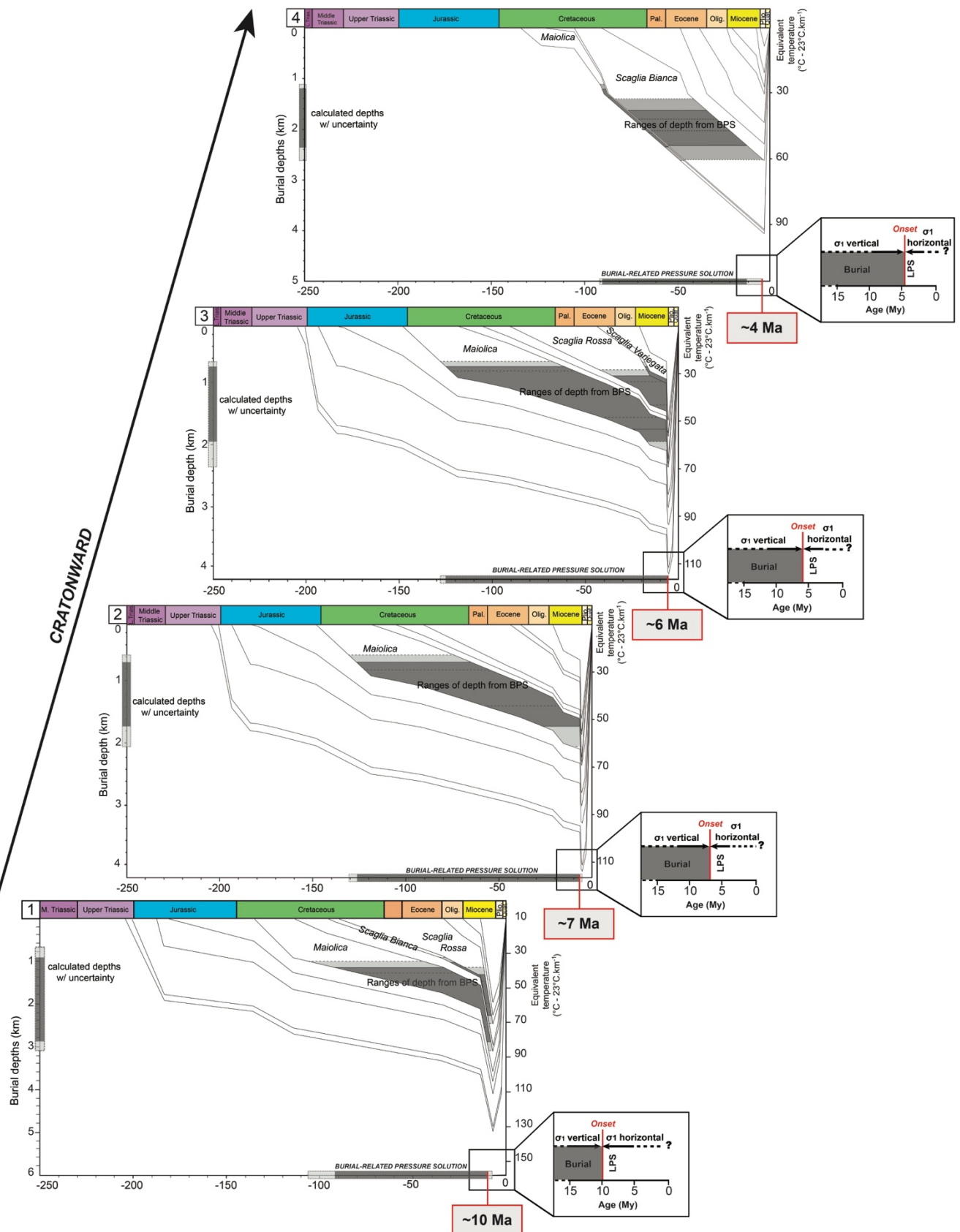


Figure 5.16- Burial models constructed for the Subasio (1), San Vicino (2), Cingoli (3) and Conero (4) anticlines considering thickness from stratigraphic and well data corrected for chemical and physical compaction. In Subasio, San Vicino and Cingoli, models are taken from works of Caricchi *et al.* (2015), Lacombe *et al.*, (2021) and Labeur *et al.*, (2021), respectively. The range of depths reconstructed from BPS roughness inversion (with uncertainty shaded in light grey) are reported for each formation as grey levels. The corresponding timing and depth of active dissolution are reported on the x axis and left y axis, respectively. Onsets of LPS, *i.e.*, the moment when σ_1 switches from vertical to horizontal, is deduced from the results of the roughness inversion process applied on sedimentary stylolites.

3- Burial depths evolution along the transect

After computation of the vertical stresses associated with the end of pressure-solution along BPS, according to the inversion method detailed in Chapter 1 and 3, burial depths are calculated from each value of the vertical stress and rounded to the closest 10 m. The corresponding depth ranges for each formation and each locality are graphically represented in Figure 5.15B using violin plots. These ranges correspond to when pressure solution along sedimentary stylolites was active, *i.e.*, the time vertical shortening (σ_1 vertical) was prevailing over horizontal shortening (Beaudoin *et al.*, 2020c; a; Labeur *et al.*, 2021; Lacombe *et al.*, 2021).

The calculated depths are also normalized relative to the top of Maiolica in each fold (Figure 5.15C). Depth data are consistent along the transect because the maximum burial depths of active pressure solution given by the SRIT are shallower than the maximum burial depth of the formation they belong to (Figure 5.16). In addition, depth ranges recorded by the different formations overlap: (i) per fold, except for the youngest formation (*i.e.* the Scaglia Variegata) in the Cingoli Anticline, which records the shallowest burial, with a median value of 850 m; (ii) between the different folds, with a deepening in Subasio, (*i.e.* entire overlap of the other depth ranges, with higher maximum burial values).

4- Determination of the onset of orogenic contraction

The assumption underlying this study is that the end of a stylolite growth is associated with the switch from vertical to horizontal σ_1 , *i.e.* with the onset of the LPS stage. This pre- or early folding compressional stage was regionally recorded, *e.g.*, Monte Catria, Conero, Cingoli and San Vicino Nero, Conero, Catria (Tavani *et al.*, 2008; Díaz General *et al.*, 2015; Beaudoin *et al.*, 2016; Labeur *et al.*, 2021; Lacombe *et al.*, 2021), with a σ_1 NE-SW-oriented related to the Apenninic contraction. Furthermore, stylolites studied are bedding-parallel and horizontal after unfolding. Stylolitization is considered as directly linked to the burial of strata under the weight of the overburden before contraction.

Beyond the knowledge of the maximum burial depth reached in the different parts of the UMAR before the onset of Apenninic contraction there, the time at which the principal stress σ_1 changes from vertical to horizontal can be estimated by coupling inversion depth data with burial models. Thus, by plotting the burial depths provided by SRIT on the reconstructed burial curves for each area of interest, the timing of the onset of LPS is estimated from west to east for the 4 anticlines. The following results are summarized in Figure 5.16: ~10 Ma in Subasio, ~7 Ma in San Vicino, ~6 Ma in Cingoli and ~4 Ma in Conero. Thus, the beginning of contraction stage is older in the inner part than in the outer part, evolving from the Tortonian to the Zacléan, corresponding to a shift of ~6 Ma over a distance of about 100 km, without overlap in the ages.

IV- CONCLUSIONS

These cases of study are four field examples of application demonstrating the robustness and reliability of this methodological combination, coupling mesostructural, geochemical and paleopiezometric analyses, to constrain and reconstruct the sequence and timing of deformation at the fold scale. The main conclusions and contributions of these studies are as follows:

- the reconstruction of fracture and deformation sequence, consistent between the three cases of anticlines. The main stages of regional deformation were recognized, such as: (i) the foreland flexure, *i.e.* E-W extension under a σ_1 vertical; (ii) NE-SW oriented contraction related to LPS; (iii) fold growth and (iv) horizontal NE-SW contraction, associated with LSFT;
- the reconstruction of burial history experienced by strata using the SRIT applied to BPS. Burial depths values are consistent between the three cases of study and with previous studies leaded in the UMAR;
- the reconstruction of timing of deformation, and particularly the estimation of the onset of Apenninic contraction, for each anticlines studied.

The methodological contributions of this approach now tested at the fold scale, a question then arises: how to go further in using this methodology to assess timing and propagation of LPS at the scale of a foreland and FTB? The next and final chapter aims to discuss the different results and interpretations presented in the last three chapters (Chapters 3, 4 and 5), both from an applicative and methodological point of view.

General discussion

I- INTRODUCTION

Chapters 3, 4 and 5 present and interpret the different results of the SRIT and its application to real geological cases.

Chapter 3 demonstrates that SRIT is a robust method (the criterion of validity being predominant). Enhancements to the signals before the inversion process, *i.e.* the application of detrend and border effect corrections, improve the quality of the results. Furthermore, the inversion of concatenated stylolites of the same morphology, and belonging to equivalent geological formations and localities, tends to improve the consistency of the results between the two analysis methods (*i.e.* FPS and AWC). How does the inversion of composite stylolites improve the quality of the results? On the other hand, two inversion results considered as valid are not necessarily consistent. In this case, what value of L_c should be used?

Chapters 4 and 5 apply the method to several field examples. These studies demonstrate the contribution of this methodology in reconstructing the timing of burial and deformation at the fold and FTB scale. Nevertheless, they also assume several study hypotheses such as the choice of a geothermal gradient value, an estimation of the chemical compaction, the simultaneous development and end of stylolitization, ... To what extent do these hypotheses have an impact on the sequence and timing of the deformations? On the other hand, the switch of scales raises the question of the evolution of the fracture sequence on a regional scale, and of the consistency of this sequence on the fold scale and on the FTB scale. Finally, considering the contributions of this methodology in the analysis of vertical stresses, is it possible to assume that it can also help in the study of horizontal stresses?

The aim of this chapter is to discuss all these elements and to attempt to answer the various questions raised.

II- METHODOLOGICAL LIMITATIONS AND IMPROVEMENTS

1- How to explain inconsistency of results?

The statistical study presented in Chapter 3 demonstrates the robustness of the SRIT applied to BPS. It also highlights that the inversion of composite stylolites favors the consistency of the results. Two hypotheses follow from this observation, linking the improved results after concatenation to (1) a signal width effect (*i.e.* the longer the signal, the more consistent the results of the inversions) or (2) a signal sampling effect (*i.e.* the larger the range of roughness, the more consistent the results of the inversions). Another test is carried out to decide between (1) and (2), consisting in the concatenation of the track of the same stylolite several times. The width of the signal is thus increased, but the roughness range remains the same. The test is performed on stylolites whose inversions by the classical method give invalid and inconsistent results. The example given in Figure 6.1 shows that the concatenation of the same track does not improve the results of the inversions, which remain invalid or inconsistent.

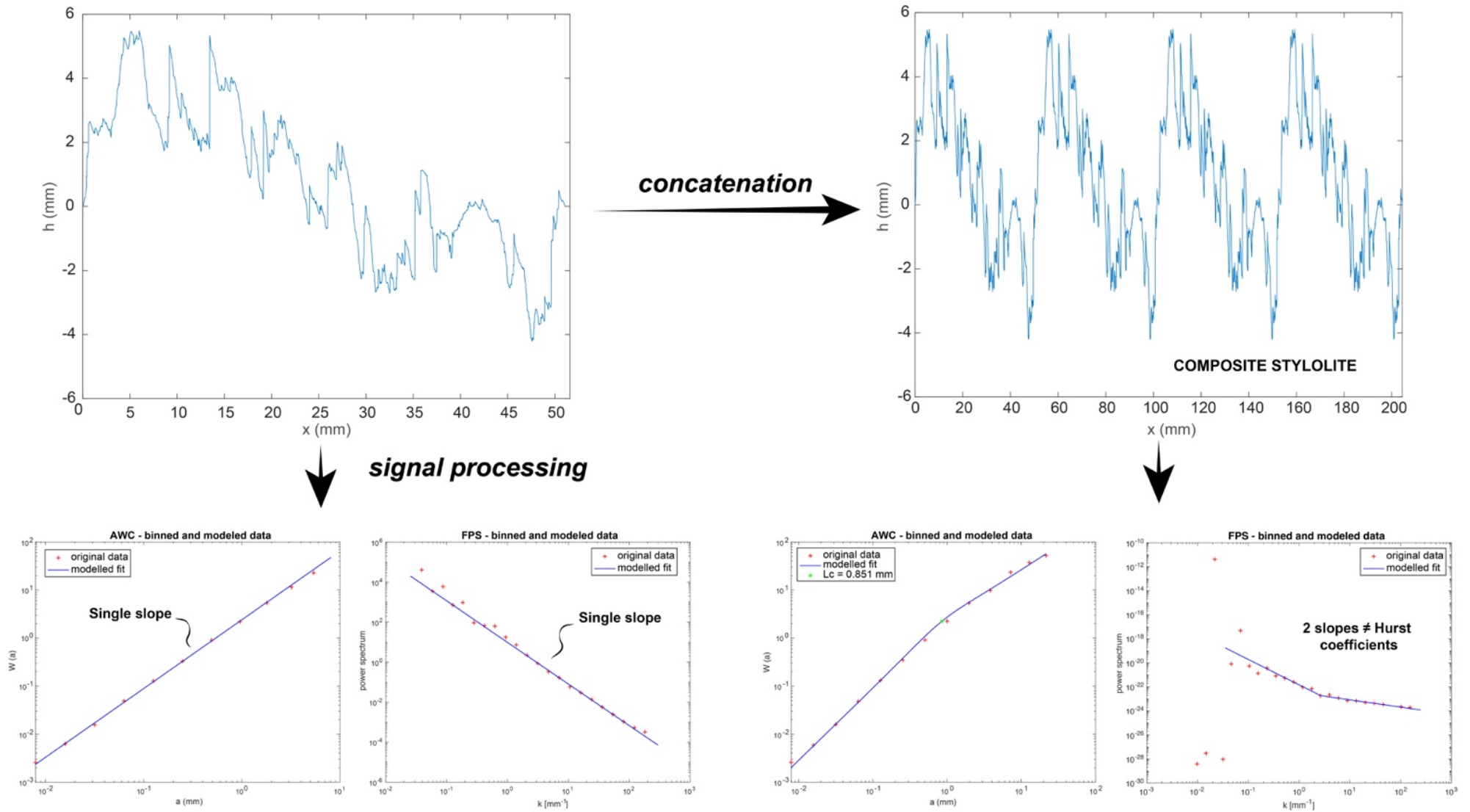


Figure 6.1- Concatenation of one single track 5 times. Non-linear regression curves are represented. Inversions are invalid before and after concatenation, demonstrating that signal length has no impact on the quality of the results.

Thus, the assumption that the validity and consistency of inversions would be better for longer tracks is definitely refuted. However, concatenation increases the number of frequencies associated with the signal (*i.e.* roughness range in the present case), and returns a more complete signal roughness range, thus increasing the quality of the regressions. The FPS seems to be very sensitive to this effect, as the concatenation significantly improves the validity of results. An interesting test would be to try to correlate the maximum local amplitude with the FPS results for this population of stylolites. The idea would be to highlight, or not, an impact of the vertical features on the validity of the L_c rendered by the FPS analysis, and thus also on the consistency of the results: if the results are invalid for high amplitude values, then this effect is verified. Finally, the robustness of classical method is confirmed thanks to the concatenation approach, the resulting inversions being valid in both cases, and all the more consistent as the roughness range is broader. The few cases where concatenation does not improve the quality of the results could then be explained by an insufficient roughness range, or by the fact that the stylolite does not fit the model, *i.e.* driven not by a chemo-mechanical model but by a physical or chemical model only.

2- Impact of stylolite morphology

Stylolite morphology could be related to the timing of the end of stylolite development, considering that (i) different morphologies can give access to different timings, and (ii) stylolites of the same morphology can form at the same time and record the same events (Ebner *et al.*, 2009b; Beaudoin *et al.*, 2019). Considering stylolites of the same morphology, if each of them individually inverted returns a value of equivalent L_c (*i.e.* valid and consistent) to L_c returned after concatenation, then they were formed at the same time and can therefore be grouped. Concatenation thus supports this morphology-timing relationship. Furthermore, this work demonstrates an impact of stylolite morphology on signal processing, both in terms of L_c values (*i.e.* lower for peak type morphology) and their statistic distribution (*i.e.* bimodal for columnar types, unimodal for peaks). Thus, this bimodal distribution suggests that the associated stylolites formed at different times (or in different areas, but local effects are assumed to be negligible as both types of morphologies are observed on all sample sites). The lowest values for peak stylolites assume that, in case of mud-supported lithology, they are more likely to record the maximum burial depth experienced by strata. Thus, morphology is a parameter that must be considered for the subsequent inversion process (*i.e.* calculation of vertical stresses and associated depths), since it impacts the results of the signal processing.

These results, associated with a recent work (Bah *et al.*, 2022), suggest that to document the maximum burial depth for mud-supported lithologies, it would be preferable to investigate class 3 stylolites (which record lower L_c , *i.e.* higher stress and depth). This statement is less true for grain-supported lithologies, as the maximum depth of burial experienced by strata is underestimated for both columnar morphologies and peak types (*e.g.* Bah *et al.*, 2022, with L_c related to grain-supported textures being significantly higher than those associated with mud-supported textures). All the data used are from mud-supported carbonate lithologies. A comparative study of these results in mud-supported

lithologies with data in grain-supported carbonates in the same study area, and for equivalent morphologies, could be conducted to determine whether lithology has any impact on the inversion process.

3- Validity and inconsistency of results, what solution(s) ?

One last case has not been discussed: what happens when the AWC and FPS inversions of the same stylolite are valid but inconsistent? For a population of stylolites in this case (n = 12, <10% of the dataset), L_c values returned by classical inversions are compared to L_c value obtained after concatenation (Figure 6.2). For single stylolites, L_c considered are those returned by AWC, FPS, and the average value of these two values. For composite stylolites, L_c is the mean value of the AWC and the FPS. There is no clear trend between L_c of composite stylolite and these returned by the classical AWC and FPS. But average L_c returned for non-concatenated stylolites overlaps L_c of composite stylolites in most cases. Concatenation therefore provides answers for this case where the inversions are valid and inconsistent: choosing the average L_c between the AWC and the FPS seems acceptable and would minimize the errors associated with this inconsistency.

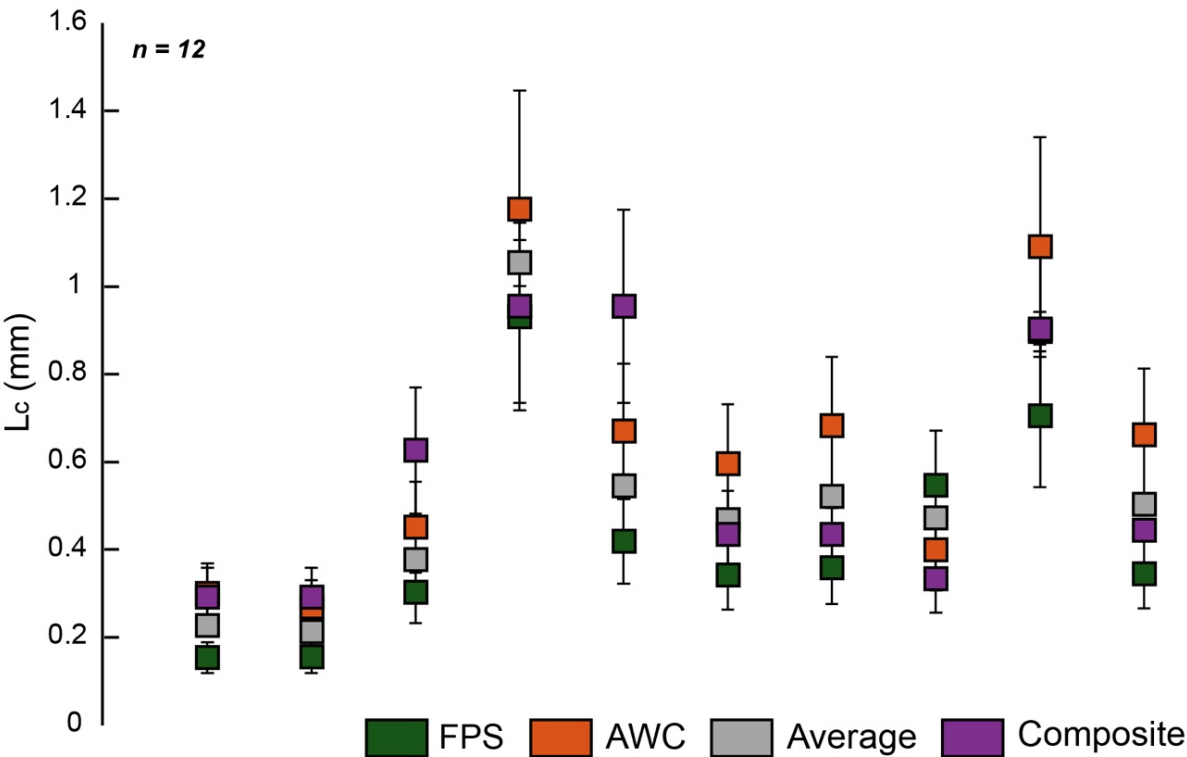


Figure 6.2- Comparison between (i) L_c returned by the classical FPS (green) and (ii) AWC (orange), their mean value (in grey) and (iv) the mean L_c obtained after concatenation (purple). 12 cases are considered, for which the inversions by the classical method return valid but inconsistent results.

III- EVOLUTION OF FRACTURE SEQUENCE IN THE STUDIED FOLDS

1- *Fracture sequence related to deformation history*

As a reminder, the UMAR underwent the following major deformation stages recorded by large networks of mesostructures, reported and interpreted for each anticline (Chapter 4 and 5 of this thesis; in Beaudoin *et al.*, 2020a; Labeur *et al.*, 2021; Lacombe *et al.*, 2021). These networks exhibit sequences that are consistent with each other and at the regional scale. Thus, the 4 stages of deformation recognized during these studies, and the associated mesostructures, are summarized below (Figure 6.3): (1) the forebulge stage, dated late Oligocene-early Miocene in the western part of the FTB and middle Miocene in the eastern part of the FTB (Brozzetti *et al.*, 2021). This early stage of deformation was related to the flexure of the downgoing lithosphere, and associated with a fracture set oriented ~N-S parallel to the flexed foreland; (2) the LPS event, an early-folding NE-SW-directed shortening related to the Apenninic contraction (Marshak *et al.*, 1982b; Storti *et al.*, 2001; Tavani *et al.*, 2008; Barchi *et al.*, 2012). The compression was dated early Miocene to the west, and middle Pliocene to the east (Brozzetti *et al.*, 2021), causing the widespread development of joints and veins striking ~NE-SW and perpendicular to the bedding, associated with tectonic stylolites with peaks of the same orientation, as well as reverse and strike-slip faults ; (3) the folding stage started by early Miocene in the western part and by late Pliocene in the eastern part of the UMAR (Calamita *et al.*, 1994). This stage was characterized by a maximum compressional stress oriented NE-SW (Tavani *et al.*, 2012b), *i.e.* parallel to regional shortening, and a local extension perpendicular to fold axis due to strata curvature at fold hinges (Beaudoin *et al.*, 2020a). Mostly, mesostructures associated with this stage of deformation were fractures oriented NW-SE and parallel to the hinge. Reactivation of normal faults and activation of strike-slip faults (*e.g.* in Monte Catria, where rotated dip-slip and rotated strike-slip faults are interpreted as syn-folding by Tavani *et al.*, 2008) were also related to this folding phase; (4) the late-stage fold tightening (LSFT), associated with a still NE-SW-trending contraction corresponded to ongoing shortening no longer accommodated, by *e.g.* limb rotation (Amrouch *et al.*, 2010a). Specific deformation structures were associated with this late contraction phase, (i) fore-thrusts in the forelimb and back-thrusts in the backlimb (Gutiérrez-Alonso & Gross, 1999; Tavani *et al.*, 2008), as observed in Subasio and Conero (Chapter 5); (ii) fractures and tectonic stylolites (of which respective planes and peaks are globally NE-SW to N-S oriented); (iii) conjugate strike-slip faults as described in Cingoli and San Vicino, related to the post-tilting horizontal NE-SW contraction. Recently, folding event was defined as the moment of shortening accommodation by pre-folding strata, from the onset to the end of the horizontal contraction at the origin of the fold (Lacombe *et al.*, 2021). Consequently, this event included LPS, fold growth and LSFT stages.

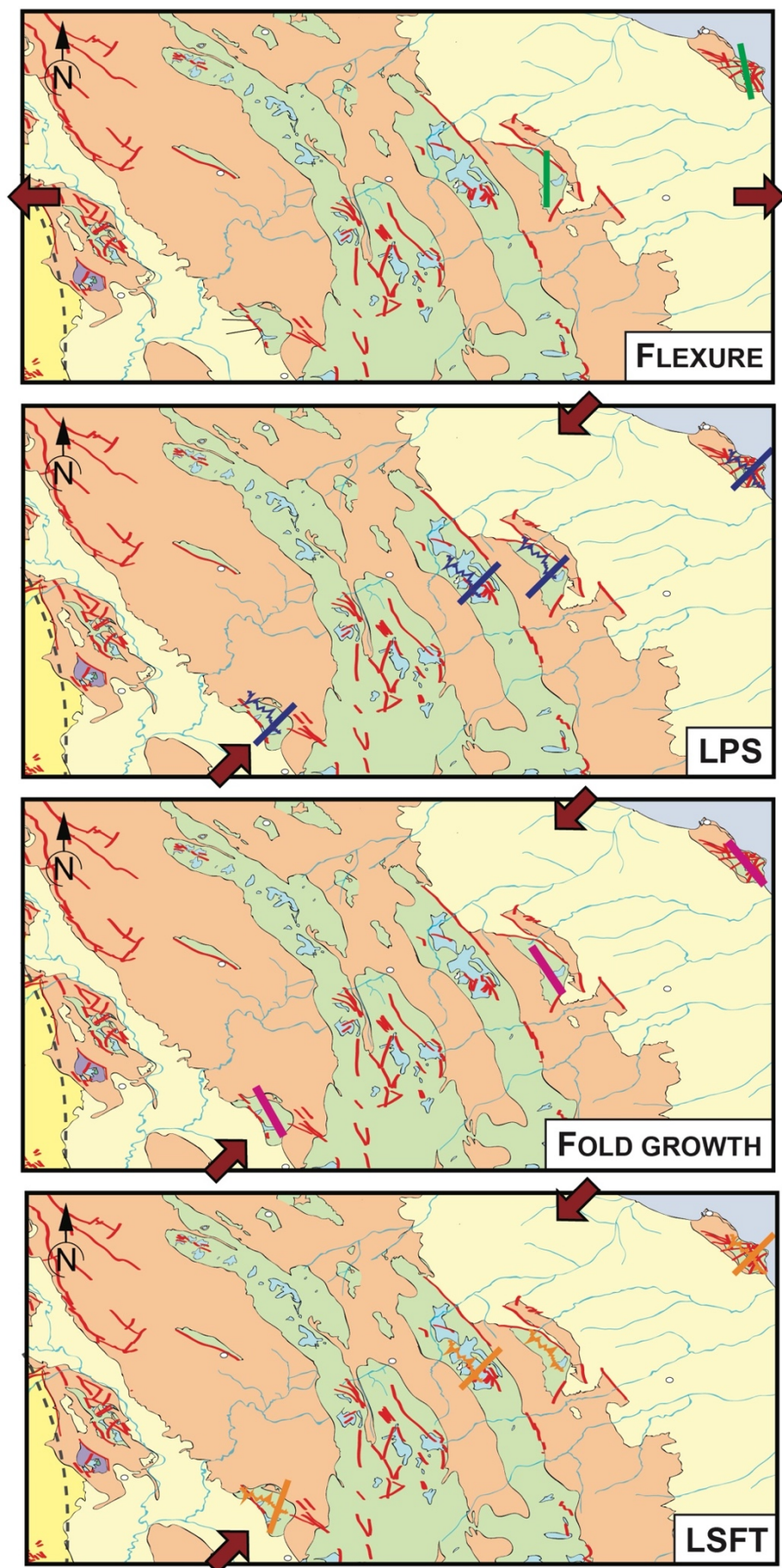


Figure 6.3- Synthesis of fracturing data at the UMAR scale. Fractures are represented by thick green, blue, pink or orange lines depending on the stage of deformation represented. The orientation of the inherited faults controlling the folding is given by the thick red lines. Red arrows indicate the direction of the maximum horizontal principal stress.

2- Contributions to the understanding of local and large-scale effects

For the different folds studied, the depth ranges deduced from the BPS inversion are equivalent for successive geological formations in the stratigraphic column, at the fold and FTB scale (Figure 5.5B). This means that the differences in thickness between the formations studied are not preserved, as the depth ranges are equivalent for strata of different ages. In this case, the development and end of stylolites would therefore be simultaneous, linked to a large-scale effect (*i.e.* development and end of stylolites respectively linked to a global burial under σ_1 vertical, and to the transition to a contractional stage under σ_1 horizontal, Figure 6.4). However, another case can be considered, for which the development and end of stylolites would be diachronic for different strata, notably due to local phenomena such as the reservoir effect and overpressure phenomena. In this case, the depth ranges recorded would vary from one formation to another, at the scale of the fold and the FTB, depending on whether they were impacted by these local phenomena (Figure 6.4).

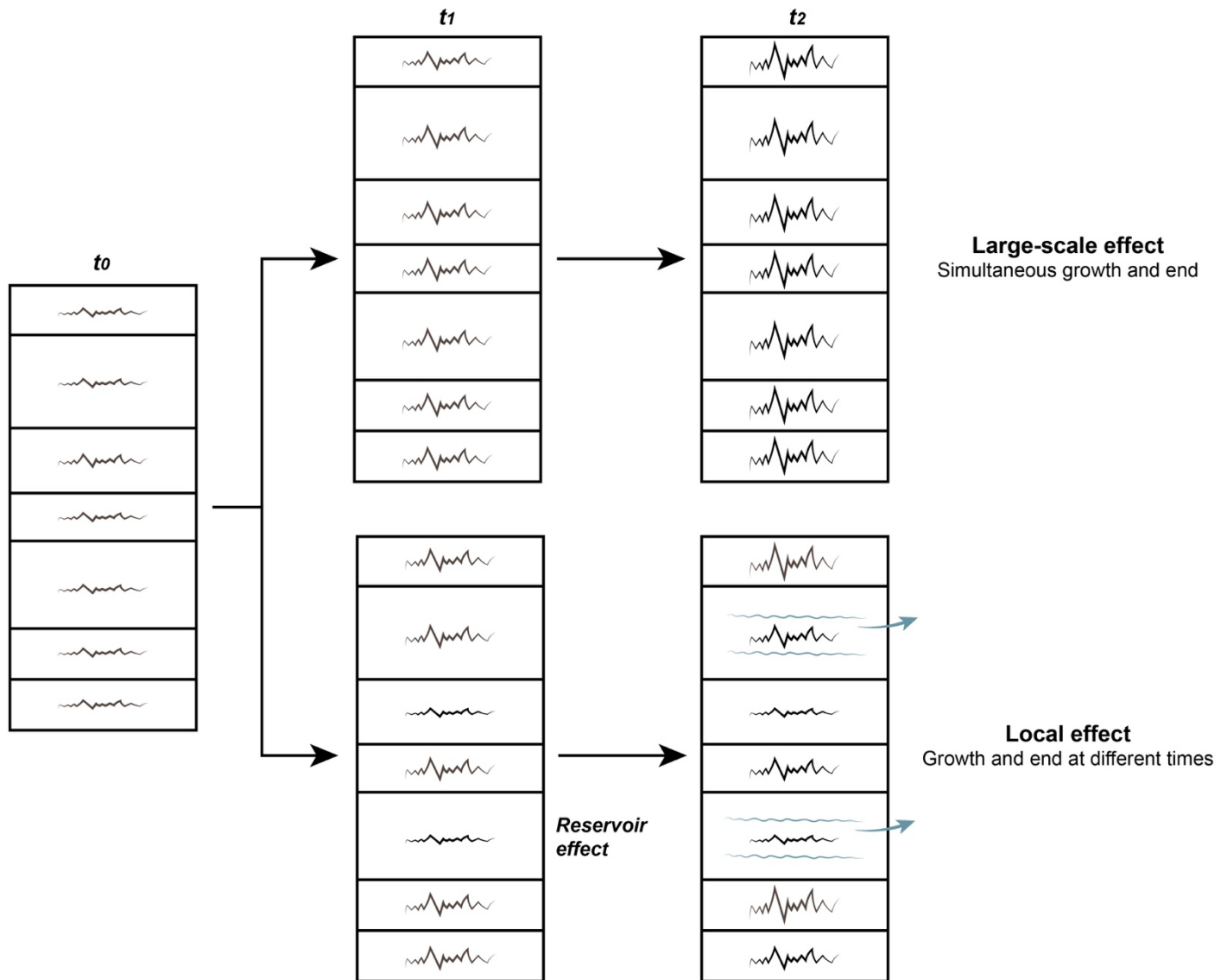


Figure 6.4- Model of stylolite growth and end over time. Two cases are illustrated: (i) linked to a large-scale effect, with simultaneous development and end of stylolites throughout the stratigraphic column; (ii) subject to local effects (*e.g.* reservoir, overpressure), causing diachronic development and end of stylolites in the different strata. Developing stylolites are represented in grey, those that are fully grown in black.

Beyond quantifying the burial recorded by the sediments over time, the SRIT applied to the BPS would also help to distinguish the large-scale effects of the phenomena, and to highlight those that predominate for a given case study. The robustness and the contributions of this methodology justify its application to real geological cases, *i.e.* one or more well-constrained folds, in an attempt to evaluate the timing and propagation of deformations related to folding.

IV- TIMING AND PROPAGATION OF FOLDING

1- At the fold scale: case of the Cingoli Anticline

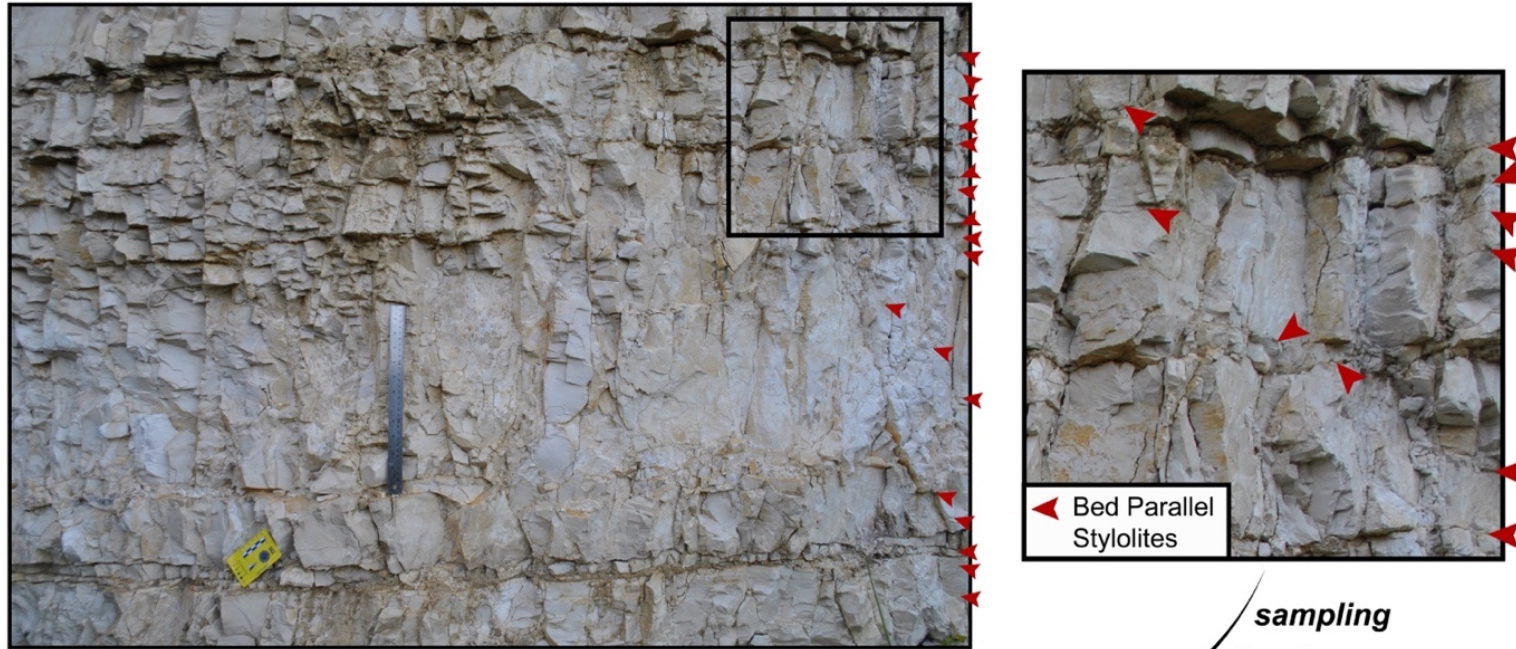
The combined study at Cingoli (Labeur *et al.*, 2021; Chapitre 4) demonstrates the reliability and contributions of sedimentary stylolite inversion in reconstructing the timing of burial and deformation. However, the use of this methodology implies some key and potentially impactful assumptions on the establishment of this timing, such as the geothermal gradient and chemical compaction values considered, as well as the location of the samples in the stratigraphic column. The aim of this section is to discuss these different elements, in order to assess their impact and the associated uncertainties.

1.1- Impact of the chemical compaction on the timing of deformations?

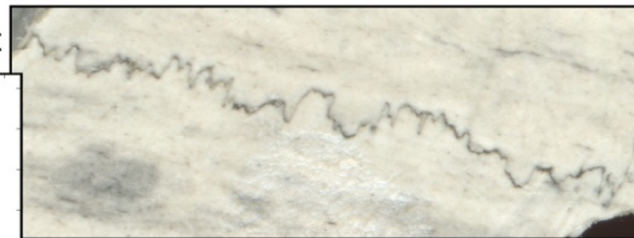
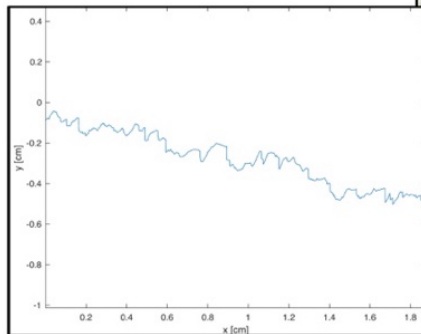
As described in Chapter 2, stylolites play an important role in this chemical compaction process, their amplitude being sometimes used as a means of direct estimation of the compaction undergone by rocks (Peacock & Azzam, 2006), and thus seem to be able to give an acceptable approximation of chemical compaction, especially in carbonate lithologies (as in the present case). In order to take into account the volume loss associated with this effect in the reconstruction of the maximum sediment thickness, the study presented for the case of Cingoli proposes the following method of estimation, based on field data (Figure 6.5).

Average number of sedimentary stylolites per meter is therefore estimated from the outcrop data (Figure 6.5). The maximum amplitude associated with each analyzed stylolite is also computed from the sample data; this step required writing a Matlab® script, which searches for the maximum tooth height for each stylolite redrawn and converted to a matrix in the initial computational steps of the inversion, with local smoothing of the signal to eliminate small scale effects. Chemical compaction is then deduced from these two parameters, calculated as the product of these two quantities, and expressed as a percentage (Figure 6.5). For the sake of reliability and robustness of the results, the process is repeated over the entire dataset. 112 estimates are thus made, distributed in 11 sites, 3 formations and corresponding to 35 beds. Statistical representation of results is further developed in the Figure 6.6, which gives the number of measurements and strata, and the standard deviation of the average number of stylolites per meter of beds, per measurement point and formation.

STEP 1 : measurement of the number of stylolites per metre : **N**



STEP 2 : computer treatment



sampling
drawing
digitalization

Compaction

Search for the height of the biggest teeth with local smoothing for each samples ; then calculation of the average : **A_{max}**

STEP 3 : calculation of chemical compaction

$$\text{Chemical compaction} = N \times \overline{A_{\max}}$$

Figure 6.5- Determination of chemical compaction: processing and calculation steps.

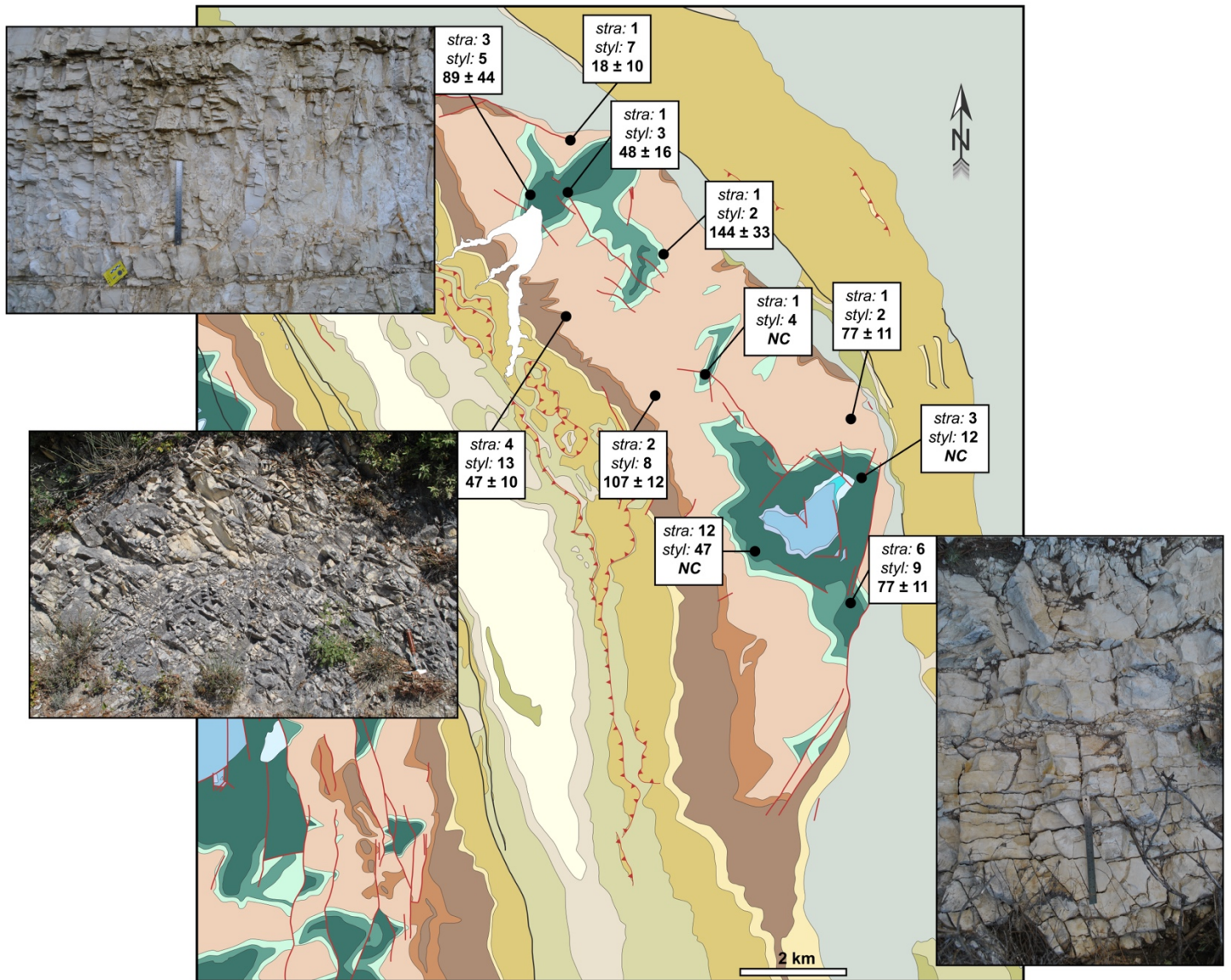


Figure 6.6- Distribution of chemical compaction data on the Cingoli Anticline, in map view. Per GPS point is indicated: the number of strata (*stra*) and the number of stylolites (*styl*) measured to calculate the compaction, and the average number of stylolites per meter of strata and the associated average deviation when the data allowed it (*NC*: not computed). The latter is calculated from field measurements: counting the number of BPS for a given rock height on each outcrop, then calculating the number of BPS per metre. Some of the outcrops studied are illustrated by field photos associated with the measurement site.

A last element for testing the reliability of this quantification is the comparison of the burial curves adding physical and chemical compaction effects with those only corrected for physical compaction. Figures 6.7 and 6.8 shows these two curves, and the resulting timing according to the methodology used and previously developed for this case study. Neglecting chemical compaction seems to generate burial curves with slightly steeper slopes and with less marked breaks in slope, sometimes shifted in time (Figure 6.7). However, the timing of the development of pressure-solution phenomena is not considered, as the method consists of estimating a quantity of shortening, then the initial thickness of the strata. Yet, several works studied the evolution of porosity in carbonate reservoirs and demonstrate the importance of early cementation in the reduction of porosity, with porosity occlusion dominating over its creation by dissolution during burial diagenesis (Ehrenberg & Nadeau, 2005; Bah *et al.*, 2022; Xu *et al.*, 2022). This last point may contribute to explain the variable appearance of the curves with or

without chemical compaction linked to pressure-solution, although the model automatically integrates a compaction law derived from natural data (notably porosity as a function of depth). Moreover, without chemical compaction, the deformation sequence remains equivalent, and the ages associated with the different stages of deformation diverge only slightly (Figure 6.8):

- (i) the flexure, which initiation is calibrated to the inflection point of the curves, is dated from 22.1 to 7.1 Ma (duration ca. 15 My), *versus* 21.2 to 6.6 Ma (duration ca. 14.6 My) when chemical compaction effects are considered;
- (ii) ages and duration of the LPS, dated from 7.1 to 5.8 Ma (ca. 1.3 My), are also close to those estimated from the curves including chemical compaction, *i.e.* 6.6 to 5.8 Ma (ca. 0.8 My).
- (iii) end of folding and beginning of the LSFT, estimated to be more recent when chemical compaction is not considered in the construction of the curves (1.8 Ma *versus* 3.1 Ma).

The shape of the burial curve potentially explains these few discrepancies in the interpretation of ages. Nevertheless, the differences observed are minor (even negligible), and the deformation sequence and timing being respected and consistent with the results and interpretations previously made and published (Labeur *et al.*, 2021) and with the existing literature as well (Calamita *et al.*, 1990, 1994; Mazzoli *et al.*, 2002; Brozzetti *et al.*, 2021).

Although the number of stylolites analyzed is relatively large, their distribution is not sufficient to cover the entire fold in a representative manner (around 1% of the fold is covered). However, the test carried out on the burial curves reflects the small part of chemical compaction compared to physical compaction: the shape of the curves remains globally stable, the deformation sequence and the associated timing are consistent and only slightly variable. Based on these observations, estimating chemical compaction from stylolites and then introducing it into burial model construction appears to be justified in the context of this methodology. Similarly to the methodologies previously considered, this chemical compaction calculation method is a rough estimate which tends to maximize the chemical compaction values. More than an exact quantification, this is more an attempt to illustrate a geological reality at the data points studied, without impacting the final interpretations. As a result, this method can therefore be considered acceptable and usable, keeping in mind that these are rough and not absolute estimates.

Finally, the impact of chemical compaction in the application of this methodology appears to be negligible, contrary to the reservoir models where compaction parameters are highly impactful (in relation to the reservoir properties such as porosity and permeability, which are strongly affected by the recorded compaction rates). The integration of chemical compaction in the construction of burial curves as quantified in this study seems justifiable, with the possibility of improving the data set in spatial and quantitative ways.

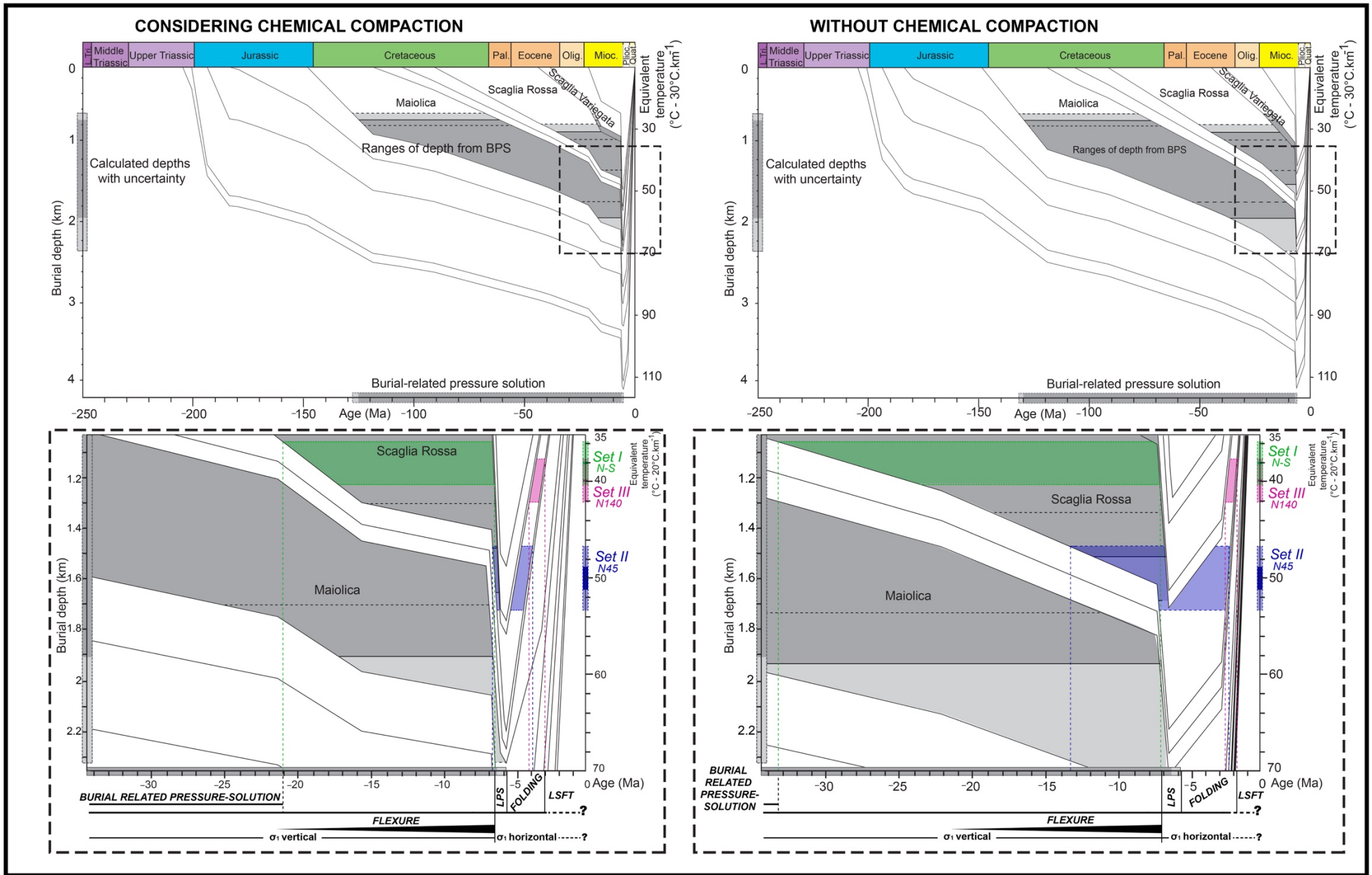


Figure 6.7- Impact of the chemical compaction on burial curves construction.

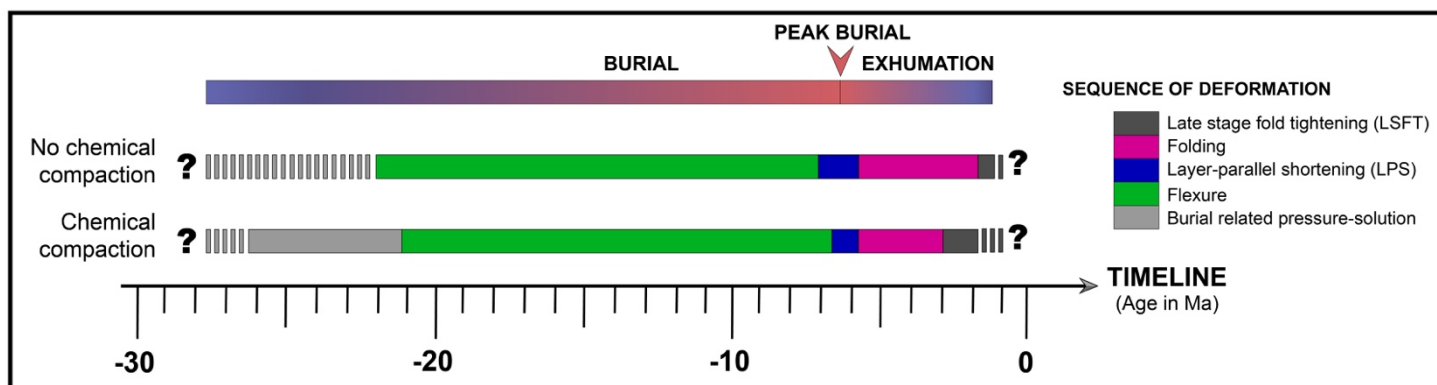


Figure 6.8- Impact of the chemical compaction on timing of deformation interpreted

1.2- Impact of the geothermal gradient on timing of deformations

This methodology implies a strong assumption on the geothermal gradient, given as input to the software. A question arises: in the framework of this methodology, is this assumption as restrictive as for other temperature-dependent methods? Thus, a sensitivity study applied in the framework of the case study, *i.e.* the Cingoli Anticline, should provide an estimate of this variability by making two parameters vary: the slope of the geothermal gradient and the surface temperature. Therefore, the methodology developed in this study, using a geothermal gradient of 23°C/km and a surface temperature of 10°C, is reiterated in 2 other configurations involving a variation of the slope, *i.e.* geotherms of 20°C/km and 30°C/km respectively. As a reminder, 23°C/km geothermal gradient value corresponds to the quaternary geothermal gradient of estimated by Caricchi *et al.* (2015) from vitrinite reflectance (dataset and previous models and studies, *e.g.* Sweeney & Burnham, 1990, Hillier *et al.*, 1995), for the northern part of the Apennines. Temperatures derived from the clumped isotopes thermometry (Labeur *et al.*, 2021) are plotted on the resulting burial models (Figure 6.9), and the deformation schedule is constrained for each of these gradients using the same methodology. All results are compared in Figure 6.10, adding results of published work of Labeur *et al.* (2021) using a 0°C surface temperature, to estimate the impacts of both the uncertainty in the geothermal gradient and the surface temperature on the deformation schedule and sequence.

The sequence of deformation stages is similar despite the variation of the geothermal gradient (Figure 6.9). In contrast, the ages of these deformation stages vary with the geothermal gradient (Figure 6.10): (i) the flexure is initiated at 21 Ma whatever the geothermal gradient considered and according to the inflexion point of burial curves. But the end age of the flexure ends varies with the geothermal gradient, younger for lower geothermal gradient values (Figure 6.10); (ii) the LPS, the duration of which increases with the geothermal gradient. While the end of the flexure remains the same, estimated at 5.8 Ma (Beaudoin *et al.*, 2020a), this stage of deformation begins later for higher geothermal gradients, *i.e.* 6.4, 6.6 and 6.8 Ma for 20, 23 and 30°C/km, respectively (Figure 6.10). The duration of this deformation phase is also impacted by the surface temperature considered, with an interval of [6.3-5.8] Ma for a temperature of 0°C, and [6.6-5.8] Ma for 10°C. Thus, as the geothermal gradient and surface temperature decrease, the LPS duration decreases (Figure 6.10); (iii) the end of fold growth and the

onset of LSFT occurred later when the geothermal gradient increases. Thus, our appraisal of the duration of deformation, and particularly of LPS and folding, is also impacted by the geothermal gradient considered: the higher the geothermal gradient, the longer the deformation stages. The inferred duration of deformations therefore varies with the geothermal gradient (for a same surface temperature of 10°C): for a variation of 1°C/km, the timing fluctuates from 0.04 to 0.13 Ma (minimum and maximum variations), and on average by 0.08 Ma, values respectively associated with a relative uncertainty of 4.8%, 8.3% and 5.8% on the age of the deformations. All these values are calculated from Figure 6.9 taking as reference the ages estimated for a geothermal gradient of 23°C/km (Caricchi *et al.*, 2015), and a surface temperature of 10°C/km. Nevertheless, the time ranges overlap for each deformation phase (Figure 6.10), regardless of the gradient considered.

The use of stylolite palaeopiezometry aims to overcome some of this problem by the possibility of considerably multiplying the data, which is not necessarily possible with conventional methods. The shape of burial rate curve is therefore an element of sensitivity impacting ages of deformations: the calibration of the ages (and in particular of the LPS) being carried out in the part of the curve where the slope is the steepest, a small shift of temperatures necessarily causes an important temporal shift. This implies a loss of sensitivity for domains with high burial rates at several times in the geological history. Burial curves related to these domains are strongly steep, and thus the estimated ages are more sensitive to geothermal gradient variations and potentially biased. Conversely, the estimation of ages for domains with low subsidence (*i.e.* associated with low slope curves) is therefore less affected by the choice of geothermal gradient and temperature. Moreover, the diminution of LPS duration with the decrease of the geothermal gradient and temperature highlights a hot or cold effect for which the geothermal gradient and the temperature have each an equivalent and non-negligible impact: the colder the system, either because of a weak geothermal gradient or a low surface temperature, the shorter the inferred duration of the LPS, always because of this important temporal shift linked to a strong geothermal gradient. In conclusion, the problem of fixing temperature values is partly solved, as the model is only sensitive to it when the burial curves are steep (*i.e.* domains with high subsidence rates)

Finally, assuming a geothermal gradient remains mandatory. However, the previously presented sensitivity study shows that the lower the subsidence rates, the lesser the impact of this assumption. In areas where tectonic deformation is important (*e.g.* fold-and-thrust belts), subsidence and uplift rates are nevertheless rarely low, and thus this assumption remains important. Although impactful, the choice of given geothermal gradient remains less constraining in the application of this methodology than for classical thermo-dependent methods. Indeed, data acquisition and processing do not involve any dependence on temperature, which has only a partial impact on interpretation (*i.e.* temporal shift related to the shape of the curves and subsidence rates). Therefore, L_c and σ_v calculation, and the estimation of associated burial depths using SRIT applied on BPS, are independent of temperature. Using absolute dating methods such as U-Pb to date the mesostructures contemporary with the BPS to which the SRIT is applied, the following data can be quantified: (i) σ_v and associated burial depth

magnitude and (ii) the age of the studied BPS development. The determination of the gradient most fitting with these data on the burial curves allows the rest of the dataset to be calibrated. The most reliable geothermal gradient can then be approximated by finding which value of geothermal gradient best coincides with these data on the burial curves. Thus, a single absolute age associated with a burial depth and curves is sufficient to calibrate the entire dataset. The problems of assumptions are thus partially overcome, since the sensitivity of the models is less, and the multiplication of direct dating such as U-Pb, expensive and often difficult to obtain, is no longer necessary (a single age being sufficient to calibrate the whole dataset). However, when subsidence rates are high, one must be aware that the inferred durations depend on the assumptions made and are thus more or less important.

Considering the impact and uncertainties associated with these different parameters, *i.e.* geothermal gradient and chemical compaction values, and sample position, the results can be discussed on a larger scale. The following section therefore discusses the use of this methodology for the assessment of the timing and propagation of folding at the FTB scale, and the new interpretations and conclusions that can be inferred.

1.3- Impact of the stylolite sampling

According to this methodology, the position of the sampled stylolites within the stratigraphic column can impact the definition of deformation ages is the position. As a matter of fact, ages can vary significantly depending on whether the stylolites are positioned at the top or at the base of the formation, as well as its thickness. Thus, for thin formations, *e.g.* the Scaglia Variegata, the inferred age does not vary significantly, the interval between the bottom and top curves being limited. In contrast, for thick formations like the Maiolica or the Scaglia Rossa, the position of stylolites is essential because the deduced ages considerably vary because of the important interval between the top and bottom of two curves defining the formation. For this study, the samples are referenced at the base as well as at the top of the formations. Tops of the curves can therefore be used to establish the timing of the deformation.

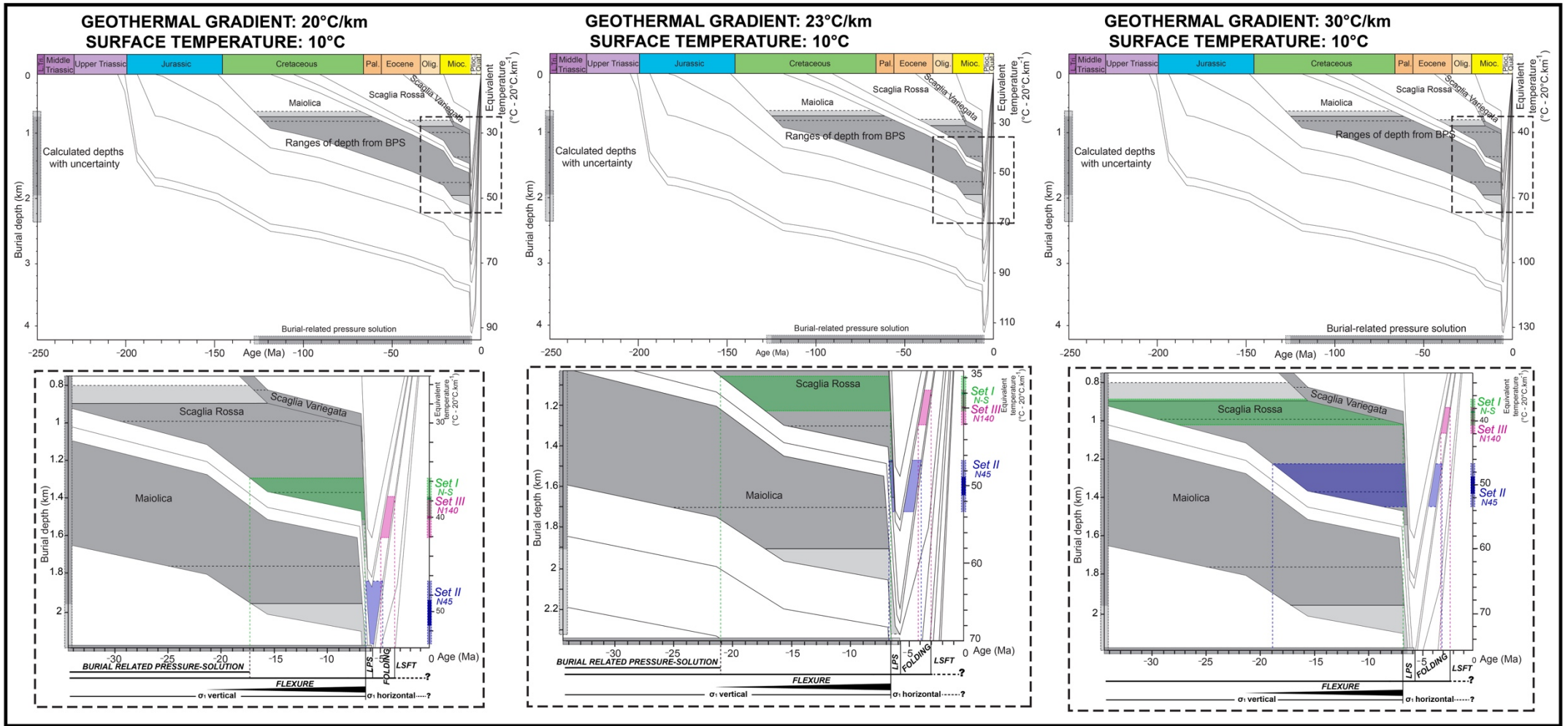


Figure 6.9- Burial models for geothermal gradients of 20°C/km, 23°C/km, and 30°C/km, considering a surface temperature of 10°C. The stratigraphic data and methodology are identical to those used in the work of *Labeur et al (2021)*.

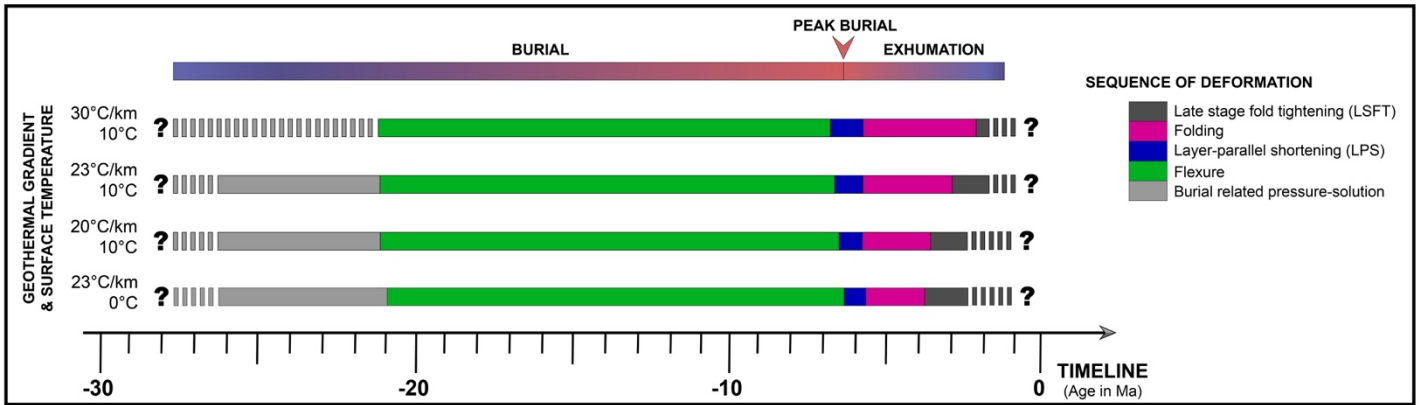


Figure 6.10- Comparison of results for the different cases considered: synthesis in terms of timing and deformation sequence;

2- At the fold-and-thrust belt scale

2.1- Shape of burial curves

A first point that deserves discussion is the difference between the burial model built for Conero and these of Subasio, San Vicino and Cingoli. The forebulge stage illustrated in the other burial models is seemingly not recorded at Conero. One possible explanation could be the position of the Conero Anticline in the system, located in the easternmost part of the belt where the bulge may not have occurred. In addition, significant evolutionary differences from the rest of the UMR were recorded. For example, Costa *et al.* (2021) suggested a significant differential subsidence related to an extensional phase in the early Pliocene followed by a compressive deformation in the middle Pliocene, which was not observed in the northern sector of the Marche region. On the other hand, differences in stratigraphic sequence were highlighted in Monte Conero from the rest of the UMR, with no exposure of the Triassic and Jurassic formations in this external part of the FTB (Fancelli & Radrizzani, 1964a; Díaz General *et al.*, 2015; Costa *et al.*, 2021) and a stratigraphic gap identified between the Scaglia Bianca and Scaglia Rossa formations (*i.e.* missing of the boundary called Bonarelli level). Moreover, this part of the FTB is on the coast and still highly exposed to marine erosion and landslides (*e.g.* Angeli *et al.*, 1992, 1996, Sirolo landslide). That's why this hiatus can be explained by a large submarine collapse, causing the transport of missing formation sediments to deeper areas of the ancient basin (Montanari & Sandroni, 1995). The shape of the curves could be impacted by these events which generate losses of volume and thickness of sediments.

2.2- Determination of the onset and of the duration of the LPS

The estimated ages for the onset of LPS, including uncertainties, are consistent with the known deformation sequence for the whole FTB. The results obtained are robust and consistent with the overall geological context. The application of the SRIT in the context of the foreland and fold-and-thrust belt is therefore validated.

For the sake of simplicity, the onset of the LPS is considered when $\sigma_v \leq \sigma_H$. The switch of σ_1 related to the onset of LPS is estimated to predate fold growth for each anticline. The works of Calamita *et al.*

(1994) on the UMAR, and these of Mazzoli *et al.* (2002) carried out in the San Vicino-Cingoli area, are based respectively on tectono-stratigraphic, seismic, and growth strata studies. They dated the initiation of compressional events to late Miocene-early Pliocene (Calamita *et al.*, 1994) with a fold growth constrained from the late Messinian to the Zanclean (ca. 6-4 Ma, Mazzoli). This timing agrees with the estimate of the onset of the LPS ~7-6 Ma for this study area (Figure 6.11). Similarly, structural and sedimentary studies (*i.e.*, identification of lower-middle Pliocene deposits affected by compressional structures) and seismic interpretations conducted at Conero proposed the onset of compressional events by the middle Pliocene (3.6 Ma, Carruba *et al.*, 2006; Costa *et al.*, 2021). This age is consistent with the timing established for this anticline, dating the initiation of the LPS at ~4 Ma. In the westernmost part of the UMAR (Subasio area), geochemical and isotopic data (Beaudoin *et al.*, 2020a) suggested an earlier compression (Tortonian-Messinian, around 8 Ma), which is in line with the possible initiation of the LPS at ~10 Ma.

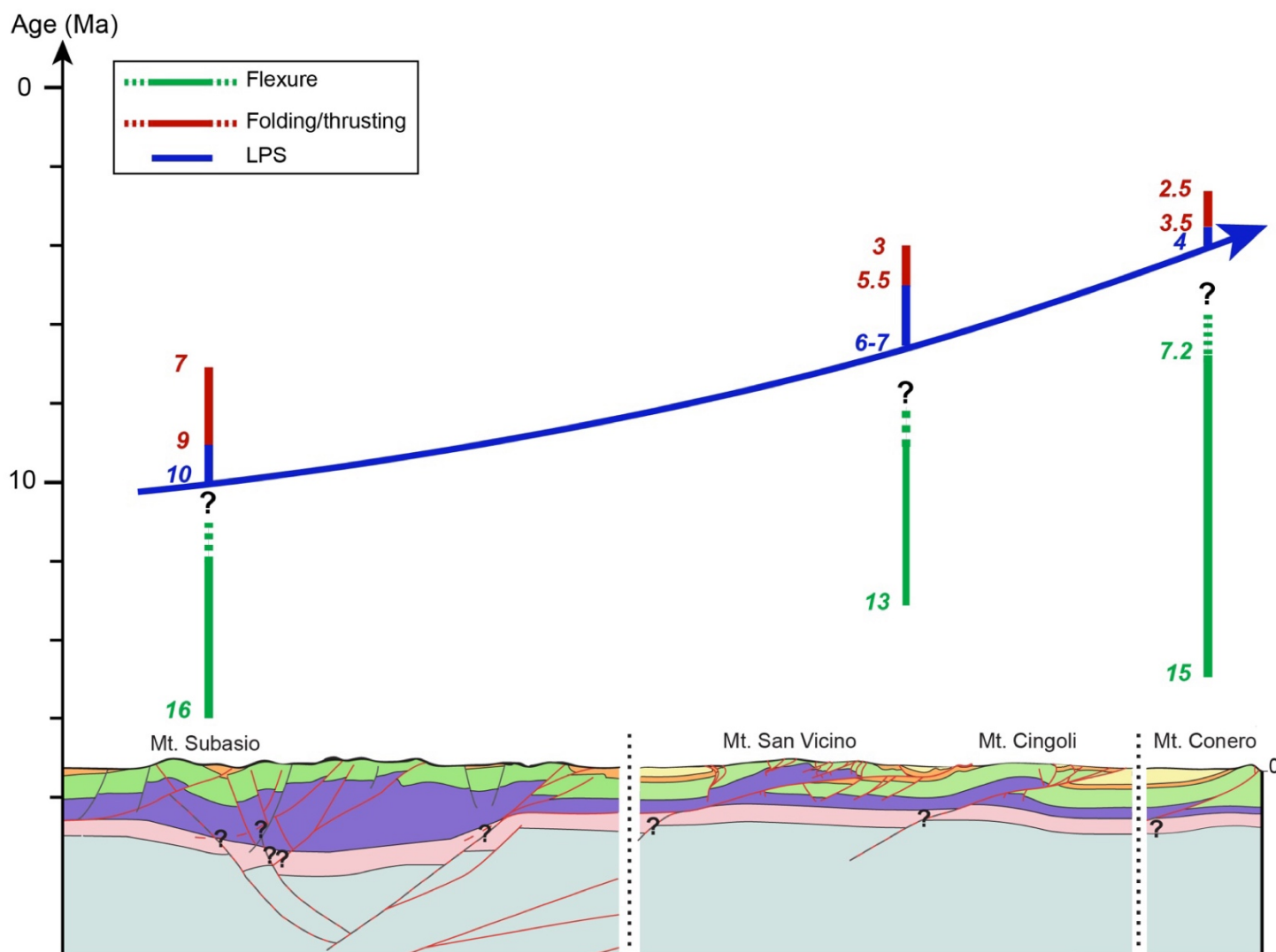


Figure 6.11- Synthesis of flexure, LPS and folding stages across the UMAR. The colours green, blue and red are associated with the onset and duration for each of these stages of deformation: green for the flexural stage and given by bibliographic data (Calamita *et al.*, 1994); Guerrero *et al.*, 2012), blue for the LPS and given by these studies, red for the folding stage and given by the work of Lacombe *et al.* (2021).

The duration of burial and the timing of the onset of contraction, inferred from the combined use of burial models and computed burial depths, are also consistent from a spatial perspective: as the burial is continuous from the Cretaceous to the late Miocene-early Pliocene and ends later in the eastern than in the western part of the UMAR, the LPS tends to affect rocks later from west to east. This likely reflects the eastward propagation of deformations during the building of the UMAR, as largely described in literature (Lavecchia *et al.*, 1988; Cello *et al.*, 1997; Ghisetti & Vezzani, 2002; Tavani *et al.*, 2012a). Considering these data, *i.e.* beginning of LPS and folding, the duration of LPS can be estimated for each anticlinal structure: ~ 1 My in Subasio, ~ 1.5 My in San Vicino, ~ 0.5 My in Cingoli and ~ 0.4 My in Conero. Thus, the duration of the LPS seems relatively similar at the scale of foreland and FTB, around a mean value of ~ 1 Ma.

2.3- Dating and quantifying the horizontal stresses build up

Another potential implication of this work would be the spatial and temporal characterization of evolution and magnitudes of horizontal stresses. The burial curves provide a quantitative estimate of the magnitude evolution of vertical stress σ_v over time. Furthermore, this work allows to calibrate the moment of σ_1 switch between vertical and horizontal, *i.e.* the moment when the condition $\sigma_v \leq \sigma_H$ is satisfied. Thus, under the assumption of a build-up model with a W-E propagation of deformation, and considering the timing of the first fold growth and for which σ_1 switch moment is estimated, two additional stress magnitudes can be quantitatively assessed:

- (i) in the area where contraction begins, the minimum magnitude of σ_H can be computed, which necessarily satisfies the condition $\sigma_v \leq \sigma_H$. σ_v corresponds to the maximum magnitude returned by the BPS inversion;
- (ii) in the front zone (contraction not yet started), where the the condition $\sigma_H < \sigma_v$ is fulfilled, the maximum magnitude of σ_H can be estimated. σ_v is deduced from burial curves, and corresponds to the maximum burial recorded by strata for a reference formation (*i.e.* same formation considered for all folds studied).

The results of this approach are summarized in Figure 6.12, which traces the evolution of σ_H and σ_v magnitudes, as well as the LPS zone evolution, in map view, cross-section, and graphically over time. The estimates of the magnitude evolution with time (plots on Figure 6.12) tend to demonstrate a coevality between the start of the fold growth, *i.e.* the decrease of the magnitude of σ_v , and the LPS initiation at the front of the belt. Such timing is also observed in other case studies of simple accretional prisms (*e.g.* Bourlange *et al.*, 2007).

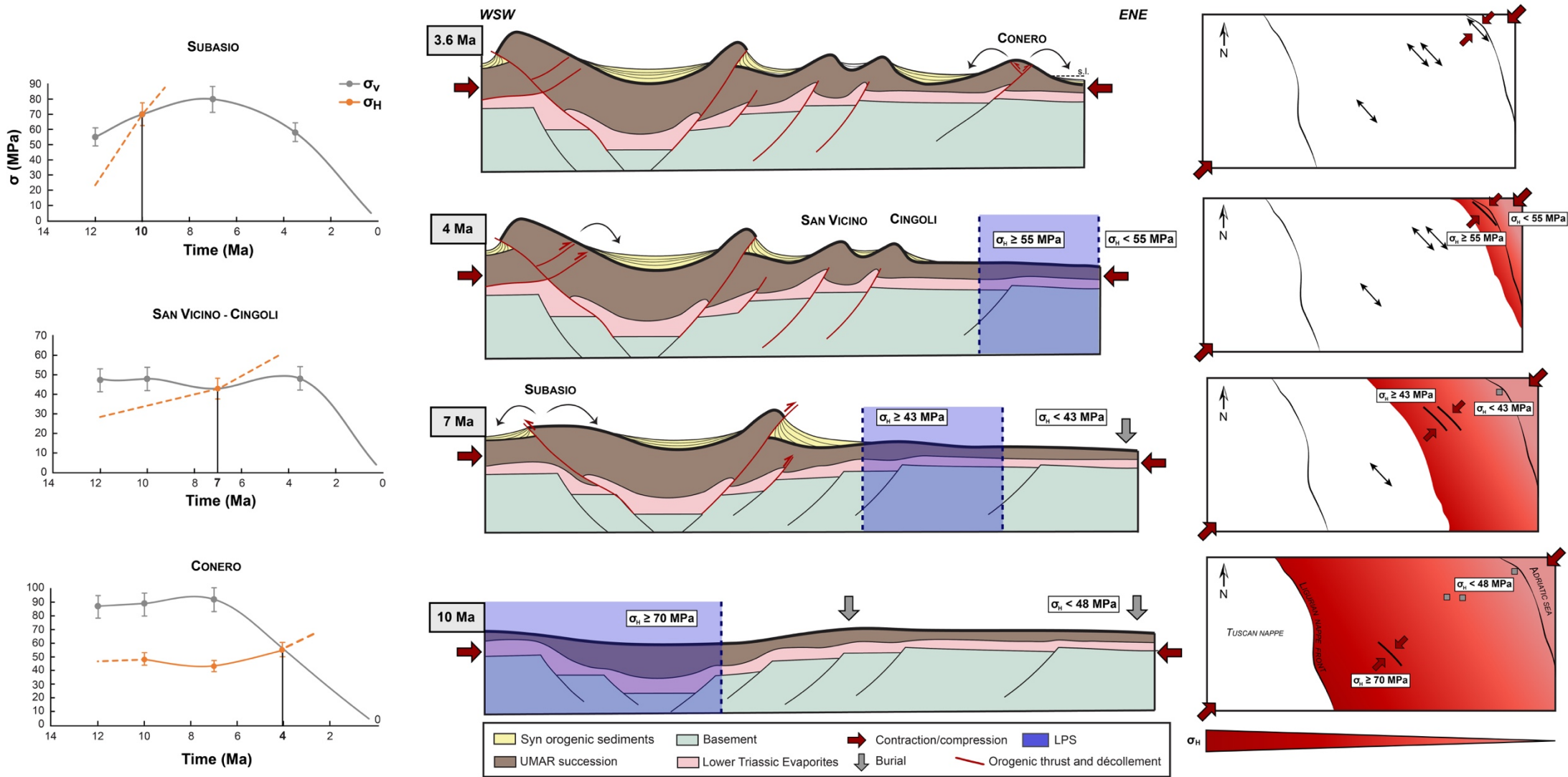


Figure 6.12- Spatial and temporal evolution of σ_v and σ_h magnitudes, in map view, cross-section and graphically. Maps and cross-sections are represented in sketch form. Vertical shortening is not calculated, and vertical scale is exaggerated on cross-sections. Magnitudes are deduced from depths returned by SRIT application on BPS and these given by burial models. The evolution of the LPS is also represented on these sections, indicated by the blue areas in transparency.

Some locks remain in this quantification of horizontal stresses. For a given area, this approach does not allow the estimation of σ_H magnitudes after the time of the σ_1 switch (Figure 6.12). Additional quantitative data are required to refine the evolution of σ_H magnitudes over time and space, which is provided by palaeopiezometers such as tectonic stylolites and calcite twins.

2.4- Debate on structural style

One last point can still be discussed: the potential contribution of this methodology to the understanding of structural style, which is still debated in the Apennines. The duration of stress/strain accumulation in rocks required to generate folding can depend on structural style (Beaudoin *et al.*, 2020b), and can be reflected to some degree by the duration of LPS. Considering this, the work Lacombe *et al.* (2021) is focused on the study of 3 anticlines differing in their structural style, and show differences in the timing and durations of deformation stages. They support that a longer LPS, corresponding to a higher level of differential stress, is required to cause the inversion of a high-angle basement normal fault and related forced folding of the undetached sedimentary cover (the Sheep Mountain Anticline) than to initiate folding of the cover above a weak decollement (Pico del Aguila, Cingoli and San Vicino, Figure 6.13A). They also explain the longer LPS at Pico del Aguila with respect to San Vicino and Cingoli likely is in line with the longer accumulation of displacement required to initiate folding oblique to the regional compression rather than perpendicular to it. In addition, the four Apennine examples studied in this PhD show that: (i) the onsets of LPS and fold growth are increasingly young from west to east; (ii) LPS and folding durations are relatively short, *i.e.* 1-2 My. All these data suggest that, at the scale of the FTB, the deformation is propagated by the decollement level, with the location of the folds in line with the inherited basement faults (Figure 6.13B).

In summary, beyond accessing the burial-deformation calendar, the inversion of sedimentary stylolites could provide insights into the timing and mode of deformation propagation at the fold and FTB scale. Thus, this methodology could be a powerful tool for understanding the structural style of the study area.

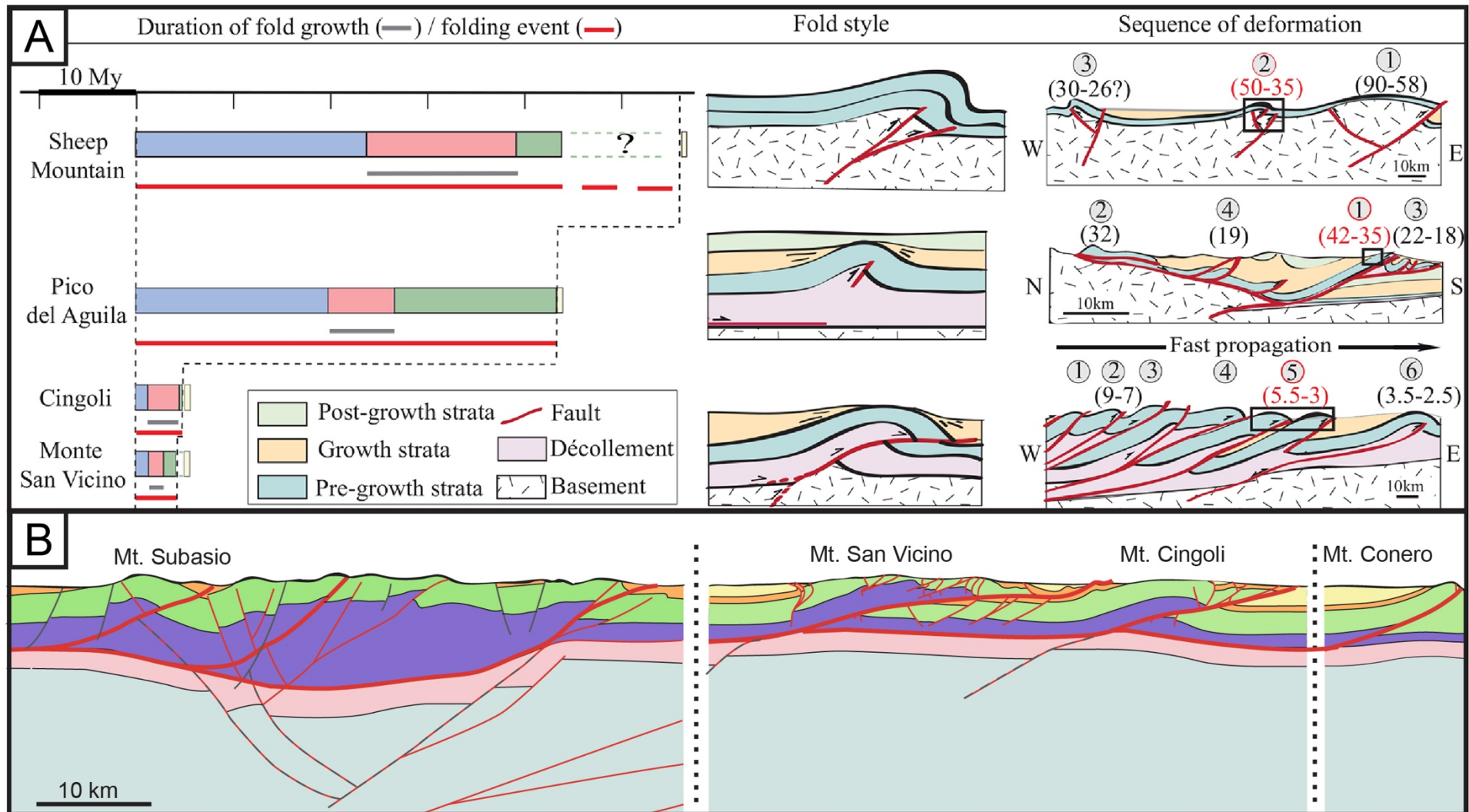


Figure 6.13- (A) Relation between durations of deformation stages of folding event, fold style (*i.e.* final fold geometry) and sequence of regional deformation. Circles 1 to 6 indicate the order of structural style development, *i.e.* sequence of folding/thrusting, with corresponding ages in Ma (in parentheses). The colour code is: blue for the LPS, red for the fold growth, green for the LSFT and yellow for the post-folding extension/compression; from Lacombe *et al.* (2021). (B) Structural style proposed for Umbria-Marche based on data from this study and previous works (Beaudoin *et al.*, 2020b; Lacombe *et al.*, 2021). The suggested model proposes a propagation of the deformation through the level of décollement, *i.e.* the diachronous formation from west to east of fault-bend folds along a flat-ramp décollement.

General conclusion

Firstly, the application of SRIT on a large dataset, and particularly the test of the signal processing methods (*i.e.* FPS and AWC) on BPS sampled in the whole UMAR, help to identify the impact factors, to unlock some methodological limits, and also to demonstrate the robustness and reliability of this palaeopiezometric method. The proposed improvements in terms of drawing, *i.e.* computer-assisted track segmentation, allow for a gain in time and efficiency before the inversion process. In addition, the proposed corrections to slope and edge effects allow for better quality inversion results, *i.e.* L_c valid and more consistent the two signal processing methods. Moreover, contributions of the comparative study between the inversion of individual and composite stylolites (*i.e.* grouping of stylolites of the same morphology and formation) are several:

- (i) first, concatenation supports and consolidates the classical SRIT method consisting in the inversion of individual stylolites;
- (ii) it also demonstrates that the inconsistency of the inversion results is most likely explained by a roughness range that is not sufficiently covered. In some cases, it is not sufficient to increase the quality of the results, most likely indicating that the inverted stylolites do not fit the model.
- (iii) it reveals the impact of morphology on the inversion results, with a differential recording of L_c values (and therefore of vertical stresses and recorded depths) depending on whether the stylolites are peaked or columnar. It also tends to support the idea that timing and morphology are linked when the results of inversions are equivalent before and after concatenation of stylolites of the same morphology.
- (iv) finally, it allows to decide when the L_c returned by the AWC and the FPS are valid but incoherent for the same stylolite, by recommending the choice of the average between these two values.

Hence, the statistical study carried out enables to answer and overcome some methodological locks. Despite the attempts at optimization, the question of minimizing the uncertainty in the determination of the cross-over length persists, the choice of the value still being left to the user. It would be interesting to consider further studies on the subject, to try to automate this part of the inversion, with a determination of the slope break that becomes partially or even totally independent of the user.

Then, the application of this innovative methodology at the scale on several folds highlights multiple implications for the study of foreland-FTB systems. The application of SRIT to BPS, coupled with the reconstruction of burial curves, allows to estimate to first order (i) the burial experienced by strata before contraction, and (ii) the onset of the LPS, assuming it corresponds to the moment when the principal stress σ_1 switches from vertical to horizontal. The recorded depths would also reveal possible local effects responsible for a diachronic stop of stylolitization. The application of this method on several anticlines allows not only to assess the evolution of vertical stress experienced by the sediments, but also the timing of the switch between σ_v and σ_H , consistent on a large scale. A second major implication of this large-scale palaeopiezometric study is the ability to trace the horizontal stress magnitude σ_H at

the time of the σ_1 switch, both at the location of the growing fold and at the front of the FTB. Thus, the evolution of horizontal stress σ_H can be estimated semi-quantatively, both spatially and temporally, and without involving the use of palaeopiezometers quantifying horizontal stress magnitudes or differentials. But, the use of these tectonic paleopiezometers such as tectonic stylolites and calcite twins would (i) complement this approach by, (ii) overcome this limitation and thus reconstruct the spatial and temporal evolution of horizontal stress at the foreland-FTB scale and (iii) definitively validate the palaeopiezometry of the BPS for the quantification of horizontal stress prior and at the beginning of contraction (*i.e.* LPS onset).

Finally, this study highlights the possible contributions of this methodology to the study of such a geological system. The potential correlation between exhumation fold and loading front, as well as the previous discussion including data from work of Lacombe *et al.* (2021) about the duration of the LPS as a function of the structural style, raise the following questions and perspectives: following this methodology, would the palaeopiezometry of the BPS allow the deep structure of the geological system studied to be highlighted? Considering previous interpretations and discussions, this kind of tool seems potentially link timing and structural style. In the case of the Apennines for example, where the deep structure is still debated, the application of this method in the inner zones (thin-skinned model), and in the outer zones (thick-skinned model with detachment level), would potentially improve the understanding of the deep structure of the FTB. The data suggest that the folds are located on inherited basement faults and are related to diachronous W-E deformation driven by the decollement level. By extension, the use of this methodology could provide the same answers in any other system where it is applicable, and where such problems remain.

References

- Accordi, G., Carbone, F., Civitelli, G., Corda, L., De Rita, D., Esu, D., Funicello, R., Kotsakis, T., Mariotti, G. and Sposato, A.** (1986) Lithofacies map of Latium-Abruzzi and neighbouring areas, scale 1: 250000.
- Agard, P., Jolivet, L., Vrielynck, B., Burov, E. and Monié, P.** (2007) Plate acceleration: The obduction trigger? *Earth Planet. Sci. Lett.*, **258**, 428–441.
- Agard, P., Omrani, J., Jolivet, L., Whitechurch, H., Vrielynck, B., Spakman, W., Monié, P., Meyer, B. and Wortel, R.** (2011) Zagros orogeny: A subduction-dominated process. *Geol. Mag.*, **148**, 692–725.
- Aharonov, E. and Katsman, R.** (2009) Interaction between pressure solution and clays in stylolite development: insights from modeling. *Am. J. Sci.*, **309**, 607–632.
- Ahmadhadi, F., Daniel, J., Azzizadeh, M. and Lacombe, O.** (2008) Evidence for pre-folding vein development in the Oligo-Miocene Asmari formation in the central Zagros Fold Belt, Iran.
- Ahmadhadi, F., Lacombe, O. and Daniel, J.-M.** (2007) Early reactivation of basement faults in Central Zagros (SW Iran): evidence from pre-folding fracture populations in Asmari Formation and lower Tertiary paleogeography. In: *Thrust Belts and Foreland Basins*, Springer, 205–228.
- Al-Hajeri, M.M., Al Saeed, M., Derks, J., Fuchs, T., Hantschel, T., Kauerauf, A., Neumaier, M., Schenk, O., Swientek, O. and Tessen, N.** (2009) Basin and petroleum system modeling. *Oilf. Rev.*, **21**, 14–29.
- Aldega, L., Botti, F. and Corrado, S.** (2007) Clay mineral assemblages and vitrinite reflectance in the Laga Basin (Central Apennines, Italy): what do they record? *Clays Clay Miner.*, **55**, 504–518.
- Aldega, L., Viola, G., Casas-Sainz, A., Marcén, M., Román-Berdiel, T. and van der Lelij, R.** (2019) Unraveling multiple thermotectonic events accommodated by crustal-scale faults in northern Iberia, Spain: Insights from K-Ar dating of clay gouges. *Tectonics*, **38**, 3629–3651.
- Aldinucci, M., Gandin, A. and Sandrelli, F.** (2008) The Mesozoic continental rifting in the Mediterranean area: Insights from the Verrucano tectofacies of southern Tuscany (Northern Apennines, Italy). *Int. J. Earth Sci.*, **97**, 1247–1269.
- Allen, P.A., Crampton, S.L. and Sinclair, H.D.** (1991) The inception and early evolution of the North Alpine Foreland Basin, Switzerland. *Basin Res.*, **3**, 143–163.
- Allen, P.A.A. and Allen, J.R.R.** (1990) Basin analysis: principles and applications, Blackwell Scientific Publications.
- Allmendinger, R.W., Cardozo, N. and Fisher, D.M.** (2013) Structural geology algorithms: Vectors and tensors. *Cambridge University Press*.
- Alvarez, W.** (2009) The historical record in the Scaglia limestone at Gubbio: Magnetic reversals and the Cretaceous-Tertiary mass extinction. *Sedimentology*, **56**, 137–148.
- Amrouch, K., Lacombe, O., Bellahsen, N., Daniel, J. and Callot, J.** (2010a) Stress and strain patterns, kinematics and deformation mechanisms in a basement-cored anticline: Sheep Mountain

Anticline, Wyoming.

- Amrouch, K., Robion, P., Callot, J.-P., Lacombe, O., Daniel, J.-M., Bellahsen, N. and Faure, J.-L.** (2010b) Constraints on deformation mechanisms during folding provided by rock physical properties: a case study at Sheep Mountain anticline (Wyoming, USA). *Geophys. J. Int.*, **182**, 1105–1123.
- Anderson, E.M.** (1951) Dynamics of Faulting and Folding. Edinburgh, UK.
- Anderson, H. and Jackson, J.** (1987) Active tectonics of the Adriatic region. *Geophys. J. Int.*, **91**, 937–983.
- Andre, G., Hirsch, C., Fourcade, S., Cathelineau, M. and Buschaert, S.** (2010) Chronology of fracture sealing under a meteoric fluid environment: Microtectonic and isotopic evidence of major Cainozoic events in the eastern Paris Basin (France). *Tectonophysics*, **490**, 214–228.
- André, G., Proudhon, B., Rebours, H. and Wileveau, Y.** (2006) Paramètres contrôlant la distribution de la fracturation: exemple dans une série marno-calcaire du Jurassique supérieur (Est du bassin de Paris). *Comptes Rendus Geosci.*, **338**, 931–941.
- Angeli, M.-G., Barbarella, M. and Pontoni, F.** (1992) Instability of a sea cliff: Sirolo landslide, Italy. 1093–1100.
- Angeli, M.-G., Pontoni, F. and Gasparetto, P.** (1996) Long term monitoring and remedial measures in a coastal landslide (Central Italy): *A.A. Balkema*, **3**, 1497–1502.
- Angelier, J.** (1984) Tectonic analysis of fault slip data sets. *J. Geophys. Res. Solid Earth*, **89**, 5835–5848.
- Angelier, J.** (1989) From orientation to magnitudes in paleostress determinations using fault slip data. *J. Struct. Geol.*, **11**, 37–50.
- Angelier, J.** (1990) Inversion of field data in fault tectonics to obtain the regional stress—III. A new rapid direct inversion method by analytical means. *Geophys. J. Int.*, **103**, 363–376.
- Antonellini, M., Tondi, E., Agosta, F., Aydin, A. and Cello, G.** (2008) Failure modes in deep-water carbonates and their impact for fault development: Majella Mountain, Central Apennines, Italy. *Mar. Pet. Geol.*, **25**, 1074–1096.
- Armstrong, P.A.** (2005) Thermochronometers in Sedimentary Basins. *Rev. Mineral. Geochemistry*, **58**, 499–525.
- Arne, D., Zentilli, M., Mukhopadhyay, P.K. and Dow, W.G.** (1994) Apatite fission track thermochronology integrated with vitrinite reflectance. In: *ACS Symposium Series, American Chemical Society*, **570**, 249–268.
- Arne, D.C., Grist, A.M., Zentilli, M., Collins, M., Embry, A. and Gentzis, T.** (2002) Cooling of the Sverdrup Basin during Tertiary basin inversion: implications for hydrocarbon exploration. *Basin Res.*, **14**, 183–205.
- Arsenikos, S., Frizon De Lamotte, D., Chamot-Rooke, N., Mohn, G., Bonneau, M.C. and**

- Blanpied, C.** (2013) Mechanism and timing of tectonic inversion in Cyrenaica (Libya): Integration in the geodynamics of the East Mediterranean. *Tectonophysics*, **608**, 319–329.
- Athy, L.F.** (1930) Density, Porosity, and Compaction of Sedimentary Rocks. *Am Assoc Pet Geol Bull.* doi: 10.1306/3d93289e-16b1-11d7-8645000102c1865d
- Aydin, A. and Basu, A.** (2005) The Schmidt hammer in rock material characterization. *Eng. Geol.*, **81**, 1–14.
- Bah, B., Beaudoin, N.E., Lacombe, O., Girard, J.-P., Gout, C., Godeau, N. and Deschamps, P.** (2022) Multi-proxy reconstruction of the burial history and porosity evolution of the TOCA carbonate formation in the Lower Congo Basin (South West Africa).
- Bally, A.W., Burbi, W., Cooper, J.C. and Ghelardoni, L.** (1986) Balanced Sections and Seismic Reflection Profiles Across the Central Apennines, Italy. *Mem. Soc. Geol. Ital.*, **77**, 63–78.
- Barchi, M., Minelli, G. and Piali, P.** (1998) The Crop 03 profile: A synthesis of results on deep structures of the Northern Apennines. *Mem. Soc. Geol. It.*, **52**, 383–405.
- Barchi, M.R., Alvarez, W. and Shimabukuro, D.H.** (2012) The Umbria-Marche Apennines as a double orogen: observations and hypotheses. *Ital. J. Geosci.*, **131**, 258–271.
- Bathurst, R.G.C.** (1972) Carbonate sediments and their diagenesis. *Elsevier*.
- Bathurst, R.G.C.** (1987) Diagenetically enhanced bedding in argillaceous platform limestones: stratified cementation and selective compaction. *Sedimentology*, **34**, 749–778.
- Baud, P., Klein, E. and Wong, T. fong** (2004) Compaction localization in porous sandstones: Spatial evolution of damage and acoustic emission activity. *J. Struct. Geol.*, **26**, 603–624.
- Baudin, F., Fiet, N., Coccioni, R. and Galeotti, S.** (1998) Organic matter characterisation of the Selli Level (Umbria-Marche Basin, central Italy). *Cretac. Res. - Cretac. RES*, **19**, 701–714.
- Beaudoin, N.** (2012) Circulations de fluides et déformation cassante au front des Rocheuses: étude intégrée du bassin du Bighorn, Wyoming, USA.
- Beaudoin, N., Gasparri, M., David, M.-E., Lacombe, O. and Koehn, D.** (2019) Bedding-parallel stylolites as a tool to unravel maximum burial depth in sedimentary basins: Application to Middle Jurassic carbonate reservoirs in the Paris basin, France. *GSA Bull.*, **131**, 1239–1254.
- Beaudoin, N., Koehn, D., Lacombe, O., Lecouty, A., Billi, A., Aharonov, E. and Parlangeau, C.** (2016) Fingerprinting stress: Stylolite and calcite twinning paleopiezometry revealing the complexity of progressive stress patterns during folding—The case of the Monte Nero anticline in the Apennines, Italy. *Tectonics*, **35**, 1687–1712.
- Beaudoin, N., Labeur, A., Lacombe, O., Koehn, D., Billi, A., Hoareau, G., Boyce, A., John, C.M., Marchegiano, M., Roberts, N.M., Millar, I.L., Claverie, F., Pecheyran, C. and Callot, J.-P.** (2020a) Regional-scale paleofluid system across the Tuscan Nappe – Umbria Marche Arcuate Ridge (northern Apennines) as revealed by mesostructural and isotopic analyses of stylolite-vein networks. *Solid Earth*. doi: 10.5194/se-2020-64

- Beaudoin, N. and Lacombe, O.** (2018) Recent and future trends in paleopiezometry in the diagenetic domain: Insights into the tectonic paleostress and burial depth history of fold-and-thrust belts and sedimentary basins. *J. Struct. Geol.*, **114**, 357–365.
- Beaudoin, N., Lacombe, O., David, M. and Koehn, D.** (2020b) Does stress transmission in forelands depend on structural style? Distinctive stress magnitudes during Sevier thin-skinned and Laramide thick-skinned layer-parallel shortening in the Bighorn Basin (USA) revealed by stylolite and calcite twinning paleopiez. *Terra Nov.*, **32**, 225–233.
- Beaudoin, N., Lacombe, O., Koehn, D., David, M.-E., Farrell, N. and Healy, D.** (2020c) Vertical stress history and paleoburial in foreland basins unravelled by stylolite roughness paleopiezometry: Insights from bedding-parallel stylolites in the Bighorn Basin, Wyoming, USA. *J. Struct. Geol.*, **136**, 104061.
- Beaudoin, N., Lacombe, O., Roberts, N.M.W. and Koehn, D.** (2018) U-Pb dating of calcite veins reveals complex stress evolution and thrust sequence in the Bighorn Basin, Wyoming, USA. *Geology*, **46**, 1015–1018.
- Beaudoin, N., Leprêtre, R., Bellahsen, N., Lacombe, O., Amrouch, K., Callot, J.-P., Emmanuel, L. and Daniel, J.-M.** (2012) Structural and microstructural evolution of the Rattlesnake Mountain Anticline (Wyoming, USA): new insights into the Sevier and Laramide orogenic stress build-up in the Bighorn Basin. *Tectonophysics*, **576**, 20–45.
- Beaudoin, N.E., Lacombe, O., Hoareau, G. and Callot, J.** (2022) Geochemistry-assisted structural geology, or how the reconstruction of the paleofluid sources and migration pathways using geochemistry sheds light on tectonics: a review of applications to calcite cements filling fractures in fold-and-thrust belts and st.
- Beaumont, C.** (1981) Foreland basins. *Geophys. J. Int.*, **65**, 291–329.
- Bellahsen, N., Fiore, P. and Pollard, D.D.** (2006a) The role of fractures in the structural interpretation of Sheep Mountain Anticline, Wyoming. *J. Struct. Geol.*, **28**, 850–867.
- Bellahsen, N., Fiore, P.E. and Pollard, D.D.** (2006b) From spatial variation of fracture patterns to fold kinematics: A geomechanical approach.
- Ben-Itzhak, L.L., Aharonov, E., Toussaint, R., Sagy, A., Laronne Ben-Itzhak, L., Aharonov, E., Toussaint, R. and Sagy, A.** (2012) Upper bound on stylolite roughness as indicator for amount of dissolution. *Earth Planet. Sci. Lett.*, **337**, 186–196.
- Benkhelil, J.** (1989) The origin and evolution of the Cretaceous Benue Trough (Nigeria). *J. African Earth Sci.*, **8**, 251–282.
- Benkhelil, J., Dainelli, P., Ponsard, J.F., Popoff, M. and Saugy, L.** (1988) The Benue trough: Wrench-fault related basin on the border of the equatorial Atlantic. In: *Developments in Geotectonics, Elsevier*, **22**, 787–788.
- Bergbauer, S. and Pollard, D.D.** (2004) A new conceptual fold-fracture model including prefolding

- joints, based on the Emigrant Gap anticline, Wyoming. *Geol. Soc. Am. Bull.*, **116**, 294–307.
- Bernoulli, D. and Jenkyns, H.** (1974) Alpine, Mediterranean and Central Atlantic Mesozoic Facies in Relation to the Early Evolution of the Tethys. In: *Modern and Ancient Geosynclinal Sedimentation*, 19, 129–160.
- Berthelon, J., Bruch, A., Colombo, D., Frey, J., Traby, R., Bouziat, A., Cacas-Stentz, M.C. and Cornu, T.** (2021) Impact of tectonic shortening on fluid overpressure in petroleum system modelling: Insights from the Neuquén basin, Argentina. *Mar. Pet. Geol.*, **127**, 104933.
- Bertotti, G., de Graaf, S., Bisdorn, K., Oskam, B., Vonhof, H.B., Bezerra, F.H.R., Reijmer, J.J.G. and Cazarin, C.L.** (2017) Fracturing and fluid-flow during post-rift subsidence in carbonates of the Jandaíra Formation, Potiguar Basin, NE Brazil. *Basin Res.*, **29**, 836–853.
- Bevan, T.G. and Moustafa, A.R.** (2012) Inverted rift-basins of northern Egypt. In: *Regional Geology and Tectonics: Phanerozoic Rift Systems and Sedimentary Basins*, Elsevier Inc., 482–507.
- Bieniawski, Z.T.** (1967a) Stability concept of brittle fracture propagation in rock. *Eng. Geol.*, **2**, 149–162.
- Bieniawski, Z.T.** (1967b) Mechanism of brittle fracture of rock: part I—theory of the fracture process. In: *International Journal of Rock Mechanics and Mining Sciences & Geomechanics Abstracts*, Elsevier, 4, 395–406.
- Bigi, G., Bonardi, G., Catalano, R., Cosentino, D., Lentini, F., Parotto, M., Sartori, R., Scandone, P. and Turco, E.** (1992) Structural model of Italy: Progetto Finalizzato Geodinamica.
- Billi, A. and Salvini, F.** (2003) Development of systematic joints in response to flexure-related fibre stress in flexed foreland plates: the Apulian forebulge case history, Italy. *J. Geodyn.*, **36**, 523–536.
- Bjørlykke, K.** (2006) Effects of compaction processes on stresses, faults, and fluid flow in sedimentary basins: examples from the Norwegian margin. *Geol. Soc. London, Spec. Publ.*, **253**, 359–379.
- Boccaletti, M., Calamita, F. and Viandante, M.G.** (2005) The lithospheric Apennine Neo-Chain developing since the Lower Pliocene as a result of the Africa-Europe convergence. *Boll. della Soc. Geol. Ital.*, **124**, 87–105.
- Bons, P.D., Elburg, M.A. and Gomez-Rivas, E.** (2012) A review of the formation of tectonic veins and their microstructures. *J. Struct. Geol.*, **43**, 33–62.
- Bosellini, A.** (1989) Dynamics of Tethyan carbonate platforms.
- Bosworth, W., Guiraud, R. and Kessler, L.G.** (1999) Late Cretaceous (ca. 84 Ma) compressive deformation of the stable platform of northeast Africa (Egypt): Far-field stress effects of the “Santonian event” and origin of the Syrian arc deformation belt. *Geology*, **27**, 633–636.
- Bourlange, S., Nd, A., He Nr, P. and Bourlange, S.** (2007) Numerical model of fluid pressure solitary wave propagation along the décollement of an accretionary wedge: application to the Nankai wedge. *Geofluids*, **7**, 323–334.
- Brandon, M.T., Roden-Tice, M.K. and Garver, J.I.** (1998) Late Cenozoic exhumation of the Cascadia

- accretionary wedge in the Olympic Mountains, northwest Washington State. *Geol. Soc. Am. Bull.*, **110**, 985–1009.
- Bray, R.J., Green, P.F. and Duddy, I.R.** (1992) Thermal history reconstruction using apatite fission track analysis and vitrinite reflectance: a case study from the UK East Midlands and Southern North Sea. *Geol. Soc. London, Spec. Publ.*, **67**, 3–25.
- Brouste, A., Renard, F., Gratier, J.P. and Schmittbuhl, J.** (2007) Variety of stylolites' morphologies and statistical characterization of the amount of heterogeneities in the rock. *J. Struct. Geol.*, **29**, 422–434.
- Brozzetti, F., Cirillo, D. and Luchetti, L.** (2021) Timing of Contractional Tectonics in the Miocene Foreland Basin System of the Umbria Pre-Apennines (Italy): An Updated Overview. *Geosciences*, **11**, 97.
- Brüch, A., Colombo, D., Frey, J., Berthelon, J., Cacas-Stentz, M.C., Cornu, T. and Gout, C.** (2021) Coupling 3D geomechanics to classical sedimentary basin modeling: From gravitational compaction to tectonics. *Geomech. Energy Environ.*, **28**, 100259.
- Bruns, B., di Primio, R., Berner, U. and Littke, R.** (2013) Petroleum system evolution in the inverted Lower Saxony Basin, northwest Germany: a 3D basin modeling study. *Geofluids*, **13**, 246–271.
- Burke, K., MacGregor, D.S. and Cameron, N.R.** (2003) Africa's petroleum systems: Four tectonic "Aces" in the past 600 million years. *Geol. Soc. Spec. Publ.*, **207**, 21–60.
- Burke, K., Steinberger, B., Torsvik, T.H. and Smethurst, M.A.** (2008) Plume Generation Zones at the margins of Large Low Shear Velocity Provinces on the core-mantle boundary. *Earth Planet. Sci. Lett.*, **265**, 49–60.
- Bushinskiy, G.I.** (1961) Stylolites. *Izv. Akad. Nauk. SSSR, Ser. Fiz*, **8**, 31–46.
- Buxton, T.M. and Sibley, D.F.** (1981) Pressure solution features in a shallow buried limestone. *J. Sediment. Petrol.*, **51**, 19–26.
- Calamita, F., Cello, G., Deiana, G. and Paltrinieri, W.** (1994) Structural styles, chronology rates of deformation, and time-space relationships in the Umbria-Marche thrust system (central Apennines, Italy). *Tectonics*, **13**, 873–881.
- Calamita, F., Cello, G., Invernizzi, C. and Paltrinieri, W.** (1990) Stile strutturale e cronologia della deformazione lungo la traversa M. S. Vicino. *Stud. Geol. Camerti*, 69–86.
- Calamita, F., Coltorti, M., Piccinini, D., Pierantoni, P., Pizzi, A., Ripepe, M., Scisciani, V. and Turco, E.** (2000) Quaternary faults and seismicity in the Umbro-Marchean Apennines (Central Italy): Evidence from the 1997 Colfiorito earthquake. *J. Geodyn.*, 1–20.
- Calamita, F. and Deiana, G.** (1988) The arcuate shape of the Umbria-Marche-Sabina Apennines (central Italy). *Tectonophysics*, **146**, 139–147.
- Calamita, F. and Deiana, G.** (1980) Evidenze di una fase tettonica distensiva del Messiniano basale nel bacino di Camerino (Appennino umbro-marchigiano).

- Calamita, F., Paltrinieri, W., Pelorosso, M., Scisciani, V. and Tavarnelli, E.** (2003) Inherited Mesozoic architecture of the Adria continental palaeomargin in the neogene central apennines orogenic system, Italy. *Boll. della Soc. Geol. Ital.*, **122**, 307–318.
- Calamita, F., Viandante, M.G. and Hegarty, K.** (2004) Pliocene-Quaternary burial/exhumation paths of the Central Apennines (Italy): Implications for the definition of the deep structure of the belt. *Boll. della Soc. Geol. Ital.*, **123**, 503–512.
- Candela, T., Renard, F., Bouchon, M., Brouste, A., Marsan, D., Schmittbuhl, J. and Voisin, C.** (2009) Characterization of Fault Roughness at Various Scales: Implications of Three-Dimensional High Resolution Topography Measurements. In: *Mechanics, Structure and Evolution of Fault Zones*, Birkhäuser Basel, 1817–1851.
- Cannon, M.J., Percival, D.B., Caccia, D.C., Raymond, G.M. and Basingthwaite, J.B.** (1997) Evaluating scaled windowed variance methods for estimating the Hurst coefficient of time series. *Phys. A Stat. Mech. its Appl.*, **241**, 606–626.
- Capuano, N. and D’Antonio, G.** (1992) Studio sedimentologico-composizionale della successione tardo-miocenica della dorsale costiera Gabicce-Pesaro. *G. di Geol.*, **54**, 107–123.
- Capuano, N., Savelli, D., Santini, S. and Tonelli, G.** (2009) Note illustrative della Carta Geologica d’Italia alla scala 1:50.000, foglio 279 Urbino.
- Cardozo, N.** (2011) Backtrip: Performs 1D “Airy type” Backstripping of Sedimentary Strata.
- Cardozo, N. and Allmendinger, R.W.** (2013) Spherical projections with OSXStereonet. *Comput. Geosci.*, **51**, 193–205.
- Caricchi, C., Aldega, L. and Corrado, S.** (2015) Reconstruction of maximum burial along the Northern Apennines thrust wedge (Italy) by indicators of thermal exposure and modeling. *Bulletin*, **127**, 428–442.
- Carlini, R., Martelli, G. and Veneri, F.** (1995) Stratigrafia della formazione Marnoso-arenacea nell’area di Borgo Pace (Appennino umbro-marchigiano): analisi composizionali di alcune torbiditi di provenienza sud-orientale.
- Carmignani, L. and Kligfield, R.** (1990) Crustal extension in the Northern Apennines: The transition from compression to extension in the Alpi Apuane Core Complex. *Tectonics*, **9**, 1275–1303.
- Carminati, E. and Doglioni, C.** (2012) Alps vs. Apennines: The paradigm of a tectonically asymmetric Earth. *Earth-Science Rev.*, **112**, 67–96.
- Carruba, S., Casnedi, R., Perotti, C.R., Tornaghi, M. and Bolis, G.** (2006) Tectonic and sedimentary evolution of the lower Pliocene Periadriatic foredeep in Central Italy. *Int. J. Earth Sci.*, **95**, 665–683.
- Casini, G., Gillespie, P.A., Vergés, J., Romaine, I., Fernández, N., Casciello, E., Saura, E., Mehl, C., Homke, S. and Embry, J.-C.** (2011) Sub-seismic fractures in foreland fold and thrust belts: insight from the Lurestan Province, Zagros Mountains, Iran. *Pet. Geosci.*, **17**, 263–282.

- Castellarin, A., Colacicchi, R., Praturlon, A. and Cantelli, C.** (1982) The Jurassic-lower Pliocene history of the Ancona-Anzio line (Central Italy). *Mem. Soc. Geol. It.*, **24**, 325–336.
- Cello, G. and Coppola, L.** (1984) Assetto geologico-strutturale dell'area anconetana e sua evoluzione plio-quadernaria. *Boll. della Soc. Geol. Ital.*, **103**, 97–109.
- Cello, G., Mazzoli, S., Tondi, E. and Turco, E.** (1997) Active tectonics in the central Apennines and possible implications for seismic hazard analysis in peninsular Italy. *Tectonophysics*, **272**, 43–68.
- Ciarapica, G. and Passeri, L.** (1998) Evoluzione paleogeografica degli Appennini. *Atti ticinensi di Sci. della terra*, **40**, 233–290.
- Ciarapica, G. and Passeri, L.** (2002) The palaeogeographic duplicity of the Apennines. *Boll. Soc. Geol. It.*, **1**, 67–75.
- Coakley, B.J. and Watts, A.B.** (1991) Tectonic controls on the development of unconformities: the North Slope, Alaska. *Tectonics*, **10**, 101–130.
- Coccioni, R., Nesci, O., Tramontana, M., Wezel, F. and Moretti, E.** (1987) Descrizione di un livello-guida “radiolaritico-bituminoso-ittiolitico” alla base delle Marne a Fucoidi nell'Appennino umbro-marchigiano. *Boll. Soc. Geol. Ital.*, **106**, 183–192.
- Coogan, J.C., Link, P.K., Kuntz, M.A. and Platt, L.B.** (1992) Structural evolution of piggyback basins in the Wyoming-Idaho-Utah thrust belt. *Reg. Geol. East. Idaho West. Wyoming Geol. Soc. Am. Mem.*, **179**, 55–81.
- Cooke, M.L.** (1997) Fracture localization along faults with spatially varying friction. *J. Geophys. Res. Solid Earth*, **102**, 22425–22434.
- Cooper, M.** (2007) Structural style and hydrocarbon prospectivity in fold and thrust belts: A global review. In: *Geological Society Special Publication*, **272**, 447–472.
- Cooper, S.P., Goodwin, L.B. and Lorenz, J.C.** (2006) Fracture and fault patterns associated with basement-cored anticlines: The example of Teapot Dome, Wyoming. *Am. Assoc. Pet. Geol. Bull.*, **90**, 1903–1920.
- Cosentino, D., Cipollari, P., Marsili, P. and Scrocca, D.** (2010) Geology of the central Apennines: A regional review. *J Virtual Explor.* doi: 10.3809/jvirtex.2009.00223
- Costa, M., Chicco, J., Invernizzi, C., Teloni, S., Pierantoni, P.P., Martinez-Frias, J., Liotta, D., Molli, G. and Cipriani, A.** (2021) Plio–Quaternary Structural Evolution of the Outer Sector of the Marche Apennines South of the Conero Promontory, Italy. *Geosci. 2021, Vol. 11, Page 184*, **11**, 184.
- Couzens-Schultz, B.A. and Azbel, K.** (2014) Predicting pore pressure in active fold–thrust systems: An empirical model for the deepwater Sabah foldbelt. *J. Struct. Geol.*, **69**, 465–480.
- Coward, M.P., De Donatis, M., Mazzoli, S., Paltrinieri, W. and Wezel, F.C.** (1999) Frontal part of the northern Apennines fold and thrust belt in the Romagna-Marche area (Italy): Shallow and deep structural styles. *Tectonics*, **18**, 559–574.
- Coward, M.P., Rex, D.C., Khan, M.A., Windley, B.F., Broughton, R.D., Luff, I.W., Petterson,**

- M.G. and Pudsey, C.J.** (1986) Collision tectonics in the NW Himalayas. *Geol. Soc. London, Spec. Publ.*, **19**, 203–219.
- Cox, S.F. and Etheridge, M.A.** (1983) Crack-seal fibre growth mechanisms and their significance in the development of oriented layer silicate microstructures. *Tectonophysics*, **92**, 147–170.
- Crampton, S.L. and Allen, P.A.** (1995) Recognition of forebulge unconformities associated with early stage foreland basin development: example from the North Alpine Foreland Basin. *Am. Assoc. Pet. Geol. Bull.*, **79**, 1495–1514.
- Croizé, D., Ehrenberg, S.N., Bjørlykke, K., Renard, F. and Jahren, J.** (2010) Petrophysical properties of bioclastic platform carbonates: Implications for porosity controls during burial. *Mar. Pet. Geol.*, **27**, 1765–1774.
- Croize, D., Renard, F. and Gratier, J.-P.** (2013) Compaction and porosity reduction in carbonates: A review of observations, theory, and experiments. *Adv. Geophys.*, **54**, 181–238.
- Cross, T.A.** (1986) Tectonic controls of foreland basin subsidence and Laramide style deformation, western United States. *Forel. basins*, 15–39.
- Currie, B.S.** (1994) “Back-bulge” to foredeep evolution of the Late Jurassic–Early Cretaceous Cordilleran foreland basin: Evidence from the Morrison and Cedar Mountain Formations, central-eastern Utah. In: *Geological Society of America Abstracts with Programs*, **26**, 9.
- Curzi, M., Aldega, L., Bernasconi, S.M., Berra, F., Billi, A., Boschi, C., Franchini, S., Van der Lelij, R., Viola, G. and Carminati, E.** (2020) Architecture and evolution of an extensionally-inverted thrust (Mt. Tancia Thrust, Central Apennines): Geological, structural, geochemical, and K–Ar geochronological constraints. *J. Struct. Geol.*, **136**, 104059.
- Damiani, A. V., Tuscano, F. and Vecchia, P.** (1995) Assetto stratigrafico-strutturale del M. Subasio e delle circostanti successioni silico-clastiche mioceniche (Umbria).
- Davis, G.A., Cong, W., Yadong, Z., Jinjiang, Z., Changhou, Z. and Gehrels, G.E.** (1998) The enigmatic Yinshan fold-and-thrust belt of northern China: New views on its intraplate contractional styles. *Geology*, **26**, 43–46.
- de Feyter, A.** (1991) Gravity tectonics and sedimentation of the Montefeltro, Italy.
- de Jager, J.** (1979) The relation between tectonics and sedimentation along the “Sillaro line” (Northern Apennines, Italy).
- Decandia, F. a.** (1982) Geologia dei Monti di Spoleto (Provincia di Perugia). *Boll. della Soc. Geol. Ital.*, **101**, 291–315.
- DeCelles, P.G. and Burden, E.T.** (1992) Non-marine sedimentation in the overfilled part of the Jurassic-Cretaceous Cordilleran foreland basin: Morrison and Cloverly Formations, central Wyoming, USA. *Basin Res.*, **4**, 291–314.
- DeCelles, P.G. and Giles, K.A.** (1996) Foreland basin systems. *Basin Res.*, **8**, 105–123.
- Deiana, G.** (1965) Osservazioni preliminari sulle condizioni stratigrafico strutturali del M. Subasio.

Boll. Soc. Geol. It., **84**, 185–192.

- Delle Rose, M., Guerrera, F., Moretti, E. and Rusciadelli, G.** (1990) Evoluzione del segmento interno dell'Avanfossa Appenninica durante il Miocene medio (Spartiacque tosco-romagnolo). *G. di Geol.*, **52**, 135–158.
- Delle Rose, M., Guerrera, F., Moretti, E., Rusciadelli, G. and CORONA, F.** (1991) The Marnoso-Arenacea Fm. between Bocca Trabaria and Campigna (Northern Apennines): lithostratigraphy from the Schlier Fm. to the Verghereto Marls Fm. in a new structural context. *G. di Geol.*, **84/2**, 291–315.
- Delle Rose, M., Guerrera, F., Renzulli, A., Ravasc Baranyai, L. and Serrano, F.** (1994a) Stratigrafia e petrografia delle Marne di Vicchio (Unità Tettonica Cervarola) dell'alta Val Tiberina (Appennino Tosco-Romagnolo).
- Delle Rose, M., Guerrera, F., Renzulli, A. and Serrano, F.** (1994b) Stratigraphic and volcanoclastic events in the Vicchio Marls Auct.(Cervarola Tectonic Unit) along the Monte Fatucchio section (northern Apennines, Italy).
- Dercourt, J., Ricou, L.E. and Vrielynck, B.** (1993) Atlas Tethys Palaeoenvironmental Maps. Gauthier-Villars, Paris, 307p., 14 cartes, 1 pl.
- Destro, N.** (1995) Release fault: A variety of cross fault in linked extensional fault systems, in the Sergipe-Alagoas Basin, NE Brazil. *J. Struct. Geol.*, **17**, 615–629.
- Di Domenica, A., Turtù, A., Satolli, S. and Calamita, F.** (2012) Relationships between thrusts and normal faults in curved belts: New insight in the inversion tectonics of the Central-Northern Apennines (Italy). *J. Struct. Geol.*, **42**, 104–117.
- Diaz General, E.N.** (2013) The Influence of Fractures on Vulnerability to Pollution of a Carbonate Aquifer: Monte Conero (Italy). alma
- Díaz General, E.N., Mollema, P.N. and Antonellini, M.** (2015) Fracture patterns and fault development in the pelagic limestones of the Monte Conero Anticline (Italy). *Ital. J. Geosci.*, **134**, 495–512.
- Dogliani, C., Merlini, S. and Cantarella, G.** (1999) Foredeep geometries at the front of the Apennines in the Ionian Sea (central Mediterranean). *Earth Planet. Sci. Lett.*, **168**, 243–254.
- Dogliani, C. and Prosser, G.** (1997) Fold uplift versus regional subsidence and sedimentation rate. *Mar. Pet. Geol.*, **14**, 179–190.
- Donelick, R.A., O'Sullivan, P.B. and Ketcham, R.A.** (2005) Apatite fission-track analysis. *Rev. Mineral. Geochemistry*, **58**, 49–94.
- Drost, K., Chew, D., Petrus, J.A., Scholze, F., Woodhead, J.D., Schneider, J.W. and Harper, D.A.T.** (2018) An image mapping approach to U-Pb LA-ICP-MS carbonate dating and applications to direct dating of carbonate sedimentation. *Geochemistry, Geophys. geosystems*, **19**, 4631–4648.
- Dubbini, A., Guerrera, F. and Sandroni, P.** (1991) Nuovi dati sullo Schlier dell'Appennino umbro-

- marchigiano. *Giorn. Geol.*, **53**, 115–130.
- Dunham, R.J.** (1962) Classification of Carbonate Rocks According to Depositional Textures. In: *Classification of Carbonate Rocks--A Symposium*, 108–121.
- Ebner, M., Koehn, D., Toussaint, R. and Renard, F.** (2009a) The influence of rock heterogeneity on the scaling properties of simulated and natural stylolites. *J. Struct. Geol.*, **31**, 72–82.
- Ebner, M., Koehn, D., Toussaint, R., Renard, F. and Schmittbuhl, J.** (2009b) Stress sensitivity of stylolite morphology. *Earth Planet. Sci. Lett.*, **277**, 394–398.
- Ebner, M., Piazzolo, S., Renard, F. and Koehn, D.** (2010a) Stylolite interfaces and surrounding matrix material: Nature and role of heterogeneities in roughness and microstructural development. *J. Struct. Geol.*, **32**, 1070–1084.
- Ebner, M., Toussaint, R., Schmittbuhl, J., Koehn, D. and Bons, P.** (2010b) Anisotropic scaling of tectonic stylolites: A fossilized signature of the stress field? *J. Geophys. Res. Solid Earth*, **115**, B06403.
- Ebner, M.J.** (2009) The development of stylolites, from small-scale heterogeneities to multi-scale roughness. Mainz, Univ., Diss., 2009
- Edwards, S.F.E. and Wilkinson, D.R.** (1982) The surface statistics of a granular aggregate. *Proc. R. Soc. London. A. Math. Phys. Sci.*, **381**, 17–31.
- Ehlers, T.A. and Farley, K.A.** (2003) Apatite (U–Th)/He thermochronometry: methods and applications to problems in tectonic and surface processes. *Earth Planet. Sci. Lett.*, **206**, 1–14.
- Ehrenberg, S.N., McArthur, J.M. and Thirlwall, M.F.** (2006) Growth, demise, and dolomitization of Miocene carbonate platforms on the Marion Plateau, offshore NE Australia. *J. Sediment. Res.*, **76**, 91–116.
- Ehrenberg, S.N. and Nadeau, P.H.** (2005) Sandstone vs. carbonate petroleum reservoirs: A global perspective on porosity-depth and porosity-permeability relationships. *Am. Assoc. Pet. Geol. Bull.*, **89**, 435–445.
- Eke, A., Herman, P., Kocsis, L. and Kozak, L.R.** (2002) Fractal characterization of complexity in temporal physiological signals. *Physiol. Meas.*, **23**, R1.
- Ekström, G., Morelli, A., Boschi, E. and Dziewonski, A.M.** (1998) Moment tensor analysis of the central Italy earthquake sequence of September–October 1997. *Geophys. Res. Lett.*, **25**, 1971–1974.
- Engelder, T.** (1999) Transitional–tensile fracture propagation: a status report. *J. Struct. Geol.*, **21**, 1049–1055.
- Engelder, T.** (1987) Joints and shear fractures in rock. *Fract. Mech. rock*, 27–69.
- Engelder, T. and Geiser, P.** (1980) On the use of regional joint sets as trajectories of paleostress fields during the development of the Appalachian Plateau, New York. *J. Geophys. Res. Solid Earth*, **85**, 6319–6341.
- Etchecopar, A.** (1984) Etude des états de contrainte en tectonique cassante et simulations de

déformations plastiques: approche mathématique.

- Evans, M.A. and Elmore, R.D.** (2006) Fluid control of localized mineral domains in limestone pressure solution structures. *J. Struct. Geol.*, **28**, 284–301.
- Evans, M.A., Lewchuk, M.T. and Elmore, R.D.** (2003) Strain partitioning of deformation mechanisms in limestones: examining the relationship of strain and anisotropy of magnetic susceptibility (AMS). *J. Struct. Geol.*, **25**, 1525–1549.
- Fancelli, R. and Radrizzani, S.** (1964a) Carta geologica d'Italia alla scala 1: 100.000 Note illustrative del Foglio 118 Ancona.
- Fancelli, R. and Radrizzani, S.** (1964b) Foglio 118 Ancona. Note III. Carta Geologica d'Italia, 42, Roma.
- Fantoni, R. and Franciosi, R.** (2010) Tectono-sedimentary setting of the Po Plain and Adriatic foreland. In: *Rendiconti Lincei, Springer*, 21, 197–209.
- Farley, K.A.** (2002) (U-Th)/He dating: Techniques, calibrations, and applications.
- Ferret, H., Roure, F., Swennen, R. and Ortuno, S.** (2000) Fluid migration placed into the deformation history of fold-and-thrust belts: an example from the Veracruz basin (Mexico). *J. Geochemical Explor.*, **69**, 275–279.
- Ferret, H., Swennen, R., Arzate, S.O. and Roure, F.** (2006) Fluid flow evolution in petroleum reservoirs with a complex diagenetic history: An example from Veracruz, Mexico. *J. geochemical Explor.*, **89**, 108–111.
- Ferret, H., Swennen, R., Ortuño, S. and Roure, F.** (2003) Reconstruction of the fluid flow history during Laramide forelandfold and thrust belt development in eastern Mexico: cathodoluminescence and $\delta^{18}\text{O}$ - $\delta^{13}\text{C}$ isotope trends of calcite-cemented fractures. *J. Geochemical Explor.*, **78**, 163–167.
- Finetti, I., Calamita, F., Crescenti, U., Del Ben, A., Forlin, E., Pipan, M., Prizzon, A., Rusciadelli, G. and Scisciani, V.** (2005) Crustal Geological Section across Central Italy from the Corsica Basin to the Adriatic Sea based on Geological and CROP Seismic Data. *Crop Proj. Deep Seism. Explor. Cent. Mediterr. Italy*, **2**, 159.
- Finetti, I.R., Boccaletti, M., Bonini, M., Ben, A., Geletti, R., Pipan, M. and Sani, F.** (2001) Crustal section based on CROP seismic data cross the North Tyrrhenian–Northern Apennines–Adriatic Sea. *Tectonophysics*, **343**, 135–163.
- Finkel, E.A. and Wilkinson, B.H.** (1990) Stylolitization as source of cement in Mississippian Salem Limestone, west-central Indiana. *Am. Assoc. Pet. Geol. Bull.*, **74**, 174–186.
- Fischer, M.P., Woodward, N.B. and Mitchell, M.M.** (1992) The kinematics of break-thrust folds. *J. Struct. Geol.*, **14**, 451–460.
- Fisher, Q.J. and Knipe, R.J.** (2001) The permeability of faults within siliciclastic petroleum reservoirs of the North Sea and Norwegian Continental Shelf. *Mar. Pet. Geol.*, **18**, 1063–1081.
- Flemings, P.B. and Jordan, T.E.** (1990) Stratigraphic modeling of foreland basins: interpreting thrust

- deformation and lithosphere rheology. *Geology*, **18**, 430–434.
- Flemings, P.B.** and **Jordan, T.E.** (1989) A synthetic stratigraphic model of foreland basin development. *J. Geophys. Res. Solid Earth*, **94**, 3851–3866.
- Fletcher, R.C.** and **Pollard, D.D.** (1981) Anticrack model for pressure solution surfaces. *Geology*, **9**, 419–424.
- Frizon de Lamotte, D., Fourdan, B., Leleu, S., Leparmentier, F.** and **de Clarens, P.** (2015) Style of rifting and the stages of Pangea breakup. *Tectonics*, **34**, 1009–1029.
- Frizon de Lamotte, D., Raulin, C., Mouchot, N., Wrobel-Daveau, J.-C., Blanpied, C.** and **Ringebach, J.-C.** (2011) The southernmost margin of the Tethys realm during the Mesozoic and Cenozoic: Initial geometry and timing of the inversion processes. *Tectonics*, **30**, n/a-n/a.
- Garduño-Martínez, D.E., Pi Puig, T., Solé, J., Martini, M.** and **Alcalá-Martínez, J.R.** (2015) K-Ar illite-mica age constraints on the formation and reactivation history of the El Doctor fault zone, central Mexico. *Rev. Mex. ciencias geológicas*, **32**, 306–322.
- Genik, G.J.** (1993) Petroleum geology of Cretaceous-Tertiary rift basins in Niger, Chad, and Central African Republic. *Am. Assoc. Pet. Geol. Bull.*, **77**, 1405–1434.
- Ghisetti, F.** and **Vezzani, L.** (2002) Normal faulting, extension and uplift in the outer thrust belt of the central Apennines (Italy): role of the Caramanico fault. *Basin Res.*, **14**, 225–236.
- Ghisetti, F.** and **Vezzani, L.** (1988) Geometric and kinematic complexities in the Marche-Abruzzi external zones (Central Apennines, Italy). *Geol. Rundschau*, **77**, 63–78.
- Godeau, N., Deschamps, P., Guihou, A., Leonide, P., Tendil, A., Gerdes, A., Hamelin, B.** and **Girard, J.-P.** (2018) U-Pb dating of calcite cement and diagenetic history in microporous carbonate reservoirs: Case of the Urgonian Limestone, France. *Geology*, **46**, 247–250.
- Gonzalez-Mercado, G.E.** (2007) Reconstruction des circulations de fluides et de la migration des hydrocarbures (modélisation Ceres 2D) le long d'un transect através la Plateforme de Córdoba et le Bassin de Veracruz, Mexique. *DES Univ. Pierre Marie Curie. Inst. Français du Pétrole Rep.*, **60112**, 40.
- Graham, J.W.** (1949) The stability and significance of magnetism in sedimentary rocks. *J. Geophys. Res.*, **54**, 131–167.
- Graham Wall, B.R., Girbacea, R., Mesonjesi, A.** and **Aydin, A.** (2006) Evolution of fracture and fault-controlled fluid pathways in carbonates of the Albanides fold-thrust belt. *Am. Assoc. Pet. Geol. Bull.*, **90**, 1227–1249.
- Grant, J.A.** (2005) Isocon analysis: A brief review of the method and applications. *Phys. Chem. Earth, Parts A/B/C*, **30**, 997–1004.
- Green, P.F., Duddy, I.R.** and **Bray, R.J.** (1995) Applications of thermal history reconstruction in inverted basins. *Geol. Soc. London, Spec. Publ.*, **88**, 149–165.
- Gresens, R.L.** (1967) Composition-volume relationships of metasomatism. *Chem. Geol.*, **2**, 47–65.

- Grohmann, C.H. and Campanha, G.A.** (2010) OpenStereo: open source, cross-platform software for structural geology analysis. In: *AGU Fall Meeting abstracts*, 2010, IN31C-06.
- Guerrera, F., Tramontana, M., Donatelli, U. and Serrano, F.** (2012) Space/time tectono-sedimentary evolution of the Umbria-Romagna-Marche Miocene Basin (Northern Apennines, Italy): A foredeep model. *Swiss J Geosci.* doi: 10.1007/s00015-012-0118-0
- Guidish, T.M., Kendall, C.G.S.C., Lerche, I., Toth, D.J. and Yarzab, R.F.** (1985) Basin Evaluation Using Burial History Calculations: an Overview. *Am. Assoc. Pet. Geol. Bull.*, **69**, 92–105.
- Guillaume, B., Dhont, D. and Brusset, S.** (2008) Three-dimensional geologic imaging and tectonic control on stratigraphic architecture: Upper Cretaceous of the Tresp Basin (south-central Pyrenees, Spain). *Am. Assoc. Pet. Geol. Bull.*, **92**, 249–269.
- Guillocheau, F., Robin, C., Allemand, P., Bourquin, S., Brault, N., Dromart, G., Friedenber, R., Garcia, J.P., Gaulier, J.M., Gaumet, F., Grosdoy, B., Hanot, F., Le Strat, P., Mettraux, M., Nalpas, T., Prijac, C., Rigoltet, C., Serrano, O. and Grandjean, G.** (2000) Meso-cenozoic geodynamic evolution of the Paris basin: 3d stratigraphic constraints. *Geodin. Acta*, **13**, 189–245.
- Guiraud, R., Bosworth, W., Thierry, J. and Delplanque, A.** (2005) Phanerozoic geological evolution of Northern and Central Africa: An overview. *J. African Earth Sci.*, **43**, 83–143.
- Gutiérrez-Alonso, G. and Gross, M.R.** (1999) Structures and mechanisms associated with development of a fold in the Cantabrian zone thrust belt, NW Spain. *J. Struct. Geol.*, **21**, 653–670.
- H. V. Dunnington** (1954) Stylolite Development Post-Dates Rock Induration. *SEPM J Sediment Res.* doi: 10.1306/d4269648-2b26-11d7-8648000102c1865d
- Harris, N.B.** (2006) Low-porosity haloes at stylolites in the feldspathic Upper Jurassic Ula sandstone, Norwegian North Sea: An integrated petrographic and chemical mass-balance approach. *J. Sediment. Res.*, **76**, 444–459.
- Hässig, M., Rolland, Y., Duretz, T. and Sosson, M.** (2016) Obduction triggered by regional heating during plate reorganization. *Terra Nov.*, **28**, 76–82.
- Hässig, M., Rolland, Y., Sosson, M., Galoyan, G., Müller, C., Avagyan, A. and Sahakyan, L.** (2013) New structural and petrological data on the Amasia ophiolites (NW Sevan-Akera suture zone, Lesser Caucasus): Insights for a large-scale obduction in Armenia and NE Turkey. *Tectonophysics*, **588**, 135–153.
- Heald, M.T.** (1955) Stylolites in Sandstones. *J. Geol.*, **63**, 101–114.
- Heller, P.L., Angevine, C.L., Winslow, N.S. and Paola, C.** (1988) Two-phase stratigraphic model of foreland-basin sequences. *Geology*, **16**, 501–504.
- Hilgers, C. and Urai, J.L.** (2002) Microstructural observations on natural syntectonic fibrous veins: implications for the growth process. *Tectonophysics*, **352**, 257–274.
- Hill, K.C. and Hayward, A.B.** (1988) Structural constraints on the Tertiary plate tectonic evolution of Italy. *Mar. Pet. Geol.*, **5**, 2–16.

- Hillier, S., Matyas, J., Matter, A. and Vasseur, G.** (1995) Illite/smectite diagenesis and its variable correlation with vitrinite reflectance in the Pannonian Basin. *Clays Clay Miner.*, **43**, 174–183.
- Hintze, J.L. and Nelson, R.D.** (1998) Violin plots: A box plot-density trace synergism. *Am. Stat.*, **52**, 181–184.
- Hippolyte, J.-C., Angelier, J. and Barrier, E.** (1995) Compressional and extensional tectonics in an arc system: example of the Southern Apennines. *J. Struct. Geol.*, **17**, 1725–1740.
- Hoareau, G., Claverie, F., Pecheyran, C., Paroissin, C., Grignard, P.-A., Motte, G., Chailan, O. and Girard, J.-P.** (2021a) Direct U–Pb dating of carbonates from micron-scale femtosecond laser ablation inductively coupled plasma mass spectrometry images using robust regression. *Geochronology*, **3**, 67–87.
- Hoareau, G., Crognier, N., Lacroix, B., Aubourg, C., Roberts, N.M.W., Niemi, N., Branellec, M., Beaudoin, N. and Ruiz, I.S.** (2021b) Combination of $\Delta 47$ and U-Pb dating in tectonic calcite veins unravel the last pulses related to the Pyrenean Shortening (Spain). *Earth Planet. Sci. Lett.*, **553**, 116636.
- Hodges, K. V., Ruhl, K.W., Wobus, C.W. and Pringle, M.S.** (2005) $40\text{Ar}/39\text{Ar}$ thermochronology of detrital minerals. *Rev. Mineral. Geochemistry*, **58**, 239–257.
- Horton, B.K., Constenius, K.N. and DeCelles, P.G.** (2004) Tectonic control on coarse-grained foreland-basin sequences: An example from the Cordilleran foreland basin, Utah. *Geology*, **32**, 637–640.
- Humphrey, E., Gomez-Rivas, E., Neilson, J., Martín-Martín, J.D., Healy, D., Yao, S. and Bons, P.D.** (2020) Quantitative analysis of stylolite networks in different platform carbonate facies. *Mar. Pet. Geol.*, **114**, 104203.
- Issler, D.R., Willett, S.D., Beaumont, C., Donelick, R.A. and Grist, A.M.** (1999) Paleotemperature history of two transects across the Western Canada Sedimentary Basin: Constraints from apatite fission track analysis. *Bull. Can. Pet. Geol.*, **47**, 475–486.
- Jacobi, R.D.** (1981) Peripheral bulge—a causal mechanism for the Lower/Middle Ordovician unconformity along the western margin of the Northern Appalachians. *Earth Planet. Sci. Lett.*, **56**, 245–251.
- Jammes, S., Tiberi, C. and Manatschal, G.** (2010) 3D architecture of a complex transcurrent rift system: The example of the Bay of Biscay-Western Pyrenees. *Tectonophysics*, **489**, 210–226.
- Jolivet, L. and Faccenna, C.** (2000) Mediterranean extension and the Africa-Eurasia collision. *Tectonics*, **19**, 1095–1106.
- Jolivet, L., Faccenna, C., Agard, P., Lamotte, D.F. De, Menant, A., Sternai, P. and Guillocheau, F.** (2016) Neo-tethys geodynamics and mantle convection: From extension to compression in Africa and a conceptual model for obduction. *Can. J. Earth Sci.*, **53**, 1190–1204.
- Jolivet, L., Frizon De Lamotte, D., Mascle, A. and Séranne, M.** (1999) The Mediterranean Basins:

- Tertiary Extension within the Alpine Orogen - an introduction. *Geol. Soc. Spec. Publ.*, **156**, 1–14.
- Jordan, T.E.** (1981) Thrust loads and foreland basin evolution, Cretaceous, western United States. *Am. Assoc. Pet. Geol. Bull.*, **65**, 2506–2520.
- Kamp, P.J.J., Webster, K.S. and Nathan, S.** (1996) Thermal history analysis by integrated modelling of apatite fission track and vitrinite reflectance data: Application to an inverted basin (Buller Coalfield, New Zealand). *Basin Res.*, **8**, 383–402.
- Karcz, Z. and Scholz, C.H.** (2003) The fractal geometry of some stylolites from the Calcare Massiccio Formation, Italy. *J. Struct. Geol.*, **25**, 1301–1316.
- Karner, G.D. and Watts, A.B.** (1983) Gravity anomalies and flexure of the lithosphere at mountain ranges. *J. Geophys. Res. Solid Earth*, **88**, 10449–10477.
- Katsman, R.** (2010) Extensional veins induced by self-similar dissolution at stylolites: Analytical modeling. *Earth Planet. Sci. Lett.*, **299**, 33–41.
- Katsman, R., Aharonov, E. and Scher, H.** (2006) Localized compaction in rocks: Eshelby's inclusion and the Spring Network Model. *Geophys Res Lett.* doi: 10.1029/2005GL025628
- Kattenhorn, S.A., Aydin, A. and Pollard, D.D.** (2000) Joints at high angles to normal fault strike: an explanation using 3-D numerical models of fault-perturbed stress fields. *J. Struct. Geol.*, **22**, 1–23.
- Katz, O., Reches, Z. and Roegiers, J.-C.** (2000) Evaluation of mechanical rock properties using a Schmidt Hammer. *Int. J. rock Mech. Min. Sci.*, **37**, 723–728.
- Koehn, D., Ebner, M., Renard, F., Toussaint, R. and Passchier, C.W.** (2012) Modelling of stylolite geometries and stress scaling. *Earth Planet. Sci. Lett.*, **341**, 104–113.
- Koehn, D., Köehler, S., Toussaint, R., Ghani, I. and Stollhofen, H.** (2022) Scaling analysis, correlation length and compaction estimates of natural and simulated stylolites. *J. Struct. Geol.*, **161**, 104670.
- Koehn, D., Renard, F., Toussaint, R. and Passchier, C.W.** (2007) Growth of stylolite teeth patterns depending on normal stress and finite compaction. *Earth Planet. Sci. Lett.*, **257**, 582–595.
- Koehn, D., Rood, M.P., Beaudoin, N., Chung, P., Bons, P.D. and Gomez-Rivas, E.** (2016) A new stylolite classification scheme to estimate compaction and local permeability variations. *Sediment. Geol.*, **346**, 60–71.
- Kohn, B.P., Feinstein, S., Foster, D.A., Steckler, M.S. and Eyal, M.** (1997) Thermal history of the eastern Gulf of Suez, II. Reconstruction from apatite fission track and $^{40}\text{Ar}/^{39}\text{Ar}$ K-feldspar measurements. *Tectonophysics*, **283**, 219–239.
- Koopman and Anton** (1983) Detachment tectonics in the Central Apennines, Italy.
- Kubler, B.** (1984) Les indicateurs des transformations physiques et chimiques dans la diagenese temperature et calorimetrie. *Thermométrie et barométrie géologiques*, **2**, 489–596.
- Kubler, B.** (1967) La cristallinité de l'illite et les zones tout à fait supérieures du métamorphisme. *Etages tectoniques*, 105–121.

- Kübler, B. and Jaboyedoff, M.** (2000) Illite crystallinity. *Comptes Rendus l'Académie des Sci. - Ser. IIA - Earth Planet. Sci.*, **331**, 75–89.
- Labeur, A., Beaudoin, N.E., Lacombe, O., Emmanuel, L., Petracchini, L., Daëron, M., Klimowicz, S. and Callot, J.-P.** (2021) Burial-deformation History of Folded Rocks Unraveled by Fracture Analysis, Stylolite Paleopiezometry and Vein Cement Geochemistry: A Case Study in the Cingoli Anticline (Umbria-Marche, Northern Apennines). *Geosciences*, **11**, 135.
- Lacombe, O.** (2007) Comparison of paleostress magnitudes from calcite twins with contemporary stress magnitudes and frictional sliding criteria in the continental crust: Mechanical implications. *J. Struct. Geol.*, **29**, 86–99.
- Lacombe, O., Amrouch, K., Mouthereau, F. and Dissez, L.** (2007) Calcite twinning constraints on late Neogene stress patterns and deformation mechanisms in the active Zagros collision belt. *Geology*, **35**, 263–266.
- Lacombe, O., Beaudoin, N., Hoareau, G., Labeur, A., Pecheyran, C. and Callot, J.-P.** (2021) Dating folding beyond folding, from layer-parallel shortening to fold tightening, using mesostructures: Lessons from the Apennines, Pyrenees and Rocky Mountains. *Solid Earth Discuss.*, 1–26.
- Lacombe, O., Bellahsen, N. and Mouthereau, F.** (2011) Fracture patterns in the Zagros Simply Folded Belt (Fars, Iran): constraints on early collisional tectonic history and role of basement faults. *Geol. Mag.*, **148**, 940–963.
- Laird, A.P. and Morley, C.K.** (2011) Development of gas hydrates in a deep-water anticline based on attribute analysis from three-dimensional seismic data. *Geosphere*, **7**, 240–259.
- Lash, G.G. and Engelder, T.** (2007) Jointing within the outer arc of a forebulge at the onset of the Alleghanian Orogeny. *J. Struct. Geol.*, **29**, 774–786.
- Laubach, S.E.** (1988) Subsurface fractures and their relationship to stress history in East Texas Basin sandstone. *Tectonophysics*, **156**, 37–49.
- Laubach, S.E.** (1989) Paleostress directions from the preferred orientation of closed microfractures (fluid-inclusion planes) in sandstone, East Texas basin, USA. *J. Struct. Geol.*, **11**, 603–611.
- Laubach, S.E., Olson, J.E. and Gale, J.F.W.** (2004) Are open fractures necessarily aligned with maximum horizontal stress? *Earth Planet. Sci. Lett.*, **222**, 191–195.
- Lavecchia, G., Minelli, G. and Piali, G.** (1988) The Umbria-Marche arcuate fold belt (Italy). *Tectonophysics*, **146**, 125–137.
- Lawton, T.F. and Trexler Jr, J.H.** (1991) Piggyback basin in the Sevier orogenic belt, Utah: Implications for development of the thrust wedge. *Geology*, **19**, 827–830.
- Lee, E.Y., Novotny, J. and Wagreich, M.** (2020) Compaction trend estimation and applications to sedimentary basin reconstruction (BasinVis 2.0). *Appl. Comput. Geosci.*, **5**, 100015.
- Li, Q., Parrish, R.R., Horstwood, M.S.A. and McArthur, J.M.** (2014) U–Pb dating of cements in

Mesozoic ammonites. *Chem. Geol.*, **376**, 76–83.

- Li, W., Frash, L.P., Welch, N.J., Carey, J.W., Meng, M. and Wigand, M.** (2021) Stress-dependent fracture permeability measurements and implications for shale gas production. *Fuel*, **290**, 119984.
- Liégeois, J.P., Benhallou, A., Azzouni-Sekkal, A., Yahiaoui, R. and Bonin, B.** (2005) The Hoggar swell and volcanism: Reactivation of the Precambrian Tuareg shield during Alpine convergence and West African Cenozoic volcanism. *Spec. Pap. Geol. Soc. Am.* 388:379–400.
- Lucente, C.C.** (2004) Topography and palaeogeographic evolution of a middle Miocene foredeep basin plain (Northern Apennines, Italy). *Sediment. Geol.*, **170**, 107–134.
- Malinverno, A. and Ryan, W.** (1986) Extension in the Tyrrhenian Sea and Shortening in the Apennines as Result of Arc Migration Driven by Sinking of the Lithosphere. *Tectonics*, **5**, 227–245.
- Mangenot, X., Bonifacie, M., Gasparrini, M., Götz, A., Chaduteau, C., Ader, M. and Rouchon, V.** (2017) Coupling $\Delta 47$ and fluid inclusion thermometry on carbonate cements to precisely reconstruct the temperature, salinity and $\delta 18O$ of paleo-groundwater in sedimentary basins. *Chem. Geol.*, **472**, 44–57.
- Manger, G.E.** (1963) Porosity and bulk density of sedimentary rocks.
- Marchegiani, L., Bertotti, G., Cello, G., Deiana, G., Mazzoli, S. and Tondi, E.** (1999) Pre-orogenic tectonics in the Umbria-Marche sector of the Afro-Adriatic continental margin. *Tectonophysics*, **315**, 123–143.
- Marfil, R., Caja, M.A., Tsige, M., Al-Aasm, I.S., Martin-Crespo, T. and Salas, R.** (2005) Carbonate-cemented stylolites and fractures in the Upper Jurassic limestones of the Eastern Iberian Range, Spain: a record of palaeofluids composition and thermal history. *Sediment. Geol.*, **178**, 237–257.
- Marshak, S., Geiser, P.A., Alvarez, W. and Engelder, T.** (1982a) Mesoscopic fault array of the northern Umbrian Apennine fold belt, Italy: geometry of conjugate shear by pressure-solution slip. *Geol. Soc. Am. Bull.*, **93**, 1013–1022.
- Marshak, S., Geiser, P.A., Alvarez, W. and Engelder, T.** (1982b) Mesoscopic fault array of the northern Umbrian Apennine fold belt, Italy: Geometry of conjugate shear by pressure-solution slip. *Geol. Soc. Am. Bull.*, **93**, 1013–1022.
- Martelli, L., Farabegoli, E., Benini, A., De Donatis, M., Severi, P. and Pizziolo, M.** (1994) The Geology of the Map 265 - S. Piero in Bagno (Northern Apennines).
- Mazzoli, S., Cello, G., Deiana, G., Galdenzi, S., Gambini, R., Mancinelli, A., Mattioni, L., Shiner, P. and Tondi, E.** (2000) Modes of foreland deformation ahead of the Apennine thrust front. *J. Czech Geol. Soc.*, **45**, 246.
- Mazzoli, S., Deiana, G., Galdenzi, S. and Cello, G.** (2002) Miocene fault-controlled sedimentation and thrust propagation in the previously faulted external zones of the Umbria-Marche Apennines, Italy. *EGU Stephan Mueller Spec. Publ. Ser.*, **1**, 195–209.
- Mazzoli, S., Pierantoni, P., Borraccini, F., Paltrinieri, W. and Deiana, G.** (2005) Geometry,

- segmentation pattern and displacement variations along a major Apennine thrust zone, central Italy. *J. Struct. Geol.* - *J STRUCT GEOL*, **27**, 1940–1953.
- McCormick, D.S. and Grotzinger, J.P.** (1992) Evolution and significance of an overfilled alluvial foreland basin: Burnside Formation (1.9 Ga), Kilohigok Basin, NWT, Canada. *Basin Res.*, **4**, 253–278.
- McDougall, I. and Harrison, T.M.** (1999) Geochronology and Thermochronology by the $^{40}\text{Ar}/^{39}\text{Ar}$ Method. *Oxford University Press on Demand*.
- Medwedeff, D.A. and Krantz, R.W.** (2002) Kinematic and analog modeling of 3-D extensional ramps: observations and a new 3-D deformation model. *J. Struct. Geol.*, **24**, 763–772.
- Mele, G. and Sandvol, E.** (2003) Deep crustal roots beneath the Northern Apennines inferred from teleseismic receiver functions. *Earth Planet. Sci. Lett.*, **211**, 69–78.
- Mele, G., Sandvol, E. and Cavinato, G.P.** (2006) Evidence of crustal thickening beneath the central Apennines (Italy) from teleseismic receiver functions. *Earth Planet. Sci. Lett.*, **249**, 425–435.
- Mirabella, F., Barchi, M., Lupattelli, A., Stucchi, E., Vulcanologia, I., Roma, S., Roma and Italia** (2008) Insights on the seismogenic layer thickness from the upper crust structure of the Umbria-Marche Apennines (Central Italy). *Tectonics*. doi: 10.1029/2007TC002134
- Mirabella, F., Ciaccio, M., Barchi, M. and Merlini, S.** (2004) The Gubbio normal fault (Central Italy): Geometry, displacement distribution and tectonic evolution. *J. Struct. Geol.*, **26**, 2233–2249.
- Mitra, G. and Yonkee, W.A.** (1985) Relationship of spaced cleavage to folds and thrusts in the Idaho-Utah-Wyoming thrust belt. *J. Struct. Geol.*, **7**, 361–373.
- Mitrovica, J.X., Beaumont, C. and Jarvis, G.T.** (1989) Tilting of continental interiors by the dynamical effects of subduction. *Tectonics*, **8**, 1079–1094.
- Mollema, P.N. and Antonellini, M.A.** (1996) Compaction bands: A structural analog for anti-mode I cracks in aeolian sandstone. *Tectonophysics*, **267**, 209–228.
- Montanari, A., Carey, S., Coccioni, R. and Deino, A.** (1994) Early Miocene tephra in the Apennine pelagic sequence: An inferred Sardinian provenance and implications for western Mediterranean tectonics. *Tectonics*, **13**, 1120–1134.
- Montanari, A., Deino, A., Coccioni, R., Langenheim, V.E., Capo, R. and Monechi, S.** (1991) Geochronology, Sr isotope analysis, magnetostratigraphy, and plankton stratigraphy across the Oligocene-Miocene boundary in the Contessa section (Gubbio, Italy). *Newsletters Stratigr.*, **23**, 151–180.
- Montanari, A. and Sandroni, P.** (1995) Le rocce del Conero raccontano: una breve guida geoescurionistica. *Parco del Conero (IS)*.
- Morley, C.K.** (2007) Development of crestal normal faults associated with deepwater fold growth. *J. Struct. Geol.*, **29**, 1148–1163.
- Motte, G., Hoareau, G., Callot, J.-P., Révillon, S., Piccoli, F., Calassou, S. and Gaucher, E.C.**

- (2021) Rift and salt-related multi-phase dolomitization: example from the northwestern Pyrenees. *Mar. Pet. Geol.*, **126**, 104932.
- Mussi, M., Nanni, T., Tazioli, A. and Vivalda, P.M.** (2017) The Mt Conero limestone ridge: The contribution of stable isotopes to the identification of the recharge area of aquifers. *Ital. J. Geosci.*, **136**, 186–197.
- Mussman, W.J. and Read, J.F.** (1986) Sedimentology and development of a passive-to convergent-margin unconformity: Middle Ordovician Knox unconformity, Virginia Appalachians. *Geol. Soc. Am. Bull.*, **97**, 282–295.
- Mutti, E., Lucchi, F.R. and Roveri, M.** (2002) Revisiting turbidites of the Marnoso-arenacea formation and their basin-margin equivalents: problems with classic models. *Excursion Guideb. Turbid. Work. ...*, 27–30.
- Nemcok, M., Schamel, S. and Gayer, R.** (2009) Thrustbelts: Structural architecture, thermal regimes and petroleum systems. *Cambridge University Press*.
- Nikishin, A., Cloetingh, S., Brunet, M.-F., Stephenson, R., Bolotov, S. and Ershov, A.** (1998) Scythian Platform, Caucasus and Black\Sea region: Mesozoic-Cenozoic tectonic history and dynamics. *Mémoires du Muséum Natl. d'Histoire Nat.*, **177**, 163–176.
- Nikishin, A.M., Okay, A.I., Tüysüz, O., Demirer, A., Amelin, N. and Petrov, E.** (2015) The Black Sea basins structure and history: New model based on new deep penetration regional seismic data. Part 1: Basins structure and fill. *Mar. Pet. Geol.*, **59**, 638–655.
- Noguera, A.M. and Rea, G.** (2000) Deep structure of the Campanian–Lucanian Arc (Southern Apennine, Italy). *Tectonophysics*, **324**, 239–265.
- O’Sullivan, P.B.** (1999) Thermochronology, denudation and variations in palaeosurface temperature: a case study from the North Slope foreland basin, Alaska. *Basin Res.*, **11**, 191–204.
- Oncken, O., Chong, G., Franz, G., Giese, P., Götze, H.-J., Ramos, V.A., Strecker, M.R. and Wigger, P.** (2006) The Andes: active subduction orogeny. *Springer Science & Business Media*.
- Ori, G.G., Roveri, M. and Vannoni, F.** (1986) Plio–Pleistocene sedimentation in the Apenninic–Adriatic foredeep (central Adriatic Sea, Italy). *Forel. basins*, 183–198.
- Otsu, N.** (1979) A threshold selection method from gray-level histograms. *IEEE Trans. Syst. Man. Cybern.*, **9**, 62–66.
- Pace, P. and Calamita, F.** (2014) Push-up inversion structures v. fault-bend reactivation anticlines along oblique thrust ramps: Examples from the Apennines fold-and-thrust belt (Italy). *J. Geol. Soc. London.*, **171**, 227–238.
- Paris B. Stockdale** (1943) Stylolites: Primary or Secondary? *SEPM J Sediment Res.* doi: 10.1306/d4269175-2b26-11d7-8648000102c1865d
- Park, W.C. and Schot, E.H.** (1968) Stylolites: Their Nature and Origin. *SEPM J Sediment Res.* doi: 10.1306/74d71910-2b21-11d7-8648000102c1865d

- Parlangeau, C.** (2017) Quantification des paléocontraintes par l'analyse des macles de la calcite : nouvelle approche d'acquisition et d'inversion des données et mécaniques du maillage. *Université Pierre et Marie Curie - Paris VI*.
- Parlangeau, C., Dimanov, A., Lacombe, O., Hallais, S. and Daniel, J.M.** (2019) Uniaxial compression of calcite single crystals at room temperature: Insights into twinning activation and development. *Solid Earth*, **10**, 307–316.
- Parlangeau, C., Lacombe, O., Schueller, S. and Daniel, J.M.** (2018) Inversion of calcite twin data for paleostress orientations and magnitudes: A new technique tested and calibrated on numerically-generated and natural data. *Tectonophysics*, **722**, 462–485.
- Parrish, R.R., Parrish, C.M. and Lasalle, S.** (2018) Vein calcite dating reveals Pyrenean orogen as cause of Paleogene deformation in southern England. *J. Geol. Soc. London.*, **175**, 425–442.
- Patton, T.L. and O'connor, S.J.** (1988) Cretaceous flexural history of northern Oman mountain foredeep, United Arab Emirates. *Am. Assoc. Pet. Geol. Bull.*, **72**, 797–809.
- Peacock, D.C.P. and Azzam, I.N.** (2006) Development and scaling relationships of a stylolite population. *J. Struct. Geol.*, **28**, 1883–1889.
- Peacock, D.C.P., Korneva, I., Nixon, C.W. and Rotevatn, A.** (2017) Changes of scaling relationships in an evolving population: The example of “sedimentary” stylolites. *J. Struct. Geol.*, **96**, 118–133.
- Peters, K.E., Curry, D.J. and Kacwicz, M.** (2012) An overview of basin and petroleum system modeling: Definitions and concepts.
- Petracchini, L., Antonellini, M., Billi, A. and Scrocca, D.** (2012) Fault development through fractured pelagic carbonates of the Cingoli anticline, Italy: Possible analog for subsurface fluid-conductive fractures. *J. Struct. Geol.*, **45**, 21–37.
- Pizzi, A. and Scisciani, V.** (2000) Methods for determining the Pleistocene-Holocene component of displacement on active faults reactivating pre-Quaternary structures: Examples from the Central Apennines (Italy). *J. Geodyn.*, **29**, 445–457.
- Plint, A.G.U.Y., Hart, B.S. and Donaldson, W.S.** (1993) Lithospheric flexure as a control on stratal geometry and facies distribution in Upper Cretaceous rocks of the Alberta foreland basin. *Basin Res.*, **5**, 69–77.
- Ponziani, F., De Franco, R., Minelli, G., Biella, G., Costanzo, F. and Piali, G.** (1995) Crustal shortening and duplication of the Moho in the Northern Apennines: A view from seismic refraction data. *Tectonophysics*, **252**, 391–418.
- Price, R.A.** (1973) Large-scale gravitational flow of supracrustal rocks, southern Canadian Rockies. *Gravity and tectonics*, **491**, 502.
- Quinlan, G.M. and Beaumont, C.** (1984) Appalachian thrusting, lithospheric flexure, and the Paleozoic stratigraphy of the eastern interior of North America. *Can. J. Earth Sci.*, **21**, 973–996.
- Quintà, A. and Tavani, S.** (2012) The foreland deformation in the south-western Basque-Cantabrian

- Belt (Spain). *Tectonophysics*, **576–577**, 4–19.
- Railsback, L.B.** (1993) Lithologic controls on morphology of pressure-dissolution surfaces (stylolites and dissolution seams) in Paleozoic carbonate rocks from the mideastern United States. *J. Sediment. Petrol.*, **63**, 513–522.
- Railsback, L.B.** and **Andrews, L.M.** (1995) Tectonic stylolites in the ‘undeformed’ Cumberland Plateau of southern Tennessee. *J. Struct. Geol.*, **17**, 911–915.
- Ramsay, J.G.** (1980) The crack–seal mechanism of rock deformation. *Nature*, **284**, 135–139.
- Ravenhurst, C.E., Willett, S.D., Donelick, R.A.** and **Beaumont, C.** (1994) Apatite fission track thermochronometry from central Alberta: Implications for the thermal history of the Western Canada sedimentary basin. *J. Geophys. Res. Solid Earth*, **99**, 20023–20041.
- Reiners, P.W.** (2005) Zircon (U–Th)/He thermochronometry. *Rev. Mineral. Geochemistry*, **58**, 151–179.
- Reiners, P.W., Farley, K.A.** and **Hickes, H.J.** (2002) He diffusion and (U–Th)/He thermochronometry of zircon: initial results from Fish Canyon Tuff and Gold Butte. *Tectonophysics*, **349**, 297–308.
- Renard, F., Bernard, D., Desrues, J.** and **Ougier-Simonin, A.** (2009) 3D imaging of fracture propagation using synchrotron X-ray microtomography. *Earth Planet. Sci. Lett.*, **286**, 285–291.
- Renard, F., Ortoleva, P.** and **Gratier, J.P.** (1997) Pressure solution in sandstones: Influence of clays and dependence on temperature and stress. *Tectonophysics*, **280**, 257–266.
- Renard, F., Schmittbuhl, J., Gratier, J.P., Meakin, P.** and **Merino, E.** (2004) Three-dimensional roughness of stylolites in limestones. *J Geophys Res Solid Earth*. doi: 10.1029/2003jb002555
- Ricci-Lucchi, F.** (1975) Depositional Cycles in Two Turbidite Formations of Northern Apennines (Italy). *J Sediment Res - J SEDIMENT RES*. doi: 10.1306/212F6CB7-2B24-11D7-8648000102C1865D
- Ricci Lucchi, F.** (1986) The foreland basin system of the Northern Apennines and related clastic wedges: A preliminary outline. *G. di Geol.*, **48**, 165–185.
- Ricci Lucchi, F.** (1981) The Marnoso-Arenacea: a migrating turbidite basin “oversupplied” by a highly efficient dispersal system. In: *Excursion Guidebook with Contributions on Sedimentology of Some Italian Basins, International Association of Sedimentologists 2nd Regional Meeting, Bologna*, 231–303.
- Ricci Lucchi, F.** and **Ori, G.G.** (1985) Field Excursion D: syn-orogenic deposits of a migrating basin system in the NW Adriatic Foreland: examples from Emilia Romagna region, Northern Apennines. In: *Excursion Guidebook: Cardiff, International Symposium on Foreland Basins*, 137–176.
- Ring, U.** and **Gerdes, A.** (2016) Kinematics of the Alpenrhein-Bodensee graben system in the Central Alps: Oligocene/Miocene transtension due to formation of the Western Alps arc. *Tectonics*, **35**, 1367–1391.
- Rispoli, R.** (1981) Stress fields about strike-slip faults inferred from stylolites and tension gashes. *Tectonophysics*, **75**, T29–T36.

- Ritts, B.D., Weislogel, A., Graham, S.A. and Darby, B.J.** (2009) Mesozoic Tectonics and Sedimentation of the Giant Polyphase Nonmarine Intraplate Ordos Basin, Western North China Block. *http://dx.doi.org/10.1080/00206810802614523*, **51**, 95–115.
- Roberts, N.M.W., Drost, K., Horstwood, M.S.A., Condon, D.J., Chew, D., Drake, H., Milodowski, A.E., McLean, N.M., Smye, A.J. and Walker, R.J.** (2020) Laser ablation inductively coupled plasma mass spectrometry (LA-ICP-MS) U–Pb carbonate geochronology: strategies, progress, and limitations. *Geochronology*, **2**, 33–61.
- Roberts, N.M.W. and Holdsworth, R.E.** (2022) Timescales of faulting through calcite geochronology: A review. *J. Struct. Geol.*, **158**, 104578.
- Roberts, N.M.W. and Walker, R.J.** (2016) U-Pb geochronology of calcite-mineralized faults: Absolute timing of rift-related fault events on the northeast Atlantic margin. *Geology*, **44**, 531–534.
- Robion, P., Grelaud, S. and Frizon de Lamotte, D.** (2007) Pre-folding magnetic fabrics in fold-and-thrust belts: Why the apparent internal deformation of the sedimentary rocks from the Minervois basin (NE — Pyrenees, France) is so high compared to the Potwar basin (SW — Himalaya, Pakistan)? *Sediment. Geol.*, **196**, 181–200.
- Rolland, A.** (2013) Rhéologie, localisation de la déformation et histoire des contraintes dans les calcaires du site de Bure.
- Rolland, A., Toussaint, R., Baud, P., Conil, N. and Landrein, P.** (2014) Morphological analysis of stylolites for paleostress estimation in limestones. *Int. J. Rock Mech. Min. Sci.*, **67**, 212–225.
- Rolland, A., Toussaint, R., Baud, P., Schmittbuhl, J., Conil, N., Koehn, D., Renard, F. and Gratier, J.** (2012) Modeling the growth of stylolites in sedimentary rocks.
- Rosenbaum, G., Lister, G.S. and Duboz, C.** (2002) Relative motions of Africa, Iberia and Europe during Alpine orogeny. *Tectonophysics*, **359**, 117–129.
- Roure, F., Andriessen, P., Callot, J.P., Faure, J.L., Ferket, H., Gonzales, E., Guilhaumou, N., Lacombe, O., Malandain, J., Sassi, W., Schneider, F., Swennen, R. and Vilasi, N.** (2010) The use of palaeo-thermo-barometers and coupled thermal, fluid flow and pore-fluid pressure modelling for hydrocarbon and reservoir prediction in fold and thrust belts. *Geol. Soc. Spec. Publ.*, **348**, 87–114.
- Roure, F., Casero, P. and Addoum, B.** (2012) Alpine inversion of the North African margin and delamination of its continental lithosphere.
- Roure, F., Swennen, R., Schneider, F., Faure, J.L., Ferket, H., Guilhaumou, N., Osadetz, K., Robion, P. and Vandeginste, V.** (2005) Incidence and importance of tectonics and natural fluid migration on reservoir evolution in foreland fold-and-thrust belts. *Oil Gas Sci. Technol.* **60**:67–106.
- Royden, L. and Karner, G.D.** (1984) Flexure of lithosphere beneath Apennine and Carpathian foredeep basins: evidence for an insufficient topographic load. *Am. Assoc. Pet. Geol. Bull.*, **68**, 704–712.

- Royden, L., Patacca, E. and Scandone, P.** (1987) Segmentation and configuration of subducted lithosphere in Italy - An important control on thrust-belt and foredeep-basin Evolution. *Geology*. doi: 10.1130/0091-7613(1987)15<714:SACOSL>2.0.CO;2
- Royden, L.H.** (1993) The tectonic expression slab pull at continental convergent boundaries. *Tectonics*, **12**, 303–325.
- Rusciadelli, G., Viandante, M.G., Calamita, F. and Cook, A.C.** (2005) Burial-exhumation history of the central Apennines (Italy), from the foreland to the chain building: thermochronological and geological data. *Terra Nov.*, **17**, 560–572.
- Rustichelli, A., Tondi, E., Agosta, F., Cilona, A. and Giorgioni, M.** (2012) Development and distribution of bed-parallel compaction bands and pressure solution seams in carbonates (Bolognano Formation, Majella Mountain, Italy). *J. Struct. Geol.*, **37**, 181–199.
- Saintot, A., Stephenson, R., Brem, A., Stovba, S. and Privalov, V.** (2003) Paleostress field reconstruction and revised tectonic history of the Donbas fold and thrust belt (Ukraine and Russia).
- Sandvol, E., Ni, J., Kind, R. and Zhao, W.** (1997) Seismic anisotropy beneath the southern Himalayas-Tibet collision zone. *J. Geophys. Res. Solid Earth*, **102**, 17813–17823.
- Santucci, S., Måløy, K.J., Delaplace, A., Mathiesen, J., Hansen, A., Haavig Bakke, J.Ø., Schmittbuhl, J., Vanel, L. and Ray, P.** (2007) Statistics of fracture surfaces. *Phys. Rev. E - Stat. Nonlinear, Soft Matter Phys.*, **75**, 016104.
- Satolli, S., Pace, P., Viandante, M.G. and Calamita, F.** (2014) Lateral variations in tectonic style across cross-strike discontinuities: an example from the Central Apennines belt (Italy). *Int. J. Earth Sci.*, **103**, 2301–2313.
- Scarascia, S., Cassinis, R. and Federici, F.** (1998) Gravity modelling of deep structures in the Northern-Central Apennines. *Mem. Soc. Geol. It.*, **52**, 231–246.
- Schmidt, V. and McDonald, D.A.** (1979) The role of secondary porosity in the course of sandstone diagenesis.
- Schmittbuhl, J., Renard, F., Gratier, J.-P.P. and Toussaint, R.** (2004) Roughness of stylolites: implications of 3D high resolution topography measurements. *Phys. Rev. Lett.*, **93**, 238501.
- Schmittbuhl, J., Vilotte, J.P. and Roux, S.** (1995) Reliability of self-affine measurements. *Phys. Rev. E*, **51**, 131–147.
- Schneider, F., Potdevin, J.L., Wolf, S. and Faille, I.** (1996) Mechanical and chemical compaction model for sedimentary basin simulators. *Tectonophysics*, **263**, 307–317.
- Scisciani, V., Agostini, S., Calamita, F., Pace, P., Cilli, A., Giori, I. and Paltrinieri, W.** (2014) Positive inversion tectonics in foreland fold-and-thrust belts: a reappraisal of the Umbria–Marche Northern Apennines (Central Italy) by integrating geological and geophysical data. *Tectonophysics*, **637**, 218–237.
- Scisciani, V., Calamita, F., Tavarnelli, E., Rusciadelli, G., Ori, G.G. and Paltrinieri, W.** (2001)

- Foreland-dipping normal faults in the inner edges of syn-orogenic basins: a case from the Central Apennines, Italy. *Tectonophysics*, **330**, 211–224.
- Scisciani, V. and Montefalcone, R.** (2005) Neogene-Quaternary evolution of the Central Apennine thrust front: Constraints from sequence and forward balancing of a regional cross-section. *Boll. della Soc. Geol. Ital.*, **124**, 579–599.
- Scisciani, V., Montefalcone, R., Mazzoli, S. and Butler, R.W.H.** (2006) Coexistence of thin-and thick-skinned tectonics: an example from the Central Apennines, Italy. *Spec. Pap. Soc. Am.*, **414**, 33.
- Scisciani, V., Rusciadelli, G. and Calamita, F.** (2000) Faglie normali nell'evoluzione tortoniano-messiniane dei bacini sinorogenici dell'Appennino centrale esterno. *Boll. della Soc. Geol. Ital.*, **119**, 715–732.
- Semeniuk, V. and Logan, B.W.** (1976) Dynamic metamorphism; processes and products in Devonian carbonate rocks Canning Basin, Western Australia. *J. Geol. Soc. Aust.*, **Special Pu**, 138.
- Servizio Geologica d'Italia** (1969) Carta geologica d'Italia alla scala 1:100 000, Foglio 123 Assisi.
- Shiner, P., Beccacini, A. and Mazzoli, S.** (2004) Thin-skinned versus thick-skinned structural models for Apulian carbonate reservoirs: constraints from the Val d'Agri Fields, S Apennines, Italy. *Mar. Pet. Geol.*, **21**, 805–827.
- Simonsen, I., Hansen, A. and Nes, O.M.** (1998) Determination of the Hurst exponent by use of wavelet transforms. *Phys. Rev. E*, **58**, 2779.
- Sinclair, H.D., Coakley, B.J., Allen, P.A. and Watts, A.B.** (1991) Simulation of foreland basin stratigraphy using a diffusion model of mountain belt uplift and erosion: an example from the central Alps, Switzerland. *Tectonics*, **10**, 599–620.
- Smith, B., Derder, M.E.M.M., Henry, B., Bayou, B., Yelles, A.K., Djellit, H., Amenna, M., Garces, M., Beamud, E., Callot, J.-P.P., Eschard, R., Chambers, A., Aifa, T., Ait Ouali, R. and Gandriche, H.** (2006) Relative importance of the Hercynian and post-Jurassic tectonic phases in the Saharan platform: a palaeomagnetic study of Jurassic sills in the Reggane Basin (Algeria). *Geophys. J. Int.*, **167**, 380–396.
- Smith, J.E.** (1971) The dynamics of shale compaction and evolution of pore-fluid pressures. *J. Int. Assoc. Math. Geol.* 1971 **33**, **3**, 239–263.
- Sobel, E.R. and Dumitru, T.A.** (1997) Thrusting and exhumation around the margins of the western Tarim basin during the India-Asia collision. *J. Geophys. Res. Solid Earth*, **102**, 5043–5063.
- Stearns, D.W. and Friedman, M.** (1972) Reservoirs in Fractured Rock. Stratigraphic Oil and Gas Fields—Classification, Exploration Methods, and Case Histories. *AAPG Mem.*, **10**, 82–106.
- Stockdale, P.B.** (1922) Stylolites : their nature and origin /. [Bloomington, Ind.,
- Stockdale, P.B.** (1926) The Stratigraphic Significance of Solution in Rocks. *J. Geol.*, **34**, 399–414.
- Stockdale, P.B.** (1936) Rare stylolites. *Am. J. Sci.*, **s5-32**, 129–133.

- Stockmal, G.S., Beaumont, C. and Boutilier, R.** (1986) Geodynamic models of convergent margin tectonics: transition from rifted margin to overthrust belt and consequences for foreland-basin development. *Am. Assoc. Pet. Geol. Bull.*, **70**, 181–190.
- Stoeckhert, F., Molenda, M., Brenne, S. and Alber, M.** (2015) Fracture propagation in sandstone and slate—Laboratory experiments, acoustic emissions and fracture mechanics. *J. Rock Mech. Geotech. Eng.*, **7**, 237–249.
- Storti, F., Rossetti, F. and Salvini, F.** (2001) Structural architecture and displacement accommodation mechanisms at the termination of the Priestley Fault, northern Victoria Land, Antarctica. *Tectonophysics*, **341**, 141–161.
- Sweeney, J.J. and Burnham, A.K.** (1990) Evaluation of a simple model of vitrinite reflectance based on chemical kinetics. *Am. Assoc. Pet. Geol. Bull.*, **74**, 1559–1570.
- Tada, R. and Siever, R.** (2003) Pressure Solution During Diagenesis. <http://dx.doi.org/10.1146/annurev.earth.17.050189.000513>, 89–118.
- Tagami, T.** (2005) Zircon fission-track thermochronology and applications to fault studies. *Rev. Mineral. Geochemistry*, **58**, 95–122.
- Talling, P.J., Lawton, T.F., Burbank, D.W. and Hobbs, R.S.** (1995) Evolution of latest Cretaceous–Eocene nonmarine deposystems in the Axhandle piggyback basin of central Utah. *Geol. Soc. Am. Bull.*, **107**, 297–315.
- Tankard, A.J.** (1986) Depositional response to foreland deformation in the Carboniferous of eastern Kentucky. *Am. Assoc. Pet. Geol. Bull.*, **70**, 853–868.
- Tavani, S., Fernandez, O. and Muñoz, J.A.** (2012a) Stress fluctuation during thrust-related folding: Boltaña anticline (pyrenees, Spain). *Geol. Soc. Spec. Publ.*, **367**, 131–140.
- Tavani, S., Snidero, M. and Muñoz, J.A.** (2014) Uplift-induced residual strain release and late-thrusting extension in the Anaran mountain front anticline, Zagros (Iran). *Tectonophysics*, **636**, 257–269.
- Tavani, S., Storti, F., Bausa, J. and Munoz, J.A.** (2012b) Late thrusting extensional collapse at the mountain front of the northern Apennines (Italy).
- Tavani, S., Storti, F., Lacombe, O., Corradetti, A., Muñoz, J.A. and Mazzoli, S.** (2015) A review of deformation pattern templates in foreland basin systems and fold-and-thrust belts: Implications for the state of stress in the frontal regions of thrust wedges. *Earth-Science Rev.*, **141**, 82–104.
- Tavani, S., Storti, F., Salvini, F. and Toscano, C.** (2008) Stratigraphic versus structural control on the deformation pattern associated with the evolution of the Mt. Catria anticline, Italy. *J. Struct. Geol.*, **30**, 664–681.
- Tavarnelli, E.** (1997) Structural evolution of a foreland fold-and-thrust belt: The Umbria-Marche Apennines, Italy. *J. Struct. Geol.*, **19**, 523–534.
- Tavarnelli, E.** (2007) Ancient synsedimentary structural control on thrust ramp development: an

- example from the Northern Apennines, Italy. *Terra Nov.*, **8**, 65–74.
- Tavarnelli, E., Butler, R.W.H., Decandia, F.A., Calamita, F., Grasso, M., Alvarez, W. and Renda, P.** (2004) Implications of fault reactivation and structural inheritance in the Cenozoic tectonic evolution of Italy. *Spec. Vol. Geol. Soc. Italy*, **186**, 209–222.
- Tembe, S., Baud, P. and Wong, T.F.** (2008) Stress conditions for the propagation of discrete compaction bands in porous sandstone. *J Geophys Res Solid Earth*. doi: 10.1029/2007JB005439
- Ten Brink, U.S. and Ben-Avraham, Z.** (1989) The anatomy of a pull-apart basin: Seismic reflection observations of the Dead Sea Basin. *Tectonics*, **8**, 333–350.
- Tondi, E., Antonellini, M., Aydin, A., Marchegiani, L. and Cello, G.** (2006) The role of deformation bands, stylolites and sheared stylolites in fault development in carbonate grainstones of Majella Mountain, Italy. *J. Struct. Geol.*, **28**, 376–391.
- Toussaint, R., Aharonov, E., Koehn, D., Gratier, J.-P., Ebner, M., Baud, P., Rolland, A. and Renard, F.** (2018) Stylolites: A review. *J. Struct. Geol.*, **114**, 163–195.
- Treloar, P.J., Rex, D.C., Guise, P.G., Coward, M.P., Searle, M.P., Windley, B.F., Petterson, M.G., Jan, M.Q. and Luff, I.W.** (1989) K-Ar and Ar-Ar geochronology of the Himalayan collision in NW Pakistan: Constraints on the timing of suturing, deformation, metamorphism and uplift. *Tectonics*, **8**, 881–909.
- Turgeon, S. and Brumsack, H.** (2006) Anoxic vs dysoxic events reflected in sediment geochemistry during the Cenomanian–Turonian Boundary Event (Cretaceous) in the Umbria–Marche Basin of central Italy. *Chem. Geol.*, **234**, 321–339.
- Van Wamel, W.A. and Zwart, P.E.** (1990) The structural geology and basin development of the Romagnan-Umbrian zone (Upper Savio- and Upper Bidente Valleys, N. Italy). *Geol. en Mijnb.*, **69**, 53–68.
- Ventura, B., Pini, G.A. and Zuffa, G.G.** (2001) Thermal history and exhumation of the Northern Apennines (Italy): evidence from combined apatite fission track and vitrinite reflectance data from foreland basin sediments. *Basin Res.*, **13**, 435–448.
- Wanless, H.R.** (1979) Limestone response to stress; pressure solution and dolomitization. *J. Sediment. Res.*, **49**, 437–462.
- Warr, L.N. and Rice, A.H.N.** (1994) Interlaboratory standardization and calibration of day mineral crystallinity and crystallite size data. *J. Metamorph. Geol.*, **12**, 141–152.
- Watts, A.B.** (2001) *Isostasy and Flexure of the Lithosphere*. Cambridge University Press.
- Westaway, R.** (1992) Seismic moment summation for historical earthquakes in Italy: tectonic implications. *J. Geophys. Res. Solid Earth*, **97**, 15437–15464.
- Wilson, M.** (1993) Magmatism and the geodynamics of basin formation. *Sediment. Geol.*, **86**, 5–29.
- Wilson, M. and Guiraud, R.** (1992) Magmatism and rifting in Western and Central Africa, from Late Jurassic to Recent times. *Tectonophysics*, **213**, 203–225.

- Withjack, M.O., Olsen, P.E. and Schlische, R.W.** (1995) Tectonic evolution of the Fundy rift basin, Canada: evidence of extension and shortening during passive margin development. *Tectonics*, **14**, 390–405.
- Wong, T.F. and Baud, P.** (1999) Mechanical compaction of porous sandstone. *Oil Gas Sci. Technol.*, **54**, 715–727.
- Woodhead, J.D. and Hergt, J.M.** (2001) Strontium, neodymium and lead isotope analyses of NIST glass certified reference materials: SRM 610, 612, 614. *Geostand. Newsl.*, **25**, 261–266.
- Wright, K., Cygan, R.T. and Slater, B.** (2001) Structure of the (101 [combining macron] 4) surfaces of calcite, dolomite and magnesite under wet and dry conditions. *Phys. Chem. Chem. Phys.*, **3**, 839–844.
- Xu, J., Deng, Y., Fu, M., Guo, R., Chen, P., Duan, G. and Ma, R.** (2022) The Nonuniform Distribution of Stylolite in Bioclastic Limestones and Its Influence on Reservoir Petro-Physical Properties—A Case Study of the Mishrif Formation from the Ah Oilfield. *Energies*, **15**, 3032.
- Yalçın, M.N., Littke, R. and Sachsenhofer, R.F.** (1997) Thermal History of Sedimentary Basins. *Pet. Basin Evol.*, 71–167.
- Yilmaz, P.O., Norton, I., Leary, D. and Chuchla, R.J.** (1996) Tectonic Evolution and Paleogeography of Europe. In: *Peri-Tethys Memoir 2: Structure and Prospects of Alpine Basins and Forelands* (Ed. P.A. Ziegler and F. (eds) Horvath), *French National Museum of Natural History*, 170, 15–45.
- Zeboudj, A., Bah, B., Lacombe, O., Beaudoin, N., Gout, C., Godeau, N., Girard, J.-P. and Deschamps, P.** (2022) Depicting past stress history at passive margins: a combination of calcite twinning and stylolite roughness paleopiezometry in supra-salt Sendji deep carbonates, lower Congo Basin, west Africa.
- Zhang, X.** (2010) Compaction of granular carbonates under conditions relevant to diagenesis and fault sealing. Utrecht University Repository
- Zoback, M. Lou, Zoback, M.D., Adams, J., Assumpção, M., Bell, S., Bergman, E.A., Blümling, P., Brereton, N.R., Denham, D., Ding, J., Fuchs, K., Gay, N., Gregersen, S., Gupta, H.K., Gvishiani, A., Jacob, K., Klein, R., Knoll, P., Magee, M., Mercier, J.L., Müller, B.C., Paquin, C., Rajendran, K., Stephansson, O., Suarez, G., Suter, M., Udias, A., Xu, Z.H. and Zhizhin, M.** (1989) Global patterns of tectonic stress. *Nat.* 1989 3416240, **341**, 291–298.

Appendices

Appendices to Chapter 3

Appendix 3.1 - Summary of the results obtained with the standard method, for stylolites sampled in the UMAR, and associated error (rate of variation and percentage of error). The colorimetric scale is qualitative, defined in Table 3.2, and highlights inversion results that are not usable (in red) and therefore not considered for the rest of the analysis. For these inversions, the associated error is not calculated, which is mentioned with **.

Sample	Lc FT (mm)	Lc AWC (mm)	VR	Δ (%)
CIN13_BPS1	0,412	0,439	0,06	6,2
CIN13_BPS2a	0,561	0,6	0,06	6,5
CIN13_BPS2b	0,91	0,766	0,19	18,8
CIN13_BPS2c	0,569	0,841	0,32	32,3
CIN13_BPS3a	0,154	0,3	0,49	48,7
CIN13_BPS3b	0,155	0,269	0,42	42,4
CIN13_BPS4	0,318	0,312	0,02	1,9
CIN14_BPS1	0,243	0,344	0,29	29,4
CIN14_BPS9	0,305	0,632	0,52	51,7
CIN3_BPS1	0,214	0,389	0,45	45,0
CIN3_BPS2	0,298	0,542	0,45	45,0
CIN3_BPS3	0,419	0,495	0,15	15,4
CIN6_BPS1	0,293	0,544	0,46	46,1
CIN6_BPS2	0,148	0,359	0,59	58,8
CIN8_BPS1	0,41	0,532	0,23	22,9
CIN8_BPS2	0,286	0,761	0,62	62,4
CIN9	0,489	0,385	0,27	27,0
CIN10_A1_BPS1b	0,536	0,364	0,47	47,3
CIN10_A1_BPS3	0,242	0,309	0,22	21,7
CIN10_A2_BPS3	0,199	0,285	0,30	30,2
CIN15_A1_BPS1	0,447	0,486	0,08	8,0
CIN15_A2_BPS1	0,916	0,838	0,09	9,3
CIN15_A3	0,326	0,377	0,14	13,5
CIN18_A1	0,302	0,451	0,33	33,0
CIN18_A2_BPS1	0,91	1,31	0,31	30,6
CIN18_A2_BPS2	1,069	1,089	0,02	1,8
CIN17_BPS2	0,539	0,849	0,37	36,5
CIN33_A_BPS1	0,561	0,733	0,23	23,5
CIN33_A_BPS2	1,051	1,081	0,03	2,8
CIN33_A_BPS3	0,46	0,455	0,01	1,1

CIN33_B	0,16	0,344	0,53	53,5
CIN40_A_BPS1	0,872	0,761	0,15	14,6
CIN40_A_BPS2	0,202	0,464	**	**
CIN40_B_BPS1	0,258	0,315	**	**
CIN40_B_BPS2	0,253	0,556	**	**
CIN40_B_BPS3	1,593	0,354	**	**
CIN38_BPS1	0,281	0,529	0,47	46,9
CIN38_BPS3	0,372	0,546	0,32	31,9
C51_BPS1	0,931	1,176	0,21	20,8
C51_BPS2	0,419	0,67	0,37	37,5
C56	0,216	0,35	0,38	38,3
C67'_BPS1	0,52	0,754	0,31	31,0
C67'_BPS2	0,269	0,582	0,54	53,8
C68	0,294	0,333	0,12	11,7
C69_BPS1	0,539	0,736	0,27	26,8
C69_BPS2	0,349	0,46	0,24	24,1
C70_BPS1	0,269	0,352	0,24	23,6
C70_BPS2	0,338	1,28	0,74	73,6
C71	0,136	0,376	0,64	63,8
C72_A_BPS1	0,518	0,503	0,03	3,0
C3_B_BPS1	1,349	1,757	0,23	23,2
C3_B_BPS2	0,799	1,384	0,42	42,3
C86_A_BPS1	0,98	1,33	0,26	26,3
C86_A_BPS2	0,393	1,001	0,61	60,7
C86_A_BPS3	0,352	0,431	0,18	18,3
C86_B	0,501	1,107	0,55	54,7
C26_A	0,872	0,872	0,00	0,0
C26_B_BPS1	0,308	0,847	0,64	63,6
C26_B_BPS2	0,901	0,98	0,08	8,1
C28_BPS2	0,443	0,474	0,07	6,5
C29_A	0,645	0,631	0,02	2,2
C29_B_BPS1	0,636	0,638	0,00	0,3
C29_B_BPS2	0,568	0,836	0,32	32,1
C30_BPS1	0,365	0,358	0,02	2,0
C30_BPS2	0,632	0,603	0,05	4,8
C30_BPS3	0,424	0,4	0,06	6,0
C79_BPS2	0,424	0,38	0,12	11,6
C15_BPS1	0,291	0,49	0,41	40,6

C15_BPS2	0,439	0,508	0,14	13,6
C87_BPS1	0,536	1,173	0,54	54,3
C87_BPS2	0,747	0,98	0,24	23,8
C21_BPS1	0,342	0,595	0,43	42,5
C21_BPS2	0,359	0,683	0,47	47,4
C21_BPS3	0,301	0,447	0,33	32,7
C2_A_BPS1	0,752	0,754	0,00	0,3
C2_A_BPS2	1,145	1,256	0,09	8,8
C2_B	0,8	1,748	0,54	54,2
CON3_BPS1	0,105	0,094	0,12	11,7
CON3_BPS2	0,259	0,146	0,77	77,4
CON5_BPS1	0,42	0,398	0,06	5,5
CON5_BPS2	1,297	0,281	3,62	361,6
CON6_BPS1	0,747	0,788	0,05	5,2
CON6_BPS2	0,3	0,235	0,28	27,7
CON6_BPS3	0,33	0,699	0,53	52,8
CON6_BPS4	1,081	0,493	**	**
CON8_BPS1	0,557	0,316	0,76	76,3
CON8_BPS2	0,385	0,557	0,31	30,9
CON8_BPS3	0,57	0,58	0,02	1,7
CON17_BPS1	0,082	0,888	**	**
CON17_BPS2	0,07	0,507	**	**
CON17_BPS3	0,045	1,153	**	**
CON17_BPS4	0,068	0,349	**	**
CON17_BPS5	0,115	0,338	**	**
CON17_BPS6	0,106	0,304	**	**
CON17_BPS7	0,079	0,935	**	**
CON17_BPS8	0,076	0,385	**	**
CON17_BPS9	0,122	0,421	**	**
CON17_BPS10	0,131	0,633	**	**
CON10_BPS1	0,546	0,399	0,37	36,8
CON10_BPS2	0,332	0,176	0,89	88,6
CON20_BPS1	0,199	0,319	**	**
CON20_BPS2	0,367	0,499	0,26	26,5
CON20_BPS3	0,662	0,649	0,02	2,0
A137T2	4,563	3,949	**	**
A137T3	1,988	5,315	**	**
A137T4	4,444	3,097	**	**

A137T5	4,471	6,276	**	**
A137T7	3,825	7,557	**	**
A137	1,539	2,701	0,43	43,0
A97_styl1BOT_0.94	0,268	1,911	**	**
A97_styl2_3.28	0,163	0,763	0,79	78,6
A97_styl3_0.88	0,32	0,624	0,49	48,7
A97_BPS1	0,604	0,435	0,39	38,9
A97_BPS2	0,29	0,61	0,52	52,5
A97_BPS3	0,119	0,201	0,41	40,8
A123-2	0,428	0,492	0,13	13,0
A123BOT	0,846	0,896	0,06	5,6
A123MID	0,591	2,771	0,79	78,7
A123TOP	0,82	1,782	0,54	54,0
VIN19_BPS1_top	0,406	2,661	**	**
VIN19_BPS1_bottom	1,157	14,595	**	**
VIN19_BPS2	0,492	3,947	**	**
VIN19_BPS3	0,961	1,83	0,47	47,5
VIN20_BPS1	0,802	1,993	0,60	59,8
VIN20_BPS2	0,97	0,883	0,10	9,9
VIN20_BPS3	0,45	0,497	0,09	9,5
VIN22_BPS1	0,648	1,227	0,47	47,2
VIN22_BPS2	0,705	1,09	0,35	35,3
VIN23	0,943	1,224	0,23	23,0
VIN24_A	0,569	1,017	0,44	44,1
VIN24_B	0,626	0,686	0,09	8,7
A21_part	0,368	1,147	0,68	67,9
A21	0,303	0,565	0,46	46,4
A21_SL_5.63	0,649	1,316	0,51	50,7
A104_BPS1	0,326	0,596	0,45	45,3
A104_BPS2	0,521	0,576	0,10	9,5
A104_BPS3	0,473	0,545	0,13	13,2
A104_BPS4	0,341	0,552	0,38	38,2
A104_BPS5	0,42	0,398	0,06	5,5
A104_BPS6	0,45	0,57	0,21	21,1
A104_BPS7	0,529	0,531	0,00	0,4
A104_BPS8	0,556	0,519	0,07	7,1
A104_BPS9	0,321	0,277	0,16	15,9
A104_BPS10	0,32	0,568	0,44	43,7

A104_BPS11	0,329	0,256	0,29	28,5
A104_BPS12	0,411	0,555	0,26	25,9
A104_BPS13	0,31	0,272	0,14	14,0
SUB25_BPS1	0,449	0,505	0,11	11,1
SUB25_BPS2	0,561	0,312	0,80	79,8
SUB27	0,592	0,308	0,92	92,2
SUB28	0,38	0,529	0,28	28,2
SUB41	0,383	0,139	**	**
SUB45_BPS1	0,29	0,282	0,03	2,8
SUB45_BPS2	0,152	0,418	0,64	63,6
SUB45_BPS3	1,012	0,969	0,04	4,4
SUB54	0,072	0,07	**	**
SUB65_BPS1	0,799	0,325	1,46	145,8
SUB65_BPS2	0,229	0,268	0,15	14,6
SUB70	0,508	0,908	0,44	44,1
SUB72_BPS1	0,597	0,549	0,09	8,7
SUB72_BPS2	0,345	0,661	0,48	47,8
SUB72_BPS3	0,261	0,237	0,10	10,1
SUB72_BPS4	0,419	0,47	0,11	10,9
SUB72_BPS5	0,245	0,888	0,72	72,4
SUB80_BPS1	0,181	0,462	0,61	60,8
SUB80_BPS2	0,266	0,365	0,27	27,1
SUB80_BPS3	0,402	0,323	0,24	24,5
SUB85_BPS1	0,264	0,602	0,56	56,1
SUB85_BPS2	0,261	0,442	0,41	41,0
SUB97	0,345	0,382	0,10	9,7
SUB98	0,792	1,26	0,37	37,1
SUB107_BPS1	0,34	0,258	0,32	31,8
SUB107_BPS2	0,189	0,225	0,16	16,0
SUB107_BPS3	0,041	0,159	0,74	74,2
SUB113_BPS1	0,151	0,227	0,33	33,5
SUB113_BPS2	0,175	0,192	0,09	8,9
SUB113_BPS3	0,06	0,104	**	**
SUB145	0,203	0,252	0,19	19,4
A165_mid_2_6.59	0,503	1,134	0,56	55,6
A165_top_ob_2_3.75	1,192	1,368	0,13	12,9
A165_bot_ob_2_6.15_styl1_1.36	0,232	0,514	0,55	54,9
A165_bot_ob_2_6.15_styl3_2,64	0,273	0,514	0,47	46,9

A165_bot_2_4.08	0,383	0,501	0,24	23,6
A165_mid_ob_6.18	1,21	1,05	0,15	15,2
A165_top_ob_5.28_styl1_0.72	0,617	0,768	0,20	19,7
A165_top_ob_5.28_styl2_4.5	0,872	1,611	0,46	45,9

Appendix 3.2 - Summary of the results obtained with the composite method, for stylolites sampled in the UMAR, and associated error (rate of variation and percentage of error). The colorimetric scale is qualitative, defined in Table 3.2, and highlights inversion results that are not usable (in red) and therefore not considered for the rest of the analysis. For these inversions, the associated error is not calculated, which is mentioned with **.

Sample	BPS number	L _c FT (mm)	L _c AWC (mm)	Δ (%)
C15	6	0,229	0,236	3
C2_A	2	1,198	1,251	4
C21	5	0,318	0,55	42
C28	2	0,694	0,639	9
C29_B	2	0,389	0,447	13
C3_B	2	1,249	1,037	20
C30	4	0,48	0,522	8
C45	2	1,208	6,983	**
C51	2	0,81	1,099	26
C67'	2	0,361	0,717	50
C69	2	0,43	0,515	17
C70	2	0,572	0,679	16
C79	2	0,432	0,328	32
C86_A	3	0,591	0,624	5
C87	2	0,856	1,044	18
CIN10_A1	4	0,221	0,277	20
CIN10_A2	2	0,31	0,224	38
CIN13	7	0,226	0,356	37
CIN14_type2	6	0,121	0,245	51
CIN14_type3	6	0,187	0,329	43
CIN15_A1	3	0,121	0,28	57
CIN15_A2	3	0,226	0,276	18
CIN17	3	1,141	1,782	36
CIN18	3	0,606	0,646	6
CIN3	3	0,247	0,45	45
CIN33	4	0,369	0,387	5
CIN38	3	0,418	0,5	16
CIN40_A	2	0,652	0,637	2

CIN40_B	3	0,461	0,744	38
CIN6	3	0,199	0,363	45
CIN8	2	0,552	0,595	7
A137	5	0,638	2,269	**
CON10	2	0,234	0,432	46
CON17	10	0,34	0,078	**
CON20	3	0,112	0,306	63
CON3	2	0,087	0,08	9
CON5	2	0,315	0,823	62
CON6	5	0,753	0,591	27
CON8	3	0,434	0,486	11
A97	3	0,883	0,825	7
A123	4	0,673	0,966	30
AN26	16	0,981	1,308	25
A21	2	0,569	0,592	4
VIN19	3	0,816	2,079	61
VIN20	3	1,045	1,474	29
VIN22	2	0,915	0,889	3
A104	13	0,597	0,593	1
A165	12	0,575	0,535	7
SUB107	3	0,199	0,254	22
SUB113	3	0,164	0,19	14
SUB25	2	0,418	0,459	9
SUB45	3	0,428	0,355	**
SUB65	2	0,347	0,423	18
SUB72	5	0,435	0,454	4
SUB80	3	0,333	0,304	10
SUB85	2	0,293	0,441	34

Appendix to Chapter 4

Appendix 4.1 - Summary table of samples used for U-Pb datings in the Cingoli Anticline. All datings were attempted on faults. None of them yielded conclusive results. The type of fault is given by the following denominations: certainly reverse (CR), normal (N) and sinistral (S);

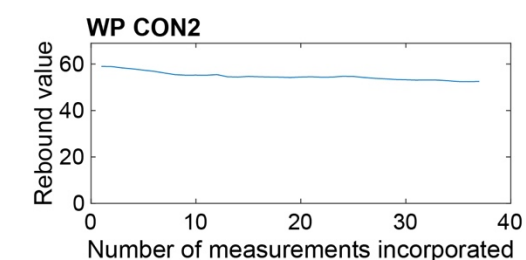
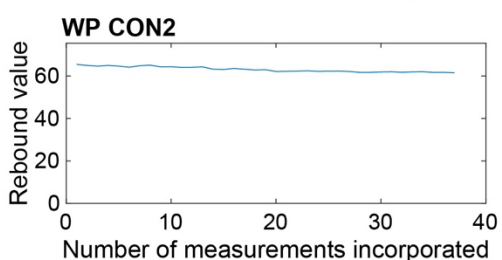
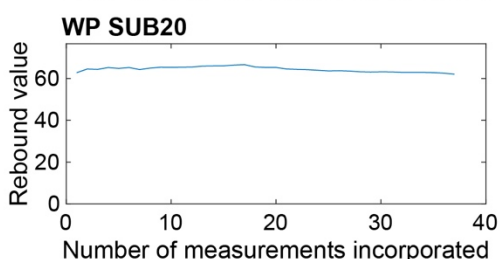
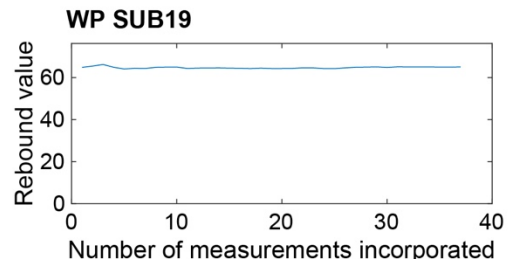
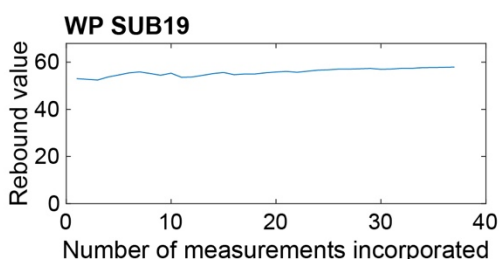
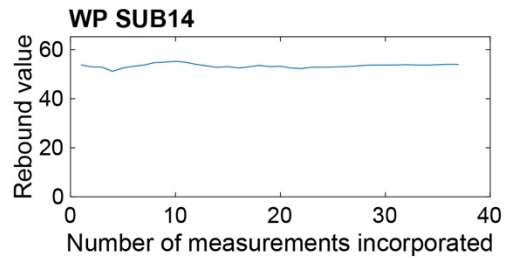
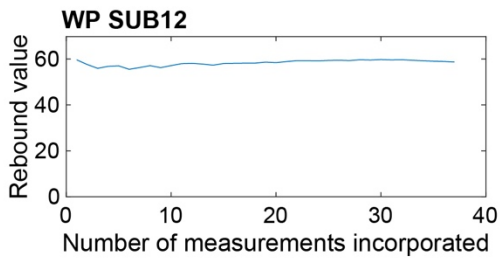
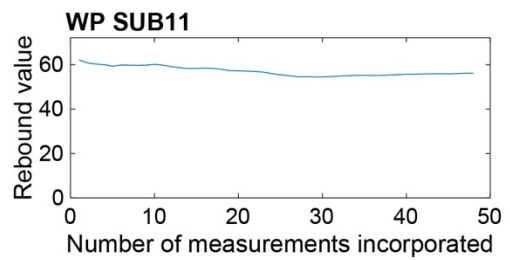
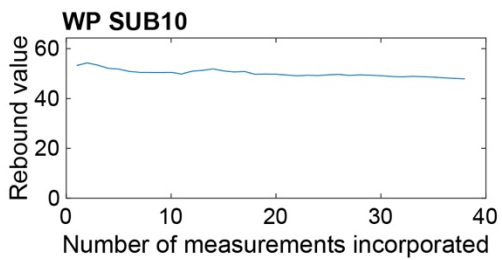
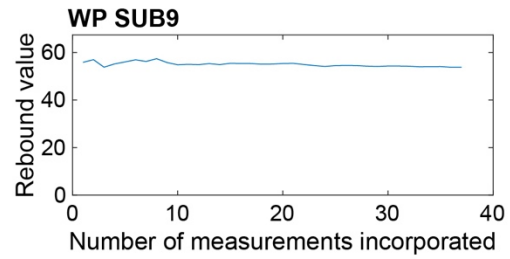
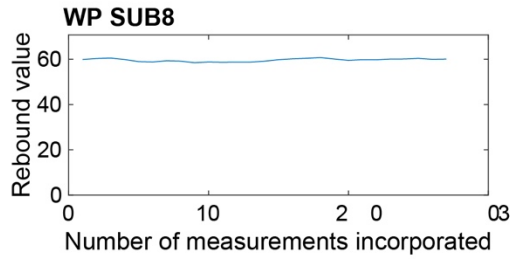
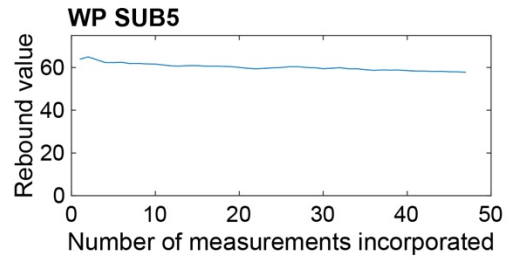
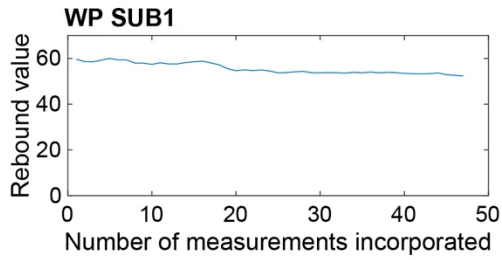
Samples	Location	GPS	Formation	S0	Type	Orientation	Pitch/PVS
CF10	Cingoli	WP_CIN6	Scaglia Bianca	30/244	CR	42/303	82E
CF16	Cingoli	WP_CIN10	Scaglia Rossa	33/344	N	50/130	83W
CF2	Cingoli	WP_CIN6	Scaglia Bianca	30/244	CR	61/210	72E
CF26	Cingoli	WP_CIN7-3	Scaglia Rossa	66/030	N	54/254	65N
CF27	Cingoli	WP_CIN7-3	Scaglia Rossa	66/030	N	50/290	115
CF28	Cingoli	WP_CIN7-3	Scaglia Rossa	66/030	S	52/063	19NW
CF29	Cingoli	WP_CIN7-3	Scaglia Rossa	66/030	N	57/283	76N
CF30	Cingoli	WP_CIN7-3	Scaglia Rossa	66/030	N	60/255	70N
CF31	Cingoli	WP_CIN20	Scaglia Variegata	55/000	S	72/337	24W
CF4	Cingoli	WP_CIN6	Scaglia Bianca	30/244	CR	27/230	47
CF9	Cingoli	WP_CIN6	Scaglia Bianca	30/244	CR	10/020	28

Appendices to Chapter 5

Appendix 5.1 - List of Schmidt Hammer results indexing the anticline, GPS and sample formation. The rebound values and associated Young's moduli are listed for each site studied.

Location	Waypoint	Formation	R value	E (GPA)
Subasio	WP SUB5	Maiolica	59	38
	WP SUB11	Maiolica	55	31
	WP SUB14	Maiolica	54	29
	WP SUB12	Scaglia Bianca	59	38
	WP SUB20	Scaglia Bianca	63	48
	WP SUB1	Scaglia Rossa	54	29
	WP SUB8	Scaglia Rossa	60	40
	WP SUB9	Scaglia Rossa	54	30
	WP SUB10	Scaglia Rossa	49	21
	WP SUB19	Scaglia Rossa	57	35
	WP SUB19	Scaglia Rossa	65	52
	Conero	WP CON2	Maiolica	62
WP CON2		Maiolica	53	28

Appendix 5.2 - Graphical representation of Schmidt Hammer measurements by sampling site. Each graph represents rebound values versus the number of measurements incorporated.



Appendix 5.3 - Published version of 2 articles which I co-authored. The first one, published on 31 August 2020 in the journal *Solid Earth* by Beaudoin *et al.*, and entitled “**Regional-scale paleofluid system across the Tuscan Nappe-Umbria-Marche Apennine Ridge (northern Apennines) as revealed by mesostructural and isotopic analyses of stylolite-vein networks**”. The second one, published on 30 September 2021 in the journal *Solid Earth* by Lacombe *et al.*, and entitled “**Dating folding beyond folding, from layer-parallel shortening to fold tightening using mesostructures: lessons from the Apennines, Pyrenees, and Rocky Mountains**”



Regional-scale paleofluid system across the Tuscan Nappe–Umbria–Marche Apennine Ridge (northern Apennines) as revealed by mesostructural and isotopic analyses of stylolite–vein networks

Nicolas E. Beaudoin¹, Aurélie Labeur^{1,2}, Olivier Lacombe², Daniel Koehn³, Andrea Billi⁴, Guilhem Hoareau¹, Adrian Boyce⁵, Cédric M. John⁷, Marta Marchegiano⁷, Nick M. Roberts⁶, Ian L. Millar⁶, Fanny Claverie⁸, Christophe Pecheyran⁸, and Jean-Paul Callot¹

¹Université de Pau et des Pays de l'Adour, E2S UPPA, LFCR, Pau, France

²Institut des Sciences de la Terre de Paris – ITeP, CNRS-INSU, Sorbonne Université, Paris, France

³GeoZentrum Nordbayern, University Erlangen-Nuremberg, Erlangen, Germany

⁴Consiglio Nazionale delle Ricerche, Roma, Italy

⁵Scottish Universities Environmental Research Centre (SUERC), East Killbride, UK

⁶Geochronology and Tracers Facility, British Geological Survey, Environmental Science Centre, Nottingham, NG12 5GG, UK

⁷Department of Earth Science & Engineering, Imperial College London, London, UK

⁸Université de Pau et des Pays de l'Adour, E2S UPPA, IPREM, Pau, France

Correspondence: Nicolas E. Beaudoin (nicolas.beaudoin@univ-pau.fr)

Received: 21 April 2020 – Discussion started: 5 May 2020

Revised: 13 July 2020 – Accepted: 23 July 2020 – Published: 31 August 2020

Abstract. We report the results of a multiproxy study that combines structural analysis of a fracture–stylolite network and isotopic characterization of calcite vein cements and/or fault coating. Together with new paleopiezometric and radiometric constraints on burial evolution and deformation timing, these results provide a first-order picture of the regional fluid systems and pathways that were present during the main stages of contraction in the Tuscan Nappe and Umbria–Marche Apennine Ridge (northern Apennines). We reconstruct four steps of deformation at the scale of the belt: burial-related stylolitization, Apenninic-related layer-parallel shortening with a contraction trending NE–SW, local extension related to folding, and late-stage fold tightening under a contraction still striking NE–SW. We combine the paleopiezometric inversion of the roughness of sedimentary stylolites – that constrains the range of burial depth of strata prior to layer-parallel shortening – with burial models and U–Pb absolute dating of fault coatings in order to determine the timing of development of mesostructures. In the western part of the ridge, layer-parallel shortening started in

Langhian time (~ 15 Ma), and then folding started at Tortonian time (~ 8 Ma); late-stage fold tightening started by the early Pliocene (~ 5 Ma) and likely lasted until recent/modern extension occurred (~ 3 Ma onward). The textural and geochemical ($\delta^{18}\text{O}$, $\delta^{13}\text{C}$, $\Delta_{47}\text{CO}_2$ and $^{87}\text{Sr}/^{86}\text{Sr}$) study of calcite vein cements and fault coatings reveals that most of the fluids involved in the belt during deformation either are local or flowed laterally from the same reservoir. However, the western edge of the ridge recorded pulses of eastward migration of hydrothermal fluids ($> 140^\circ\text{C}$), driven by the tectonic contraction and by the difference in structural style of the subsurface between the eastern Tuscan Nappe and the Umbria–Marche Apennine Ridge.

1 Introduction

The upper crust is the locus of omnipresent fluid migrations that occur at all scales, leading to strain localization, earthquake triggering, and georesource generation, distribution and storage (e.g. Cartwright, 2007; Andresen, 2012; Bjørlykke, 1994, 1993; Lacombe and Rolland, 2016; Lacombe et al., 2014; Roure et al., 2005; Agosta et al., 2016). Carbonate rocks host an important part of the world's exploited hydrocarbons, strategic ores, and water resources (Agosta et al., 2010). It is thus a fundamental topic to depict the history of fluid migration in deformed carbonates. Such knowledge not only impacts both the prediction and monitoring of energy prospects and potential storage areas but also may help refine our understanding of what mechanisms facilitate fluid migrations during diagenesis of the sedimentary rocks, along with temporal and spatial scales of fluid flow.

Fluid migration and accumulation events are strongly controlled by tectonics, especially by the related development of large-scale faults and fracture networks. Indeed, structural studies established that fracture networks in folded reservoirs are not exclusively related to the local folding history (Stearns and Friedman, 1972) and can also be influenced by burial history (Becker et al., 2010; Laubach et al., 2010, 2019) and long-term regional deformation (Lacombe et al., 2011; Quintà and Tavani, 2012; Tavani and Cifelli, 2010; Tavani et al., 2015; Bellahsen et al., 2006; Bergbauer and Pollard, 2004; Ahmadhadi et al., 2008; Sassi et al., 2012; Beaudoin et al., 2012; Amrouch et al., 2010). In fold-and-thrust belts and orogenic forelands, the complex deformation history can be unravelled by studying the development of mesoscale structures such as faults, veins, and stylolites (Tavani et al., 2015). Several deformational stages often affect the strata in such settings, starting with extension related to foreland flexure and bulging layer-parallel shortening (so-called *pre-folding* if kinematically unrelated with folding, *early-folding* otherwise). Once contraction is accommodated by strata tilting syn-folding, strata curvature-related structures develop under local extension. After the tilting is over, continuous contraction leads to the late-stage fold tightening. Mesoscale structures developing during the so-called *post-folding* events are kinematically unrelated with folding.

In the past decades, a significant volume of work has been conducted in order to reconstruct past fluid migrations through either localized fault systems or distributed sub-seismic fracture networks from the scale of a single fold to that of the basin itself (Engelder, 1984; Reynolds and Lister, 1987; McCaig, 1988; Evans et al., 2010; Evans and Hobbs, 2003; Evans and Fischer, 2012; Forster and Evans, 1991; Cruset et al., 2018; Lacroix et al., 2011; Travé et al., 2000, 2007; Bjørlykke, 2010; Callot et al., 2017a, b; Roure et al., 2005, 2010; Van Geet et al., 2002; Vandeginste et al., 2012; Vilasi et al., 2009; Barbier et al., 2012; Beaudoin et al., 2011, 2013, 2014, 2015; Fischer et al., 2009; Lefticariu et al., 2005; Di Naccio et al., 2005). In some cases, fluid migration

is stratigraphically compartmentalized and directed by compressive tectonic stress. In other cases, mineralization records an infill of meteoric fluids flowing downward or of hydrothermal fluids (i.e. hotter than the host rock they precipitated in) flowing upward, either from the basin or the basement rocks through large-scale faults or décollement (Roure et al., 2005; Vandeginste et al., 2012; Cruset et al., 2018; Lacroix et al., 2011; Travé et al., 2000, 2007; De Graaf et al., 2019; Callot et al., 2010; Beaudoin et al., 2011, 2014; Bertotti et al., 2017; Gonzalez et al., 2013; Lucca et al., 2019; Mozafari et al., 2019; Storti et al., 2018; Vannucchi et al., 2010).

This contribution reports an orogen-scale paleofluid flow study in the northern Apennines (Italy). The study builds upon the mesostructural and geochemical analysis of vein and stylolite networks within the competent Jurassic–Oligocene carbonate platform along a transect running across the Tuscan Nappe and the Umbria–Marche Apennine Ridge (UMAR) (Fig. 1a). The data collection was organized to cover a large area comprising several folds in order to be able to differentiate regional trends from local, fold-related ones. We focused on identifying and characterizing first-order pattern of mesostructures – faults, fractures, and stylolites – associated with layer-parallel shortening and with thrust-related folding, along with the isotopic measurements ($\delta^{18}\text{O}$, $\delta^{13}\text{C}$, $^{87}\text{Sr}/^{86}\text{Sr}$), clumped-isotope measurements ($\Delta_{47}\text{CO}_2$), and U–Pb absolute dating of their calcite cements. Without an appraisal of which fracture trends are relevant to the large-scale (i.e. regional) tectonic evolution, there is a risk to otherwise capture mesostructural and geochemical signals of local meaning only. In order to discuss the local versus hydrothermal fluid origin, we also reconstructed burial curves using strata thickness we correct from physical and chemical compaction. Novel constraints are added to the timing and minimal depth of layer-parallel shortening-related deformation based on the study of the roughness of bedding-parallel stylolites, the inversion of which reliably returns the maximum depth at which compaction under a vertical maximum principal stress was prevailing in the strata. U–Pb absolute dating of calcite steps on mesoscale faults further constrains the timing of folding. Such a multiproxy approach – one that combines structural analysis of fracture–stylolite networks and isotopic characterization of cements/coatings, together with new constraints on burial evolution and deformation timing – provides a picture of the regional fluid pathways during the Apenninic contraction.

2 Geological setting

The Neogene-to-Quaternary Apennines fold-and-thrust belt formed during the convergence of Eurasia and Africa (Lavecchia, 1988; Elter et al., 2012). It is associated with the eastward retreating subduction of the Adriatic Plate under the European Plate. The Apennines extend from the Po Plain to the Calabrian Arc and are divided into two main arcs, the

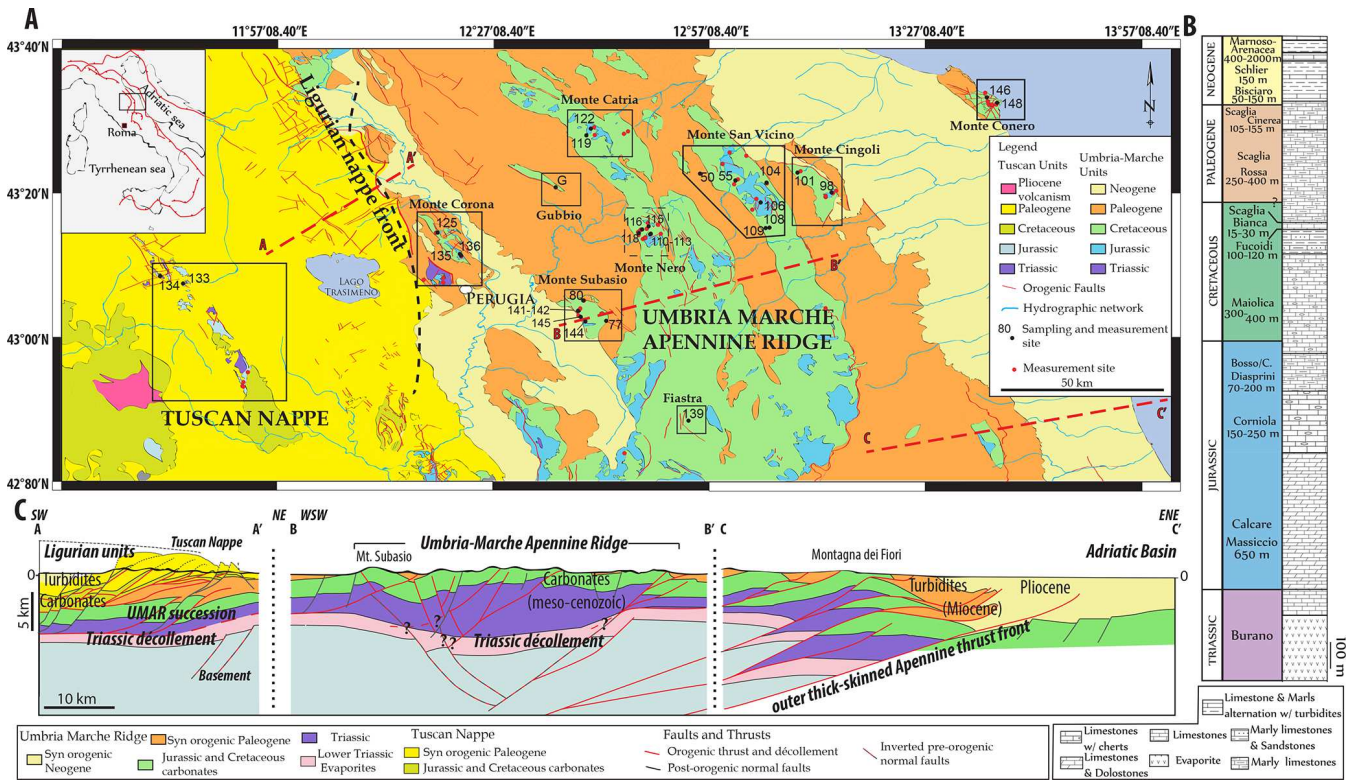


Figure 1. (A) Simplified geological map of the study area, with locations of the sampling and measurement sites. Frames relate to the fracture study areas used in Fig. 4. Exact location of measurement sites is reported as black and red points, and labelled black points also represent the sampling sites for geochemical analysis. (B) Stratigraphic column based on stratigraphic and well data from the central part of the UMAR, after Centamore et al. (1979). (C) Crustal-scale composite cross section based on published seismic data interpretations; A-A' modified after Carboni et al. (2020); B-B' and C-C' after Scisciani et al. (2014). Note that both tectonic style (thick skinned and thin skinned) are represented by question marks for the UMAR.

northern Apennines that extend down to the south of the UMAR and the Southern Apennines that cover the remaining area down to the Calabrian Arc (Carminati et al., 2010). The evolution of the Apennines is characterized by a roughly eastward migration of thrust fronts and associated foredeep basins, superimposed by post-orogenic extension at the rear of the eastward propagating orogenic belt (Cello et al., 1997; Tavani et al., 2012; Lavecchia, 1988; Ghisetti and Vezzani, 2002).

The study area, the Tuscan Nappe and the Umbria–Marche Apennines Ridge, comprises a succession of carbonate rocks, Upper Triassic to Oligocene in age, which corresponds to a carbonate platform (Lavecchia, 1988; Carminati et al., 2010). The Umbrian carbonate units overlie early Triassic evaporites that act as a décollement level and that are themselves unconformably overlying the crystalline basement rocks (Fig. 1b). Above the platform, Miocene turbidite deposits record the progressive eastward involvement of the platform into the fold-and-thrust belt (Calamita et al., 1994). In the western part of the area, the belt is a thin-skinned assembly of piggy-back duplex folds (Fig. 1c), the so-called Tuscan Nappe, the folding and thrusting of which started

by the late Aquitanian (ca. 23–20.43 Ma) and lasted until the Langhian (ca. 16 to 13.8 Ma; Carboni et al., 2020). The UMAR is an arcuate ridge exhibiting an eastward convex shape, with a line connecting Perugia and Ancona separating a northern part where structural trends are oriented NW–SE, from a southern part where structure trends are oriented N–S (Calamita and Deiana, 1988). Burial models suggest that from Burdigalian to early Messinian times, the Tuscan Nappe was further buried under the allochthonous Ligurian thrust sheet, reaching locally up to 1 km in thickness (Caricchi et al., 2015). In the eastern part (now UMAR), the foreland was progressively folded and thrustured from the Lower Miocene in the westernmost part of the current ridge to the Messinian in the foreland of the ridge (Mazzoli et al., 2002). UMAR was considered a thin-skinned thrust belt where shortening was accommodated by stacking and duplexing of sedimentary units detached above a décollement level located in the Triassic evaporites (Conti and Gelmini, 1994; Carboni et al., 2020). The seismic profile of the CROsta Profonda (CROP) project led authors to interpret the UMAR as resulting from thick-skinned tectonics, where the basement is involved in shortening (Barchi et al., 1998) through the positive inver-

sion of normal faults inherited from the Jurassic Tethyan rifting (Fig. 1c). Even if the interpretation of basement-involved shortening is more accepted now, the subsurface geometry is still debated, with some models involving shallow duplexes (Tavernelli et al., 2004; Mirabella et al., 2008), while in more recent works surface folds are rather interpreted as related to high-angle thrusts that either sole within the mid-Triassic décollement or involve the basement (Scisciani et al., 2014, 2019; Butler et al., 2004) (Fig. 1c). For the latter interpretations, the style of deformation of the UMAR strongly contrasts with the style of deformation of the Tuscan Nappe where shortening is accommodated by allochthonous, far-travelled duplex nappes (Carboni et al., 2020) (Fig. 1c). The cross section in Fig. 1c also implies that at least part of the motion on the décollement level at the base of the Tuscan Nappe postdates the westernmost activation of steep thrusts of the UMAR, as the thrust at the base of the Tuscan Nappe cuts and offsets the west-verging basement fault in the area of Monte Subasio. Currently, the whole Tuscan Nappe–UMAR area is experiencing extension, with numerous active normal faults developing trenches, as the contraction front migrated toward the Adriatic Sea (d'Agostino et al., 2001).

Our sampling focused on the carbonate formations cropping out from W to E in the Cetona area located west from Perugia in the Tuscan Nappe – Monte Corona, Monte Subasio, the Gubbio area, Spoleto Area, Monte Nero, Monte Catria, Monte San Vicino, and Monte Cingoli in the UMAR, as well as Monte Conero, the youngest on-shore anticline related to the Apenninic compression, located on the coast line (Fig. 1a). The sampled units comprise, following the stratigraphic order (Fig. 1b): the Triassic anhydrites and dolostones of the Anidridi di Burano Formation focusing on the limestone and marl intercalation at the top; (2) Liassic massive dolomites of the Calcare Massiccio Fm. (Hettangian to Sinemurian, ca. 203–195 Ma); (3) the grey Jurassic limestones with chert beds of the Corniola Fm. (Sinemurian–Pleisbachian, ca. 195–184 Ma); (4) the micritic limestones, marls, and cherts of the Calcare Diasprini Fm (Bajocian–Tithonian, ca. 160–140 Ma); (5) the white limestones with chert beds of the Maiolica Fm. (Tithonian–Aptian, ca. 140–110 Ma); (6) the marly limestones of the Fucoidi Fm. (Aptian–Albian, ca. 110–100 Ma); (7) the white marly limestones of the Scaglia Bianca Fm. (Albian–Turonian, ca. 100–90 Ma); (8) the pink marly limestones of the Scaglia Rossa Fm. (Turonian–Priabonian, ca. 90–37 Ma); and (9) the grey marly limestones of the Scaglia Cinerea Fm. (Priabonian–Aquitanian, ca. 37–21 Ma). Up to 3000 m of Miocene turbidites were deposited when the area of interest was the foredeep ahead of the advancing fold-and-thrust belt and during fold development, including clay-rich limestones and silts of Marnoso–Aranacea (Aquitanian–Tortonian, ca. 21–7 Ma); in the eastern part of the ridge (east of the Cingoli anticline), thicker foredeep deposits are Messinian to Pliocene (ca. 7 to 3 Ma) in age.

3 Methods

The approach adopted relies on structural and geochemical analyses, the results of which are combined to establish a scenario of fluid flow and fluid–rock interaction during deformation of the Umbria–Marche Apennine Ridge in the northern Apennines.

3.1 Mesostructural analysis of joints, veins, and striated fault planes

Approximately ~ 1300 joint and vein orientations, along with tectonic stylolite orientations, were measured along a WSW–ENE transect going from Cetona in the Tuscan Nappe to Monte Conero on the coastline (Fig. 1a). For each measurement site, fractures and tectonic stylolites were measured. Tectonic stylolites considered are either bedding-perpendicular dissolution planes displaying horizontal peaks after unfolding or vertical dissolution planes displaying horizontal peaks in the current bed attitude. Crosscutting and abutment relationships between mesostructures were carefully observed in the field (Fig. 2) and checked in thin sections under the optical microscope when possible (Fig. 3). Poles to fractures and stylolite peaks were projected on Schmidt stereograms, lower hemisphere, in the current attitude of the strata (raw) and after unfolding (unfolded) (Fig. 4). Assuming the same mode of deformation (i.e. mode I opening) and consistent chronological relationships and orientation, we use the pole density obtained from Fisher statistical analysis to define the sets of joints and/or veins which are the most documented and representative at fold scale. Tectonic stylolite planes and peaks were measured, and we consider that the average orientation of the stylolite peaks at the fold scale represents the orientation of the horizontal maximum principal stress (σ_1), as peaks grow parallel to the main shortening direction (Koehn et al., 2007). To complement this mesostructural analysis, striated fault planes were measured (1) in the Langhian carbonates from the Camerino syncline west from Monte San Vicino and (2) in the forelimb of Monte Subasio, with one site in the Scaglia Cinerea and one site in the Scaglia Rossa e Bianca. At each site, paleostress orientations (local trend and plunge) and regimes (reverse, extensional, strike-slip) were calculated using inversion techniques (Angelier, 1984) discussed in Lacombe (2012). Published studies in the UMAR highlight the complexity of fracture patterns at the fold scale that record several phases of stress perturbation and stress/block rotation due to the local tectonics and structural inheritance (Tavani et al., 2008; Petracchini et al., 2012; Beaudoin et al., 2016; Díaz General et al., 2015). In order to capture the mesostructural and fluid flow evolution at the regional scale during layer-parallel shortening and folding, we gathered the most represented fractures by structure, regardless of the structural complexity in the individual folds and corrected them from the local bedding dip using an open-source

stereodiagram rotation program (Grohmann and Campanha, 2010) to discriminate between early, syn-, and late folding features.

3.2 Inversion of sedimentary stylolites

Bedding-parallel stylolites are rough dissolution surfaces that developed in carbonates in flat laying strata during burial at the time when σ_1 was vertical. As proposed by Schmittbuhl et al. (2004) and later developed by Koehn et al. (2012), Ebner et al. (2009b, 2010), Rolland et al. (2014) and Beaudoin et al. (2019, 2020), the 1D roughness of a track along the bedding-parallel stylolite (i.e. difference in height between two points along the track) results from a competition between roughening forces (i.e. pining on non-soluble particles in the rocks) and smoothing forces (i.e. the surface energy at scale typically < 1 mm and the elastic energy at scale > 1 mm). The stylolite growth model (Koehn et al., 2007; Ebner et al., 2009a; Rolland et al., 2012; Toussaint et al., 2018) predicts that the surface energy-controlled scale returns a steep slope characterized by a roughness exponent (so-called Hurst exponent) of 1.1 ± 0.1 , while the elastic energy-controlled scale returns a gentle slope with a roughness exponent of 0.5 to 0.6 (Fig. 5). The length at which the change in roughness exponent occurs, called the crossover length (L_c , in mm), is directly related to the magnitude of differential and mean stress ($\sigma_d = \sigma_1 - \sigma_3$ and $\sigma_m = \frac{\sigma_1 + \sigma_2 + \sigma_3}{3}$, respectively, in Pa) prevailing in the strata at the time the stylolite stopped to be an active dissolution surface following

$$L_c = \frac{\gamma E}{\beta \sigma_m \sigma_d}, \quad (1)$$

where E is the Young modulus of the rock (in Pa), γ is the solid-fluid interfacial energy (in J m^{-2}), and $\beta = \nu(1-2\nu)/\pi$, a dimensionless constant with ν being the Poisson ratio. Samples of bedding-parallel stylolites of which peaks were perpendicular to the dissolution plane were collected in specific points of the study area, and several stylolites were inverted. The inversion process follows the method described in Ebner et al. (2009b). Samples were cut perpendicular to the stylolite, hand polished to enhance the visibility of the track while being cautious to not altering the peaks, and scanned at high resolution (12 800 pixel per inches), and the 1D track was hand drawn with a pixel-based software (GIMP). Each track was analysed as a periodic signal by using the average wavelet spectrum with Daubechies D4 wavelets (Fig. 5) (Ebner et al., 2009b; Simonsen et al., 1998). In the case of bedding-parallel stylolites related to compaction and burial, the method assumes isotropic horizontal stress ($\sigma_v \gg \sigma_h = \sigma_H$). This assumption can be checked by considering different tracks of the same sample, as horizontal stress isotropy during pressure solution implies a constant value of the crossover length regardless of the track direction.

This leads to simplify Eq. (1) (Schmittbuhl et al., 2004) as

$$\sigma_v^2 = \frac{\gamma E}{\alpha L_c}, \quad (2)$$

with

$$\alpha = \frac{(1-2\nu) \cdot (1+\nu)^2}{30\pi(1-\nu)^2}. \quad (3)$$

According to the sampled formation, we used the solid-fluid interfacial energy γ of 0.24 J m^{-2} for dolomite and of 0.32 J m^{-2} for calcite (Wright et al., 2001). As an approximation for the material mechanical properties, we use a Poisson ratio of $\nu = 0.25 \pm 0.05$ and the average Young modulus derived from the Jurassic–Eocene competent core of $E = 24.2 \text{ GPa}$ (Beaudoin et al., 2016). It is important to note that because of the nonlinear regression method we use – and because of uncertainty on the mechanical parameters of the rock at the time it dissolved – the uncertainty on the stress has been calculated to be about 12 % (Rolland et al., 2014). As the dissolution occurs along a fluidic film (Koehn et al., 2012; Rolland et al., 2012; Toussaint et al., 2018), the stylolite roughness is unaffected by local fluid overpressure until the system is fluidized and hydro-fractures (Vass et al., 2014), meaning it is possible to translate vertical stress magnitude directly into depth if considering an average dry rock density for clastic and carbonate sediments (2400 g m^{-3} ; Manger, 1963), without any additional assumption on the past thermal gradient or fluid pressure (Beaudoin and Lacombe, 2018). This technique has already provided meaningful results in various settings (Bertotti et al., 2017; Rolland et al., 2014; Beaudoin et al., 2019, 2020).

Sedimentary stylolites also yield quantitative information on the volume of dissolved rocks during burial (Toussaint et al., 2018), the minimum of which can be approached in 1D by measuring the amplitude of the highest peak along the stylolite track (Table 1) and multiplying this height value (in m) by the average density of stylolites (number per metre) derived from field spacing measurement (Fig. 2c–d; in m).

3.3 O and C stable isotopes

Calcite cements in tectonic veins related either to layer-parallel shortening or to strata curvature at fold hinges were studied petrographically (Fig. 3). The vein textures were characterized in thin sections under an optical microscope, and possible post-cementation diagenesis such as dissolution or replacement were checked under cathodoluminescence, using a cathodoluminescence CITL CCL 8200 Mk4 operating under constant gun condition of 15 kV and 300 μA . To perform oxygen and carbon stable isotope analysis on the cements that were the most likely to record the conditions of fluid precipitation at the time the veins opened, we selected those veins that (1) show no obvious evidence of shear; (2) the texture of which was elongated blocky or fibrous (Fig. 3; Bons et al., 2012); and (3) show homogeneous

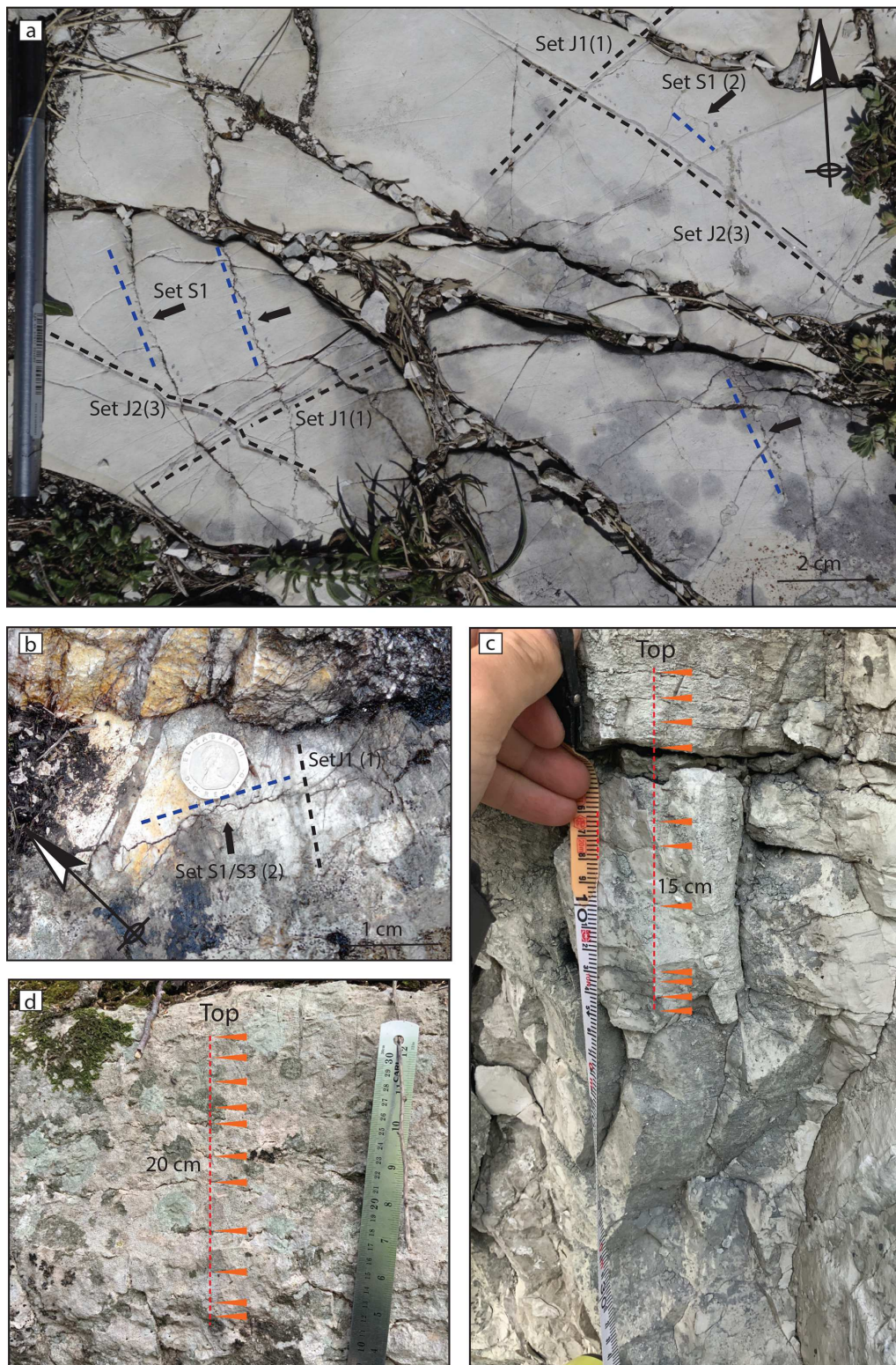


Figure 2. Field photographs showing chronological relationships between veins, joints, and stylolites. (a) Monte Nero and (b) Monte Cingoli sets are reported along with local chronological order between brackets, as deduced from crosscutting and abutment relationships displayed. Dotted lines depict the labelled fracture and tectonic stylolite orientation in black and blue, respectively. Bedding-parallel stylolites spacing from (c) the Maiolica Fm. (Monte Subasio) and (d) the Massiccio Fm. (Monte Cingoli). Intersections between bedding-parallel stylolites and scanline are pointed out with orange arrows.

Table 1. Results of stylolite roughness inversion applied on bedding-parallel stylolites.

Sample	GPS	Structure	Formation	Dissolution (mm)	Lc (mm)*	E (GPa)	ν	γ	σv (Pa)	Depth (m)
A165	165	Subasio	Scaglia Bianca	2.7	1.059	23.2	0.25	0.32	21 811 000	926
	165	Subasio	Scaglia Bianca	2.0	1.306	23.2	0.25	0.32	19 640 000	834
	165	Subasio	Scaglia Bianca	0.6	0.46	23.2	0.25	0.32	33 093 000	1406
	165	Subasio	Scaglia Bianca	0.5	0.486	23.2	0.25	0.32	32 196 000	1368
	165	Subasio	Scaglia Bianca	1.3	0.434	23.2	0.25	0.32	34 070 000	1447
	165	Subasio	Scaglia Bianca	3.1	0.971	23.2	0.25	0.32	22 778 000	967
	165	Subasio	Scaglia Bianca	1.3	1.488	23.2	0.25	0.32	18 400 000	782
AN26	110	Nero	Maiolica	3.1	1.073	23.2	0.25	0.32	21 668 000	920
	110	Nero	Maiolica	2.8	1.535	23.2	0.25	0.32	18 116 000	769
	110	Nero	Maiolica	1.7	1.463	23.2	0.25	0.32	18 557 000	788
	110	Nero	Maiolica	2.2	1.071	23.2	0.25	0.32	21 688 000	921
	110	Nero	Maiolica	3.0	1.29	23.2	0.25	0.32	19 762 000	839
	110	Nero	Maiolica	2.2	1.073	23.2	0.25	0.32	22 661 000	962
	110	Nero	Maiolica	1.8	1.596	23.2	0.25	0.32	17 767 000	755
	110	Nero	Maiolica	6.4	0.659	23.2	0.25	0.32	27 649 000	1174
110	Nero	Maiolica	2.7	0.696	23.2	0.25	0.32	26 904 000	1143	
AN16	115	Nero	Maiolica	2.7	1.279	23.2	0.25	0.32	19 847 000	843
A137	148	Conero	Scaglia Bianca	5.2	2.073	23.2	0.25	0.32	15 589 000	662
A123-2	130	Gubbio	Corniola	2.1	0.428	23.2	0.25	0.32	34 308 000	1457
A123	130	Gubbio	Corniola	1.3	0.791	23.2	0.25	0.32	25 237 000	1072
	130	Gubbio	Corniola	1.8	2.35	23.2	0.25	0.32	14 642 000	622
	130	Gubbio	Corniola	2.3	1.457	23.2	0.25	0.32	18 595 000	790
A21	104	San Vincino	Maiolica	2.1	0.906	23.2	0.25	0.32	23 581 000	1002
	104	San Vincino	Maiolica	3.4	0.787	23.2	0.25	0.32	25 414 000	1079
A104	138	Spoletto	Scaglia Bianca	8.5	0.655	23.2	0.25	0.32	27 733 000	1178
	138	Spoletto	Scaglia Bianca	2.8	0.634	23.2	0.25	0.32	28 189 000	1197
	138	Spoletto	Scaglia Bianca	0.7	0.66	23.2	0.25	0.32	27 628 000	1174
	138	Spoletto	Scaglia Bianca	0.6	1.22	23.2	0.25	0.32	20 321 000	863
	138	Spoletto	Scaglia Bianca	3.4	0.749	23.2	0.25	0.32	25 935 000	1102
	138	Spoletto	Scaglia Bianca	2.5	1.322	23.2	0.25	0.32	19 521 000	829

* Crossover length given within 23 % uncertainty. Vertical stress σv given within 12 % uncertainty using for Young modulus $E = 23.2$ GPa (Beaudoin et al., 2014), Poisson ratio $\nu = 0.25$, and interfacial energy $\gamma = 0.32$ J m⁻². Depth calculated using dry density of rock $d = 2400$ g m⁻³, acceleration of the gravitational field $g = 9.81$ m s⁻².

cement under cathodoluminescence (Fig. 3), precluding any later diagenetic alteration.

To begin with, 0.5 mg of calcite powder was manually collected for each of 58 veins and 54 corresponding host rocks (sampled ~ 2 cm away from veins) in various structures and formations along the transect, in both Tuscan Nappe and UMAR. Carbon and oxygen stable isotopes were analysed on an Analytical Precision AP2003 mass spectrometer equipped with a separate acid injector system. Samples (calcite or dolomite) were placed in glass vials to conduct a reaction with 105 % H₃PO₄ under a helium atmosphere at 90 °C, overnight. Results are reported in Table 2, in permil relative to Vienna PeeDee Belemnite (‰ VPDB). Mean analytical reproducibility based on replicates of the SUERC labora-

tory standard MAB-2 (Carrara marble) was around ± 0.2 ‰ for both carbon and oxygen. MAB-2 is an internal standard extracted from the same Carrara marble quarry, as is the IAEA-CO208 1 international standard. It is calibrated against IAEA-CO-1 and NBS-19 and has exactly the same C and O isotope values as IAEA-CO-1 (-2.5 ‰ and 2.4 ‰ VPDB, respectively).

3.4 ⁸⁷Sr/⁸⁶Sr measurements

Sr-isotope analysis was performed at the Geochronology and Tracers Facility, British Geological Survey. First, 2–10 mg of sample was weighed into 15 mL Savillex teflon beakers and dissolved in 1–2 mL of 10 % Romil uPA acetic acid. After evaporating to dryness, the samples were converted to chlo-

Table 2. Results of stable isotopic analyses of O, C, and $^{87}\text{Sr}/^{86}\text{Sr}$.

Sample	GPS	Structure	Formation	Set	$\delta^{18}\text{O}$ Vein (‰ VPDB)	$\delta^{13}\text{C}$ Vein (‰ VPDB)	$\delta^{18}\text{O}$ HR (‰ VPDB)	$\delta^{13}\text{C}$ HR (‰ VPDB)	$^{87}\text{Sr}/^{86}\text{Sr}_V$	$^{87}\text{Sr}/^{86}\text{Sr}_{HR}$
A94V	134	Cetona	Retian*	J1	-3.2	0.2	-3.2	-4.6		
A93V	134	Cetona	Retian*	J1	-2.9	1.6	-2.5	-3.8		
A95V	134	Cetona	Retian*	J1	-0.5	2.5	-3.2	-4.5		
A92V	134	Cetona	Retian*	J1	-4.3	2.3				
A89V	133	Cetona	Retian*	J1	-2.4	2.4	-3.6	-4.9		
A84V	133	Cetona	Retian*	J2	-2.2	1.8	-2.3	-3.6		
A86V	133	Cetona	Retian*	J2	-5.1	-9.7	-3.9	-5.3		
A76F	125	Corona	Maliolica	F1	-6.7	-1.4	-2.1	2.3		
A76V2	125	Corona	Maliolica	J1	-15.1	1.9	-2.1	2.3		
A76V1	125	Corona	Maliolica	J1	-11.2	-0.5	-2.1	2.3		
A72V	125	Corona	Maliolica	J2	-5.6	2.0	-1.3	1.8		
A76V3	125	Corona	Maliolica	J2	-9.1	0.7	-2.1	2.3		
A77V2	125	Corona	Maliolica	J2	-11.6	1.7	-2.2	1.8		
A77V1	125	Corona	Maliolica	J2	-11.5	1.8	-2.9	2.7		
A96V	135	Corona	Rosso Amonitico	J1	-16.8	2.2	-2.7	2.0		
A97bV1	135	Corona	Rosso Amonitico	J1	-6.4	0.6	-2.7	1.7		
A97bV2	135	Corona	Rosso Amonitico	J1	-9.3	-0.1	-2.7	1.7		
A98V1	136	Corona	Corniola	J1	-3.6	1.7	-2.3	1.4		
A98V2	136	Corona	Corniola	J2	-4.7	1.7	-2.3	1.4		
A121V	G	Gubbio	Maliolica	J2	-2.4	2.0	-2.6	2.1		
A112V1	141	Subasio	Massiccio	J2	-15.8	1.4				
A111V	141	Subasio	Massiccio	J2	-16.6	1.8	-3.3	1.1	0.707644	0.707366
A118V	145	Subasio	Scaglio Rossa	J2	-16.3	1.7	-2.2	2.3	0.707690	0.707827
A120V	145	Subasio	Scaglia Rossa	J2	-14.9	1.7	-2.3	2.5		
A116V	144	Subasio	Massiccio	J3					0.707437	0.707580
SUB15	77	Subasio	Scaglia Cinerea	F1	-3.5	1.3				
SUB17	77	Subasio	Scaglia Cinerea	F1	-3.6	1.3				
SUB30	81	Subasio	Scaglia Cinerea	F1	-4.0	1.5				
A28V	106	Subasio	Massiccio*	J1	-5.8	1.6				
A59V	119	Catria	Maliolica	J1	1.4	2.3	-1.8	2.6		
A73V	122	Catria	Massiccio*	J1	-0.2	2.4	0.4	-1.0		
A63V	122	Catria	Massiccio*	J1	0.5	2.3	-0.3	-1.7		
A66V	122	Catria	Massiccio*	J2	-2.5	2.3	-1.5	-2.9		
A65	122	Catria	Massiccio*	J1	2.0	1.9				
A56V	118	Nero	Scaglia Cinera	J1	-0.9	2.5	-2.7	2.3		
A57bV	118	Nero	Scaglia Cinera	J1	-2.7	2.7	-2.9	2.4	0.707461	0.707382
A53V1	116	Nero	Maliolica	J1	-2.1	1.8	-2.8	2.2	0.707519	
A53V2	116	Nero	Maliolica	J1	1.6	1.9	-2.8	2.2		
A52V	115	Nero	Maliolica	J1	1.3	1.6	-2.2	1.3		
A50V1	113	Nero	Maliolica	J1	-0.7	2.3	-2.3	1.9		
A50V2	113	Nero	Maliolica	J1	3.5	2.3	-2.3	1.9		
A47V	112	Nero	Maliolica	J1	3.7	2.2				
A46V	112	Nero	Maliolica	J2	2.7	1.8	-1.9	2.1		
A44V	111	Nero	Maliolica	J1	3.6	2.0	-2.1	2.2		
A43V	110	Nero	Maliolica	J2	-0.7	1.9	-2.1	1.4		
A107F	139	Spoleto	Scaglia Rossa	F1	-4.2	2.4	-2.5	2.7		
A107V	139	Spoleto	Scaglia Rossa	J1	-3.7	2.5	-2.5	2.7		
A104V1	139	Spoleto	Scaglia Rossa	J2	-3.7	1.8	-2.0	2.6		
A27V	106	San Vicinno	Massiccio	J1	-1.1	1.9	-0.9	2.0		
A40F	109	San Vicinno	Scaglia Bianca	F1	-5.9	1.6	-2.0	3.0		
A38V	109	San Vicinno	Scaglia Bianca	J2	-7.3	-3.0	-2.7	2.6	0.707646	0.707778
A18V	104	San Vicinno	Maliolica	J1	2.1	1.9	-1.3	1.7		
A74V1	104	San Vicinno	Maliolica	J2	2.1	2.1	-1.2	2.2		
A74V2	104	San Vicinno	Maliolica	J2	2.5	2.3	-1.2	2.2		
A32V	108	San Vicinno	Scaglia Bianca	J1	-3.4	2.2	-2.5	2.3	0.707415	0.707778
A29V	108	San Vicinno	Scaglia Bianca	J1	-3.6	2.0	-2.1	1.8		
A34V	108	San Vicinno	Scaglia Bianca	J1	-2.7	2.2	-2.0	2.3		
A30V	108	San Vicinno	Scaglia Bianca	J2	-0.3	2.4	-2.1	2.0		
A39V	109	San Vicinno	Scaglia Rossa	J2	-4.1	0.3				
FAB3	50	San Vicinno	Langhian Flysh	F2	-2.5	0.5				
FAB6	50	San Vicinno	Langhian Flysh	F2	-2.5	0.4				
A14V	101	Cingoli	Scaglia	J2			-1.3	2.8		
A129bF	146	Conero	Scaglia	F1	2.1	2.0	-1.4	2.4		
A129bV	146	Conero	Scaglia	F1	-0.1	2.0	-1.4	2.4		
A126V	146	Conero	Scaglia	J2	0.6	2.4				
A133V	148	Conero	Fucoidi	J1			-1.4	1.5		
CON6	68	Conero	Scaglia Rossa	J1	0.0	1.5				
A135V	148	Conero	Fucoidi	J1	0.3	1.1	-1.4	0.8		

* Values were corrected to reflect the fact that host rocks is dolomite; HR stands for host rock, V stands for vein.

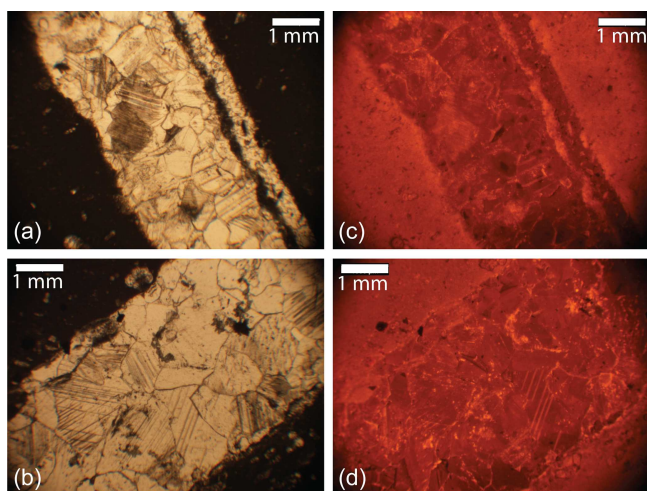


Figure 3. (a, b) Photomicrographs of various veins in plain polarized light, (c, d) with corresponding view under cathodoluminescence; top one is a set J1 vein from the Scaglia Fm., while the bottom one is a set J2 from the Maiolica Fm.

ride form using 2 mL of Teflon-distilled HCl. The samples were then dissolved in ca. 1 mL of calibrated 2.5 M HCl in preparation for column chemistry and centrifuged. Samples were pipetted onto quartz–glass columns containing 4 mL of AG50x8 cation exchange resin. Matrix elements were washed off the column using 48 mL of calibrated 2.5 M HCl and discarded. Sr was collected in 12 mL of 2.5 M HCl and evaporated to dryness.

Sr fractions were loaded onto outgassed single Re filaments using a TaO activator solution and analysed in a Thermo-Electron Triton mass spectrometer in multi-dynamic mode. Data are normalized to $^{86}\text{Sr}/^{88}\text{Sr} = 0.1194$. Three analyses of the NBS987 standard run with the samples gave a value of 0.710250 ± 0.000001 (1SD).

3.5 Carbonate clumped-isotope paleothermometry ($\Delta_{47}\text{CO}_2$)

Clumped-isotope analyses were carried out in the Qatar Stable Isotope Laboratory at Imperial College London. The technique relies on the tendency for heavy isotopes (^{13}C , ^{18}O) to “clump” together in the same carbonate molecule, which varies only by temperature. Since the clumping of heavy isotopes within a molecule is a purely stochastic process at high temperature but is systematically over-represented (relative to randomly distributing isotopes among molecules) at low temperature, the “absolute” temperature of carbonate precipitation can be constrained using clumped-isotope abundances.

The clumped-isotopes laboratory methods at Imperial College follow the protocol of Dale et al. (2014) as adapted for the automated clumped-isotope measurement system IBEX (Imperial Batch EXtraction) system (Cruset et al., 2016).

Typical sample size was 3.5 mg of calcite powder per replicate. Measurement of ^{13}C – ^{18}O ordering in sample calcite was achieved by measurement of the relative abundance of the $^{13}\text{C}^{18}\text{O}^{16}\text{O}$ isotopologues (mass 47) in acid-evolved CO_2 and is referred to in this paper as $\Delta_{47}\text{CO}_2$. A single run on the IBEX comprises 40 analyses, 30% of which are standards. Each analysis takes about 2 h. The process starts with 10 min of reaction of the carbonate powder in a common acid bath containing 105% orthophosphoric acid at 90 °C to liberate CO_2 . The CO_2 gas is then captured in a water/ CO_2 trap maintained at liquid nitrogen temperature and then moved through a hydrocarbon trap filled with Porapak and a second water trap using helium as carrier gas. At the end of the cleaning process, the gas is transferred into a cold finger attached to the mass spectrometer and into the bellows of the mass spectrometer. Following transfer, analyte CO_2 was measured on a dual-inlet Thermo MAT 253 mass spectrometer (MS “Pinta”). The reference gas used is a high-purity CO_2 , with the following reference values: -37.07‰ $\delta^{13}\text{C}_{\text{VPDB}}$ and 8.9‰ $\delta^{18}\text{O}_{\text{VSMOW}}$. Measurements comprise eight acquisitions each with seven cycles with 26 s integration time. A typical acquisition time is 20 min, corresponding to a total analysis time of 2 s.

Data processing was carried out in the freely available stable isotope management software, *Easotope* (<https://www.easotope.org>, last access: 19 February 2020, John and Bowen, 2016). The raw $\Delta_{47}\text{CO}_2$ is corrected in three steps. First, mass spectrometer nonlinearity was corrected by applying a “pressure baseline correction” (Bernasconi et al., 2013). Next, the Δ_{47} results were projected in the absolute reference frame or carbon dioxide equilibrated scale (CDES; Dennis et al., 2011) based on routinely measured ETH1, ETH2, ETH3, ETH4 and Carrara marble (ICM) carbonate standards (Meckler et al., 2014; Muller et al., 2017). The last correction to the raw Δ_{47} was to add an acid correction factor of 0.082‰ to obtain a final $\Delta_{47}\text{CO}_2$ value (Defliese et al., 2015). Temperatures of precipitation were then estimated using the equation of Davies and John (2019). The bulk isotopic value of $\delta^{18}\text{O}$ was corrected for acid digestion at 90 °C by multiplying the value by 1.0081 using the published fractionation factor valid for calcite (Kim et al., 2007). Contamination was monitored by observing the values on mass 48 and 49 from each measurement, using a Δ_{48} offset value $>0.5\text{‰}$ and/or a 49 parameter values >0.3 as a threshold to exclude individual replicates from the analysis (Davies and John, 2019).

3.6 U–Pb absolute dating of veins and faults

The calcite U–Pb geochronology was conducted in two different ways (specific methodology of which is reported in the Supplement):

- LA-ICPMS trace elements and U–Pb isotope mapping were performed at the Geochronology and Tracers Facility, British Geological Survey, UK, on six vein sam-

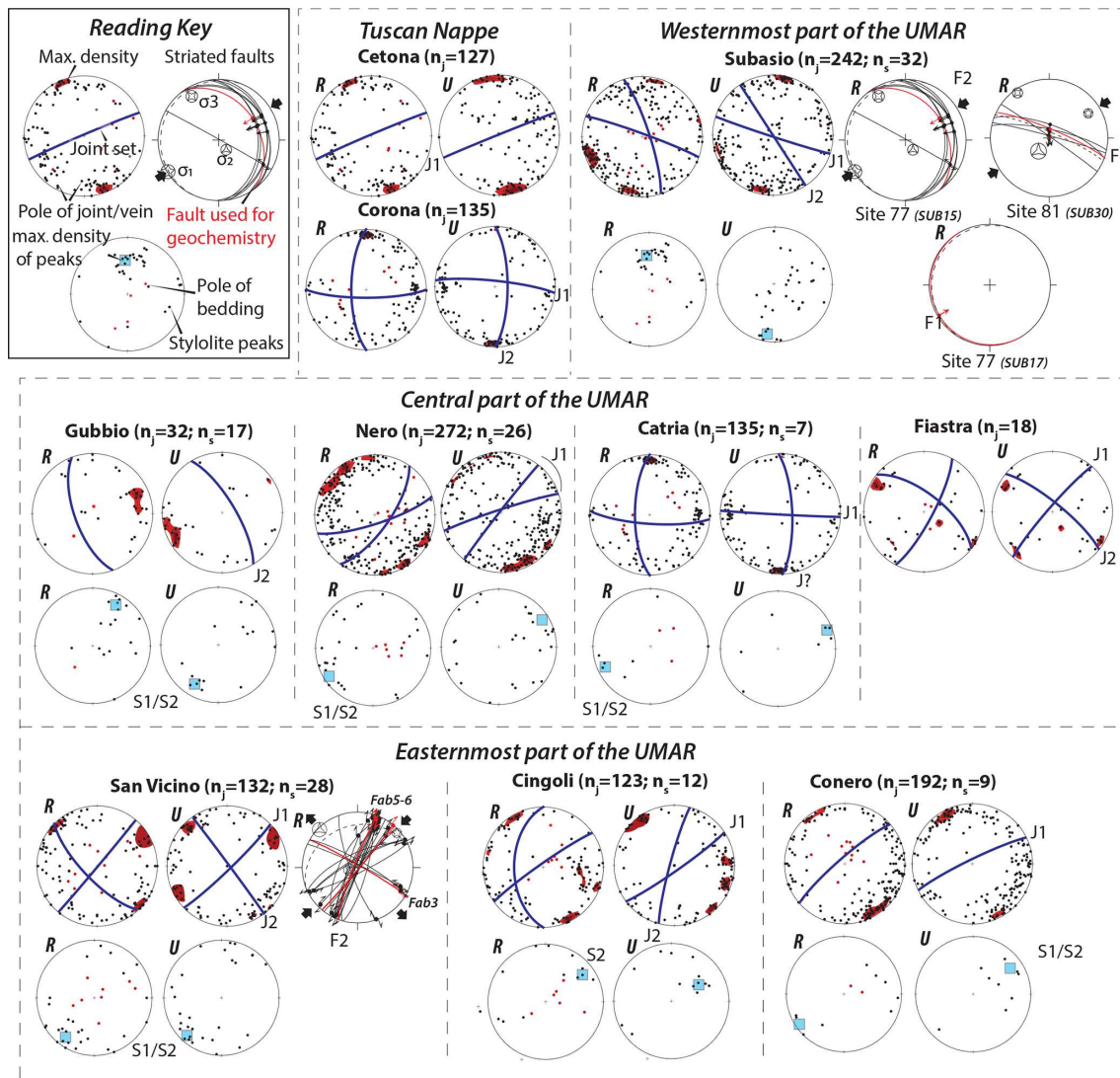


Figure 4. Poles of measured joints and veins and stylolite peaks projected on Schmidt stereograms, lower hemisphere, for the different structures. Data are projected in the current attitude of the strata (left, *R*), with pole to bedding in red, and after unfolding (right, *U*). Red areas represent highest density according to Fischer statistical analysis using the software OpenStereo, and main fracture set average orientations are represented as blue planes. For tectonic stylolite peaks, the blue square represents highest density according to Fischer statistical analysis. Striated fault inversion results are reported in the current attitude of the strata (bedding as dashed line).

ples. Data were generated using a Nu Instruments Atom single collector inductively coupled plasma mass spectrometer coupled to a NWR193UC laser ablation system fitted with a TV2 cell, following protocol reported previously (Roberts et al., 2017; Roberts and Walker, 2016). Laser parameters were 110 μm spots, ablated at 10 Hz for 30 s with a fluence of 7 J cm^{-2} . WC1 (Roberts et al., 2017) was used as a primary reference material for Pb/U ratios and NIST614 for Pb/Pb ratios; no secondary reference materials were run during the session. Additional constraints on U–Pb composition were calculated from the Pb and U masses measured during the trace element mapping. Baselines were

subtracted in Iolite, and Pb/Pb and Pb/U ratios were calculated offline in Excel. No normalization was conducted, as the raw ratios are suitable accurate to assess

- LA-ICPMS U–Pb isotope mapping approach was undertaken at the Institut des Sciences Analytiques et de Physico-Chimie pour l’Environnement et les Matériaux (IPREM) Laboratory (Pau, France). All the 29 samples were analysed with a 257 nm femtosecond laser ablation system (Lambda3, Nexeya, Bordeaux, France) coupled to an HR-ICPMS Element XR (ThermoFisher Scientific, Bremen, Germany) fitted with the Jet Interface (Donard et al., 2015). The method is based on the

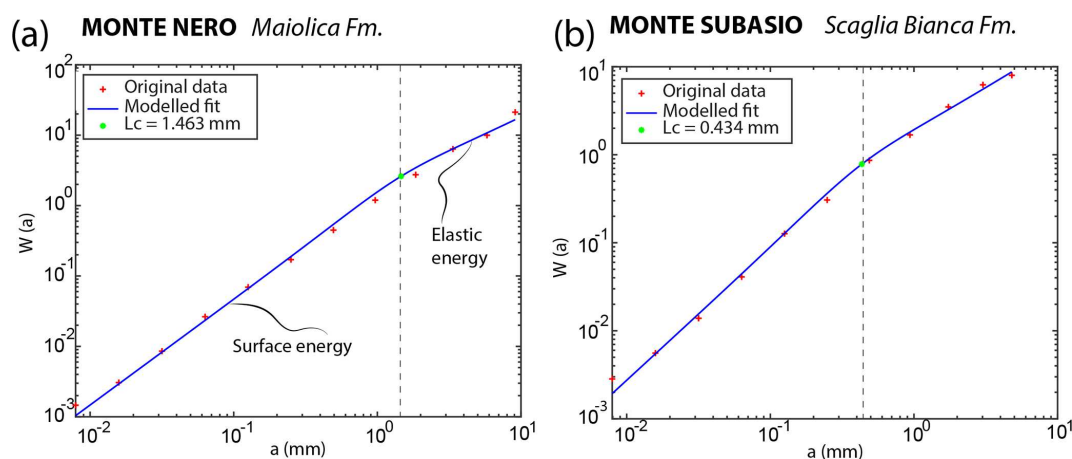


Figure 5. Examples of results of stylolite roughness inversion, with signal analysis by Average Wavelet in Monte Nero (a) and in Monte Subasio (b).

construction of isotopic maps of the elements of interest for dating (U, Pb, Th) from ablation along lines, with ages calculated from the pixel values (Hoareau et al., 2020). The ablation was made in a helium atmosphere (600 mL min^{-1}), and 10 mL min^{-1} of nitrogen was added to the helium flow before mixing with argon in the ICPMS. Measured wash out time of the ablation cell was $\sim 500 \text{ ms}$ for helium gas. The LA-ICPMS coupling was tuned daily, and the additional Ar carrier gas flow rate, torch position, and power were adjusted so that the U/Th ratio was close to 1 ± 0.05 when ablating the glass SRM NIST612. Detector cross-calibration and mass bias calibration were checked daily. The laser and HR-ICPMS parameters used for U–Pb dating are detailed in the Supplement.

4 Results

4.1 Mesostructural analysis of joints, veins, and striated fault planes

Based on the average orientation and the angle to the local fold axis, we group veins and joints in two main sets labelled J (Fig. 4):

- Set J1 comprises joints and veins at high angle to bedding, of which direction is perpendicular to the local strike of fold axis, i.e. E–W to NE–SW with respect to the arcuate shape of the folds. The trend of this set J1 evolves as follows: E–W in the westernmost part (Cetona, Subasio), E–W to NE–SW in the central part (Catria, Nero), NE–SW in the eastern part of the chain (San Vicino, Cingoli), and ENE–WSW in the far foreland (Conero).
- Set J2 comprises joints and veins at high angle to bedding that strike parallel to the local trend of the fold

hinge, i.e. NW–SE in the ridge to N–S in the outermost part of the belt, where the arcuate shape is more marked.

Note that as set J1 strikes perpendicular to the strike of local strata, it is impossible to infer a pre-, syn-, or post-tilting (post-tilting then called J3 hereinafter) origin for its development. In most cases though, abutment relationships establish a relative chronology with set J1 predating set J2 (Fig. 3). The veins of sets J1 and J2 show twinned calcite grains (Fig. 3) with mostly thin and rectilinear twins (thickness $< 5 \mu\text{m}$; Fig. 3). Another set comprising joints striking N–S and oblique to the direction of the fold axis is documented in Monte Catria. It is also encountered at other locations but can be regarded as a second-order set at the regional scale on a statistical basis. This set could be tentatively related to lithospheric flexure (Mazzoli et al., 2002; Tavani et al., 2012), but as it is the least represented in our data, it will not be considered hereinafter.

Most tectonic stylolites have peaks striking NE–SW (Fig. 4), but they can be split in two sets labelled S based on the orientation of their planes with respect to the local bedding.

- Set S1 comprises bed-perpendicular, vertical stylolite planes containing horizontal peaks in the unfolded attitude of strata;
- Set S2 comprises: vertical stylolite planes containing horizontal peaks in the current attitude of strata (set S2).

S1 and S2 were not always easily distinguished when both occurred at the fold scale because (1) stylolite data were often collected in shallow dipping strata, (2) peaks are not always perfectly perpendicular to the stylolite planes, and (3) the orientation data are scattered with intermediate plunges of the peaks. Another set showing stylolite planes with N–S peaks parallel to bedding is documented at Monte Subasio only,

thus will not be considered in the regional sequence of deformation.

Finally, inversion of in-plane striation of mesoscale reverse and strike-slip conjugate fault population reveals (1) a NE–SW contraction in the unfolded attitude of the strata (early folding set F1, flexural-slip related, bedding-parallel reverse faults) and (2) a NE–SW contraction in the current attitude of the strata (late folding set F2, strike-slip conjugate faults and reverse faults).

4.2 Inversion of sedimentary stylolites

The paleopiezometric study of 30 bedding-parallel stylolites returned a range of burial depths, across the UMAR, from W to E, reported in Table 1. To ensure that the stress on the horizontal plane was isotropic, the stylolite inversion technique was applied on two orthogonal tracks for each stylolite. Reported L_c correspond to stylolite where both L_c values are similar within uncertainty. Most data come from the western part of the UMAR: in the Subasio Anticline ($n = 7$), the depth returned by the Scaglia Bianca and the lower part of the Scaglia Rossa fms. ranges from ca. 800 ± 100 to ca. 1450 ± 150 m. In Fiastra area ($n = 6$), the depth returned for the Maiolica Fm. ranges from 800 ± 100 to 1200 ± 150 m. In the Gubbio fault area ($n=4$), the depth returned for the Jurassic Corniola Fm. ranges from 600 ± 70 to 1450 ± 150 m. In Monte Nero ($n = 11$), the depth data published by Beaudoin et al. (2016) and updated here range from 750 ± 100 to 1350 ± 150 m in the Maiolica. Fewer data come from the western part of the UMAR: in Monte San Vicino ($n = 2$), the depth returned for the Maiolica Fm. ranges from 1000 ± 100 to 1050 ± 100 m. Finally, the depth reconstructed for the lower part of the Scaglia Rossa is 650 ± 70 m in the foreland at Conero Anticline ($n = 1$). The maximum height of peaks along the studied stylolite tracks ranges from 0.6 to 8.5 mm ($n = 30$) with a mean value of 2.6 mm. Spacing values for these stylolites were measured on outcrops (Fig. 2) and range from 1 to 2 cm, averaging the number of stylolite per metre to 70. Considering that dissolution is isotropic along the stylolite plane, the volume of rock loss in relation to the chemical compaction is $\sim 18\%$.

4.3 O and C stable isotopes

At the scale of the study area, most formations cropping out were sampled (Table 2), and oxygen isotopic values of the vein cements and striated fault coatings range from -16.8% to 3.7% VPDB, while in the host rocks values range from -5.3% to 0.4% VPDB. Carbon isotopic values range from -9.7% to 2.7% VPDB and from 0.0% to 3.5% VPDB in the veins and in the host rock, respectively (Fig. 6a–b). Isotopic values are represented either according to the structure where they have been sampled in, irrespective of the structural position in the structure (i.e. limbs or hinge), or according to the set they belong to, differentiating the sets J1, J2,

F1, and F2 (Fig. 6a). At the scale of the belt, isotopic values of host rocks are very similar, the only noteworthy point being that the Triassic carbonates have lower $\delta^{18}\text{O}$ than the rest of the column ($\delta^{18}\text{O}$ of -5.5% to -3.5% versus -3.2% to -1.0% VPDB; Fig. 6b). Considering the vein cements, the $\delta^{13}\text{C}$ values are rather similar in all structures and in all sets, a vast majority of veins showing cements with values of $1.5 \pm 1.5\%$ VPDB. In most structures, the $\delta^{13}\text{C}$ values of the veins are similar to the $\delta^{13}\text{C}$ values of the host rock, with the notable exception of the veins hosted in Triassic carbonates of the Cetona anticline, where the shift between $\delta^{13}\text{C}$ values of veins and $\delta^{13}\text{C}$ values of host rocks ranges from $+4.0\%$ VPDB to $+7.5\%$ VPDB (Fig. 6c). The $\delta^{18}\text{O}$ values range from -6.0% VPDB to $+3.7\%$ VPDB in most of the structures and formation, irrespectively of vein set. However, veins sampled in Monte Subasio and Monte Corona return very negative $\delta^{18}\text{O}$ values $< -15.0\%$ VPDB (Fig. 6a). The shift between the $\delta^{18}\text{O}$ value of the vein and the $\delta^{18}\text{O}$ value of the surrounding host rock (Fig. 6d) increases from the western part of the belt (down to -15.0% VPDB in Monte Corona and Monte Subasio) to the central and eastern part of the belt (up to $+5.0\%$ VPDB in Monte Nero, Monte San Vicino, and Monte Conero).

4.4 $^{87}\text{Sr}/^{86}\text{Sr}$ measurements

Analyses were carried out on seven veins and six corresponding host rocks, distributed over three structures of the UMAR (Monte Subasio, Monte Nero, and Monte San Vicino, from the hinterland to the foreland) and three formations (the Calcare Massiccio, the Maiolica, and the Scaglia fms.; Fig. 7, Table 2). Vein sets sampled are the J1, J2, and J3 sets described in the whole area. $^{87}\text{Sr}/^{86}\text{Sr}$ values of host rocks differ according to the formations, being the highest in the Scaglia Rossa Fm. ($^{87}\text{Sr}/^{86}\text{Sr} \approx 0.70780$), intermediate in the Calcare Massiccio Fm. ($^{87}\text{Sr}/^{86}\text{Sr} \approx 0.70760$), and the lowest in both the Scaglia Bianca and the Maiolica Fm. ($^{87}\text{Sr}/^{86}\text{Sr} \approx 0.70730$). $^{87}\text{Sr}/^{86}\text{Sr}$ values of host rocks are in line with expected values for seawater at the time of their respective deposition (McArthur et al., 2001). $^{87}\text{Sr}/^{86}\text{Sr}$ values of veins scatter from 0.70740 to 0.70770, with lower values in Monte Nero and in Monte San Vicino (0.707415 to 0.707646, irrespectively of fracture set) and higher values in Monte Subasio (0.707644 to 0.707690, set J2). One vein cement of J3 in Monte Subasio returned a lower $^{87}\text{Sr}/^{86}\text{Sr}$ value of 0.707437.

4.5 Carbonate clumped-isotope paleothermometry ($\Delta_{47}\text{CO}_2$)

Sixteen samples were analysed, including cements of NE–SW (J1) and NW–SE (J2) pre-folding vein sets, along with coatings of early folding reverse (F1) and late folding strike-slip conjugate mesoscale faults (F2). Regardless of the structural position in the individual folds, $\Delta_{47}\text{CO}_2$ values for veins (Table 3) range from 0.511 ± 0.004 to $0.608 \pm 0.000\%$

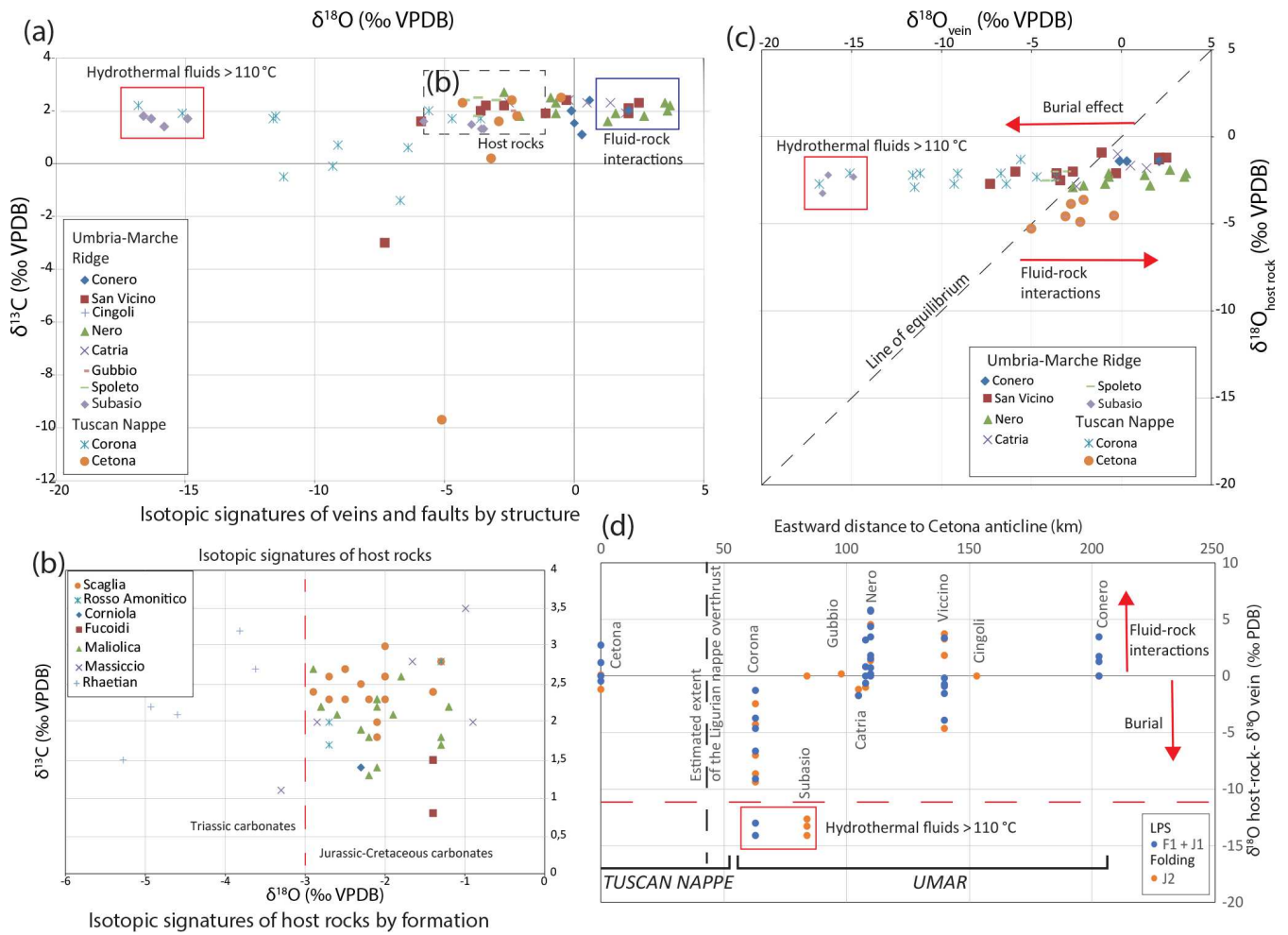


Figure 6. (a) Plot of $\delta^{13}\text{C}$ vs. $\delta^{18}\text{O}$ (‰ VPDB) of veins represented by structure. Frames represent the different type of fluid system. (b) Plot of $\delta^{13}\text{C}$ vs $\delta^{18}\text{O}$ (‰ VPDB) of host rocks represented by structure. (c) Plot of $\delta^{13}\text{C}_{\text{vein}}$ vs. $\delta^{13}\text{C}_{\text{host}}$ (‰ VPDB) of veins represented by structures. (d) Plot of the difference between $\delta^{18}\text{O}$ of host rocks and $\delta^{18}\text{O}$ of veins (‰ VPDB) vs. eastward distance from the Cetona Anticline towards the Adriatic Basin across the strike of the UMAR. Data are represented by tectonic sets. The proposed extension of the Ligurian nappe overthrust is reported after Caricchi et al. (2014); red frames and arrows represent the fluid systems.

CDES in Monte Corona ($n = 3$), from 0.468 ± 0.032 to 0.574 ± 0.000 ‰ CDES in Monte Subasio ($n = 5$), from 0.662 ± 0.004 to 0.685 ± 0.052 ‰ CDES in Monte Nero ($n = 2$), from 0.568 ± 0.035 to 0.658 ± 0.018 ‰ CDES in Monte San Vicino and the syncline to its west ($n = 4$), from 0.601 ± 0.032 to 0.637 ± 0.013 ‰ CDES in Monte Catria ($n = 2$), and is 0.643 ± 0.044 ‰ CDES in Monte Conero. Corresponding $\delta^{18}\text{O}$ and $\delta^{13}\text{C}$ are reported in Table 2. Analysis of $\Delta_{47}\text{CO}_2$ returns the precipitation temperature (T), and the oxygen isotopic values of the mineralizing fluid can be calculated using the $\delta^{18}\text{O}$ of the mineral, the clumped-isotope temperature and the fractionation equation of Kim and O’Neil (1997) providing the fractionation coefficient as a function of the temperature (Fig. 8). Veins and faults belong to the Calcare Massiccio Fm., the Maiolica Fm., the Scaglia Fm., and the marls of the Langhian (Table 3). In the

outermost structure studied of the UMAR (Monte Corona), the fractures of set J2 ($n = 2$) yield consistent precipitation temperatures $T = 106 \pm 8$ °C and $\delta^{18}\text{O}_{\text{fluids}} = 0.0 \pm 1.8$ ‰ VSMOW; the sample of the set J1 yields $T = 56 \pm 16$ °C and $\delta^{18}\text{O}_{\text{fluids}} = -1.1 \pm 1.8$ ‰ VSMOW; in the UMAR, at the Subasio anticline, set F1 ($n = 3$) returns temperatures T ranging from 80 ± 5 to 141 ± 19 °C and a corresponding $\delta^{18}\text{O}_{\text{fluids}}$ ranging from 8.4 ± 1.0 ‰ to 16.1 ± 2.1 ‰ VSMOW, while the set J2 yields $T = 71 \pm 0$ °C and $\delta^{18}\text{O}_{\text{fluids}} = -5.2 \pm 0.0$ ‰ VSMOW; in Monte Nero, set J1 ($n = 2$) yields consistent $T = 30 \pm 15$ °C and $\delta^{18}\text{O}_{\text{fluids}} = [2.7 \pm 2.4, 6.8 \pm 0.2]$ ‰ VSMOW; in the syncline on the west of Monte San Vicino, set F2 ($n = 2$) returns $T = 36 \pm 4$ to 70 ± 7 °C and $\delta^{18}\text{O}_{\text{fluids}} = 2.5 \pm 0.7$ ‰ to 8.3 ± 1.2 ‰ VSMOW; in Monte San Vicino, set J1 yields $T = 47 \pm 5$ °C and $\delta^{18}\text{O}_{\text{fluids}} = 3 \pm 1.1$ ‰ VSMOW, while set J2 yields $T = 74 \pm 10$ °C and $\delta^{18}\text{O}_{\text{fluids}} =$

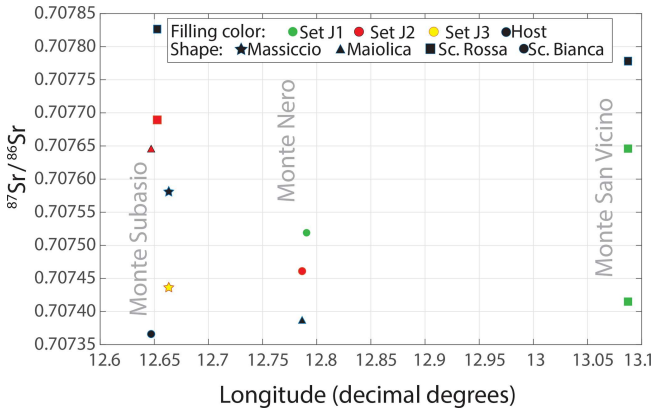


Figure 7. Plot of $^{87}\text{Sr}/^{86}\text{Sr}$ values vs. longitude, with filling colour related to tectonic set and point shape related to host rock formation. Note that the host-rock values are equivalent to the related formation seawater values.

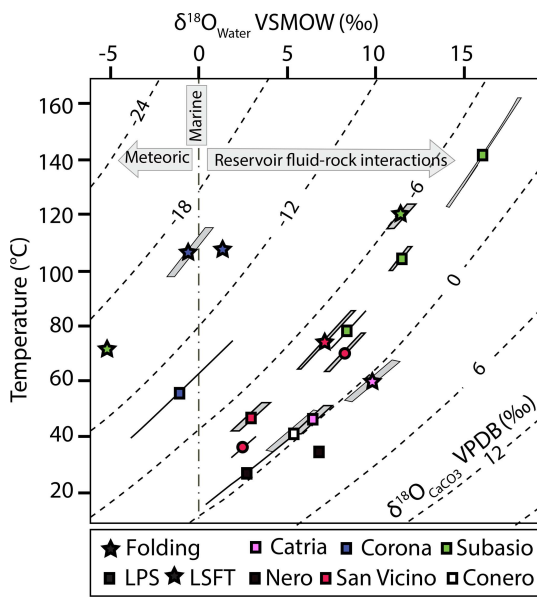


Figure 8. Plot of $\delta^{18}\text{O}_{\text{fluid}}$ (‰ VSMOW) vs precipitation temperature ($^{\circ}\text{C}$) obtained from clumped-isotope analyses along with uncertainties reported as greyed contours. Dotted oblique lines are the measured $\delta^{18}\text{O}_{\text{CaCO}_3}$ of the vein cements (‰ VPDB). Shape of the points correspond to tectonic set (layer-parallel shortening being U1 and compatible faults and folding U2), while filling colour relates to structure. LPS stands for layer-parallel shortening; LSFT stands for late-stage fold tightening.

7.2 ± 1.6 ‰ VSMOW. In Monte Catria, the sample of set J1 was characterized by a fluid with $\delta^{18}\text{O}_{\text{fluids}} = 8.6 \pm 0.7$ ‰ VSMOW precipitated at $T = 44 \pm 4$ °C, the sample of set J2 by a fluid with $\delta^{18}\text{O}_{\text{fluids}} = 11.1 \pm 2.3$ ‰ VSMOW precipitated at $T = 59 \pm 10$ °C. In the easternmost structure (Monte Conero), the sample of J1 was characterized by a fluid with $\delta^{18}\text{O}_{\text{fluids}} = 5.8 \pm 2.4$ ‰ VSMOW precipitated at $T = 42 \pm 12$ °C.

Sample name	GPS	Structure	Host formation	Set	Temperature ($^{\circ}\text{C}$)	Min T ($^{\circ}\text{C}$)	Max T ($^{\circ}\text{C}$)	Fluid $\delta^{18}\text{O}$ (‰ VSMOW) (mean)	Fluid $\delta^{18}\text{O}$ (‰ VSMOW) (min)	Fluid $\delta^{18}\text{O}$ (‰ VSMOW) (max)	$\delta^{47}\text{‰}$ CDES (final)	$\delta^{47}\text{‰}$ CDES SD (final)
A74A	125	Corona	Maiolica	J2	106.4	98.0	115.4	-0.5	-1.8	0.9	0.514	0.023
A77-130	125	Corona	Maiolica	J2	107.6	106.0	109.3	1.4	1.2	1.7	0.511	0.004
A77-40	125	Corona	Maiolica	J1	55.9	39.9	74.7	-1.1	-3.9	1.9	0.608	0.000
A120	145	Subasio	Scaglia Rossa	J2	71.7	71.7	71.7	-5.2	-5.2	-5.1	0.574	0.000
A28	106	Subasio	Massiccio	J1	119.1	114.8	123.6	11.3	10.7	12.0	0.495	0.011
SUB15	77	Subasio	Scaglia Cinerea	F1	78.3	71.7	85.3	8.4	7.4	9.5	0.561	0.022
SUB17	77	Subasio	Scaglia Cinerea	F1	140.9	122.9	161.8	16.1	14.0	18.2	0.468	0.032
SUB30	81	Subasio	Scaglia Cinerea	F1	104.4	100.1	108.9	11.4	10.8	12.1	0.516	0.012
A52	115	Nero	Maiolica	J1	34.7	33.9	35.5	6.8	6.6	7.0	0.662	0.004
A56	118	Nero	Scaglia Rossa	J1	27.2	15.9	39.9	2.7	0.3	5.2	0.685	0.052
A29	108	San Vicino	Scaglia Rossa	J1	47.3	42.5	52.4	3.0	1.9	4.0	0.628	0.021
A39	109	San Vicino	Scaglia Rossa	J2	74.5	64.7	85.2	7.2	5.6	8.8	0.568	0.035
FAB3	50	San Vicino	Langhan Fysch	F2	36.5	32.8	40.3	2.5	1.7	3.3	0.658	0.018
FAB6	50	San Vicino	Langhan Fysch	F2	70.3	63.7	77.4	8.3	7.1	9.4	0.576	0.024
A59	119	Catria	Maiolica	J1	44.3	40.7	48.0	8.6	7.8	9.3	0.637	0.013
A65	122	Catria	Massiccio	J2	59.0	49.2	69.7	11.1	8.9	13.4	0.601	0.032
CON6	68	Conero	Scaglia Rossa	J1	41.6	30.7	53.8	5.8	3.4	8.3	0.643	0.044

Table 3. Fluid precipitation temperature and oxygen isotopic values derived from clumped-isotope analysis results.

4.6 U–Pb absolute dating of veins and faults

All samples from veins, whatever the set they belong to, are revealed to have a U/Pb ratio not high enough to return an age, with too low a U content and/or dominated by common lead (see the Supplement), which seems to be common in tectonic veins (Roberts et al., 2020). Of the 35 samples screened, two faults returned variable U/Pb and Pb/Pb ratios, allowing the calculation of accurate ages (FAB5 and FAB6) by applying the robust regression approach (Hoareau et al., 2020). In sample FAB5, the pixels with higher U/Pb ratios made it possible to obtain identical ages within the limits of uncertainty for the different plots in spite of a majority of pixel values dominated by common lead (5.03 ± 1.2 , 4.92 ± 1.3 , and 5.28 ± 0.95 Ma for the TW (Tera Wasserburg), the 86TW, and the isochron plot, respectively) (Fig. 9a). The rather large age uncertainties are consistent with the moderately high RSE values, but the d-MSWD values close to 1 indicate good alignment of discretized data (Fig. 9b). In sample FAB6, the mapping approach returned distinct ages according to the plot considered because of low U/Pb ratios (from 2.17 ± 1.4 to 6.53 ± 2 Ma). Keeping in mind their low reliability, the ages obtained for this sample grossly point toward precipitation younger than ~ 8 Ma.

5 Interpretation

5.1 Sequence of fracturing events and related regional compressional and extensional trends

The previously defined joint and vein, fault, and stylolite sets were compared and gathered in order to reconstruct the deformation history at the scale of the belt. We interpret the mesostructural network as resulting from three stages of regional deformation, supported by already published fold-scale fracture sequence (Tavani and Cifelli, 2010; Tavani et al., 2008; Petracchini et al., 2012; Beaudoin et al., 2016; Díaz General et al., 2015; Di Naccio et al., 2005; Vignaroli et al., 2013) and in line with the ones observed in most recent studies (see Evans and Fischer, 2012; Tavani et al., 2015a, for reviews):

Layer-parallel shortening stage: chronological relationships suggest that set J1 formed before set J2. Set J1 is kinematically consistent with set S1 that recorded bedding-parallel, NE–SW directed Apenninic contraction, except in some places where sets J1 and S1 rather formed under a slight local rotation/perturbations of the NE–SW directed compression as a result of structural inheritance and/or of the arcuate shape of the fold. Bedding-parallel reverse faults of set F1 also belong to this LPS stage as they are likely to develop at an early stage of fold growth (Tavani et al., 2015).

Folding stage: set J2 reflects local extension perpendicular to fold axis and associated with strata curvature at fold hinges. The extensional trend, i.e. the trend of J2 joints and/or

veins, changes as a function of curvature of fold axes in map view. We also interpret the stylolite peaks of which orientation are intermediate between set S1 and S2 (Fig. 4) as related to the folding stage (Roure et al., 2005).

Late-stage fold tightening: some tectonic stylolites with horizontal peaks striking NE–SW (set S2) and some veins and/or joints (set J3) postdate strata tilting, like the strike-slip and reverse faults of set F2. All these mesostructures formed slightly after the fold has locked, still under a NE–SW contractional trend which is now oriented at a high angle to bedding. They mark a late stage of fold tightening, when shortening is no longer accommodated, by e.g. limb rotation.

5.2 Burial depth evolution and timing of contractional deformation

Stylolite roughness inversion applied to bedding-parallel stylolites provides access to the maximum depth experienced by the strata at the time vertical shortening was prevailing over horizontal shortening (σ_1 vertical) (Ebner et al., 2009b; Koehn et al., 2007; Beaudoin et al., 2016, 2019, 2020; Beaudoin and Lacombe, 2018; Rolland et al., 2014; Bertotti et al., 2017). In this study, we compare the depth range returned by the inversion of a population of bedding-parallel stylolites to a local burial model (Fig. 10) reconstructed from the strata thickness documented in wells located in the western–central part of the UMAR (Nero–Catria area) (Centamore et al., 1979; Tavani et al., 2008). The resulting burial curves were constructed from the present-day strata thicknesses corrected from (1) chemical compaction by increasing the thickness by an estimated 18 %, then from (2) physical compaction by using the open-source software *backstrip* (PetroMehas), considering initial porosity of 70 % for the carbonates and 40 % for the sandstones, and compaction coefficients of 0.58 and 0.30 derived from exponential decrease of porosity with increasing burial for the carbonates and sandstones, respectively (Watts, 2001). The timing of exhumation was further constrained by published paleogeothermometric studies and by the sedimentary record (Caricchi et al., 2014; Mazzoli et al., 2002). To the west, tectonic reconstructions and organic matter paleothermometry applied to the Tuscan Nappe (Caricchi et al., 2014) revealed that most of this unit locally underwent more burial because it was underthrust below the Ligurian Nappe but that the western front of the Ligurian Nappe did not reach Monte Corona (Caricchi et al., 2014). We therefore consider a unique burial curve for the whole western UMAR, and we project the range of depth values at which individual bedding-parallel stylolite stopped being active on the burial curves of the formations hosting the bedding-parallel stylolites. Recent application of this technique, coupled with absolute dating of vein cements (Beaudoin et al., 2018), showed that the greatest depth that a population of bedding-parallel stylolites recorded was reached nearly at the time corresponding to the age of the oldest layer-parallel shortening-related veins, suggesting that it is

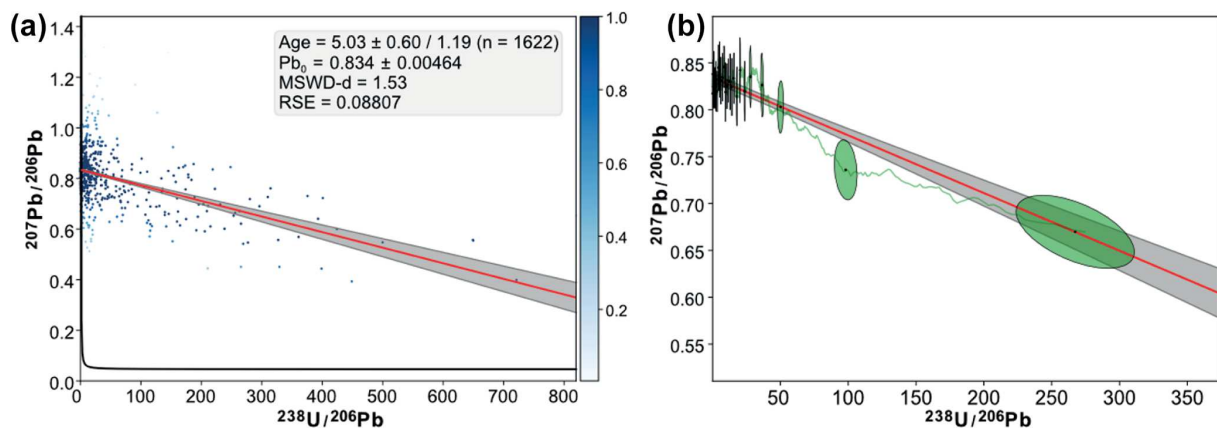


Figure 9. (a) Tera–Wasserburg concordia plot obtained from LA-ICPMS U–Pb dating of FAB5 calcite sample. The age was obtained by robust regression through the U–Pb image pixel values. The scale bar corresponds to the weight of each pixel as determined by robust regression. (b) Same plot but with discretized data represented as ellipses (one ellipse = 60 pixels). The running mean (window = 60 pixels) is also shown as a green line.

possible to constrain the timing at which horizontal principal stress overcame the vertical principal stress, switching from burial-related stress regime (σ_1 vertical) to layer-parallel shortening (σ_1 horizontal) (Beaudoin et al., 2020). In the case of the UMAR, 800 m is the minimum depth at which dissolution stopped along bedding-parallel stylolite planes, regardless of the studied formations. This confirms that burial-related pressure solution (i.e. chemical vertical compaction) likely initiated at depth shallower than 800 m (Ebner et al., 2009b; Rolland et al., 2014; Beaudoin et al., 2019, 2020).

Figure 10 also shows that bedding-parallel stylolites were active mainly from the Cretaceous (age of deposition of the platform) until Langhian times (~ 15 Ma), which suggests that σ_1 likely switched from vertical to horizontal at ca. 15 Ma. For the sake of simplicity, we will consider this age of 15 Ma for the onset of layer-parallel shortening, but one must keep in mind that taking into account a 12 % uncertainty on the magnitude of the maximum vertical stress derived from stylolite roughness inversion, hence ± 12 % on the determined depth, yields a 19–12 Ma possible time span for the onset of layer-parallel shortening (from Burdigalian to Serravalian) (Fig. 10). Syn-folding sedimentary deposits pins the beginning of folding of the UMAR to the Tortonian (11–7.3 Ma) in the west and to the Messinian (7.3–5.3 Ma) in the east (onshore) (Calamita et al., 1994). Consequently, in the central and western parts of the UMAR, we propose that the layer-parallel shortening stage of Apennine contraction lasted about ~ 7 Myr (from 15–8 Ma – Langhian to Tortonian) before folding occurred. Absolute dating of faults related to late-stage fold tightening in the central part of the UMAR further indicates that fold development was over by ~ 5 Ma, i.e. by the beginning of the Pliocene (5.3–1.75 Ma). We can therefore estimate an average duration of folding in the western–central part of the UMAR of ~ 3 Ma. Knowing

the oldest record of post-orogenic extensional tectonics in the UMAR is mid-Pliocene (~ 3 Ma) (Barchi, 2010), we can also estimate the duration of the late-stage fold tightening to ~ 2 Ma. In total, the probable period when the compressive horizontal principal stress σ_1 was higher in magnitude than the vertical stress (i.e. until post-orogenic extension) lasted for 9 Myr in the western–central part of the UMAR. We propose an average duration of fold growth about 3 Ma, quite in accordance with previous attempts to constrain fold growth duration elsewhere using either syntectonic sedimentation (3–10 Ma; Holl and Anastasio, 1993; Anastasio et al., 2018) – up to 24 Ma with quiescent periods in between growth pulses (Masferro et al., 2002) – or mechanical or kinematic modelling applied to natural cases (1–8 Ma; Suppe et al., 1992; Yamato et al., 2011). The combination of bedding-parallel stylolite inversion, burial models and U–Pb dating of vein cements/fault coatings yields a valuable insight into the timing of the different stages of contraction in a fold-and-thrust belt (Beaudoin et al., 2018).

5.3 Paleofluid system evolution

The combined use of bedding-parallel stylolites inversion and burial curves constrains the absolute timing of layer-parallel shortening, folding, and late-stage fold tightening in the UMAR (Fig. 10). The further combination of this calendar with the knowledge of the past geothermal gradient as reconstructed from organic matter studies in the eastern part of the Tuscan Nappe (23 °C km $^{-1}$; Caricchi et al., 2014) therefore yields the expected temperature within the various strata at the time vein sets J1, J2, and J3 and faults F1 and F2 formed. Then it is possible to identify whether fluids precipitated at thermal equilibrium or not during the Apenninic contraction. Overall, most calcite grains from vein cements show thin (thickness < 5 μ m) and rectilinear twins, suggest-

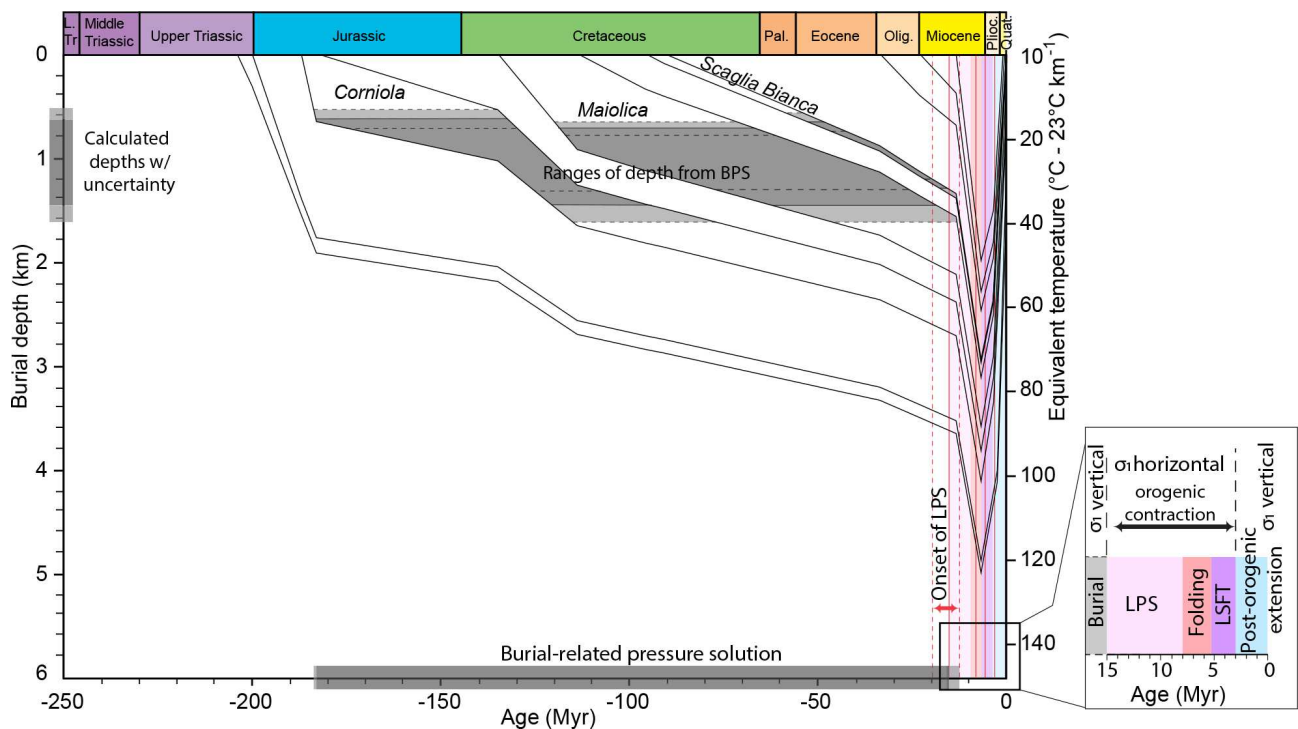


Figure 10. Burial model constructed considering thickness from well data (central UMAR) corrected from both chemical and physical compaction. The range of depths reconstructed from bedding-parallel stylolite roughness inversion (with uncertainty) are reported for each formation as grey shades. The derived corresponding timing and depth of active dissolution are reported on the *x* axis and left *y* axis, respectively. The timing of the deformation is reported on the righthand side in the inset. The onset of layer-parallel shortening is deduced from the latest bedding-parallel stylolite to have been active; the effect of the 12 % uncertainty is represented by dashed red lines; the onset of late-stage fold tightening is given by U–Pb dating of fault coating in this study. The timing of folding and post-orogenic extension are reported from published sedimentary data (see text for more detailed explanations). LPS stands for layer-parallel shortening and LSFT for late-stage fold tightening.

ing deformation at temperatures below 170 °C (Ferrill et al., 2004; Lacombe, 2010), in line with the maximum expected temperature reached by the Upper Triassic–Eocene carbonate reservoir (120 °C; Fig. 10). The fact $\delta^{13}\text{C}$ values of veins are very close to the $\delta^{13}\text{C}$ values of the surrounding host rocks (Fig. 6c), while the $\delta^{18}\text{O}$ values of the veins are different from the $\delta^{18}\text{O}$ values of the host rocks (Fig. 6d), suggests against that the fluids’ original isotopic signatures were lost due to rock buffering. The similarity of $\delta^{13}\text{C}$ values of veins compared to local host rock, along with the $^{87}\text{Sr}/^{86}\text{Sr}$ values of the veins, which are in accordance with the expected values of the host rocks (Fig. 7) (McArthur et al., 2001), points towards very limited exchange between stratigraphic reservoirs and rules out external fluid input into the system. Indeed, other potential fluid reservoirs such as lower Triassic evaporites seawater have $^{87}\text{Sr}/^{86}\text{Sr}$ values significantly higher (0.70800–0.70820) than the highest $^{87}\text{Sr}/^{86}\text{Sr}$ values documented in the UMAR (Monte Subasio: 0.70760–0.70769; Fig. 7). These characteristics indicate a closed fluid system in most of the UMAR, with formational fluids precipitating at thermal equilibrium, limited reservoir fluid–host

rock interactions in the reservoirs, and limited cross-strata fluid migrations.

When considering $\delta^{18}\text{O}$ and $\Delta_{47}\text{CO}_2$ values, the folds in the westernmost part of the UMAR, Monte Corona, and Monte Subasio require a different interpretation from the other folds of the UMAR (Fig. 6d). Indeed, the $\delta^{18}\text{O}_{\text{fluids}}$ values derived from $\Delta_{47}\text{CO}_2$ measurements, which are higher in Monte Subasio (8 ‰ to 16 ‰ VSMOW; Fig. 8) than in the rest of the UMAR (from 0 ‰ to 8 ‰ VSMOW; Fig. 8), suggest a fractionation usually interpreted as the result of rock dissolution during fluid migration (Clayton et al., 1966; Hitchon and Friedman, 1969) if considering an environment with limited connection between reservoirs and no implication of external fluids, i.e. where fluids are sourced locally from the marine carbonates. Thus, $\delta^{18}\text{O}_{\text{fluids}}$ values in the western part of the UMAR point towards a higher degree of reservoir fluid–rock interaction there. This interpretation based on limited $\Delta_{47}\text{CO}_2$ measurements can be further extended by considering the $\delta^{18}\text{O}$ values of the veins, significantly higher than the $\delta^{18}\text{O}$ values of their host rocks in the westernmost part of the UMAR, hence supporting a higher degree of fluid–rock interaction in this area regardless of

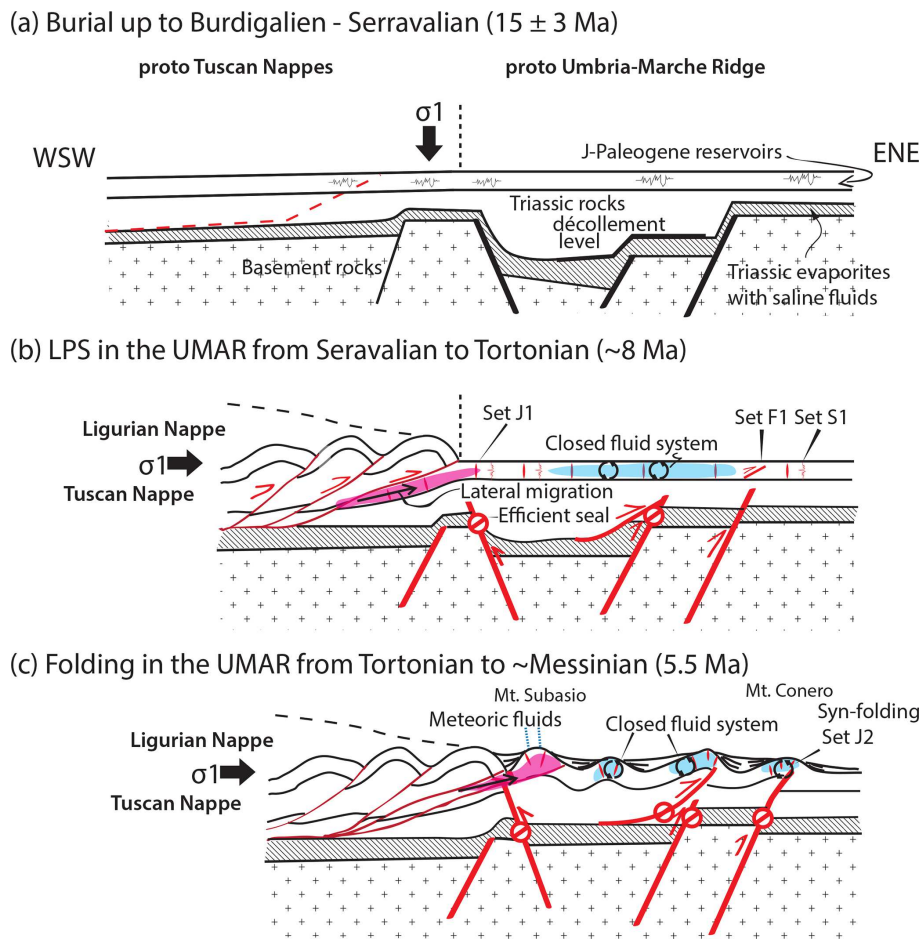


Figure 11. Conceptual model representing fracture development and regional-scale fluid migration during the formation of the Tuscan Nappes and Umbria–Marche Apennine Ridge. Red areas represent the extent of eastward pulses of hydrothermal fluids. Blue areas represent closed fluid system at the scale of the carbonate reservoirs. Potential effects of flexural event reported during upper Burdigalian and Lower Messinian in the eastern part of the belt (Mazzoli et al., 2002; Tavani et al., 2012) have not been documented in our dataset and, therefore, are not considered in this scenario.

the considered fracture set (Fig. 6). However, $\delta^{18}\text{O}_{\text{fluids}}$ values derived from the $\Delta_{47}\text{CO}_2$ measurements in the set J2 vein of Monte Subasio return a value of $\delta^{18}\text{O}_{\text{fluids}}$ consistent with fluid–rock interaction (11‰ VSMOW), while another one returns a significantly lower value of $\delta^{18}\text{O}_{\text{fluids}}$ (−5‰ VSMOW) that can be interpreted as infiltration of meteoric water (Fig. 8). Such evidence for both formational fluids with higher degree of fluid–rock interactions and meteoric fluids at Monte Subasio lead us to propose that the dataset reflects an alternation of fluid source during folding in the area.

Temperatures of precipitation are consistent with the predicted temperatures of host rocks considering the formation and timing of fracture development in most of the UMAR at all times of deformation (Figs. 6, 7, 10). This is different in Monte Corona and Monte Subasio where veins precipitated from fluids at higher temperature than the predicted temperatures for the host rock. In the Maiolica Fm. at Monte

Corona, J2 veins with high value of $\delta^{18}\text{O}_{\text{fluids}}$ returned a temperature $>100^\circ\text{C}$, while the maximum predicted temperature during folding is $<90^\circ\text{C}$. In the Scaglia Fm. at Monte Subasio, the layer-parallel shortening-related veins (J1) and faults (F1) precipitated from fluids much hotter ($105\text{--}140^\circ$) than the predicted temperature during layer-parallel shortening ($<70^\circ\text{C}$). In contrast, the J2 vein in the Scaglia Fm. at Monte Subasio precipitated at 70°C , i.e. at thermal equilibrium if considering burial history (Fig. 10). A hydrothermal dolomitizing fluid migration event was documented in the southeastern part of the UMAR (Montagna dei Fiori) and interpreted as vertical fluid migration from deeper Jurassic reservoirs (Mozafari et al., 2019; Storti et al., 2018). But the reconstructed fluid temperatures (100°C) and $\delta^{18}\text{O}_{\text{fluids}}$ (6‰ VSMOW) are still much lower than the ones reconstructed from the fluids involved in Monte Subasio ($105\text{--}140^\circ\text{C}$; 9‰ to 15‰ VSMOW), supporting that a different fluid system was prevailing in the westernmost part of the

belt during layer-parallel shortening, folding, and late-stage fold tightening compared to central–eastern UMAR.

6 Discussion

6.1 Fluid origin and engine of fluid migration in the westernmost Umbria–Marche Apennine Ridge

During layer-parallel shortening and folding, a temperature of fluid precipitation of up to 140 °C, i.e. significantly higher than the local host-rock temperature, implies that fluids flowed from depth >4 km, while a high $\delta^{18}\text{O}_{\text{fluids}}$ reflects a high degree of reservoir fluid–rock interaction. Considering the subsurface geometry of the UMAR (Fig. 1) and discarding any input of external fluids originated from the lower Triassic formations or from the basement on the basis of $^{87}\text{Sr}/^{86}\text{Sr}$ values, we propose that the fluids originated from the westward lateral extension of the carbonate platform reservoir that was buried under the Tuscan and Ligurian Nappes (Caricchi et al., 2014; Carboni et al., 2020). The coexistence inside a single deformation stage (layer-parallel shortening or folding) of both local/meteoric fluids and hydrothermal brines that migrated from depths can be explained by transient flushes into the system of hydrothermal fluids flowing from deeply buried parts of the same, stratigraphically continuous, reservoir (Bachu, 1995; Garven, 1995; Machel and Cavell, 1999; Oliver, 1986).

We therefore propose that the fluid system prevailing at Monte Corona and at Monte Subasio reflects an eastward, tectonically driven, flow of hydrothermal fluids under the influence of the Tuscan Nappe (Fig. 11), where shortening was accommodated by stacked nappes detached above the Triassic décollement level. That contrasts with the closed fluid system documented in the remainder of the UMAR, where shortening is distributed on deep-rooted faults. We propose that the long-term migration engine was a difference in hydraulic head due to the lateral variation in the burial depth of the reservoir related to the stacked Tuscan and Ligurian nappes west from the UMAR (up to 4 km for the Scaglia Fm.; Caricchi et al., 2014), which does not affect the UMAR (burial up to 3 km for the Scaglia Fm.; Figs. 10, 11b). The resulting hydraulic gradient allowed for the eastward fluid migration within the reservoir, enhanced by layer-parallel shortening and related fracture development (Roure et al., 2005). As the paleodepth variation was related to the thickness of the nappes stacking rather than to a foreland-type slope, the UMAR would then have formed a “plateau” without any large-scale lateral fluid migration (Fig. 11b). The inferred pulses of hydrothermal fluids (“hot flashes” in the sense of Machel and Cavell, 1999) also imply a strong influence of foreland-ward propagation of contractional deformation on the eastward fluid expulsion (Oliver, 1986).

6.2 Influence of tectonic style on fluid flow during deformation history

If considering a thin-skinned tectonic model for the UMAR with shallow, low-angle thrusts rooting into the Triassic evaporitic décollement (Fig. 1) (Bally et al., 1986), one would expect some influence of Triassic fluids signatures to be involved in the reservoir paleohydrology at the time faults were active or during folding, as illustrated in similar salt-detached fold systems in the Pyrenees, in the Appalachians, and in the Sierra Madre Oriental (Lacroix et al., 2011; Travé et al., 2000; Evans and Hobbs, 2003; Evans and Fischer, 2012; Fischer et al., 2009; Smith et al., 2012; Lefticariu et al., 2005). On the other hand, if considering a thick-skinned tectonic model with high-angle thrusts crossing the Triassic down to the basement, it becomes more likely that these thrusts did not act as efficient conduits for deep fluids (evaporitic fluids or basement fluids) as fault damage zones in calcium-sulfates evaporites of the area can remain non permeable, if the displacement along the faults is smaller than the nonpermeable layer thickness (De Paola et al., 2008). This contrasts with paleohydrological studies of basement cored folds, where high-angle thrusts allow hot flashes of hydrothermal fluids into the overlying cover (Beaudoin et al., 2011; Evans and Fischer, 2012) in the absence of evaporites. Thus, the lack of Triassic influence in our paleofluid dataset, especially with respect to the low $^{87}\text{Sr}/^{86}\text{Sr}$ values, seems to support a thick-skinned tectonic style of deformation in the UMAR (Fig. 11c). This fluid flow model therefore outlines important differences between belts where shortening is localized and accommodated by shallow nappe stacking, typical from thin-skinned belts, and belts where shortening is instead distributed on basement-cored folds related to high-angle thrusts, as commonly encountered in thick-skinned belts (Lacombe and Bellahsen, 2016). Tectonically induced fluid flow during layer-parallel shortening in response to hydraulic gradient and lateral tectonic contraction has also been described in other thin-skinned belts, such as the Canadian Rocky Mountains (Vandeginste et al., 2012; Roure et al., 2010; Machel and Cavell, 1999; Qing and Mountjoy, 1992), or in Venezuela (Schneider et al., 2002, 2004; Roure et al., 2003) where lithospheric bulging was at the origin of the depth difference leading to hydraulic gradient-driven fluid migration. The presented case study shows how stacking of sedimentary units typical of thin-skinned tectonics strongly influences the fluid system beyond the morphological front of the belt and allows occurrence of large-scale fluid migration.

7 Conclusions

Our study of the vein–fault–tectonic stylolite populations distributed in Jurassic to Eocene limestone rocks at the scale of the thin-skinned Tuscan Nappe and presumably thick-

skinned Umbria–Marche Apennine Ridge reveals the occurrence of several fracture/stylolite sets that support a three-stage (meso)structural evolution of the Apenninic contraction: (1) layer-parallel shortening is reconstructed by a set of joint/veins striking NE–SW to E–W, perpendicular to the local trend of the fold, alongside with stylolite peaks striking NE–SW and early folding bedding-parallel reverse faults; (2) the folding stage is recorded by fold-parallel mode I joints and veins; (3) the late-stage fold tightening is recorded by post-tilting, late folding stylolite peaks and joints and veins, and also mesoscale reverse and strike-slip faults.

Thanks to burial models coupled to bedding-parallel stylolite paleopiezometry, along with (unfortunately scarce) U–Pb absolute dating of strike-slip faults related to late-stage fold tightening, we were able to reconstruct the timing of the onset and the duration of the Apennine contraction. The layer-parallel shortening likely started by Langhian time (ca. 15 Ma) and lasted for ca. 7 Myr. Folding started by the Tortonian time (ca. 8 Ma, as constrained by the sedimentary record of growth strata) and lasted ca. 3 Myr. Indeed, absolute dating of fault coatings implies that late-stage fold tightening started by the beginning of Pliocene (ca. 5 Ma), itself lasting for 2 Myr before post-orogenic extension affected strata since mid-Pliocene (3 Ma).

Accessing the starting and ending time of deformation in the UMAR also allowed us to predict the depth and expected temperatures of the paleofluids during fracturing assuming fluids precipitated at thermal equilibrium. By characterizing the cements related to sets of veins and faults using $\delta^{18}\text{O}$ and $\delta^{13}\text{C}$, $^{87/86}\text{Sr}$, and $\Delta_{47}\text{CO}_2$ values, we show that different paleofluid systems occurred during layer-parallel shortening and folding from west to east of the section. In the westernmost folds of the UMAR located beyond the arrow of the Ligurian Nappe thrusting over the Tuscan Nappe, we highlight a local fluid system with transient large-scale lateral, stratigraphically compartmentalized hydrothermal fluid migration. In contrast, these pulses are not documented in the rest of the UMAR and its foreland, where the fluid system always remained closed. We tentatively relate this change in fluid system to a lateral change in tectonic style of deformation across the belt, from thin skinned in the Tuscan Nappe to rather thick skinned in the UMAR. Beyond regional implications, the combination of stylolite roughness inversion and burial history reconstruction, linked to reliable estimates of the past geothermal gradient, appears as a powerful tool to unravel coupled structural and fluid flow evolution in fold-and-thrust belts.

Data availability. All data are available in the tables and in the Supplement.

Supplement. The supplement related to this article is available online at: <https://doi.org/10.5194/se-11-1617-2020-supplement>.

Author contributions. NEB, OL, DK, AnB, and JPC were involved in the overall writing of the paper led by NEB; NEB, OL, DK, and AnB collected structural data and rock samples in the field; NEB, AL, and OL conducted microstructural inversion; GH, AdB, CJ, MM, NR, ILM, FC, and CP designed experiments and collected the geochemical data and wrote the related parts of the paper and appendices. All authors critically reviewed the multiple drafts of the paper.

Competing interests. The authors declare that they have no conflict of interest.

Special issue statement. This article is part of the special issue “Faults, fractures, and fluid flow in the shallow crust”. It is not associated with a conference.

Acknowledgements. Nicolas E. Beaudoin is funded through the ISITE programme E2S, supported by ANR PIA and Région Nouvelle-Aquitaine. Authors also thank two anonymous reviewers for insightful comments that improved the manuscript and Randolph Williams for his editorial work.

Financial support. This research has been supported by the Natural Environmental Research Council (grant no. IP-1494-1114), the European Union’s Seventh Framework Programme (grant no. 316889), the Sorbonne Université (grant no. C14313), the Région Nouvelle-Aquitaine, and the Agence Nationale de la Recherche (Projet Investissement d’Avenir (programme E2S)).

Review statement. This paper was edited by Randolph Williams and reviewed by two anonymous referees.

References

- Agosta, F., Alessandroni, M., Antonellini, M., Tondi, E., and Giorgioni, M.: From fractures to flow: A field-based quantitative analysis of an outcropping carbonate reservoir, *Tectonophysics*, 490, 197–213, <https://doi.org/10.1016/j.tecto.2010.05.005>, 2010.
- Agosta, F., Luetkemeyer, P. B., Lamarche, J., Crider, J. G., and Lacombe, O.: An introduction to the Special Issue: The role of fluids in faulting and fracturing in carbonates and other upper crustal rocks, *Tectonophysics*, 690, 1–3, 2016.
- Ahmadhadi, F., Daniel, J. M., Azzizadeh, M., and Lacombe, O.: Evidence for pre-folding vein development in the Oligo-Miocene Asmari Formation in the Central Zagros Fold Belt, Iran, *Tectonics*, 27, <https://doi.org/10.1029/2006TC001978>, 2008.
- Amrouch, K., Lacombe, O., Bellahsen, N., Daniel, J. M., and Callot, J. P.: Stress and strain patterns, kinematics and deformation mechanisms in a basement-cored anticline: Sheep Mountain Anticline, Wyoming, *Tectonics*, 29, TC1005, <https://doi.org/10.1029/2009TC002525>, 2010.

- Anastasio, D., Kodama, K., and Parés, J.: Episodic deformation rates recovered from growth strata, Pyrenees, Search and Discovery Article, 30553, 2018.
- Andresen, K. J.: Fluid flow features in hydrocarbon plumbing systems: What do they tell us about the basin evolution?, *Mar. Geol.*, 332, 89–108, 2012.
- Angelier, J.: Tectonic analysis of fault slip data sets, *J. Geophys. Res.-Sol. Ea.*, 89, 5835–5848, 1984.
- Bachu, S.: Synthesis and model of formation-water flow, Alberta Basin, Canada, *AAPG Bull.*, 79, 1159–1178, 1995.
- Bally, A., Burbi, L., Cooper, C., and Ghelardoni, R.: Balanced cross sections and seismic reflection profiles across the central Apennines Mem, *Soc. Geol. It.*, 35, 275–310, 1986.
- Barbier, M., Hamon, Y., Callot, J.-P., Floquet, M., and Daniel, J.-M.: Sedimentary and diagenetic controls on the multiscale fracturing pattern of a carbonate reservoir: The Madison Formation (Sheep Mountain, Wyoming, USA), *Mar. Petrol. Geol.*, 29, 50–67, <https://doi.org/10.1016/j.marpetgeo.2011.08.009>, 2012.
- Barchi, M., De Feyter, A., Magnani, M., Minelli, G., Pialli, G., and Sotera, B.: Extensional tectonics in the Northern Apennines (Italy): evidence from the CROP03 deep seismic reflection line, *Mem. Soc. Geol. It.*, 52, 527–538, 1998.
- Barchi, M.: The Neogene-Quaternary evolution of the Northern Apennines: crustal structure, style of deformation and seismicity, in: *The Geology of Italy: tectonics and life along plate margins*, edited by: Beltrando, M., Peccerillo, A., Mattei, M., Conticelli, S., and Doglioni, C., *Journal of the Virtual Explorer*, Electronic Edition, ISSN 1441-8142, Vol. 36, paper 11, <https://doi.org/10.3809/jvirtex.2010.00220>, 2010.
- Beaudoin, N., Bellahsen, N., Lacombe, O., and Emmanuel, L.: Fracture-controlled paleohydrogeology in a basement-cored, fault-related fold: Sheep Mountain Anticline, Wyoming, United States, *Geochem. Geophys. Geosy.*, 12, Q06011, <https://doi.org/10.1029/2010gc003494>, 2011.
- Beaudoin, N., Leprêtre, R., Bellahsen, N., Lacombe, O., Amrouch, K., Callot, J.-P., Emmanuel, L., and Daniel, J.-M.: Structural and microstructural evolution of the Rattlesnake Mountain Anticline (Wyoming, USA): new insights into the Sevier and Laramide orogenic stress build-up in the Bighorn Basin, *Tectonophysics*, 576, 20–45, 2012.
- Beaudoin, N., Lacombe, O., Bellahsen, N., and Emmanuel, L.: Contribution of studies of sub-seismic fracture populations to paleohydrological reconstructions (Bighorn Basin, USA), *Proced. Earth Plan. Sc.*, 7, 57–60, 2013.
- Beaudoin, N., Bellahsen, N., Lacombe, O., Emmanuel, L., and Pironon, J.: Crustal-scale fluid flow during the tectonic evolution of the Bighorn Basin (Wyoming, USA), *Basin Res.*, 26, 403–435, <https://doi.org/10.1111/bre.12032>, 2014.
- Beaudoin, N., Koehn, D., Lacombe, O., Lecouty, A., Billi, A., Aharonov, E., and Parlangeau, C.: Fingerprinting stress: Stylolite and calcite twinning paleopiezometry revealing the complexity of progressive stress patterns during folding-The case of the Monte Nero anticline in the Apennines, Italy, *Tectonics*, 35, 1687–1712, <https://doi.org/10.1002/2016tc004128>, 2016.
- Beaudoin, N. and Lacombe, O.: Recent and future trends in paleopiezometry in the diagenetic domain: Insights into the tectonic paleostress and burial depth history of fold-and-thrust belts and sedimentary basins, *J. Struct. Geol.*, 114, 357–365, <https://doi.org/10.1016/j.jsg.2018.04.001>, 2018.
- Beaudoin, N., Lacombe, O., Roberts, N. M. W., and Koehn, D.: U-Pb dating of calcite veins reveals complex stress evolution and thrust sequence in the Bighorn Basin, Wyoming, USA, *Geology*, 46, 1015–1018, <https://doi.org/10.1130/g45379.1>, 2018.
- Beaudoin, N., Gasparrini, M., David, M.-E., Lacombe, O., and Koehn, D.: Bedding-parallel stylolites as a tool to unravel maximum burial depth in sedimentary basins: Application to Middle Jurassic carbonate reservoirs in the Paris basin, France, *GSA Bull.*, 131, 1239–1254, <https://doi.org/10.1130/b32064.1>, 2019.
- Beaudoin, N., Huyghe, D., Bellahsen, N., Lacombe, O., Emmanuel, L., Mouthereau, F., and Ouahnon, L.: Fluid systems and fracture development during syn-depositional fold growth: example from the Pico del Aguila Anticline, Sierras Exteriores, Southern Pyrenees, Spain, *J. Struct. Geol.*, 70, 23–38, 2015.
- Beaudoin, N., Lacombe, O., Koehn, D., David, M.-E., Farrell, N., and Healy, D.: Vertical stress history and paleoburial in foreland basins unravelled by stylolite roughness paleopiezometry: Insights from bedding-parallel stylolites in the Bighorn Basin, Wyoming, USA, *J. Struct. Geol.*, 136, 104061, <https://doi.org/10.1016/j.jsg.2020.104061>, 2020.
- Becker, S., Eichhubl, P., Laubach, S. E., Reed, R. M., Lander, R., and Bodnar, R.: A 48 my history of fracture opening, temperature, and fluid pressure: Cretaceous Travis Peak Formation, East Texas basin, *Bulletin*, 122, 1081–1093, 2010.
- Bellahsen, N., Fiore, P., and Pollard, D. D.: The role of fractures in the structural interpretation of Sheep Mountain Anticline, Wyoming, *J. Struct. Geol.*, 28, 850–867, 2006.
- Bergbauer, S. and Pollard, D. D.: A new conceptual fold-fracture model including prefolding joints, based on the Emigrant Gap anticline, Wyoming, *Geol. Soc. Am. Bull.*, 116, 294–307, 2004.
- Bernasconi, S. M., Hu, B., Wacker, U., Fiebig, J., Breitenbach, S. F., and Rutz, T.: Background effects on Faraday collectors in gas-source mass spectrometry and implications for clumped isotope measurements, *Rapid Commun. Mass Spectr.*, 27, 603–612, 2013.
- Bertotti, G., de Graaf, S., Bisdorf, K., Oskam, B., Vonhof, H., H. R. Bezerra, F., J. G. Reijmer, J., and L. Cazarin, C.: Fracturing and fluid-flow during post-rift subsidence in carbonates of the Jandaíra Formation, Potiguar Basin, NE Brazil, *Basin Res.*, 29, 836–853, <https://doi.org/10.1111/bre.12246>, 2017.
- Bjørlykke, K.: Fluid flow in sedimentary basins, *Sediment. Geol.*, 86, 137–158, 1993.
- Bjørlykke, K.: Fluid-flow processes and diagenesis in sedimentary basins, *Geol. Soc. Lond.*, 78, 127–140, 1994.
- Bjørlykke, K.: Subsurface Water and Fluid Flow in Sedimentary Basins, in: *Petroleum Geoscience*, edited by: Bjørlykke, K., Springer, Berlin, Heidelberg, 651 pp., https://doi.org/10.1007/978-3-642-34132-8_10, 2015.
- Bons, P. D., Elburg, M. A., and Gomez-Rivas, E.: A review of the formation of tectonic veins and their microstructures, *J. Struct. Geol.*, 43, 33–62, 2012.
- Butler, R. W. H., Mazzoli, S., Corrado, S., Donatis, M. D., Bucci, D. D., Gambini, R., Naso, G., Nicolai, C., Scrocca, D., Shiner, P., and Zucconi, V.: Applying Thick-skinned Tectonic Models to the Apennine Thrust Belt of Italy – Limitations and Implications, *AAPG Memoir*, 82, 647–667, 2004.
- Calamita, F. and Deiana, G.: The arcuate shape of the Umbria-Marche-Sabina Apennines (central Italy), *Tectonophysics*, 146, 139–147, 1988.

- Calamita, F., Cello, G., Deiana, G., and Paltrinieri, W.: Structural styles, chronology rates of deformation, and time-space relationships in the Umbria-Marche thrust system (central Apennines, Italy), *Tectonics*, 13, 873–881, 1994.
- Callot, J.-P., Breesch, L., Guilhaumou, N., Roure, F., Swennen, R., and Vilasi, N.: Paleo-fluids characterisation and fluid flow modelling along a regional transect in Northern United Arab Emirates (UAE), *Arab. J. Geosci.*, 3, 413–437, 2010.
- Callot, J.-P., Roure, F., Faure, J.-L., and Tarapoanca, M.: Kinematic, thermal, and petroleum modeling of the northern Emirates, in: *Petroleum System Analysis – Case Studies: AAPG Memoir*, edited by: AbuAli, M. A., Moretti, I., and Nordgård Bolås, H. M., 135–164, 2017a.
- Callot, J.-P., Sassi, W., Roure, F., Hill, K., Wilson, N., and Divies, R.: Pressure and Basin Modeling in Foothill Belts: A Study of the Kutubu Area, Papua New Guinea Fold and Thrust Belt, in: *Petroleum Systems Analysis: AAPG Memoir*, edited by: AbuAli, M. A., Moretti, I., and Nordgård Bolås, H. M., 114, 165–190, 2017b.
- Carboni, F., Brozzetti, F., Mirabella, F., Cruciani, F., Porreca, M., Ercoli, M., Back, S., and Barchi, M. R.: Geological and geophysical study of a thin-skinned tectonic wedge formed during an early collisional stage: the Trasimeno Tectonic Wedge (Northern Apennines, Italy), *Geol. Mag.*, 157, 213–232, 2020.
- Caricchi, C., Aldega, L., and Corrado, S.: Reconstruction of maximum burial along the Northern Apennines thrust wedge (Italy) by indicators of thermal exposure and modeling, *Geol. Soc. Am. Bull.*, 127, 428–442, <https://doi.org/10.1130/b30947.1>, 2014.
- Caricchi, C., Aldega, L., and Corrado, S.: Reconstruction of maximum burial along the Northern Apennines thrust wedge (Italy) by indicators of thermal exposure and modeling, *Bulletin*, 127, 428–442, 2015.
- Carminati, E., Lustrino, M., Cuffaro, M., and Doglioni, C.: Tectonics, magmatism and geodynamics of Italy: What we know and what we imagine, *Journal of the Virtual Explorer*, 36, 1–59, <https://doi.org/10.3809/jvirtex.2010.00226>, 2010.
- Cartwright, J.: The impact of 3D seismic data on the understanding of compaction, fluid flow and diagenesis in sedimentary basins, *J. Geol. Soc.*, 164, 881–893, 2007.
- Cello, G., Mazzoli, S., Tondi, E., and Turco, E.: Active tectonics in the central Apennines and possible implications for seismic hazard analysis in peninsular Italy, *Tectonophysics*, 272, 43–68, 1997.
- Centamore, E., Chiocchini, M., Chiocchini, U., Dramis, F., Giardini, G., Jacobacci, A., Martelli, G., Micarelli, A., and Potetti, M.: Carta Geologica d'Italia alla scala 1 : 50.000, Note Illustrative Fo. 301 “Fabriano”, 1979.
- Clayton, R., Friedman, I., Graf, D., Mayeda, T., Meents, W., and Shimp, N.: The origin of saline formation waters: 1. Isotopic composition, *J. Geophys. Res.*, 71, 3869–3882, 1966.
- Conti, S. and Gelmini, R.: Miocene-Pliocene tectonic phases and migration of foredeep-thrust belt system in Northern Apennines, *J Mem. Soc. Geol. It.*, 48, 261–274, 1994.
- Cruset, D., Cantarero, I., Travé, A., Vergés, J., and John, C. M.: Crestal graben fluid evolution during growth of the Puig-reig anticline (South Pyrenean fold and thrust belt), *J. Geodynam.*, 101, 30–50, 2016.
- Cruset, D., Cantarero, I., Vergés, J., John, C. M., Muñoz-López, D., and Travé, A.: Changes in fluid regime in syn-orogenic sediments during the growth of the south Pyrenean fold and thrust belt, *Glob. Planet. Change*, 171, 207–224, <https://doi.org/10.1016/j.gloplacha.2017.11.001>, 2018.
- d’Agostino, N., Jackson, J., Dramis, F., and Funicello, R.: Interactions between mantle upwelling, drainage evolution and active normal faulting: an example from the central Apennines (Italy), *Geophys. J. Int.*, 147, 475–497, 2001.
- Dale, A., John, C. M., Mozley, P. S., Smalley, P., and Muggerridge, A. H.: Time-capsule concretions: unlocking burial diagenetic processes in the Mancos Shale using carbonate clumped isotopes, *Earth Planet. Sc. Lett.*, 394, 30–37, 2014.
- Davies, A. J. and John, C. M.: The clumped ($^{13}\text{C}^{18}\text{O}$) isotope composition of echinoid calcite: Further evidence for “vital effects” in the clumped isotope proxy, *Geochim. Cosmochim. Ac.*, 245, 172–189, 2019.
- De Graaf, S., Nooitgedacht, C. W., Le Goff, J., Van Der Lubbe, J. H., Vonhof, H. B., and Reijmer, J. J.: Fluid-flow evolution in the Albanide fold-thrust belt: Insights from hydrogen and oxygen isotope ratios of fluid inclusions, *AAPG Bull.*, 103, 2421–2445, 2019.
- Defliese, W. F., Hren, M. T., and Lohmann, K. C.: Compositional and temperature effects of phosphoric acid fractionation on Δ^{47} analysis and implications for discrepant calibrations, *Chem. Geol.*, 396, 51–60, 2015.
- Dennis, K. J., Affek, H. P., Passey, B. H., Schrag, D. P., and Eiler, J. M.: Defining an absolute reference frame for “clumped” isotope studies of CO_2 , *Geochem. Cosmochim. Ac.*, 75, 7117–7131, 2011.
- De Paola, N., Collettini, C., Faulkner, D. R., and Trippetta, F.: Fault zone architecture and deformation processes within evaporitic rocks in the upper crust, *Tectonics*, 27, TC4017, <https://doi.org/10.1002/2017GC007097>, 2008.
- Di Naccio, D., Boncio, P., Cirilli, S., Casaglia, F., Morettini, E., Lavecchia, G., and Brozzetti, F.: Role of mechanical stratigraphy on fracture development in carbonate reservoirs: Insights from outcropping shallow water carbonates in the Umbria-Marche Apennines, Italy, *J. Volcanol. Geoth. Res.*, 148, 98–115, <https://doi.org/10.1016/j.jvolgeores.2005.03.016>, 2005.
- Díaz General, E. N., Mollema, P. N., and Antonellini, M.: Fracture patterns and fault development in the pelagic limestones of the Monte Conero Anticline (Italy), *Ital. J. Geosci.*, 134, 495–512, 2015.
- Donard, A., Pottin, A.-C., Pointurier, F., and Pécheyran, C.: Determination of relative rare earth element distributions in very small quantities of uranium ore concentrates using femtosecond UV laser ablation–SF-ICP-MS coupling, *J. Anal. Atom. Spectrom.*, 30, 2420–2428, 2015.
- Ebner, M., Koehn, D., Toussaint, R., and Renard, F.: The influence of rock heterogeneity on the scaling properties of simulated and natural stylolites, *J. Struct. Geol.*, 31, 72–82, <https://doi.org/10.1016/j.jsg.2008.10.004>, 2009a.
- Ebner, M., Koehn, D., Toussaint, R., Renard, F., and Schmittbuhl, J.: Stress sensitivity of stylolite morphology, *Earth Planet. Sc. Lett.*, 277, 394–398, <https://doi.org/10.1016/j.epsl.2008.11.001>, 2009b.
- Ebner, M., Piazzolo, S., Renard, F., and Koehn, D.: Stylolite interfaces and surrounding matrix material: Nature and role of heterogeneities in roughness and mi-

- crostructural development, *J. Struct. Geol.*, 32, 1070–1084, <https://doi.org/10.1016/j.jsg.2010.06.014>, 2010.
- Elter, F. M., Elter, P., Eva, C., Eva, E., Kraus, R. K., Padovano, M., and Solarino, S.: An alternative model for the recent evolution of the Northern–Central Apennines (Italy), *J. Geodynam.*, 54, 55–63, 2012.
- Engelder, T.: The role of pore water circulation during the deformation of foreland fold and thrust belts, *J. Geophys. Res.-Sol. Ea.*, 89, 4319–4325, 1984.
- Evans, M. and Hobbs, G.: Fate of “warm” migrating fluids in the central Appalachians during the Late Paleozoic Alleghanian orogeny, *J. Geochem. Expl.*, 78, 327–331, 2003.
- Evans, M. A., Tollo, R., Bartholomew, M., Hibbard, J., and Karabinos, P.: Temporal and spatial changes in deformation conditions during the formation of the Central Appalachian fold-and-thrust belt: Evidence from joints, vein mineral paragenesis, and fluid inclusions, From Rodinia to Pangea: The Lithotectonic Record of the Appalachian Region, 206, 477–552, 2010.
- Evans, M. A. and Fischer, M. P.: On the distribution of fluids in folds: A review of controlling factors and processes, *J. Struct. Geol.*, 44, 2–24, 2012.
- Ferrill, D. A., Morris, A. P., Evans, M. A., Burkhard, M., Groshong Jr, R. H., and Onasch, C. M.: Calcite twin morphology: a low-temperature deformation geothermometer, *J. Struct. Geol.*, 26, 1521–1529, 2004.
- Fischer, M. P., Higuera-Díaz, I. C., Evans, M. A., Perry, E. C., and Lefticariu, L.: Fracture-controlled paleohydrology in a map-scale detachment fold: Insights from the analysis of fluid inclusions in calcite and quartz veins, *J. Struct. Geol.*, 31, 1490–1510, 2009.
- Forster, C. B. and Evans, J. P.: Hydrogeology of thrust faults and crystalline thrust sheets: Results of combined field and modeling studies, *Geophys. Res. Lett.*, 18, 979–982, 1991.
- Garven, G.: Continental-scale groundwater flow and geologic processes, *Annu. Rev. Earth Pl. Sc.*, 23, 89–117, 1995.
- Ghissetti, F. and Vezzani, L.: Normal faulting, extension and uplift in the outer thrust belt of the central Apennines (Italy): role of the Caramanico fault, *Basin Res.*, 14, 225–236, 2002.
- Gonzalez, E., Ferket, H., Callot, J.-P., Guilhaumou, N., Ortuno, F., and Roure, F.: Paleoburial, hydrocarbon generation and migration in the Cordoba platform and Veracruz basin: Insights from fluid inclusion studies and 2D-modelling, *SEPM Spec. P.*, 103, 167–186, 2013.
- Grohmann, C. H. and Campanha, G.: OpenStereo: open source, cross-platform software for structural geology analysis, AGU Fall Meeting Abstracts, IN31C-06, 2010.
- Hitchon, B. and Friedman, I.: Geochemistry and origin of formation waters in the western Canada sedimentary basin – I. Stable isotopes of hydrogen and oxygen, *Geochim. Cosmochim. Ac.*, 33, 1321–1349, 1969.
- Hoareau, G., Claverie, F., Pecheyran, C., Paroissin, C., Grignard, P.-A., Motte, G., Chailan, O., and Girard, J.-P.: Direct U-Pb dating of carbonates from micron scale fsLA-ICPMS images using robust regression, *Geochronology Discuss.*, <https://doi.org/10.5194/gchron-2020-10>, in review, 2020.
- Holl, J. E. and Anastasio, D. J.: Paleomagnetically derived folding rates, southern Pyrenees, Spain, *Geology*, 21, 271–274, 1993.
- John, C. M. and Bowen, D.: Community software for challenging isotope analysis: First applications of “Easotope” to clumped isotopes, *Rapid Commun. Mass Sp.*, 30, 2285–2300, 2016.
- Kim, S.-T. and O’Neil, J. R.: Equilibrium and nonequilibrium oxygen isotope effects in sythetic carbonates, *Geochim. Cosmochim. Ac.*, 61, 3461–3475, 1997.
- Kim, S.-T., Mucci, A., and Taylor, B. E.: Phosphoric acid fractionation factors for calcite and aragonite between 25 and 75 °C: revisited, *Chem. Geol.*, 246, 135–146, 2007.
- Koehn, D., Renard, F., Toussaint, R., and Passchier, C.: Growth of stylolite teeth patterns depending on normal stress and finite compaction, *Earth Planet. Sc. Lett.*, 257, 582–595, <https://doi.org/10.1016/j.epsl.2007.03.015>, 2007.
- Koehn, D., Ebner, M., Renard, F., Toussaint, R., and Passchier, C. W.: Modelling of stylolite geometries and stress scaling, *Earth Planet. Sc. Lett.*, 341, 104–113, <https://doi.org/10.1016/j.epsl.2012.04.046>, 2012.
- Lacombe, O.: Calcite twins, a tool for tectonic studies in thrust belts and stable orogenic forelands, *Oil Gas Sci. Technol.*, 65, 809–838, 2010.
- Lacombe, O., Bellahsen, N., and Mouthereau, F.: Fracture patterns in the Zagros Simply Folded Belt (Fars, Iran): constraints on early collisional tectonic history and role of basement faults, *Geol. Mag.*, 148, 940–963, <https://doi.org/10.1017/s001675681100029x>, 2011.
- Lacombe, O.: Do fault slip data inversions actually yield “paleostresses” that can be compared with contemporary stresses? A critical discussion, *C. R. Geosci.*, 344, 159–173, 2012.
- Lacombe, O., Swennen, R., and Caracausi, A.: An introduction to the Special Issue of Marine and Petroleum Geology: Fluid-rock-tectonics interactions in basins and orogens, *Mar. Petrol. Geol.*, 55, 1–5, 2014.
- Lacombe, O. and Bellahsen, N.: Thick-skinned tectonics and basement-involved fold–thrust belts: insights from selected Cenozoic orogens, *Geol. Mag.*, 153, 763–810, <https://doi.org/10.1017/s0016756816000078>, 2016.
- Lacombe, O. and Rolland, Y.: An introduction to the Special Issue: Fluids in crustal deformation: Fluid flow, fluid-rock interactions, rheology, melting and resources, *J. Geodynam.*, 101, 1–4, 2016.
- Lacroix, B., Buatier, M., Labaume, P., Travé, A., Dubois, M., Charpentier, D., Ventalon, S., and Convert-Gaubier, D.: Microtectonic and geochemical characterization of thrusting in a foreland basin: Example of the South-Pyrenean orogenic wedge (Spain), *J. Struct. Geol.*, 33, 1359–1377, <https://doi.org/10.1016/j.jsg.2011.06.006>, 2011.
- Laubach, S. E., Eichhubl, P., Hilgers, C., and Lander, R. H.: Structural diagenesis, *J. Struct. Geol.*, 32, 1866–1872, <https://doi.org/10.1016/j.jsg.2010.10.001>, 2010.
- Laubach, S. E., Lander, R., Criscenti, L. J., Anovitz, L. M., Urai, J., Pollyea, R., Hooker, J. N., Narr, W., Evans, M. A., and Kerisit, S. N.: The role of chemistry in fracture pattern development and opportunities to advance interpretations of geological materials, *Rev. Geophys.*, 57, 1065–1111, 2019.
- Lavecchia, G.: The Tyrrhenian-Apennines system: structural setting and seismotectogenesis, *Tectonophysics*, 147, 263–296, 1988.
- Lefticariu, L., Perry, E. C., Fischer, M. P., and Banner, J. L.: Evolution of fluid compartmentalization in a detachment fold complex, *Geology*, 33, 69–72, 2005.
- Lucca, A., Storti, F., Balsamo, F., Clemenzi, L., Fondriest, M., Burgess, R., and Toro, G. d.: From Submarine to Subaerial Out-of-Sequence Thrusting and Gravity-Driven Extensional Fault-

- ing: Gran Sasso Massif, Central Apennines, Italy, *Tectonics*, 38, 4155–4184, <https://doi.org/10.1029/2019TC005783>, 2019.
- Machel, H. G. and Cavell, P. A.: Low-flux, tectonically-induced squeegee fluid flow, *B. Can. Petrol. Geol.*, 47, 510–533, 1999.
- Manger, G. E.: Porosity and bulk density of sedimentary rocks, *USGS Bull.*, 1144-E, 47–55, 1963.
- Masaferro, J. L., Bulnes, M., Poblet, J., and Eberli, G. P.: Episodic folding inferred from syntectonic carbonate sedimentation: the Santaren anticline, Bahamas foreland, *Sediment. Geol.*, 146, 11–24, 2002.
- Mazzoli, S., Deiana, G., Galdenzi, S., and Cello, G.: Miocene fault-controlled sedimentation and thrust propagation in the previously faulted external zones of the Umbria-Marche Apennines, Italy, *EGU Stephan Mueller Special Publication Series*, 1, 195–209, 2002.
- McArthur, J. M., Howarth, R., and Bailey, T.: Strontium isotope stratigraphy: LOWESS version 3: best fit to the marine Sr-isotope curve for 0–509 Ma and accompanying look-up table for deriving numerical age, *J. Geol.*, 109, 155–170, 2001.
- McCaig, A. M.: Deep fluid circulation in fault zones, *Geology*, 16, 867–870, 1988.
- Meckler, A. N., Ziegler, M., Millán, M. I., Breitenbach, S. F., and Bernasconi, S. M.: Long-term performance of the Kiel carbonate device with a new correction scheme for clumped isotope measurements, *Rapid Commun. Mass Sp.*, 28, 1705–1715, 2014.
- Mirabella, F., Barchi, M., Lupattelli, A., Stucchi, E., and Ciaccio, M.: Insights on the seismogenic layer thickness from the upper crust structure of the Umbria-Marche Apennines (central Italy), *Tectonics*, 27, TC1010, <https://doi.org/10.1029/2007TC002134>, 2008.
- Mozafari, M., Swennen, R., Balsamo, F., Desouky, H. E., Storti, F., and Taberner, C.: Fault-controlled dolomitization in the Montagna dei Fiori Anticline (Central Apennines, Italy): record of a dominantly pre-orogenic fluid migration, *Solid Earth*, 10, 1355–1383, <https://doi.org/10.5194/se-10-1355-2019>, 2019.
- Muller, I. A., Violay, M. E. S., Storck, J. C., Fernandez, A., van Dijk, J., Madonna, C., and Bernasconi, S. M.: Clumped isotope fractionation during phosphoric acid digestion of carbonates at 70 °C, *Chem. Geol.*, 449, 1–14, <https://doi.org/10.1016/j.chemgeo.2016.11.030>, 2017.
- Oliver, J.: Fluids expelled tectonically from orogenic belts: Their role in hydrocarbon migration and other geologic phenomena, *Geology*, 14, 99–102, 1986.
- Petracchini, L., Antonellini, M., Billi, A., and Scrocca, D.: Fault development through fractured pelagic carbonates of the Cingoli anticline, Italy: Possible analog for subsurface fluid-conductive fractures, *J. Struct. Geol.*, 45, 21–37, <https://doi.org/10.1016/j.jsg.2012.05.007>, 2012.
- Qing, H. and Mountjoy, E.: Large-scale fluid flow in the Middle Devonian Presqu'île Barrier, Western Canada sedimentary basin, *Geology*, 20, 903–906, 1992.
- Quintà, A. and Tavani, S.: The foreland deformation in the southwestern Basque–Cantabrian Belt (Spain), *Tectonophysics*, 576, 4–19, 2012.
- Reynolds, S. J. and Lister, G. S.: Structural aspects of fluid-rock interactions in detachment zones, *Geology*, 15, 362–366, 1987.
- Roberts, N. M. and Walker, R. J.: U–Pb geochronology of calcite-mineralized faults: Absolute timing of rift-related fault events on the northeast Atlantic margin, *Geology*, 44, 531–534, 2016.
- Roberts, N. M., Rasbury, E. T., Parrish, R. R., Smith, C. J., Horstwood, M. S., and Condon, D. J.: A calcite reference material for LA-ICP-MS U–Pb geochronology, *Geochem. Geophys. Geosy.*, 18, 2807–2814, 2017.
- Roberts, N. M. W., Drost, K., Horstwood, M. S. A., Condon, D. J., Chew, D., Drake, H., Milodowski, A. E., McLean, N. M., Smye, A. J., Walker, R. J., Haslam, R., Hodson, K., Imber, J., Beaudoin, N., and Lee, J. K.: Laser ablation inductively coupled plasma mass spectrometry (LA-ICP-MS) U–Pb carbonate geochronology: strategies, progress, and limitations, *Geochronology*, 2, 33–61, <https://doi.org/10.5194/gchron-2-33-2020>, 2020.
- Rolland, A., Toussaint, R., Baud, P., Schmittbuhl, J., Conil, N., Koehn, D., Renard, F., and Gratier, J.-P.: Modeling the growth of stylolites in sedimentary rocks, *J. Geophys. Res.-Sol. Ea.*, 117, B06403, <https://doi.org/10.1029/2011jb009065>, 2012.
- Rolland, A., Toussaint, R., Baud, P., Conil, N., and Landrein, P.: Morphological analysis of stylolites for paleostress estimation in limestones, *Int. J. Rock Mech. Min.*, 67, 212–225, <https://doi.org/10.1016/j.ijrmm.2013.08.021>, 2014.
- Roure, F., Bordas-Lefloch, N., Toro, J., Aubourg, C., Guilhaumou, N., Hernandez, E., Lecornec-Lance, S., Rivero, C., Robion, P., and Sassi, W.: Petroleum systems and reservoir appraisal in the sub-Andean basins (eastern Venezuela and eastern Colombian foothills), *AAPG Memoirs*, 79, 750–775, 2003.
- Roure, F., Swennen, R., Schneider, F., Faure, J., Ferket, H., Guilhaumou, N., Osadetz, K., Robion, P., and Vandeginste, V.: Incidence and importance of tectonics and natural fluid migration on reservoir evolution in foreland fold-and-thrust belts, *Oil Gas Sci. Technol.*, 60, 67–106, 2005.
- Roure F., Andriessen P., Callot J.-P., Ferket H., Gonzalez E., Guilhaumou N., Hardebol N., Lacombe O., Malandain J., Mougou P., Muska K., Ortuno S., Sassi W., Swennen R., and Vilasi N.: The use of paleo-thermo-barometers and coupled thermal, fluid flow and pore fluid pressure modelling for hydrocarbon and reservoir prediction in fold-and-thrust belts, in: “Hydrocarbons in Contractual Belts”, *Geol. Soc. Lond. Special Publ.*, 348, 87–114, <https://doi.org/10.1144/SP348.6>, 2010.
- Sassi, W., Guiton, M., Leroy, Y., Daniel, J.-M., and Callot, J.-P.: Constraints on bed scale fracture chronology with a FEM mechanical model of folding: The case of Split Mountain (Utah, USA), *Tectonophysics*, 576, 197–215, 2012.
- Schmittbuhl, J., Renard, F., Gratier, J. P., and Toussaint, R.: Roughness of stylolites: implications of 3D high resolution topography measurements, *Phys. Rev. Lett.*, 93, 238501, <https://doi.org/10.1103/PhysRevLett.93.238501>, 2004.
- Schneider, F., Faure, J., and Roure, F.: Methodology for basin modeling in complex area: examples from Eastern Venezuelan and Canadian Foothills, *AAPG Hedberg Conference “Deformation History, Fluid Flow Reconstruction and Reservoir Appraisal in Foreland Fold and Thrust Belts”*, 14–18, 2002.
- Schneider, F., Pagel, M., and Hernandez, E.: Basin modeling in a complex area: Example from the Eastern Venezuelan foothills, in: *Deformation, fluid flow, and reservoir appraisal in foreland fold and thrust belts: AAPG Hedberg Series*, edited by: Swennen, R., Roure, F., and Granath, J. W., 357–369, 2004.
- Scisciani, V., Agostini, S., Calamita, F., Pace, P., Cilli, A., Giori, I., and Paltrinieri, W.: Positive inversion tectonics in foreland fold-and-thrust belts: a reappraisal of the Umbria–Marche Northern

- Apennines (Central Italy) by integrating geological and geophysical data, *Tectonophysics*, 637, 218–237, 2014.
- Scisciani, V., Patruno, S., Tavarnelli, E., Calamita, F., Pace, P., and Iacopini, D.: Multi-phase reactivations and inversions of Paleozoic–Mesozoic extensional basins during the Wilson cycle: case studies from the North Sea (UK) and the Northern Apennines (Italy), *Geol. Soc. Lond. Special Publ.*, 470, 205–243, <https://doi.org/10.1144/sp470-2017-232>, 2019.
- Simonsen, I., Hansen, A., and Nes, O. M.: Determination of the Hurst exponent by use of wavelet transforms, *Phys. Rev. E*, 58, 2779, <https://doi.org/10.1103/PhysRevE.58.2779>, 1998.
- Smith, A. P., Fischer, M. P., and Evans, M. A.: Fracture-controlled palaeohydrology of a secondary salt weld, La Popa Basin, NE Mexico, *Geol. Soc. Lond. Special Publ.*, 363, 107–130, 2012.
- Stearns, D. W. and Friedman, M.: Reservoirs in fractured rock: Geologic exploration methods, AAPG Special Volumes M16, 82–106, 1972.
- Storti, F., Balsamo, F., Mozafari, M., Koopman, A., Swennen, R., and Taberner, C.: Syn-Contractional Overprinting Between Extension and Shortening Along the Montagna Dei Fiori Fault During Plio-Pleistocene Antiformal Stacking at the Central Apennines Thrust Wedge Toe, *Tectonics*, 37, 3690–3720, <https://doi.org/10.1029/2018tc005072>, 2018.
- Suppe, J., Chou, G. T., and Hook, S. C.: Rates of folding and faulting determined from growth strata, in: *Thrust tectonics*, Springer, 105–121, 1992.
- Tavani, S., Storti, F., Salvini, F., and Toscano, C.: Stratigraphic versus structural control on the deformation pattern associated with the evolution of the Mt. Catria anticline, Italy, *J. Struct. Geol.*, 30, 664–681, <https://doi.org/10.1016/j.jsg.2008.01.011>, 2008.
- Tavani, S. and Cifelli, F.: Deformation pattern analysis and tectonic implications of a décollement level within the Central Apennines (Italy), *Geol. J.*, 45, 582–596, <https://doi.org/10.1002/gj.1198>, 2010.
- Tavani, S., Storti, F., Bausà, J., and Muñoz, J. A.: Late thrusting extensional collapse at the mountain front of the northern Apennines (Italy), *Tectonics*, 31, TC4019, <https://doi.org/10.1029/2011tc003059>, 2012.
- Tavani, S., Storti, F., Lacombe, O., Corradetti, A., Muñoz, J., and Mazzoli, S.: A review of deformation pattern templates in foreland basin systems and fold-and-thrust belts: Implications for the state of stress in the frontal regions of thrust wedges, *Earth-Sci. Rev.*, 141, 82–104, 2015.
- Tavarnelli, E., Butler, R., Decandia, F., Calamita, F., Grasso, M., Alvarez, W., Renda, P., Crescenti, U., and D’offizi, S.: Implications of fault reactivation and structural inheritance in the Cenozoic tectonic evolution of Italy, *The Geology of Italy, Special*, 1, 209–222, 2004.
- Toussaint, R., Aharonov, E., Koehn, D., Gratier, J. P., Ebner, M., Baud, P., Rolland, A., and Renard, F.: Stylolites: A review, *J. Struct. Geol.*, 114, 163–195, <https://doi.org/10.1016/j.jsg.2018.05.003>, 2018.
- Travé, A., Calvet, F., Sans, M., Vergés, J., and Thirlwall, M.: Fluid history related to the Alpine compression at the margin of the south-Pyrenean Foreland basin: the El Guix anticline, *Tectonophysics*, 321, 73–102, 2000.
- Travé, A., Labaume, P., and Vergés, J.: Fluid systems in foreland fold-and-thrust belts: an overview from the Southern Pyrenees, in: *Thrust belts and foreland basins*, Springer, 93–115, 2007.
- Van Geet, M., Swennen, R., Durmishi, C., Roure, F., and Muchez, P.: Paragenesis of Cretaceous to Eocene carbonate reservoirs in the Ionian fold and thrust belt (Albania): relation between tectonism and fluid flow, *Sedimentology*, 49, 697–718, 2002.
- Vandeginste, V., Swennen, R., Allaey, M., Ellam, R. M., Osadetz, K., and Roure, F.: Challenges of structural diagenesis in foreland fold-and-thrust belts: a case study on paleofluid flow in the Canadian Rocky Mountains West of Calgary, *Mar. Petrol. Geol.*, 35, 235–251, 2012.
- Vannucchi, P., Remitti, F., Bettelli, G., Boschi, C., and Dallai, L.: Fluid history related to the early Eocene-middle Miocene convergent system of the Northern Apennines (Italy): Constraints from structural and isotopic studies, *J. Geophys. Res.*, 115, B05405, <https://doi.org/10.1029/2009JB006590>, 2010.
- Vass, A., Koehn, D., Toussaint, R., Ghani, I., and Piazzolo, S.: The importance of fracture-healing on the deformation of fluid-filled layered systems, *J. Struct. Geol.*, 67, 94–106, <https://doi.org/10.1016/j.jsg.2014.07.007>, 2014.
- Vignaroli, G., Pinton, A., De Benedetti, A. A., Giordano, G., Rossetti, F., Soligo, M., and Berardi, G.: Structural compartmentalisation of a geothermal system, the Torre Alfina field (central Italy), *Tectonophysics*, 608, 482–498, 2013.
- Vilasi, N., Malandain, J., Barrier, L., Callot, J.-P., Amrouch, K., Guilhaumou, N., Lacombe, O., Muska, K., Roure, F., and Swennen, R.: From outcrop and petrographic studies to basin-scale fluid flow modelling: The use of the Albanian natural laboratory for carbonate reservoir characterisation, *Tectonophysics*, 474, 367–392, 2009.
- Watts, A. B.: *Isostasy and Flexure of the Lithosphere*, Cambridge University Press, 458 pp., 2001.
- Wright, K., Cygan, R. T., and Slater, B.: Structure of the (101 [combining macron] 4) surfaces of calcite, dolomite and magnesite under wet and dry conditions, *Phys. Chem. Chem. Phys.*, 3, 839–844, 2001.
- Yamato, P., Kaus, B. J., Mouthereau, F., and Castellort, S.: Dynamic constraints on the crustal-scale rheology of the Zagros fold belt, Iran, *Geology*, 39, 815–818, 2011.



Dating folding beyond folding, from layer-parallel shortening to fold tightening, using mesostructures: lessons from the Apennines, Pyrenees, and Rocky Mountains

Olivier Lacombe¹, Nicolas E. Beaudoin², Guilhem Hoareau², Aurélie Labeur², Christophe Pecheyran³, and Jean-Paul Callot²

¹Institut des Sciences de la Terre de Paris, Sorbonne Université, CNRS, Paris, France

²Laboratoire des Fluides Complexes et de leurs Réservoirs, Université de Pau et des Pays de l'Adour, E2S UPPA, CNRS-TOTAL, Pau, France

³Institut des Sciences Analytiques et de Physico-Chimie pour l'Environnement et les Matériaux, Université de Pau et des Pays de l'Adour, E2S UPPA, Pau, France

Correspondence: Olivier Lacombe (olivier.lacombe@sorbonne-universite.fr)

Received: 18 June 2021 – Discussion started: 23 June 2021

Revised: 26 August 2021 – Accepted: 6 September 2021 – Published: 30 September 2021

Abstract. Dating syntectonic sedimentary sequences is often seen as the unique way to constrain the initiation, duration, and rate of folding as well as the sequence of deformation in the shallow crust. Beyond fold growth, however, deformation mesostructures accommodate the internal strain of pre-folding strata before, during, and after strata tilting. Absolute dating of syn-folding mesostructures may help constrain the duration of fold growth in the absence of preserved growth strata. Absolute dating of mesostructures related to early-folding layer-parallel shortening and late fold tightening provides an access to the timing and duration of the entire folding event. We compile available ages from the literature and provide new U–Pb ages of calcite cements from veins and faults from four folds (Apennines, Pyrenees, Rocky Mountains). Our results not only better constrain the timing of fold growth but also reveal a contraction preceding and following folding, the duration of which might be a function of the tectonic style and regional sequence of deformation. This study paves the way for a better appraisal of folding lifetime and processes and stress evolution in folded domains.

1 Introduction

Quantifying the rates and duration of deformation processes is key to understanding how the continental crust deforms. Quite a lot is known about rates and duration of ductile deformation in the lower crust, for instance that shear zones can be active for tens to hundreds of millions of years (Schneider et al., 2013; Mottram et al., 2015). However, less is known about the duration and rates of folding processes in the upper crust. Short-term folding rates are usually captured by studying deformed terraces and alluvial fan ridges associated with active folds, and the dating of the inception and lifetime of folds is based on the extrapolation of these short-term rates back in time assuming a steady deformation rate.

The other classical means of constraining the age and rate of upper-crustal folding consists of dating growth strata. In orogenic forelands, contractional deformation causes folding of the pre-deformational sedimentary sequence, and when sedimentation occurs continuously during deformation, growth strata are deposited synchronously with folding. Growth strata often show a characteristic pattern, such as decreasing dips up-section toward the limbs of the fold, fan-like geometry, and unconformities (Riba, 1976; Fig. 1). Several factors control growth strata patterns, such as kink-band migration, fold uplift, limb rotation and lengthening rates, as well as sedimentation and erosion rates (Suppe et al., 1992; Storti and Poblet, 1997). Chronostratigraphic constraints are

critical for defining the duration and rate of fold growth (Butler and Lickorish, 1997). Dating the base of the growth strata defines the youngest initiation age for the fold, while post-growth strata conceal the final geometry of the fold and mark the end of folding (Fig. 1).

However, preserved growth strata are not ubiquitous/are rare, and the folded multilayer typically includes only pre-growth strata. Also, the fold growth may be highly discontinuous through time, deformation being episodic at all timescales with tectonic uplift pulses of different duration and intensity interrupted by periods of variable extent in which no fold growth occurred (Masferro et al., 2002; Carrigan et al., 2016; Anastasio et al., 2017). Where available, the study of syntectonic unconformities (Barnes, 1996) or terraces (Mueller and Suppe, 1997) otherwise suggests that the growth of some folds may be caused by earthquake-related slip on active faults, which is by its nature discontinuous. These studies emphasize the difficulty in extrapolating fold growth rates back in time. The age of fold initiation obtained by assuming steady shortening, deposition, and fold growth rates is therefore at best strongly biased and at worst false, so the duration of fold growth remains poorly constrained.

Folded sedimentary layers usually exhibit brittle mesostructures such as faults, joints, veins, and stylolites (e.g. Tavani et al., 2015, and references therein). These mesostructures accommodate the internal strain of strata during folding but also before strata started to be tilted and after tilting, i.e. when shortening can no longer be accommodated by fold growth (Fig. 1). Several deformation stages can typically be identified in folded pre-compressional strata, starting with pre-shortening extension related to foreland flexure and bulging, followed by layer-parallel shortening (LPS, horizontal shortening of flat-lying strata) (Amrouch et al., 2010a; Callot et al., 2010; Lacombe et al., 2011; Tavani et al., 2006, 2008, 2011, 2012; Rocher et al., 2000; Beaudoin et al., 2012, 2016; Branellec et al., 2015). Continuing horizontal stress loading and shortening usually leads to folding, associated with strata tilting and curvature, which are accommodated by flexural slip in the fold limbs and tangential longitudinal strain (outer-arc extension and inner-arc compression) at the fold hinge. The fold “locks” when limb rotation and/or kink-band migration cannot accommodate shortening anymore. At that stage, strata tilting is over but continuous horizontal shortening leads to late-stage fold tightening (LSFT), accommodated by late mesostructures developing irrespective of bedding dip (Fig. 1) (Amrouch et al., 2010a; Tavani et al., 2015).

Despite recent efforts (Wang et al., 2016; Grobe et al., 2019; Curzi et al., 2020; Cruset et al., 2020, 2021), the dating of the early-, syn-, and late-folding mesostructures has received poor attention, although it is key to constraining not only the absolute timing of folding in the absence of growth strata but also the entire duration of the fold-related contractional stages and the associated stress evolution from build-up to release. We explore hereinafter the possibility to de-

fine the age and duration of folding by investigating how and for how long pre-folding strata have been accommodating shortening from the onset to the end of the horizontal contraction from which the fold originated, an event we define as the folding event (Fig. 1). This approach will help better constrain the duration of fold growth, by directly dating the syn-folding mesostructures but also by bracketing the timing of fold growth through the dating of the mesostructures that immediately predate and postdate strata tilting. Doing so will also enable us to capture the duration of the LPS and LSFT. These two deformation stages have been overlooked since they accommodate much less shortening than folding itself. However, they correspond to key periods of time for large-scale fluid flow and related ore deposition in fold-and-thrust belts and sedimentary basins (e.g. Roure et al., 2005; Evans and Fischer, 2012; Beaudoin et al., 2014). For this purpose, we consider four natural folds for which we either compile existing data or provide new estimates of the age of LPS, fold growth, and LSFT. Three of our examples are from fold-and-thrust belts (Apennines, Pyrenees) and one from the Laramide basement-cored folding province (Rocky Mountains). We show that mesostructures can be used to constrain the timing and duration of fold growth and/or of shortening preceding and following folding. Our results not only provide new estimates of the duration of folding but also establish that the overall duration of the folding event may strongly vary as a function of the tectonic style of deformation. Beyond regional implications, this study paves the way to a better mechanical appraisal of contractional deformation and stress evolution in folded domains.

2 Methods for dating the folding event using mesostructures

In this paper, we focus on easily recognizable mesostructures that develop in the same contractional stage and under the same regional trend of horizontal shortening as folding. We report neither on microstructures such as calcite twins (Cradock et al., 1993; Lacombe et al., 2007, 2009; Rocher et al., 1996; Hnat et al., 2011; see review by Lacombe, 2010) nor on rock physical properties such as anisotropy of magnetic susceptibility (e.g. Aubourg et al., 2010; Amrouch et al., 2010b; Branellec et al., 2015; Weil and Yonkee, 2012). The main reason is that although both of them have been shown to be suitable recorders of the stress and strain history of folded strata (Lacombe et al., 2012), their precise dating remains out of reach to date.

In the four folds that we investigated, the sequence and age of mesostructures were established by various dating approaches, the methodologies of which are briefly recalled below (Fig. 2). Note that strata from which mesostructures were dated are mainly pre-folding strata and that there have been few (if any) attempts at directly dating mesostructures that developed within growth strata. The reason is that the of-

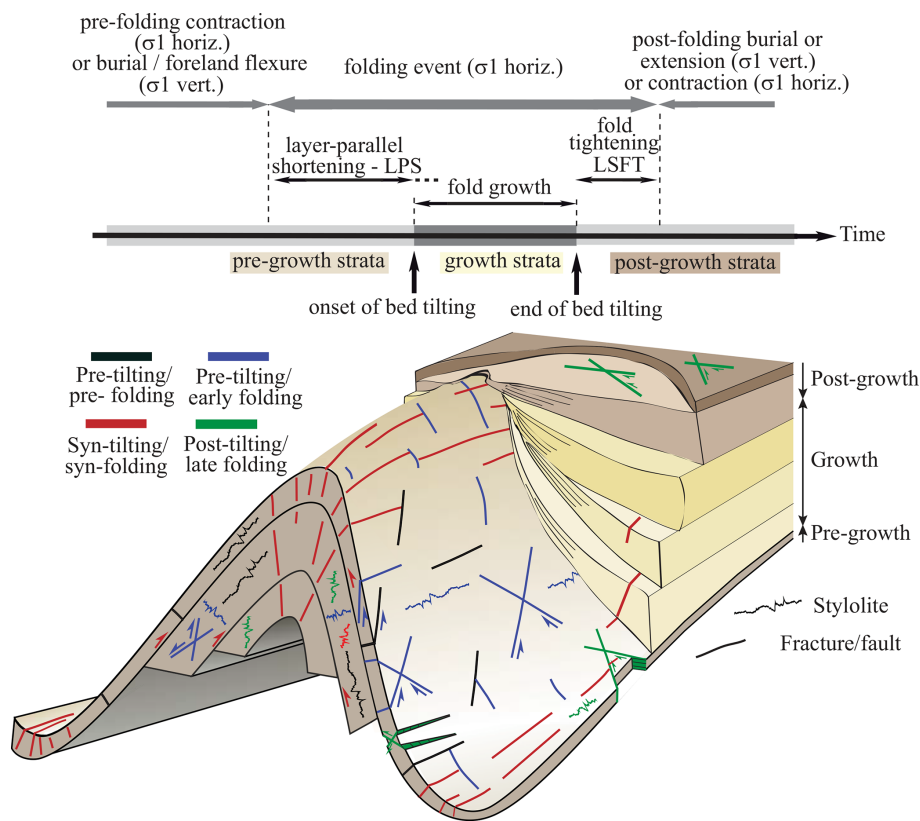


Figure 1. Concept of folding event and associated mesostructures and growth strata.

ten poorly indurated syn-folding formations are less prone to fracturing and calcite cementation at the time of deformation compared to pre-folding, well-indurated formations, which is evidenced by the paucity of fracture studies in syn-tectonic strata (e.g. Shackleton et al., 2011).

2.1 Sequence of mesostructures related to the fold history

The characterization of the sequence of deformation was based on field measurements of stylolites, faults, joints, and veins and their grouping into sets according to their statistical orientation, deformation mode, and relative chronology established from abutting and crosscutting relationships (Fig. 2a). Their timing with respect to fold growth (i.e. early-, syn-, and late-folding mesostructures) was further established by considering their current and unfolded attitude at the fold hinge and limbs (e.g. Beaudoin et al., 2012, 2016; Tavani et al., 2015) (Fig. 1).

Field observations (e.g. Bellahsen et al., 2006; Ahmadhadi et al., 2008; Tavani et al., 2015) and numerical modelling (Guiton et al., 2003; Sassi et al., 2012) have emphasized the widespread reactivation during folding of joints and veins formed during pre-folding stages. The role of reactivation should not be, and has not been, overlooked in our study; however, for the sake of reliable absolute dating we focused

on faults and veins the characteristics of which support that they newly formed at each deformation stage and show neither textural nor petrographic evidence of multiple opening or shearing events, be it at the mesoscale or at the microscale.

2.2 Dating veins and faults

Calcite-bearing veins and faults (Fig. 2a) can be dated by combining the absolute precipitation temperature of the fluids from which calcite cements formed as given by carbonate clumped isotope Δ_{47} thermometry with the burial-time history of strata (Fig. 2b and d). Provided that (1) cementation was nearly coeval with fracturing, (2) the geotherm can be reliably estimated, and (3) stable isotope geochemistry points to fluid precipitation at thermal equilibrium with the host rock, clumped isotope thermometry of cements combined with strata burial history yields the absolute timing of the successive vein sets and hence the timing of the related deformation stages (Fig. 2d) (Labeur et al., 2021).

Calcite cements can also be directly dated by carbonate geochronology (Fig. 2b). Laser-ablation–inductively-coupled-plasma–mass-spectrometry (LA-ICP-MS) U–Pb dating of calcite consistently reveals the age of brittle deformation events (Roberts and Walker, 2016; Nuriel et al., 2017; Hansman et al., 2018; Beaudoin et al., 2018; Roberts et al., 2020) (Fig. 2b and d), provided that cementation was

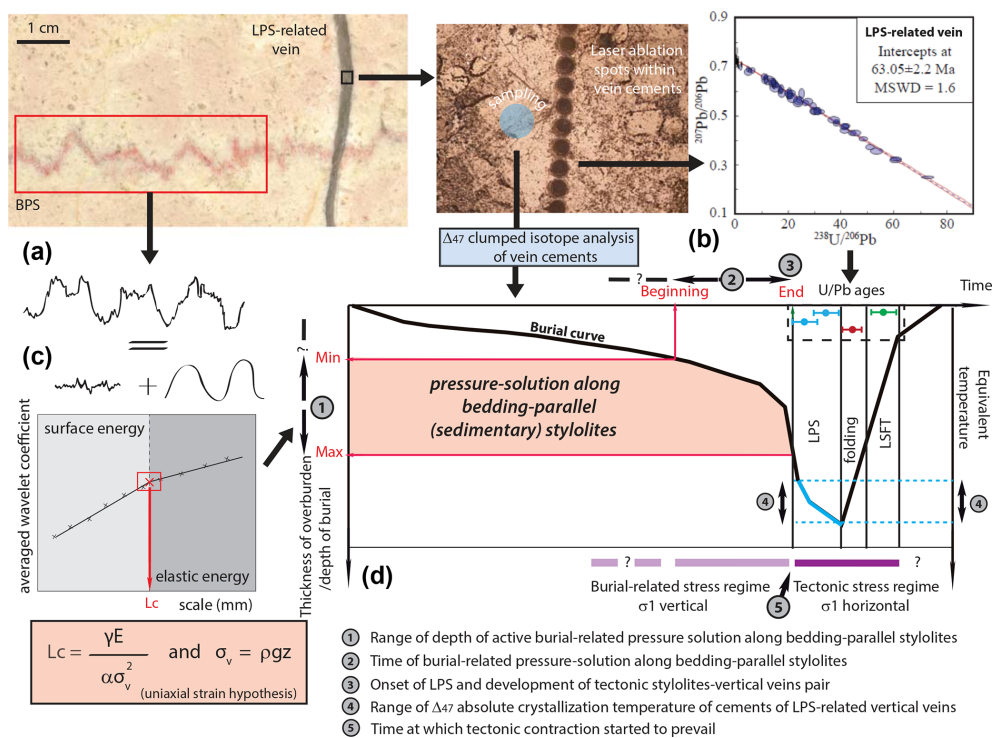


Figure 2. Principle of the dating of mesostructures related to the folding event. (a) Photograph of a bedding-parallel sedimentary stylolite cut by a vertical vein related to layer-parallel shortening (LPS). (b) Principle of dating calcite veins using LA-ICP-MS, with laser ablation spots and final Tera-Wasserburg diagram. (c) Principle of inversion of the roughness of sedimentary stylolites for stress. σ_v is the vertical stress, $\alpha = ((1 - 2\nu) \cdot (1 + \nu)^2) / (30\pi(1 - \nu)^2)$, γ is the solid–fluid interfacial energy, ν is the Poisson ratio, E is the Young modulus, ρ is the dry density, g is the gravitational field acceleration, and z is the depth. (d) Principle of the combination of U–Pb dating and absolute Δ_{47} thermometry of calcite cements (here for LPS-related veins) with maximum depth of burial-related dissolution inferred from roughness inversion of sedimentary stylolites and burial-time evolution of strata to derive the timing of deformation stages during the folding event.

coeval with fracturing and that no later fluid infiltration and/or calcite recrystallization occurred (Roberts et al., 2021).

2.3 Combining sedimentary stylolite roughness inversion for paleodepth and burial history to constrain the onset of LPS

The onset of LPS corresponds to the time at which the maximum principal stress σ_1 switched from a vertical attitude related to compaction and/or to foreland flexural extension to a horizontal attitude in response to tectonic contraction (Beaudoin et al., 2020a). In order to constrain the timing of this switch, our approach relies on the capability of bedding-parallel, sedimentary stylolite (Fig. 2a) to fossilize the magnitude of the vertical stress σ_1 at the time at which dissolution stopped. Indeed, signal analysis (e.g. wavelets) of the final roughness of a sedimentary stylolite returns scale-dependent power laws, of which the transition length (crossover length L_c) scales with the magnitude of the vertical stress $\sigma_v = \sigma_1$ (Schmittbuhl et al., 2004; Toussaint et al., 2018) (Fig. 2c). By analysing a population of sedimentary stylolites with this inversion technique, which has been

validated by numerous studies (Ebner et al., 2009; Rolland et al., 2012, 2014; Bertotti et al., 2017; Beaudoin et al., 2016, 2019, 2020a, b), one can estimate the maximum burial depth at which pressure solution was active, with 12 % uncertainty (Rolland et al., 2014). Combining this depth with the burial-time evolution of the strata as derived from well data and/or exposed stratigraphic successions reveals the time at which compaction-driven pressure solution was halted in the rock because of the switch from a vertical to a horizontal σ_1 and thus the age of the onset of LPS (Fig. 2d). The validity of such an approach has been established on the basis of the comparison of the age of the onset of LPS determined this way with the oldest U–Pb absolute age of LPS-related veins (Beaudoin et al., 2020a).

3 Dating natural folding events

3.1 Cingoli and San Vicino Anticlines (Apennines)

The San Vicino and Cingoli anticlines belong to the Umbria–Marche Apennine Ridge (UMAR, Fig. 3a). Apenninic deformation occurred by the Tortonian in the west of UMAR to the

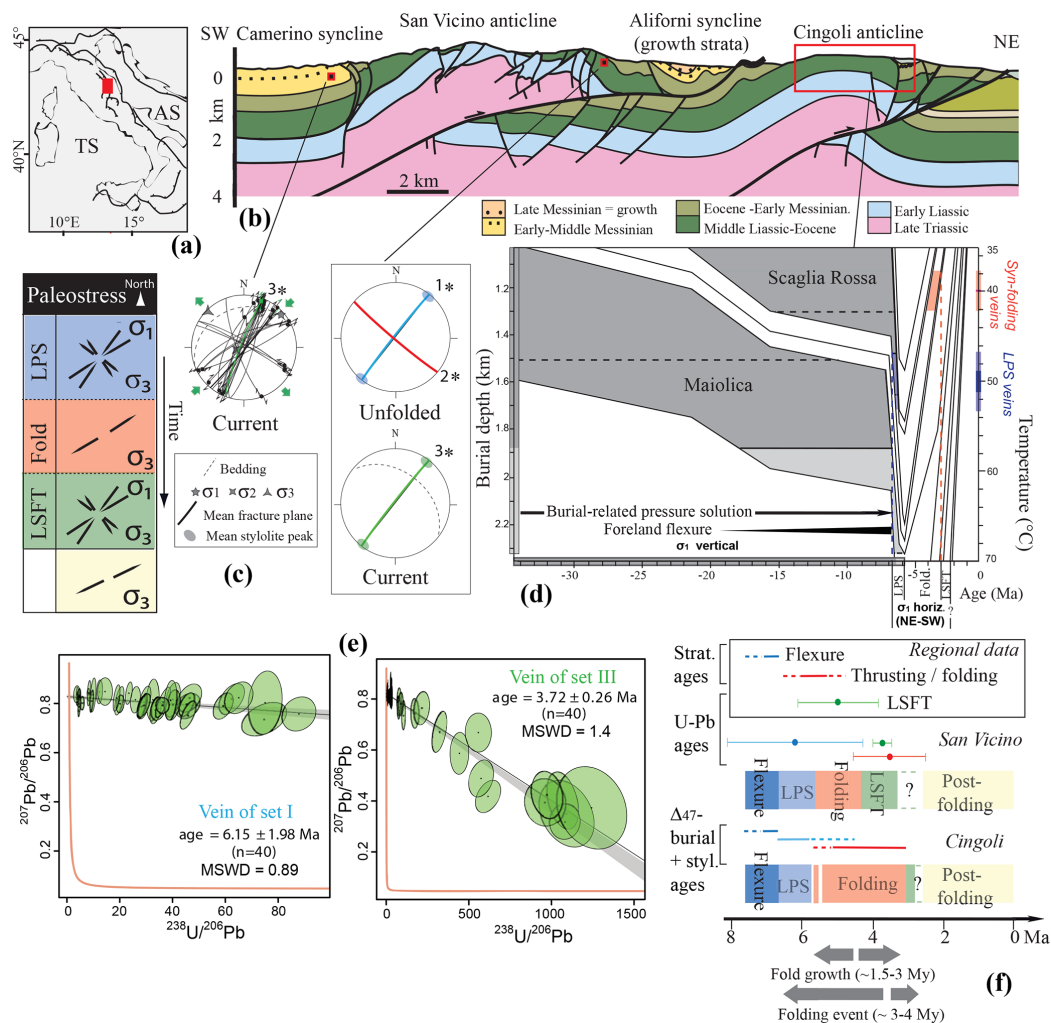


Figure 3. San Vicino and Cingoli anticlines. (a) Location (AS: Adriatic Sea; TS: Tyrrhenian Sea). (b) Cross section (modified after Mazzoli et al., 2002). (c) Orientation of the main sets of mesostructures (relative chronology, 1 to 3), reported in current or unfolded attitude on a lower-hemisphere Schmidt stereonet, and associated paleostress evolution; * denotes mesostructures dated using U–Pb. (d) Burial model of Cingoli constructed considering thickness from stratigraphic and well data corrected for chemical and physical compaction (modified after Labeur et al., 2021). The range of depths reconstructed from sedimentary stylolite roughness inversion (with uncertainty shaded in light grey) is reported for each formation as grey levels. The results of clumped isotope analysis (i.e. temperatures of precipitation of vein cements at thermal equilibrium with the host rock) are reported for LPS-related veins (blue) and syn-folding veins (red). The deduced timing of the deformation stages is reported. (e) Age dating results for veins from the San Vicino anticline: Tera–Wasserburg concordia plots for carbonate samples showing $^{238}\text{U}/^{206}\text{Pb}$ vs. $^{207}\text{Pb}/^{206}\text{Pb}$ for veins of sets I (LPS-related) and III (LSFT-related) (n – no. of spots). MSWD – mean square of weighted deviates. (f) Timing and duration of deformation stages. Regional data are from Mazzoli et al. (2002) (flexure), Calamita et al. (1994) (folding and thrusting), and Beaudoin et al. (2020b) (LSFT). Colour code for (c, f): dark blue – flexure-related extension; blue – layer-parallel shortening (LPS); red – fold growth; green – late-stage fold tightening (LSFT); yellow – post-folding extension.

late Messinian–early Pliocene in the east, reaching the Adriatic domain in the late Pliocene–Pleistocene (Calamita et al., 1994). UMAR has been undergoing post-orogenic extension since ~ 3 Ma, being younger eastward and marked by recent or active normal faults cutting through the nappe stack (Barchi, 2010). The San Vicino and the Cingoli anticlines involve platform carbonates overlain by a hemipelagic succession detached above Triassic evaporites. The folds formed in the late Messinian–early Pliocene (~ 6 – 5 Ma) as indicated

by growth strata preserved in the nearby Aliforni syncline (Fig. 3b), following a period of foreland flexure-related extension marked by pre-contractual normal faults associated with turbidite deposition lasting until the early Messinian (~ 6.5 Ma) (Calamita et al., 1994; Mazzoli et al., 2002).

Field analysis in the Cingoli and San Vicino fault-bend anticlines (Fig. 3b) has revealed three main sets of mesostructures (Beaudoin et al., 2020b; Labeur et al., 2021). Set I consists of vertical veins perpendicular to both bedding and fold

axis and striking NE–SW, associated with bed-perpendicular tectonic stylolites with peaks trending NE–SW and plunging parallel to bedding dip which, after unfolding, indicates NE–SW-directed LPS. Set II veins are bed-perpendicular and strike NW–SE, parallel to the fold axis; they abut or cut across set I veins and formed in response to outer-arc extension at the fold hinge. Set III comprises NE–SW-striking veins closely associated with tectonic stylolites with horizontal peaks trending NE–SW – both veins and tectonic stylolites being vertical regardless of the bedding dip – and with conjugate vertical strike-slip faults which formed during a post-tilting horizontal NE–SW contraction, i.e. LSFT (Fig. 3c).

Labeur et al. (2021) focused on the Cingoli anticline to reconstruct the burial history of the early Cretaceous Maiolica Fm and the Paleocene Scaglia Rossa Fm. The authors carried out an extensive inversion of the roughness of sedimentary stylolites from these formations to constrain the maximum depth at which compaction-related dissolution was active. The results are shown in Fig. 3d, together with the timing of veins from sets I and II as deduced from Δ_{47} thermometry (Labeur et al., 2021) by considering a $23\text{ }^{\circ}\text{C km}^{-1}$ geotherm (Caricchi et al., 2015) and a $10\text{ }^{\circ}\text{C}$ surface temperature. The resulting timing for LPS, fold growth, and LSFT is shown in Fig. 3f.

To extend the published dataset to the San Vicino Anticline, veins from sets I, II, and III were sampled in the Maiolica Fm to perform U–Pb analyses for absolute dating. Selected veins display antitaxial, elongated blocky, or blocky textures (Bons et al., 2012) ensuring that the cements precipitated during, or soon after, vein opening. Cathodoluminescence observations further support the homogeneity of the cements (Fig. 4) as well as the absence of any vein reopening and calcite recrystallization or fluid infiltration that might cause anomalous younger (reset) ages (Roberts et al., 2021). U–Pb dating of calcite cements was conducted using LA-ICP-MS at the Institut des Sciences Analytiques et de Physico-Chimie pour l’Environnement et les Matériaux (IPREM) laboratory (Pau, France). Ages were determined from the total-Pb/U–Th algorithm of Vermeesch (2020), are quoted at 95 % confidence, and include the propagation of systematic uncertainties. Sample information, a detailed methodology, and results are provided in the Supplement. Three veins from the San Vicino anticline yielded reliable ages: $6.1 \pm 2\text{ Ma}$ for the set I vein, $3.5 \pm 1\text{ Ma}$ for the set II vein, and $3.7 \pm 0.3\text{ Ma}$ for the set III vein (Fig. 3e). The large uncertainties in the U–Pb age from the set II vein lead to some overlap with the dates of set I and set III veins (Fig. 3f). However, these veins have distinctive orientations, a consistent relative chronology, and distinctive C and O stable isotopic signatures of their cements while being sampled in the same parts of the fold (Beaudoin et al., 2020b). These observations support that these veins were not cemented by the same fluid and hence were not cemented coevally. The absolute vein ages, combined with existing time constraints

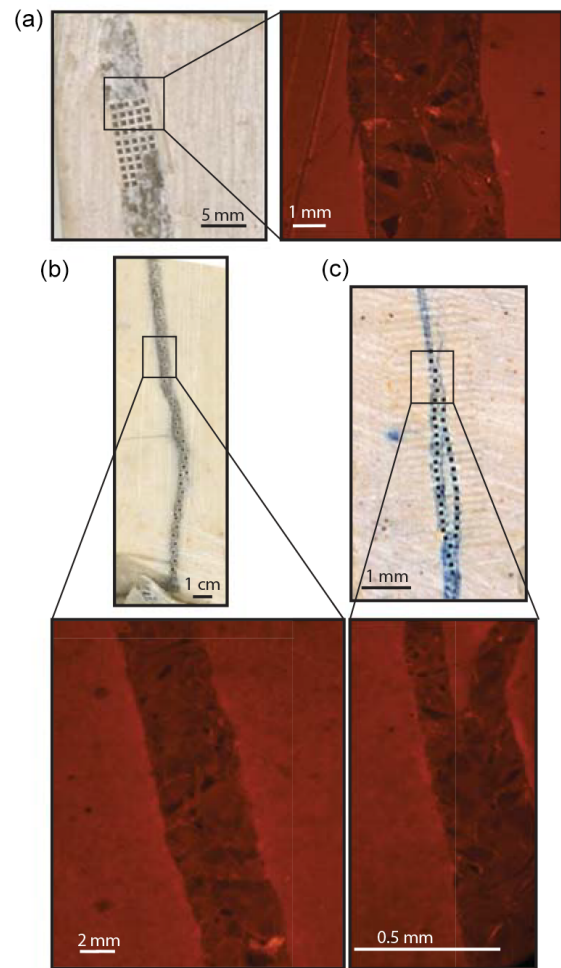


Figure 4. Two-dimensional scans of veins dated by LA-ICP-MS U–Pb geochronology from the San Vicino anticline, with the location of the ablation spots and diagenetic state observed under cathodoluminescence microscopy. (a) Sample A16 (LPS-related vein). (b) Sample A19 (syn-folding vein). (c) Sample A20 (LSFT-related vein).

(Fig. 3f), indicate that LPS occurred from ~ 6.5 to 5.5 Ma for both anticlines, followed by fold growth between ~ 5.5 and $\sim 3.5\text{ Ma}$, with a seemingly slightly longer duration in Cingoli than in San Vicino. LSFT started $\sim 5\text{ Ma}$ in the Camerino syncline (Beaudoin et al., 2020b), $\sim 4.5\text{ Ma}$ in San Vicino, and $\sim 3\text{ Ma}$ in Cingoli and possibly lasted until the onset of post-orogenic extension in eastern UMAR (~ 2.5 – 2 Ma , Fig. 3f). The entire folding event was thus very short, having lasted 3–4 Myr considering both anticlines as a whole (Fig. 3f).

3.2 Pico del Aguila Anticline (Pyrenees)

The Pico del Aguila is a N160° E-trending anticline in the southern Pyrenees (Fig. 5a), markedly oblique to the south Pyrenean thrust front. It formed in response to Pyrenean

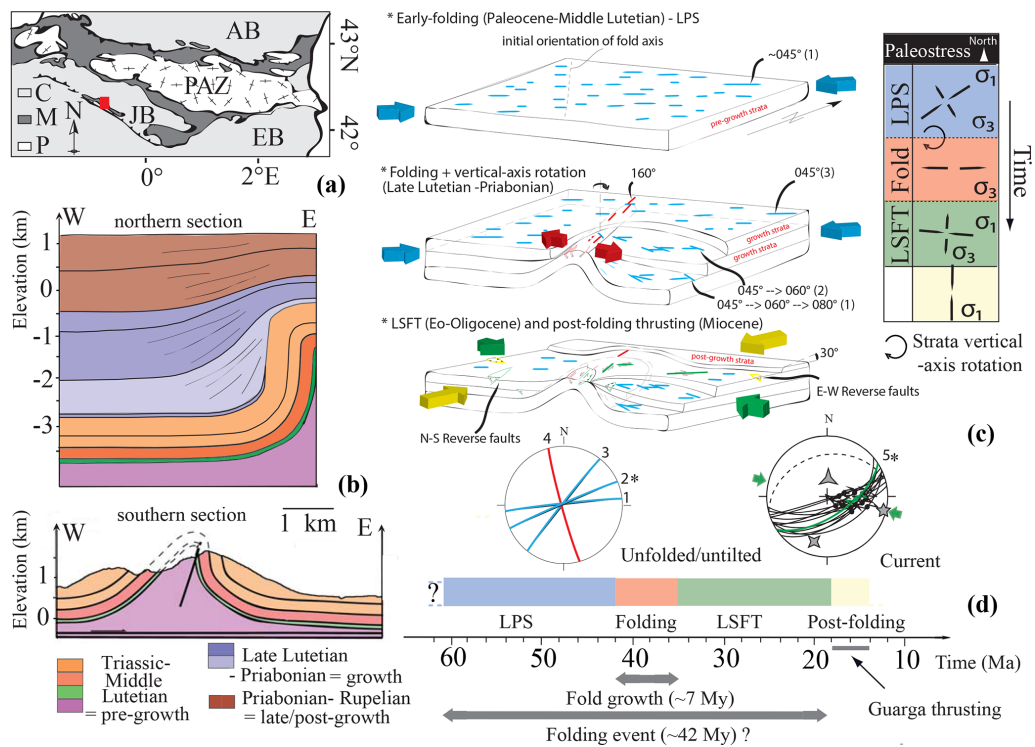


Figure 5. Pico del Aguila anticline. (a) Location (AB: Aquitaine Basin; JB: Jaca Basin; EB: Ebro Basin; PAZ: Pyrenean Axial Zone; P: Paleozoic; M: Mesozoic; C: Cenozoic). (b) Cross sections (north: modified after Poblet et al., 1997; south: modified after Beaudoin et al., 2015). (c) Orientation of the main sets of mesostructures (relative chronology, 1 to 5), reported in current or unfolded attitude on a lower-hemisphere Schmidt stereonet (same key as Fig. 3), and associated structural and paleostress evolution. Block diagrams modified after Beaudoin et al. (2015); * denotes mesostructures dated using U–Pb. (d) Timing and duration of deformation stages. Colour code for (c, d): blue – layer-parallel shortening (LPS); red – fold growth; green – late-stage fold tightening (LSFT); yellow – post-folding compression.

thrusting and detachment folding above Triassic evaporites (Poblet and Hardy, 1995; Vidal Royo et al., 2009, Fig. 5b). Growth strata (Fig. 5b) indicate that the fold developed by the late Lutetian–Priabonian (~ 42–35 Ma, Hogan and Burbank, 1996), before it was passively tilted and transported southward over the Guarga basement thrust (Jolivet et al., 2007).

Beaudoin et al. (2015) investigated the fracturing history of the Pico del Aguila (Fig. 5c). Three sets of bed-perpendicular joints/veins, oriented N080, N060, and N045° E (from the oldest to the youngest as established from abutting/cross-cutting relationships), were recognized. These three sets formed in progressively younging strata in response to a NE–SW-directed shortening while the area was undergoing a vertical axis 30–40° clockwise rotation (Fig. 5c). This rotation agrees with the Bartonian–Priabonian clockwise rotation of 15–50° around a vertical axis identified from paleomagnetism (Pueyo et al., 2002). The field study also revealed bed-perpendicular joints oriented N160° E and N–S-trending normal faults which formed during fold growth in response to outer-arc extension at the fold hinge (Fig. 5c). The end of the fold-related fracturing history (LSFT) is marked by the formation of N–S-trending reverse faults and by the transpressional reactivation of earlier ENE-striking

joints under an E–W compression resulting from the local rotation of the regional NE–SW compression (Beaudoin et al., 2015). Post-folding, E–W-trending reverse faults ultimately developed under the same N–S compression as the Guarga thrust (Fig. 5c).

U–Pb dating of calcite cements reveals that the veins related to the NE–SW-directed LPS formed as early as ~ 61 ± 3 Myr ago, while late oblique-slip reverse faults (LSFT) and post-folding E–W reverse faults were dated to 19 ± 5 and 18–14 ± 3 Ma, respectively (Hoareau et al., 2021). LPS, folding, and LSFT therefore lasted ~ 19 Myr (61–42 Ma), ~ 7 Myr (42–35 Ma), and ~ 17 Myr (35–18 Ma), respectively (Fig. 5d).

3.3 Sheep Mountain Anticline (Rocky Mountains)

The Sheep Mountain anticline is a thrust-related, basement-cored NW–SE-striking fold that developed in the Bighorn basin (Fig. 6a and b) during the late Cretaceous–Paleogene Laramide contraction. Three main joint/vein sets were recognized there (Fig. 6c, Bellahsen et al., 2006; Amrouch et al., 2010a; Barbier et al., 2012). Set I consists of bed-perpendicular, WNW–ESE-oriented veins associated with tectonic stylolites with ~WNW–ESE horizontal peaks (after

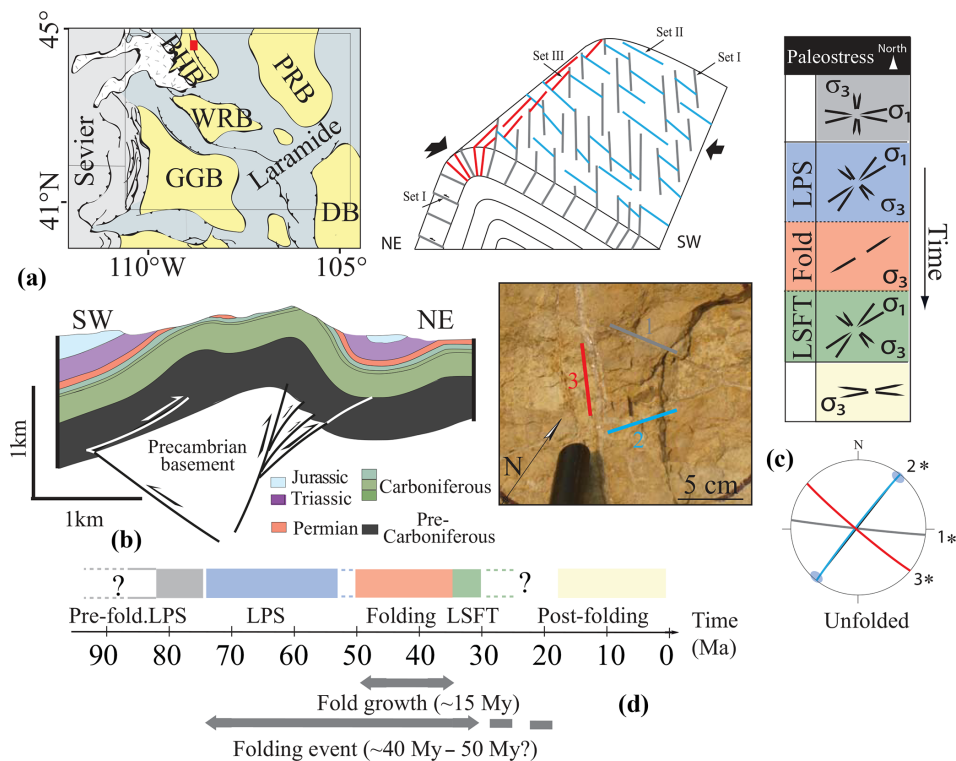


Figure 6. Sheep Mountain anticline. **(a)** Location (BHB: Bighorn basin; WRB: Wind River Basin; PRB: Powder River Basin; GGB: Greater Green River Basin; DB: Denver Basin). **(b)** Cross section (modified after Amrouch et al., 2010); **(c)** Orientation of the main sets of veins (relative chronology, 1 to 3), shown on a field photograph and on a block diagram of the final fold geometry, reported in unfolded attitude on a lower-hemisphere Schmidt stereonet (same key as Fig. 3), and associated structural and paleostress evolution; * denotes mesostructures dated using U–Pb. **(d)** Timing and duration of the deformation stages. Colour code for **(c, d)**: grey – pre-folding layer-parallel shortening kinematically unrelated to folding; blue – layer-parallel shortening (LPS); red – fold growth; green – late-stage fold tightening (LSFT); yellow – post-folding extension.

unfolding) (Amrouch et al., 2010a, 2011). This set formed prior to folding under a horizontal σ_1 trending WNW–ESE, likely transmitted from the distant thin-skinned Sevier orogen at the time the Bighorn basin was still part of the Sevier undeformed foreland. Set II comprises vertical, bed-perpendicular joints/veins striking NE–SW, i.e. perpendicular to the fold axis. These veins are associated with tectonic stylolites with horizontal peaks oriented NE–SW and witness a NE–SW-directed Laramide LPS (Varga, 1993; Amrouch et al., 2010a; Weil and Yonkee, 2012). The joints/veins of set III are bed-perpendicular and abut or cut across the veins of the former sets. They strike NW–SE, i.e. parallel to the fold axis, and their distribution mainly at the hinge zone of the fold supports their development in response to outer-arc extension at the hinge of the growing anticline (Fig. 6c). Widespread reverse and strike-slip faults also formed during LPS and LSFT, while bedding-parallel slip surfaces developed during fold growth (Amrouch et al., 2010a).

Veins from sets I, II, and III were dated by means of U–Pb (Beaudoin et al., 2018). Set I veins yielded ages between 81 and 72 Ma, supporting their pre-Laramide formation. The Laramide LPS-related veins were dated to 72–50 Ma. The

age of set III veins constrains the timing of folding in the absence of preserved growth strata to 50–35 Ma (Beaudoin et al., 2018). Laramide LPS and fold growth therefore lasted ~ 20 –25 Myr and ~ 15 Myr, respectively (Fig. 6d). The duration of the LSFT is poorly constrained, being bracketed between 35 Ma and the onset of the Basin and Range extension and Yellowstone hot-spot activity at ~ 17 Ma (Camp et al., 2015, Fig. 6d).

4 Discussion and conclusion

The absolute dating of mesostructures definitely confirms the sequence of deformation usually deduced from orientation data and relative chronology with respect to bedding attitude, which includes LPS, fold growth (e.g. strata tilting), and LSFT (Fig. 1). This sequence is valid for the four folds studied, despite the San Vicino, Cingoli and Pico del Aguila anticlines developed above a decollement in a fold-and-thrust belt, while the Sheep Mountain anticline formed as a basement-cored forced fold above a basement thrust. The overall consistency between the ages of growth strata when

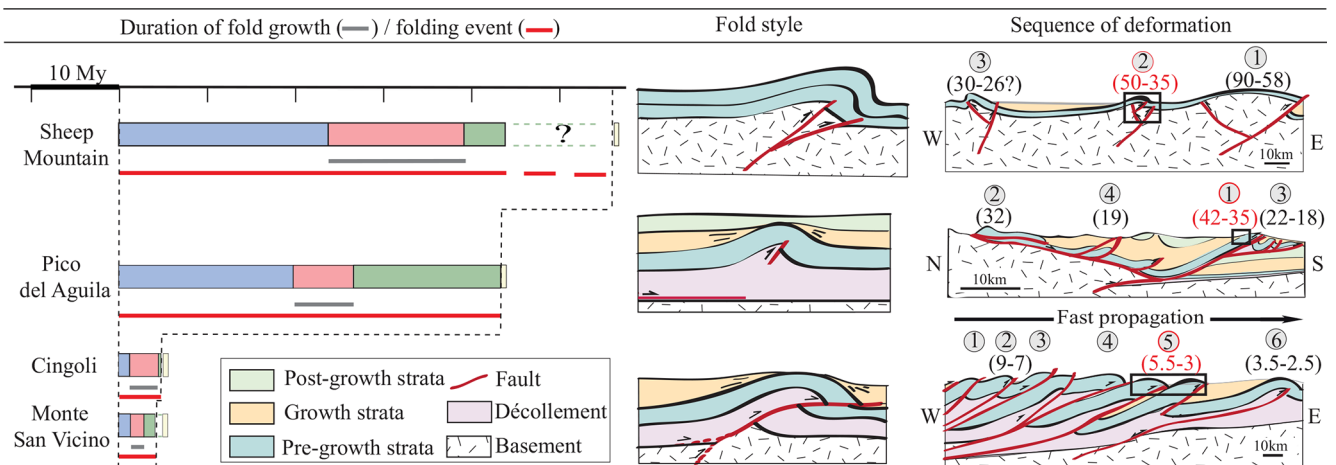


Figure 7. Compared durations of the deformation stages of the folding event, fold style (i.e. final fold geometry) and sequence of regional deformation for the four studied folds (circled numbers 1 to 6: order of structural development, i.e. sequence of folding/thrusting, with corresponding ages in Ma (in parentheses)); red: from this study; black: from the literature (Beaudoin et al., 2018, for Wyoming, Jolivet et al., 2007, for the Pyrenees, Calamita et al., 1994, and Curzi et al., 2020, for the Apennines). Colour code: blue – layer-parallel shortening (LPS); red – fold growth; green – late-stage fold tightening (LSFT); yellow – post-folding extension/compression.

preserved, the time constraints derived from our multi-proxy analysis coupling isotopic geochemistry of cements and stylolite paleopiezometry, and the U–Pb ages on early-, syn-, and late-folding mesostructures demonstrates the reliability of our approach. Minor age overlaps are observed only when the duration of each deformation stage was shorter than age uncertainties, i.e. in the case of recent and rapid deformation (San Vicino and Cingoli, Fig. 3f). Note that age overlaps could also relate to the fact that LPS and fold growth may slightly overlap, as documented in the Sibillini thrust anticline, i.e. the southern continuation of the San Vicino anticline (Tavani et al., 2012).

In the four investigated anticlines, fold growth lasted between 1.5 and 15 Ma, in accordance with previous estimates of fold growth duration elsewhere using either syntectonic sedimentation (Holl and Anastasio, 1993; Anastasio et al., 2017) or mechanical modelling (Yamato et al., 2011). Moreover, our study quantifies for the first time the duration of the contraction before and after fold growth. The results unexpectedly reveal that LPS and LSFT, which accommodate lower amounts of shortening than fold growth but which are associated with substantial – if not most of – small-scale rock damage, may have lasted much longer than fold growth itself. Such a trend could be key for the understanding of the history of foreland basins, including the mechanical evolution of strata and past fluid flow dynamics (Roure et al., 2005; Beaudoin et al., 2014).

Dating precisely the onset of LPS, whatever the technique used (U–Pb geochronology or absolute thermometry of calcite cements of mesostructures) is difficult because the entire range of vein ages may not be captured with certainty due to limited sampling. However, the onset of LPS can be further constrained either by the sedimentary record of the

foreland flexure preceding contraction (San Vicino) or by the estimate of the time at which compaction-related pressure solution along sedimentary stylolites is halted in the rocks in response to the switch of σ_1 axis from vertical to horizontal (Cingoli). The end of LSFT is also difficult to constrain precisely, but an upper bound is given by the change from fold-related shortening to a new regional state of stress. The latter is illustrated by the onset of post-orogenic extension in eastern UMAR (Fig. 3), by the late Pyrenean compression in the Pico del Aguila area (Fig. 5), and by the Basin and Range extension in the Laramide province (Fig. 6).

The four examples of folds also show that the overall duration of the folding event is variable (Fig. 7). Fold growth lasted longer in the case of forced folding above a high-angle basement thrust (Sheep Mountain) compared to fault-bend folding (San Vicino and Cingoli) along a flat-ramp decollement and detachment folding (Pico del Aguila) above a weak detachment layer in the cover (Fig. 7). The rapid fold growth and the relatively short LSFT in San Vicino and Cingoli are in line with the high rates of contraction and migration of deformation in the Apennines (Calamita et al., 1994, Fig. 7). In contrast, LSFT appears to last longer when folding is anchored to a high-angle basement thrust or when the fold is located at the front of the orogenic wedge, i.e. when the later propagation of deformation is limited or slow or when it occurs in a complex sequence (Pico del Aguila and Sheep Mountain, Fig. 7). The duration of LPS reflects to some degree the duration of the stress/strain accumulation in rocks required to generate folding, which can depend on the structural style (Beaudoin et al., 2020c). Our results support that a longer LPS (and a higher level of differential stress as well) is required to cause the inversion of a high-angle basement normal fault and related forced folding of the undetached

sedimentary cover (Sheep Mountain) than to initiate folding of the cover above a weak decollement (Pico del Aguila, Cingoli and San Vicino, Fig. 7). The longer LPS at Pico del Aguila with respect to San Vicino and Cingoli (Fig. 7) likely reflects the longer accumulation of displacement required to initiate folding oblique to the regional compression rather than perpendicular to it. It is worth noting that at first glance the fracture pattern (e.g. Tavani et al., 2015) remains basically similar whatever the overall duration of the folding event and related deformation stages.

In summary, beyond regional implications, this study demonstrates that pre-, syn-, and post-tilting mesostructures that formed under the same contraction as folding can be successfully dated. Our results bring for the first time absolute time constraints on the age and duration of the entire folding event for several upper-crustal folds formed in different contractional settings. In particular, we not only better constrain the age and duration of the fold growth stage but also the onset and duration of the layer-parallel shortening stage that predates folding and the duration and end of the late-stage fold tightening. Because the duration of each deformation stage is found to depend on the structural style and/or the regional sequence of deformation, our results emphasize the need to more carefully consider the entire folding event for a better appraisal of folding processes and stress/strain evolution in orogenic forelands and for a more accurate prediction of host rock damage and fluid migrations in naturally fractured reservoirs within folded domains.

Data availability. Data are either available in the Supplement or come from properly cited literature (Sect. 3).

Supplement. The supplement related to this article is available online at: <https://doi.org/10.5194/se-12-2145-2021-supplement>.

Author contributions. Conceptualization was carried out by OL and NEB. Data acquisition was done by all authors. Visualization was carried out by OL, NEB, GH, and AL. NEB was responsible for funding acquisition. NEB and OL prepared the original draft of the paper. OL, NEB, GH, JPC reviewed and edited the paper.

Competing interests. The contact author has declared that neither they nor their co-authors have any competing interests.

Disclaimer. Publisher's note: Copernicus Publications remains neutral with regard to jurisdictional claims in published maps and institutional affiliations.

Acknowledgements. The authors would like to thank the two anonymous reviewers for their constructive comments, as well as

Fabrizio Storti, Catherine Mottram, and Stephen Marshak for their comments on an earlier version of the paper. The authors also thank topical editor Virginia Toy for editorial handling.

Financial support. Nicolas Beaudoin is funded through the ISITE programme E2S, supported by ANR PIA and Region Nouvelle-Aquitaine.

Review statement. This paper was edited by Virginia Toy and reviewed by two anonymous referees.

References

- Ahmadhadi, F., Daniel, J. M., Azzizadeh, M., and Lacombe, O.: Evidence for pre-folding vein development in the Oligo-Miocene Asmari Formation in the Central Zagros Fold Belt, Iran, *Tectonics*, 27, TC1016, <https://doi.org/10.1029/2006TC001978>, 2008.
- Amrouch, K., Lacombe, O., Bellahsen, N., Daniel, J. M., and Callot, J. P.: Stress and strain patterns, kinematics and deformation mechanisms in a basement-cored anticline: Sheep Mountain Anticline, Wyoming, *Tectonics*, 29, TC1005, <https://doi.org/10.1029/2009TC002525>, 2010a.
- Amrouch, K., Robion, P., Callot, J. P., Lacombe, O., Daniel, J. M., Bellahsen, N., and Faure, J. L.: Constraints on deformation mechanisms during folding provided by rock physical properties: a case study at Sheep Mountain anticline (Wyoming, USA), *Geophys. J. Int.*, 182, 1105–1123, 2010b.
- Amrouch, K., Beaudoin, N., Lacombe, O., Bellahsen, N., and Daniel, J. M.: Paleostress magnitudes in folded sedimentary rocks, *Geophys. Res. Lett.*, 38, L17301, <https://doi.org/10.1029/2011GL048649>, 2011.
- Anastasio, D., Kodama, K., and Parés, J.: Episodic deformation rates recovered from growth strata, Pyrenees, Search and Discovery, AAPG Datapages/Search and Discovery Article #90291, AAPG Annual Convention and Exhibition, Houston, Texas, 2–5 April 2017, 30553, 2017.
- Aubourg, C., Smith, B., Eshraghi, A., Lacombe, O., Authemayou, C., Amrouch, K., Bellier O., and Mouthereau, F.: New magnetic fabric data and their comparison with palaeostress markers in the Western Fars Arc (Zagros, Iran): tectonic implications, *Geol. Soc. Sp.*, 330, 97–120, 2010.
- Barbier, M., Leprêtre, R., Callot, J. P., Gasparrini, M., Daniel, J. M., Hamon, Y., Lacombe O., and Floquet, M.: Impact of fracture stratigraphy on the paleo-hydrogeology of the Madison Limestone in two basement-involved folds in the Bighorn basin (Wyoming, USA), *Tectonophysics*, 576, 116–132, 2012.
- Barchi, M.: The Neogene–Quaternary evolution of the Northern Apennines: crustal structure, style of deformation and seismicity, *J. Virtual Explor.*, 36, 11, <https://doi.org/10.3809/jvirtex.2010.00220>, 2010.
- Barnes P. M.: Active folding of Pleistocene unconformities on the edge of the Australian–Pacific plate boundary zone, offshore North Canterbury, New Zealand, *Tectonics*, 15, 623–640, 1996.
- Beaudoin, N., Leprêtre, R., Bellahsen, N., Lacombe, O., Amrouch, K., Callot, J. P., Emmanuel, L., and Daniel, J. M.: Structural and microstructural evolution of the Rattlesnake Mountain Anticline

- (Wyoming, USA): New insights into the Sevier and Laramide orogenic stress build-up in the Bighorn Basin, *Tectonophysics*, 576–577, 20–45, 2012.
- Beaudoin, N., Bellahsen, N., Lacombe, O., Emmanuel, L., and Pironon, J.: Crustal-scale fluid flow during the tectonic evolution of the Bighorn Basin (Wyoming, USA), *Basin Res.*, 26, 403–435, 2014.
- Beaudoin, N., Huyghe, D., Bellahsen, N., Lacombe, O., Emmanuel, L., Mouthereau, F., and Ouahnon, L.: Fluid systems and fracture development during syn-depositional fold growth: example from the Pico del Aguila Anticline, Sierras Exteriores, Southern Pyrenees, Spain, *J. Struct. Geol.*, 70, 23–38, 2015.
- Beaudoin, N., Koehn, D., Lacombe, O., Lecouty, A., Billi, A., Aharonov, E., and Parlangeau, C.: Fingerprinting stress: Stylolite and calcite twinning paleopiezometry revealing the complexity of progressive stress patterns during folding—The case of the Monte Nero anticline in the Apennines, Italy, *Tectonics*, 35, 1687–1712, 2016.
- Beaudoin, N., Lacombe, O., Roberts, N. M. W., and Koehn, D.: U–Pb dating of calcite veins reveals complex stress evolution and thrust sequence in the Bighorn Basin, Wyoming, USA, *Geology*, 46, 1015–1018, 2018.
- Beaudoin, N., Gasparrini, M., David, M. E., Lacombe, O., and Koehn, D.: Bedding-parallel stylolites as a tool to unravel maximum burial depth in sedimentary basins: application to Middle Jurassic carbonate reservoirs in the Paris basin, France, *Geol. Soc. Am. Bull.*, 131, 1239–1254, 2019.
- Beaudoin, N. E., Lacombe, O., Koehn, D., David, M. E., Farrell, N., and Healy, D.: Vertical stress history and paleoburial in foreland basins unravelled by stylolite roughness paleopiezometry: Insights from bedding-parallel stylolites in the Bighorn Basin, Wyoming, USA, *J. Struct. Geol.*, 136, 104061, <https://doi.org/10.1016/j.jsg.2020.104061>, 2020a.
- Beaudoin, N., Labeur, A., Lacombe, O., Koehn, D., Billi, A., Hoareau, G., Boyce, A., John, C. M., Marchegiano, M., Roberts, N. M., Millar, I. L., Claverie, F., Pecheyran, C., and Callot, J. P.: Regional-scale paleofluid system across the Tuscan Nappe–Umbria Marche Apennine Ridge (northern Apennines) as revealed by mesostructural and isotopic analyses of stylolite-vein networks, *Solid Earth*, 11, 1617–1641, 2020b.
- Beaudoin, N., Lacombe, O., David, M. E., and Koehn, D.: Does stress transmission in forelands depend on structural style? Distinctive stress magnitudes during Sevier thin-skinned and Laramide thick-skinned layer-parallel shortening in the Bighorn Basin (USA) revealed by stylolite and calcite twinning paleopiezometry, *Terra Nova*, 32, 225–233, 2020c.
- Bellahsen, N., Fiore, P., and Pollard, D. D.: The role of fractures in the structural interpretation of Sheep Mountain Anticline, Wyoming, *J. Struct. Geol.*, 28, 850–867, 2006.
- Bertotti, G., de Graaf, S., Bisdorf, K., Oskam, B., Vonhof, H. B., Bezerra, F. H. R., Reijmer, J. J. G., and Cazarin, C. L.: Fracturing and fluid-flow during post-rift subsidence in carbonates of the Jandaíra Formation, Potiguar Basin, NE Brazil, *Basin Res.*, 29, 836–853, 2017.
- Bons, P. D., Elburg, M. A., and Gomez-Rivas, E.: A review of the formation of tectonic veins and their microstructures, *J. Struct. Geol.*, 43, 33–62, 2012.
- Branellac, M., Callot, J. P., Nivière, B., and Ringenbach, J. C.: The fracture network, a proxy for mesoscale deformation: Constraints on layer parallel shortening history from the Malargüe fold and thrust belt, Argentina, *Tectonics*, 34, 623–647, 2015.
- Butler, R. W. H. and Lickorish, W. H.: Using high-resolution stratigraphy to date fold and thrust activity: examples from the Neogene of south-central Sicily, *J. Geol. Soc. London*, 154, 633–643, 1997.
- Calamita, F., Cello, G., Deiana, G., and Paltrinieri, W.: Structural styles, chronology rates of deformation, and time-space relationships in the Umbria–Marche thrust system (central Apennines, Italy), *Tectonics*, 13, 873–881, 1994.
- Callot, J. P., Robion, P., Sassi, W., Guiton, M. L. E., Kallel, N., Daniel, J. M., Mengus, J. M., and Schmitz, J.: Magnetic characterisation of folded aeolian sandstones: interpretation of magnetic fabric in diamagnetic rocks, *Tectonophysics*, 495, 230–245, 2010.
- Camp, V. E., Pierce, K. L., and Morgan, L. A.: Yellowstone plume trigger for Basin and Range extension, and coeval emplacement of the Nevada–Columbia Basin magmatic belt, *Geosphere*, 1, 203–225, 2015.
- Caricchi, C., Aldega, L., and Corrado, S.: Reconstruction of maximum burial along the Northern Apennines thrust wedge (Italy) by indicators of thermal exposure and modeling, *Geol. Soc. Am. Bull.*, 127, 428–442, 2015.
- Carrigan, J. H., Anastasio, D. J., Kodama, K. P., and Parés, J. M.: Fault-related fold kinematics recorded by terrestrial growth strata, Sant Llorenç de Morunys, Pyrenees Mountains, NE Spain, *J. Struct. Geol.*, 91, 161–176, 2016.
- Craddock, J. P., Jackson, M., van der Pluijm, B. A., and Versical, R. T.: Regional shortening fabrics in eastern North America: Far-field stress transmission from the Appalachian–Ouachita Orogenic Belt, *Tectonics*, 12, 257–264, 1993.
- Cruset, D., Vergés, J., Albert, R., Gerdes, A., Benedicto, A., Cantarero, I., and Travé, A.: Quantifying deformation processes in the SE Pyrenees using U–Pb dating of fracture-filling calcites, *J. Geol. Soc. London*, 177, 1186–1196, 2020.
- Cruset, D., Vergés, J., Rodrigues, N., Belenguer, J., Pascual-Cebrian, E., Almar, Y., Perez-Caceres, I., Macchiavelli, C., Trave, A., Beranoaguirre, A., Albert, R., Gerdes, A., and Messenger, G.: U–Pb dating of carbonate veins constraining timing of beef growth and oil generation within Vaca Muerta Formation and compression history in the Neuquén Basin along the Andean fold and thrust belt, *Mar. Petrol. Geol.*, 132, 105204, <https://doi.org/10.1016/j.marpetgeo.2021.105204>, 2021.
- Curzi, M., Aldega, L., Bernasconi, S. M., Berra, F., Billi, A., Boschi, C., Franchini, S., Van der Lelij, R., Viola, G., and Carminati, E.: Architecture and evolution of an extensionally-inverted thrust (Mt. Tancia Thrust, Central Apennines): Geological, structural, geochemical, and K–Ar geochronological constraints, *J. Struct. Geol.*, 136, 104059, <https://doi.org/10.1016/j.jsg.2020.104059>, 2020.
- Ebner, M., Koehn, D., Toussaint, R., Renard, F., and Schmittbuhl, J.: Stress sensitivity of stylolite morphology, *Earth Planet. Sc. Lett.*, 277, 394–398, 2009.
- Evans, M. A. and Fischer, M. P.: On the distribution of fluids in folds: A review of controlling factors and processes, *J. Struct. Geol.*, 44, 2–24, 2012.
- Grobe, A., von Hagke, C., Littke, R., Dunkl, I., Wübbeler, F., Muecher, P., and Urai, J. L.: Tectono-thermal evolution of Oman’s Mesozoic passive continental margin under the obducting Semail

- Ophiolite: a case study of Jebel Akhdar, Oman, *Solid Earth*, 10, 149–175, 2019.
- Guiron M. L., Sassi W., Leroy Y., and Gauthier B. D.: Mechanical constraints on the chronology of fracture activation in folded Devonian sandstones of the western Moroccan Anti-Atlas, *J. Struct. Geol.*, 25, 1317–1330, 2003.
- Hansman, R. J., Albert, R., Gerdes, A., and Ring, U.: Absolute ages of multiple generations of brittle structures by U–Pb dating of calcite, *Geology*, 46, 207–210, 2018.
- Hnat, J. S. and van der Pluijm, B. A.: Foreland signature of indenter tectonics: Insights from calcite twinning analysis in the Tennessee salient of the Southern Appalachians, USA, *Lithosphere*, 3, 317–327, 2011.
- Hoareau, G., Crognier, N., Lacroix, B., Aubourg, C., Roberts, N. W., Niemi, N., Branellac, M., Beaudoin, N. E., and Suárez Ruiz, I.: Combination of $\Delta 47$ and U–Pb dating in tectonic calcite veins unravel the last pulses related to the Pyrenean Shortening (Spain), *Earth Planet. Sc. Lett.*, 553, 116636, <https://doi.org/10.1016/j.epsl.2020.116636>, 2021.
- Hogan, P. J. and Burbank, D. W.: Evolution of the Jaca piggyback basin and emergence of the external Sierras, southern Pyrenees, in: *Tertiary Basins of Spain*, edited by: Friend, P. F. and Dabrio, C. J., Cambridge Univ. Press, Cambridge, 153–160, 1996.
- Holl, J. E. and Anastasio, D. J.: Paleomagnetically derived folding rates, southern Pyrenees, Spain, *Geology*, 21, 271–274, 1993.
- Jolivet, M., Labaume, P., Monie, P., Brunel, M., Arnaud, N., and Campani, M.: Thermochronology constraints for the propagation sequence of the south Pyrenean basement thrust system (France–Spain), *Tectonics* 26, TC5007, <https://doi.org/10.1029/2006TC002080>, 2007.
- Labeur, A., Beaudoin, N. E., Lacombe, O., Emmanuel, L., Petracchini, L., Daëron, M., Klimowicz, S., and Callot, J.-P.: Burial-deformation history of folded rocks unraveled by fracture analysis, stylolite paleopiezometry and vein cement geochemistry: A case study in the Cingoli Anticline (Umbria–Marche, Northern Apennines), *Geosciences*, 11, 135, <https://doi.org/10.3390/geosciences11030135>, 2021.
- Lacombe, O.: Calcite twins, a tool for tectonic studies in thrust belts and stable orogenic forelands, *Oil Gas Sci. Technol.*, 65, 809–838, 2010.
- Lacombe, O., Amrouch, K., Mouthereau, F., and Dissez, L.: Calcite twinning constraints on late Neogene stress patterns and deformation mechanisms in the active Zagros collision belt, *Geology*, 35, 263–266, 2007.
- Lacombe, O., Malandain, J., Vilasi, N., Amrouch, K., and Roure, F.: From paleostresses to paleoburial in fold–thrust belts: preliminary results from calcite twin analysis in the Outer Albanides, *Tectonophysics* 475, 128–141, 2009.
- Lacombe, O., Bellahsen, N., and Mouthereau, F.: Fracture patterns in the Zagros Simply Folded Belt (Fars, Iran): constraints on early collisional tectonic history and role of basement faults, *Geol. Mag.*, 148, 940–963, 2011.
- Lacombe, O., Tavani, S., and Soto, R.: Into the deformation history of folded rocks, Special Issue, *Tectonophysics*, 576–577, 1–3, 2012.
- Masaferrero, J. L., Bulnes, M., Poblet, J., and Eberli, G. P.: Episodic folding inferred from syntectonic carbonate sedimentation: the Santaren anticline, Bahamas foreland, *Sediment. Geol.*, 146, 11–24, 2002.
- Mazzoli, S., Deiana, G., Galdenzi, S., and Cello, G.: Miocene fault-controlled sedimentation and thrust propagation in the previously faulted external zones of the Umbria–Marche Apennines, Italy, *EGU Stephan Mueller Special Publication Series*, 1, 195–209, 2002.
- Mottram, C. M., Parrish, R. R., Regis, D., Warren, C. J., Argles, T. W., Harris, N. B., and Roberts, N. M.: Using U–Th–Pb petrochronology to determine rates of ductile thrusting: Time windows into the Main Central Thrust, Sikkim Himalaya, *Tectonics*, 34, 1355–1374, 2015.
- Mueller, K. and Suppe, J.: Growth of Wheeler Ridge anticline, California: geomorphic evidence for fault-bend folding behavior during earthquakes, *J. Struct. Geol.*, 19, 383–396, 1997.
- Nuriel P., Weinberger R., Kylander-Clark A. R. C., Hacker B. R., and Craddock J. P.: The onset of the Dead Sea transform based on calcite age-strain analyses, *Geology*, 45, 587–590, 2017.
- Poblet, J. and Hardy, S.: Reverse modelling of detachment folds; application to the Pico del Aguila anticline in the south-central Pyrenees (Spain), *J. Struct. Geol.*, 17, 1707–1724, 1995.
- Poblet, J., McClay, K., Storti, F., and Munoz, J. A.: Geometry of syntectonic sediments associated with single-layer detachment folds, *J. Struct. Geol.*, 19, 369–381, 1997.
- Pueyo, E. L., Millan, H., and Pocoví, A.: Rotation velocity of a thrust: a paleomagnetic study in the External Sierras (Southern Pyrenees), *Sediment. Geol.*, 146, 191–208, 2002.
- Riba, O.: Syntectonic unconformities of the Alto Cardener, Spanish Pyrenees: A genetic interpretation, *Sediment. Geol.*, 15, 213–233, 1976.
- Roberts, N. M. and Walker, R. J.: U–Pb geochronology of calcite-mineralized faults: Absolute timing of rift-related fault events on the northeast Atlantic margin, *Geology*, 44, 531–534, 2016.
- Roberts, N. M., Žák, J., Vacek, F., and Sláma, J.: No more blind dates with calcite: Fluid-flow vs. fault-slip along the Očkov thrust, Prague Basin, *Geosci. Front.*, 12, 101143, <https://doi.org/10.1016/j.gsf.2021.101143>, 2021.
- Roberts, N. M. W., Drost, K., Horstwood, M. S. A., Condon, D. J., Chew, D., Drake, H., Milodowski, A. E., McLean, N. M., Smye, A. J., Walker, R. J., Haslam, R., Hodson, K., Imber, J., Beaudoin, N., and Lee, J. K.: Laser ablation inductively coupled plasma mass spectrometry (LA-ICP-MS) U–Pb carbonate geochronology: strategies, progress, and limitations, *Geochronology*, 2, 33–61, 2020.
- Rocher, M., Lacombe, O., Angelier, J., and Chen H. W.: Mechanical twin sets in calcite as markers of recent collisional events in a fold-and-thrust belt: evidence from the reefal limestones of southwestern Taiwan, *Tectonics* 15, 984–996, 1996.
- Rocher, M., Lacombe, O., Angelier, J., Deffontaines, B., and Verdier, F.: Cenozoic folding and faulting in the south Aquitaine Basin (France): insights from combined structural and paleostress analyses, *J. Struct. Geol.*, 22, 627–645, 2000.
- Rolland, A., Toussaint, R., Baud, P., Schmittbuhl, J., Conil, N., Koehn, D., Renard, F., and Gratier, J.-P.: Modeling the growth of stylolites in sedimentary rocks, *J. Geophys. Res.*, 117, B06403, <https://doi.org/10.1029/2011JB009065>, 2012.
- Rolland, A., Toussaint, R., Baud, P., Conil, N., and Landrein, P.: Morphological analysis of stylolites for paleostress estimation in limestones, *Int. J. Rock Mech. Min. Sci.*, 67, 212–225, <https://doi.org/10.1016/j.ijrmm.2013.08.021>, 2014.

- Roure, F., Swennen, R., Schneider, F., Faure, J. L., Ferket, H., Guilhaumou, N., Osadetz, K., Robion, P., and Vandeginste, V.: Incidence and Importance of Tectonics and Natural Fluid Migration on Reservoir Evolution in Foreland Fold-And-Thrust Belts, *Oil Gas Sci. Technol.*, 60, 67–106, 2005.
- Sassi, W., Guiton, M., Leroy, Y. M., Kallel, N., Callot, J. P., Daniel, J. M., Lerat, O., and Faure, J. L.: Constraints on mechanical modelling of folding provided by matrix deformation and fracture network analysis: The case of Split Mountain (Utah, USA), *Tectonophysics*, 576–577, 197–215, 2012.
- Schmittbuhl, J., Renard, F., Gratier, J. P., and Toussaint, R.: Roughness of stylolites: implications of 3D high resolution topography measurements, *Phys. Rev. Lett.*, 93, 238501, <https://doi.org/10.1103/PhysRevLett.93.238501>, 2004.
- Schneider, S., Hammerschmidt, K., and Rosenberg, C. L.: Dating the longevity of ductile shear zones: Insight from $^{40}\text{Ar}/^{39}\text{Ar}$ in situ analyses, *Earth Planet. Sc. Lett.*, 369, 43–58, 2013.
- Shackleton, J. R., Cooke, M. L., Verges, J., and Sima, T.: Temporal constraints on fracturing associated with fault-related folding at Sant Corneli anticline, Spanish Pyrenees, *J. Struct. Geol.*, 33, 5–19, 2011.
- Storti, F. and Poblet, J.: Growth stratal architectures associated to decollement folds and fault-propagation folds. Inferences on fold kinematics, *Tectonophysics*, 282, 353–373, 1997.
- Suppe, J., Chou, G. T., and Hook, S. C.: Rates of folding and faulting determined from growth strata, in: *Thrust Tectonics*, edited by: McClay, K. R., Chapman & Hall, Suffolk, 105–121, 1992.
- Tavani, S., Storti, F., Fernández, O., Muñoz, J. A., and Salvini, F.: 3-D deformation pattern analysis and evolution of the Añiscló anticline, southern Pyrenees, *J. Struct. Geol.*, 28, 695–712, 2006.
- Tavani, S., Storti, F., Salvini, F., and Toscano, C.: Stratigraphic versus structural control on the deformation pattern associated with the evolution of the Mt. Catria anticline, Italy, *J. Struct. Geol.*, 30, 664–681, 2008.
- Tavani, S., Mencos, J., Bausà, J., and Muñoz, J. A.: The fracture pattern of the Sant Corneli Bóixols oblique inversion anticline (Spanish Pyrenees), *J. Struct. Geol.*, 33, 1662–1680, 2011.
- Tavani, S., Storti, F., Bausa, J., and Muñoz, J. A.: Late thrusting extensional collapse at the mountain front of the northern Apennines (Italy), *Tectonics*, 31, TC4019, <https://doi.org/10.1029/2011TC003059>, 2012.
- Tavani, S., Storti, F., Lacombe, O., Corradetti, A., Muñoz, J., and Mazzoli, S.: A review of deformation pattern templates in foreland basin systems and fold-and-thrust belts: Implications for the state of stress in the frontal regions of thrust wedges, *Earth-Sci. Rev.*, 141, 82–104, 2015.
- Toussaint, R., Aharonov, E., Koehn, D., Gratier, J. P., Ebner, M., Baud, P., Rolland, A., and Renard, F.: Stylolites: A review, *J. Struct. Geol.*, 114, 163–195, 2018.
- Varga, R. J.: Rocky Mountain foreland uplifts: products of a rotating stress field or strain partitioning?, *Geology*, 21, 1115–1118, 1993.
- Vermeesch, P.: Unifying the U–Pb and Th–Pb methods: joint isochron regression and common Pb correction, *Geochronology*, 2, 119–131, 2020.
- Vidal-Royo, O., Koyi, H. A., and Muñoz, J. A.: Formation of orogen-perpendicular thrusts due to mechanical contrasts in the basal décollement in the Central External Sierras (Southern Pyrenees, Spain), *J. Struct. Geol.*, 31, 523–539, 2009.
- Weil, A. B. and Yonkee, W. A.: Layer-parallel shortening across the Sevier fold-thrust belt and Laramide foreland of Wyoming: spatial and temporal evolution of a complex geodynamic system, *Earth Planet. Sc. Lett.*, 357–358, 405–420, 2012.
- Yamato, P., Kaus, B. J., Mouthereau, F., and Castellort, S.: Dynamic constraints on the crustal-scale rheology of the Zagros fold belt, Iran, *Geology*, 39, 815–818, 2011.
- Wang, Y., Zwingmann, H., Zhou, L., Lo, C.-H., Viola, G., and Hao, J.: Direct dating of folding events by $^{40}\text{Ar}/^{39}\text{Ar}$ analysis of synkinematic muscovite from flexural-slip planes, *J. Struct. Geol.*, 83, 46–59, 2016.